2015

Physics-model-based Optimization and Feedback Control of the Current Profile Dynamics in Fusion Tokamak Reactors

Justin Edwin Barton
Lehigh University

Physics-model-based Optimization and Feedback Control of the Current Profile Dynamics in Fusion Tokamak Reactors

by

Justin E. Barton

Presented to the Graduate and Research Committee
of Lehigh University
in Candidacy for the Degree of
Doctor of Philosophy
in
Mechanical Engineering

Lehigh University
(January 2015)

Final Dissertation Signature Sheet

Approved and recommended for acceptance as a dissertation in partial fulfillment of the requirements for the degree of Doctor of Philosophy.

Date

Professor Eugenio Schuster, Dissertation Advisor

Accepted Date

Committee Members:

Professor D. Gary Harlow

Professor Mayuresh V. Kothare

Professor Arnold H. Kritz

Professor Donald O. Rockwell

Acknowledgements

This dissertation benefited from the valuable contributions of several persons whom the author would like to acknowledge.

Firstly, I would like to express my deepest gratitude to my advisor, Professor Eugenio Schuster, for lending his guidance, support, and expertise throughout my dissertation work at Lehigh University, and for providing me with many outstanding opportunities, such as performing experiments in the DIII-D tokamak, completing a visiting research assistantship with colleagues in Switzerland, and attending a meeting of Nobel Laureates.

I would like to thank the scientists and engineers of the DIII-D National Fusion Facility at General Atomics, in particular Dr. David A. Humphreys, who provided unwavering support and encouragement during the completion of this dissertation. Additionally, I would like to thank Dr. Michael L. Walker, Dr. John R. Ferron, Dr. Tim C. Luce, Dr. Al W. Hyatt, Dr. Francesca Turco, Benjamin G. Penaflor, and Robert D. Johnson for their many invaluable contributions to the modeling, control algorithm implementation, and experimental testing work carried out on DIII-D during this dissertation.

I would like to sincerely thank Dr. Jo Lister and Dr. Karim Besseghir for hosting my visiting research assistantship at the Centre de Recherches en Physique des Plasmas (CRPP) in Switzerland. I am particularly thankful for the time they devoted to

helping me greatly increase my understanding of plasma physics through fruitful discussions, for providing me the opportunity to contribute to studying control solutions for ITER, and allowing me to utilize the DINA-CH&CRONOS free boundary tokamak simulation code. Also, I would like to thank Dr. Federico Felici and Dr. Olivier Sauter for the opportunity to become involved with a collaborative research project on the TCV tokamak.

Furthermore, I would like to thank the members and alumni of the Laboratory for Control of Complex Physical Systems at Lehigh University, Dr. Mark D. Boyer, Dr. Wenyu Shi, William P. Wehner, and Zeki O. Ilhan, for their many collaborations, assistance, and camaraderie during the completion of this work. Additionally, I would like to thank Dr. Yongsheng Ou and Dr. Chao Xu for devoting time to passing along their knowledge during the onset of my graduate studies.

I also would like to thank my dissertation committee members at Lehigh University, Professor D. Gary Harlow, Professor Mayuresh V. Kothare, Professor Arnold H. Kritz, and Professor Donald O. Rockwell, for providing their support during the completion of my dissertation work.

Finally, and most of all, I am grateful to my family, in particular my parents and brother, for providing endless support, encouragement, and optimism, without which the completion of this dissertation would not have been possible.

Contents

List of Tables

List of Figures

Abstract

As the demand for energy continues to increase, the need to develop alternative energy sources to complement (and one day replace) conventional fossil fuels is becoming increasingly important. One such energy source is nuclear fusion, which has the potential to provide a clean source of energy and possesses an abundant fuel supply. However, due to the technological difficulty in creating the conditions necessary for controlled fusion to occur, nuclear fusion is not yet commercially viable. The tokamak is a device that utilizes magnetic fields to confine the reactants, which are in the plasma state, and it is one of the most promising devices capable of achieving controlled fusion. The ITER tokamak project is the next phase of tokamak development and will be the first tokamak reactor to explore the burning plasma (one with a significant amount of fusion reactions) operating regime.

In order for ITER to meet its demanding goals, extensive research has been conducted to develop advanced tokamak operating scenarios characterized by a high fusion gain, good plasma confinement, magnetohydrodynamic stability, and a significant fraction of noninductively driven plasma current to maximize the plasma performance and potentially enable steady-state operation. As the dynamics of the tokamak plasma magnetic and kinetic states are highly coupled, distributed, nonlinear systems that exhibit many instabilities, it is extremely difficult to robustly achieve advanced operating scenarios. Therefore, active control of the plasma dynamics has significant potential to improve the ability to access advanced operating regimes. One of the

key plasma properties investigated in the development of advanced scenarios is the plasma current profile because of its intimate relationship to plasma energy/particle transport and to plasma stability limits that are approached by increasing the plasma pressure. The plasma density and temperature profiles are also important parameters due to their close relationship to the amount of generated fusion power, to the total plasma stored energy, and to the amount of noninductive current drive. In tokamaks, the current and electron temperature profiles are coupled through resistive diffusion, noninductive current drive, and plasma energy/particle transport. As a result, integrated algorithms for current profile and electron temperature profile control will be necessary to maintain plasma stability, optimize plasma performance, and respond to changing power demand in ITER, and eventually a commercial, power producing tokamak reactor.

In this work, model-based feedforward and feedback algorithms are developed to control the plasma current profile and thermal state dynamics with the goal of improving the ability to achieve robust tokamak operation. A first-principles-driven (FPD), physics-based approach is employed to develop models of the plasma response to the available actuators, which provides the freedom to handle the trade-off between the physics accuracy and the tractability for control design of the models. A numerical optimization algorithm to synthesize feedforward trajectories for the tokamak actuators that steer the plasma through the tokamak operating space to achieve a predefined target scenario (characterized by a desired current profile and total stored energy), subject to the plasma dynamics (described by the developed physics-based model), actuator constraints, and plasma state constraints, is developed. Additionally, robust feedback control algorithms for current profile, combined current profile + total stored energy, and simultaneous current profile + electron temperature profile control are synthesized for various tokamaks by embedding a FPD model into the control design process.

Examples of the performance of the controllers in simulations (DIII-D, ITER, and TCV tokamaks) and DIII-D experiments are presented to illustrate the potential and versatility of the employed control methodology. The DIII-D experimental tests demonstrate the potential physics-model-based profile control has to provide a systematic approach for the development and robust sustainment of advanced scenarios. The ITER simulations demonstrate the ability to drive the current profile to a stationary target while simultaneously modulating the amount of fusion power that is generated. Finally, the TCV simulations demonstrate the ability to drive the current and electron temperature profiles to a self consistent target, as well as to maintain the current profile in a stationary condition while simultaneously modulating the electron temperature profile between equilibrium points.

Chapter 1

Introduction

As a result of more countries becoming industrialized and the world population rising, the demand for energy continues to increase. Several energy sources will be employed to help society as a whole meet this growing energy demand, such as fossil fuels, renewable energies, and nuclear energy. Currently, the major source of the world's energy is produced by burning fossil fuels, such as coal, natural gas, and oil. These conventional energy sources are becoming more environmentally friendly through the development of technologies to capture and store greenhouse gases (such as carbon dioxide) that are produced by burning the fossil fuels. However, even though the sources are becoming cleaner and their availability is not expected to be depleted for several hundred years, it is predicted that there will be an energy shortfall in the near future (possibly in less than 50 years) at the world's current rate of energy consumption [16,17]. As a result, the need to develop alternative energy sources to complement (and one day replace) conventional fossil fuels is becoming increasingly important.

Solar, wind, hydroelectric, and geothermal power are examples of renewable energy sources that possess many attractive options to complement fossil fuel energy production. These energy sources do not generate potentially harmful greenhouse

gases to produce electricity, which makes them attractive from an environmental perspective. Also, the fuel supply for renewable sources is theoretically unlimited, which makes them attractive from a sustainability point-of-view. However, despite these advantages, there are also several hurdles that limit the applicability of renewable energy sources to completely make up for the predicted energy shortfall. Renewable energy sources can only be installed where their respective fuel sources (sun, wind, falling water, etc.) are plentiful, which may result in difficulties in redistributing the produced power from the generation site to the consumer. Also, since these energy sources rely on the availability of sunlight, wind, etc., there may not be a constant supply of electricity from renewable power plants. Therefore, enhancements to the electrical power grid need to be developed to cope with this inconsistent supply, such as integration of energy storage technologies into the power grid. Finally, renewable energy sources currently lack a sufficient power density (power produced divided by the land area needed to generate the power) compared to other energy generation sources.

Nuclear energy, generated from the processes of nuclear fission (splitting of heavy nuclei) or nuclear fusion (combining of light nuclei), on the other hand provides a larger power density comparable with conventional fossil fuel energy sources. As a result, nuclear fission and fusion have a significant potential to help meet growing energy demands. Nuclear fission is currently a mature commercial technology that supplies a significant portion of the world's energy needs. However, despite the advantages that nuclear fission possesses, such as being an alternative energy source that can produce a constant supply of electricity while not generating any greenhouse gases, there are several aspects of this energy source that may limit its ability to continue growing. Some of the disadvantages of nuclear fission reactors are related to proliferation issues and the possibility of a nuclear accident characterized by a large, uncontrolled release of energy, as well as the fact that they produce long-lasting (can

be on the order of 1000's of years) radioactive waste that must be properly stored to avoid detrimental environmental effects.

Like nuclear fission, nuclear fusion does not produce any greenhouse gases, but in contrast to nuclear fission, nuclear fusion poses no threat of a nuclear accident. Additionally, fusion possess an abundant fuel supply[1] that can potentially last for thousands of years and produces radioactive waste that can be properly disposed of on a much shorter timescale (on the order to 10's to 100's of years) compared to fission. Research towards developing controlled nuclear fusion reactors has been ongoing for the past 60 years. However, due to the extreme technological difficulty in creating the conditions necessary for controlled fusion to occur, nuclear fusion is not yet a commercially viable energy source. The work in this dissertation focuses on developing control solutions to improve the performance of and the ability to robustly operate nuclear fusion tokamak devices.

1.1 Introduction to nuclear fusion

Nuclear fusion is the process by which two light nuclei "fuse" together to form one heavier nucleus, and in the process, energy is released according to the relation

$$E_p - E_r = (m_r - m_p)\, c^2, \tag{1.1}$$

where E denotes energy, m denotes mass, c denotes the speed of light in a vacuum, and $(\cdot)_i$, for $i \in [r, p]$, defines quantities related to the reactants ($i = r$) and products ($i = p$) of the reaction, respectively. Presently, the two nuclei most often considered for the fusion reaction are deuterium (D) and tritium (T), which are isotopes of hydrogen,

[1]The most often considered reactants for the fusion reaction are deuterium and tritium, which are isotopes of hydrogen. Deuterium naturally occurs in seawater, and tritium, which is radioactive, can be produced from lithium, which is found in the Earth's crust.

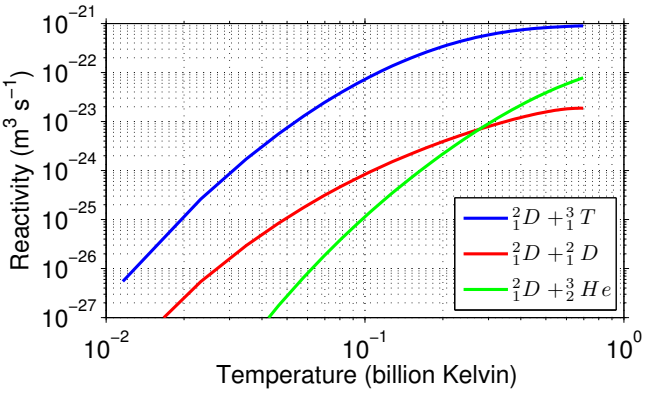

Figure 1.1: Reactivity versus temperature for various fusion reactions calculated using the results obtained in [1].

because the $D-T$ reactivity is higher at lower temperatures than other possible fusion reactions (see Fig. 1.1). The $D-T$ fusion reaction is shown schematically in Fig. 1.2 and can be expressed mathematically as

$$ {}^2_1D + {}^3_1T \rightarrow {}^4_2He + {}^1_0n + Q_{DT}, \tag{1.2} $$

where He denotes a helium nucleus, n denotes a neutron, and Q_{DT} is the amount of energy produced in the reaction. In the notation ${}^a_bC$, a denotes the atomic mass number, b denotes the atomic number, and C denotes the element. The helium nucleus produced in this reaction (${}^4_2He$) is commonly referred to as an alpha particle (α), i.e., ${}^4_2He \equiv \alpha$, in the fusion community. The amount of energy that is released in this reaction is 17.6 mega electron volts (MeV)[2], i.e., $Q_{DT} = 17.6$ MeV. The energy generated in the reaction is divided amongst the products according to the inverse proportion of their masses, i.e.,

$$ \begin{aligned} E_\alpha &= \frac{m_n}{m_n + m_\alpha} Q_{DT} = 3.5 \text{ MeV}, \\ E_n &= \frac{m_\alpha}{m_n + m_\alpha} Q_{DT} = 14.1 \text{ MeV}. \end{aligned} \tag{1.3} $$

[2] 1 electron volt (eV) is equal to $1.60217646 \times 10^{-19}$ Joules (J).

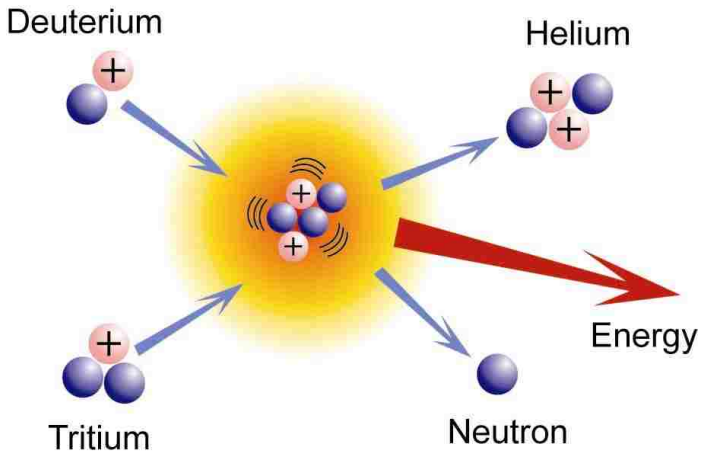

Figure 1.2: Schematic of the deuterium $({}^{2}_{1}D)$ tritium $({}^{3}_{1}T)$ nuclear fusion reaction. The products are a helium nucleus $({}^{4}_{2}He)$, which carries 3.5 MeV of energy and a neutron $({}^{1}_{0}n)$, which carries 14.1 MeV of energy.

This relation is obtained by applying the principles of conservation of linear momentum and conservation of energy (assuming the reactants are stationary) to the reaction (1.2). Conservation of linear momentum applied to the reaction (1.2) results in

$$\begin{aligned} 0 = m_\alpha v_\alpha + m_n v_n \quad &\Rightarrow \quad v_n = -\frac{m_\alpha}{m_n} v_\alpha \quad \Rightarrow \\ v_n^2 = \left(\frac{m_\alpha}{m_n}\right)^2 v_\alpha^2 \quad &\Rightarrow \quad v_n^2 = 2\frac{m_\alpha}{m_n^2} E_\alpha \quad \Rightarrow \quad E_n = \frac{m_\alpha}{m_n} E_\alpha, \end{aligned} \tag{1.4}$$

where m_i, v_i, and $E_i = (1/2) m_i v_i^2$, for $i \in [\alpha, n]$, denote the mass, velocity, and kinetic energy of the α particle and neutron, respectively. Conservation of energy applied to the reaction (1.2) results in

$$Q_{DT} = E_\alpha + E_n = E_\alpha \left(1 + \frac{m_\alpha}{m_n}\right), \tag{1.5}$$

where we have utilized (1.4). The relations shown in (1.3) are then obtained from (1.4) and (1.5).

Due to the Coulombic repulsion force that exists between the positively charged nuclei, the fusion reactants must be kept under high pressure and heated to a high

temperature (on the order of 100 million degrees Kelvin) so that the nuclei possess enough kinetic energy to overcome this repulsive force and get close enough together where the strong nuclear force dominates, resulting in the nuclei fusing. The reactivity of the reactant nuclei is dependent on the nuclei velocity distribution, which is a bounded nonlinear function of the nuclei temperature, and only becomes significant when the temperature is higher than 10 million degrees Kelvin. By examining Fig. 1.1, we see that at around 100 million degrees Kelvin, the $D-T$ reactivity is larger than one order of magnitude higher than other possible fusion reactions. At these high temperatures, the reactant gas mixture is in the plasma state, which means the positively charged nuclei and negatively charged electrons disassociate from one another and are free to move about independently of one another.

There are three ways to confine the nuclei in the environment necessary for fusion reactions to occur: gravitational confinement, inertial confinement, and magnetic confinement. Gravitational confinement is only possible in stars because the mass needed to generate the required gravitational force is extremely large. The second confinement approach is inertial confinement, where a rapid pulse of energy is directed onto the surface of a fuel pellet which causes the pellet to implode, thus generating the required high pressures and temperatures needed for fusion to occur. Finally, as the reactant mixture is in the plasma state, it can conduct electricity and therefore interact with magnetic fields which can be used to confine the plasma, as shown in Fig. 1.3, in various magnetic configurations to create the conditions necessary for fusion to occur. Arguably, the magnetic confinement technique is the most promising approach for achieving controlled fusion on Earth, and one of the most promising magnetic confinement devices is the tokamak[3] [18].

[3]Russian acronym which translates to toroidal chamber with magnetic coils.

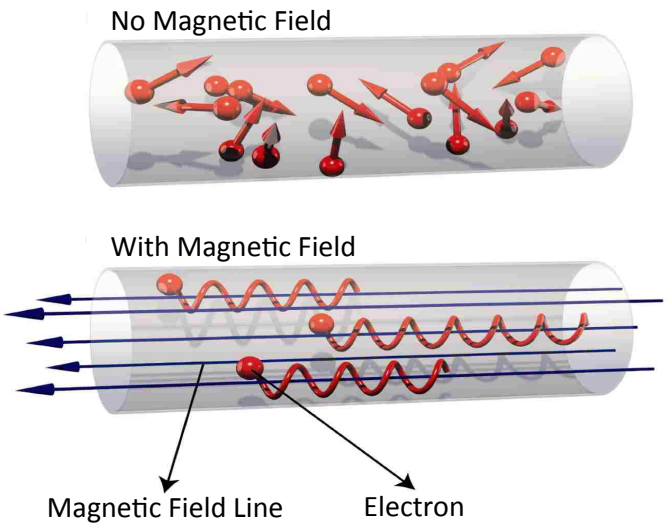

Figure 1.3: Charged particles confined by an applied magnetic field. Due to the Lorentz force $\mathbf{F} = q(\mathbf{E}+\mathbf{v}\times\mathbf{B})$, where q is the particle charge, $\mathbf{v}$ is the particle velocity, $\mathbf{E}$ is the electric field, and $\mathbf{B}$ is the magnetic field, the charged particles are confined in the direction perpendicular to the magnetic field lines but are free to move in the direction parallel to the magnetic field lines.

1.2 Magnetic confinement: The tokamak

If the magnetic configuration shown in Fig. 1.3 is used to attempt to confine the plasma in a fixed volume (tube where the magnetic field lines run the length of the tube), plasma confinement would eventually be lost due to the particles escaping through the ends of the tube. Therefore, to eliminate these *end losses*, the tokamak device [18] closes the tube in on itself to obtain a doughnut structure. A schematic of the various coil systems used to generate the magnetic fields in a tokamak machine is shown in Fig. 1.4. The long way around the device is denoted as the toroidal direction, and the short way around the device is denoted as the poloidal direction.

The tokamak employs various coil systems to generate the total helical magnetic field (red line in Fig. 1.4) to confine the plasma in a fixed toroidal volume. The main confining toroidal magnetic field (purple arrow in Fig. 1.4) is generated by the toroidal field coils (purple D shaped coils in Fig. 1.4). The toroidal magnetic field decreases

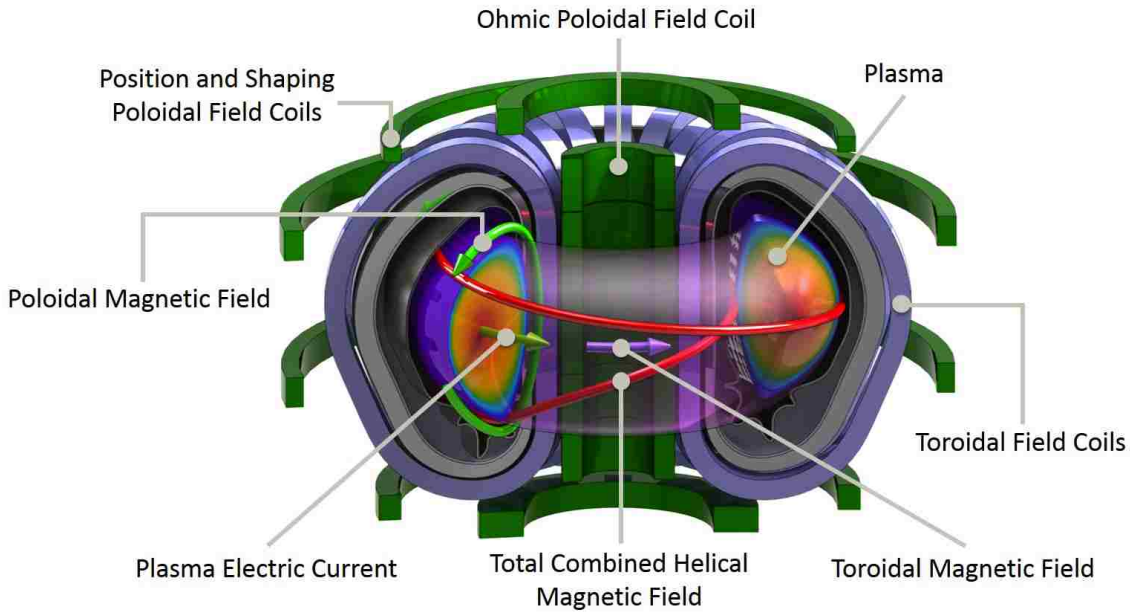

Figure 1.4: Schematic of the tokamak machine for confining a plasma.

as the distance from the center of the machine increases. This radial gradient results in the plasma particles drifting vertically inside the machine, and the drift direction is charge dependent, i.e., the ions and electrons drift in opposite directions. This charge separation consequently generates a vertical electric field in the plasma. The interaction of this electric field with the toroidal magnetic field results in the plasma particles drifting horizontally outward towards the tokamak walls. Thus, the toroidal magnetic field alone can not completely confine the plasma. Therefore, a poloidal magnetic field (green arrow in Fig. 1.4 that wraps around the tube) is also needed to completely confine the plasma in a fixed volume. The combination of the toroidal and poloidal magnetic fields generates a total confining helical magnetic field structure (red line in Fig. 1.4). As the plasma particles travel along this helical path, they continuously drift vertically in the machine due to the toroidal magnetic field radial gradient as previously discussed. However, as the particles travel along the helical path, they spend some time above and some time below the horizontal mid-plane of the machine. Therefore, averaged over many transits around the torus, the plasma

particles tend to stay at a given spatial location relative to the center of the plasma. Thus the total helical magnetic field produces an averaging of the plasma particle vertical drifts such that the total net vertical drift is almost exactly zero. Therefore, there is no charge separation, and consequently, no vertical electric field is produced. As a result the plasma is confined in a fixed toroidal volume. In the tokamak, the poloidal magnetic field is primarily generated by exploiting the ability of the plasma to conduct electrical current. The plasma electric current (green arrow in Fig. 1.4) is traditionally driven through a transformer action, where the ohmic poloidal field coil (green coils in the center of the machine in Fig. 1.4) acts as the primary circuit and the plasma acts as the secondary circuit. Finally, the position and shaping poloidal field coils (green coils on the exterior of the machine in Fig. 1.4) are used to push and pull on the plasma to control its position and shape within the device.

In a well confined tokamak plasma, the plasma kinetic pressure (density multiplied by temperature) is a maximum at the center of the plasma (red region of the plasma in Fig. 1.4). An important property of the tokamak plasma is referred to as the plasma beta (β), which is defined as

$$\beta = \frac{\text{plasma kinetic pressure}}{\text{magnetic pressure}}. \tag{1.6}$$

The plasma β is a measure of how efficiently the applied magnetic pressure is being utilized to confine the plasma kinetic pressure. Naturally, the higher β is, the better. Different regimes of tokamak operation exist with different levels of plasma confinement and are characterized by the pressure profile that is present in the machine. A schematic of the pressure profiles observed in low confinement (L-mode) and high confinement (H-mode) operating regimes are shown in Figs. 1.5(a-b). In L-mode, the pressure gradient is limited over the whole plasma cross section and is governed by a high level of turbulence which enhances the radial transport. A region with a

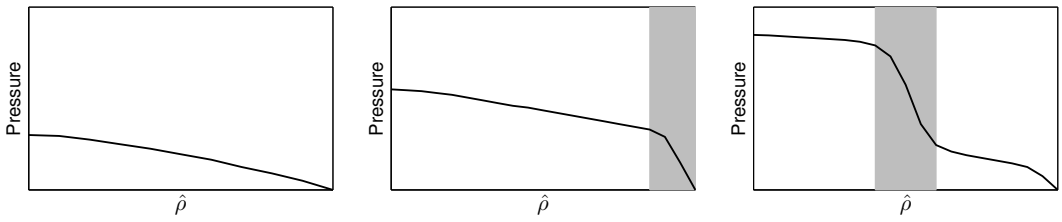

Figure 1.5: Schematic of the pressure profiles observed (a) in L-mode, (b) in H-mode, and (c) with an internal transport barrier (ITB) [2]. The variable $\hat{\rho}$ is used to denote the spatial coordinate (left = center of plasma (red region of plasma in Fig. 1.4) and right = boundary of plasma (purple region of plasma in Fig. 1.4)). Regions of reduced radial transport (gray-shaded areas) are observed where large pressure gradients are present, i.e., at the plasma edge in H-mode and in the plasma core for an ITB.

large pressure gradient at the edge of the plasma, which is associated with a local reduction of the turbulent transport, is a characteristic of an H-mode plasma. Similarly, an internal transport barrier (ITB) is characterized by a large pressure gradient in the plasma core as shown in Fig. 1.5(c) [2]. As the product of the pressure and the volume encapsulated by the region of higher pressure increases, larger amounts of stored energy in the plasma are produced. This results in higher values of β which is advantageous for the development of a power producing reactor.

There are multiple devices around the world studying various aspects of tokamak research, from plasma physics, to plasma control, to technological issues, such as plasma-material interaction, with the goal of building the scientific and technological basis needed to develop a commercial fusion reactor. Some examples are JET in the United Kingdom, ASDEX-Upgrade in Germany, Tore Supra in France, TCV in Switzerland, EAST in China, JT-60U in Japan, KSTAR in South Korea, and DIII-D, NSTX-U, and Alcator C-Mod in the United States. As all modern day tokamaks rely on induction (transformer action) to drive current in the plasma (necessary to maintain plasma confinement), tokamaks are inherently pulsed devices. The process of creating, forming, and terminating the plasma is commonly referred to as a plasma

discharge, or shot, in the tokamak community. The tokamak discharge can roughly be divided up into four phases:

1. *Breakdown phase*: During this phase, the plasma is created by ionizing the reactant gas inside the tokamak vacuum vessel chamber.

2. *Ramp-up phase*: During this phase, the plasma current is brought from its initial value of zero up to its desired steady-state value. Additionally, other quantities that characterize the plasma, for example density and temperature, are brought to their desired values.

3. *Flattop phase*: This is the most important phase of the tokamak discharge and is the phase where the production of energy should happen. During this phase, all of the quantities that characterize the plasma should remain as constant as possible.

4. *Ramp-down phase*: During this phase, the plasma current is driven to zero and the plasma is terminated.

Modern tokamak devices are at the point where they can produce almost as much energy as is required to heat the plasma. The next phase of tokamak development is the ITER tokamak project [3], which will be the first tokamak device to produce a significant amount of fusion power and hence be the first machine to explore the burning plasma operating regime. The products of the $D-T$ fusion reaction are a charged α particle (carries 3.5 MeV, or 20%, of the generated energy) and a neutron (carries 14.1 MeV, or 80%, of the generated energy) as shown in (1.2). As fusion reactions occur, the deuterium and tritium fuel will need to be replenished inside the reactor and subsequently heated to the temperatures where further reactions can occur. As the alpha particle product of the $D-T$ reaction is charged, it will remain confined by the magnetic field in the tokamak. Therefore, as the α particle collides

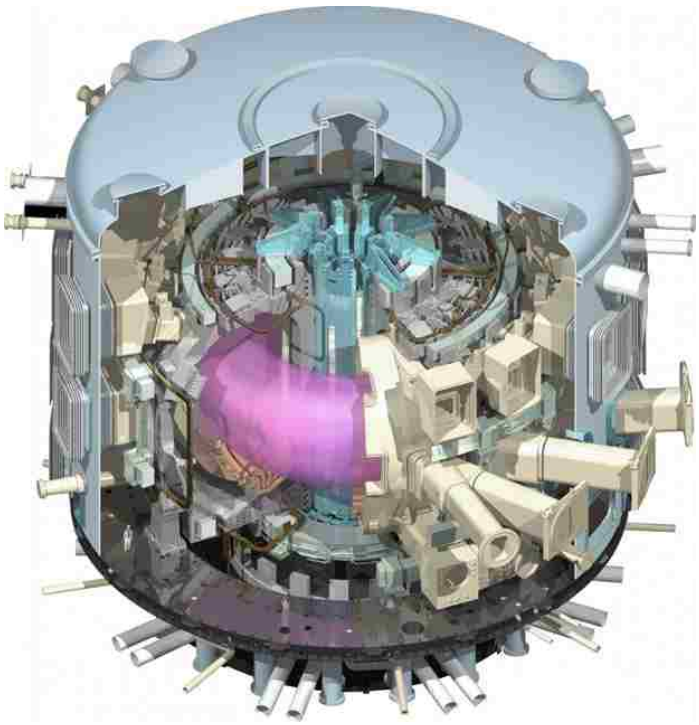

Figure 1.6: Schematic of the ITER tokamak [3]. Note the size of the person in the lower left hand side of the figure.

with particles already present in the plasma, it will impart some of its energy to these particles. This is referred to as plasma self-heating. A burning plasma is one in which a significant portion of the power needed to sustain the fusion reaction is generated by the α particle heating. As the neutron product of the $D-T$ reaction has no charge, it will not be confined by the magnetic field in the tokamak and therefore leave the plasma. As the neutron interacts with the confining structure, its energy will be converted into heat, which can be utilized in a conventional Rankine cycle to produce electricity. A schematic of ITER is shown in Fig. 1.6.

1.3 Control problems in tokamaks

In order for the ITER project to meet its demanding project goals, extensive research has been conducted to find advanced tokamak operating scenarios [19] that

are characterized by a high fusion gain, good plasma confinement, magnetohydrodynamic (MHD) stability, and a noninductively driven plasma current[4]. The ability to drive the plasma current in the tokamak through completely noniductive means could potentially lead to the realization of a "steady-state" tokamak reactor. If these performance objectives are achieved, the cost and size of fusion reactors could be greatly reduced. The dynamics of the tokamak plasma are highly coupled, distributed, nonlinear systems that exhibit many instabilities. Therefore, active control to stabilize/suppress these plasma instabilities and to optimize the performance of the plasma has significant potential improve the ability to access advanced operating regimes. A complete description of the various control problems in tokamaks is beyond the scope of this dissertation, however, a few of the most relevant problems are briefly highlighted in the following. See [20, 21] for an introduction to many of these control problems.

The first class of control problems are typically referred to as magnetic control problems, and consist of employing the tokamak poloidal field coils (green coils in Fig. 1.4) to control the location of the plasma inside the machine (for vertically elongated plasmas, ones that are taller than they are wide, the plasma vertical position is unstable), the value of the plasma current, as well as the shape (boundary) of the plasma. Advances in plasma position, current, and shape control are described in [22–31]. A second class of control problems are related to the stabilization/suppression of plasma MHD instabilities. These instabilities are usually triggered in high performance plasmas and limit the achievable plasma β. If these instabilities are triggered, they result in a reduction of the plasma confinement, which lowers the plasma stored energy. While not normally catastrophic, if left uncontrolled, these instabilities can lead to

[4]The ratio between the amount of fusion power (P_{fus}) produced to the amount of external power (P_{ext}) that is needed to heat the plasma is defined as the fusion gain (Q) of a scenario, i.e., $Q = P_{fus}/P_{ext}$. Two of the ITER project goals are to demonstrate operation at $Q = 10$ with an inductively driven plasma current and operation at $Q = 5$ with a largely noninductivley driven plasma current.

plasma-terminating disruptions[5]. Some examples of plasma MHD instabilities are: resistive wall modes (RWMs), edge localized modes (ELMs), and neoclassical tearing modes (NTMs). Advances in RWM control can be found in [32–41], and advances in NTM stabilization can be found in [42–48].

Finally, as the tokamak plasma is a distributed system, the spatial distribution of the plasma toroidal current density, particle density, particle temperature, etc., plays an important role in the stability, as well as the performance, of a given operating condition. The spatial distribution of these plasma quantities are typically referred to as profiles, e.g., current profile, density profile, temperature profile, in the tokamak community. Current profile control is usually referred to as *magnetic profile* control and *kinetic profile* control refers to the control of the plasma kinetic quantities (density, temperature, etc.). The work in this dissertation focuses on developing strategies for current profile control, combined current profile + total stored energy control, and simultaneous current profile + electron temperature profile control.

The various control algorithms on any given machine are integrated together to form the machine's Plasma Control System (PCS). A schematic of the various components of a tokamak PCS, and how a machine operator would interact with this system, is shown in Fig. 1.7. The work in this dissertation focuses on developing components (specifically the Actuator Trajectory Optimizer and Model-based Feedback Controller in Fig. 1.7) of the PCS relevant to control of the plasma current profile and thermal state dynamics. Also in this work, physics-based, control-oriented models of the plasma current profile and thermal state dynamics are developed that can be used to simulate the evolution of these plasma quantities. Subsequently, these models are interfaced with the PCS, i.e., they replace the Tokamak in Fig. 1.7, to test the implementation and performance of, and ensure effective interaction between, the

[5]A plasma disruption is a condition where the plasma current is extinguished and the energy of the plasma particles is rapidly lost to the surrounding structure.

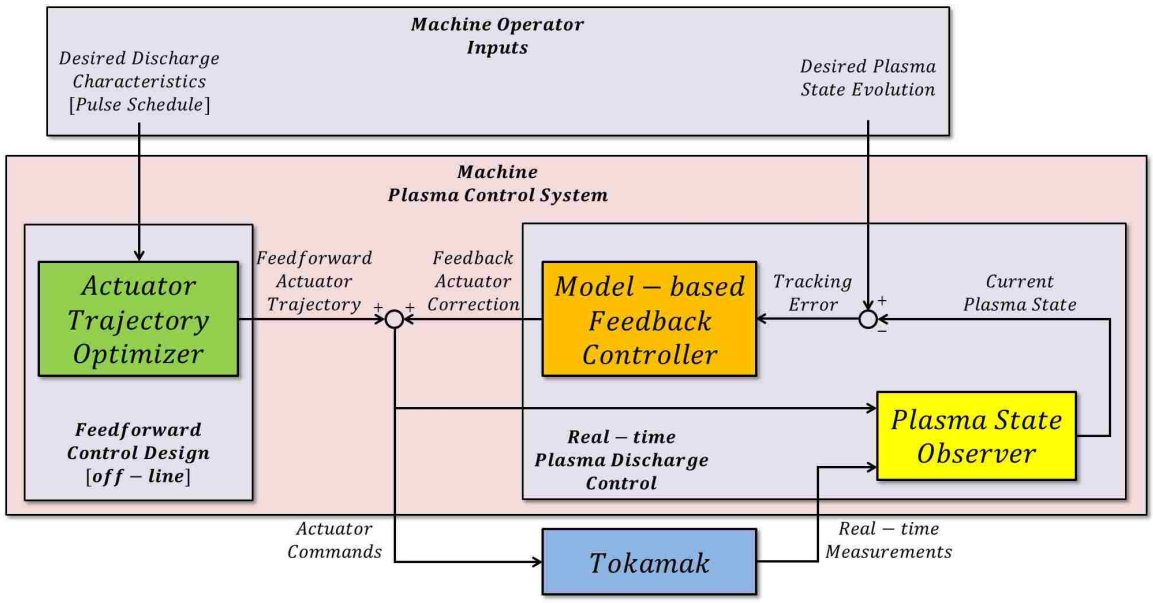

Figure 1.7: Schematic of the various components of a tokamak Plasma Control System (PCS), how a machine operator would interface with the PCS, and how the PCS would interface with the tokamak.

developed control components through simulations prior to experimental testing.

In an fully operational, power producing tokamak reactor, the PCS will need to be able to maintain the plasma state in a predefined operational space ensuring stability and safety limits are not violated, stabilize numerous plasma instabilities, optimize the evolution of average plasma parameters and plasma profiles, avoid or mitigate plasma disruptions, and be able to respond to any abnormal event requiring a change in the control action in a seamless fashion. This will require the development of optimized, yet robust, integrated algorithms that can coordinate the sharing of the available actuation capabilities to control multiple strongly coupled plasma parameters [49]. The development of this overarching PCS architecture, as well as the development of the individual control algorithms, is an active area of research, and many of the solutions will be needed for ITER.

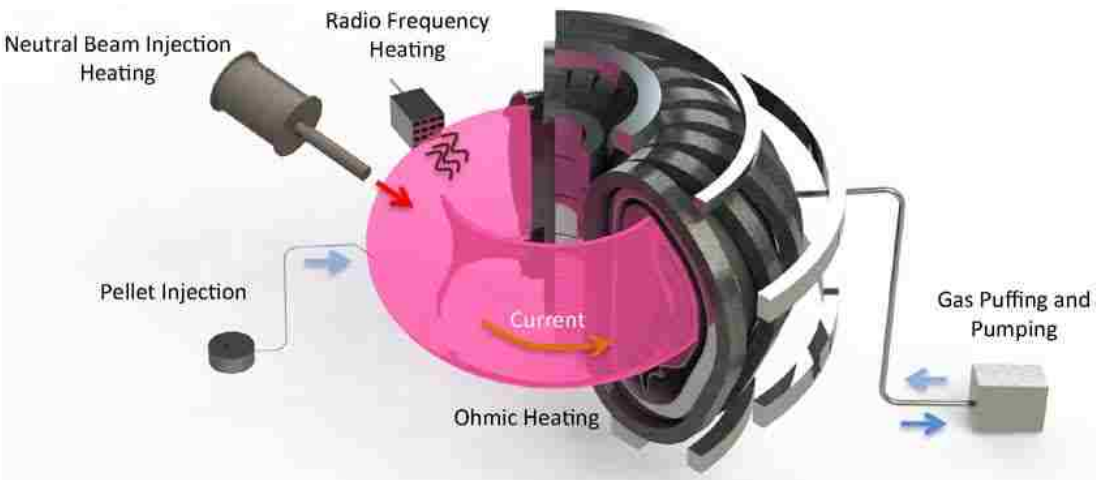

Figure 1.8: Actuators that can be used for plasma profile control [4].

1.4 Current profile control

There are several actuators that can be used to manipulate the plasma current profile evolution in the tokamak (shown in Fig. 1.8). The first actuator is the total plasma current, which is controlled by the poloidal field coil system through induction. By controlling the total current inside the plasma, the internal current profile can be modified through resistive diffusion. Also, since the plasma is slightly resistive, some of the plasma current is dissipated into heat. The plasma resistivity scales inversely with the plasma electron temperature, therefore, at high temperatures the resistive diffusion is low, which tends to freeze the current profile evolution. The second actuator is neutral beam injection (NBI). Injecting beams of highly energetic neutral particles into the plasma provides a source of noninductive current as well as plasma heating through collisions. The third actuator is radio-frequency heating/current-drive. The frequency can be tuned to excite the electrons or ions by power from electron cyclotron and ion cyclotron launchers, respectively. The radio frequency waves can be injected into the plasma in a variety of ways, and various combinations of electron/ion cyclotron heating (ECRH/ICRH) and electron/ion cyclotron current drive (ECCD/ICCD) can be obtained. The neutral beam injectors and radio

frequency wave launchers comprise a given machine's auxiliary heating and current drive (H&CD) system. The final actuator is the plasma electron density, which is controlled by gas-feed and pellet launchers. However, tight control of the electron density in experiments is challenging due to large recycling at the tokamak walls.

Recent work towards the development of advanced tokamak operating scenarios is described in [50–59]. The goal in these works is to study the formation of advanced scenarios with a high bootstrap current fraction so as to minimize the necessary amount of auxiliary current drive needed to maintain the plasma at the desired operating point [53]. The bootstrap current is a self-generated, noninductive current in the plasma that is associated with particles that cannot complete their helical orbit around the machine. These particles are therefore called trapped particles. In the presence of the radial pressure gradient that is produced by the magnetic confinement, more trapped particles move in one toroidal direction than in the other. As a result, a net current is produced which is called the bootstrap current [60]. A key plasma property that is investigated in the development of advanced scenarios is the safety factor profile (q profile) [18] because of its close relationship to plasma energy/particle transport [61, 62], which affect both the magnitudes and gradients of the plasma temperature and density profiles, and to plasma stability limits that are approached by increasing the plasma pressure [63, 64]. The temperature and density gradients are important due to their relationship to the bootstrap current, and the temperature and density profiles themselves are important due to their relationship to the fusion gain of a scenario and to the amount of current that can be driven by auxiliary sources [53, 65, 66].

The safety factor is defined as the ratio between number of times (n) a magnetic field line goes toroidally (the long way) around tokamak to number of times (m) it goes around poloidally (the short way) before it closes in on itself, i.e., it reaches the same point in space that it originated from. Mathematically, the local q value at a

specific location in the plasma can be expressed as

$$q = \frac{n}{m}. \tag{1.7}$$

During a tokamak discharge, the toroidal field coils produce an approximately constant toroidal magnetic field. As a result, n is approximately constant at a given spatial location in the plasma. If the shape of the plasma boundary is controlled at a steady-state equilibrium, the poloidal field coil currents are nearly constant as well. Therefore, changes in the poloidal magnetic field, and hence the value of m at a given spatial location in the plasma, are dominated by changes in the spatial distribution of the toroidal current density in the machine. Therefore, the q profile is seen to be dependent on the toroidal current profile and vice versa. As a result, the current profile and the q profile are often utilized interchangeably in the tokamak community to describe the magnetic state of the plasma.

Finally, advanced scenarios aim to operate at high values of the plasma β to maximize the bootstrap current fraction, however, MHD instabilities, such as NTMs, can be triggered in these regimes [67], which in turn limit the plasma performance and can lead to plasma-terminating disruptions. Obtaining a suitable target current profile in the plasma may provide sufficiently stabilizing effects near rational q surfaces to mitigate NTM formation and contribute to maximizing the bootstrap current [59]. This complex set of interactions makes the problems of predicting (using models) and achieving (in experiments) advanced scenarios extremely challenging. Also, as advanced scenarios operate close to operational boundaries, variations in the plasma evolution can lead to difficulties with reproducibility. These factors motivate the design of controllers to regulate the plasma current profile to improve the ability to access advanced modes of operation. This is the main focus of this dissertation.

Algorithms to control the plasma parameters can be developed by employing either

non-model-based or model-based control techniques. Most likely, non-model-based single-input-single-output (SISO) control loops will not be able to satisfy the plasma profile control performance requirements needed for ITER because the SISO control loops cannot account for the multiple effects a given actuator has on the plasma evolution. Additionally, non-model-based controllers require trial-and-error tuning and are not conducive to developing integrated algorithms to control coupled plasma parameters, which requires coordinated actuator sharing, both of which are impractical for use on ITER. Model-based control is motivated by the coupled, nonlinear, multivariable, distributed parameter dynamics of the plasma. In the development of model-based controllers, the dominant physics of the system is embedded into the control design process through a multi-input-multi-output (MIMO) control-oriented dynamic model. Therefore, the developed controllers know in which direction to actuate to generate a desired response in the plasma state evolution and can be designed to share the available actuation capabilities. As a result, model-based control design inherently reduces the need for trial-and-error tuning of the algorithm and has the potential to meet the demanding control requirements of ITER.

To develop model-based controllers (control algorithms), control-oriented models that describe the plasma response to the actuators, i.e., poloidal field coil voltages, electron cyclotron heating/current-drive, etc., must first be developed. These models can be obtained by employing either data-driven or first-principles-driven (FPD), physics-based modeling techniques. Data-driven models are developed by mainly considering the response of the system output, i.e., the plasma parameters to be controlled, around a specified reference state due to modulations in the system actuators, and little if any physical understanding is incorporated into the model. As a result of the model identification process, most data-driven models are inherently linear, and are only valid around the reference plasma state adopted during the data identification process. This in turn may limit the effectiveness of controllers designed

by utilizing these models when the plasma state deviates from the adopted reference state. Also, as the data-driven models are strongly dependent on system input-output data, dedicated identification experiments are needed on each device, and potentially for each operating scenario, to develop the models.

A substantial physics effort has been ongoing for several years to develop predictive models for the evolution of the magnetic and kinetic plasma profiles in toroidal plasmas. The core of these first-principles models are the fundamental physical laws that govern the behavior of the plasma, such as conservation equations (mass, momentum, energy, charge) and Maxwell's equations, for instance. These physics models have been incorporated into complex simulation codes utilized to model the plasma dynamics and predict the evolution of the plasma in existing and future tokamak devices, with some examples being TRANSP [12], ONETWO [68], CORSICA [69], ASTRA [70], DINA-CH&CRONOS [5–9], and FASTRAN [71]. The goal in developing FPD, control-oriented models is the conversion of these physics models into a form *suitable for control design*. Where first-principles knowledge of a particular plasma parameter is either to complex for control design or not fully understood, such as the plasma thermal conductivity, general physical observations, which are not unique to any one machine, and experimental/simulated data are used to close the first-principles model by developing a simplified model of the plasma parameter in question, thereby obtaining a *first-principles-driven* model.

It is important to note that FPD, physics-based models are developed with control design in mind. Consequently, the models need only capture the dominant physics of the plasma dynamics that are relevant to the control objective since one of the main characteristics of feedback control is the ability to deal with model uncertainties, such as unmodeled dynamics that have a relatively small influence on the plasma state evolution from a control design point-of-view. Additionally, FPD models have the advantages of being (i) extendable to various MHD equilibrium configurations

and operating scenarios, (ii) able to incorporate the nonlinear coupling between the various plasma parameters, and (iii) able to explicitly describe the temporal and spatial evolution of the plasma profiles in response to nonlinear control actuation. As these models mainly rely on fundamental physical laws, they can readily be adapted to a given operating scenario (characterized by a specified magnetic configuration, heating/current-drive scheme, etc.) in a given tokamak, as preexisting experimental data from the machine of interest, or in the case of ITER, simulated data from an advanced simulation code, is all that is needed to close the model. Finally, FPD modeling provides the freedom of arbitrarily handling the trade-off between the simplicity of the model and both its physics accuracy and its range of validity, which will of course be reflected in the model-based controller's performance and capability. In this dissertation, the focus is on employing FPD, physics-based models to control the plasma dynamics.

1.4.1 Prior work

Advances in current profile control at the JET, DIII-D, Tore Supra, and JT-60U tokamaks are described in [72–82]. Experiments at the DIII-D tokamak focus on creating the desired current profile during the ramp-up and early flattop phases of the discharge with the goal of actively maintaining this target profile throughout the remainder of the discharge. During the initial phase of the discharge, feedback control of the value of q at the center of the plasma and the minimum q value across the spatial domain has been demonstrated at DIII-D by changing the plasma conductivity through electron heating [75] . The employed controller requests a power level to the actuator, either ECRH or NBI, that is equal to a preprogrammed feedforward value plus the error in q times a proportional gain. The q profile is obtained in real-time from the motional Stark effect (MSE) diagnostic measurement. If the sampling rate of the q profile is reduced, because the MSE beam is modulated rather than run

continuously, the non-model-based controller has been observed to become unstable causing the q profile to oscillate. This behavior, along with the strong coupling between the magnetic and kinetic plasma profiles and the high dimensionality of the problem, motivates the design of a model-based controller that takes into account the dynamics of the q profile in response to the available actuators and has the potential for improved performance.

By following a data-driven modeling approach, linear, dynamic, plasma profile response models were obtained from experimental data by performing system identification experiments in JET [74], JT-60U, and DIII-D [76]. The models were identified by exploiting the different time scales of the magnetic and kinetic variables and were subsequently used to design controllers to control the plasma current profile. The designed controllers use the heating and current drive systems to regulate the plasma profiles around desired target profiles during the flattop phase of the plasma discharge [74, 77, 78]. However, as the identified models are linear, they are only valid around the reference plasma state adopted during the system identification experiment. Therefore, the effectiveness of the controllers designed based on these models may be limited when the plasma state moves away from the reference state.

Alternatively, a first-principles-driven, physics-based approach can be employed to design control algorithms to regulate plasma conditions. Progress towards physics-based, control-oriented modeling of the magnetic and kinetic plasma profile evolutions in L-mode scenarios has been recently reported in [13, 83, 84]. Advances in developing physics-model-based algorithms to control the plasma dynamics in various tokamaks can be found in [85–94].

1.4.2 Results of this work

The control strategy we employ to control the current profile dynamics is a feedforward + feedback control scheme, where the feedforward control commands are

computed off-line and the feedback control commands are computed on-line. The objective of the feedforward controller is to achieve a target plasma state evolution throughout the discharge while taking into account actuator constraints, such as the maximum available amount of auxiliary heating and current-drive power and total plasma current ramp-up rate, and plasma state constraints. The objective of the feedback controller is to reject the effects that external disturbances have on the plasma, overcome the uncertainties in the model used for the control design, and regulate the plasma state around the target.

In this work, firstly, a general physics-based modeling approach is developed to convert the physics model that describes the current profile evolution in the tokamak into a form suitable for control design by developing physics-based, control-oriented models of the electron density, the electron temperature, the plasma resistivity, and the noninductive current drives in response to the available control actuators. Subsequently, the FPD, physics-based model is tailored to L-mode and H-mode scenarios in DIII-D, to H-mode burning plasma scenarios in ITER, and L-mode scenarios in TCV, demonstrating the flexibility of the developed approach. The model prediction is then compared to the evolution of experimentally-achieved/advanced-simulation-predicted plasma parameters.

Secondly, a model of the plasma dynamics is embedded into a numerical optimization algorithm to synthesize feedforward trajectories for the tokamak actuators that steer the plasma through the tokamak operating space to a predefined target scenario. In this way, actuator trajectories can be designed by exploiting the accumulated knowledge gained by the plasma physics community regarding both the multivariable, coupled, nonlinear, distributed plasma dynamics and plasma stability limits. Ideally, one would like to embed the complex simulation codes described in [5–9, 12, 68–71] into the numerical optimization algorithm. However, as these codes

contain highly sophisticated models of the plasma dynamics, they require a substantial amount of computational time to simulate a plasma discharge. As many state-of-the-art optimization algorithms use an iterative approach to find the optimal solution to a problem [95], a more computationally efficient model of the plasma dynamics is needed in practice. Therefore, we utilize the developed FPD, physics-based model, as models of this complexity can be used to simulate a tokamak discharge with a computational time on the order of seconds, and as a result, are ideal candidates for the models that can be embedded in an iterative optimization algorithm. Advances in actuator trajectory optimization in L-mode scenarios at the DIII-D and TCV tokamaks that employ physics-based models of the plasma dynamics can be found in [14, 96, 97]. In this work, the developed optimization algorithm is employed to design feedforward actuator trajectories to achieve various different target plasma conditions in L-mode and H-mode scenarios in the DIII-D tokamak, and the optimized trajectories are subsequently tested in DIII-D experiments.

Finally, feedback control algorithms to control the current profile evolution in L-mode and H-mode scenarios in the DIII-D and TCV tokamaks are designed by embedding a FPD, physics-based model of the plasma dynamics into the control design process. The effectiveness of the controllers in tracking a desired current profile evolution is demonstrated in simulations and in DIII-D experiments. In order to experimentally test the feedback controllers in DIII-D, a general framework for real-time feedforward + feedback control of magnetic and kinetic plasma profiles was implemented in the DIII-D PCS. A valuable result of the experimental tests is an investigation into the minimum number of variables that must be controlled to achieve robust scenario execution. The L-mode DIII-D experiments represent the first successful demonstration of FPD, physics-model-based, closed-loop full q profile control in a tokamak device. In conjunction with the work presented in this dissertation, the work described in [98, 99] was also part of this initial experimental

campaign. Subsequently, the control philosophy described in [98,99] was extended to actively control the q profile in DIII-D H-mode scenarios [100,101] through feedback.

1.5 Combined current and kinetic profile control

The current profile and the electron temperature profile are intimately coupled in tokamaks through resistive diffusion, auxiliary current-drive efficiency, bootstrap current drive, ohmic heating, and plasma energy/particle transport. In reactor relevant high confinement scenarios, particle and energy transport barriers just inside the plasma boundary are formed, which improve the plasma performance and result in the formation of large gradients in both the plasma density and temperature. These gradients increase the complexity of the coupling between the magnetic and kinetic plasma parameters via the increase of the plasma self-generated bootstrap current in H-mode scenarios compared to L-mode scenarios, where the bootstrap effects are relatively small because of the lower plasma temperature and density gradients in this operating mode [2] (see Fig. 1.5). To optimize the fusion power, the plasma density and temperature profiles must also simultaneously be controlled. The volume-averaged plasma stored energy is related to these kinetic plasma profiles and can alternatively be controlled to regulate the fusion power. As the current and electron temperature profiles are intimately coupled (particularly in reactor relevant scenarios), integrating methodologies for current profile control with strategies to control the kinetic state of the plasma is crucial to developing the ability to robustly achieve and maintain high performance plasma targets, in particular on long-pulse devices such as ITER where the resistive current diffusion time constant is comparable to the discharge time. This capability can enable the study of desired regimes, control the proximity to stability limits, and maximize the physics output of the executed plasma discharges.

1.5.1 Prior work

Algorithms for simultaneous control of the current profile and a volume average representation of the plasma thermal state (plasma β, total fusion power) following a data-driven approach have recently been developed. These controllers have been tested in H-mode DIII-D experiments [102–105] and in advanced tokamak ITER operating scenarios [103] through simulations with the simplified plasma transport code METIS [106]. Additionally, following a data-driven approach, an algorithm for simultaneous control the current profile and the gyro-normalized electron temperature gradient profile was designed for JET and tested through simulations [74]. Finally an algorithm for simultaneous control of the current and electron temperature profiles based on real-time estimation of linearized static plasma profile response models is described in [107]. This algorithm was subsequently tested in advanced tokamak ITER operating scenarios through simulations with the CRONOS code [7].

1.5.2 Results of this work

In this work, feedback algorithms for simultaneous current profile + total stored energy control in H-mode scenarios in the DIII-D and ITER tokamaks are designed by embedding a FPD, physics-based model of the plasma dynamics into the control design process. The effectiveness of the controllers in tracking a desired current profile + total stored energy evolution is demonstrated in DIII-D and ITER based on simulations with the FPD, physics-based model developed in this work. In particular, the ITER simulations demonstrate the ability of the feedback controller to maintain the current profile at a stationary target while simultaneously modulating the amount of fusion power that is generated. Additionally, a feedback algorithm for simultaneous current + electron temperature profile control in L-mode scenarios in the TCV tokamak is designed by following a FPD, physics-based approach. The effectiveness

of the feedback controller is demonstrated through simulations with the RAPTOR code [13–15], which is a simplified physics-based code (similar to one developed in this work), where the current profile is maintained at a stationary target while simultaneously modulating the electron temperature profile between equilibrium points. The ability to maintain the current profile at a stationary target (to maintain plasma stability) while modulating the thermal state of the plasma (to respond to changing power demand) is an essential capability that will be needed for a commercial, power producing tokamak reactor.

1.6 Dissertation outline

The organization of this dissertation is as follows.

Chapter 2

In this chapter, a general physics-based modeling approach is developed to convert the physics model that describes the current profile evolution in the tokamak into a form suitable for control design. This is accomplished by developing physics-based, control-oriented models of the electron density, the electron temperature, the plasma resistivity, and the noninductive current drives in response to the available control actuators. Subsequently, the FPD model is tailored to L-mode and H-mode operating scenarios in multiple tokamaks, demonstrating the flexibility of the employed methodology. The model's predictive capabilities are demonstrated through comparison to the evolution of experimentally-achieved/advanced-simulation-predicted plasma parameters.

This work was presented at the 54th Annual Meeting of the APS Division of Plasma Physics [108] and the 52nd IEEE Conference on Decision and Control [109].

Chapter 3

In this chapter, a robust feedback controller for current profile control in L-mode scenarios in the DIII-D tokamak is designed by employing the FPD, physics-based model described in [83]. A general framework for real-time feedforward + feedback control of magnetic and kinetic plasma profiles is implemented in the DIII-D PCS. A tokamak simulation model (Simserver) that can interface with the control algorithm implemented in the DIII-D PCS is developed, which enables closed-loop simulations with the real-time code to be executed to debug the algorithm prior to experimental testing. The effectiveness of the feedback controller is demonstrated through simulations and DIII-D experiments. These experiments, along with those described in [98, 99], represent the first demonstration of FPD, physics-based, closed-loop control of the entire current profile in a tokamak.

This feedback control design, control algorithm implementation in the DIII-D PCS, and experimental testing of the controller was presented at the 53rd Annual Meeting of the APS Division of Plasma Physics [110], the 2012 American Control Conference (best student paper award finalist) [111], the 24th IAEA Fusion Energy Conference [112], and published in Nuclear Fusion [113].

The Simserver development work was presented at the 52nd Annual Meeting of the APS Division of Plasma Physics [114] and published in Fusion Engineering and Design [115].

Chapter 4

In this chapter, a FPD, physics-model-based algorithm is developed to optimize plasma startup conditions in L-mode scenarios in the DIII-D tokamak by achieving a specified target q profile at the end of the current ramp-up phase of the discharge. A feedforward + feedback scheme is utilized to control the q profile. The physics-based

model developed in chapter 2 is embedded in a numerical optimization algorithm to design feedforward trajectories for the available actuators. A unique characteristic of the feedforward trajectories obtained by solving the optimization problem is the regulation of the plasma current ramp-up rate to achieve the target q profiles. The feedback controller is employed to add robustness to the control scheme and account for drifts due to external plasma disturbances. Additionally, the feedback controller is designed to be robust to uncertainties in the electron density, electron temperature, and plasma resistivity profiles, respectively. Experimental results in DIII-D are presented to demonstrate the potential of the feedforward + feedback controller to improve the ability to robustly achieve various different target q profile at the end of the current ramp-up phase of the discharge.

This work was presented at the 56th Annual Meeting of the APS Division of Plasma Physics [116].

Chapter 5

In this chapter, the feedforward and feedback controllers designed in chapter 4 are extended to H-mode scenarios in the DIII-D tokamak. The physics-based model developed in chapter 2 is embedded in a numerical optimization algorithm to design feedforward trajectories for the available actuators that steer the plasma through the tokamak operating space to reach a target plasma state (characterized by the current profile and plasma stored energy) in such a way that the achieved state is as stationary in time as possible. Additionally, feedback controllers for current profile and for simultaneous current profile and plasma stored energy control are designed following the approach presented in chapter 4. The feedforward and feedback controllers are tested in DIII-D experiments. The experimental tests demonstrate the potential physics-model-based profile control has to provide a systematic approach for the development and robust sustainment of advanced scenarios, as well as provide insight

into physics aspects important to robust scenario execution. The current profile (not including energy control) feedback controller is shown to be able to effectively control the current profile when the plasma stored energy is relatively close to the target. This indicates the need for integrated current profile and stored energy control to further enhance the ability to achieve robust scenario execution. Through simulations with the physics-based model developed in chapter 2, the ability of the combined current profile and stored energy feedback controller to track a desired target is demonstrated.

This work was presented at the 55th Annual Meeting of the APS Division of Plasma Physics [117], the 19th IFAC World Congress [118, 119], and the 25th IAEA Fusion Energy Conference [120].

Chapter 6

In this chapter, a feedback controller for simultaneous q profile and plasma stored energy control in H-mode burning plasma scenarios in the ITER tokamak is designed. The controller is designed with a two-loop structure, where the total plasma current and the auxiliary sources that heat and drive noninductive current in the plasma are employed to the control the q profile, and the auxiliary sources that only heat the plasma are employed to control the plasma stored energy. The q profile controller is designed to be robust to uncertainties in the electron density, electron temperature, and plasma resistivity profiles, respectively. The ability of the two control loops to interact together effectively is demonstrated through simulations with the physics-based model developed in chapter 2 by first tracking a nominal target, and then modulating the generated fusion power while maintaining the current profile in a stationary condition.

This work was presented at the 52nd IEEE Conference on Decision and Control [121].

Chapter 7

In this chapter, feedback algorithms for q profile control in L-mode scenarios in the TCV tokamak are synthesized. The controllers are designed to put emphasis on achieving the target q profile in different spatial regions, to respond differently to errors in the q profile, and to be robust to uncertainties in the plasma electron temperature and plasma resistivity profiles. The performance of each controller is tested though simulations with the RAPTOR code, where the ability of each controller to track multiple different target profiles is demonstrated.

This work was presented at the 53rd IEEE Conference on Decision and Control [122].

Chapter 8

In this chapter, a feedback controller for simultaneous current and electron temperature profile control in L-mode scenarios in the TCV tokamak is designed following a FPD, physics-based approach. The electron thermal conductivity profile is modeled as an uncertainty, and the controller is designed to be robust to an expected uncertainty range. The RAPTOR code is used to test the capabilities of the controller. The performance of the integrated profile controller is demonstrated by first tracking a nominal target, and then modulating the electron temperature profile between equilibrium points while maintaining the current profile in a stationary condition.

This work was submitted to the 2015 American Control Conference [123].

Chapter 9

In this chapter, the contributions of this dissertation are summarized, and some possible directions of future research are discussed.

Chapter 2

Physics-based modeling of the plasma current profile dynamics

2.1 Introduction

Towards the goal of developing control algorithms to achieve and maintain a desired plasma magnetic state in the tokamak, in this chapter, a general control-oriented physics-based modeling approach is developed to obtain a *first-principles-driven* (FPD) model of the plasma current profile dynamics in tokamaks. We begin the model development process by considering the well known one-dimensional poloidal magnetic flux diffusion equation [124,125], which describes the resistive diffusion of the poloidal magnetic flux in the tokamak in response to the electric field due to induction, the noninductive current driven by the auxiliary heating and current-drive (H&CD) system, and the neoclassical bootstrap effect. This physics model is subsequently converted into a form suitable for control design by developing simplified control-oriented versions of physics-based models of the electron density, the electron temperature, the plasma resistivity, and the noninductive current-drives (auxiliary and bootstrap). The objective in developing the simplified physics-based models of

the plasma parameters is to capture the dominant physics that describe how the control actuators affect the plasma parameters.

The approach employed to develop the control-oriented models is inspired by the approach presented in [83], where a FPD model of the poloidal magnetic flux dynamics valid for low confinement (L-mode) scenarios in the DIII-D tokamak was developed. The approach developed in this work extends the work described in [83] in many critical areas. Firstly, the effects of the auxiliary H&CD actuators are modeled independently to exploit the full capabilities of a given machine's H&CD system. Additionally, the ability to include various kinds of auxiliary current drive sources, such as electron cyclotron current drive and neutral beam injection current drive, is included in the model. Secondly, the bootstrap current and fusion power are included in the model. This allows the developed FPD model to be applied to reactor relevant, high confinement (H-mode) operating scenarios where the bootstrap current provides a significant fraction of the total current density, and in the case of ITER, to burning plasma scenarios where a significant portion of the plasma heating power is provided by the α power. Finally, the developed approach (and corresponding numerical simulation code) is readily tailored to different machines of interest.

This chapter is organized as follows. We begin by providing a derivation of the Grad–Shafranov equation [126], which is a two-dimensional, nonlinear, elliptic partial differential equation (PDE) that describes the magnetohydrodynamic (MHD) equilibrium distribution of the poloidal magnetic flux at any given time in the tokamak plasma, in section 2.2. The derivation provided follows the one described in [127]. In section 2.3, a deviation of the the poloidal magnetic flux diffusion equation is provided. The derivation provided follows the one described in [124]. The control-oriented, physics-based models of the plasma parameters in response to the control actuators are discussed in section 2.4. In section 2.5, the, nonlinear FPD model of the plasma poloidal magnetic flux dynamics is obtained by coming the magnetic diffusion

equation with the control-oriented models, and various parameters that are utilized to characterize tokamak operating scenarios (and their relationship to the poloidal magnetic flux), such as the current profile and the safety factor profile (q profile), are defined in section 2.6. In sections 2.7 through 2.10, the FPD model is tailored to L-mode and H-mode scenarios in the DIII-D, ITER, and TCV tokamaks, respectively, demonstrating the flexibility of the developed approach. The model prediction is then compared to the evolution of experimentally-achieved/advanced-simulation-predicted plasma parameters. Finally, conclusions are discussed in section 2.11.

2.2 Tokamak plasma MHD equilibrium

A tokamak plasma magnetohydrodynamic equilibrium is governed by the static, time independent form of the full MHD equations:

$$\mathbf{j} \times \mathbf{B} = \nabla p, \qquad \text{(Momentum Equation)} \tag{2.1}$$

$$\nabla \times \mathbf{B} = \mu_0 \mathbf{j}, \qquad \text{(Ampere's Law)} \tag{2.2}$$

$$\nabla \cdot \mathbf{B} = 0, \qquad \text{(Gauss's Law)} \tag{2.3}$$

where $\mathbf{B}$ is the magnetic field, $\mathbf{j}$ is the current density, p is the fluid pressure, and μ_0 is the vacuum magnetic permeability. We begin by defining the cylindrical coordinate system (R, ϕ, Z) shown in Fig. 2.1, where R denotes the radial direction, Z denotes the vertical direction, and ϕ denotes the angle necessary to obtain a right-handed system. We use the quantities $\mathbf{e}_R$, $\mathbf{e}_\phi$, and $\mathbf{e}_Z$ to denote unit vectors along the appropriate directions. At each point in space, the direction parallel to the unit vector $\mathbf{e}_\phi$ is called the toroidal direction and the plane perpendicular to this direction is called the poloidal direction. In this coordinate system, a generic vector $\mathbf{A}$, with

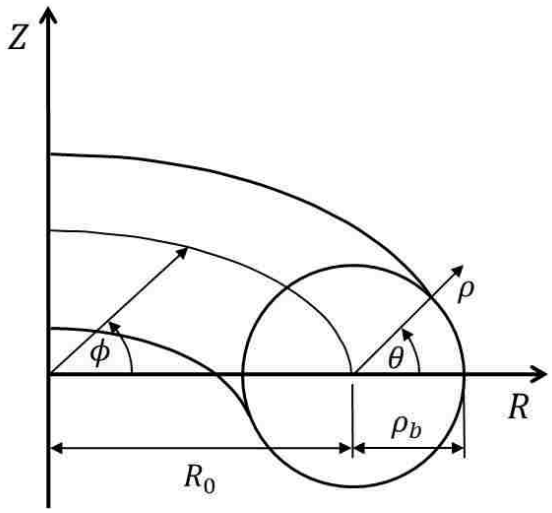

Figure 2.1: Coordinate systems employed to describe plasma quantities: cylindrical system (R, ϕ, Z) and flux surface system (ρ, ϕ, θ). The geometric major radius of the tokamak is denoted by R_0 and ρ_b denotes the value of ρ at the plasma boundary.

components A_R, A_ϕ, and A_Z, is defined as

$$\mathbf{A} = A_R \mathbf{e}_R + A_\phi \mathbf{e}_\phi + A_Z \mathbf{e}_Z.$$

Finally, as the geometric configuration of the tokamak is symmetric about the Z-axis, we assume that all relevant physical quantities are independent of the toroidal angle ϕ, which implies for a general quantity A

$$\frac{\partial}{\partial \phi} A = 0.$$

We begin by defining the total magnetic field as

$$\mathbf{B} = B_R \mathbf{e}_R + B_\phi \mathbf{e}_\phi + B_Z \mathbf{e}_Z, \tag{2.4}$$

and from Gauss's Law (2.3), the magnetic field components must satisfy

$$\nabla \cdot \mathbf{B} = \frac{1}{R}\frac{\partial (RB_R)}{\partial R} + \frac{1}{R}\frac{\partial B_\phi}{\partial \phi} + \frac{\partial B_Z}{\partial Z} = 0 \quad \Rightarrow \quad \frac{1}{R}\frac{\partial (RB_R)}{\partial R} + \frac{\partial B_Z}{\partial Z} = 0. \tag{2.5}$$

Next, we define the poloidal stream function ψ as the flux per unit radian of magnetic field passing through a disk $\mathbf{S}_Z$ of radius R that is perpendicular to $\mathbf{e}_Z$, which is expressed as

$$\psi(R, Z) = \frac{1}{2\pi}\int \mathbf{B} \cdot d\mathbf{S}_Z = \frac{1}{2\pi}\int_0^{2\pi}\int_0^R B_Z(\tau, Z) d\phi \tau d\tau = \int_0^R \tau B_Z(\tau, Z) d\tau. \tag{2.6}$$

Differentiating (2.6) with respect to R, we obtain

$$\frac{\partial \psi}{\partial R} = RB_Z,$$

and differentiating (2.6) with respect to Z and using (2.5), we obtain

$$\frac{\partial \psi}{\partial Z} = \int_0^R \tau \frac{\partial B_Z}{\partial Z} d\tau = -\int_0^R \tau \frac{1}{\tau}\frac{\partial (\tau B_R)}{\partial \tau} d\tau = -RB_R.$$

Therefore, the magnetic field components B_R and B_Z depend on the poloidal stream function ψ through the relations

$$\begin{aligned} B_R &= -\frac{1}{R}\frac{\partial \psi}{\partial Z}, \\ B_Z &= \frac{1}{R}\frac{\partial \psi}{\partial R}. \end{aligned} \tag{2.7}$$

By employing (2.7), the magnetic field (2.4) can be written as

$$\mathbf{B} = B_\phi \mathbf{e}_\phi + \mathbf{B}_\theta, \tag{2.8}$$

where the poloidal magnetic field $\mathbf{B}_\theta$ is defined as

$$\begin{aligned}\mathbf{B}_\theta &= \frac{1}{R}\nabla\psi \times \mathbf{e}_\phi = \frac{1}{R}\left(\frac{\partial\psi}{\partial R}\mathbf{e}_R + \frac{1}{R}\frac{\partial\psi}{\partial\phi}\mathbf{e}_\phi + \frac{\partial\psi}{\partial Z}\mathbf{e}_Z\right) \times \mathbf{e}_\phi \\ &= -\frac{1}{R}\frac{\partial\psi}{\partial Z}\mathbf{e}_R + \frac{1}{R}\frac{\partial\psi}{\partial R}\mathbf{e}_Z. \end{aligned} \tag{2.9}$$

Finally, in a well confined tokamak plasma, nested surfaces of constant ψ are obtained as shown in Fig. 2.2, and these surfaces are referred to as magnetic flux surfaces. By noting that

$$\begin{aligned}\nabla\psi \cdot \mathbf{B} &= \left(\frac{\partial\psi}{\partial R}\mathbf{e}_R + \frac{1}{R}\frac{\partial\psi}{\partial\phi}\mathbf{e}_\phi + \frac{\partial\psi}{\partial Z}\mathbf{e}_Z\right) \cdot \left(-\frac{1}{R}\frac{\partial\psi}{\partial Z}\mathbf{e}_R + B_\phi\mathbf{e}_\phi + \frac{1}{R}\frac{\partial\psi}{\partial R}\mathbf{e}_Z\right) \\ &= -\frac{1}{R}\frac{\partial\psi}{\partial R}\frac{\partial\psi}{\partial Z} + \frac{1}{R}\frac{\partial\psi}{\partial R}\frac{\partial\psi}{\partial Z} = 0, \end{aligned} \tag{2.10}$$

we see that the helical magnetic field lines lie on the magnetic flux surfaces. The limiting magnetic flux surface, which approaches a single magnetic field line, is called the magnetic axis. The definition of the function ψ given in (2.6) results in ψ having the same sign as the physical poloidal magnetic flux and ψ is related to the poloidal magnetic flux Ψ via the relation $\Psi = 2\pi\psi$. Additionally with this definition, the function ψ is a maximum at the magnetic axis for a positive plasma current (flowing in the counter-clockwise direction when looking down on the tokamak).

By utilizing Ampere's Law (2.2), we can obtain an expression for the electrical current density. Substituting (2.8) into (2.2) we obtain

$$\begin{aligned}\mu_0\mathbf{j} = \nabla \times \mathbf{B} &= \left(\frac{1}{R}\frac{\partial B_Z}{\partial\phi} - \frac{\partial B_\phi}{\partial Z}\right)\mathbf{e}_R + \left(\frac{\partial B_R}{\partial Z} - \frac{\partial B_Z}{\partial R}\right)\mathbf{e}_\phi + \frac{1}{R}\left(\frac{\partial(RB_\phi)}{\partial R} - \frac{\partial B_R}{\partial\phi}\right)\mathbf{e}_Z \\ &= -\frac{\partial B_\phi}{\partial Z}\mathbf{e}_R + \left(-\frac{1}{R}\frac{\partial^2\psi}{\partial Z^2} - \frac{1}{R}\frac{\partial^2\psi}{\partial R^2} + \frac{1}{R^2}\frac{\partial\psi}{\partial R}\right)\mathbf{e}_\phi + \frac{1}{R}\left(R\frac{\partial B_\phi}{\partial R} + B_\phi\right)\mathbf{e}_Z. \end{aligned} \tag{2.11}$$

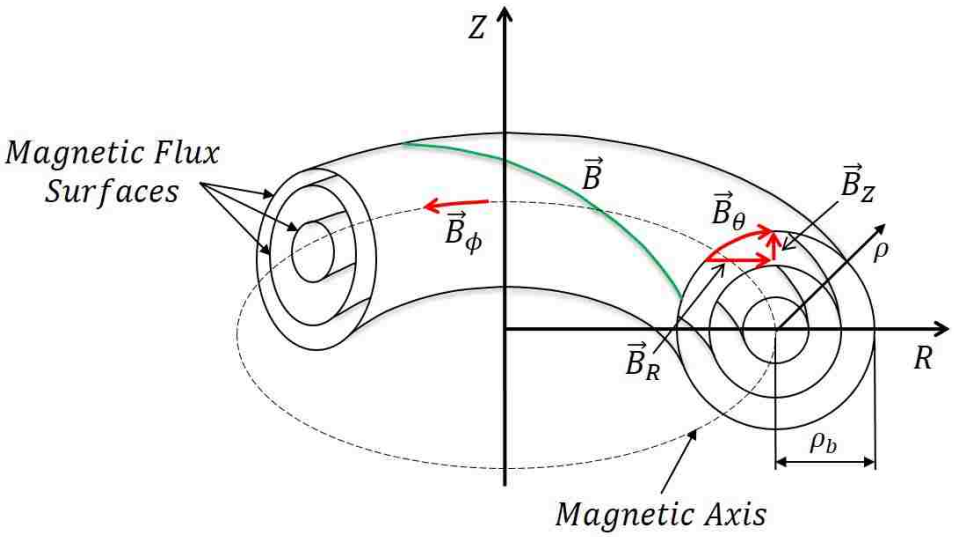

Figure 2.2: Toroidal magnetic flux surfaces (defined by a constant poloidal magnetic flux) in a tokamak. The coordinates (R, Z) define the radial and vertical coordinates in the poloidal plane. The total helical magnetic field ($\vec{B}$) is composed of a toroidal component ($\vec{B}_\phi$) and a poloidal component ($\vec{B}_\theta$), respectively. The poloidal component is in turn composed of a radial component ($\vec{B}_R$) and vertical component ($\vec{B}_Z$). The limiting flux surface at the plasma core is called the magnetic axis. The quantity ρ is any arbitrary quantity that is constant on each magnetic flux surface within the plasma and can be used to index the magnetic flux surfaces.

By defining the differential elliptic operator $\Delta^*\psi$ as

$$\begin{aligned}
\Delta^*\psi = R^2\nabla\cdot\frac{\nabla\psi}{R^2} &= R^2\nabla\cdot\left(\frac{1}{R^2}\left[\frac{\partial\psi}{\partial R}\mathbf{e}_R+\frac{1}{R}\frac{\partial\psi}{\partial\phi}\mathbf{e}_\phi+\frac{\partial\psi}{\partial Z}\mathbf{e}_Z\right]\right)\\
&= R^2\left[\frac{1}{R}\frac{\partial}{\partial R}\left(R\frac{1}{R^2}\frac{\partial\psi}{\partial R}\right)+\frac{1}{R}\frac{\partial}{\partial\phi}\left(\frac{1}{R^3}\frac{\partial\psi}{\partial\phi}\right)+\frac{\partial}{\partial Z}\left(\frac{1}{R^2}\frac{\partial\psi}{\partial Z}\right)\right]\\
&= R^2\left[\frac{1}{R}\frac{\partial}{\partial R}\left(\frac{1}{R}\frac{\partial\psi}{\partial R}\right)+\frac{1}{R^2}\frac{\partial^2\psi}{\partial Z^2}\right]\\
&= R\frac{\partial}{\partial R}\left(\frac{1}{R}\frac{\partial\psi}{\partial R}\right)+\frac{\partial^2\psi}{\partial Z^2},
\end{aligned} \tag{2.12}$$

we can express (2.11) as

$$\mu_0\mathbf{j} = \left(-\frac{1}{R}\Delta^*\psi\right)\mathbf{e}_\phi+\frac{1}{R}\nabla(RB_\phi)\times\mathbf{e}_\phi, \tag{2.13}$$

where

$$-\frac{1}{R}\Delta^*\psi = -\frac{\partial}{\partial R}\left(\frac{1}{R}\frac{\partial\psi}{\partial R}\right) - \frac{1}{R}\frac{\partial^2\psi}{\partial Z^2} = -\frac{1}{R}\frac{\partial^2\psi}{\partial Z^2} - \frac{1}{R}\frac{\partial^2\psi}{\partial R^2} + \frac{1}{R^2}\frac{\partial\psi}{\partial R}$$

and

$$\begin{aligned}\frac{1}{R}\nabla(RB_\phi)\times\mathbf{e}_\phi &= \frac{1}{R}\left[\frac{\partial(RB_\phi)}{\partial R}\mathbf{e}_R + \frac{1}{R}\frac{\partial(RB_\phi)}{\partial\phi}\mathbf{e}_\phi + \frac{\partial(RB_\phi)}{\partial Z}\mathbf{e}_Z\right]\times\mathbf{e}_\phi \\ &= \frac{1}{R}\left[\left(R\frac{\partial B_\phi}{\partial R} + B_\phi\right)\mathbf{e}_R + R\frac{\partial B_\phi}{\partial Z}\mathbf{e}_Z\right]\times\mathbf{e}_\phi \\ &= -\frac{\partial B_\phi}{\partial Z}\mathbf{e}_R + \frac{1}{R}\left(R\frac{\partial B_\phi}{\partial R} + B_\phi\right)\mathbf{e}_Z.\end{aligned}$$

The final condition that the electrical currents and magnetic fields inside the plasma must satisfy so that the plasma is in MHD equilibrium is given by the momentum equation (2.1). The momentum equation (2.1) can be decomposed into 3 components, along $\mathbf{B}$, $\mathbf{j}$, and $\nabla\psi$ (normal to the magnetic flux surfaces). By noting that $\mathbf{B}\cdot\nabla p = 0$ and $\mathbf{j}\cdot\nabla p = 0$, we see that the pressure gradient is orthogonal to both the magnetic field and electrical current density. Evaluating the component of (2.1) parallel to $\mathbf{B}$ results in

$$\mathbf{B}\cdot\nabla p = 0 \quad\Rightarrow\quad \left(\frac{1}{R}\nabla\psi\times\mathbf{e}_\phi\right)\cdot\nabla p = 0 \quad\Rightarrow\quad \mathbf{e}_\phi\cdot\left(\frac{1}{R}\nabla\psi\times\nabla p\right) = 0. \quad (2.14)$$

Evaluating the component of (2.1) parallel to $\mathbf{j}$ results in

$$\begin{aligned}\mathbf{j}\cdot\nabla p = 0 \quad &\Rightarrow \quad \left(\frac{1}{\mu_0 R}\nabla(RB_\phi)\times\mathbf{e}_\phi\right)\cdot\nabla p = 0 \\ &\Rightarrow \quad \frac{1}{\mu_0 R}\mathbf{e}_\phi\cdot\left(\nabla(RB_\phi)\times\nabla p\right) = 0. \qquad (2.15)\end{aligned}$$

From (2.14), we see that ∇p is parallel to $\nabla\psi$, which implies p is constant on a magnetic flux surface, i.e., $p = p(\psi)$. From (2.15), we see that $\nabla(RB_\phi)$ is parallel

to ∇p (and therefore $\nabla\psi$), which implies RB_ϕ is also constant of a magnetic flux surface, i.e., $RB_\phi = F = F(\psi)$. Finally, evaluating the component of (2.1) parallel to $\nabla\psi$ results in

$$\nabla\psi \cdot (\mathbf{j} \times \mathbf{B}) = \nabla\psi \cdot \nabla p. \tag{2.16}$$

By employing (2.13) and (2.8), the term $\nabla\psi \cdot (\mathbf{J} \times \mathbf{B})$ is evaluated as

$$\begin{aligned}
\nabla\psi \cdot (\mathbf{j} \times \mathbf{B}) &= \nabla\psi \cdot \left(-\frac{1}{\mu_0 R}\Delta^*\psi \mathbf{e}_\phi + \frac{1}{\mu_0 R}\nabla F \times \mathbf{e}_\phi \right) \times \left(\frac{F}{R}\mathbf{e}_\phi + \frac{1}{R}\nabla\psi \times \mathbf{e}_\phi \right) \\
&= \nabla\psi \cdot \left(-\frac{1}{\mu_0 R^2}\Delta^*\psi \left[\mathbf{e}_\phi \times \left(-\frac{\partial\psi}{\partial Z}\mathbf{e}_R + \frac{\partial\psi}{\partial R}\mathbf{e}_Z \right) \right] \right. \\
&\quad \left. + \frac{1}{\mu_0 R^2} F \frac{\partial F}{\partial\psi} \left[\left(-\frac{\partial\psi}{\partial Z}\mathbf{e}_R + \frac{\partial\psi}{\partial R}\mathbf{e}_Z \right) \times \mathbf{e}_\phi \right] \right) \\
&= -\nabla\psi \cdot \left(\frac{1}{\mu_0 R^2}\Delta^*\psi \nabla\psi + \frac{1}{\mu_0 R^2} F \frac{dF}{d\psi}\nabla\psi \right) \\
&= -(\nabla\psi \cdot \nabla\psi)\left(\frac{1}{\mu_0 R^2}\Delta^*\psi + \frac{1}{\mu_0 R^2} F \frac{dF}{d\psi} \right),
\end{aligned} \tag{2.17}$$

where we have used the definition $\nabla F(\psi) = [\partial F/\partial\psi]\,\nabla\psi$. The term $\nabla\psi \cdot \nabla p$ is evaluated as

$$\nabla\psi \cdot \nabla p = (\nabla\psi \cdot \nabla\psi)\frac{dp}{d\psi}, \tag{2.18}$$

where we have used the definition $\nabla p(\psi) = [\partial p/\partial\psi]\,\nabla\psi$.

The Grad–Shafranov equation [126] is then obtained by combining (2.16)-(2.18) and is expressed as

$$\Delta^*\psi + \mu_0 R^2 \frac{dp}{d\psi} + F\frac{dF}{d\psi} = 0. \tag{2.19}$$

Note that the poloidal stream function ψ is both a dependent and an independent variable in (2.19). The Grad–Shafranov equation is a two-dimensional, nonlinear, elliptic partial differential equation that describes the equilibrium distribution of ψ (in the poloidal plane) at any given time in the tokamak plasma. A typical distribution of the poloidal magnetic flux in a tokamak plasma is shown in Fig. 2.3. The magnetic

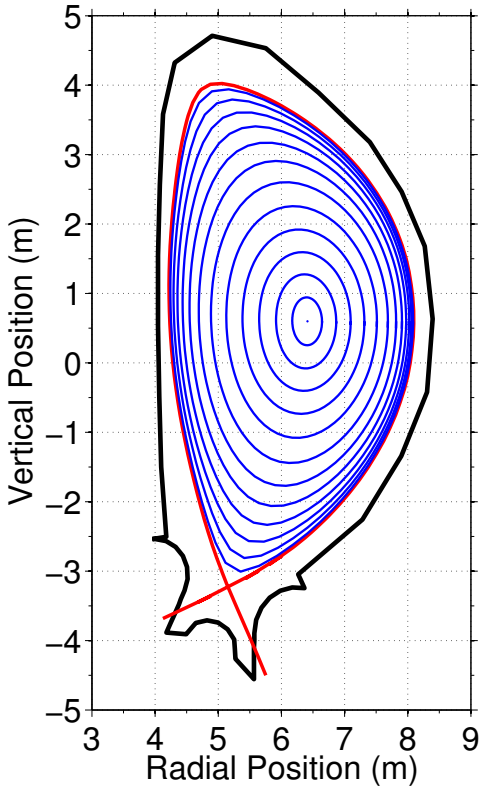

Figure 2.3: Magnetic flux surface geometry in the ITER tokamak (computed by the DINA-CH&CRONOS [5–9] free-boundary tokamak simulation code). The individual magnetic flux surfaces are shown in blue, the plasma boundary is shown in red and the first wall is shown in black.

field (2.8) and current density (2.13) written in terms of ψ and F are expressed as

$$\mathbf{B} = \frac{1}{R}\nabla\psi \times \mathbf{e}_\phi + \frac{F}{R}\mathbf{e}_\phi, \tag{2.20}$$

$$\mathbf{j} = \frac{1}{\mu_0 R}\frac{dF}{d\psi}\nabla\psi \times \mathbf{e}_\phi - \frac{1}{\mu_0 R}\Delta^*\psi\mathbf{e}_\phi. \tag{2.21}$$

2.3 Plasma poloidal magnetic flux diffusion equation

We now introduce the poloidal magnetic flux diffusion equation, which describes the resistive diffusion of the poloidal magnetic flux in the plasma. Any arbitrary quantity that is constant on each magnetic flux surface within the plasma can be used to index the magnetic flux surfaces. In this work, we choose the mean effective minor radius, ρ, of the magnetic flux surface, i.e.,

$$\Phi(\rho) = \pi B_{\phi,0}\rho^2, \tag{2.22}$$

as the indexing variable, where Φ is the toroidal magnetic flux and $B_{\phi,0}$ is the vacuum toroidal magnetic field at the geometric major radius R_0 of the tokamak. The normalized effective minor radius is defined as $\hat{\rho} = \rho/\rho_b$, where ρ_b is the normalized mean effective minor radius of the last closed magnetic flux surface.

We begin by noting that some physical quantities are constant on a magnetic flux surface, such as ψ, p, and F as shown in the previous section, while other physical quantities are not constant on a magnetic flux surface. Therefore, to derive equations for physical quantities that are not constant on a magnetic flux surface, we introduce the concept of a flux-surface average. The flux-surface average of a generic quantity A is defined as

$$\langle A \rangle = \frac{\partial}{\partial V}\int_V A dV, \tag{2.23}$$

where V is the volume enclosed by a magnetic flux surface and the differential volume is defined as $dV = RdRd\phi dZ$. The toroidal magnetic flux is defined as the magnetic field passing through the surface $\mathbf{S}_\phi$ ($dS_\phi = dRdZ$) that is perpendicular to $\mathbf{e}_\phi$

$$\Phi = \int \mathbf{B}\cdot d\mathbf{S}_\phi = \int B_\phi dS_\phi = \frac{1}{2\pi}\int_V \frac{F}{R}|\nabla\phi| dV = \frac{1}{2\pi}\int_V \frac{F}{R^2} dV. \tag{2.24}$$

Therefore, we can define the quantities $\partial\Phi/\partial V$ and $\partial V/\partial\rho$ as

$$\frac{\partial\Phi}{\partial V} = \frac{1}{2\pi}\frac{\partial}{\partial V}\int_V \frac{F}{R^2}dV = \frac{F}{2\pi}\left\langle\frac{1}{R^2}\right\rangle \tag{2.25}$$

and

$$V' = \frac{\partial V}{\partial\rho} = \frac{\partial V}{\partial\Phi}\frac{\partial\Phi}{\partial\rho} = \frac{2\pi}{F}\left\langle\frac{1}{R^{-2}}\right\rangle 2\pi B_{\phi,0}\rho = \frac{4\pi^2\rho B_{\phi,0}}{F}\left\langle\frac{1}{R^{-2}}\right\rangle, \tag{2.26}$$

which will be useful in the derivation of the poloidal magnetic flux diffusion equation.

The poloidal magnetic flux diffusion equation is a statement of Ohm's Law projected along the direction parallel to the magnetic field lines and then averaged over a flux surface. Ohm's Law describes the evolution of the inductive component of the plasma current density and is stated as

$$\mathbf{E} + \mathbf{v}\times\mathbf{B} = \eta(\mathbf{j} - \mathbf{j_{ni}}), \tag{2.27}$$

where $\mathbf{E}$ is the electric field, $\mathbf{v}$ is the average velocity of the particles in the plasma, η is the plasma resistivity, and $\mathbf{j_{ni}}$ is the total noninductive current density. Evaluating the component of (2.27) parallel to $\mathbf{B}$ and flux-surface averaging the resulting equation results in

$$\langle\mathbf{E}\cdot\mathbf{B}\rangle + \langle(\mathbf{v}\times\mathbf{B})\cdot\mathbf{B}\rangle = \eta\langle(\mathbf{j}-\mathbf{j_{ni}})\cdot\mathbf{B}\rangle \quad\Rightarrow\quad \eta j_{||} = E_{||} + \eta j_{ni}, \tag{2.28}$$

where

$$j_{||} = \langle\mathbf{j}\cdot\mathbf{B}\rangle/B_{\phi,0},$$
$$E_{||} = \langle\mathbf{E}\cdot\mathbf{B}\rangle/B_{\phi,0},$$
$$j_{ni} = \langle\mathbf{j_{ni}}\cdot\mathbf{B}\rangle/B_{\phi,0}.$$

The poloidal magnetic flux diffusion equation is obtained by rewriting the terms $j_{||}$ and $E_{||}$ in terms of ψ. By employing (2.20) and (2.21), the term $\langle \mathbf{j} \cdot \mathbf{B} \rangle / B_{\phi,0}$ is evaluated as

$$\begin{aligned}
\frac{\langle \mathbf{j} \cdot \mathbf{B} \rangle}{B_{\phi,0}} &= \frac{1}{B_{\phi,0}} \frac{\partial}{\partial V} \int_V \left(\frac{1}{\mu_0 R} \frac{dF}{d\psi} \nabla\psi \times \mathbf{e}_\phi - \frac{1}{\mu_0 R} \Delta^* \psi \mathbf{e}_\phi \right) \cdot \left(\frac{1}{R} \nabla\psi \times \mathbf{e}_\phi + \frac{F}{R} \mathbf{e}_\phi \right) dV \\
&= \frac{1}{B_{\phi,0}} \frac{\partial}{\partial V} \int_V \left(-\frac{F}{\mu_0 R^2} \Delta^* \psi + \frac{1}{\mu_0 R^2} \frac{\partial F}{\partial \psi} \nabla\psi \cdot \nabla\psi \right) dV \\
&= \frac{1}{B_{\phi,0}} \frac{\partial}{\partial V} \int_V \left(-\frac{F}{\mu_0} \nabla \cdot \frac{\nabla\psi}{R^2} + \frac{1}{\mu_0 R^2} \frac{\partial F}{\partial \psi} \nabla\psi \cdot \nabla\psi \right) dV \\
&= -\frac{F}{\mu_0 B_{\phi,0}} \left\langle \nabla \cdot \frac{\nabla\psi}{R^2} \right\rangle + \frac{1}{\mu_0 B_{\phi,0}} \frac{\partial F}{\partial \psi} \left\langle \frac{1}{R^2} \nabla\psi \cdot \nabla\psi \right\rangle, \\
&= -\frac{F}{\mu_0 B_{\phi,0}} \frac{\partial}{\partial V} \left\langle \frac{\nabla\psi}{R^2} \cdot \nabla V \right\rangle + \frac{1}{\mu_0 B_{\phi,0}} \frac{\partial F}{\partial \rho} \frac{\partial \psi}{\partial \rho} \left\langle \frac{1}{R^2} \nabla\rho \cdot \nabla\rho \right\rangle \\
&= -\frac{F}{\mu_0 B_{\phi,0}} \frac{\partial}{\partial V} \left\{ \left\langle \frac{\nabla\rho}{R^2} \cdot \nabla V \right\rangle \frac{\partial \psi}{\partial \rho} \right\} + \frac{1}{\mu_0 B_{\phi,0}} \frac{\partial F}{\partial \rho} \frac{\partial \psi}{\partial \rho} \left\langle \frac{1}{R^2} \nabla\rho \cdot \nabla\rho \right\rangle \\
&= -\frac{F}{\mu_0 B_{\phi,0} V'} \frac{\partial}{\partial \rho} \left\{ V' \left\langle \frac{|\nabla\rho|^2}{R^2} \right\rangle \frac{\partial \psi}{\partial \rho} \right\} + \frac{1}{\mu_0 B_{\phi,0}} \frac{\partial F}{\partial \rho} \frac{\partial \psi}{\partial \rho} \left\langle \frac{|\nabla\rho|^2}{R^2} \right\rangle \\
&= -\frac{F^2}{\mu_0 B_{\phi,0} V'} \left[\frac{1}{F} \frac{\partial}{\partial \rho} \left\{ V' \left\langle \frac{|\nabla\rho|^2}{R^2} \right\rangle \frac{\partial \psi}{\partial \rho} \right\} - \frac{V'}{F^2} \frac{\partial F}{\partial \rho} \frac{\partial \psi}{\partial \rho} \left\langle \frac{|\nabla\rho|^2}{R^2} \right\rangle \right] \\
&= -\frac{F^2}{\mu_0 B_{\phi,0} V'} \frac{\partial}{\partial \rho} \left\{ \frac{V'}{F} \left\langle \frac{|\nabla\rho|^2}{R^2} \right\rangle \frac{\partial \psi}{\partial \rho} \right\},
\end{aligned} \tag{2.29}$$

where we have used (2.12), the property

$$\langle \nabla \cdot \mathbf{A} \rangle = \frac{\partial}{\partial V} \langle \mathbf{A} \cdot \nabla V \rangle,$$

and the definitions $\nabla\rho(\psi) = [\partial\rho/\partial\psi]\nabla\psi$ and $\nabla V(\psi) = [\partial V/\partial\psi]\nabla\psi$. By employing Faraday's Law, which is stated as

$$-\frac{\partial \mathbf{B}}{\partial t} = \nabla \times \mathbf{E}, \tag{2.30}$$

where t is the time, it can be shown that [124, 125]

$$\frac{\partial \psi}{\partial t} = -\frac{\langle \mathbf{E} \cdot \mathbf{B} \rangle}{F \langle R^{-2} \rangle}. \tag{2.31}$$

The term $\langle \mathbf{E} \cdot \mathbf{B} \rangle / B_{\phi,0}$ is then evaluated as

$$\frac{\langle \mathbf{E} \cdot \mathbf{B} \rangle}{B_{\phi,0}} = -\frac{F}{B_{\phi,0} \langle R^2 \rangle} \frac{\partial \psi}{\partial t}. \tag{2.32}$$

A derivation of (2.31) following the one described in [124] is now discussed. Firstly, we consider a magnetic flux surface ($\mathbf{S}_\psi$) defined by $\psi =$ constant that is moving with a constant velocity $\mathbf{u}_\psi$, which is defined by the relation

$$\frac{d}{dt}(\psi) = \frac{\partial \psi}{\partial t} + \mathbf{u}_\psi \cdot \nabla \psi = 0. \tag{2.33}$$

The toroidal magnetic flux enclosed by a magnetic flux surface is defined by (2.24), and the time rate of change of toroidal flux Φ that is enclosed by the surface $\mathbf{S}_\psi$ is evaluated as

$$\begin{aligned}
\left.\frac{\partial \Phi}{\partial t}\right|_{\psi=\text{constant}} &= \frac{\partial}{\partial t} \int \mathbf{B} \cdot d\mathbf{S}_\psi = \frac{1}{2\pi} \frac{\partial}{\partial t} \int \mathbf{B} \cdot \nabla \phi dV \\
&= \frac{1}{2\pi} \int \frac{\partial \mathbf{B}}{\partial t} \cdot \nabla \phi dV + \frac{1}{2\pi} \oint_{S_\psi} (\mathbf{B} \cdot \nabla \phi) \, \mathbf{u}_\psi \cdot d\mathbf{S}_\psi \quad \text{(see (2.35))} \\
&= \frac{1}{2\pi} \int \frac{\partial \mathbf{B}}{\partial t} \cdot \nabla \phi dV + \frac{1}{2\pi} \oint_{S_\psi} (\mathbf{B} \cdot \nabla \phi) \, \mathbf{u}_\psi \cdot \frac{\nabla \psi}{|\nabla \psi|} dS_\psi,
\end{aligned} \tag{2.34}$$

where we have used the relation $d\mathbf{S}_\psi = (\nabla \psi / |\nabla \psi|) dS_\psi$ and the theorem

$$\frac{\partial C}{\partial t} = \int \frac{\partial A}{\partial t} dV + \oint_{S_\psi} A \mathbf{u}_\psi \cdot d\mathbf{S}_\psi, \tag{2.35}$$

where $A(R, \phi, Z, t)$ is a general scalar field and $C(t) = \int A dV$ is a scalar. By employing Faraday's Law (2.30), the first term of (2.34) can be expressed as a surface

integral by employing the Divergence Theorem as

$$\begin{aligned}
\frac{1}{2\pi}\int \frac{\partial \mathbf{B}}{\partial t}\cdot\nabla\phi dV &= -\frac{1}{2\pi}\int (\nabla\times\mathbf{E})\cdot\nabla\phi dV \quad \text{(Faraday's Law)} \\
&= -\frac{1}{2\pi}\int \left[\nabla\cdot(\mathbf{E}\times\nabla\phi)+\mathbf{E}\cdot(\nabla\times\nabla\phi)\right] dV \quad \text{(Vector Identity)} \\
&= -\frac{1}{2\pi}\int \nabla\cdot(\mathbf{E}\times\nabla\phi)\, dV \quad \text{(Vector Identity)} \\
&= -\frac{1}{2\pi}\oint_{S_\psi} (\mathbf{E}\times\nabla\phi)\cdot\frac{\nabla\psi}{|\nabla\psi|}dS_\psi \quad \text{(Divergence Theorem)} \\
&= -\frac{1}{2\pi}\oint_{S_\psi} \mathbf{E}\cdot(\nabla\phi\times\nabla\psi)\frac{1}{|\nabla\psi|}dS_\psi \quad \text{(Vector Identity)} \\
&= -\frac{1}{2\pi}\oint_{S_\psi} \mathbf{E}\cdot\left(\frac{1}{R}\frac{\partial\psi}{\partial Z}\mathbf{e}_R-\frac{1}{R}\frac{\partial\psi}{\partial R}\mathbf{e}_Z\right)\frac{1}{|\nabla\psi|}dS_\psi \\
&= \frac{1}{2\pi}\oint_{S_\psi} \mathbf{E}\cdot\mathbf{B}_\theta\frac{1}{|\nabla\psi|}dS_\psi, \qquad (2.36)
\end{aligned}$$

where we have used (2.9). Evaluating the component of (2.30) parallel to $\nabla\psi$ results in

$$\nabla\psi\cdot\frac{\partial\mathbf{B}}{\partial t} = -\nabla\psi\cdot(\nabla\times\mathbf{E})\,. \qquad (2.37)$$

The left-hand-side of (2.37) can be evaluated as follows. Since the magnetic field lines lie on the magnetic flux surfaces, we know from (2.10) that $\nabla\psi\cdot\mathbf{B}=0$. Therefore, we can write

$$\frac{\partial}{\partial t}(\nabla\psi\cdot\mathbf{B}) = \nabla\psi\cdot\frac{\partial\mathbf{B}}{\partial t}+\mathbf{B}\cdot\frac{\partial}{\partial t}(\nabla\psi)=0,$$

which implies that

$$\nabla\psi\cdot\frac{\partial\mathbf{B}}{\partial t} = -\mathbf{B}\cdot\frac{\partial}{\partial t}(\nabla\psi) = -\mathbf{B}\cdot\nabla\frac{\partial\psi}{\partial t}. \qquad (2.38)$$

The right-hand-side of (2.37) is evaluated as

$$
\begin{aligned}
-\nabla\psi\cdot(\nabla\times\mathbf{E}) &= -\nabla\cdot(\mathbf{E}\times\nabla\psi)-\mathbf{E}\cdot(\nabla\times\nabla\psi) \quad \text{(Vector Identity)}\\
&= -\nabla\cdot(\mathbf{E}\times\nabla\psi) \quad \text{(Vector Identity)}\\
&= -\nabla\cdot\left([E_R\mathbf{e}_R+E_\phi\mathbf{e}_\phi+E_Z\mathbf{e}_Z]\times\left[\frac{\partial\psi}{\partial R}\mathbf{e}_R+\frac{1}{R}\frac{\partial\psi}{\partial\phi}\mathbf{e}_\phi+\frac{\partial\psi}{\partial Z}\mathbf{e}_Z\right]\right)\\
&= -\nabla\cdot\left(\frac{\partial\psi}{\partial Z}E_\phi\mathbf{e}_R+\left[\frac{\partial\psi}{\partial R}E_Z-E_R\frac{\partial\psi}{\partial Z}\right]\mathbf{e}_\phi-\frac{\partial\psi}{\partial R}E_\phi\mathbf{e}_Z\right)\\
&= -\nabla\cdot\left(\frac{\partial\psi}{\partial Z}E_\phi\mathbf{e}_R-\frac{\partial\psi}{\partial R}E_\phi\mathbf{e}_Z\right) \text{ as } \nabla\cdot\left(\left[\frac{\partial\psi}{\partial R}E_Z-E_R\frac{\partial\psi}{\partial Z}\right]\mathbf{e}_\phi\right)=0\\
&= \nabla\cdot(R\mathbf{B}_\theta E_\phi)\\
&= \nabla\cdot(\mathbf{B}RE_\phi) \text{ as } \nabla\cdot(RB_\phi E_\phi\mathbf{e}_\phi)=0\\
&= RE_\phi(\nabla\cdot\mathbf{B})+\mathbf{B}\cdot\nabla(RE_\phi) \quad \text{(Vector Identity)}\\
&= \mathbf{B}\cdot\nabla(RE_\phi) \quad \text{(Gauss's Law (2.3))},
\end{aligned}
\tag{2.39}
$$

where we have used (2.9). Therefore, combining (2.37)-(2.39), we obtain

$$
\frac{\partial\psi}{\partial t}=-RE_\phi=-\mathbf{u}_\psi\cdot\nabla\psi, \tag{2.40}
$$

where we have used (2.33). Combining (2.34) with (2.36) and (2.40), we obtain

$$
\begin{aligned}
\left.\frac{\partial\Phi}{\partial t}\right|_{\psi=\text{constant}} &= \frac{1}{2\pi}\oint_{S_\psi}\mathbf{E}\cdot\mathbf{B}_\theta\frac{1}{|\nabla\psi|}dS_\psi+\frac{1}{2\pi}\oint_{S_\psi}(\mathbf{B}\cdot\nabla\phi)\,RE_\phi\frac{1}{|\nabla\psi|}dS_\psi\\
&= \frac{1}{2\pi}\oint_{S_\psi}(\mathbf{E}\cdot\mathbf{B}_\theta+B_\phi E_\phi)\,\frac{1}{|\nabla\psi|}dS_\psi\\
&= \frac{1}{2\pi}\oint_{S_\psi}(\mathbf{E}\cdot\mathbf{B})\,\frac{1}{|\nabla\psi|}dS_\psi\\
&= \frac{1}{2\pi}\frac{\partial V}{\partial\psi}\langle\mathbf{E}\cdot\mathbf{B}\rangle,
\end{aligned}
\tag{2.41}
$$

where the last equivalence relation follows from the definition of the flux-surface

average operation [124]. Finally, from the relation

$$\left.\frac{\partial \Phi}{\partial t}\right|_{\Phi=\text{constant}} = \left.\frac{\partial \Phi}{\partial t}\right|_{\psi=\text{constant}} + \frac{\partial \Phi}{\partial V}\frac{\partial V}{\partial \psi}\left.\frac{\partial \psi}{\partial t}\right|_{\Phi=\text{constant}} \equiv 0,$$

we obtain (2.31) by solving for $\partial\psi/\partial t$, which is evaluated as

$$\left.\frac{\partial \psi}{\partial t}\right|_{\Phi=\text{constant}} = -\frac{\partial V}{\partial \Phi}\frac{\partial \psi}{\partial V}\left.\frac{\partial \Phi}{\partial t}\right|_{\Phi=\text{constant}} = -\frac{1}{2\pi}\frac{\partial V}{\partial \Phi}\langle \mathbf{E}\cdot\mathbf{B}\rangle = -\frac{\langle \mathbf{E}\cdot\mathbf{B}\rangle}{F\langle R^{-2}\rangle}, \tag{2.42}$$

where we have used (2.25) and (2.41).

By combining (2.28), (2.29), and (2.32) we obtain

$$-\eta\frac{F^2}{\mu_0 B_{\phi,0}V'}\frac{\partial}{\partial \rho}\left\{\frac{V'}{F}\left\langle\frac{|\nabla\rho|^2}{R^2}\right\rangle\frac{\partial \psi}{\partial \rho}\right\} = -\frac{F}{B_{\phi,0}\langle R^2\rangle}\frac{\partial \psi}{\partial t} + \eta j_{ni},$$

which can be rearranged to obtain

$$\frac{\partial \psi}{\partial t} = \frac{\eta F\langle R^2\rangle}{\mu_0 V'}\frac{\partial}{\partial \rho}\left\{\frac{V'}{F}\left\langle\frac{|\nabla\rho|^2}{R^2}\right\rangle\frac{\partial \psi}{\partial \rho}\right\} + \frac{\eta B_{\phi,0}\langle R^2\rangle}{F}j_{ni}. \tag{2.43}$$

We now rewrite (2.43) by using (2.26), the definition of the normalized mean effective minor radius of the magnetic flux surface ($\hat{\rho} = \rho/\rho_b$), and the geometric factors

$$\hat{F}(\hat{\rho}) = \frac{R_0 B_{\phi,0}}{F} \qquad \hat{G}(\hat{\rho}) = \left\langle\frac{R_0^2}{R^2}|\nabla\rho|^2\right\rangle \qquad \hat{H}(\hat{\rho}) = \frac{\hat{F}}{\left\langle R_0^2/R^2\right\rangle}, \tag{2.44}$$

to obtain the poloidal magnetic flux diffusion equation [124,125], which is expressed as

$$\frac{\partial \psi}{\partial t} = \frac{\eta}{\mu_0\rho_b^2\hat{F}^2}\frac{1}{\hat{\rho}}\frac{\partial}{\partial \hat{\rho}}\left(\hat{\rho}\hat{F}\hat{G}\hat{H}\frac{\partial \psi}{\partial \hat{\rho}}\right) + R_0\hat{H}\eta j_{ni}. \tag{2.45}$$

The boundary conditions are given by

$$\left.\frac{\partial \psi}{\partial \hat{\rho}}\right|_{\hat{\rho}=0} = 0 \qquad \left.\frac{\partial \psi}{\partial \hat{\rho}}\right|_{\hat{\rho}=1} = -\frac{\mu_0}{2\pi}\frac{R_0}{\hat{G}(1)\hat{H}(1)}I_p(t), \tag{2.46}$$

where $I_p(t)$ is the total plasma current. The model (2.45)-(2.46) makes the simplifying assumption that the magnetic geometry is fixed in time, which excludes two potential sources of flux: (i) a change in ρ_b, either by a change in the shape of the last closed flux surface or in $B_{\phi,0}$ and (ii) a change in location of the geometric center of the interior flux surfaces relative to that of the last closed flux surface, such as changes in the Shafranov shift that occur during a plasma energy or internal inductance change. The assumption that the plasma surface can be considered fixed assumes that a separate poloidal field (PF) coil controller, which is not considered, provides this fixed surface on a faster timescale than the energy confinement.

2.4 Physics-based modeling of plasma parameters

In this section, we develop simplified physics-based, control-oriented models of the electron density, the electron temperature, the plasma resistivity, and the noninductive current drives in response to the available control actuators (total plasma current, auxiliary heating and current-drive system, electron density) to convert the physics model (2.45)-(2.46) into a form suitable for control design, hence obtaining a *first-principles-driven* model of the poloidal magnetic flux dynamics. In this work, physical quantities are used as actuators, although they are quantities which are themselves controlled by feedback loops. Thus, quantities such as the total plasma current and electron density are considered as actuators since they appear as control inputs in the physics models. In other words, the control algorithms developed in this work will generate references for the respective physical quantities that are sent to the dedicated feedback control loops that command the physical actuators on the tokamak. Additionally, we exploit the fact that the dynamics of the physical actuator feedback control loops are faster than that of the system we are controlling, i.e., we assume that

the dedicated control loops are able to instantaneously follow the references generated by the controllers developed in this work. As a result, the fact that the physical quantities have power supplies and gas valves is not taken into account here.

The objective in developing simplified physics-based models of the plasma parameters is to capture the dominant physics that describe how the control actuators affect the plasma parameters, and hence the ψ profile evolution. We emphasize the models developed are not designed for physical understanding, rather they are meant to capture the dominant physics which affect the overall system dynamics that are relevant for control design, i.e., the input-output relationship of the system. This implies that a controller synthesized by employing the control-oriented model only needs to know about the physics that are relevant to its design objective. The control-oriented models (and hence the first-principles-driven model) can then be tailored to a given operating scenario in a given machine of interest by employing experimental and simulated (from an advanced physics simulation code TRANSP [12], DINA-CH&CRONOS [5–9], etc.) data.

2.4.1 Electron density modeling

In the formulation of the electron density model, we assume the control action employed to regulate the electron density only weakly affects the radial distribution of the electrons. Therefore, the electron density evolution $n_e(\hat{\rho}, t)$ is modeled as

$$n_e(\hat{\rho}, t) = n_e^{prof}(\hat{\rho})\bar{n}_e(t), \tag{2.47}$$

where n_e^{prof} is a reference electron density profile and $\bar{n}_e$ is the line average electron density, which is typically utilized to specify the electron density in present tokamak operation. Note that n_e^{prof} is obtained by evaluating the experimental/simulated n_e at a reference time $t_{r_{n_e}}$, i.e., $n_e^{prof}(\hat{\rho}) = n_e(\hat{\rho}, t_{r_{n_e}})/\bar{n}_e(t_{r_{n_e}})$.

2.4.2 Electron temperature modeling

In the formulation of the model of the electron temperature (T_e) evolution, we assume a tight coupling between the electron and ion species in the plasma, i.e., $T_e(\hat{\rho},t) \approx T_i(\hat{\rho},t)$ and $n_e(\hat{\rho},t) \approx n_i(\hat{\rho},t)$, where $T_i(\hat{\rho},t)$ and $n_i(\hat{\rho},t)$ are the ion temperature and density profiles, respectively.

Physics model approach: Electron heat transport equation

Under the simplifying assumption of a fixed magnetic geometry (both the plasma boundary as well as the orientation of the internal magnetic flux surfaces), and assuming diffusion is the dominant heat transport mechanism in the tokamak plasma, the electron temperature dynamics are given by the electron heat transport equation [7]

$$\frac{3}{2}\frac{\partial}{\partial t}\left[n_e T_e\right] = \frac{1}{\rho_b^2 \hat{H}}\frac{1}{\hat{\rho}}\frac{\partial}{\partial \hat{\rho}}\left[\hat{\rho}\frac{\hat{G}\hat{H}^2}{\hat{F}}\left(\chi_e n_e \frac{\partial T_e}{\partial \hat{\rho}}\right)\right] + Q_e, \tag{2.48}$$

with boundary conditions

$$\left.\frac{\partial T_e}{\partial \hat{\rho}}\right|_{\hat{\rho}=0} = 0 \qquad T_e\big|_{\hat{\rho}=1} = T_{e,bdry}, \tag{2.49}$$

where $\chi_e(\hat{\rho},t)$ is the electron thermal conductivity, $Q_e(\hat{\rho},t)$ is the total electron heating power density, and $T_{e,bdry}$ is the electron temperature at the plasma boundary, which is assumed constant. Typically, the electron temperature is specified in units of kilo-electron-volts (keV) in the plasma physics community.

The total electron heating power density is expressed as

$$Q_e(\hat{\rho},t) = \frac{1}{k_{JkeV}}\left[Q_{ohm}(\hat{\rho},t) + \sum_{i=1}^{n_{aux}} Q_{aux_i}(\hat{\rho},t) - Q_{rad}(\hat{\rho},t) + \eta_{fus}Q_{fus}(\hat{\rho},t)\right], \tag{2.50}$$

where Q_{ohm} is the ohmic heating power density, Q_{aux_i} is the power density produced by

the individual auxiliary sources, Q_{rad} is the radiated power density, Q_{fus} is the fusion power density, n_{aux} is the total number of individual auxiliary heating sources, η_{fus} represents the effectiveness of the fusion power in heating the plasma, and $k_{JkeV} = e \times 1\text{V} \times 1000$, where e is the elementary charge. Due to the assumption of a tight coupling between the electron and ion species in the plasma, we have neglected the explicit electron-ion equilibration power density. The ohmic power density is modeled as

$$Q_{ohm}(\hat{\rho}, t) = j_{tor}(\hat{\rho}, t)^2 \eta(\hat{\rho}, t), \tag{2.51}$$

where the total toroidal current density is expressed as [70]

$$j_{tor}(\hat{\rho}, t) = -\frac{1}{\mu_0 \rho_b^2 R_0 \hat{H}} \frac{1}{\hat{\rho}} \frac{\partial}{\partial \hat{\rho}} \left(\hat{\rho} \hat{G} \hat{H} \frac{\partial \psi}{\partial \hat{\rho}} \right).$$

The individual auxiliary power densities are modeled as

$$\begin{aligned} Q_{aux_i}(\hat{\rho}, t) &= k^q_{aux_i} Q^{dep}_{aux_i}(\hat{\rho}) \eta_{aux_i} P_{aux_i}(t) \\ &= Q^{ref}_{aux_i}(\hat{\rho}) \eta_{aux_i} P_{aux_i}(t), \end{aligned} \tag{2.52}$$

where $k^q_{aux_i}$ is a normalizing constant, $Q^{dep}_{aux_i}$ is a reference power density deposition profile for each auxiliary source, the effectiveness each respective source has on heating the plasma is captured through the efficiency constant η_{aux_i}, $P_{aux,i}$ is the power injected through the i-th auxiliary source, and $Q^{ref}_{aux,i} = k^q_{aux_i} Q^{dep}_{aux_i}$. Note that $Q^{dep}_{aux,i}$ is obtained by evaluating the experimental/simulated $Q_{aux,i}$ at a reference time $t_{r_{T_e}}$, i.e., $Q^{dep}_{aux,i}(\hat{\rho}) = Q_{aux,i}(\hat{\rho}, t_{r_{T_e}})$. The constant $k^q_{aux_i}$ is also evaluated at the time $t_{r_{T_e}}$ and is expressed as $k^q_{aux_i} = 1/[\eta_{aux_i} P_{aux_i}(t_{r_{T_e}})]$. The radiated power density is comprised of Bremsstrahlung, line, and cyclotron radiation losses. In modern tokamaks,

the dominant radiative power density losses are due to Bremsstrahlung radiation[1], which is modeled as [18]

$$Q_{rad}(\hat{\rho},t) = k_{brem} Z_{eff} n_e(\hat{\rho},t)^2 \sqrt{T_e(\hat{\rho},t)}, \tag{2.53}$$

where $k_{brem} = 5.5 \times 10^{-37}$ $\mathrm{Wm}^3/\sqrt{\mathrm{keV}}$ is the Bremsstrahlung radiation coefficient and Z_{eff} is the effective average charge of the ions in the plasma, which is defined as

$$Z_{eff} = \frac{1}{n_e} \sum_{\text{all ions}} n_j Z_j^2,$$

where n_j and Z_j are the density and charge of the j-th ion species. In this work, we assume Z_{eff} to be constant in space and time. The fusion power density (for a deuterium (D) and tritium (T) fuel) is expressed as

$$Q_{fus}(\hat{\rho},t) = Q_{DT} n_D(\hat{\rho},t) n_T(\hat{\rho},t) \left\langle \sigma v \right\rangle_{DT}(\hat{\rho},t) k_{JeV}, \tag{2.54}$$

where $Q_{DT} = 17.6$ MeV is the energy released in each $D-T$ reaction, $n_D(\hat{\rho},t)$ and $n_T(\hat{\rho},t)$ are the density of the deuterium and tritium ions, respectively, and $k_{JeV} = e \times 1\mathrm{V}$. The deuterium-tritium reactivity $\left\langle \sigma v \right\rangle_{DT}$ is dependent on the velocity distribution of the deuterium and tritium ions, which is a bounded nonlinear function of the deuterium and tritium temperature $T_{DT}(\hat{\rho},t)$. From [1], $\left\langle \sigma v \right\rangle_{DT}$ is given in units of $\mathrm{cm}^3 \cdot \mathrm{s}^{-1}$ by

$$\left\langle \sigma v \right\rangle_{DT}(\hat{\rho},t) = \exp\left(\frac{a_1}{T_{DT}^r} + a_2 + a_3 T_{DT} + a_4 T_{DT}^2 + a_5 T_{DT}^3 + a_6 T_{DT}^4 \right), \tag{2.55}$$

where T_{DT} is in keV, the constants a_i and r are given in Table I of [1], and we have

[1] Whenever a charged particle experiences an acceleration/deceleration, i.e., a change in velocity, it will radiate electromagnetic energy, which is referred to as Bremsstrahlung radiation. In a plasma, coulomb scattering collisions will cause acceleration/deceleration of charged particles and will therefore result in the emission of Bremsstrahlung radiation.

neglected non-thermal ions which might enhance the reactivity.

Singular perturbation approach: Exploiting characteristic time scale difference between energy confinement and resistive current diffusion

Ideally, one would like to model the evolution of the electron temperature profile using the electron heat transport equation (2.48)-(2.49). However, due to the complexity of modeling the local thermal transport, i.e., χ_e, it is difficult to model the electron temperature dynamics in this way. The local thermal transport is intimately dependent on the local magnetic and kinetic state of the plasma [61,62], and closed-form expressions, i.e., explicit first-principles knowledge, that represent this complex interaction do not exist. There are multiple computationally intensive numerical simulation codes that calculate plasma transport coefficients, under some approximations, for a given plasma state, with some examples being GLF [128] and GLF23 (a linearized version of GLF) [129]. Alternatively, closed-form expressions for plasma transport can be derived from empirical scalings, with some examples being Coppi–Tang [130] and Bohm–Gyrobohm [131]. Finally, expressions for how the electron temperature responds to changes in the control actuators can be obtained from scaling laws [83,84]. In this work, we utilize the scaling law approach.

Under the assumption of a tight coupling between the electron and ion species in the plasma, the plasma kinetic pressure (p) and total stored thermal energy density (E_d) are expressed as

$$\begin{aligned} p(\hat{\rho},t) &= k_{JkeV}\left[n_e(\hat{\rho},t)T_e(\hat{\rho},t) + n_i(\hat{\rho},t)T_i(\hat{\rho},t)\right] \\ &= 2k_{JkeV}n_e(\hat{\rho},t)T_e(\hat{\rho},t), \end{aligned} \tag{2.56}$$

$$\begin{aligned} E_d(\hat{\rho},t) &= k_{JkeV}\left[\frac{3}{2}n_e(\hat{\rho},t)T_e(\hat{\rho},t) + \frac{3}{2}n_i(\hat{\rho},t)T_i(\hat{\rho},t)\right] \\ &= 3k_{JkeV}n_e(\hat{\rho},t)T_e(\hat{\rho},t). \end{aligned} \tag{2.57}$$

The expression for E_d given in (2.57) results from the assumption that the distribution of the plasma particles in energy is given by a Maxwell-Boltzmann distribution, which is derived from statistical mechanics. Note that the Maxwell-Boltzmann distribution only strictly applies to systems of particles that are in thermodynamic equilibrium, i.e., a system that possesses no strong sinks/sources of particles or energy. In fusion relevant plasmas, this is generally not the case as there are strong sinks (particle and energy loss from the plasma) and sources (particle fueling, auxiliary and fusion heating). Nevertheless, it is observed that many phenomena in fusion plasmas are well represented by assuming a Maxwell-Boltzmann distribution. The stored thermal energy (E) in the plasma is expressed as

$$E(t) = \int_0^1 E_d(\hat{\rho}, t) \frac{\partial V}{\partial \hat{\rho}} d\hat{\rho} = 3 k_{JkeV} \langle n_e \rangle_V \langle T_e \rangle_V V_p, \tag{2.58}$$

where $\langle \cdot \rangle_V$ denotes the volume-average operation $1/V_p \int_V (\cdot) dV$ and V_p denotes the total plasma volume. Additionally, under the fixed magnetic geometry assumption, the plasma power balance equation is given by the ordinary differential equation

$$\begin{aligned} \frac{dE}{dt} &= -P_{loss}(t) + P_{ohm}(t) + P_{aux}(t) - P_{rad}(t) + \eta_{fus} P_{fus}(t), \\ &= -\frac{E}{\tau_E(t)} + P_{tot}(t), \end{aligned} \tag{2.59}$$

where $P_{loss} = E/\tau_E$ is the total power crossing the plasma boundary, τ_E is the global energy confinement time, P_{ohm} is the ohmic power, P_{aux} is the total auxiliary heating and current-drive power, P_{rad} is the radiated power, P_{fus} is the fusion power, and

$$P_{tot} = P_{ohm} + P_{aux} - P_{rad} + \eta_{fus} P_{fus} \tag{2.60}$$

is the total power injected into the plasma.

The characteristic energy confinement time in the plasma is much faster than the

characteristic resistive current diffusion time. Therefore, the temperature is always in quasi-equilibrium on the time-scale of the poloidal magnetic flux evolution. As a result, we neglect the temporal dynamics of the electron temperature in the development of the electron temperature evolution model, as we are mainly concerned with capturing the dominant physical effects that the electron temperature has on the poloidal magnetic flux profile evolution. Evaluating (2.59) at steady state ($d/dt = 0$), we obtain

$$\frac{3k_{JkeV}\langle n_e\rangle_V\langle T_e\rangle_V V_p}{\tau_E} = P_{tot}. \tag{2.61}$$

Various energy confinement scaling expressions have been developed over the years to fit experimentally observed plasma behavior, such as the IPB98(y,2) [132] and Goldston scaling expressions [133]. Typically, these scaling expressions are proportional to the actuators utilized for plasma control, i.e., $\tau_E \propto I_p^{\gamma_s} P_{tot}^{\varepsilon_s} n_e^{\zeta_s}$, where γ_s, ε_s, and ζ_s depend on the scaling expression utilized. If, as with the IPB98(y,2) and Goldston scaling expressions, τ_E is not an explicit function of the temperature, we can solve (2.61) for the temperature to obtain

$$\langle T_e\rangle_V \propto I_p^{\gamma_s} P_{tot}^{(1+\varepsilon_s)} \langle n_e\rangle_V^{(\zeta_s-1)}. \tag{2.62}$$

Utilizing the results of this analysis, we model the slowly evolving (on the resistive current diffusion time scale) electron temperature evolution $T_e(\hat{\rho}, t)$ as a static map of the control actuators, which is expressed as

$$T_e(\hat{\rho}, t) = k_{T_e}(\hat{\rho}) T_e^{prof}(\hat{\rho}) I_p(t)^{\gamma} P_{tot}(t)^{\varepsilon} n_e(\hat{\rho}, t)^{\zeta}, \tag{2.63}$$

where k_{T_e} is a normalizing profile and $T_e^{prof}(\hat{\rho})$ is a reference electron temperature profile. The constants γ, ε, and ζ describe how the temperature scales with the various parameters. Note that T_e^{prof} is obtained by evaluating the experimental/simulated T_e

at a reference time $t_{r_{T_e}}$, i.e., $T_e^{prof}(\hat{\rho}) = T_e(\hat{\rho}, t_{r_{T_e}})$. The constant k_{T_e} is also evaluated at the time $t_{r_{T_e}}$ and is expressed as

$$k_{T_e}(\hat{\rho}) = \left[I_p(t_{r_{T_e}})^{\gamma} P_{tot}(t_{r_{T_e}})^{\varepsilon} n_e(\hat{\rho}, t_{r_{T_e}})^{\zeta} \mathrm{A}^{\gamma} \cdot \mathrm{W}^{\varepsilon} \cdot \mathrm{m}^{(-3)^{\zeta}} \right]^{-1}. \tag{2.64}$$

In low performance (L-mode) tokamak operating scenarios (characterized by low energy confinement) there are no abrupt changes in particle and energy transport across the spatial domain. As a result, the plasma density and temperature exhibit a smooth behavior across the entire spatial domain in this regime. Therefore, the electron temperature model (2.63) is applicable across the entire spatial domain. In contrast, high performance (H-mode) tokamak operating scenarios are characterized by particle and energy transport barriers [18] just inside the plasma boundary. These transport barriers improve the plasma performance (a higher energy confinement compared to L-mode) and result in the formation of large gradients in both the plasma density and temperature. Therefore, the plasma density and temperature may exhibit a different behavior in the plasma core (inside of the transport barriers) and near the plasma boundary (outside of the transport barriers) in this regime. This behavior can be incorporated into the formulation of the electron temperature model by modeling the electron temperature evolution as

$$\begin{aligned} T_e(\hat{\rho}, t) = {} & k_{T_e}^1(\hat{\rho}) \left[T_e^{prof}(\hat{\rho}) - T_e^{prof}(\hat{\rho}_{tb}) \right] I_p(t)^{\gamma} P_{tot}(t)^{\varepsilon} n_e(\hat{\rho}, t)^{\zeta} \\ & + k_{T_e}^2(\hat{\rho}_{tb})^{\omega} T_e^{prof}(\hat{\rho}_{tb}) I_p(t)^{\lambda} P_{tot}(t)^{\nu} n_e(\hat{\rho}_{tb}, t)^{\xi} \end{aligned} \tag{2.65}$$

in the plasma core ($0 \leq \hat{\rho} < \hat{\rho}_{tb}$) and as

$$T_e(\hat{\rho}) = k_{T_e}^2(\hat{\rho})^{\omega} T_e^{prof}(\hat{\rho}) I_p(t)^{\lambda} P_{tot}(t)^{\nu} n_e(\hat{\rho}, t)^{\xi} \tag{2.66}$$

outside of the edge energy transport barrier ($\hat{\rho}_{tb} \leq \hat{\rho} \leq 1$), where $k_{T_e}^1$ and $k_{T_e}^2$ are

normalizing profiles and $\hat{\rho}_{tb}$ is the spatial location of the edge energy transport barrier. The constants γ, ε, and ζ describe how the temperature in the plasma core scales with the various parameters. The constants λ, ν, and ξ describe how the temperature outside of the edge energy transport barrier scales with the various parameters. Note that the constant ω is 1 if the temperature outside of the edge energy transport barrier scales with the various parameters and is 0 otherwise. The constants $k^1_{T_e}$ and $k^2_{T_e}$ are evaluated at the time $t_{r_{T_e}}$ and are expressed as

$$\begin{aligned} k^1_{T_e}(\hat{\rho}) &= \left[I_p(t_{r_{T_e}})^{\gamma} P_{tot}(t_{r_{T_e}})^{\varepsilon} n_e(\hat{\rho}, t_{r_{T_e}})^{\zeta} \mathrm{A}^{\gamma} \cdot \mathrm{W}^{\varepsilon} \cdot \mathrm{m}^{(-3)\zeta} \right]^{-1}, \\ k^2_{T_e}(\hat{\rho}) &= \left[I_p(t_{r_{T_e}})^{\lambda} P_{tot}(t_{r_{T_e}})^{\nu} n_e(\hat{\rho}, t_{r_{T_e}})^{\xi} \mathrm{A}^{\lambda} \cdot \mathrm{W}^{\nu} \cdot \mathrm{m}^{(-3)\xi} \right]^{-1}, \end{aligned} \tag{2.67}$$

where $k^1_{T_e}$ is defined on the interval $0 \leq \hat{\rho} < \hat{\rho}_{tb}$ and $k^2_{T_e}$ is defined on the interval $\hat{\rho}_{tb} \leq \hat{\rho} \leq 1$.

We now describe the models of the individual plasma heating sources in (2.59). The ohmic power can be obtained from (2.51) and is expressed as

$$P_{ohm}(t) = \int_0^1 Q_{ohm}(\hat{\rho}, t) \frac{\partial V}{\partial \hat{\rho}} d\hat{\rho} \approx \mathcal{R}_p(t) I_p(t)^2, \tag{2.68}$$

where $\mathcal{R}_p$ is the global plasma resistance, which is expressed as

$$\mathcal{R}_p(t) \approx 2\pi R_0 \Big/ \int_0^1 \left[\frac{1}{\eta(\hat{\rho}, t)} \frac{\partial S}{\partial \hat{\rho}} d\hat{\rho} \right],$$

where S is the poloidal cross-sectional area enclosed by a magnetic flux surface within the plasma. The auxiliary heating and current-drive actuators considered in this work are electron cyclotron (ec) sources, ion cyclotron (ic) sources, and neutral beam injection (nbi) sources. Therefore, the total auxiliary heating and current-drive power

is expressed as

$$P_{aux}(t) = \sum_{i=1}^{n_{ec}} \eta_{ec_i} P_{ec_i}(t) + \sum_{i=1}^{n_{ic}} \eta_{ic_i} P_{ic_i}(t) + \sum_{i=1}^{n_{nbi}} \eta_{nbi_i} P_{nbi_i}(t), \tag{2.69}$$

where P_{ec_i} is the power injected through the individual electron cyclotron (gyrotron) launchers, P_{ic_i} is the power injected through the individual ion cyclotron launchers, P_{nbi_i} is the power injected through the individual neutral beam injectors, and n_{ec}, n_{ic}, and n_{nbi} are the total number of gyrotron, ion cyclotron, and neutral beam launchers, respectively. The effectiveness each respective source has on heating the plasma is captured through the efficiency constants η_{ec_i}, η_{ic_i}, and η_{nbi_i}, respectively. The radiated power can be obtained from (2.53) and is expressed as

$$P_{rad}(t) = \int_0^1 Q_{rad}(\hat{\rho}, t) \frac{\partial V}{\partial \hat{\rho}} d\hat{\rho}. \tag{2.70}$$

Finally, the fusion power can be obtained from (2.54) and is expressed as

$$P_{fus}(t) = \int_0^1 Q_{fus}(\hat{\rho}, t) \frac{\partial V}{\partial \hat{\rho}} d\hat{\rho}. \tag{2.71}$$

Under our working assumption of an approximately equal electron and ion temperature we evaluate (2.55) with $T_{DT} = T_e$.

2.4.3 Plasma resistivity modeling

The plasma resistivity η scales inversely with the electron temperature. In this work, we model the plasma resistivity by utilizing a simplified Spitzer resistivity model, which we express as

$$\eta(\hat{\rho}, t) = \frac{k_{sp}(\hat{\rho}) Z_{eff}}{T_e(\hat{\rho}, t)^{3/2}}. \tag{2.72}$$

The profile k_{sp} is obtained from the experimental/simulated η at a reference time t_{r_η} and is expressed as

$$k_{sp}(\hat{\rho}) = \frac{\eta(\hat{\rho}, t_{r_\eta}) T_e(\hat{\rho}, t_{r_\eta})^{3/2}}{Z_{eff}} \ \Omega\mathrm{m}(\mathrm{keV})^{3/2}. \tag{2.73}$$

Neoclassical corrections to this formula exist in the literature [134, 135], however, in this work, we neglect these corrections, which can nonetheless be significant, to retain the main temperature dependence.

2.4.4 Noninductive current drive modeling

The total noninductive current drive is produced by the combination of the auxiliary sources and the bootstrap current [60] and is expressed as

$$j_{ni}(\hat{\rho}, t) = j^{tot}_{aux}(\hat{\rho}, t) + j_{bs}(\hat{\rho}, t), \tag{2.74}$$

where j^{tot}_{aux} is the total current density driven by the auxiliary sources and j_{bs} is the current density driven by the bootstrap current. The total auxiliary current drive is generated by the electron cyclotron and neutral beam injection sources and is expressed as

$$j^{tot}_{aux}(\hat{\rho}, t) = \sum_{i=1}^{n_{ec}} j_{ec_i}(\hat{\rho}, t) + \sum_{i=1}^{n_{nbi}} j_{nbi_i}(\hat{\rho}, t), \tag{2.75}$$

where j_{ec_i} is the current density generated by the individual gyrotron launchers and j_{nbi_i} is the current density generated by the individual neutral beam injectors. In the operating scenarios considered in this work, the ion cyclotron launchers are configured to provide only heating power to the plasma.

Electron cyclotron and neutral beam injection current drive

We model each auxiliary current-drive source as the time varying power injected through each actuator multiplied by a constant deposition profile in space. The current density provided by each auxiliary source is modeled as

$$\begin{aligned} j_i(\hat{\rho},t) &= k_i(\hat{\rho}) j_i^{dep}(\hat{\rho}) \frac{T_e(\hat{\rho},t)^\delta}{n_e(\hat{\rho},t)} \eta_i P_i(t) \\ &= j_i^{ref}(\hat{\rho}) \frac{T_e(\hat{\rho},t)^\delta}{n_e(\hat{\rho},t)} \eta_i P_i(t), \end{aligned} \tag{2.76}$$

where $i \in [ec_1, \ldots, ec_{n_{ec}}, nbi_1, \ldots, nbi_{n_{nbi}}]$, k_i is a normalizing profile, j_i^{dep} is a reference current density deposition profile for each auxiliary source, the term T_e^δ/n_e represents the current-drive efficiency, and $j_i^{ref} = k_i j_i^{dep}$. Note that j_i^{dep} is obtained by evaluating the experimental/simulated j_i at a reference time $t_{r_{aux}}$, i.e., $j_i^{dep}(\hat{\rho}) = j_i(\hat{\rho}, t_{r_{aux}})$. The constant k_i is also evaluated at the time $t_{r_{aux}}$ and is expressed as

$$k_i(\hat{\rho}) = \frac{n_e(\hat{\rho}, t_{r_{aux}})}{T_e(\hat{\rho}, t_{r_{aux}})^\delta \eta_i P_i(t_{r_{aux}})} \frac{\mathrm{m}^{-3}}{\mathrm{keV}^\delta \cdot \mathrm{W}}. \tag{2.77}$$

The auxiliary neutral beam heating and current-drive models, (2.69) and (2.76), respectively, neglect the slowing down time (τ_s) of the fast ions (injected neutral particles) [18] and assume the particles and their energy are instantaneously thermalized (deposited) in the plasma. If this physical mechanism is determined to be significant based on the analysis of experimental data, a first-order filter could straightforwardly be included in the models to describe this physical mechanism, i.e.,

$$\dot{P}_{nbi} = -\frac{1}{\tau_s} P_{nbi} + \frac{1}{\tau_s} P_{nbi}^{inj}, \tag{2.78}$$

where P_{nbi}^{inj} is the power injected through the neutral beam source and P_{nbi} (input to (2.69) and (2.76)) is the absorbed power. Finally, for electron cyclotron current

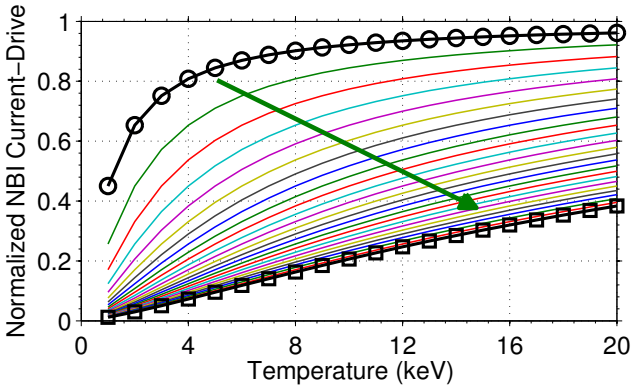

Figure 2.4: Normalized neutral beam driven current (2.79) as a function of temperature for a specific plasma composition and various values of the injected neutral particle energy (from 40 keV to 1 MeV). The green arrow denotes increasing injected particle energy. Note E_{beam} = 40 keV (black line + circle) and E_{beam} = 1 MeV (black line + square).

drive, $\delta = 1$ [66] and for neutral beam current drive, δ is dependent on the energy of the injected particles [65]. From [65] the normalized neutral beam driven current (I^*_{cd}) is expressed as a function of the temperature as

$$I^*_{cd}(T_e) = c_1 \left(\frac{T_e}{T_c}\right)^{3/2} \frac{(T_c/T_e)^{3/2}}{c_1 + c_2\,(T_c/T_e) + (T_c/T_e)^{3/2}}, \tag{2.79}$$

where c_1, c_2, and T_c are constants related to the composition of the plasma and the characteristics of the injected neutral particles (type and energy of particles). Note that $T_c \propto E_{beam}$, where E_{beam} is the energy of the injected neutral particles. A comparison of I^*_{cd} as a function temperature for various values of the injected neutral particle energy is shown in Fig. 2.4. As shown in the figure, the behavior of the neutral beam driven current changes as the energy of the injected particles increases. For low injected particle energies, the behavior can be approximated as $I^*_{cd} \propto \sqrt{T_e}$, and for high injected particle energies, the behavior can be approximated as $I^*_{cd} \propto T_e$.

Bootstrap current drive

The bootstrap current is a self-generated current in the plasma that is associated with particles that cannot complete a helical orbit around the magnetic axis. These particles are therefore called trapped particles. In the presence of the radial pressure gradient that is produced by the magnetic confinement, more trapped particles move in one toroidal direction than in the other. As a result, a net current is produced which is called the bootstrap current [60]. From [134, 135], we write the bootstrap current as

$$j_{bs}(\hat{\rho},t) = \frac{RB_{\phi}}{B_{\phi,0}} p_e \left[\mathcal{L}_{31} \left\{ \frac{1}{p_e}\frac{\partial p_e}{\partial \psi} + \frac{1}{p_e}\frac{\partial p_i}{\partial \psi} \right\} + \mathcal{L}_{32}\frac{1}{T_e}\frac{\partial T_e}{\partial \psi} + \mathcal{L}_{34}\alpha\frac{1-R_{pe}}{R_{pe}}\frac{1}{T_i}\frac{\partial T_i}{\partial \psi} \right], \quad (2.80)$$

where p_e denotes the electron pressure, p_i denotes the ion pressure, and $R_{pe} = p_e/p$. Under the assumption of a tight coupling between the electron and ion species in the plasma, we rewrite (2.80) as

$$\begin{aligned} j_{bs}(\hat{\rho},t) = \frac{k_{JkeV}R_0}{\hat{F}(\hat{\rho})} \left(\frac{\partial \psi}{\partial \hat{\rho}}\right)^{-1} \Bigg[& 2\mathcal{L}_{31}(\hat{\rho}) T_e(\hat{\rho},t) \frac{\partial n_e}{\partial \hat{\rho}} \\ & + \left\{ 2\mathcal{L}_{31}(\hat{\rho}) + \mathcal{L}_{32}(\hat{\rho}) + \alpha(\hat{\rho})\mathcal{L}_{34}(\hat{\rho}) \right\} n_e(\hat{\rho},t) \frac{\partial T_e}{\partial \hat{\rho}} \Bigg], \end{aligned} \quad (2.81)$$

where the coefficients $\mathcal{L}_{31}$, $\mathcal{L}_{32}$, $\mathcal{L}_{34}$, and α depend on the magnetic configuration of a particular plasma equilibrium and on particle collisionality in the plasma. As the bootstrap current is driven by the radial pressure gradient (the terms $T_e\,[\partial n_e/\partial\hat{\rho}]$ and $n_e\,[\partial T_e/\partial\hat{\rho}]$ in (2.81)), we note that in L-mode operating scenarios, j_{bs} will be relatively small as the plasma density and temperature profiles exhibit a smooth behavior across the spatial domain. However, in H-mode operating scenarios, large gradients in the plasma density and temperate result from the formation of edge particle and energy transport barriers. Therefore, j_{bs} represents a significant portion of the total current density in these operating scenarios, and as a result the complexity of the coupling

between the magnetic and kinetic states is increased.

2.5 First-principles-driven physics-based model of plasma poloidal magnetic flux dynamics

By combining the physics-based models of the electron density (2.47), electron temperature (2.65)-(2.66), plasma resistivity (2.72), and noninductive current-drives (2.74)-(2.76) and (2.81) with the magnetic diffusion equation model (2.45)-(2.46), we obtain our desired *first-principles-driven*, physics-based, control-oriented model of the poloidal magnetic flux profile evolution. At this time, we stress that we have included the dominant physics properties of the tokamak plasma that are critical to the evolution of the poloidal magnetic flux profile in response to the various actuators used for control, and have neglected others. An example of this is illustrated by including Z_{eff} for plasma resistivity (2.72) and Bremsstrahlung radiation (2.53), but not for fuel dilution. Our purpose is to include the dominant features, which will ultimately be verified by modeling as well as the performance of control algorithms designed by employing the developed model.

By defining the control input vector as

$$u = \left[P_{ec_1}, \ldots, P_{ec_{n_{ec}}}, P_{ic_1}, \ldots, P_{ic_{n_{ic}}}, P_{nbi_1}, \ldots, P_{nbi_{n_{nbi}}}, \bar{n}_e, I_p\right],$$

the first-principles-driven, nonlinear, partial differential equation (PDE) model is expressed as

$$\begin{aligned}\frac{\partial \psi}{\partial t} = {} & f_\eta\left(\hat{\rho}, u(t)\right) \frac{1}{\hat{\rho}} \frac{\partial}{\partial \hat{\rho}} \left(\hat{\rho} D_\psi \frac{\partial \psi}{\partial \hat{\rho}} \right) + \sum_{i=1}^{n_{ec}} f_{ec_i}\left(\hat{\rho}, u(t)\right) P_{ec_i}(t) \\ & + \sum_{i=1}^{n_{nbi}} f_{nbi_i}\left(\hat{\rho}, u(t)\right) P_{nbi_i}(t) + f_{bs}\left(\hat{\rho}, u(t)\right) \left(\frac{\partial \psi}{\partial \hat{\rho}} \right)^{-1}, \end{aligned} \tag{2.82}$$

with boundary conditions

$$\left.\frac{\partial\psi}{\partial\hat{\rho}}\right|_{\hat{\rho}=0} = 0 \qquad \left.\frac{\partial\psi}{\partial\hat{\rho}}\right|_{\hat{\rho}=1} = -k_{I_p} I_p(t), \tag{2.83}$$

where the parameters f_η, f_{ec_i}, f_{nbi_i}, and f_{bs} are functions of the model parameters, the diffusion coefficient D_ψ is defined as $D_\psi(\hat{\rho}) = \hat{F}(\hat{\rho})\hat{G}(\hat{\rho})\hat{H}(\hat{\rho})$, and $k_{I_p} = [\mu_0 R_0] \,/\, \left[2\pi\hat{G}(1)\hat{H}(1)\right]$. In the case where the electron temperature scales with the control actuators in the same way across the entire spatial domain, i.e., the electron temperature is expressed as (2.63), the spatial and temporal dependence in the model parameters f_η, f_{ec_i}, f_{nbi_i}, and f_{bs} can be separated, and (2.82) can be expressed as

$$\begin{aligned}\frac{\partial\psi}{\partial t} = {} & f_\eta\left(\hat{\rho}\right) u_\eta(t) \frac{1}{\hat{\rho}} \frac{\partial}{\partial\hat{\rho}}\left(\hat{\rho} D_\psi \frac{\partial\psi}{\partial\hat{\rho}}\right) + \sum_{i=1}^{n_{ec}} f_{ec_i}\left(\hat{\rho}\right) u_{ec_i}(t) \\ & + \sum_{i=1}^{n_{nbi}} f_{nbi_i}\left(\hat{\rho}\right) u_{nbi_i}(t) + f_{bs}\left(\hat{\rho}\right) u_{bs}(t) \left(\frac{\partial\psi}{\partial\hat{\rho}}\right)^{-1},\end{aligned} \tag{2.84}$$

where

$$\begin{aligned}
f_\eta(\hat{\rho}) &= \frac{k_{sp}(\hat{\rho}) Z_{eff}}{\mu_0 \rho_b^2 \hat{F}(\hat{\rho})^2} \left[k_{T_e}(\hat{\rho}) T_e^{prof}(\hat{\rho}) n_e^{prof}(\hat{\rho})^\zeta\right]^{-3/2}, \\
f_{ec_i}(\hat{\rho}) &= R_0 \hat{H}(\hat{\rho}) k_{sp}(\hat{\rho}) Z_{eff} \left[k_{T_e}(\hat{\rho}) T_e^{prof}(\hat{\rho}) n_e^{prof}(\hat{\rho})^\zeta\right]^{-1/2} \frac{j_{ec_i}^{ref}(\hat{\rho})}{n_e^{prof}(\hat{\rho})}, \\
f_{nbi_i}(\hat{\rho}) &= R_0 \hat{H}(\hat{\rho}) k_{sp}(\hat{\rho}) Z_{eff} \left[k_{T_e}(\hat{\rho}) T_e^{prof}(\hat{\rho}) n_e^{prof}(\hat{\rho})^\zeta\right]^{(-3/2+\delta)} \frac{j_{nbi_i}^{ref}(\hat{\rho})}{n_e^{prof}(\hat{\rho})}, \\
f_{bs}(\hat{\rho}) &= \frac{k_{JkeV} R_0^2 \hat{H}(\hat{\rho}) k_{sp}(\hat{\rho}) Z_{eff}}{\hat{F}(\hat{\rho})} \left[k_{T_e}(\hat{\rho}) T_e^{prof}(\hat{\rho}) n_e^{prof}(\hat{\rho})^\zeta\right]^{-3/2} \\
&\quad \times \Bigg[\left\{2\mathcal{L}_{31}(\hat{\rho}) + \mathcal{L}_{32}(\hat{\rho}) + \alpha(\hat{\rho})\mathcal{L}_{34}(\hat{\rho})\right\} n_e^{prof}(\hat{\rho}) \frac{d}{d\hat{\rho}} \left(k_{T_e}(\hat{\rho}) T_e^{prof}(\hat{\rho}) n_e^{prof}(\hat{\rho})^\zeta\right) \\
&\quad + 2\mathcal{L}_{31}(\hat{\rho}) \left[k_{T_e}(\hat{\rho}) T_e^{prof}(\hat{\rho}) n_e^{prof}(\hat{\rho})^\zeta\right] \frac{d}{d\hat{\rho}} \left(n_e^{prof}(\hat{\rho})\right) \Bigg],
\end{aligned} \tag{2.85}$$

and the control inputs are defined as

$$
\begin{aligned}
u_\eta(t) &= \left[I_p(t)^\gamma P_{tot}(t)^\varepsilon \bar{n}_e(t)^\zeta\right]^{-3/2}, \\
u_{ec_i}(t) &= \left[I_p(t)^\gamma P_{tot}(t)^\varepsilon \bar{n}_e(t)^\zeta\right]^{-1/2} \bar{n}_e(t)^{-1} P_{ec_i}(t), \\
u_{nbi_i}(t) &= \left[I_p(t)^\gamma P_{tot}(t)^\varepsilon \bar{n}_e(t)^\zeta\right]^{(-3/2+\delta)} \bar{n}_e(t)^{-1} P_{nbi_i}(t), \\
u_{bs}(t) &= \left[I_p(t)^\gamma P_{tot}(t)^\varepsilon \bar{n}_e(t)^\zeta\right]^{-1/2} \bar{n}_e(t).
\end{aligned} \tag{2.86}
$$

From (2.84), we see that the magnetic diffusion equation admits actuation not only through interior control ($u_{ec_i}, u_{nbi_i}, u_{bs}$) and boundary control ($I_p$), but also through u_η, which we name *diffusivity control* in this work. Simulated and experimental data can now be utilized to tailor the control-oriented models (and hence the first-principles-driven model (2.82)-(2.83)) to a given operating scenario in a given machine of interest.

In order to simulate the FPD, physics-based model, we spatially discretize the infinite dimensional PDE (2.82)-(2.83) by employing a finite difference method, where the non-dimensional spatial domain of interest ($\hat{\rho} \in [0, 1]$) is represented by m_ψ discrete nodes. By utilizing the finite difference method, a general function $f(\hat{\rho})$ is approximated as $\hat{f} = [f_1, \ldots, f_i, \ldots, f_{m_\psi}]$, where f_i is the value of f at the discrete node i, for $i \in [1, \ldots, m_\psi]$. This representation yields spatial derivative approximations of order $(\Delta\hat{\rho})^2$ at the evenly spaced interior nodes ($i \in [2, \ldots, m_\psi - 1]$) of

$$
\left(\frac{\partial f}{\partial \hat{\rho}}\right)\bigg|_i \approx \frac{f_{i+1} - f_{i-1}}{2\Delta\hat{\rho}} \qquad \left(\frac{\partial^2 f}{\partial \hat{\rho}^2}\right)\bigg|_i \approx \frac{f_{i+1} - 2f_i + f_{i-1}}{(\Delta\hat{\rho})^2},
$$

where $\Delta\hat{\rho} = 1/\left[m_\psi - 1\right]$. After spatially discretizing (2.82) and taking into account the boundary conditions (2.83), we obtain a nonlinear finite dimensional ordinary

differential equation model defined by

$$\dot{\hat{\psi}} = f_{\psi}(\hat{\psi}, u),$$

where $\hat{\psi} = [\psi_2, \ldots, \psi_i, \ldots, \psi_{m_\psi - 1}]^T \in \mathbb{R}^{n_\psi}$ is the magnetic state vector, ψ_i is the value of ψ at the discrete nodes, $f_\psi \in \mathbb{R}^{n_\psi}$ is a nonlinear function of the magnetic states and control inputs, and $n_\psi = m_\psi - 2$. The boundary conditions (2.83) are discretized as

$$\begin{aligned} 0 &= -3\psi_1 + 4\psi_2 - \psi_3, \\ 0 &= k_{I_p} I_p(t) + \left(-3\psi_{m_\psi} + 4\psi_{m_\psi - 1} - \psi_{m_\psi - 2}\right) / \left(-2\Delta\hat{\rho}\right). \end{aligned}$$

By defining the augmented state vector as

$$x = \begin{bmatrix} \hat{\psi} \\ E \end{bmatrix} \in \mathbb{R}^{(n_\psi + 1)},$$

we can write the magnetic and thermal system dynamics as

$$\dot{x} = \begin{bmatrix} f_\psi(\hat{\psi}, u) \\ -\dfrac{E}{\tau_E} + P_{tot}(x, u) \end{bmatrix} = F_{\psi,E}(x, u) \in \mathbb{R}^{(n_\psi + 1)}, \tag{2.87}$$

where the energy confinement scaling expression employed is the IPB98(y,2) scaling law [132]

$$\begin{aligned} \tau_E = {} & 0.0562 H_{H98(y,2)} I_p(\mathrm{MA})^{0.93} R_0(\mathrm{m})^{1.39} a(\mathrm{m})^{0.58} \bar{n}_e(10^{19}\mathrm{m}^{-3})^{0.41} \\ & \times B_{\phi,0}(\mathrm{T})^{0.15} A_{eff}^{0.19} \kappa^{0.78} P_{tot}(\mathrm{MW})^{-0.69}, \end{aligned} \tag{2.88}$$

where $H_{H98(y,2)}$ is the energy confinement enhancement factor, a is the plasma minor

radius, A_{eff} is the effective mass number of the hydrogenic ion species in the plasma, and κ is the plasma elongation. We then integrate (2.87) in time by employing a fully implicit numerical scheme, i.e.,

$$\frac{x_{k+1} - x_k}{\Delta t} = F_{\psi,E}(x_{k+1}, u_k), \tag{2.89}$$

where x_k and u_k denote the plasma state and control input, respectively, at the time step t_k, x_{k+1} denotes the plasma state at the next time step, and Δt denotes the simulation time step. The plasma magnetic and thermal state evolution can be obtained by iteratively solving (2.89) at each simulation time step from a given initial condition $x_0 = x(t_0)$, where t_0 is the simulation starting time.

2.6 Physics parameters utilized to define plasma scenarios

There are many plasma parameters related to the plasma magnetic and thermal states, ψ and E, respectively, that will be of interest in determining the type of operating scenarios that are or can be achieved and their performance. The parameters considered in this work are the safety factor profile (q profile), the total toroidal current density (j_{tor}), the normalized plasma beta (β_N), and the plasma loop voltage profile (U_p). The safety factor profile is related to the spatial gradient of the poloidal magnetic flux profile and is defined as

$$q(\hat{\rho}, t) = -\frac{d\Phi}{d\Psi} = -\frac{d\Phi}{2\pi d\psi} = -\frac{\frac{\partial \Phi}{\partial \rho}\frac{\partial \rho}{\partial \hat{\rho}}}{2\pi \frac{\partial \psi}{\partial \hat{\rho}}} = -\frac{B_{\phi,0}\rho_b^2 \hat{\rho}}{\partial \psi / \partial \hat{\rho}}, \tag{2.90}$$

where we have utilized the definitions of the mean effective minor radius of the magnetic flux surfaces $\Phi(\rho) = \pi B_{\phi,0}\rho^2$ and the normalized mean effective minor radius $\hat{\rho} = \rho/\rho_b$. The toroidal current density is also related to the poloidal magnetic flux spatial gradient and is defined as [70]

$$j_{tor}(\hat{\rho},t) = -\frac{1}{\mu_0\rho_b^2 R_0 \hat{H}}\frac{1}{\hat{\rho}}\frac{\partial}{\partial\hat{\rho}}\left(\hat{\rho}\hat{G}\hat{H}\frac{\partial\psi}{\partial\hat{\rho}}\right). \tag{2.91}$$

By examining (2.90) and (2.91), we see that the local safety factor value is roughly inversely related to the local toroidal current density amplitude in tokamaks as $q \propto (\partial\psi/\partial\hat{\rho})^{-1}$ and $j_{tor} \propto (\partial\psi/\partial\hat{\rho})^2 + (\partial\psi/\partial\hat{\rho})$. The normalized plasma beta is related to the plasma stored energy and is defined as

$$\beta_N = \beta_t[\%]\frac{aB_{\phi,0}}{I_p[\mathrm{MA}]} \qquad \beta_t = \frac{\langle p\rangle_V}{B_{\phi,0}^2/(2\mu_0)} = \frac{(2/3)(E/V_p)}{B_{\phi,0}^2/(2\mu_0)}, \tag{2.92}$$

where β_t is the toroidal plasma beta [18] and we have utilized (2.56)-(2.57). The plasma loop voltage profile is related to the temporal derivative of the poloidal magnetic flux profile and is defined as

$$U_p(\hat{\rho},t) = -\frac{\partial\Psi}{\partial t} = -2\pi\frac{\partial\psi}{\partial t}. \tag{2.93}$$

2.7 Tailoring physics-based model to L-mode scenarios in DIII-D

We now employ DIII-D experimental data, and data computed by the TRANSP advanced tokamak simulation code [12] configured to the DIII-D geometry, to tailor the FPD, physics-based model to L-mode plasma scenarios in DIII-D. In section 2.7.1, the model parameters tailored to the DIII-D tokamak are presented and in

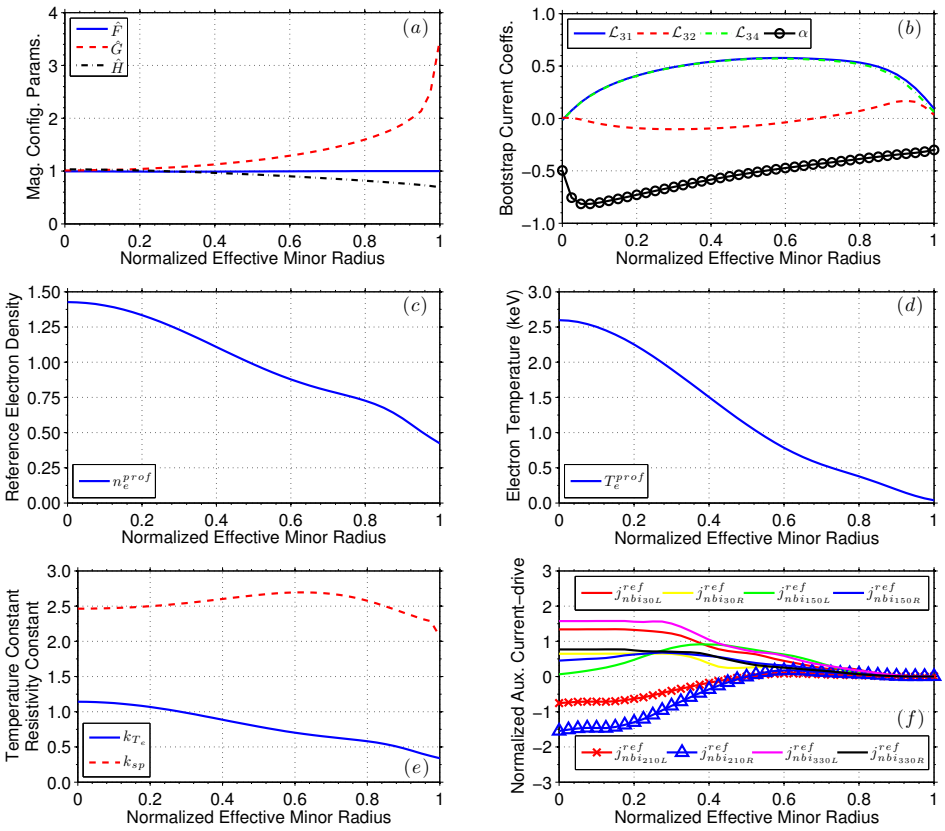

Figure 2.5: Model parameters tailored to L-mode scenarios in the DIII-D tokamak: (a) magnetic equilibrium configuration parameters $\hat{F}(\hat{\rho})$, $\hat{G}(\hat{\rho})$, and $\hat{H}(\hat{\rho})$, (b) bootstrap current coefficients $\mathcal{L}_{31}(\hat{\rho})$, $\mathcal{L}_{32}(\hat{\rho})$, $\mathcal{L}_{34}(\hat{\rho})$, and $\alpha(\hat{\rho})$, (c) reference electron density profile $n_e^{prof}(\hat{\rho})$, (d) reference electron temperature profile $T_e^{prof}(\hat{\rho})$ (keV), (e) electron temperature coefficient k_{T_e} (10^{10} m^{-3}A^{-1}W$^{-1/2}$) and plasma resistivity coefficient k_{sp} (10^{-8} Ω m keV$^{3/2}$), (e) normalized auxiliary neutral beam injection ($j^{ref}_{nbi_i}$), for $i \in$ [30L/R,150L/R,210L/R,330L/R], current-drive reference profiles (10^{18} m^{-3}keV$^{-1/2}$W^{-1}A m^{-2}).

sections 2.7.2 and 2.7.3 simulation studies that compare the evolution of the plasma parameters predicted by the FPD, physics-based model to the plasma parameters experimentally achieved in the DIII-D tokamak are discussed.

2.7.1 Model parameters tailored to DIII-D

As we are modeling L-mode scenarios in DIII-D, there are no abrupt changes in particle and energy transport in the plasma, and the temperature exhibits a smooth

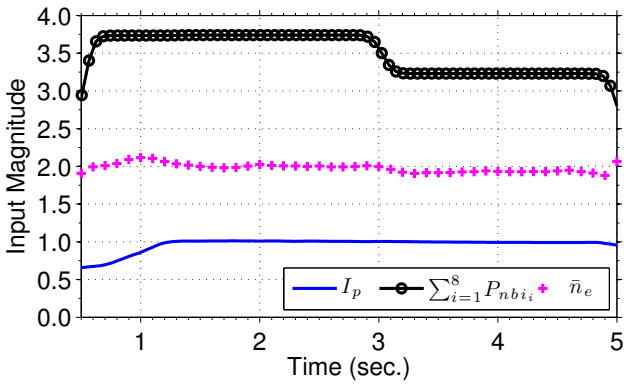

Figure 2.6: Control inputs applied during FPD, physics-based model simulation and DIII-D experimental discharge #146411 (current in MA, power in MW, and density in 10^{19} m^{-3}).

behavior across the entire spatial domain. Therefore, we model the electron temperature evolution as in (2.63), and we choose the constants in this model as $\gamma = 1$, $\varepsilon = 0.5$, and $\zeta = -1$. This choice qualitatively describes the slowly evolving electron temperature in response to the control actuators, i.e., the observation of (i) an increase in plasma confinement, and hence an increase in temperature, with increasing plasma current, and (ii) a decrease in plasma confinement with increasing total injected power [133]. Also, by changing the electron density, the electron temperature is modified for a given electron pressure.

The parameters related to the magnetic configuration of the plasma equilibrium, the reference profiles for the various models, and the normalizing profiles are shown in Fig. 2.5. The auxiliary heating and current-drive actuators on DIII-D considered in this work are 8 individual neutral beam injection sources, referred to by the names 30L/R, 150L/R, 210L/R, and 330L/R, respectively, where L and R denoted left and right beam lines, respectively. The current-drive deposition profiles for each source are shown in Fig. 2.5(f). The 30L/R and 330L/R neutral beams inject power into the plasma in the co-current direction (same direction as the total plasma current) with deposition profiles that are peaked at the magnetic axis (referred to as on-axis neutral

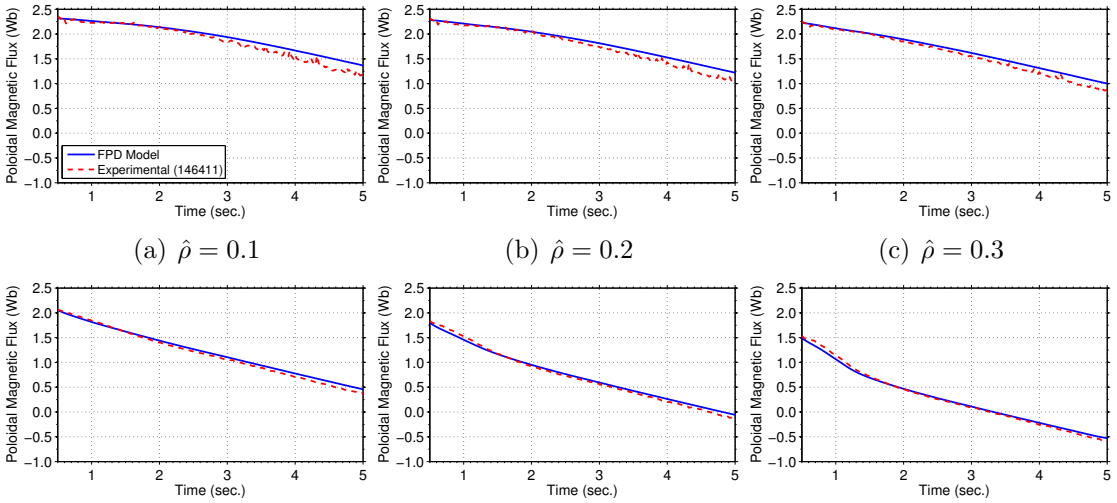

(a) $\hat{\rho} = 0.1$ (b) $\hat{\rho} = 0.2$ (c) $\hat{\rho} = 0.3$

(d) $\hat{\rho} = 0.5$ (e) $\hat{\rho} = 0.7$ (f) $\hat{\rho} = 0.95$

Figure 2.7: Time trace of poloidal magnetic flux Ψ at various normalized effective minor radii for the model comparison simulation test in section 2.7.2.

beam injection). The 150L/R neutral beams inject power into the plasma in the co-current direction with deposition profiles that are peaked away from the magnetic axis in the spatial region $\hat{\rho} \in [0.3, 0.5]$ (referred to as off-axis neutral beam injection). Finally, the 210L/R neutral beams inject power into the plasma in the counter-current direction (opposite direction as the total plasma current) with deposition profiles that are peaked at the magnetic axis (referred to as counter-current neutral beam injection). The energy of the injected neutral particles on DIII-D is 80 keV, therefore, the constant in the neutral beam current-drive model (2.76) is chosen as $\delta = 1/2$ [65] (see Fig. 2.4). The heating efficiency constants for the auxiliary heating and current-drive actuators are taken as $\eta_{nbi_i} = 1$ for $i \in$ [30L/R,150L/R,210L/R,330L/R]. The hydrogenic ion species in the considered DIII-D plasmas are solely deuterium ($A_{eff} = 2$). As the plasma temperature in DIII-D is not hot enough to produce a significant probability of deuterium-deuterium fusion reactions occurring, we choose the fusion heating constant as $\eta_{fus} = 0$. Finally, the other model constants are $B_{\phi,0} = 2.0$ T, $R_0 = 1.6955$ m, $\rho_b = 0.82$ m, and $Z_{eff} = 1.5$.

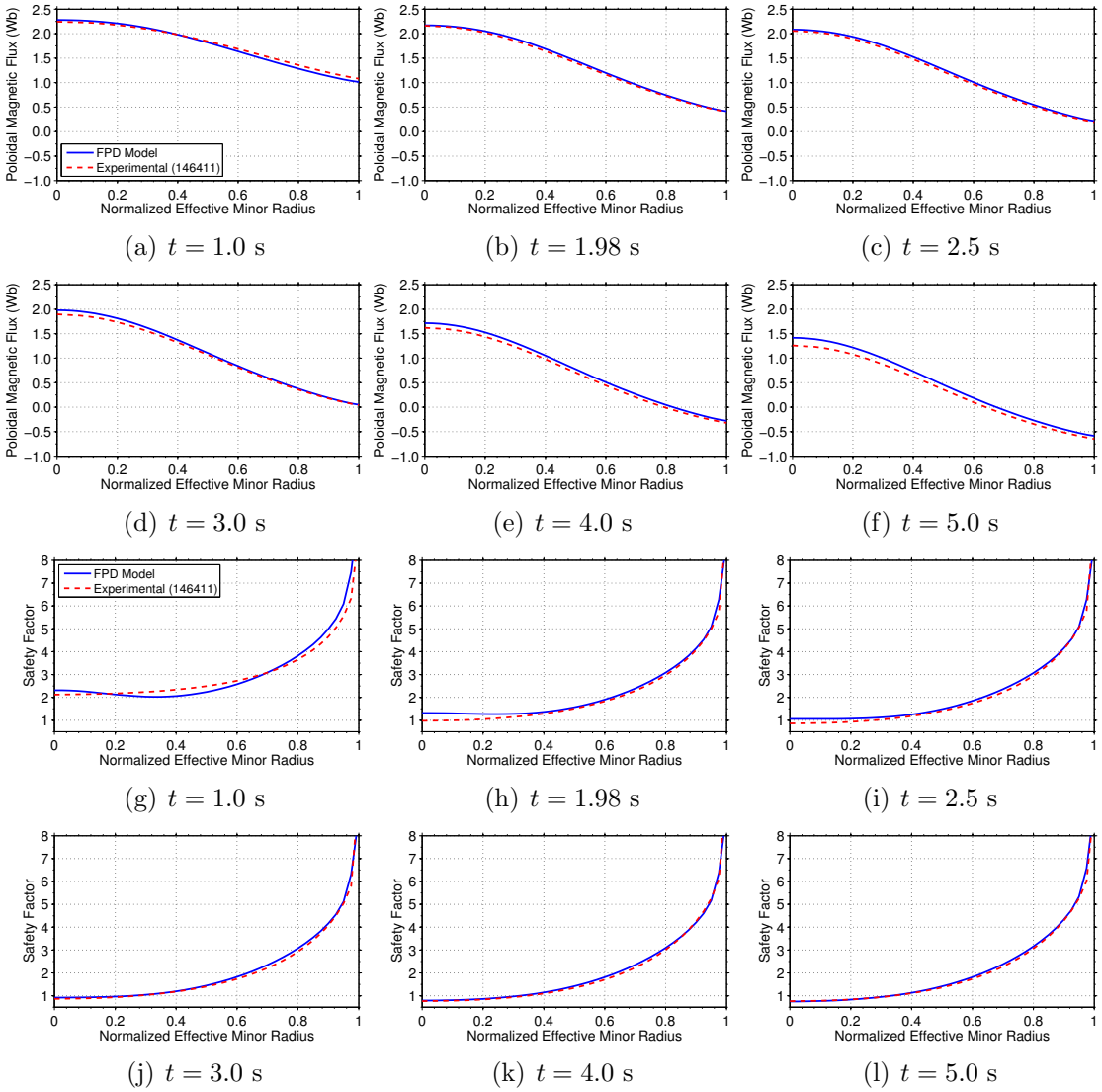

(a) $t = 1.0$ s (b) $t = 1.98$ s (c) $t = 2.5$ s

(d) $t = 3.0$ s (e) $t = 4.0$ s (f) $t = 5.0$ s

(g) $t = 1.0$ s (h) $t = 1.98$ s (i) $t = 2.5$ s

(j) $t = 3.0$ s (k) $t = 4.0$ s (l) $t = 5.0$ s

Figure 2.8: (a-f) Poloidal magnetic flux profile $\Psi(\hat{\rho})$ at various times and (g-l) safety factor profile $q(\hat{\rho})$ at various times for the model comparison simulation test in section 2.7.2.

2.7.2 Comparison between model predicted and experimentally achieved (#146411) plasma parameters

We now describe a simulation study that compares the evolution of the plasma parameters predicted by the first-principles-driven, physics-based model to the experimentally achieved plasma parameters in DIII-D shot 146411. The control inputs (total plasma current, total neutral beam injection power, and line average electron density) applied during both the simulation and the experiment are shown in Fig. 2.6. The plasma magnetic state evolution predicted by the FPD, physics-based model is now compared to the experimentally achieved magnetic state evolution. Figure 2.7 shows the evolution of the poloidal magnetic flux Ψ at various normalized effective minor radii, Figs. 2.8(a-f) show a comparison of the FPD, physics-based model predicted and experimentally achieved poloidal magnetic flux $\Psi(\hat{\rho})$ profiles at various times, and Figs. 2.8(g-l) show a comparison of the FPD, physics-based model predicted and experimentally achieved safety factor $q(\hat{\rho})$ profiles at various times. As shown in the figures, the FPD, physics-based model predicted plasma magnetic state evolution shows good agreement with the experimentally achieved plasma parameters. The FPD, physics-based model predicted poloidal magnetic flux diffuses at a slightly slower rate in the plasma core compared to the experimentally achieved poloidal magnetic flux during the time interval $t \in [3.0, 5.0]$ s (see Figs. 2.7(a-c) and 2.8(d-f)). This indicates that the physics-based model predicted plasma resistivity is slightly lower than the experimentally achieved plasma resistivity.

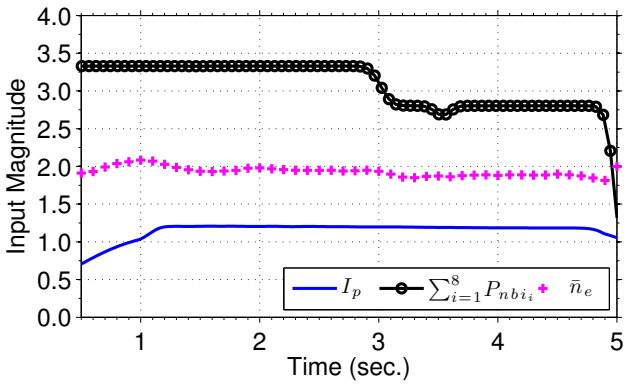

Figure 2.9: Control inputs applied during FPD, physics-based model simulation and DIII-D experimental discharge #145477 (current in MA, power in MW, and density in 10^{19} m^{-3}).

2.7.3 Comparison between model predicted and experimentally achieved (#145477) plasma parameters

We now describe a simulation study that compares the evolution of the plasma parameters predicted by the first-principles-driven, physics-based model to the experimentally achieved plasma parameters in DIII-D shot 145477. The control inputs (total plasma current, total neutral beam injection power, and line average electron density) applied during both the simulation and the experiment are shown in Fig. 2.9. The plasma magnetic state evolution predicted by the FPD, physics-based model is now compared to the experimentally achieved magnetic state evolution. Figure 2.10 shows a comparison of the FPD, physics-based model predicted and experimentally achieved safety factor $q(\hat{\rho})$ profiles at various times. As shown in the figures, the FPD, physics-based model predicted plasma magnetic state evolution shows good agreement with the experimentally achieved plasma parameters.

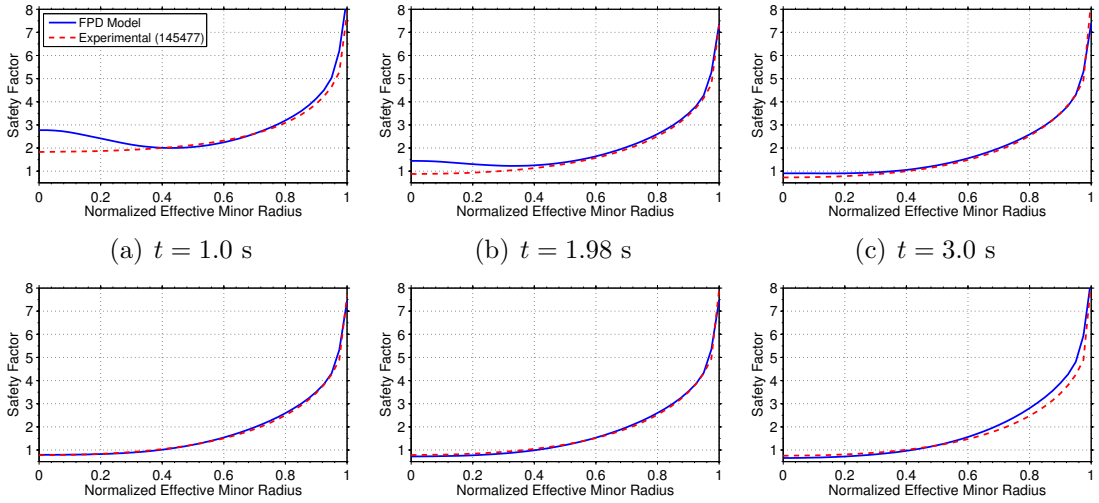

(a) $t = 1.0$ s (b) $t = 1.98$ s (c) $t = 3.0$ s

(d) $t = 3.5$ s (e) $t = 4.0$ s (f) $t = 5.0$ s

Figure 2.10: Safety factor profile $q(\hat{\rho})$ at various times for the model comparison simulation test in section 2.7.3.

2.8 Tailoring physics-based model to H-mode scenarios in DIII-D

We now employ DIII-D experimental data, and data computed by the TRANSP advanced tokamak simulation code [12] configured to the DIII-D geometry, to tailor the FPD, physics-based model to H-mode plasma scenarios in DIII-D that have energy and particle transport barriers just inside the plasma boundary. In section 2.8.1, the model parameters tailored to the DIII-D tokamak are presented and in sections 2.8.2 and 2.8.3 simulation studies that compare the evolution of the plasma parameters predicted by the FPD, physics-based model to the plasma parameters experimentally achieved in the DIII-D tokamak and analyzed by the TRANSP code are discussed.

2.8.1 Model parameters tailored to DIII-D

Based on the TRANSP analyzed electron temperature profile evolution, we first note that the electron temperature exhibits a similar behavior across the entire spatial

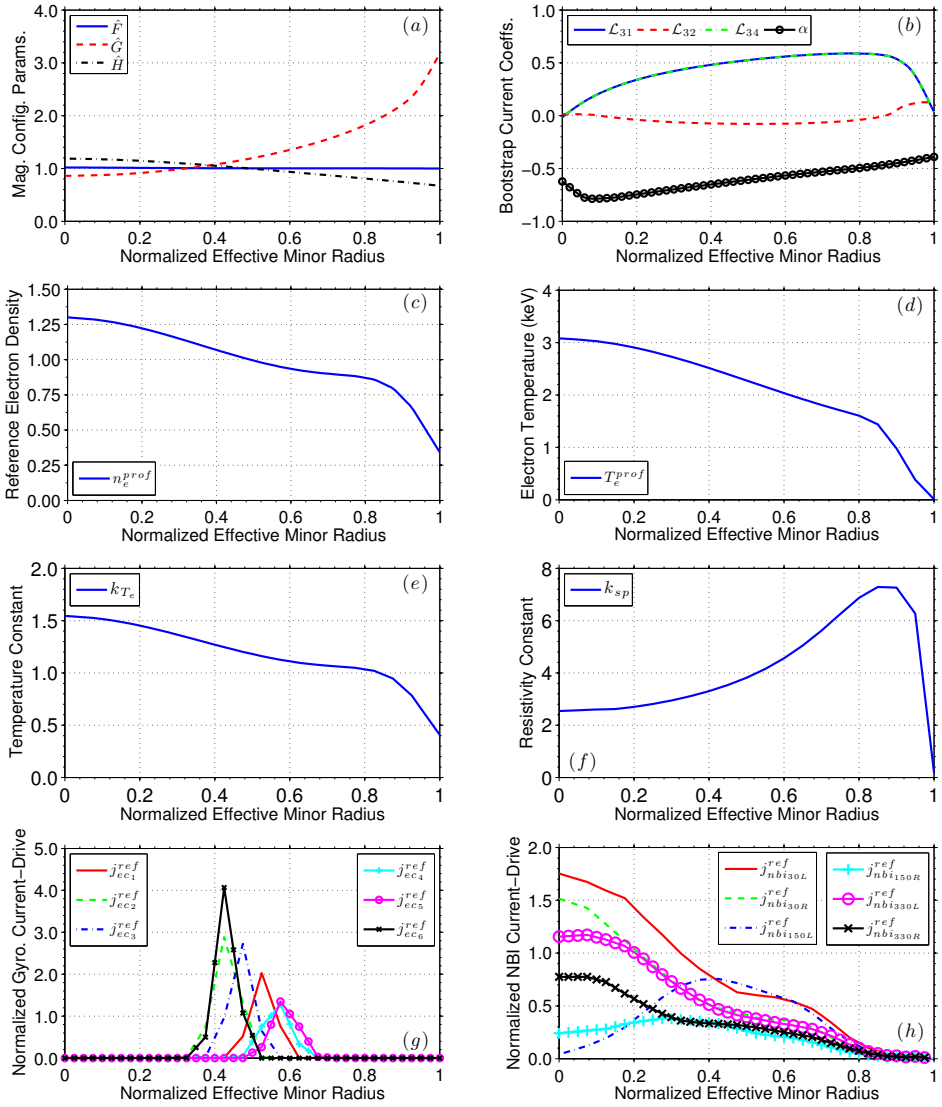

Figure 2.11: Model parameters tailored to H-mode scenarios in the DIII-D tokamak: (a) magnetic equilibrium configuration parameters $\hat{F}(\hat{\rho})$, $\hat{G}(\hat{\rho})$, and $\hat{H}(\hat{\rho})$,(b) bootstrap current coefficients $\mathcal{L}_{31}(\hat{\rho})$, $\mathcal{L}_{32}(\hat{\rho})$, $\mathcal{L}_{34}(\hat{\rho})$, and $\alpha(\hat{\rho})$, (c) reference electron density profile $n_e^{prof}(\hat{\rho})$, (d) reference electron temperature profile $T_e^{prof}(\hat{\rho})$ (keV), (e) electron temperature coefficient k_{T_e} (10^{10} $\mathrm{m}^{-3}\mathrm{A}^{-1}\mathrm{W}^{-1/2}$), (f) plasma resistivity coefficient k_{sp} (10^{-8} Ω m $\mathrm{keV}^{3/2}$), (g) normalized auxiliary electron cyclotron (j_{eci}^{ref}), for $i \in [1,2,3,4,5,6]$, current-drive reference profiles (10^{18} m^{-3} keV $^{-1}\mathrm{W}^{-1}$ A m^{-2}), and (h) normalized auxiliary neutral beam injection ($j_{nbi_i}^{ref}$), for $i \in$ [30L/R,150L/R,330L/R], current-drive reference profiles (10^{18} $\mathrm{m}^{-3}\mathrm{keV}^{-1/2}\mathrm{W}^{-1}$A m^{-2}).

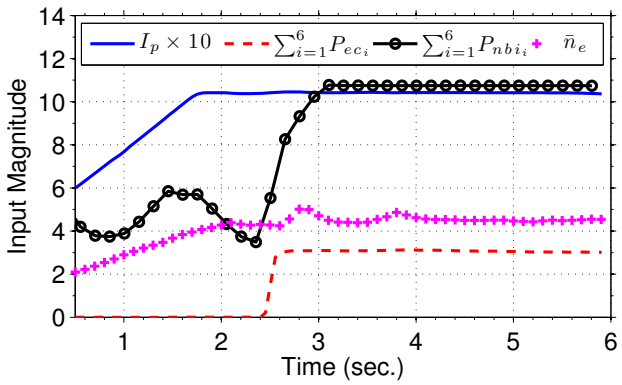

Figure 2.12: Control inputs applied during FPD, physics-based model simulation and DIII-D experimental discharge #147634 (current in MA, power in MW, and density in 10^{19} m^{-3}).

domain (both inside and outside the transport barrier). Therefore, we model the electron temperature evolution as in (2.63), and we choose the constants in this model as $\gamma = 1$, $\varepsilon = 0.5$, and $\zeta = -1$. This choice qualitatively describes the slowly evolving electron temperature in response to the control actuators, i.e., the observation of (i) an increase in plasma confinement, and hence an increase in temperature, with increasing plasma current, and (ii) a decrease in plasma confinement with increasing total injected power [133]. Also, by changing the electron density, the electron temperature is modified for a given electron pressure.

The parameters related to the magnetic configuration of the plasma equilibrium, the reference profiles for the various models, and the normalizing profiles are shown in Fig. 2.11. The auxiliary heating and current-drive actuators on DIII-D considered in this work are 6 individual electron cyclotron sources, which are grouped together to form 1 effective source for control, and 6 individual neutral beam injection sources, which are referred to by the names 30L/R, 150L/R, and 330L/R, respectively. The current-drive deposition profiles for each source are shown in Fig. 2.11(g-h). The 30L/R and 330L/R neutral beams inject power into the plasma in the co-current direction (same direction as the total plasma current) with deposition profiles that

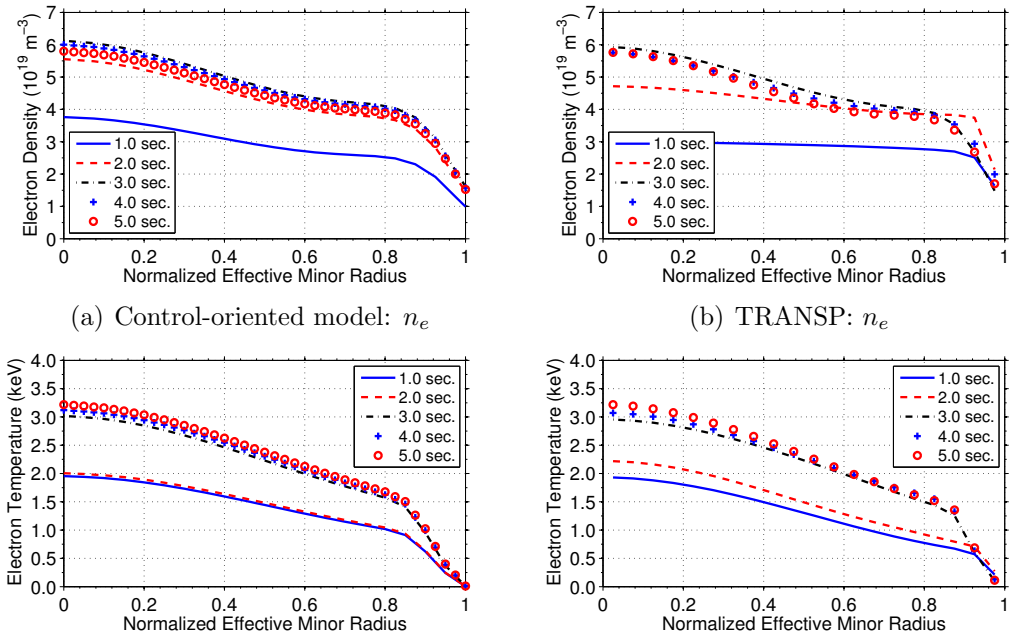

(a) Control-oriented model: n_e

(b) TRANSP: n_e

(c) Control-oriented model: T_e

(d) TRANSP: T_e

Figure 2.13: Electron density profile evolution computed via: (a) physics-based control-oriented model and (b) TRANSP, and electron temperature profile evolution computed via: (c) physics-based control-oriented model and (d) TRANSP for the model comparison simulation test in section 2.8.2.

are peaked at the magnetic axis (referred to as on-axis current drive). The electron cyclotron sources and the 150L/R neutral beams inject power into the plasma in the co-current direction with deposition profiles that are peaked away from the magnetic axis (referred to as off-axis current drive). Note that counter-current injection neutral beam sources (210L/R sources in section 2.7.1) are not utilized in these scenarios as they have been observed to increase the possibly of triggering MHD instabilities in DIII-D H-mode scenarios. The energy of the injected neutral particles on DIII-D is 80 keV, therefore, the constant in the neutral beam current-drive model (2.76) is chosen as $\delta = 1/2$ [65] (see Fig. 2.4). The heating efficiency constants for the auxiliary heating and current-drive actuators are taken as $\eta_{ec_i} = 1$ for $i \in [1, 2, \ldots, 6]$ and as $\eta_{nbi_i} = 1$ for $i \in$ [30L/R,150L/R,330L/R]. The hydrogenic ion species in the considered DIII-D plasmas are solely deuterium ($A_{eff} = 2$). As the

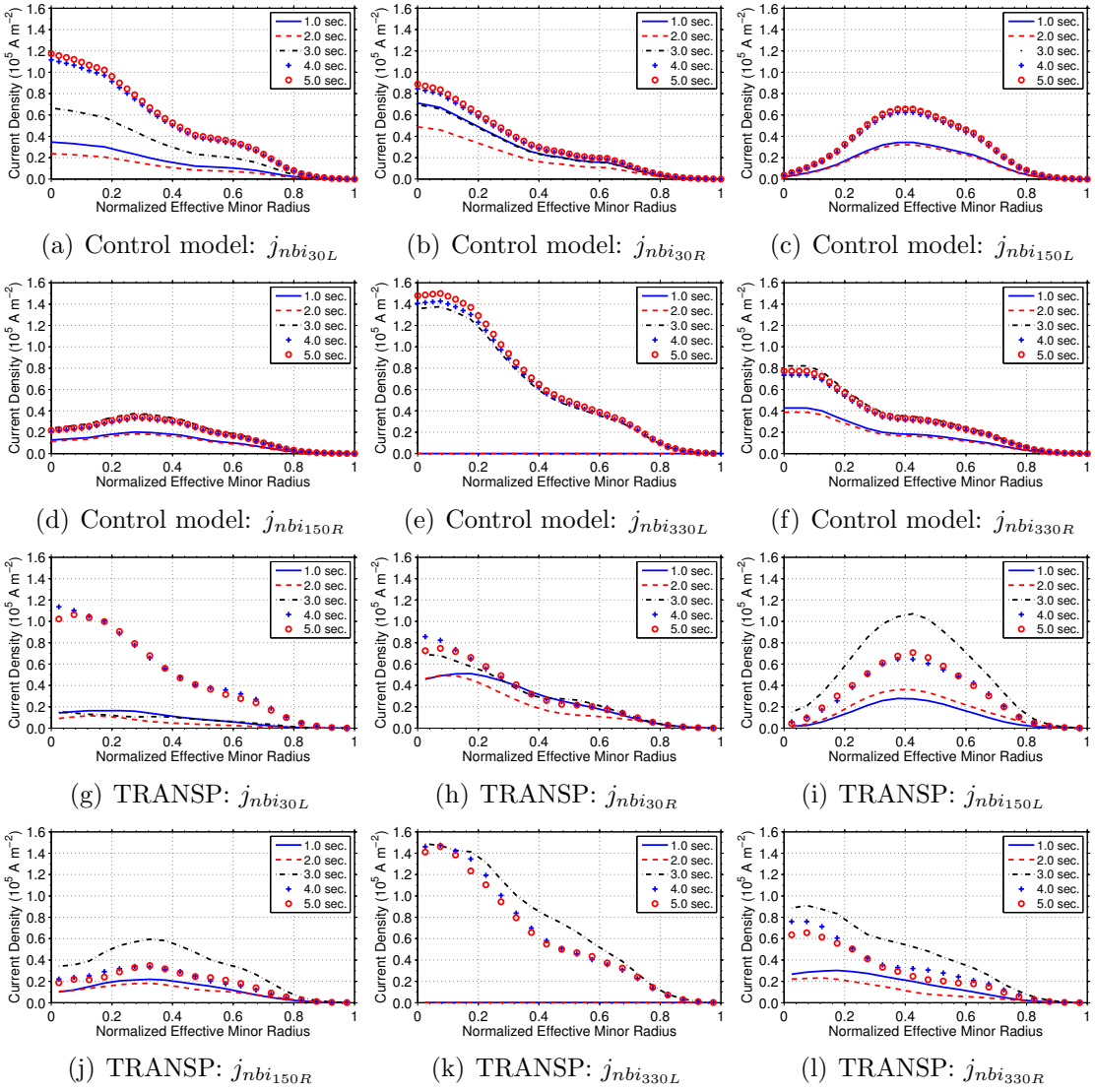

(a) Control model: $j_{nbi_{30L}}$ (b) Control model: $j_{nbi_{30R}}$ (c) Control model: $j_{nbi_{150L}}$

(d) Control model: $j_{nbi_{150R}}$ (e) Control model: $j_{nbi_{330L}}$ (f) Control model: $j_{nbi_{330R}}$

(g) TRANSP: $j_{nbi_{30L}}$ (h) TRANSP: $j_{nbi_{30R}}$ (i) TRANSP: $j_{nbi_{150L}}$

(j) TRANSP: $j_{nbi_{150R}}$ (k) TRANSP: $j_{nbi_{330L}}$ (l) TRANSP: $j_{nbi_{330R}}$

Figure 2.14: Neutral beam injection current-drive evolution computed via: (a-f) physics-based control-oriented model and (g-l) TRANSP for the model comparison simulation test in section 2.8.2.

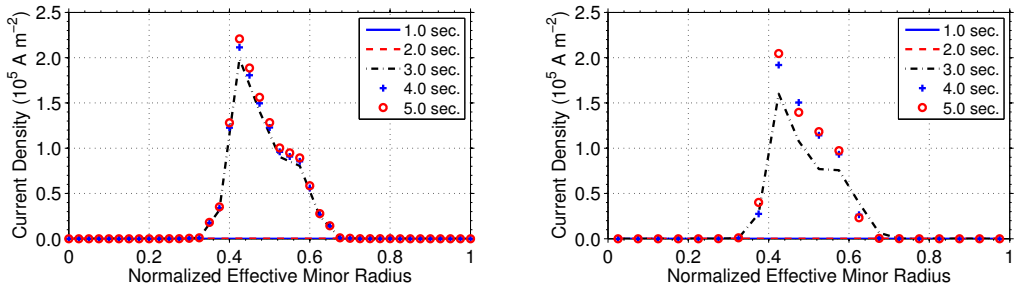

(a) Control-oriented model: j_{ec}

(b) TRANSP: j_{ec}

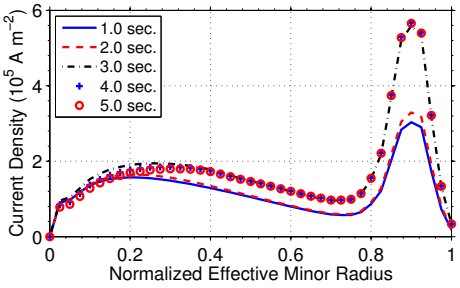

(c) Control-oriented model: j_{bs}

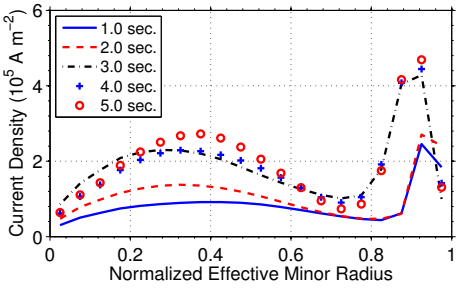

(d) TRANSP: j_{bs}

Figure 2.15: Total electron cyclotron current-drive evolution computed via: (a) physics-based control-oriented model and (b) TRANSP, and bootstrap current-drive evolution computed via: (c) physics-based control-oriented model and (d) TRANSP for the model comparison simulation test in section 2.8.2.

plasma temperature in DIII-D is not hot enough to produce a significant probability of deuterium-deuterium fusion reactions occurring, we choose the fusion heating constant as $\eta_{fus} = 0$. Based on the experimentally measured energy confinement time (during the high performance phase of the discharge), the energy confinement enhancement factor is chosen as $H_{H98(y,2)} = 1.4$. Finally, the other model constants are $B_{\phi,0} = 1.65$ T, $R_0 = 1.6955$ m, $a = 0.6$ m, $\rho_b = 0.82$ m, $\kappa = 1.8$, and $Z_{eff} = 1.75$.

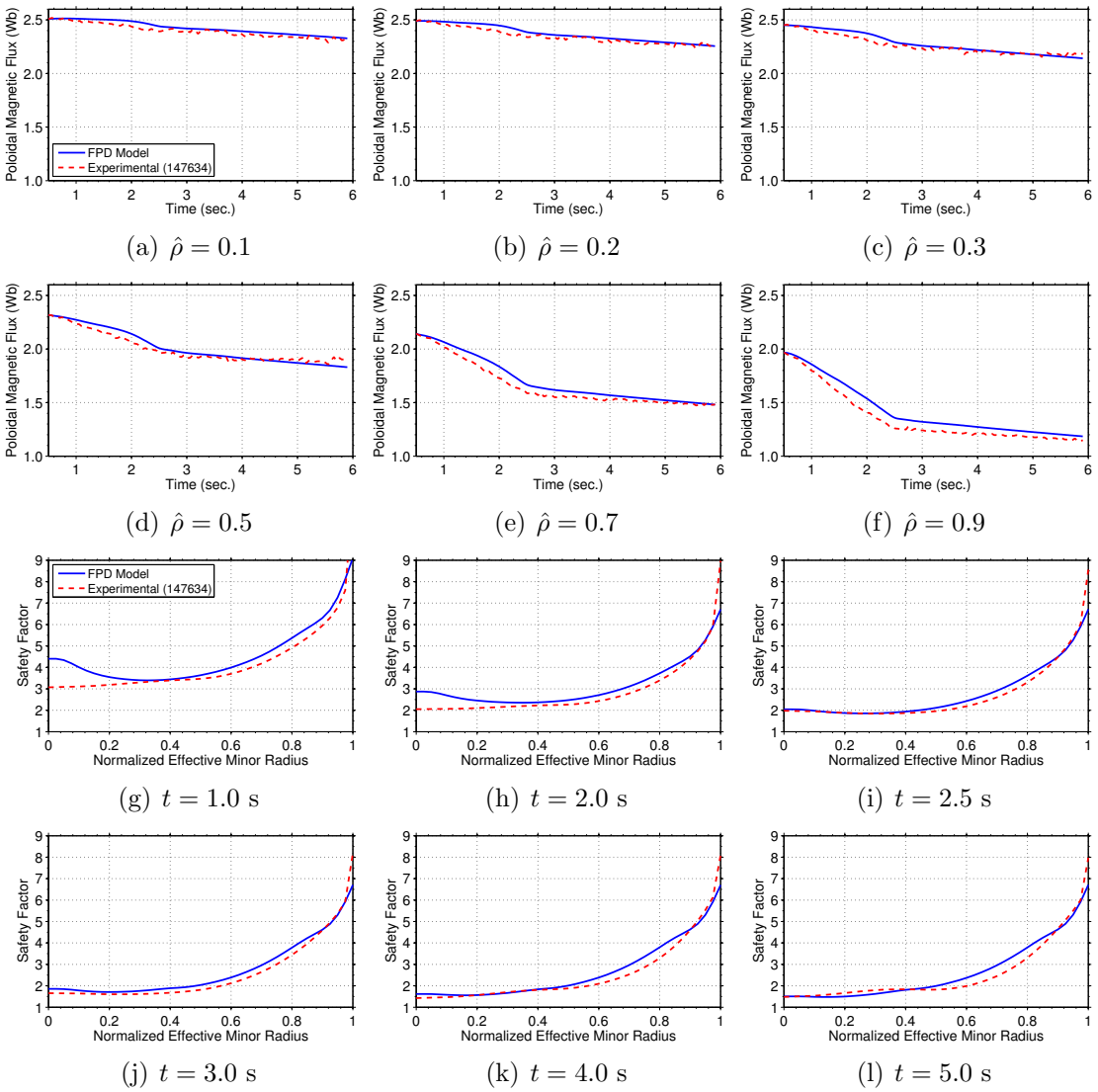

(a) $\hat{\rho} = 0.1$ (b) $\hat{\rho} = 0.2$ (c) $\hat{\rho} = 0.3$

(d) $\hat{\rho} = 0.5$ (e) $\hat{\rho} = 0.7$ (f) $\hat{\rho} = 0.9$

(g) $t = 1.0$ s (h) $t = 2.0$ s (i) $t = 2.5$ s

(j) $t = 3.0$ s (k) $t = 4.0$ s (l) $t = 5.0$ s

Figure 2.16: (a-f) Time trace of poloidal magnetic flux Ψ at various normalized effective minor radii and (g-l) safety factor profile $q(\hat{\rho})$ at various times for the model comparison simulation test in section 2.8.2.

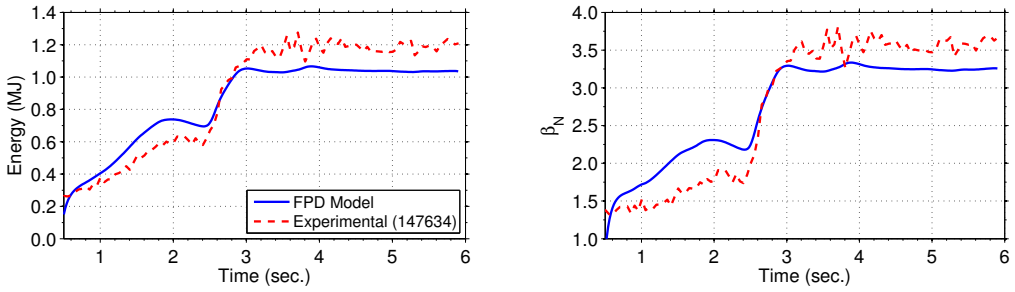

(a) $E(t)$ (b) $\beta_N(t)$

Figure 2.17: (a) Plasma stored energy E versus time and (b) plasma normalized beta β_N versus time for the model comparison simulation test in section 2.8.2.

2.8.2 Comparison between model predicted and experimentally achieved (#147634) plasma parameters

We now describe a simulation study that compares the evolution of the plasma parameters predicted by the first-principles-driven, physics-based model to the experimentally achieved plasma parameters in DIII-D shot 147634. The control inputs (total plasma current, total electron cyclotron power, total neutral beam injection power, and line average electron density) applied during both the simulation and the experiment are shown in Fig. 2.12. We begin the analysis of the FPD model's prediction capabilities by first comparing the prediction of the physics-based models of the electron density, electron temperature, and noninductive current-drive source evolutions to the TRANSP analyzed plasma parameter evolutions. Figures 2.13(a-b) show the electron density profile, Figs. 2.13(c-d) show the electron temperature profile, Fig. 2.14 shows the individual neutral beam injection noninductive current drive, and Fig. 2.15 shows the total electron cyclotron and bootstrap noninductive current-drive sources at various times computed by both the physics-based models and TRANSP. The trends of the physics-based model predicted plasma parameters show good agreement with the TRANSP results. As shown in Figs. 2.14(g-l) and 2.15(b), TRANSP predicts that the spatial noninductive current deposition location

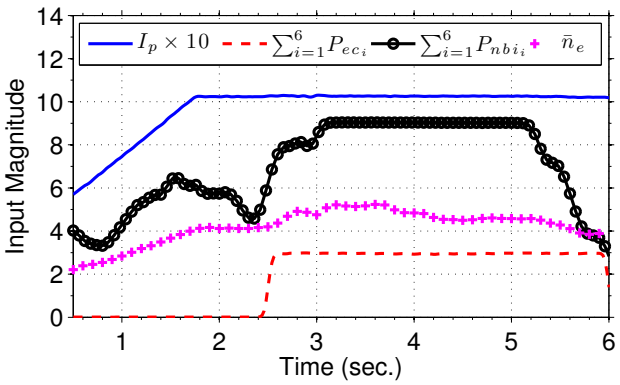

Figure 2.18: Control inputs applied during FPD, physics-based model simulation and DIII-D experimental discharge #154358 (current in MA, power in MW, and density in 10^{19} m^{-3}).

of the neutral beam injectors and gyrotron launchers remains reasonably constant throughout the experiment. Therefore, the physics-based model assumption of constant neutral beam injection and gyrotron current deposition profiles appears appropriate for the scenarios considered.

We now compare the plasma magnetic and thermal state evolution, ψ and E, as well as the plasma parameters related to these plasma states, the q profile and the normalized plasma beta (β_N), predicted by the FPD, physics-based model to the experimentally achieved plasma parameters. Figure 2.16(a-f) shows the evolution of the poloidal magnetic flux Ψ at various normalized effective minor radii, Figs. 2.16(g-l) shows a comparison of the FPD, physics-based model predicted and experimentally achieved safety factor $q(\hat{\rho})$ profiles at various times, and Fig. 2.17 shows a comparison of the FPD, physics-based model predicted and experimentally achieved plasma stored energy E and normalized plasma beta β_N. As shown in the figures, the FPD, physics-based model predicted plasma magnetic and thermal state evolution shows good agreement with the experimentally achieved plasma parameters. The plasma stored energy (and hence plasma β_N) is slightly over predicted by the physics-based model during the time interval $t \in [0.5, 2.5]$ s because a constant energy confinement

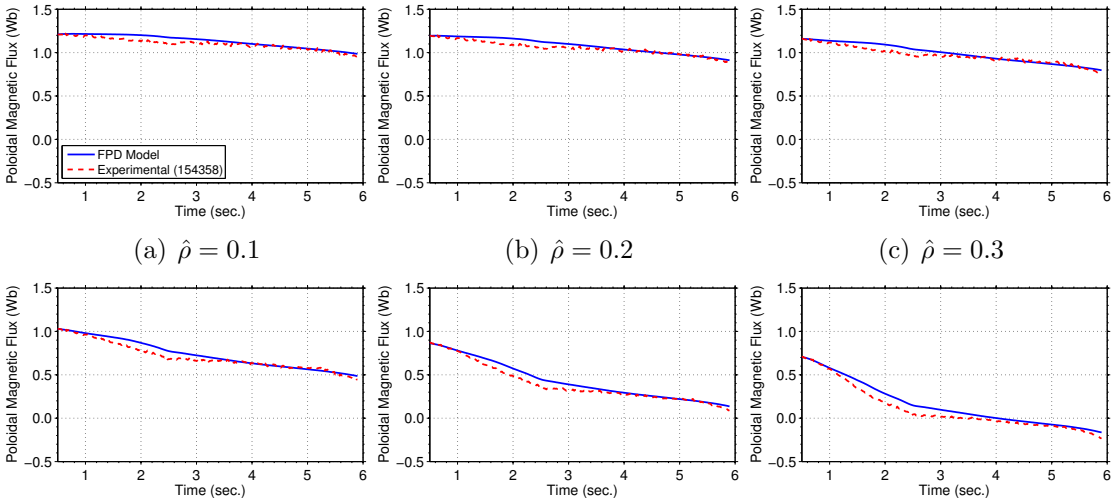

(a) $\hat{\rho} = 0.1$ (b) $\hat{\rho} = 0.2$ (c) $\hat{\rho} = 0.3$

(d) $\hat{\rho} = 0.5$ (e) $\hat{\rho} = 0.7$ (f) $\hat{\rho} = 0.9$

Figure 2.19: Time trace of poloidal magnetic flux Ψ at various normalized effective minor radii for the model comparison simulation test in section 2.8.3.

enhancement factor is employed throughout the simulation. In actuality, the thermal transport evolves during the discharge (from a value characterized by $H_{H98(y,2)} \approx 0.9$ during the time interval $t \in [0.5, 2.5]$ s to a value characterized by $H_{H98(y,2)} \approx 1.4$ during the time interval $t \in [3.0, 6.0]$ s) based on the magnetic and kinetic state of the plasma [61,62] as discussed in section 2.4.2. However, as closed-form expressions that represent this complex interaction do not exist, we chose to employ a constant energy confinement enhancement factor throughout the simulation. Finally, the plasma stored energy (and hence plasma β_N) is slightly under predicted by the physics-based model during the time interval $t \in [3.0, 6.0]$ s because the plasma power balance equation (2.59)-(2.60) neglects the contribution that the fast ions (particles that have not thermalized) in the plasma have to the total plasma stored energy[2].

[2]E-mail correspondence with Dr. John R. Ferron at General Atomics, San Diego, CA, USA.

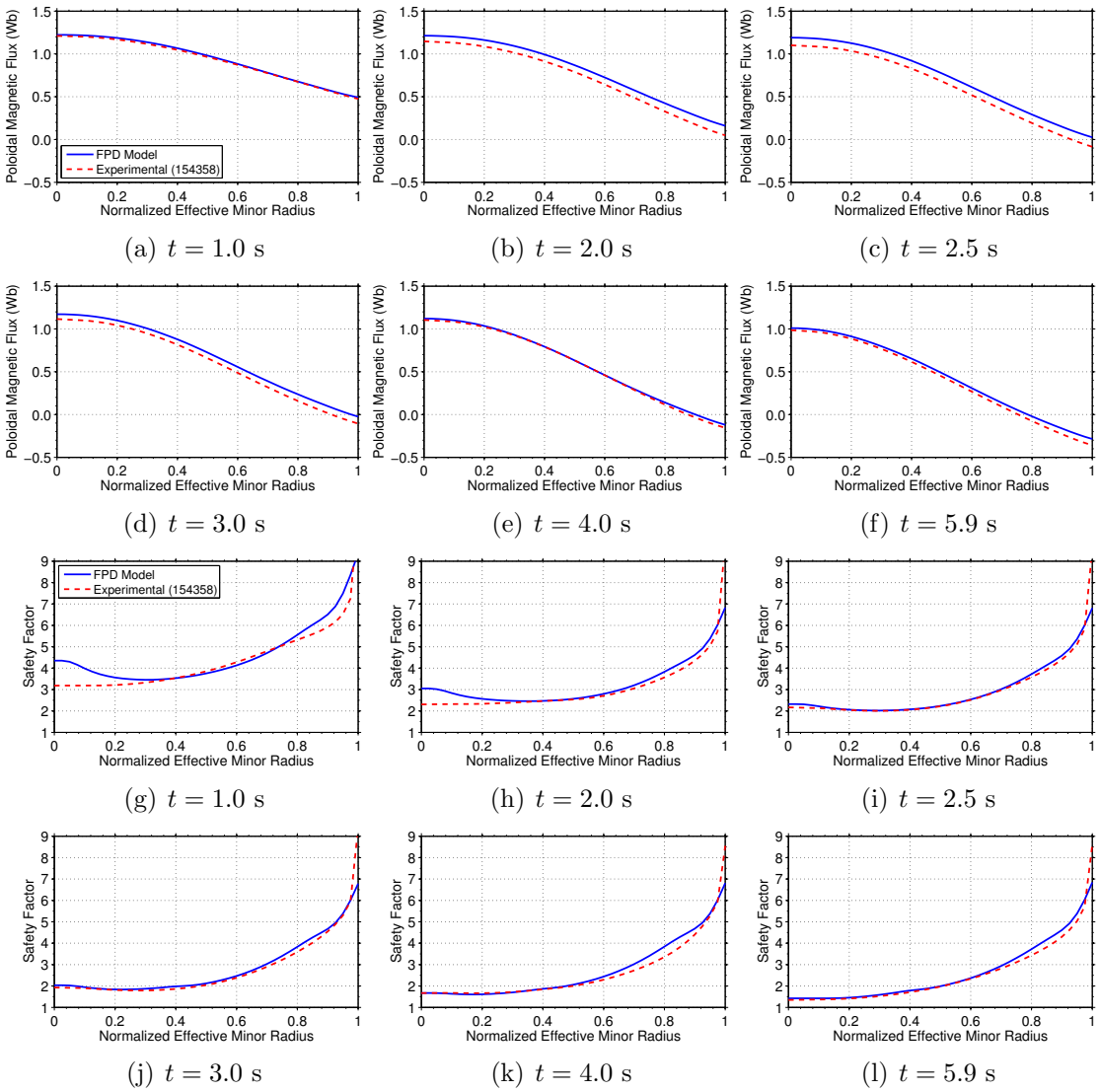

(a) $t = 1.0$ s (b) $t = 2.0$ s (c) $t = 2.5$ s

(d) $t = 3.0$ s (e) $t = 4.0$ s (f) $t = 5.9$ s

(g) $t = 1.0$ s (h) $t = 2.0$ s (i) $t = 2.5$ s

(j) $t = 3.0$ s (k) $t = 4.0$ s (l) $t = 5.9$ s

Figure 2.20: (a-f) Poloidal magnetic flux profile $\Psi(\hat{\rho})$ at various times and (g-l) safety factor profile $q(\hat{\rho})$ at various times for the model comparison simulation test in section 2.8.3.

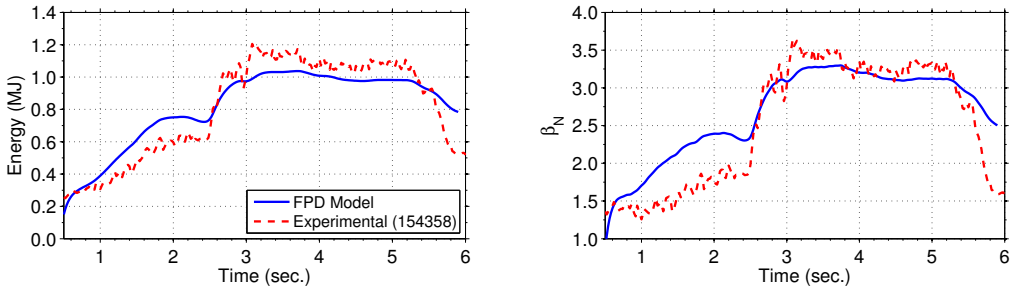

(a) $E(t)$ (b) $\beta_N(t)$

Figure 2.21: (a) Plasma stored energy E versus time and (b) plasma normalized beta β_N versus time for the model comparison simulation test in section 2.8.3.

2.8.3 Comparison between model predicted and experimentally achieved (#154358) plasma parameters

We now describe a simulation study that compares the evolution of the plasma parameters predicted by the first-principles-driven, physics-based model to the experimentally achieved plasma parameters in DIII-D shot 154358. The control inputs (total plasma current, total electron cyclotron power, total neutral beam injection power, and line average electron density) applied during both the simulation and the experiment are shown in Fig. 2.18. The plasma magnetic and thermal state evolution predicted by the FPD, physics-based model is now compared to the experimentally achieved magnetic and thermal state evolution. Figure 2.19 shows the evolution of the poloidal magnetic flux Ψ at various normalized effective minor radii, Figs. 2.20(a-f) show a comparison of the FPD, physics-based model predicted and experimentally achieved poloidal magnetic flux $\Psi(\hat{\rho})$ profiles at various times, Figs. 2.20(g-l) show a comparison of the FPD, physics-based model predicted and experimentally achieved safety factor $q(\hat{\rho})$ profiles at various times, and and Fig. 2.21 shows a comparison of the FPD, physics-based model predicted and experimentally achieved plasma stored energy E and normalized plasma beta β_N. As shown in the figures, the FPD, physics-based model predicted plasma magnetic and thermal state

evolution shows good agreement with the experimentally achieved plasma parameters. The physics-based model predicted plasma stored energy (and hence plasma β_N) exhibits the same behavior in comparison to the experimentally achieved plasma stored energy as observed in section 2.8.2.

2.9 Tailoring physics-based model to H-mode scenarios in ITER

We now employ the DINA-CH&CRONOS free-boundary simulation code [5–9] configured to the ITER geometry to obtain simulated data of the plasma state evolution to tailor the FPD, physics-based model to H-mode burning plasma (one with a significant number of fusion reactions) scenarios in ITER that have energy and particle transport barriers just inside the plasma boundary. This advanced simulation code couples the free-boundary plasma equilibrium and current diffusion solver DINA-CH [6] with the plasma heat and particle transport solver CRONOS [7] and employs complex physics models to predict the plasma magnetic and thermal state evolution in the tokamak through exhaustive consumption of computational resources. DINA-CH&CRONOS is currently configured to execute with a prescribed electron density evolution and calculates anomalous heat conductivity profiles using a global transport model, KIAUTO [136]. The radial heat conductivity profile dependence for the core plasma is computed using a Gyrobohm-like formula. Additionally, the auxiliary H&CD source profiles are recomputed by DINA-CH&CRONOS on a one second time interval, and the plasma evolves with constant auxiliary powers in-between these auxiliary source profile updates. In section 2.9.1, the model parameters tailored to the ITER tokamak are presented and in section 2.9.2 a simulation study that compares the evolution of the plasma parameters predicted by the FPD, physics-based model

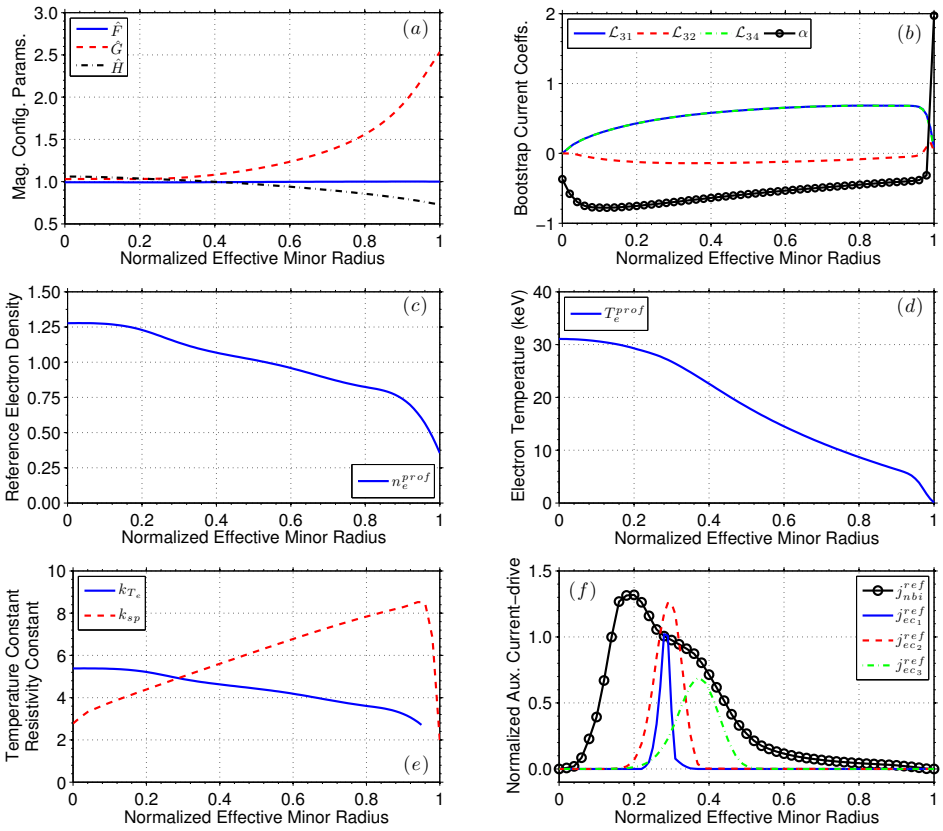

Figure 2.22: Model parameters tailored to the ITER tokamak: (a) magnetic equilibrium configuration parameters $\hat{F}(\hat{\rho})$, $\hat{G}(\hat{\rho})$, and $\hat{H}(\hat{\rho})$,(b) bootstrap current coefficients $\mathcal{L}_{31}(\hat{\rho})$, $\mathcal{L}_{32}(\hat{\rho})$, $\mathcal{L}_{34}(\hat{\rho})$, and $\alpha(\hat{\rho})$, (c) reference electron density profile $n_e^{prof}(\hat{\rho})$, (d) reference electron temperature profile $T_e^{prof}(\hat{\rho})$ (keV), (e) electron temperature coefficient $k_{T_e} = k_{T_e}^1$ (10^8 m^{-3}A^{-1}W$^{-1/2}$), note $k_{T_e}^2 = 1$, and plasma resistivity coefficient k_{sp} (10^{-8} Ω m keV$^{3/2}$), (e) normalized auxiliary neutral beam injection (j_{nbi}^{ref}) and electron cyclotron ($j_{ec_1}^{ref}$, $j_{ec_2}^{ref}$, $j_{ec_3}^{ref}$) current-drive reference profiles (10^{17} m^{-3}keV^{-1}W^{-1}A m^{-2}).

and DINA-CH&CRONOS is discussed.

2.9.1 Model parameters tailored to ITER

Based on the DINA-CH&CRONOS predicted electron temperature profile evolution, we first note that the electron temperature exhibits a different behavior in the plasma core (inside of the transport barrier) and near the plasma boundary (outside of the transport barrier). Therefore, we model the electron temperature evolution as in

(2.65)-(2.66), and we choose the constants in this model as $\gamma = 1$, $\varepsilon = 0.5$, $\zeta = -1$ and $\lambda = \nu = \xi = \omega = 0$, which models the temperature outside of the edge energy transport barrier as stiff. This choice qualitatively describes the slowly evolving electron temperature in the core of the plasma in response to the control actuators, i.e., the observation of (i) an increase in plasma confinement, and hence an increase in temperature, with increasing plasma current, and (ii) a decrease in plasma confinement with increasing total injected power [133]. Also, by changing the electron density, the electron temperature is modified for a given electron pressure. The auxiliary heating and current-drive actuators on ITER considered in this work are 3 independently configurable gyrotron launchers, 1 ion cyclotron launcher, and co-current-injection neutral beam launchers. In the considered operating scenarios, (i) the ion cyclotron launcher is configured to provide only heating power to the plasma and (ii) the neutral beam launchers are configured to inject particles at the same off-axis radial location, therefore, we group them together to form 1 total neutral beam launcher. The energy of the injected neutral particles on ITER is 1 MeV, therefore, the constant in the neutral beam current-drive model (2.76) is chosen as $\delta = 1$ [65] (see Fig. 2.4).

The parameters related to the magnetic configuration of the plasma equilibrium, the reference profiles for the various models, and the normalizing profiles are shown in Fig. 2.22. The heating efficiency constants for the auxiliary heating and current-drive actuators are taken as the ratio between the power absorbed by the plasma (calculated by DINA-CH&CRONOS) and the power requested for each individual actuator, and the efficiency constants are $\eta_{ec_i} = 1$ for $i = 1, 2, 3$, $\eta_{ic} = 0.85$, and $\eta_{nbi} = 1$. Neglecting the alpha particle and impurity densities, the charge neutrality condition in the plasma is approximated as $n_e(\hat{\rho}, t) \approx n_D(\hat{\rho}, t) + n_T(\hat{\rho}, t) \approx 2n_{DT}(\hat{\rho}, t)$, where we assume a 50:50 mix of deuterium and tritium ions and n_{DT} is the deuterium-tritium density. Under these assumptions, we approximate the fusion power density

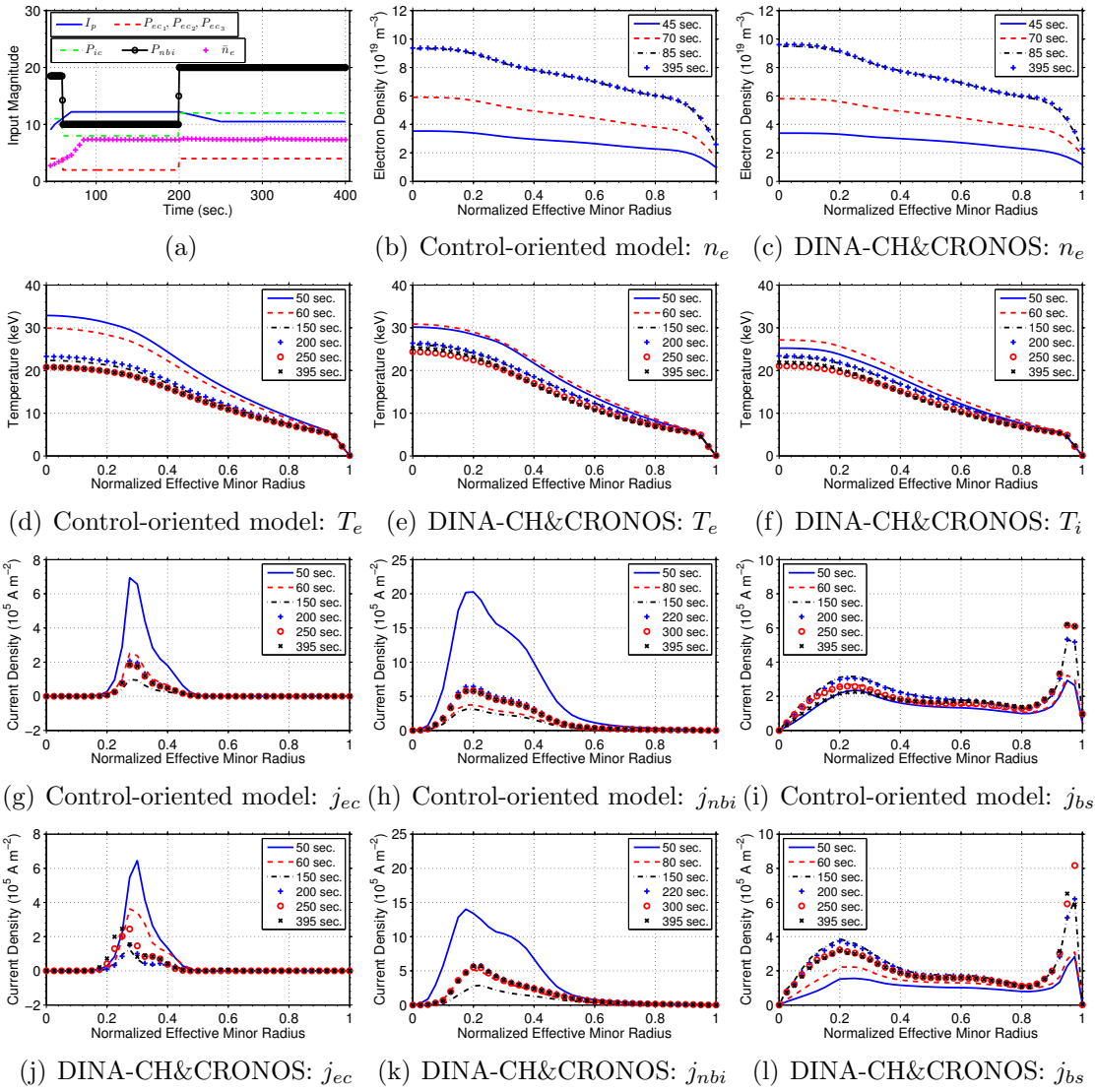

(a) (b) Control-oriented model: n_e (c) DINA-CH&CRONOS: n_e

(d) Control-oriented model: T_e (e) DINA-CH&CRONOS: T_e (f) DINA-CH&CRONOS: T_i

(g) Control-oriented model: j_{ec} (h) Control-oriented model: j_{nbi} (i) Control-oriented model: j_{bs}

(j) DINA-CH&CRONOS: j_{ec} (k) DINA-CH&CRONOS: j_{nbi} (l) DINA-CH&CRONOS: j_{bs}

Figure 2.23: (a) Control inputs applied during FPD, physics-based model and DINA-CH&CRONOS simulations (current in MA, power in MW and density in 10^{19} m^{-3}), electron density profile evolution computed via: (b) physics-based control-oriented model and (c) DINA-CH&CRONOS, electron temperature profile evolution computed via: (d) physics-based control-oriented model and (e) DINA-CH&CRONOS, (f) ion temperature evolution computed via DINA-CH&CRONOS, noninductive current-drive evolution computed via physics-based control-oriented model: (g) total gyrotron, (h) neutral beam injection, and (i) bootstrap, and noninductive current-drive evolution computed via DINA-CH&CRONOS: (j) total gyrotron, (k) neutral beam injection, and (l) bootstrap for the model comparison simulation test in section 2.9.2.

(2.54) as

$$Q_{fus}(\hat{\rho},t) \approx Q_{DT}\left(\frac{n_e(\hat{\rho},t)}{2}\right)^2 \left\langle \sigma v \right\rangle_{DT}(\hat{\rho},t) k_{JeV}, \tag{2.94}$$

and we chose the heating efficiency constant related to fusion heating in (2.60) as $\eta_{fus} = 0.15$ so that the plasma stored energy predicted by the simplified physics-based model (2.58) matches the plasma stored energy simulated by DINA-CH&CRONOS. Employing these heating efficiency constants, the energy confinement enhancement factor is chosen as $H_{H98(y,2)} = 1.3$ [8], so that the power balance equation (2.59) predicts the same energy confinement enhancement, and hence plasma stored energy, as DINA-CH&CRONOS. Finally, the other model constants are $B_{\phi,0} = 5.3$ T, $R_0 = 6.2$ m, $a = 2.0$ m, $\rho_b = 2.62$ m, $\hat{\rho}_{tb} = 0.95$, $\kappa = 1.7$, $Z_{eff} = 1.7$, and $A_{eff} = 2.5$ (results from a 50:50 mix of deuterium ($A = 2$) and tritium ($A = 3$)).

2.9.2 Comparison between model and DINA-CH&CRONOS predicted plasma parameters

We now describe a simulation study that compares the evolution of the plasma parameters predicted by the first-principles-driven, physics-based model and by the DINA-CH&CRONOS free-boundary simulation code [5–9]. We emphasize the scenario studied is not meant to be representative of any one specific standard ITER operating scenario but is meant to determine the ability of the FPD, physics-based model to predict the plasma magnetic and thermal state evolution in response to changes in the control actuators. As the FPD, physics-based model is designed for the high performance phase of the discharge, we start the simulations just after the plasma transitions from L-mode to H-mode in this particular simulated scenario at the time $t = 45$ s, which is still in the plasma current ramp-up phase. The control inputs (total plasma current, individual gyrotron launcher, ion cyclotron launcher, and neutral beam injection powers, and line average electron density) applied during

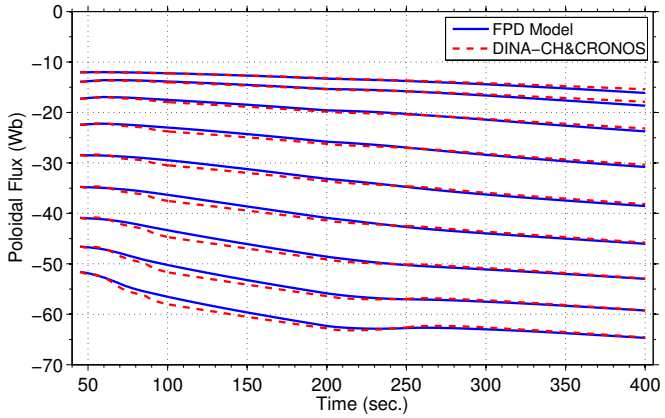

Figure 2.24: Time trace of poloidal magnetic flux Ψ at various normalized effective minor radii (top to bottom $\hat{\rho} = 0.1, 0.2, \ldots, 0.8, 0.9$) for the model comparison simulation test in section 2.9.2.

both simulations are shown in Fig. 2.23(a). We begin the analysis of the FPD model's prediction capabilities by first comparing the prediction of the physics-based models of the electron density, electron temperature, and noninductive current-drive source evolutions to the DINA-CH&CRONOS predicted plasma parameter evolutions. Figures 2.23(b-c) show the electron density profile, Figs. 2.23(d-f) show the electron and ion temperature profiles, and Figs. 2.23(g-l) show the total gyrotron, neutral beam injection, and bootstrap noninductive current-drive sources at various times during the simulations computed by both the physics-based models and DINA-CH&CRONOS.

The trends of the physics-based model predicted plasma parameters show good agreement with the DINA-CH&CRONOS predicted results. Firstly, as shown in Figs. 2.23(e-f), DINA-CH&CRONOS predicts the electron and ion temperature profiles evolve in a similar fashion, which suggests the physics-based model assumption of an approximately equal electron and ion temperature appears appropriate for the scenarios considered. Secondly, as shown in Figs. 2.23(j-k), DINA-CH&CRONOS predicts that the spatial noninductive current deposition location of the gyrotron launchers and neutral beam injectors remains reasonably constant throughout the simulation. Therefore, the physics-based model assumption of constant gyrotron and

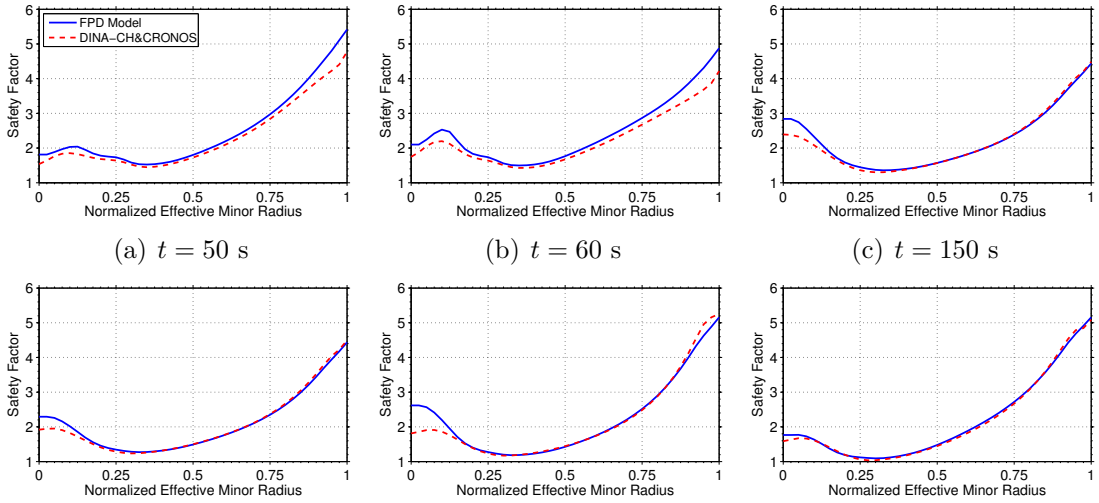

(a) $t = 50$ s (b) $t = 60$ s (c) $t = 150$ s

(d) $t = 200$ s (e) $t = 250$ s (f) $t = 395$ s

Figure 2.25: Safety factor profile $q(\hat{\rho})$ at various times for the model comparison simulation test in section 2.9.2.

neutral beam injection current deposition profiles also appears appropriate for the scenarios considered. Finally, as shown in Figs. 2.23(h) and 2.23(k), the physics-based model prediction of the noninductive current driven by the neutral beam injectors agrees reasonably well with the neutral beam driven noninductive current predicted by DINA-CH&CRONOS. However, the physics-based model neglects the slowing down time of the fast ions, assuming the particles and their energy are instantaneously thermalized, but this physical mechanism is taken into account by DINA-CH&CRONOS. This effect can be seen at the time $t = 50$ s during the simulations. A first-order filter could straightforwardly be included in the simplified model to describe this physical mechanism as discussed in section 2.4.4 (see (2.78)).

We now compare the plasma magnetic and thermal state evolution, ψ and E, respectively, as well as the plasma parameters related to these plasma states, the q profile, the toroidal current density (j_{tor}), the plasma loop voltage profile (U_p), and the normalized plasma beta (β_N) predicted by the FPD, physics-based model and DINA-CH&CRONOS. Figure 2.24 shows the evolution of the poloidal magnetic flux

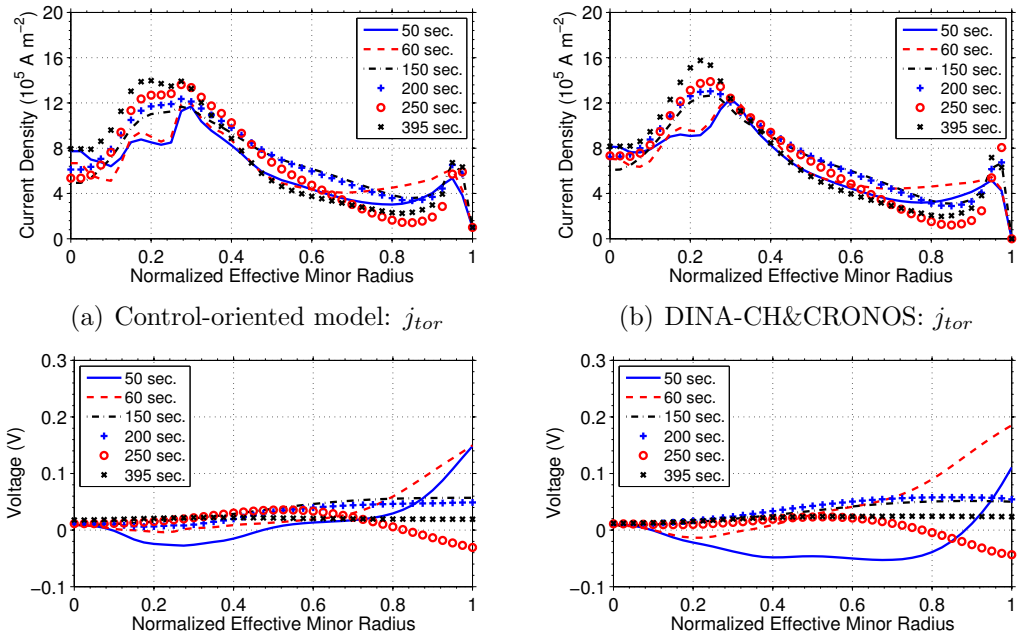

(a) Control-oriented model: j_{tor}

(b) DINA-CH&CRONOS: j_{tor}

(c) Control-oriented model: U_p

(d) DINA-CH&CRONOS: U_p

Figure 2.26: Toroidal current density evolution computed via: (a) FPD, physics-based, control-oriented model and (b) DINA-CH&CRONOS, and loop voltage profile evolution computed via: (c) FPD, physics-based, control-oriented model and (d) DINA-CH&CRONOS for the model comparison simulation test in section 2.9.2.

Ψ at various normalized effective minor radii, Figs. 2.25 and 2.26 show a comparison of the FPD, physics-based model predicted and DINA-CH&CRONOS predicted safety factor $q(\hat{\rho})$, toroidal current density $j_{tor}(\hat{\rho})$, and loop voltage $U_p(\hat{\rho})$ profiles, respectively, at various times, and Fig. 2.27 shows a comparison of the FPD, physics-based model predicted and DINA-CH&CRONOS predicted plasma stored energy E, normalized plasma beta β_N, and fusion power P_{fus}.

The scenario studied can be broken into four time sections: (i) 45−85 s, (ii) 85−200 s, (iii) $200-250$ s, and (iv) $250-400$ s, as shown in Fig. 2.23(a). During section (i) of the simulation, the control inputs are modified in time from their initial values to a first set of constant values and during section (ii) of the simulation, the control inputs remain stationary. During section (iii) of the simulation, the control inputs are

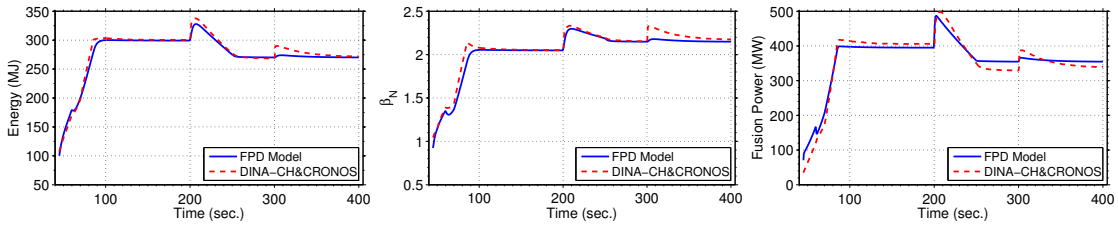

(a) $E(t)$ (b) $\beta_N(t)$ (c) $P_{fus}(t)$

Figure 2.27: (a) Plasma stored energy E versus time, (b) plasma normalized beta β_N versus time, and (c) fusion power P_{fus} versus time for the model comparison simulation test in section 2.9.2.

again modified to a second set of constant values and again remain stationary during section (iv) of the simulation. This sequence of actuator waveforms provides the opportunity to determine the ability of the FPD, physics-based model to predict the plasma magnetic and thermal state evolution during both transient and stationary conditions in plasma actuation. Figures 2.24-2.27 show that the trends of the FPD, physics-based model predicted plasma magnetic and thermal state evolution, as well as the other parameters related to these plasma states, show good agreement with the DINA-CH&CRONOS predicted results during both transient and stationary plasma actuation conditions. The discontinuity in the plasma stored energy, normalized beta, and fusion power predicted by DINA-CH&CRONOS at 300 s, shown in Fig. 2.27, is a numerical artifact in the plasma evolution that results from a slight inconsistency between the plasma state in a simulation that is restarted from a previously executed simulation.

2.10 Tailoring physics-based model to L-mode scenarios in TCV

We now employ the RAPTOR code [13–15], which is a simplified physics-based code (similar to one developed in this work) that simulates the plasma Ψ and T_e profile

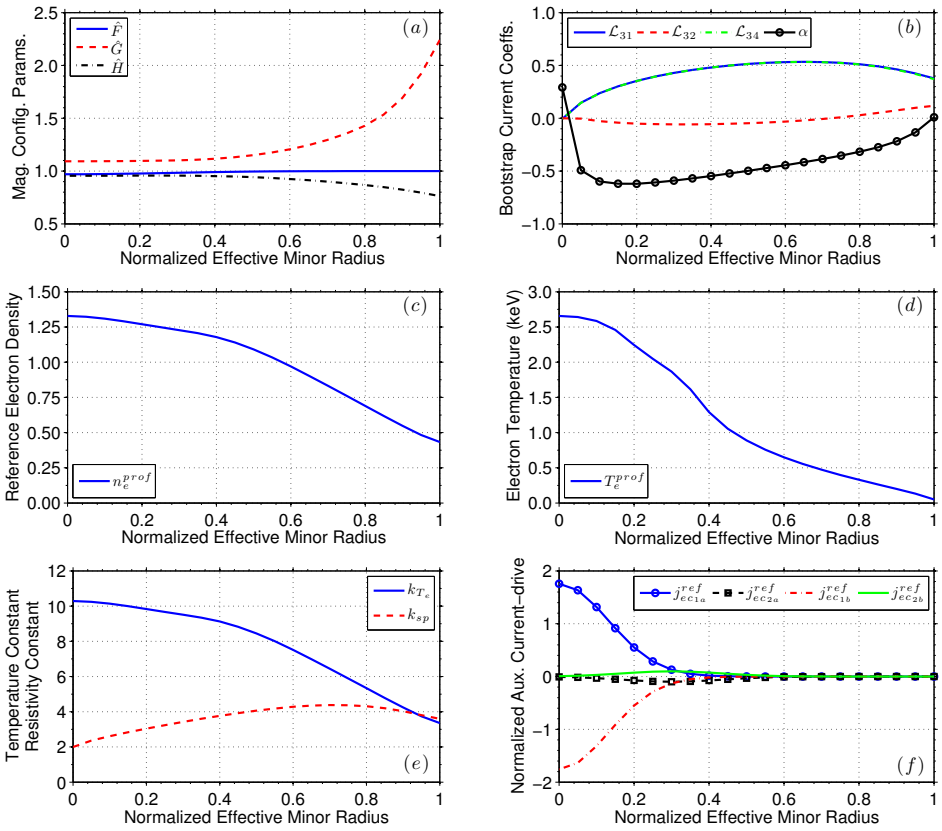

Figure 2.28: Model parameters tailored to the TCV tokamak: (a) magnetic equilibrium configuration parameters $\hat{F}(\hat{\rho})$, $\hat{G}(\hat{\rho})$, and $\hat{H}(\hat{\rho})$, (b) bootstrap current coefficients $\mathcal{L}_{31}(\hat{\rho})$, $\mathcal{L}_{32}(\hat{\rho})$, $\mathcal{L}_{34}(\hat{\rho})$, and $\alpha(\hat{\rho})$, (c) reference electron density profile $n_e^{prof}(\hat{\rho})$, (d) reference electron temperature profile $T_e^{prof}(\hat{\rho})$ (keV), (e) electron temperature coefficient k_{T_e} (10^{10} m^{-3}A^{-1}W$^{-1/2}$) and plasma resistivity coefficient k_{sp} (10^{-8} Ω m keV$^{3/2}$), and (f) normalized auxiliary electron cyclotron ($j_{ec_i}^{ref}$), for $i \in$ [1a,2a,1b,2b], current-drive reference profiles (10^{20} m^{-3}keV^{-1}W^{-1}A m^{-2}).

evolution, configured to the TCV geometry to obtain simulated data of the plasma state evolution to tailor the FPD, physics-based model to L-mode plasma scenarios in TCV. In section 2.10.1, the model parameters tailored to the TCV tokamak are presented and in section 2.10.2 a simulation study that compares the evolution of the plasma parameters predicted by the FPD, physics-based model and RAPTOR is discussed.

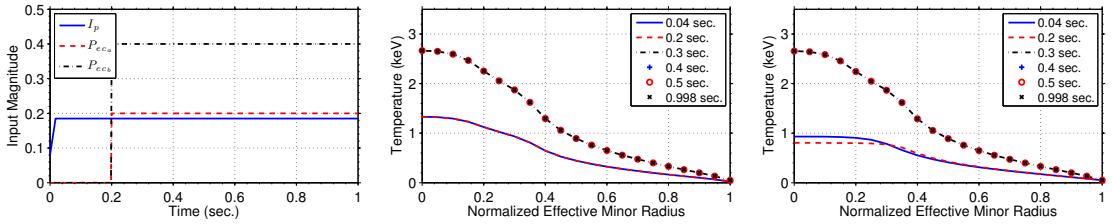

(a) (b) Control-oriented model: T_e (c) RAPTOR: T_e

Figure 2.29: (a) Control inputs applied during simulations (current in MA and power in MW) and electron temperature profile evolution computed via: (b) physics-based control-oriented model and (c) RAPTOR for the model comparison simulation test in section 2.10.2.

2.10.1 Model parameters tailored to TCV

As we are modeling L-mode scenarios in TCV, there are no abrupt changes in particle and energy transport in the plasma, and the temperature exhibits a smooth behavior across the entire spatial domain. Therefore, we model the electron temperature evolution as in (2.63), and we choose the constants in this model as $\gamma = 1$, $\varepsilon = 0.5$, and $\zeta = -1$. This choice qualitatively describes the slowly evolving electron temperature in response to the control actuators, i.e., the observation of (i) an increase in plasma confinement, and hence an increase in temperature, with increasing plasma current, and (ii) a decrease in plasma confinement with increasing total injected power [133]. Also, by changing the electron density, the electron temperature is modified for a given electron pressure.

The parameters related to the magnetic configuration of the plasma equilibrium, the reference profiles for the various models, and the normalizing profiles are shown in Fig. 2.28. The auxiliary heating and current-drive actuators on TCV considered in this work are 4 electron cyclotron launchers that are grouped into 2 clusters (denoted as a and b). The current-drive deposition profiles for each source are shown in Fig. 2.28(f). The gyrotrons in cluster a are configured as follows: 1 on-axis co-current-injection source ($j^{ref}_{ec_{1a}}$ in Fig. 2.28(f)) and 1 off-axis counter-current-injection source

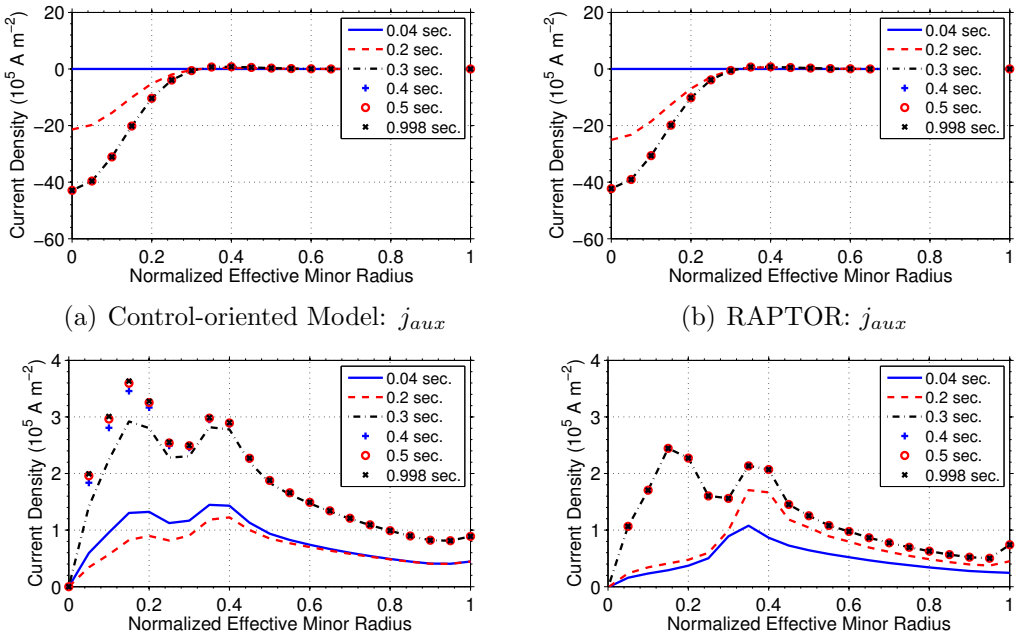

(a) Control-oriented Model: j_{aux}

(b) RAPTOR: j_{aux}

(c) Control-oriented model: j_{bs}

(d) RAPTOR: j_{bs}

Figure 2.30: Auxiliary noninductive current-drive evolution computed via: (a) physics-based control-oriented model and (b) RAPTOR, and bootstrap current-drive evolution computed via: (c) physics-based control-oriented model and (d) RAPTOR for the model comparison simulation test in section 2.10.2.

($j^{ref}_{ec_{2a}}$ in Fig. 2.28(f)), and the gyrotrons in cluster b are configured as follows: 1 on-axis counter-current-injection source ($j^{ref}_{ec_{1b}}$ in Fig. 2.28(f)) and 1 off-axis co-current-injection source ($j^{ref}_{ec_{2b}}$ in Fig. 2.28(f)). In this work, the heating efficiency constants for the auxiliary heating and current-drive actuators are taken as $\eta_{ec_i} = 1$ for $i \in$ [1a,2a,1b,2b]. The hydrogenic ion species in the considered TCV plasmas are solely deuterium ($A_{eff} = 2$). As the plasma temperature in TCV is not hot enough to produce a significant probability of deuterium-deuterium fusion reactions occurring, we choose the fusion heating constant as $\eta_{fus} = 0$. Also, the electron density profile is assumed constant in the considered scenarios. Finally, the other model constants are $B_{\phi,0} = 1.44$ T, $R_0 = 0.88$ m, $\rho_b = 0.3013$ m, and $Z_{eff} = 3.5$.

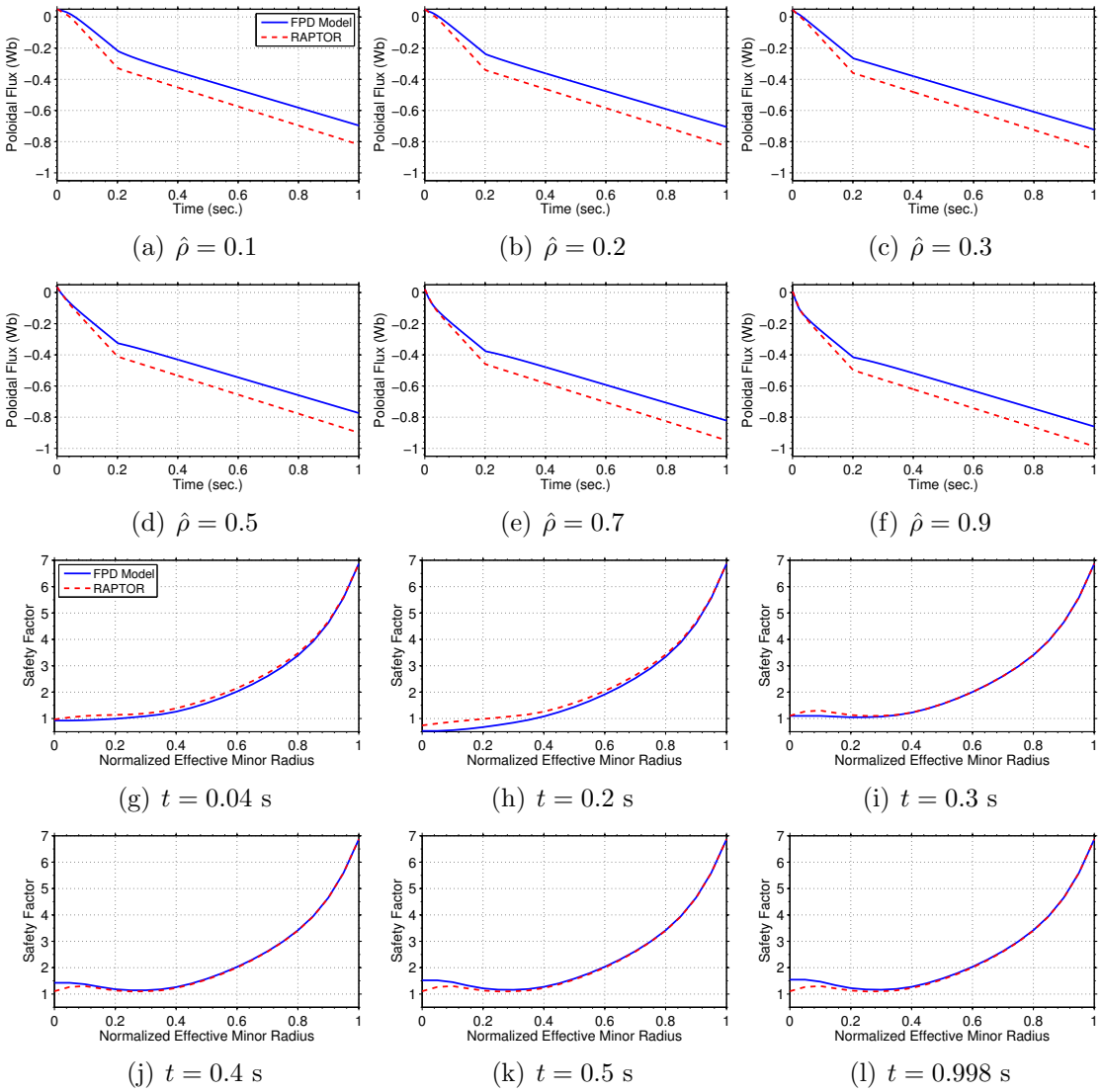

(a) $\hat{\rho} = 0.1$ (b) $\hat{\rho} = 0.2$ (c) $\hat{\rho} = 0.3$

(d) $\hat{\rho} = 0.5$ (e) $\hat{\rho} = 0.7$ (f) $\hat{\rho} = 0.9$

(g) $t = 0.04$ s (h) $t = 0.2$ s (i) $t = 0.3$ s

(j) $t = 0.4$ s (k) $t = 0.5$ s (l) $t = 0.998$ s

Figure 2.31: (a-f) Time trace of poloidal magnetic flux Ψ at various normalized effective minor radii and (g-l) safety factor profile $q(\hat{\rho})$ at various times for the model comparison simulation test in section 2.10.2.

2.10.2 Comparison between model and RAPTOR predicted plasma parameters

We now describe a simulation study that compares the evolution of the plasma parameters predicted by the first-principles-driven, physics-based model and the RAPTOR code [13–15]. The control inputs (total plasma current and gyrotron cluster powers) applied during both simulations are shown in Fig. 2.29(a). We begin the analysis of the FPD model's prediction capabilities by first comparing the prediction of the physics-based models of the electron temperature and noninductive current-drive source evolutions to the RAPTOR predicted plasma parameter evolutions. Figures 2.29(b-c) show the electron temperature profiles and Fig. 2.30 shows the total gyrotron and bootstrap noninductive current-drive sources at various times during the simulations computed by both the physics-based models and RAPTOR. The trends of the physics-based model predicted plasma parameters show good agreement with the RAPTOR predicted results. We now compare the plasma magnetic state evolution predicted by the FPD, physics-based model and RAPTOR. Figures 2.31(a-f) show the evolution of the poloidal magnetic flux Ψ at various normalized effective minor radii and Figs. 2.31(g-l) show a comparison of the FPD, physics-based model predicted and RAPTOR predicted safety factor $q(\hat{\rho})$ profiles at various times. As shown in the figures, the FPD, physics-based model predicted plasma magnetic evolution shows good agreement with the RAPTOR predicted results. The constant offset that develops between the FPD, physics-based model predicted and RAPTOR predicted Ψ profile evolution (shown in Figs. 2.31(a-f)) is due to the slight mismatch between the physics-based model predicted and RAPTOR predicted T_e profile evolution (shown in Figs. 2.29(b-c)) during the initial phase of the simulations ($t \in [0, 0.2]$ s). The electron temperature predicted by the physics-based model is slightly higher than the RAPTOR predicted electron temperature during that time interval. As

a result, the physics-based model predicted plasma resistivity is slightly lower than the RAPTOR predicted plasma resistivity. This results in the FPD, physics-based model predicted poloidal magnetic flux diffusing slower than the RAPTOR predicted poloidal magnetic flux.

2.11 Conclusion

A derivation of the plasma poloidal magnetic flux diffusion equation was provided. This equation describes the resistive diffusion of the poloidal magnetic flux in the tokamak in response to the electric field due to induction, the noninductive current driven by the auxiliary H&CD system, and the bootstrap effect. This physics model was subsequently converted into a form suitable for control design by developing simplified control-oriented versions of physics-based models of the electron density, electron temperature, plasma resistivity, and the noninductive current-drives in response to the available control actuators. The FPD, physics-based model was tailored to L-mode and H-mode scenarios in the DIII-D, ITER, and TCV tokamaks, respectively, demonstrating the flexibility of the developed approach. Finally, the model prediction was shown to be in good agreement with the evolution of experimentally-achieved/advanced-simulation-predicted plasma parameters in the studied operating scenarios. For the remainder of this dissertation, the developed model will be employed to 1.) optimize feedforward trajectories for the tokamak actuators that steer the plasma through the tokamak operating space to reach target plasma scenarios, 2.) design feedback controllers to regulate plasma conditions to maintain desired operating scenarios, and 3.) verify the ability of the designed algorithms to drive the plasma to desired targets through simulations.

Chapter 3

Current profile control in low confinement scenarios in the DIII-D tokamak

3.1 Introduction

In this chapter, a first-principles-driven (FPD), physics-model-based, robust feedback algorithm for current profile control in low confinement (L-mode) operating scenarios in the DIII-D tokamak is designed. The choice of L-mode operating scenarios rather than high confinement (H-mode) operating scenarios is based on the fact that the coupling between the magnetic and kinetic plasma parameters is not as strong in this operating regime. As a result, the dynamics of the current profile evolution in L-mode are simplified, which reduces the complexity of the model-based control design process. Therefore, L-mode operating scenarios are more attractive for initial demonstration of the technical feasibility of controlling the current profile evolution in closed-loop experiments with controllers synthesized from first-principles-driven models. Once the methodology is validated, the focus will be on extending the approach

to high performance scenarios by incorporating the effects of the bootstrap current in the FPD model of the system and synthesizing closed-loop controllers for this more complex operating mode.

The robust feedback controller is synthesized by embedding the control-oriented model of the poloidal magnetic flux evolution developed in [83] into the control design process. In this particular model of the poloidal magnetic flux evolution, the magnetic diffusion equation is combined with empirical correlations for the electron density, the electron temperature, the plasma resistivity, and the auxiliary current drive developed from physical observations and experimental data from L-mode discharges in DIII-D. Secondly, the auxiliary current drive actuators are lumped into a single input, and the noninductive bootstrap current is neglected due to its effects being relatively small in L-mode discharges, in this model. The actuators employed for current profile control are the total plasma current, the total average neutral beam injection power, and the line average electron density. Finally, the feedback controller is tested in simulations and experiments in the DIII-D tokamak. These experiments, along with those described in [98, 99], represent the first successful demonstration of FPD, physics-based, closed-loop control of the entire current profile in a tokamak.

This chapter is organized as follows. In section 3.2, the control-oriented, partial differential equation (PDE) model for the evolution of the poloidal flux profile valid for L-mode discharges is introduced. The governing infinite dimensional PDE is approximated by a finite dimensional system of ordinary differential equations to facilitate the synthesis of a feedback controller by employing a truncated Taylor series expansion in space. While the state of the reduced-order model is linearized around a given feedforward operating trajectory, the control input nonlinearities are preserved through a nonlinear transformation, and a time varying state-space representation of

the deviation dynamics is derived in section 3.3. In section 3.4, the time varying state-space system is represented as an uncertain state-space model, i.e., a nominal time-invariant model plus a bounded uncertain component, which is then formulated into a robust control framework. The part of the plant output we can effectively control is determined by employing a singular value decomposition of the static gain matrix of the nominal plant model in section 3.5, which is combined with the dynamic response of the system around the given feedforward trajectory to synthesize a robust feedback controller. In section 3.6, the feedback controller is synthesized by first considering the nominal model and then analyzing the stability of the closed-loop system in the presence of the model uncertainty. A general framework for real-time feedforward + feedback control of the magnetic and kinetic plasma profiles is implemented in the DIII-D Plasma Control System (PCS), and a simulation simserver (Simserver) that can interface with the DIII-D PCS is developed in section 3.7. In section 3.8 we test the feedback controller in Simserver simulations with the real-time code utilized in the DIII-D PCS, and in section 3.9 the feedback controller is tested in reference tracking and disturbance rejection experiments in the DIII-D tokamak. Finally, conclusions are discussed in section 3.10.

3.2 Partial differential equation model of system dynamics

The control-oriented model of the poloidal magnetic flux evolution derived in [83] is given in normalized cylindrical coordinates by the magnetic diffusion equation

$$\frac{\partial \psi}{\partial t} = f_1(\hat{\rho}) u_1(t) \frac{1}{\hat{\rho}} \frac{\partial}{\partial \hat{\rho}} \left(\hat{\rho} f_4(\hat{\rho}) \frac{\partial \psi}{\partial \hat{\rho}} \right) + f_2(\hat{\rho}) u_2(t) \tag{3.1}$$

with boundary conditions

$$\left.\frac{\partial \psi}{\partial \hat{\rho}}\right|_{\hat{\rho}=0} = 0 \qquad \left.\frac{\partial \psi}{\partial \hat{\rho}}\right|_{\hat{\rho}=1} = -k_3 u_3(t), \tag{3.2}$$

where the functions $f_1(\hat{\rho})$, $f_2(\hat{\rho})$, $f_4(\hat{\rho})$, and the geometrical constant k_3 are defined in [83], and the control inputs are expressed as

$$u_1(t) = \left(\frac{\bar{n}_e(t)}{I_p(t)\sqrt{P_{tot}(t)}}\right)^{3/2} \qquad u_2(t) = \frac{\sqrt{P_{tot}(t)}}{I_p(t)} \qquad u_3(t) = I_p(t). \tag{3.3}$$

The poloidal stream function is denoted by ψ, which is closely related to the poloidal magnetic flux Ψ ($\Psi = 2\pi\psi$), t is the time, $\bar{n}_e(t)$ is the line average electron density, $P_{tot}(t)$ is the total average neutral beam injection power, and $I_p(t)$ is the total plasma current. The normalized effective minor radius $\hat{\rho} = \rho/\rho_b$ is the spatial variable employed to index the magnetic flux surfaces, where ρ is the mean effective minor radius of the magnetic flux surface, i.e., $\Phi(\rho) = \pi B_{\phi,0}\rho^2$, Φ is the toroidal magnetic flux, $B_{\phi,0}$ is the vacuum toroidal magnetic field at the geometric major radius R_0 of the tokamak, and ρ_b is the mean effective minor radius of the last closed magnetic flux surface.

The control inputs $u_1(t)$, $u_2(t)$, and $u_3(t)$ of the magnetic diffusion equation have large order of magnitude differences which is not conducive to developing a feedback control algorithm that uses all of the available actuators to their fullest extent. Therefore, we normalize (3.1) by determining the maximum feedforward values of the three control inputs, which are denoted as $u_{1_{norm}}$, $u_{2_{norm}}$, and $u_{3_{norm}}$ respectively. The control inputs are scaled as $u_1^s(t) = u_1(t)/u_{1_{norm}}$, $u_2^s(t) = u_2(t)/u_{2_{norm}}$, and $u_3^s(t) = u_3(t)/u_{3_{norm}}$, and the parameters in the governing PDE (3.1) are scaled as $f_1^s(\hat{\rho}) = u_{1_{norm}} f_1(\hat{\rho})$, $f_2^s(\hat{\rho}) = u_{2_{norm}} f_2(\hat{\rho})$, and $k_3^s = u_{3_{norm}} k_3$, where $(\cdot)^s$ denotes a scaled quantity. Now each control input can vary between the same magnitude range,

i.e., zero to one, and a feedback controller can be designed to use the full range of each actuator. The superscript s used to denote the scaled control inputs and equation parameters is dropped for the remainder of this chapter in order to simplify notation.

In the plasma physics community, the toroidal current profile in tokamaks (j_{tor}) is usually specified in terms of the safety factor profile (q profile) as this quantity is intimately related to the stability and performance of a tokamak plasma operating scenario [61, 62] (see section 2.6 for the explicit relationship these quantities have to the poloidal magnetic flux). In particular, the q profile is defined in (2.90) and repeated here for convenience as

$$q(\hat{\rho},t) = -\frac{d\Phi}{d\Psi} = -\frac{d\Phi}{2\pi d\psi} = -\frac{B_{\phi,0}\rho_b^2\hat{\rho}}{\partial\psi/\partial\hat{\rho}}. \tag{3.4}$$

Because the q profile is inversely dependent on the gradient of the poloidal stream function $\partial\psi/\partial\hat{\rho}$, it is chosen to be the controlled variable and is denoted by

$$\theta(\hat{\rho},t) \equiv \partial\psi/\partial\hat{\rho}(\hat{\rho},t). \tag{3.5}$$

In order to obtain a PDE for $\theta(\hat{\rho},t)$, (3.1) is expanded using the chain rule as

$$\frac{\partial\psi}{\partial t} = f_1 u_1(t)\frac{1}{\hat{\rho}}\left[\hat{\rho}\frac{\partial\psi}{\partial\hat{\rho}}\frac{df_4}{d\hat{\rho}} + f_4\frac{\partial\psi}{\partial\hat{\rho}} + \hat{\rho}f_4\frac{\partial^2\psi}{\partial\hat{\rho}^2}\right] + f_2 u_2(t). \tag{3.6}$$

Inserting (3.5) into (3.6) results in the following PDE

$$\frac{\partial\psi}{\partial t} = f_1(\hat{\rho})u_1(t)\frac{1}{\hat{\rho}}\left[\hat{\rho}\theta f_4'(\hat{\rho}) + f_4(\hat{\rho})\theta + \hat{\rho}f_4(\hat{\rho})\frac{\partial\theta}{\partial\hat{\rho}}\right] + f_2(\hat{\rho})u_2(t), \tag{3.7}$$

where $(\cdot)' = d/d\hat{\rho}$. By differentiating (3.7) with respect to $\hat{\rho}$, the PDE governing the

evolution of $\theta(\hat{\rho}, t)$ is found to be

$$\frac{\partial \theta}{\partial t} = \left[h_0(\hat{\rho}) \frac{\partial^2 \theta}{\partial \hat{\rho}^2} + h_1(\hat{\rho}) \frac{\partial \theta}{\partial \hat{\rho}} + h_2(\hat{\rho}) \theta \right] u_1(t) + h_3(\hat{\rho}) u_2(t), \tag{3.8}$$

with boundary conditions

$$\theta(0, t) = 0 \qquad \theta(1, t) = -k_3 u_3(t), \tag{3.9}$$

where

$$\begin{aligned} h_0(\hat{\rho}) &= f_1(\hat{\rho}) f_4(\hat{\rho}), \\ h_1(\hat{\rho}) &= f_1'(\hat{\rho}) f_4(\hat{\rho}) + f_1(\hat{\rho}) f_4(\hat{\rho})/\hat{\rho} + 2 f_1(\hat{\rho}) f_4'(\hat{\rho}), \\ h_2(\hat{\rho}) &= f_1'(\hat{\rho}) f_4'(\hat{\rho}) + f_1'(\hat{\rho}) f_4(\hat{\rho})/\hat{\rho} + f_1(\hat{\rho}) f_4'(\hat{\rho})/\hat{\rho} \\ &\quad - f_1(\hat{\rho}) f_4(\hat{\rho})/\hat{\rho}^2 + f_1(\hat{\rho}) f_4''(\hat{\rho}), \\ h_3(\hat{\rho}) &= f_2'(\hat{\rho}). \end{aligned} \tag{3.10}$$

The model (3.8)-(3.10) is the starting point for the development of the feedback controller design. This first-principles-driven, control-oriented, PDE model contains the physics information of how the dynamics of the poloidal flux gradient profile are influenced by the control actuators. The goal is to now convert the physics information contained in the model into a form suitable to synthesize a feedback controller, thus allowing the physics contained in the model to be embedded into the feedback controller.

3.3 Model reduction via spatial discretization

In order to facilitate the design of a feedback controller, the governing infinite dimensional PDE (3.8) is approximated by a finite dimensional system of ordinary

differential equations (ODEs). This is accomplished by discretizing (3.8) in space by using a truncated Taylor series expansion to approximate the spatial derivatives while leaving the time domain continuous [137]. The non-dimensional spatial domain of interest ($\hat{\rho} \in [0, 1]$) is represented by m_θ nodes, and the spacing between the nodes ($\Delta\hat{\rho}$) is defined as $\Delta\hat{\rho} = 1/(m_\theta - 1)$. Central finite difference spatial derivative approximations of order $(\Delta\hat{\rho})^2$ are used in the interior node region, $2 \leq i \leq (m_\theta - 1)$. After applying the spatial derivative approximations to (3.8) and taking into account the boundary conditions (3.9), we obtain a matrix representation for the reduced-order model

$$\dot{\alpha}(t) = \Gamma\alpha(t)v_1(t) + \Omega v_2(t) + \Pi v_3(t), \tag{3.11}$$

where the vector $\alpha = [\theta_2, \ldots, \theta_{m_\theta - 1}] \in \mathbb{R}^{n_\theta}$ is the state of the system at the interior discrete nodes, the vector

$$[v_1(t), v_2(t), v_3(t)] = [u_1(t), u_2(t), u_1(t)u_3(t)] \in \mathbb{R}^3 \tag{3.12}$$

is the control input, $\Gamma \in \mathbb{R}^{n_\theta \times n_\theta}$, $\Omega \in \mathbb{R}^{n_\theta}$, and $\Pi \in \mathbb{R}^{n_\theta}$ are the system matrices, and $n_\theta = m_\theta - 2$. The system matrices for the interior node $i = 2$ are defined as

$$\begin{aligned}
\Gamma_{1,1} &= h_2(\Delta\hat{\rho}) - \frac{2h_0(\Delta\hat{\rho})}{(\Delta\hat{\rho})^2}, \\
\Gamma_{1,2} &= \frac{h_0(\Delta\hat{\rho})}{(\Delta\hat{\rho})^2} + \frac{h_1(\Delta\hat{\rho})}{2\Delta\hat{\rho}}, \\
\Omega_1 &= h_3(\Delta\hat{\rho}), \\
\Pi_1 &= 0.
\end{aligned} \tag{3.13}$$

The system matrices for the interior node region, $3 \leq i \leq (m_\theta - 2)$, are defined as

$$\begin{aligned}
\Gamma_{i-1,i-2} &= \frac{h_0(\Delta x)}{(\Delta\hat{\rho})^2} - \frac{h_1(\Delta x)}{2\Delta\hat{\rho}}, \\
\Gamma_{i-1,i-1} &= h_2(\Delta x) - \frac{2h_0(\Delta x)}{(\Delta\hat{\rho})^2}, \\
\Gamma_{i-1,i} &= \frac{h_0(\Delta x)}{(\Delta\hat{\rho})^2} + \frac{h_1(\Delta x)}{2\Delta\hat{\rho}}, \\
\Omega_{i-1} &= h_3(\Delta x), \\
\Pi_{i-1} &= 0,
\end{aligned} \tag{3.14}$$

where $\Delta x = (i-1)\Delta\hat{\rho}$. The system matrices for the interior node $i = m_\theta - 1$ are defined as

$$\begin{aligned}
\Gamma_{m_\theta-2,m_\theta-2} &= h_2(\Delta x^*) - \frac{2h_0(\Delta x^*)}{(\Delta\hat{\rho})^2}, \\
\Gamma_{m_\theta-2,m_\theta-3} &= \frac{h_0(\Delta x^*)}{(\Delta\hat{\rho})^2} - \frac{h_1(\Delta x^*)}{2\Delta\hat{\rho}}, \\
\Omega_{m_\theta-2} &= h_3(\Delta x^*), \\
\Pi_{m_\theta-2} &= -k_3\left(\frac{h_0(\Delta x^*)}{(\Delta\hat{\rho})^2} + \frac{h_1(\Delta x^*)}{2\Delta\hat{\rho}}\right),
\end{aligned} \tag{3.15}$$

where $\Delta x^* = (m_\theta - 2)\Delta\hat{\rho}$. All other entries in the Γ system matrix are zero. The values of θ at the boundary nodes $i = 1$ and $i = m_\theta$ are known from (3.10) and are therefore not included in the reduced-order model (3.11).

Let $\alpha_{FF}(t)$ and $v_{FF}(t)$ be the feedforward trajectories of the states and control inputs respectively with initial condition $\alpha_{FF}(0)$. These feedforward trajectories satisfy

$$\dot{\alpha}_{FF}(t) = \Gamma\alpha_{FF}(t)v_{1_{FF}}(t) + \Omega v_{2_{FF}}(t) + \Pi v_{3_{FF}}(t). \tag{3.16}$$

By defining the perturbation variables $x(t) = \alpha(t) - \alpha_{FF}(t)$ and $v_{FB}(t) = v(t) - v_{FF}(t)$, where $x(t)$ is the deviation away from the feedforward state trajectories and $v_{FB}(t)$ is

the output of the to-be-designed feedback controller, we can obtain a model suitable for tracking control design. Inserting the perturbation variables into (3.11) results in

$$\dot{\alpha}_{FF} + \dot{x} = \Gamma\big(\alpha_{FF} + x\big)\big(v_{1_{FF}} + v_{1_{FB}}\big) + \Omega\big(v_{2_{FF}} + v_{2_{FB}}\big) + \Pi\big(v_{3_{FF}} + v_{3_{FB}}\big). \quad (3.17)$$

By using (3.16), we can express (3.17) as

$$\dot{x} = \Gamma v_{1_{FF}} x + \Gamma\big(\alpha_{FF} + x\big)v_{1_{FB}} + \Omega v_{2_{FB}} + \Pi v_{3_{FB}}. \quad (3.18)$$

Due to the term $\Gamma x v_{1_{FB}}$, equation (3.18), which describes the behavior of the deviation dynamics, is bilinear (nonlinearity resulting from the product between the control input and the state). In addition, the control inputs $v_{1_{FB}}$, $v_{2_{FB}}$, and $v_{3_{FB}}$ are nonlinear functions of the real actuators as shown by the nonlinear transformations (3.3) and (3.12). While we neglect in this work the bilinear state behavior by assuming that the feedback control input v_{FB} is able to keep the deviation of the system state away from the feedforward state trajectory small, i.e., $\alpha_{FF} >> x$, we preserve the dominant control input nonlinearities through the nonlinear transformations (3.3) and (3.12). An approximate linearization of the state dynamics can therefore be obtained by neglecting the nonlinear term, i.e.,

$$\big(\alpha_{FF} + x\big) \approx \alpha_{FF}, \quad (3.19)$$

and rewriting (3.18) as

$$\dot{x} = \Gamma v_{1_{FF}} x + \Gamma \alpha_{FF} v_{1_{FB}} + \Omega v_{2_{FB}} + \Pi v_{3_{FB}}. \quad (3.20)$$

Simulations and experiments show the closed-loop system to be robust to this approximation and indicate no need for the extra burden of taking into account the bilinear

state behavior during the control synthesis, which is indeed possible. The deviation dynamics (3.20) can be written as a linear time-variant (LTV), dynamic, state-space model, i.e.,

$$\begin{aligned} \dot{x} &= A(t)x + B(t)v_{FB} \\ y &= Cx + Dv_{FB} \end{aligned} \tag{3.21}$$

where $A(t) = \Gamma v_{1_{FF}}(t) \in \mathbb{R}^{n_\theta \times n_\theta}$, $B(t) = [\Gamma \alpha_{FF}(t), \Omega, \Pi] \in \mathbb{R}^{n_\theta \times 3}$, $C = I_{n_\theta} \in \mathbb{R}^{n_\theta \times n_\theta}$ where I_{n_θ} is an $n_\theta \times n_\theta$ identity matrix, $D = 0 \in \mathbb{R}^{n_\theta \times 3}$, $x \in \mathbb{R}^{n_\theta}$, $y \in \mathbb{R}^{n_\theta}$, and $v_{FB} = [v_{1_{FB}}, v_{2_{FB}}, v_{3_{FB}}]^T \in \mathbb{R}^3$. Here α, and therefore x, is assumed measurable. A linear control law for the inputs $v_{1_{FB}}(t)$, $v_{2_{FB}}(t)$, and $v_{3_{FB}}(t)$ can now be determined and combined with the nonlinear inverse transformations resulting from (3.3) and (3.12) to produce an overall nonlinear control law for $I_p(t)$, $P_{tot}(t)$, and $\bar{n}_e(t)$.

The first-principles-driven linear model for the deviation dynamics (3.21) is similar in structure to the linear plasma response models obtained by performing system identification experiments. However, there are some subtle differences between the two types of models. Firstly, the first-principles-driven deviation model can be obtained around any feedforward reference trajectory of the system while the data-driven deviation model can only be obtained around the reference plasma state adopted during the identification process. Secondly, the first-principles-driven deviation model is time varying, therefore, it provides information on how the deviation dynamics evolve throughout the discharge while the data-driven deviation model is time invariant. Finally, the first-principles-driven deviation model is able to capture the nonlinear effect the control actuators have on the current profile evolution through the transformations (3.3) and (3.12), while the data-driven deviation model can only capture the linear effect the control actuators have on the current profile evolution.

3.4 Manipulation of dynamic model into robust control framework

We now have a LTV model describing the dynamic behavior of the system around any given feedfoward operating trajectory that we can use to synthesize a feedback controller. However, most linear control design techniques are suited for time-invariant model dynamics, i.e., the state-space matrices A, B, C, D of the model are not a function of time. Therefore, we choose to model the time-varying system (3.21) as a nominal time-invariant model plus a bounded uncertain component. We then seek to design a feedback controller to stabilize the closed-loop system for all allowable uncertain perturbations.

The control inputs $v_{FF}(t)$ are chosen to produce a desired trajectory of the system $\alpha_{FF}(t)$ [96, 97], therefore, both time varying quantities are bounded. We choose to model the time varying parameters $v_{1_{FF}}(t)$ and $\alpha_{FF}(t)$ in the definition of the system matrices of (3.21) as a nominal value plus a bounded uncertain component, i.e.,

$$v_{1_{FF}}(t) \in \gamma_v\Big(1+\beta_v\delta_v\Big) \qquad \alpha_{i_{FF}}(t) \in \gamma_\alpha^i\Big(1+\beta_\alpha^i\delta_\alpha^i\Big), \tag{3.22}$$

where $\gamma_v = (v_{1_{FF_{max}}} + v_{1_{FF_{min}}})/2$, $\gamma_\alpha^i = (\alpha_{i_{FF_{max}}} + \alpha_{i_{FF_{min}}})/2$, $\beta_v = (v_{1_{FF_{max}}} - v_{1_{FF_{min}}})/(2\gamma_v)$, and $\beta_\alpha^i = (\alpha_{i_{FF_{max}}} - \alpha_{i_{FF_{min}}})/(2\gamma_\alpha^i)$ with $|\delta_v| \leq 1$ and $|\delta_\alpha^i| \leq 1$ where $i = 1, 2, \ldots, n_\theta$. Since the vector α_{FF} contains the value of θ at the n_θ nodes and the parameter $v_{1_{FF}}$ is a scalar, this method of modeling the time varying parameters produces $n_\theta + 1$ uncertain parameters. By inserting the models (3.22) into (3.21) and defining the total uncertainty vector δ as $\delta = [\delta_\alpha^1, \ldots, \delta_\alpha^{n_\theta}, \delta_v] \in \mathbb{R}^{n_\theta+1}$, the state-space

matrices $A(t)$, $B(t)$, C, D in (3.21) are expressed as

$$\begin{aligned} A(t) &= A_0 + \sum_{m=1}^{n_\theta+1} \delta_m A_m^* \qquad B(t) = B_0 + \sum_{m=1}^{n_\theta+1} \delta_m B_m^*, \\ C &= C_0 + \sum_{m=1}^{n_\theta+1} \delta_m C_m^* \qquad D = D_0 + \sum_{m=1}^{n_\theta+1} \delta_m D_m^*, \end{aligned} \tag{3.23}$$

where

$$A_0 = \gamma_v \Gamma \qquad B_{0_k} = \left[\sum_{i=1}^{n_\theta} \gamma_\alpha^i \Gamma_{k,i}, \Omega_k, \Pi_k \right] \qquad C_0 = I_{n_\theta} \qquad D_0 = 0, \tag{3.24}$$

and

$$\begin{aligned} A^*_{1,2,\ldots,n_\theta} &= 0 \qquad A^*_{n_\theta+1} = \gamma_v \beta_v \Gamma, \\ B^*_{m_k} &= \left[\left(\gamma_\alpha^m \beta_\alpha^m \right) \Gamma_{k,m}, 0, 0 \right] \quad \text{for } m = 1, 2, \ldots, n_\theta \qquad B^*_{n_\theta+1} = 0, \\ C^*_{1,2,\ldots,n_\theta+1} &= 0 \qquad D^*_{1,2,\ldots,n_\theta+1} = 0, \end{aligned} \tag{3.25}$$

where $k = 1, 2, \ldots, n_\theta$, $\Gamma_{k,i}$ denotes the k-th row i-th column component of Γ, B_{0_k} and $B^*_{m_k}$ denote the k-th component of B_0 and B^*_m, respectively, and I_{n_θ} denotes the $n_\theta \times n_\theta$ identity matrix. The state-space matrices A_0, B_0, C_0, D_0 represent the nominal system, δ_m denotes the m-th component of δ, and the state-space matrices A^*_m, B^*_m, C^*_m, D^*_m represent the influence that each uncertain parameter δ_m has on the system.

A linear system with state-space matrices A, B, C, D has a transfer function representation $G(s) = C(sI_{n_\theta} - A)^{-1}B + D$ that describes the relationship between the system's inputs and outputs, i.e., $y = G(s)v_{FB}$, where s denotes the Laplace variable and n_θ is the number of states of the system. If we insert the representation of the state-space matrices (3.23) into the transfer function representation of the system, the nominal model will be coupled with the uncertain parameters δ_m for

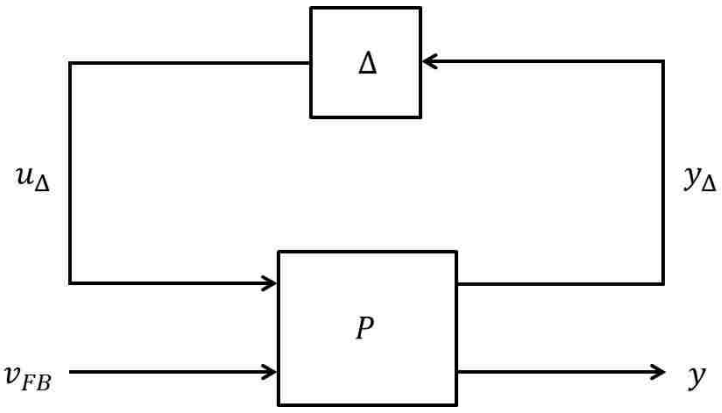

Figure 3.1: General $P - \Delta$ control configuration with model uncertainty.

$m = 1, \ldots, n_\theta + 1$. By exploiting the structure of the state matrices in (3.23), we can separate the uncertain parameters from the nominal parameters by grouping the uncertain parameters into a structured uncertainty matrix $\Delta = \text{diag}\{\delta\}$ to express the feedback system in the conventional $P - \Delta$ robust control framework shown in Fig. 3.1 by employing the method outlined in [138], where $P(s)$ is the generalized transfer function of the system. If the transfer function $P \in \mathbb{R}^{(q_T+n_\theta)\times(q_T+3)}$, where q_T is the rank of the uncertainty matrix Δ, is partitioned as

$$P = \begin{bmatrix} P_{11} & P_{12} \\ P_{21} & P_{22} \end{bmatrix}, \tag{3.26}$$

the input-output equations of the generalized transfer function are

$$\begin{aligned} y_\Delta &= P_{11}u_\Delta + P_{12}v_{FB}, \\ y &= P_{21}u_\Delta + P_{22}v_{FB}, \end{aligned} \tag{3.27}$$

where $P_{11} \in \mathbb{R}^{q_T\times q_T}$, $P_{12} \in \mathbb{R}^{q_T\times 3}$, $P_{21} \in \mathbb{R}^{n_\theta\times q_T}$, $P_{22} \in \mathbb{R}^{n_\theta\times 3}$, $y_\Delta \in \mathbb{R}^{q_T}$, $u_\Delta \in \mathbb{R}^{q_T}$, $y \in \mathbb{R}^{n_\theta}$, and $v_{FB} \in \mathbb{R}^3$. The relationship between the system transfer function $G(s)$ and the generalized transfer function $P(s)$ and the uncertainty matrix Δ is expressed

as

$$G(s) = P_{22}(s) + P_{21}(s)\Delta\left[I_{q_T} - P_{11}(s)\Delta\right]^{-1}P_{12}(s), \tag{3.28}$$

where I_{q_T} is a $q_T \times q_T$ identity matrix. An overview of the employed technique is provided in Appendix A.

By examining (3.27), it can be seen that the transfer function P contains information on how both the nominal system and the uncertain parameters affect the output of the system y. The output of the system is driven by the feedback control input v_{FB} and the uncertain input perturbation u_Δ through the transfer functions P_{22} and P_{21}, respectively. The uncertain input perturbation is driven by the uncertain output perturbation y_Δ through the uncertain matrix Δ (see Fig. 3.1). Finally, the output perturbation is driven by the feedback control input v_{FB} and the uncertain input perturbation u_Δ through the transfer functions P_{12} and P_{11}, respectively. If there were no uncertain perturbations, i.e., $\Delta = 0$, the input-output equation of the system would be reduced to

$$y = P_{22}v_{FB}. \tag{3.29}$$

Therefore, the transfer function P_{22} describes the nominal response of the system, and the transfer functions P_{11}, P_{12}, and P_{21} describe how the uncertain parameters affect the output of the system.

3.5 Evaluation of relevant control channels

It is desired that the controlled output $y(t)$ be able to track a reference value $r(t)$, therefore, we define the tracking error $e(t)$ as

$$e(t) = r(t) - y(t). \tag{3.30}$$

The conditions to bring the tracking error exactly to zero are typically not met because the number of controlled outputs (n_θ) is larger than the number of controlled inputs (3). As a result, we can only independently control 3 linear combinations of the output of the system. Therefore, in order to synthesize an effective feedback controller, it is necessary to determine which output directions are the most controllable and which input directions are the most influential. If these directions are not identified, the feedback controller could actuate in a direction that the system does not respond to and a lot of control energy could be spent for a marginal improvement in the value of the tracking error. The technique we employ to evaluate and decouple the most relevant control channels is based on a singular value decomposition (SVD) of the static (steady-state) gain matrix of the nominal state-space system A_0, B_0, C_0, D_0.

The relationship between the outputs y and the inputs v_{FB} of the nominal system is expressed in terms of the nominal transfer function $G_0(s)$ which is defined as

$$y = G_0(s)v_{FB} \qquad \text{where } G_0(s) = C_0(sI_{n_\theta} - A_0)^{-1}B_0 + D_0. \tag{3.31}$$

The nominal input-output relation in steady state (i.e., $s \to 0$) is expressed as

$$\bar{y} = \bar{G}_0\bar{v}_{FB} = \big(- C_0(A_0)^{-1}B_0 + D_0\big)\bar{v}_{FB}, \tag{3.32}$$

where $\bar{y}$ denotes the steady-state output, $\bar{v}_{FB}$ denotes the steady-state input, and $\bar{G}_0$ denotes the steady-state gain of the plant $G_0(s)$ (i.e., $s \to 0$). We next define the "weighted" transfer function $\tilde{G}_0$ and its economy size SVD as

$$\tilde{G}_0 = Q^{1/2}\bar{G}_0R^{-1/2} = U\Sigma V^T, \tag{3.33}$$

where $\Sigma = \text{diag}\{\sigma_1, \sigma_2, \sigma_3\} \in \mathbb{R}^{3\times3}$ is a diagonal matrix of steady-state singular values with $\sigma_1 > \sigma_2 > \sigma_3 > 0$ and $U \in \mathbb{R}^{n_\theta\times3}$ and $V \in \mathbb{R}^{3\times3}$ are matrices that

possess the following properties $V^TV = VV^T = I, U^TU = I$. We have introduced the positive definite matrices $Q \in \mathbb{R}^{n_\theta \times n_\theta}$ and $R \in \mathbb{R}^{3\times 3}$ to weight the relative tracking performance and control effort. Using (3.33), the input-output relation (3.32) is expressed as

$$\bar{y} = \bar{G}_0 \bar{v}_{FB} = Q^{-1/2}\tilde{G}_0 R^{1/2}\bar{v}_{FB} = Q^{-1/2}U\Sigma V^T R^{1/2}\bar{v}_{FB}. \tag{3.34}$$

We note that the columns of the matrix $Q^{-1/2}U\Sigma$ define a basis for the subspace of obtainable steady-state output values. Therefore, any obtainable steady-state output can be written as a linear combination $\bar{y}^* \in \mathbb{R}^3$ of the basis vectors, and we can write

$$\bar{y} = Q^{-1/2}U\Sigma\bar{y}^* \iff \bar{y}^* = \Sigma^{-1}U^TQ^{1/2}\bar{y}. \tag{3.35}$$

As the obtainable steady-state outputs are given by (3.35), this implies that only the component of the reference vector that lies in the subspace $Q^{-1/2}U\Sigma$ will be able to be tracked in steady state, and we can define the quantity

$$\bar{r}^* = \Sigma^{-1}U^TQ^{1/2}\bar{r} \in \mathbb{R}^3, \tag{3.36}$$

which represents the trackable components of the reference. By defining

$$\bar{v}^*_{FB} = V^TR^{1/2}\bar{v}_{FB} \iff \bar{v}_{FB} = R^{-1/2}V\bar{v}^*_{FB}, \tag{3.37}$$

where $\bar{v}^*_{FB} \in \mathbb{R}^3$, and by employing (3.35) and (3.34), a decoupled relationship between the outputs $\bar{y}^*$ and the inputs $\bar{v}^*_{FB}$ is obtained as

$$\bar{y}^* = \Sigma^{-1}U^TQ^{1/2}\bar{y} = \Sigma^{-1}U^TQ^{1/2}Q^{-1/2}U\Sigma V^TR^{1/2}\bar{v}_{FB} = \bar{v}^*_{FB}. \tag{3.38}$$

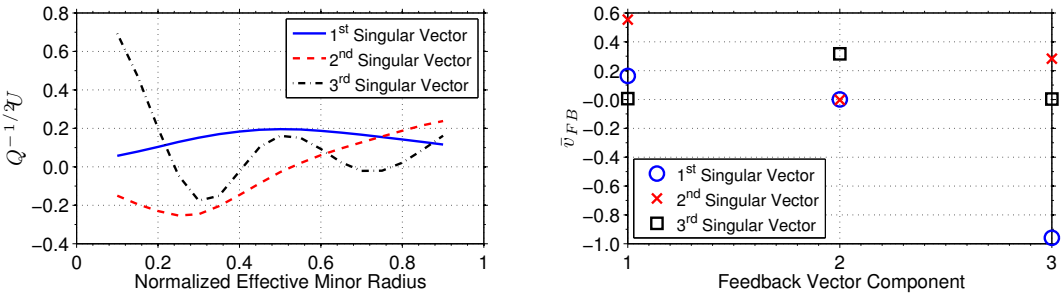

(a) (b)

Figure 3.2: Steady-state (a) reference output singular vectors and (b) input singular vectors for θ profile control in DIII-D L-mode scenarios.

We note that some of the singular values σ_i may have a small magnitude relative to others and may be chosen to be neglected in the control synthesis to avoid potentially spending a significant amount of control effort for only a marginal improvement in the tracking error (3.30). We therefore partition the singular values into k_s significant singular values Σ_s and $3 - k_s$ negligible singular values Σ_{ns}. The significant components of the reference, output, and input vectors can then be defined as $\bar{r}_s^* = \Sigma_s^{-1} U_s^T Q^{1/2} \bar{r} \in \mathbb{R}^{k_s}$, $\bar{y}_s^* = \Sigma_s^{-1} U_s^T Q^{1/2} \bar{y} \in \mathbb{R}^{k_s}$, and $\bar{v}_{FB_s}^* = V_s^T R^{1/2} \bar{v}_{FB} \in \mathbb{R}^{k_s}$, respectively, where $U_s \in \mathbb{R}^{n_\theta \times k_s}$ and $V_s \in \mathbb{R}^{3 \times k_s}$ are the components of U and V associated with the significant singular values. A detailed overview of the SVD technique employed evaluate the relevant control channels is provided in Appendix B.

The singular vectors of the basis for the subspace of obtainable steady-state output values $Q^{-1/2}U$ are shown in Fig. 3.2(a). The corresponding singular vectors associated with the steady-state input values $R^{-1/2}V$ are shown in Fig. 3.2(b). The associated singular values are $\sigma_1 = 7.9360$, $\sigma_2 = 0.2738$, and $\sigma_3 = 0.0015$, which are the result of the dynamic model assumptions, the actuator configuration, and the input scaling. As evidenced by the magnitude of the first singular value relative to the others, the first output singular vector is the dominant shape of an achievable steady-state profile, according to the model. In order to generate this profile shape, the feedback

controller can actuate in the direction associated with the first input singular vector, which contains a strong contribution from the boundary feedback control component $v_{3_{FB}}$. As the value of the singular value decreases, a larger amount of control effort is needed along the direction of the associated input singular vector to produce a significant contribution to the steady-state profile in the direction of the associated output singular vector.

3.6 Feedback control problem formulation

The control goal is to design a feedback controller that can minimize the tracking error (3.30) while using as little feedback control effort as possible, achieve a set of specified performance objectives, and robustly stabilize the system by controlling the significant portion of the output of the system (3.27). A schematic of this control problem is shown in Fig. 3.3. The blocks $\Sigma_s^{-1}U_s^TQ^{1/2}$ and $R^{-1/2}V_s$ are used to obtain a one-to-one relationship between the outputs and the inputs of the system, which provides us the ability to synthesize a square feedback controller K. The block $\Sigma_s^{-1}U_s^TQ^{1/2}$ extracts the significant component of the tracking error e_s^* from the error signal e. The feedback controller is driven by the error e_s^* and outputs the significant component of the feedback control input $v_{FB_s}^*$. Finally, the block $R^{-1/2}V_s$ is used to compute the feedback control input v_{FB} that is applied to the system from the control signal $v_{FB_s}^*$. The outputs of the closed-loop system Z_1 and Z_2 are defined as $Z_1 = W_pe_s^*$ and $Z_2 = W_uv_{FB_s}^*$, where W_p and W_u are frequency dependent functions that will be used to optimize the closed-loop performance of the system during the controller design process by minimizing the frequency-weighted tracking error (Z_1) and control effort (Z_2).

The feedback system is expressed in the conventional $\Delta - P^* - K$ robust control design framework shown in Fig. 3.4, where P^* is the generalized plant and $r_s^* =$

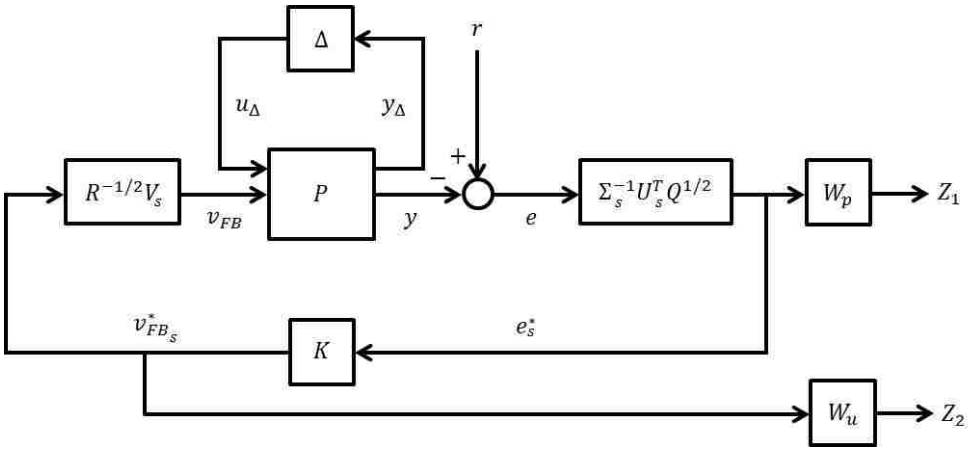

Figure 3.3: Schematic of control problem formulation for θ profile feedback control design in DIII-D L-mode scenarios.

$\Sigma_s^{-1}U_s^TQ^{1/2}r$. By defining the transfer functions

$$\begin{aligned} G_{DC} &= \Sigma_s^{-1}U_s^TQ^{1/2}P_{22}R^{-1/2}V_s, \\ T_{y_\Delta v} &= P_{12}R^{-1/2}V_s, \\ T_{yu_\Delta} &= \Sigma_s^{-1}U_s^TQ^{1/2}P_{21}, \end{aligned} \tag{3.39}$$

the input-output equations of the generalized plant P^* are

$$\left[\begin{array}{c} y_\Delta \\ Z_1 \\ Z_2 \\ \hline e^*_s \end{array}\right] = \left[\begin{array}{cc|c} P^*_{11} & P^*_{12} & P^*_{13} \\ P^*_{21} & P^*_{22} & P^*_{23} \\ P^*_{31} & P^*_{32} & P^*_{33} \\ \hline P^*_{41} & P^*_{42} & P^*_{43} \end{array}\right] \left[\begin{array}{c} u_\Delta \\ r^*_s \\ \hline v^*_{FB_s} \end{array}\right] = \left[\begin{array}{c|c} \tilde{P}^*_{11} & \tilde{P}^*_{12} \\ \hline \tilde{P}^*_{21} & \tilde{P}^*_{22} \end{array}\right] \left[\begin{array}{c} u_\Delta \\ r^*_s \\ \hline v^*_{FB_s} \end{array}\right], \tag{3.40}$$

where

$$\begin{array}{lll} P^*_{11} = P_{11} & P^*_{21} = -W_pT_{yu_\Delta} & P^*_{31} = 0 \\ P^*_{12} = 0 & P^*_{22} = W_p & P^*_{32} = 0 \\ P^*_{13} = T_{y_\Delta v} & P^*_{23} = -W_pG_{DC} & P^*_{33} = W_u \\ P^*_{41} = -T_{yu_\Delta} & P^*_{42} = I & P^*_{43} = -G_{DC}. \end{array}$$

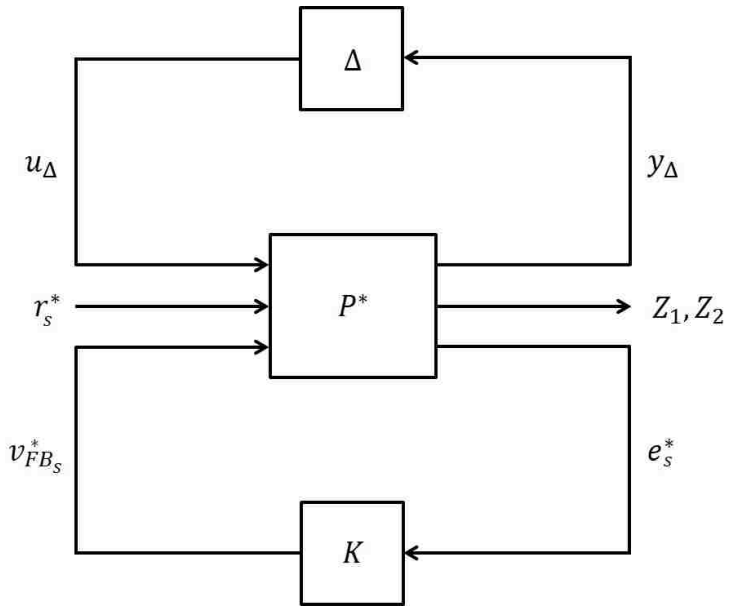

Figure 3.4: Model in conventional $\Delta - P^* - K$ robust control design framework.

The system (3.40) can be written in the conventional $N - \Delta$ closed-loop control analysis configuration shown in Fig. 3.5 by using the definition of the lower linear fractional transformation (LFT), which is denoted as F_l, between P^* and K, i.e.,

$$N = F_l(P^*, K) = \tilde{P}_{11}^* + \tilde{P}_{12}^* K (I - \tilde{P}_{22}^* K)^{-1} \tilde{P}_{21}^*. \tag{3.41}$$

By using the definitions

$$\begin{aligned} S_{DC_O} &= (I + G_{DC} K)^{-1}, \\ T_{DC_O} &= G_{DC} K (I + G_{DC} K)^{-1}, \\ I &= S_{DC_O} + T_{DC_O}, \end{aligned} \tag{3.42}$$

where S_{DC_O} is the decoupled output sensitivity function and T_{DC_O} is the decoupled output complementary sensitivity function, the system (3.40) is expressed in the $N-\Delta$

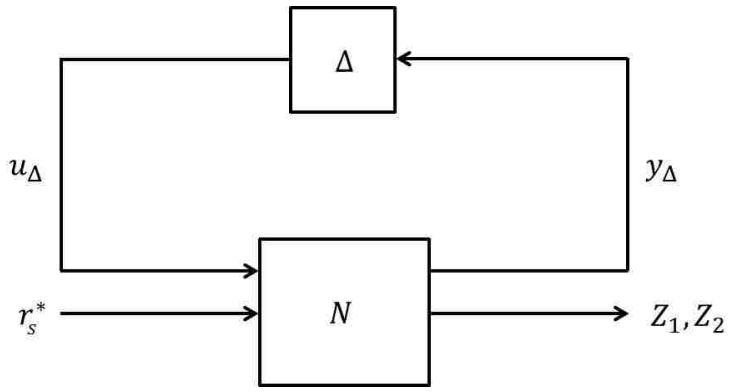

Figure 3.5: General $N - \Delta$ closed-loop control analysis configuration with model uncertainty.

framework as

$$\begin{bmatrix} y_\Delta \\ Z_1 \\ Z_2 \end{bmatrix} = N \begin{bmatrix} u_\Delta \\ r_s^* \end{bmatrix} \quad N = \begin{bmatrix} N_{11} & N_{12} \\ N_{21} & N_{22} \\ N_{31} & N_{32} \end{bmatrix} = \begin{bmatrix} P_{11} - T_{y_\Delta v} K S_{DC_O} T_{yu_\Delta} & T_{y_\Delta v} K S_{DC_O} \\ -W_p S_{DC_O} T_{yu_\Delta} & W_p S_{DC_O} \\ -W_u K S_{DC_O} T_{yu_\Delta} & W_u K S_{DC_O} \end{bmatrix}. \tag{3.43}$$

One possible approach to designing a feedback controller K is to directly take the uncertainty Δ into account during the design process by employing the μ-synthesis technique [10]. This technique aims to synthesize a feedback controller that robustly stabilizes the system by iterating between controller design and robust stability analysis in a systematic sequence of steps. This approach would guarantee that the designed controller would robustly stabilize the system, however, the computational complexity of this design technique is high, and the iterations may not converge to the best solution. Therefore, we adopt a different approach to synthesize a feedback controller. The technique we employ is to design a nominal controller K to achieve the specified control goals for the nominal closed-loop system, i.e., we assume $\Delta = 0$. We then take the uncertainty Δ into account by analyzing the robust stability of the system with this nominal controller. If the controller successfully robustly stabilizes

the system, we have achieved all of our control goals. If the controller does not robustly stabilize the system, we must repeat the process of designing a controller for the nominal system while relaxing the performance objectives of the closed-loop system. With this purpose in mind, the nominal performance condition of the closed-loop system (3.43) and the control problem are expressed as

$$\begin{bmatrix} Z_1 \\ Z_2 \end{bmatrix} = \begin{bmatrix} W_p S_{DC_O} \\ W_u K S_{DC_O} \end{bmatrix} \begin{bmatrix} r_s^* \end{bmatrix} \quad \Rightarrow \quad \min_K \left\| \begin{matrix} W_p S_{DC_O} \\ W_u K S_{DC_O} \end{matrix} \right\|_\infty, \quad \forall \omega, \tag{3.44}$$

where $||\cdot||_\infty$ denotes the H_∞ norm. The frequency dependent weight functions $W_p(s)$ and $W_u(s)$ are chosen to shape (place upper bounds on the magnitude of) the closed-loop transfer functions and are parameterized as [10]

$$W_p(s) = \frac{\left(s/\sqrt{M_p} + \omega_p\right)^2}{\left(s + \omega_p\sqrt{H_p^*}\right)^2} \qquad W_u(s) = \frac{\left(s/\sqrt{M_u} + \omega_u\right)^2}{\left(s + \omega_u\sqrt{H_u^*}\right)^2}, \tag{3.45}$$

where $M_p = 1$, $H_p^* = 10^{-6}$, $\omega_p = 1$, $M_u = 1$, $H_u^* = 10^{0.1}$, and $\omega_u = 10$. If we are able to find a controller K that minimizes the stacked norm of the transfer functions $W_p S_{DC_O}$ and $W_u K S_{DC_O}$, we will have minimized the effect a change in the reference r_s^* has on the error e_s^* while using as little feedback control effort $v_{FB_s}^*$ as possible and achieved a desired performance in the response of the nominal closed-loop system to changes in the reference r_s^*. Therefore, by solving the minimization problem (3.44), we have synthesized a controller that minimizes (3.30) while using as little control effort as possible and produces a desired closed-loop response of the system. An introduction to the design of feedback controllers by employing the H_∞ closed-loop shaping technique is provided in Appendix C.

The feedback controller K found by solving (3.44) is written in state-space form

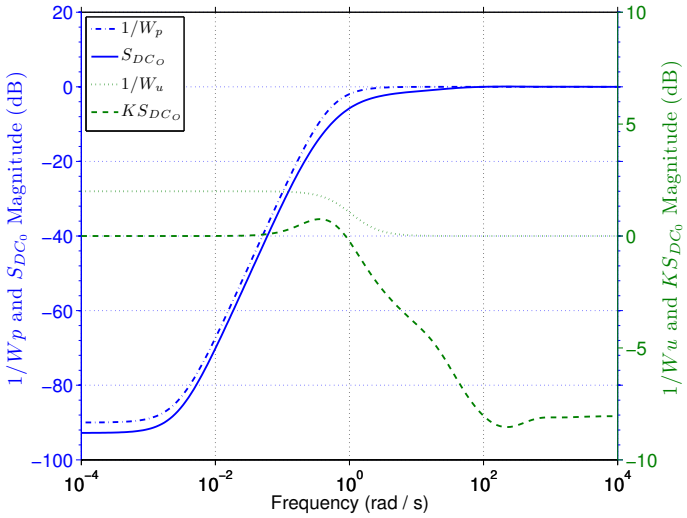

Figure 3.6: Maximum singular value diagram of: inverse of performance weight $1/W_p$ (dash-dot), transfer function S_{DC_o} (solid), inverse of performance weight $1/W_u$ (dot), and transfer function KS_{DC_o} (dash).

as

$$\begin{aligned} \dot{x}_{fb} &= A_{fb}x_{fb} + B_{fb}e_s^*, \\ v_{FB_s}^* &= C_{fb}x_{fb} + D_{fb}e_s^*, \end{aligned} \tag{3.46}$$

where the vector $x_{fb} \in \mathbb{R}^{n_{fb}}$ is the internal controller states, $A_{fb} \in \mathbb{R}^{n_{fb}\times n_{fb}}$, $B_{fb} \in \mathbb{R}^{n_{fb}\times k_s}$, $C_{fb} \in \mathbb{R}^{k_s\times n_{fb}}$, and $D_{fb} \in \mathbb{R}^{k_s\times k_s}$ are the controller system matrices, and n_{fb} is the number of controller states. For this controller design, the significant singular values are chosen as $\Sigma_s = \sigma_1$, and the negligible singular values are chosen as $\Sigma_{ns} = \text{diag}\{\sigma_2, \sigma_3\}$, i.e., $k_s = 1$. By neglecting the second and third singular values, the feedback controller will be able to actuate the system in the direction associated with the first input singular vector shown in Fig. 3.2(b) to produce the dominate shape of an achievable steady-state profile associated with the first output singular vector shown in Fig. 3.2(a). To analyze the closed-loop performance of the nominal system, the frequency response of the magnitude of the maximum singular value of

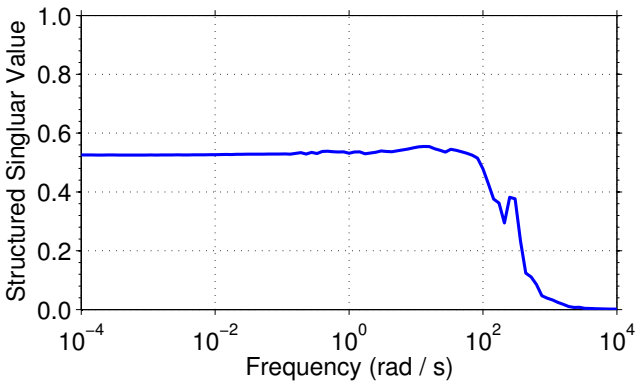

Figure 3.7: Structured singular value μ versus frequency.

the upper bounds $1/W_p$ and $1/W_u$ along with the achieved transfer functions S_{DC_O} and KS_{DC_O} computed with the nominal controller (3.46) are shown in Fig. 3.6. As can be seen from the figure, the desired shapes of the transfer functions S_{DC_O} and KS_{DC_O} are achieved, and the control goals for the nominal closed-loop system are therefore achieved. To analyze the robust stability of the closed-loop system, the structure of the uncertainty in the $N-\Delta$ control analysis framework is now taken into account. Because the uncertainty has a defined structure, $\Delta = \text{diag}\{\delta\}$, we can define the structured singular value μ as

$$\mu\big(N_{11}(j\omega)\big) = \frac{1}{\min\{k_m | \det(I - k_m N_{11}\Delta) = 0\}}, \tag{3.47}$$

where N_{11} is the closed-loop transfer function between y_Δ and u_Δ, i.e., $y_\Delta = N_{11}u_\Delta$ (see (3.43)). The closed-loop system is robustly stable for all allowable perturbations if and only if $\mu\big(N_{11}(j\omega)\big) < 1$, $\forall\omega$ [10]. A plot of μ versus frequency is shown in Fig. 3.7, and as can be seen from the figure, the robust stability condition is satisfied with the nominal controller (3.46). Therefore, the controller (3.46) achieves all of our closed-loop control specifications.

The inputs that are applied to the system P are the control signals v_{FB} and the

measurements that are available from the system P are the error signals e. Therefore, we must convert the input and output of the controller (3.46) to these signals. This is accomplished by substituting the relationships $e_s^* = \Sigma_s^{-1} U_s^T Q^{1/2} e$ and $v_{FB} = R^{-1/2} V_s v_{FB_s}^*$ into (3.46). Finally, the multi-input-multi-output feedback controller $\hat{K} \in \mathbb{R}^{3 \times n_\theta}$ is expressed in state-space form as

$$\begin{aligned} \dot{x}_{fb} &= A_{fb} x_{fb} + B_{fb} \Sigma_s^{-1} U_s^T Q^{1/2} e, \\ v_{FB} &= R^{-1/2} V_s C_{fb} x_{fb} + R^{-1/2} V_s D_{fb} \Sigma_s^{-1} U_s^T Q^{1/2} e. \end{aligned} \tag{3.48}$$

3.7 Control algorithm implementation in the DIII-D Plasma Control System

In this section we describe the implementation of a real-time feedforward + feedback algorithm for magnetic and kinetic profile control in the DIII-D Plasma Control System (PCS). We provide in section 3.7.1 an overview of the algorithm designed in this chapter. In section 3.7.2, we describe the generalized framework for real-time feedforward + feedback control of magnetic and kinetic plasma profiles implemented in the DIII-D PCS. Finally, in section 3.7.3 we present a simulation simserver that can interface with the DIII-D PCS to test the correctness of the real-time implementation of the control framework and to determine the effectiveness of proposed controllers.

3.7.1 Overview of feedforward + feedback control algorithm

The overall feedforward + feedback control algorithm synthesized from the first-principles-driven model of the poloidal flux profile evolution can be summarized as

follows. The feedforward control inputs are computed as

$$\begin{aligned} u_{1_{FF}}(t) &= \left(\frac{\bar{n}_{e_{FF}}(t)}{I_{p_{FF}}(t)\sqrt{P_{tot_{FF}}(t)}} \right)^{3/2}, \\ u_{2_{FF}}(t) &= \frac{\sqrt{P_{tot_{FF}}(t)}}{I_{p_{FF}}(t)}, \\ u_{3_{FF}}(t) &= I_{p_{FF}}(t), \end{aligned} \tag{3.49}$$

where $I_{p_{FF}}(t)$, $P_{tot_{FF}}(t)$, and $\bar{n}_{e_{FF}}(t)$ are determined off-line [96, 97]. In accordance with (3.11), the feedforward control inputs are modified as

$$v_{1_{FF}} = u_{1_{FF}} \qquad v_{2_{FF}} = u_{2_{FF}} \qquad v_{3_{FF}} = u_{1_{FF}} u_{3_{FF}}. \tag{3.50}$$

Finally, the closed-loop control inputs are computed as

$$\begin{aligned} v_1 &= v_{1_{FF}} + v_{1_{FB}} u_{1_{norm}}, \\ v_2 &= v_{2_{FF}} + v_{2_{FB}} u_{2_{norm}}, \\ v_3 &= v_{3_{FF}} + v_{3_{FB}} u_{1_{norm}} u_{3_{norm}}, \end{aligned} \tag{3.51}$$

where $(\cdot)_{FF}$ denotes a feedforward quantity and $(\cdot)_{FB}$ denotes a feedback quantity computed on-line via (3.48). The closed-loop signals for the control actuators $I_p(t)$, $P_{tot}(t)$, and $\bar{n}_e(t)$ are computed as

$$I_p(t) = \frac{v_3}{v_1} \qquad P_{tot}(t) = \left(\frac{v_2 v_3}{v_1} \right)^2 \qquad \bar{n}_e(t) = \frac{v_2 v_3^2}{v_1^{4/3}}. \tag{3.52}$$

3.7.2 Generalized framework for real-time plasma profile control

A general framework for real-time feedforward + feedback control of magnetic and kinetic plasma profiles + a scalar quantity has been implemented in the DIII-D PCS. The magnetic profiles that can be controlled are: the safety factor (q), the rotational transform ($\iota = 1/q$), the poloidal magnetic flux (Ψ), or the poloidal magnetic flux gradient (θ). The kinetic profiles that can be controlled are: the electron temperature (T_e), the ion temperature (T_i), or the toroidal rotation velocity (V_ϕ). The scalar quantities that can be controlled are: the normalized plasma beta (β_N), the minimum value of q (q_{min}), or the plasma internal inductance (l_i). The selected magnetic profile can be controlled at 21 evenly spaced points on the domain $\hat{\rho} \in [0, 1]$, and the selected kinetic profiles can be controlled at 11 evenly spaced points on the domain $\hat{\rho} \in [0, 1]$. The feedback portion of the controller was interfaced with the real-time EFIT (rtEFIT) equilibrium reconstruction code [11] for magnetic profile control and with the real-time charge-exchange recombination (rtCER) code [139] for kinetic profile control. The control scheme in this chapter has only been designed to control the magnetic poloidal flux gradient profile, therefore, only the magnetic profile portion of the control algorithm implemented in the DIII-D PCS is described below.

The diagnostics provided to the PCS by rtEFIT are: a measured value of the total plasma current I_p^{meas}, the poloidal stream function at the magnetic axis ψ_{axis} and at the plasma boundary ψ_{bdry}, and the safety factor q on a normalized flux spatial domain ψ_n where

$$\psi_n = \frac{\psi - \psi_{axis}}{\psi_{bdry} - \psi_{axis}}. \tag{3.53}$$

The safety factor $q(\psi_n^{rt})$ is provided by rtEFIT at 64 evenly spaced points

$$\psi_{n_k}^{rt} = 0, 1/64, 2/64, \ldots, 63/64. \tag{3.54}$$

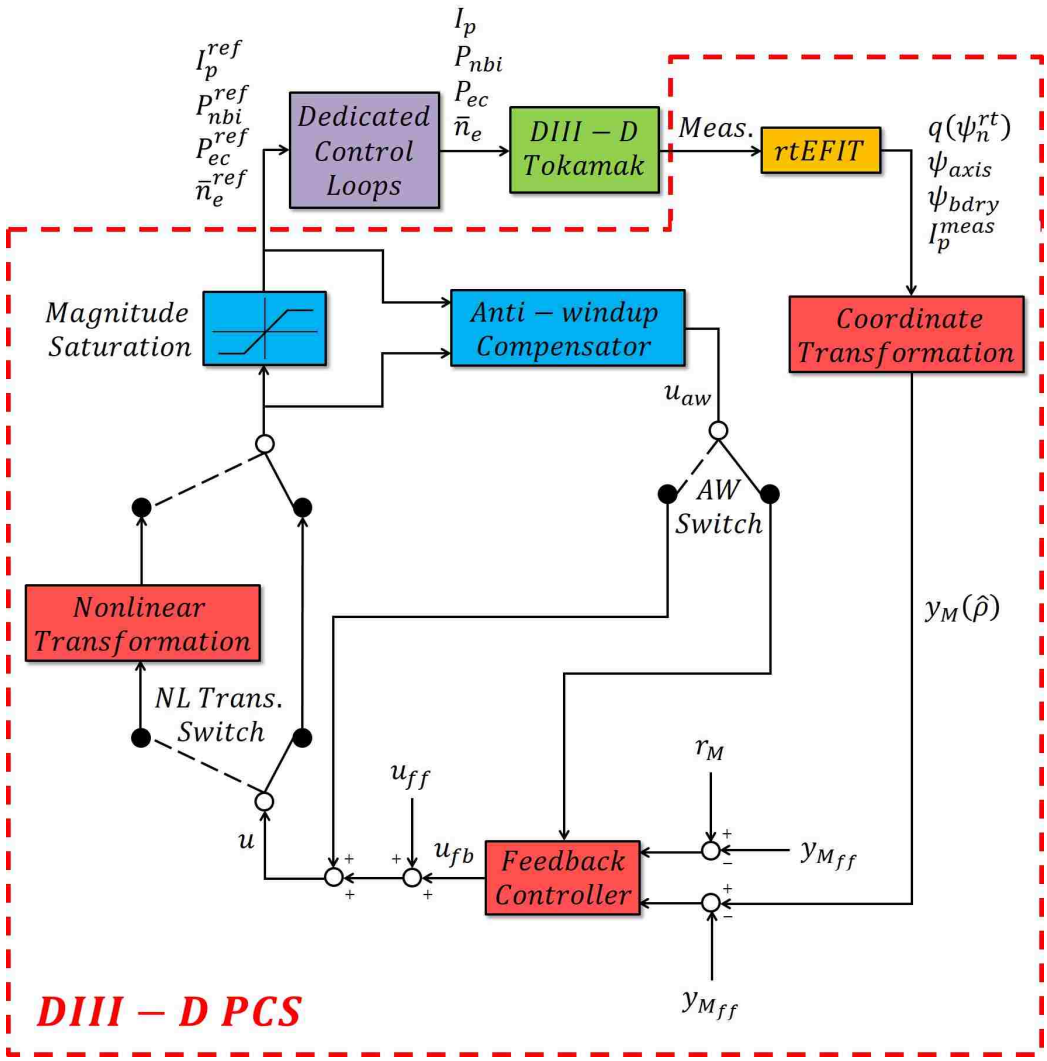

Figure 3.8: Configuration between the DIII-D tokamak and the DIII-D PCS real-time code for magnetic profile control.

The feedback portion of the controller is implemented as a discrete time state-space system with a sampling time of 20 milliseconds. This sampling time is set based on the modulation of the neutral beam injector utilized to acquire Motional Stark Effect (MSE) diagnostic data that is used to obtain measurements of the q profile in real-time. In this case the MSE beam is modulated on for 10 milliseconds then off for 10 milliseconds.

The configuration between the generalized real-time code running in the DIII-D

PCS and the DIII-D tokamak is shown in Fig. 3.8. The Coordinate Transformation block in the PCS is an algorithm that is executed to construct the selected magnetic profile $y_M(\hat{\rho})$, either q, ι, Ψ, or θ, controlled by the Feedback Controller from the data provided by the rtEFIT algorithm $q(\psi_n^{rt})$, ψ_{axis}, ψ_{bdry}, and I_p^{meas}. See Appendix D for a detailed description of this algorithm. By implementing the Feedback Controller with separate input signals, $r_M - y_{M_{ff}}$ and $y_M - y_{M_{ff}}$, where r_M represents the target (desired system output) and $y_{M_{ff}}$ represents a reference output (for example a value of the system output around which a linear model of the system dynamics is obtained), controllers designed with different tracking error definitions can be employed with the same implementation configuration. The Feedback Controller outputs a general feedback control signal (u_{fb}) that is added to a general feedfoward control signal (u_{ff}) to produce a general total control signal (u). Here, the variable u is employed to denote any *general control input*, i.e., it is not to be misinterpreted as the value of the intermediate control signals (3.49) for the algorithm designed in this chapter. In the case of control algorithm designed in this chapter (see section 3.7.1), the signal u in Fig. 3.8 would correspond to the control inputs v defined in (3.50)-(3.51). The nonlinear transformation switch (NL Trans. Switch) is used to indicate whether or not post processing of the signals generated by the overall controller is required. If post processing is required, the NL Trans. Switch is set to the left position and the Nonlinear Transformation block in the PCS converts the control signals prescribed by the feedforward + feedback controller to the signals for the physical control variables. If the Feedback Controller directly generates signals for the physical control variables, the NL Trans. Switch is set to the right position and the control signal u is directly sent to the Magnitude Saturation block in the PCS. In the case of the control algorithm designed in this chapter (see section 3.7.1), post processing of the control signals is required (NL Trans. Switch set to the left), and the Nonlinear Transformation block represents the conversion (3.52) of the outputs prescribed by the feedforward

+ feedback controller to the physical control variables $I_p(t)$, $P_{tot}(t)$, and $\bar{n}_e(t)$.

If the feedfoward + feedback controller drives the physical control actuators to saturation, causing any integral component of the feedback controller to wind up, undesirable oscillations in the system could develop. Therefore, some type of anti-windup design is necessary to ensure that the closed-loop system remains well behaved in the presence of actuator saturation. The approach taken here is to augment the feedforward + feedback controller with a separate anti-windup compensation feedback. The Anti-windup Compensator outputs a signal u_{aw} that is designed to mitigate the effect that actuator magnitude saturation has on the closed-loop performance. Various methods exist to design anti-windup compensators that achieve this goal [140]. The anti-windup switch (AW Switch) is used to indicate whether the output of the Anti-windup Compensator is designed to affect the input (right position) or the output (left position) of the feedback portion of the combined controller. In the case of control algorithm designed in this chapter, an anti-windup scheme that affects the input of the Feedback Controller (AW Switch set to the right) is employed. See [141] for an example of the employed anti-windup augmentation.

Finally, it is important to note that the requests made by the combined feedforward + feedback controller are the references to the Dedicated Control Loops commanding the physical actuators on DIII-D. For example, in the case of the plasma current, a proportional-integral-derivative (PID) loop regulates the ohmic poloidal field coil voltage so the plasma current (I_p), which is measured by a Rogowski loop and includes both inductive and noninductive current components, follows the desired waveform requested by the feedforward + feedback algorithm (I_p^{ref}). Similarly to the case of the plasma current, a PID loop regulates gas puffing to make the line average electron density measured by a CO_2 interferometer ($\bar{n}_e$) follow the combined controller requested density ($\bar{n}_e^{ref}$). Finally, the neutral beam and electron cyclotron control loops manage the individual neutral beam and gyrotron modulation (P_{nbi} and

P_{ec}) to follow the average neutral beam and electron cyclotron power requests made by the feedforward + feedback controller (P_{nbi}^{ref} and P_{ec}^{ref}). Experiments in DIII-D have shown the possibility of controlling both the plasma current and the neutral beam and electron cyclotron powers very accurately. However, the control of the line average electron density appears more challenging.

3.7.3 Simserver architecture for validating implemented algorithms

The simulation simserver (Simserver) architecture is a valuable simulation environment which is used for testing algorithms running in the DIII-D PCS, and its architecture is shown in Fig. 3.9. It incorporates a tokamak simulation model that is used to test the PCS in realistic closed-loop simulations. The simulation model accepts control inputs from the PCS and then generates simulated diagnostics. A test switch connects the PCS (left) to either the DIII-D tokamak (upper right) or the DIII-D simulated tokamak (bottom right) depending on which mode of operation is selected. The Matlab/Simulink modeling environment is used to model the major features of the tokamak, and the only restriction on the Simulink models is that their inputs and outputs must be consistent with the input and output channels in the PCS. This type of simulation is used to determine the effectiveness of controllers and correctness of their real-time implementation before experimental tests are conducted [142].

In order to carry out a Simserver simulation, a Simulink model of the magnetic diffusion equation (3.1) was developed and integrated into a Simserver that can interface with the DIII-D PCS [115]. To construct the model, the governing infinite dimensional PDE (3.1)-(3.2) is approximated by a finite dimensional system of ODEs. The process used to obtain the reduced-order model is the same one used in section 3.3, where the non-dimensional spatial domain is represented as m_ψ nodes while the

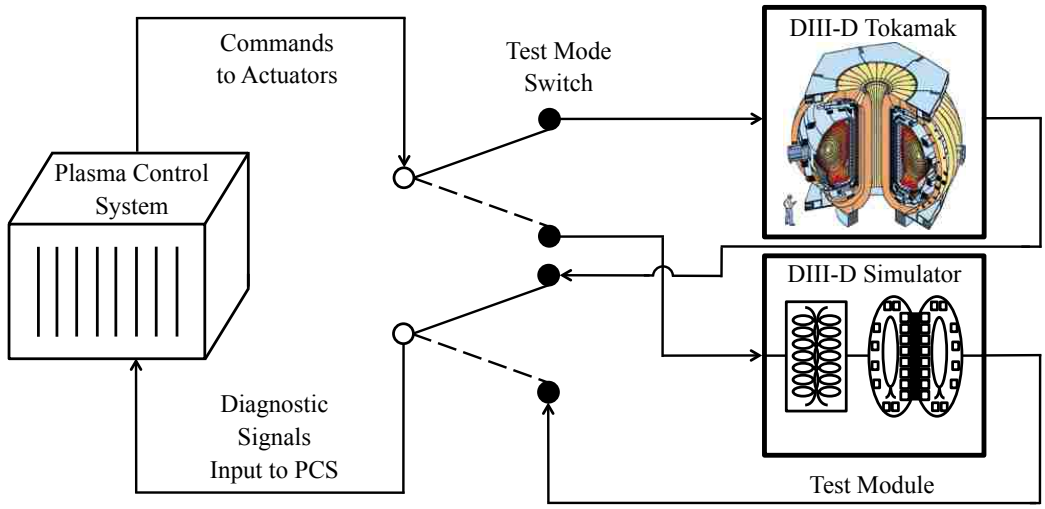

Figure 3.9: Simserver architecture for validating control algorithms in the DIII-D PCS.

time domain is left continuous. This discretization process results in $m_\psi - 2$ ordinary differential equations that can be integrated in time to simulate the the poloidal magnetic flux profile evolution in response to the control actuator signals. In order to be compatible with the diagnostics provided to the PCS by rtEFIT, the Simulink model of the magnetic diffusion equation is required to output the plasma current $I_p(t)$, the poloidal stream function at the magnetic axis ψ_{axis} and at the plasma boundary ψ_{bdry}, and the safety factor $q(\psi_n^{rt})$.

3.8 Simserver simulation testing of control algorithm

In this section, we show results from a Simserver simulation used to test the implementation of the control algorithm (3.49)-(3.52) in the DIII-D PCS and to demonstrate the effectiveness of the proposed control algorithm. In order to test the feedback controller in a realistic tokamak operating scenario, we need to generate simulation conditions where there is a mismatch (i) between the actual and the assumed initial

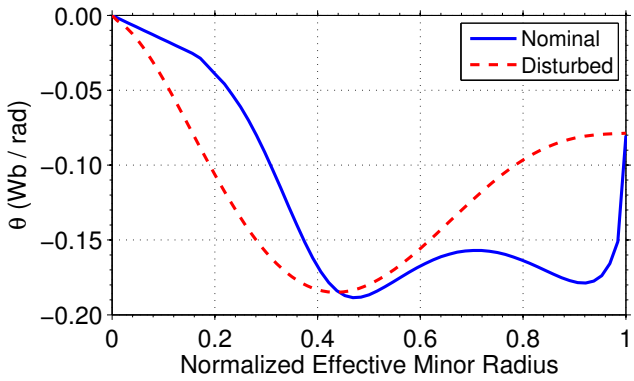

Figure 3.10: (Simulation reference tracking): Initial poloidal flux gradient profile $\theta(\hat{\rho})$ at time $t = 0.5$ s.

conditions and (ii) between the actual plant and the model used for the control design. The nominal initial poloidal flux gradient profile $\theta(\hat{\rho})$ is shown in Fig. 3.10, which is extracted from DIII-D shot 129412 at an experimental time of $t = 0.5$ s. In order to satisfy the first simulation condition requirement, we perturb the initial θ profile as shown in Fig. 3.10. We denote as the nominal model the PDE model of the θ profile evolution in a tokamak presented in section 3.2 and described in detail in [83]. This nominal model is used to design both the feedforward and the feedback controllers. In order to satisfy the second simulation condition requirement, we perturb the nominal electron temperature and noninductive current density models (described in [83]) by 10 % in order to produce a plant (disturbed model) that is different from the nominal model used to synthesize the control algorithm. These simulation conditions provide the means to test the feedback controller in a realistic operating scenario where there is a mismatch between the actual and the assumed initial conditions and between the plant and the model.

We now describe the setup for a test conducted to determine the reference tracking capabilities of the feedback controller through simulation with the real-time code utilized in the DIII-D PCS. We begin by producing a target poloidal flux gradient profile evolution $\theta_{tar}(\hat{\rho}, t)$ by executing a feedfoward-control-only simulation with the

optimal feedforward control inputs $v_{FF_{Opt}}$ [96,97]. For this simulation, the Simserver simulates the nominal model with the nominal initial condition. Next, we produce a second poloidal flux gradient profile evolution $\theta_{FF}(\hat{\rho},t)$ that is different from the target evolution $\theta_{tar}(\hat{\rho},t)$. This is accomplished by generating a non-optimal set of feedfoward control trajectories v_{FF} by perturbing the optimal feedfoward control inputs and then executing another feedfoward-control-only simulation with these perturbed control inputs. For this simulation, the Simserver simulates the disturbed model (plant) with the perturbed initial condition. Finally, we determine the ability of the feedback controller to track the target profile evolution $\theta_{tar}(\hat{\rho},t)$ by executing a feedforward + feedback control simulation. For this simulation, the Simserver simulates the disturbed model (plant) with the perturbed initial condition. The setup of the feedforward + feedback simulation is as follows. The feedback controller is on for the duration of the simulation, the non-optimal feedforward control inputs v_{FF} are used, and the reference vector is set according to $r_M(\hat{\rho},t) = \theta_{tar}(\hat{\rho},t)$. The tracking error e is defined at any time t during the simulation as

$$\begin{aligned} e &= (r_M - y_{M_{FF}}) - (y_M - y_{M_{FF}}) \\ &= \left[\theta_{tar}(\hat{\rho}) - \theta_{FF}(\hat{\rho})\right] - \left[\theta(\hat{\rho}) - \theta_{FF}(\hat{\rho})\right] = \theta_{tar}(\hat{\rho}) - \theta(\hat{\rho}), \end{aligned} \tag{3.55}$$

which in turn implies the feedback controller is trying to drive the θ profile to the desired target profile.

The ramp-up phase of the simulated discharges corresponds to an experimental time $t = [0.5, 1.7]$ s, and the early flattop phase of the simulated discharges is associated with the experimental time $t = [1.7, 2.9]$ s. A comparison between the target profile, the θ profile achieved by the plant (disturbed model) with feedforward + feedback control, and the θ profile achieved by the plant with feedforward-only control at the times $t = 1.7$ s, $t = 2.3$ s, and $t = 2.9$ s is shown in Figs. 3.11(a-c).

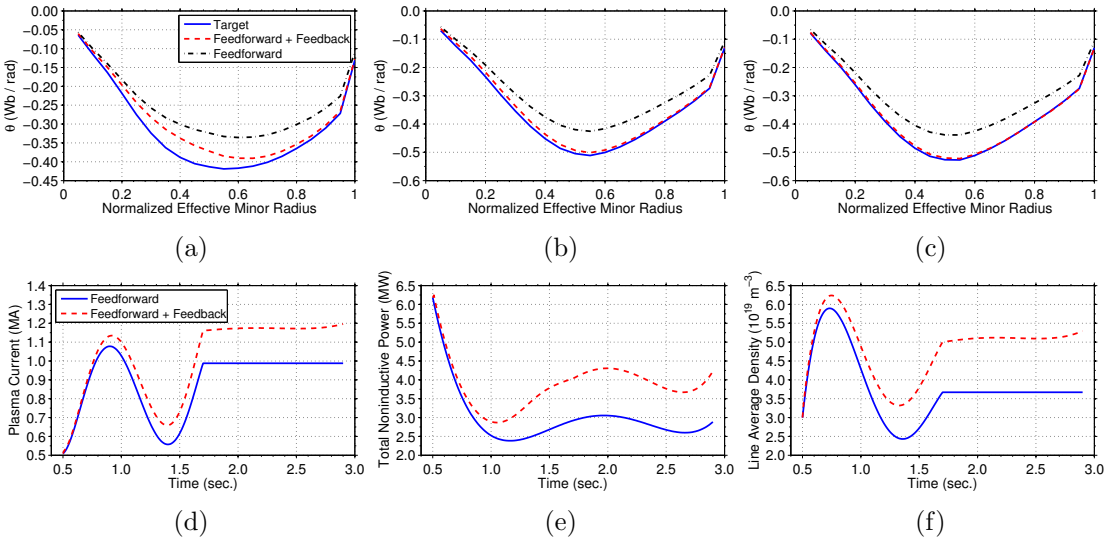

Figure 3.11: (Simulation reference tracking): Poloidal flux gradient profile $\theta(\hat{\rho})$ at time (a) $t = 1.7$ s, (b) $t = 2.3$ s, and (c) $t = 2.9$ s and control trajectory comparison: (d) plasma current (MA), (e) total noninductive power (MW), and (f) line average electron density (10^{19} m^{-3}).

During the ramp-up phase, the feedback controller reacts to the initial tracking error and begins to drive the plant towards the target. At the end of the ramp-up phase, the modification of the θ profile of the plant towards the target profile is evident as shown in Fig. 3.11(a). As the feedforward + feedback simulation progresses into the beginning of the flattop phase, the feedback controller is able to successfully drive the plant to the target profile and then regulate the θ profile evolution around the target trajectory as shown in Figs. 3.11(b-c). A comparison of the feedforward and feedforward + feedback control trajectories for $I_p(t)$, $P_{tot}(t)$, and $\bar{n}_e(t)$ is shown in Figs. 3.11(d-f). In order to (i) track the target profile evolution, (ii) overcome the disturbance in the initial θ profile, and (iii) overcome the uncertainty in the plant, the feedback component of the combined controller modifies the non-optimal feedforward control trajectories throughout the feedforward + feedback simulation.

3.9 Experimental testing of control algorithm

The actuators used to manipulate the poloidal flux gradient profile evolution $\theta(\hat{\rho}, t)$ have a limited ability to drive the system towards a desired target profile based on the physical design of the DIII-D tokamak. As a result, there are a limited number of target profiles that are physically achievable by the machine no matter what type of profile control strategy is employed. The control actuators themselves are also physically constrained in magnitude as well as rate of change, which further reduces the range of target profiles achievable for a given initial θ profile. The goal of the experimental tests was to verify that the feedback controller synthesized from a first-principles-driven model of the poloidal flux profile evolution is able to drive the system to a target profile that is physically achievable by the machine. Towards this goal, we first sought a target poloidal flux gradient profile evolution $\theta_{tar}(\hat{\rho}, t)$ that was physically achievable by the machine. We executed a feedfoward-control-only discharge with a nominal set of feedforward control inputs $v_{FF_{Nom}}$ in DIII-D shot 145477, and from this discharge we extracted a physically achievable target profile evolution that we employed to test the feedback controller in reference tracking and disturbance rejections experiments.

3.9.1 Reference tracking

In this section we describe the results of a test designed to determine the reference tracking capabilities of the feedback controller in the DIII-D tokamak during the ramp-up and early flattop phases of the discharge. We first produced a poloidal flux gradient profile evolution $\theta_{FF}(\hat{\rho}, t)$ that was different from the target evolution $\theta_{tar}(\hat{\rho}, t)$. This profile evolution was obtained by perturbing the nominal feedfoward control inputs to obtain a second set of feedfoward control inputs $v_{FF_{Ptrb}}$ and executing a feedfoward-control-only discharge in DIII-D shot 146411. Next, we determined the

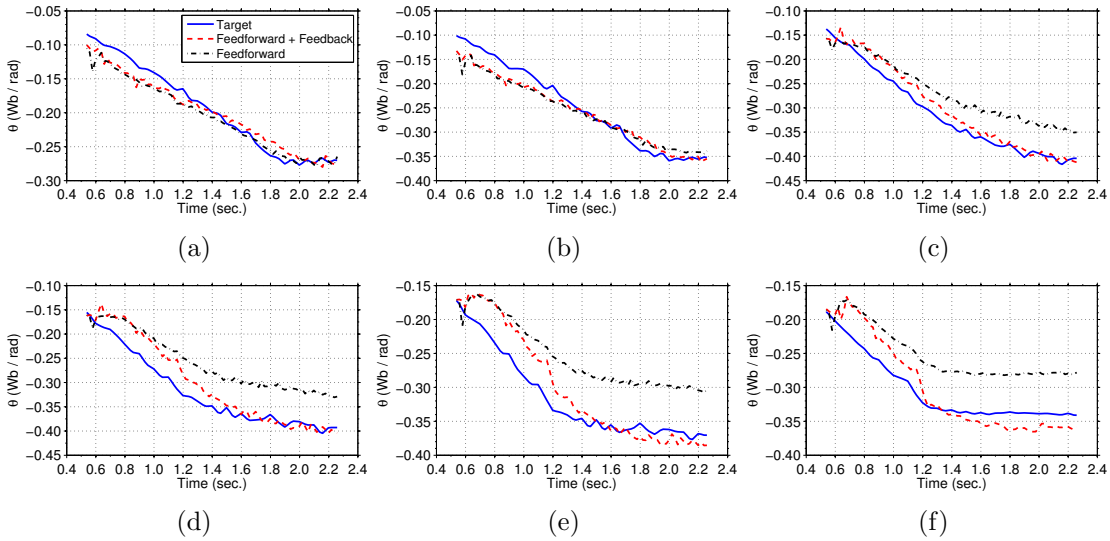

Figure 3.12: (Experiment reference tracking (DIII-D shot 146458)): Time trace of poloidal flux gradient θ at normalized radii (a) $\hat{\rho} = 0.3$, (b) $\hat{\rho} = 0.4$, (c) $\hat{\rho} = 0.6$, (d) $\hat{\rho} = 0.7$, (e) $\hat{\rho} = 0.8$, and (f) $\hat{\rho} = 0.9$.

ability of the feedback controller to track the target profile evolution $\theta_{tar}(\hat{\rho}, t)$ by executing a feedforward + feedback control discharge in DIII-D shot 146458. During this discharge, the feedback controller was on for the duration of the experiment, the feedforward control inputs $v_{FF_{Ptrb}}$ were used as the feedforward component of the combined controller, and the reference vector was set according to $r_M(\hat{\rho}, t) = \theta_{tar}(\hat{\rho}, t)$. As seen in (3.55), this choice of the reference vector implies the feedback controller was trying to drive the θ profile to the desired target profile.

In the reference tracking experiment, the ramp-up phase was associated with the time $t = [0.5, 1.2]$ s, and the early flattop phase corresponded to the time $t = (1.2, 2.25]$ s. Time traces of the poloidal flux gradient θ at normalized radii $\hat{\rho} = 0.3$, 0.4, 0.6, 0.7, 0.8, and 0.9 achieved during the target discharge, the feedforward + feedback controlled discharge, and the feedforward controlled discharge are shown in Fig. 3.12. The feedback controller can manipulate the θ profile evolution through diffusivity, interior, and boundary actuation. Due to the fact that the boundary actuation is one of the more influential actuators as shown in Fig. 3.2(b), the feedback controller can

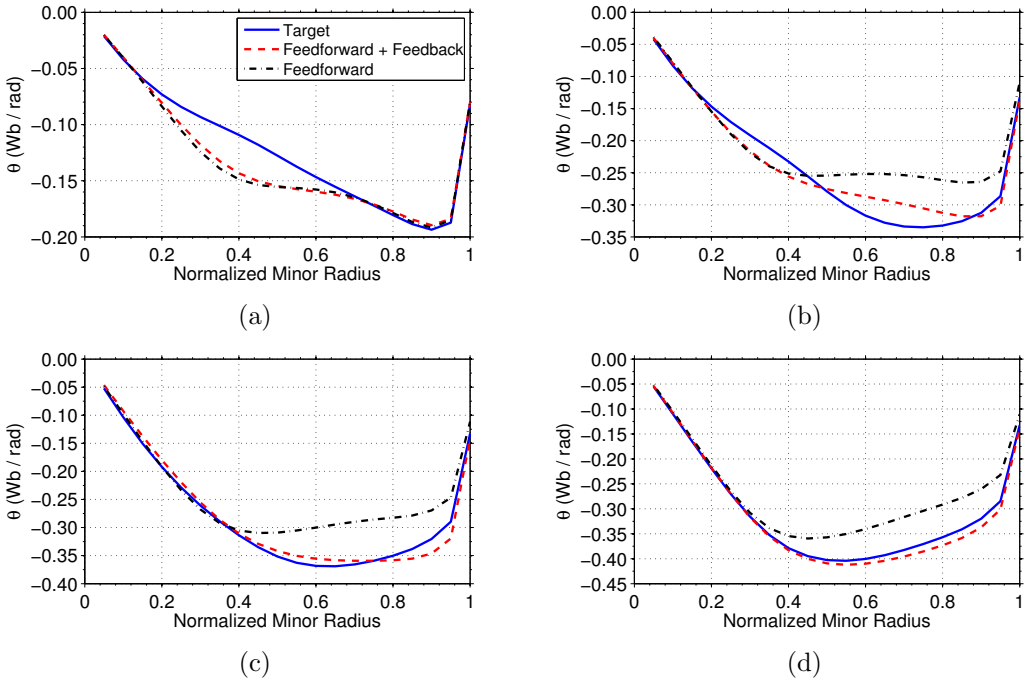

Figure 3.13: (Experiment reference tracking (DIII-D shot 146458)): Poloidal flux gradient profile $\theta(\hat{\rho})$ at time (a) $t = 0.538$ s, (b) $t = 1.218$ s, (c) $t = 1.618$ s, and (d) $t = 2.258$ s.

more effectively control the θ profile near the plasma boundary because of the spatial proximity of the actuator and the controlled quantity. Therefore, a tracking error in the interior of the plasma will take longer to be eliminated because the control action applied at the plasma boundary will have to diffuse towards the center of the plasma. This behavior is shown in Figs. 3.12(c-f) for the time traces of the θ at normalized radii $\hat{\rho} = 0.6$, 0.7, 0.8, and 0.9 achieved in the feedforward + feedback controlled discharge. During this discharge, the θ evolution at $\hat{\rho} = 0.6$ and 0.7 was initially below the desired target evolution. Therefore, the feedback controller caused θ at $\hat{\rho} = 0.8$ and 0.9 to overshoot the desired target evolution at these spatial locations in order to cause the θ evolution at $\hat{\rho} = 0.6$ and 0.7 to increase towards the target evolution through diffusion. Once the target θ evolution was achieved at $\hat{\rho} = 0.6$ and 0.7 at the time $t = 2.0$ s as shown in Figs. 3.12(c-d), the feedback controller began

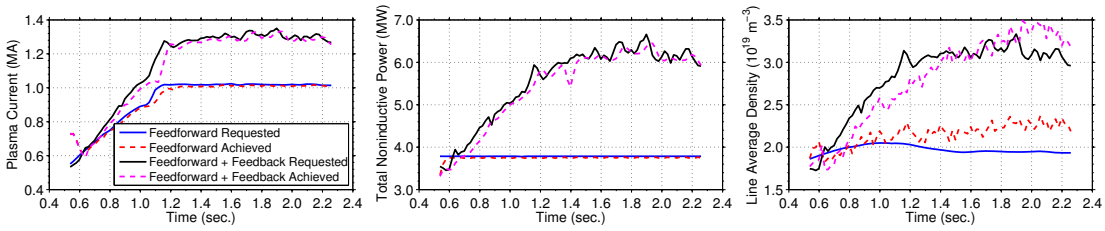

(a) (b) (c)

Figure 3.14: (Experiment reference tracking (DIII-D shot 146458)): Control trajectory comparison: (a) plasma current (MA), (b) total noninductive power (MW), and (c) line average electron density (10^{19} m^{-3}).

to reduce the tracking error at the normalized radii $\hat{\rho} = 0.8$ and 0.9 during the time interval $t = [2.0, 2.25]$ s as shown in Figs. 3.12(e-f).

A comparison between the target profile, the $\theta(\hat{\rho})$ profile achieved in the feedforward + feedback controlled discharge, and the $\theta(\hat{\rho})$ profile achieved in the feedforward controlled discharge at various times is shown in Fig. 3.13. Due to the nonlinear behavior of the tokamak plasma and the physical limitations of the actuators to manipulate the θ profile evolution, there was no guarantee that the feedback controller would be able to drive the θ profile evolution in the feedforward + feedback controlled discharge to the target profile evolution from the perturbed initial condition shown in Fig. 3.13(a). During the ramp-up phase of the feedforward + feedback controlled discharge, the feedback controller began to drive the plasma towards the target profile by modifying the perturbed feedforward actuator trajectories as shown in Figs. 3.13(b-c). At the end of the early flattop phase of the feedforward + feedback controlled discharge, the feedback controller was able to drive the θ profile as close as possible to the target profile as shown in Fig. 3.13(d).

A comparison of the actuator trajectories during the feedforward controlled discharge and during the feedforward + feedback controlled discharge is shown in Fig. 3.14. In order to track the target profile evolution, the feedback component of the combined controller modified the actuator trajectories throughout the feedforward +

feedback controlled discharge. Also shown in Fig. 3.14 is the ability of the dedicated control loops commanding the physical actuators to follow the requests made by the control algorithm. The control loops commanding the total plasma current and the total average neutral beam power were able to follow the requests very well, and the control loop commanding the line average electron density was able to follow the request reasonably well.

3.9.2 Disturbance rejection

In this section we describe the results of a test designed to determine the disturbance rejection capabilities of the feedback controller in the DIII-D tokamak during the flattop phase of the discharge. To determine the ability of the feedback controller to reject an artificial input disturbance, a feedforward + disturbance + feedback controlled discharge was executed in DIII-D shot 146153. During this discharge, the nominal feedforward control inputs $v_{FF_{Nom}}$ were used during the time interval $t = [0.5, 2)$ s (ramp-up and early flattop phases) with the feedback controller off. During the time interval $t = [2, 5]$ s (flattop phase), a disturbance was added to the nominal feedforward actuator trajectories. The disturbance was added according to

$$\begin{aligned} v_{1_{FF_{Dis}}} &= u_{1_{FF_{Nom}}}, \\ v_{2_{FF_{Dis}}} &= u_{2_{FF_{Nom}}}, \\ v_{3_{FF_{Dis}}} &= u_{1_{FF_{Nom}}}\big[u_{3_{FF_{Nom}}} - 0.1\big], \end{aligned} \tag{3.56}$$

to produce a feedforward + disturbance set of control inputs $v_{FF_{Dis}}$. By examining (3.52) it can be seen that this disturbance will propagate into each of the three control actuators $I_p(t)$, $P_{tot}(t)$, and $\bar{n}_e(t)$. The feedback controller was turned on and

off throughout this discharge according to

$$v_{FB} = \begin{cases} 0.5 \text{ to } 2.2 \text{ s} & \text{OFF} \\ 2.2 \text{ to } 2.7 \text{ s} & \text{ON} \\ 2.7 \text{ to } 3.2 \text{ s} & \text{OFF} \\ 3.2 \text{ to } 5.0 \text{ s} & \text{ON} \end{cases}, \tag{3.57}$$

to see the effect the disturbance had on the plasma and to determine the ability of the feedback controller to reject the disturbance and regulate the θ profile evolution around the target profile evolution. The reference vector was set according to $r_M(\hat{\rho}, t) = \theta_{tar}(\hat{\rho}, t)$, which implies the feedback controller was trying to regulate the θ profile around the desired target profile.

A comparison between the target profile and the $\theta(\hat{\rho})$ profile achieved during DIII-D shot 146153 (FF + Dist. + FB) at several times throughout the discharge is shown in Figs. 3.15(a-f). When the disturbance was initially introduced to the plasma at the time $t = 2.0$ s, the θ profile was close to the desired target profile as shown in Fig. 3.15(a). During the time interval $t = [2.0, 2.2]$ s, the disturbance slightly moved the θ profile away from the target profile as shown in Fig. 3.15(b). At the time $t = 2.2$ s, the feedback controller was turned on and it was able to reject the effects of the disturbance. This resulted in the target profile being successfully achieved when the feedback controller was turned off at the time $t = 2.7$ s as shown in Fig. 3.15(c). During the time interval $t = [2.7, 3.2]$ s, the θ profile again drifted away from the target profile due to the disturbance as shown in Fig. 3.15(d). Finally, the feedback controller was turned on for the remainder of the discharge at the time $t = 3.2$ s, and it was once again able to reject the effects the disturbance had on the θ profile evolution. This resulted in the θ profile evolution being driven to and then successfully regulated around the target profile evolution as shown in Figs. 3.15(e-f).

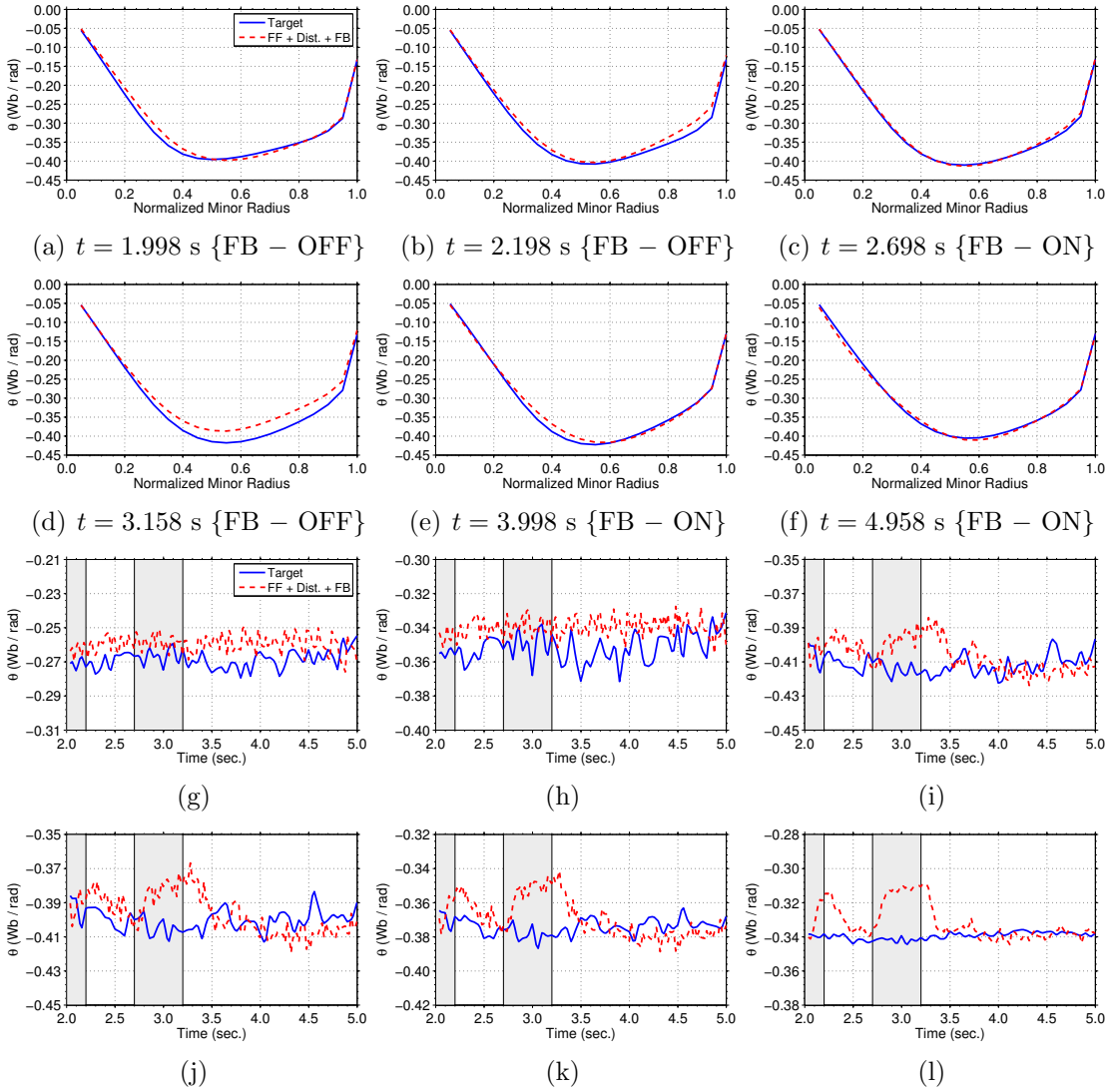

(a) $t = 1.998$ s {FB − OFF} (b) $t = 2.198$ s {FB − OFF} (c) $t = 2.698$ s {FB − ON}

(d) $t = 3.158$ s {FB − OFF} (e) $t = 3.998$ s {FB − ON} (f) $t = 4.958$ s {FB − ON}

(g) (h) (i)

(j) (k) (l)

Figure 3.15: (Experiment disturbance rejection (DIII-D shot 146153)): Poloidal flux gradient profile $\theta(\hat{\rho})$ at time (a) $t = 1.998$ s, (b) $t = 2.198$ s, (c) $t = 2.698$ s, (d) $t = 3.158$ s, (e) $t = 3.998$ s, and (f) $t = 4.958$ s, and time trace of poloidal flux gradient θ at normalized radii (g) $\hat{\rho} = 0.3$, (h) $\hat{\rho} = 0.4$, (i) $\hat{\rho} = 0.6$, (j) $\hat{\rho} = 0.7$, (k) $\hat{\rho} = 0.8$, and (l) $\hat{\rho} = 0.9$. Gray-shaded region denotes when feedback controller is off.

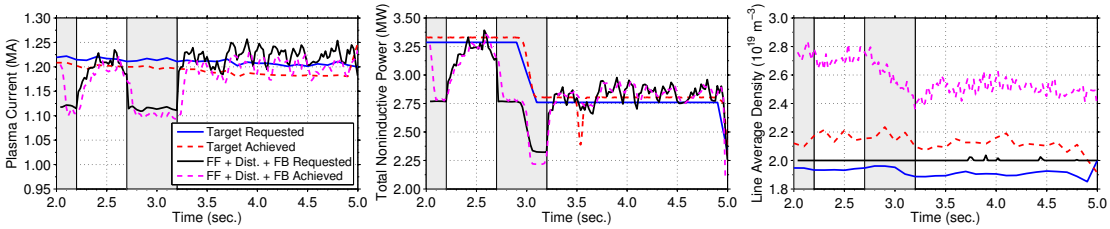

(a) (b) (c)

Figure 3.16: (Experiment disturbance rejection (DIII-D shot 146153)): Control trajectory comparison: (a) plasma current (MA), (b) total noninductive power (MW), and (c) line average electron density (10^{19} m^{-3}). Gray-shaded region denotes when feedback controller is off.

Time traces of θ at normalized radii $\hat{\rho} = 0.3$, 0.4, 0.6, 0.7, 0.8, and 0.9 achieved during the target discharge and DIII-D shot 146153 are shown in Figs. 3.15(g-l). The effect the uncontrolled disturbance had on the θ profile evolution can be seen in the time traces of θ at normalized radii $\hat{\rho} = 0.6$, 0.7, 0.8, and 0.9 as shown in Figs. 3.15(i-l). During the time intervals $t = [2.0, 2.2]$ s and $t = (2.7, 3.2]$ s when the feedback controller was off, the disturbance caused θ to drift away from the target. Also shown in these time traces of θ is the ability of the feedback controller to reject the effects of the disturbance and regulate θ around the target during the time intervals $t = (2.2, 2.7]$ s and $t = (3.2, 5.0]$ s when the feedback controller was on.

A comparison of the actuator trajectories during the target discharge and during the feedforward + disturbance + feedback controlled discharge is shown in Fig. 3.16. In order to regulate the θ profile around the target profile and reject the effects of the disturbance, the feedback component of the combined controller modified the actuator trajectories throughout the discharge. The actuator limits during this control test

were

$$0.3 \text{ MA} \leq I_p(t) \leq 1.5 \text{ MA},$$
$$2.24 \text{ MW} \leq P_{tot}(t) \leq 4.4275 \text{ MW},$$
$$2 \times (10)^{19} \text{ m}^{-3} \leq \bar{n}_e(t) \leq 10 \times (10)^{19} \text{ m}^{-3}. \tag{3.58}$$

As can be seen in Fig. 3.16(c), the combined control algorithm drove the line average electron density request to saturation, however, the line average electron density requested by the control algorithm was around $1.9 \times (10)^{19}$ m^{-3}. Therefore, the level of actuator saturation was small, and the anti-windup compensator was able to successfully keep the closed-loop system well behaved in the presence of the actuator saturation. Also shown in Fig. 3.16 is the ability of the dedicated control loops commanding the physical actuators to follow the requests made by the combined control algorithm. The control loops commanding the total plasma current and the total average neutral beam power were able to follow the requests very well, but the control loop commanding the line average electron density was not able to follow the request very well. This resulted in an additional, unintentional disturbance the feedback controller needed to overcome.

3.10 Conclusion

A robust feedback controller was synthesized to control the poloidal flux gradient profile evolution in the DIII-D tokamak from a first-principles-driven model of the poloidal flux profile evolution. A general framework for real-time feedforward + feedback control of magnetic and kinetic plasma profiles was successfully implemented in the DIII-D PCS. The feedback component of the control algorithm was interfaced with the available real-time measurements and successfully tested experimentally during

both the ramp-up and flattop phases of L-mode discharges. Even though the model used to synthesize the feedback controller neglected the effects of the bootstrap current, the adequate performance of the feedback controller during the flattop phase of the discharge can be attributed to the facts that the effects of the bootstrap current on the θ profile evolution are typically small in L-mode plasmas and the feedback controller is robust against the unmodeled bootstrap current dynamics in this operating regime. These experiments, along with those described in [98, 99], mark the first time ever a first-principles-driven, model-based, closed-loop full magnetic profile controller was successfully implemented and tested in a tokamak device.

Chapter 4

Optimization of plasma startup conditions in the DIII-D tokamak

4.1 Introduction

Advanced tokamak scenarios operate close to operational boundaries in terms of both proximity to stability limits (to maximize plasma performance) and available actuation capabilities. As a result, variations in the plasma evolution due to drifts caused by external plasma disturbances, such as variability in the condition of the tokamak walls, plasma impurities, the plasma response to the actuators, and actuator faults, can lead to difficulties with reproducibility of target plasma conditions. The initial creation and formation of the plasma is a particularly sensitive phase of the discharge to plasma variation. In this chapter, a first-principles-driven (FPD), physics-model-based control algorithm is developed to remove residual variability in the plasma state at the end of the initial creation and formation phase of the discharge (defined here at the time $t = 0.4$ s). This is accomplished by developing a feedforward + feedback scheme to optimize plasma startup conditions in low confinement (L-mode) scenarios in the DIII-D tokamak by achieving a specified target safety factor profile (q profile)

at the end of the current ramp-up phase of the discharge.

The physics-based model developed in chapter 2 is embedded in a numerical optimization algorithm to design feedforward trajectories for the available actuators (total plasma current, auxiliary heating and current-drive (H&CD) system, line average electron density) that steer the plasma through the tokamak operating space to reach a target q profile, subject to actuator, plasma state, and operating scenario constraints. The auxiliary H&CD actuators on DIII-D considered in this chapter are 8 individual neutral beam injection (NBI) sources, referred to by the names 30L/R,150L/R, 210L/R, 330L/R, where L and R denoted left and right beam lines, respectively. The 30L/R and 330L/R neutral beams inject power into the plasma in the co-current direction (same direction as the total plasma current) with deposition profiles that are peaked in the center of the plasma (referred to as on-axis NBI). The 150L/R neutral beams inject power into the plasma in the co-current direction with deposition profiles that are peaked away from the plasma core (referred to as off-axis NBI). Finally, the 210L/R neutral beams inject power into the plasma in the counter-current direction (opposite direction as the total plasma current) with deposition profiles that are peaked in the center of the plasma (referred to as counter-current NBI). The feedback controller is synthesized by following a FPD approach and is employed to add robustness to the control scheme and account for drifts due to external plasma disturbances. For feedback control design, we chose to model the kinetic plasma parameters (electron density, electron temperature, and plasma resistivity) as a nominal model plus a bounded uncertain model. These uncertain models are then combined with the physics model that describes the poloidal magnetic flux profile evolution in the tokamak (the magnetic diffusion equation) to obtain the FPD model of the system dynamics that is embedded into the feedback control design process. The feedback controller is synthesized by employing *robust control techniques* [10] and is designed to achieve a desired closed-loop system performance while guaranteeing

that the controller maintains closed-loop system stability for the range of the kinetic plasma parameters captured by the uncertain models.

This chapter is organized as follows. In section 4.2, the actuator trajectory optimization problem is formulated. The optimization problem is solved by employing the sequential quadratic programming (SQP) technique [95], and the optimized actuator trajectories are tested in DIII-D experiments in section 4.3. A unique characteristic of the feedforward trajectories obtained by solving the optimization problem is the regulation of the plasma current ramp-up rate to achieve the target q profiles. In section 4.4, a robust feedback algorithm to control the rotational transform profile (ι profile), which is defined as $\iota = 1/q$, is designed. Experimental results in DIII-D are presented to demonstrate the potential of the feedforward + feedback controller to improve the ability to robustly achieve various different target q profiles at the end of the current ramp-up phase of the discharge in section 4.5. Finally, conclusions are discussed in section 4.6.

4.2 Plasma startup optimization by feedforward actuator trajectory design

The toroidal current profile in tokamaks (j_{tor}) is usually specified in terms of the safety factor profile, or its inverse the rotational transform profile, as this quantity is intimately related to the stability and performance of a tokamak plasma operating scenario [61, 62] (see section 2.6 for the explicit relationship these quantities have to the poloidal magnetic flux (Ψ)). In particular, the q profile is defined in (2.90) and repeated here for convenience as

$$q(\hat{\rho},t) = \frac{1}{\iota(\hat{\rho},t)} = -\frac{d\Phi}{d\Psi} = -\frac{d\Phi}{2\pi d\psi} = -\frac{B_{\phi,0}\rho_b^2\hat{\rho}}{\partial\psi/\partial\hat{\rho}}, \tag{4.1}$$

where t is the time, ψ is the poloidal stream function, which is closely related to the poloidal magnetic flux ($\Psi = 2\pi\psi$). The normalized effective minor radius $\hat{\rho} = \rho/\rho_b$ is the spatial variable employed to index the magnetic flux surfaces, where ρ is the mean effective minor radius of the magnetic flux surface, i.e., $\Phi(\rho) = \pi B_{\phi,0}\rho^2$, Φ is the toroidal magnetic flux, $B_{\phi,0}$ is the vacuum toroidal magnetic field at the geometric major radius R_0 of the tokamak, and ρ_b is the mean effective minor radius of the last closed magnetic flux surface.

4.2.1 Target plasma state: Cost functional definition

The optimization problem goal is to design startup actuator trajectories that steer the plasma from an assumed initial condition through the tokamak operating space to reach a target q profile ($q^{tar}(\hat{\rho})$) at the end of the current ramp-up phase of the discharge. We denote the time that coincides with the end of the current ramp-up as t_f. Therefore, the proximity of the achieved q profile to the target at the time t_f can be described by the cost functional

$$J(t_f) = \int_0^1 W_q(\hat{\rho}) \left[q^{tar}(\hat{\rho}) - q(\hat{\rho}, t_f)\right]^2 d\hat{\rho}, \tag{4.2}$$

where $W_q(\hat{\rho})$ is a positive function used to weight which portions of the q profile are more important relative to the others.

4.2.2 Plasma state dynamics

In chapter 2, a general first-principles-driven, physics-based model of the poloidal magnetic flux profile (and hence the q profile) evolution was derived. The model was subsequently tailored to L-mode operating scenarios in the DIII-D tokamak in section 2.7. The nonlinear, physics-based partial differential equation (PDE) model of the

poloidal flux evolution tailored to DIII-D L-mode scenarios is expressed as

$$\frac{\partial \psi}{\partial t} = f_\eta\left(\hat{\rho}\right) u_\eta(t) \frac{1}{\hat{\rho}} \frac{\partial}{\partial \hat{\rho}} \left(\hat{\rho} D_\psi(\hat{\rho}) \frac{\partial \psi}{\partial \hat{\rho}} \right) + \sum_{i=1}^{n_{nbi}} f_{nbi_i}\left(\hat{\rho}\right) u_{nbi_i}(t) + f_{bs}\left(\hat{\rho}\right) u_{bs}(t) \left(\frac{\partial \psi}{\partial \hat{\rho}} \right)^{-1}, \tag{4.3}$$

with boundary conditions

$$\left.\frac{\partial \psi}{\partial \hat{\rho}}\right|_{\hat{\rho}=0} = 0 \qquad \left.\frac{\partial \psi}{\partial \hat{\rho}}\right|_{\hat{\rho}=1} = -k_{I_p} u_{I_p}(t), \tag{4.4}$$

where f_η, f_{nbi_i}, and f_{bs} are defined in (2.85), D_ψ is a parameter pertaining to the magnetic configuration of a particular plasma equilibrium, n_{nbi} is the number of individual neutral beam injectors, and k_{I_p} is a geometrical constant defined in (2.83). The diffusivity (u_η), interior (u_{nbi_i}, u_{bs}), and boundary (u_{I_p}) control terms are expressed as

$$\begin{aligned}
u_\eta(t) &= \left[I_p(t) P_{tot}(t)^{1/2} \bar{n}_e(t)^{-1} \right]^{-3/2}, \\
u_{nbi_i}(t) &= \left[I_p(t) P_{tot}(t)^{1/2} \bar{n}_e(t)^{-1} \right]^{-1} \bar{n}_e(t)^{-1} P_{nbi_i}(t), \\
u_{bs}(t) &= \left[I_p(t) P_{tot}(t)^{1/2} \bar{n}_e(t)^{-1} \right]^{-1/2} \bar{n}_e(t), \\
u_{I_p}(t) &= I_p(t),
\end{aligned} \tag{4.5}$$

where $I_p(t)$ is the total plasma current, $P_{tot}(t)$ is the total power injected into the plasma, which is defined as

$$P_{tot}(t) = P_{ohm}(t) + \sum_{i=1}^{n_{nbi}} P_{nbi_i}(t) - P_{rad}(t), \tag{4.6}$$

where $P_{ohm}(t)$ is the ohmic power (defined in (2.68)), $P_{nbi_i}(t)$ are the individual neutral beam injection powers, $P_{rad}(t)$ is the radiated power (defined in (2.70)), and $\bar{n}_e(t)$ is the line average electron density.

To simulate the physics-based model, we spatially discretize the infinite dimensional PDE (4.3)-(4.4) by employing a finite difference method, where the spatial domain ($\hat{\rho} \in [0,1]$) is represented by m_ψ discrete nodes. After spatially discretizing (4.3) and taking into account the boundary conditions (4.4), we obtain a nonlinear finite dimensional ordinary differential equation (ODE) model defined by

$$\dot{x} = f_\psi(x,u), \tag{4.7}$$

where $x = [\psi_2, \ldots, \psi_{m_\psi - 1}]^T \in \mathbb{R}^{n_\psi}$ is the magnetic state vector, ψ_i, for $i = 2, \ldots, m_\psi - 1$, is the value of ψ at the i-th node, $u = [P_{nbi_1}, \ldots, P_{nbi_{n_{nbi}}}, \bar{n}_e, I_p]^T \in \mathbb{R}^{n_{act}}$ is the control input vector, $n_{act} = n_{nbi} + 2$, $f_\psi \in \mathbb{R}^{n_\psi}$ is a nonlinear function of the plasma magnetic states and control inputs, and $n_\psi = m_\psi - 2$. We then integrate (4.7) in time by employing a fully implicit numerical scheme, i.e.,

$$\frac{x_{k+1} - x_k}{\Delta t} = f_\psi(x_{k+1}, u_k), \tag{4.8}$$

where x_k and u_k denote the state and control input, respectively, at the time step t_k, x_{k+1} denotes the state at the next time step t_{k+1}, and Δt is the simulation time step. The magnetic state evolution can be obtained by iteratively solving (4.8) at each time step from a given initial condition at time t_0, i.e., $x_0 = x(t_0)$.

4.2.3 Control actuator trajectory parameterization

We parameterize the trajectories of the i-th control actuator (u_i) by a finite number of parameters (n_{p_i}) at discrete points in time (t_{p_i}), i.e., $t_{p_i} = [t_0, t_1, \ldots, t_k, \ldots, t_k = t_f] \in \mathbb{R}^{n_{p_i}}$. During the time interval $t \in (t_k, t_{k+1})$ the i-th control input is determined by

linear interpolation as

$$u_i(t) = u_i(t_k) + [u_i(t_{k+1}) - u_i(t_k)] \frac{t - t_k}{t_{k+1} - t_k}. \tag{4.9}$$

By combining all of the parameters utilized to represent each individual actuator trajectory into a vector

$$\tilde{\theta} = \left[u_1^1, \ldots, u_1^{n_{p_1}}, \ldots, u_i^1, \ldots, u_i^{n_{p_i}}, \ldots, u_{n_{act}}^1, \ldots, u_{n_{act}}^{n_{p_{n_{act}}}} \right], \tag{4.10}$$

where $\tilde{\theta} \in \mathbb{R}^{n_p^{tot}}$ and $n_p^{tot} = \sum_{i=1}^{n_{act}} n_{p_i}$, we can write the parameterized control actuator trajectories as

$$u(t) = \Pi(t)\tilde{\theta}, \tag{4.11}$$

where $\Pi(t) \in \mathbb{R}^{n_{act} \times n_p^{tot}}$ is a piecewise linear function of time. Some of the parameters in the vector (4.10) may be chosen to be fixed due to the desire to obtain an operating condition at the time t_f with a specific set of characteristics (for example a final plasma current $(I_p(t_f))$), or to provide the ability to acquire diagnostic data (for example requiring a constant power in a neutral beam injector). Therefore, the subset of free parameters in the vector (4.10) can be combined into a vector of to-be-optimized parameters which we define as $\theta \in \mathbb{R}^{n_{opt}}$ where $n_{opt} \leq n_p^{tot}$.

4.2.4 Actuator constraints

The actuator magnitude constraints are given by

$$I_p^{min} \leq I_p(t) \leq I_p^{max}, \tag{4.12}$$

$$P_{nbi}^{min} \leq P_{nbi_i}(t) \leq P_{nbi}^{max}, \quad i = 1, \ldots, n_{nbi}, \tag{4.13}$$

where $(\cdot)^{min}$ and $(\cdot)^{max}$ represent the minimum and maximum limits, respectively. The actuator rate constraints are given by

$$-I_{p,max}^{d'} \leq \frac{dI_p}{dt} \leq I_{p,max}^{u'}, \tag{4.14}$$

where $I_{p,max}^{d'}$ and $I_{p,max}^{u'}$ are the maximum total plasma current ramp-down and ramp-up rates, respectively. The actuator constraints (4.12)-(4.14) can be combined together and written in terms of the to-be-optimized parameters θ in a compact matrix form as

$$A_u^{lim}\theta \leq b_u^{lim}. \tag{4.15}$$

4.2.5 Plasma state and operating scenario constraints

The magnetohydrodynamic (MHD) stability limit related to the plasma magnetic states considered in this work is expressed as

$$q_{min}(t) \geq q_{min}^{lim}, \tag{4.16}$$

where $q_{min}(t) = \min\{q(\hat{\rho}, t)\}$ and q_{min}^{lim} is a constant chosen to be slightly greater than one to avoid the onset of sawtooth oscillations[1] [18]. In order for the plasma to remain in the L-mode operating regime, the net power across the plasma surface, P_{net}, must be lower than a threshold power [143, 144], $P_{threshold}$, i.e.,

$$P_{net}(t) \leq P_{threshold}(t). \tag{4.17}$$

[1]Sawtooth oscillations are periodic reconnections of the magnetic flux surfaces which degrade the plasma confinement and can be the precursor to more serious MHD instabilities that can lead to plasma-terminating disruptions.

In this chapter, the net power across the plasma surface is approximated as

$$P_{net}(t) \approx P_{aux}(t) = \sum_{i=1}^{n_{nbi}} P_{nbi_i}(t), \tag{4.18}$$

where P_{aux} is the total auxiliary power injected into the plasma. The threshold power is determined by analyzing data from DIII-D experiments in which the plasma transitioned from the low confinement to the high confinement (H-mode) regime during the discharge, and the threshold power was found to follow the expression given by[2]

$$P_{threshold}(t) = 2\left[\bar{n}_{e19}(t)\right]^{3/4}, \tag{4.19}$$

where $\bar{n}_{e19}$ is the line average electron density in units of 10^{19} m^{-3}. We next chose to formulate the constraint (4.16) as an integral constraint [145]. This provides us the ability to reduce the number of constraints imposed on the optimization problem solution. The constraint (4.16) is expressed as an integral constraint as

$$c_{mhd}^{lim}(x(t)) = \int_{t_0}^{t_f} \max\{0, q_{min}^{lim} - q_{min}(t)\}dt \leq 0. \tag{4.20}$$

The operating mode constraint (4.17)-(4.19), depends directly on the to-be-optimized parameters θ, but in a nonlinear manner. Therefore, we chose to also formulate this constraints as a integral constraint as

$$c_{lh}^{lim}(\theta) = \int_{t_0}^{t_f} \max\{0, P_{net}(t) - P_{threshold}(t)\}dt \leq 0. \tag{4.21}$$

4.2.6 Optimization problem statement and solution method

The nonlinear, constrained, actuator trajectory optimization problem is now to determine the to-be-optimized parameters θ that minimize the cost functional (4.2)

[2]Analysis performed by Dr. Tim C. Luce at General Atomics, San Diego, CA, USA.

subject to the plasma dynamics (4.7), the control actuator trajectory parameterization (4.11), the actuator and operating scenario constraints (4.15) and (4.21), and the plasma state constraint (4.20). This optimization problem is written mathematically as

$$\min_{\theta} \quad J(t_f) = J(x(t_f)), \tag{4.22}$$

such that

$$\begin{aligned} \dot{x} &= f_{\psi}(x, u), \\ u(t) &= \Pi(t)\tilde{\theta}, \\ A_u^{lim}\theta &\leq b_u^{lim}, \\ c_{lh}^{lim}(\theta) &\leq 0, \\ c_{mhd}^{lim}(x(t)) &\leq 0. \end{aligned} \tag{4.23}$$

We solve this optimization problem by employing a method called sequential quadratic programming (SQP) [95]. The SQP solution method is predicated on determining a local minimizer of the nonlinear program (NLP) (4.22)-(4.23) by iteratively solving a sequence of quadratic programs (QP). At each iteration we have a current estimate of a local minimizer of the NLP and a QP which minimizes a quadratic approximation of the original system Hamiltonian subject to a linear approximation of the system constraints around the current estimate. The solution of each QP then yields a step toward the solution of the original NLP. An overview of the SQP technique is provided in Appendix E.

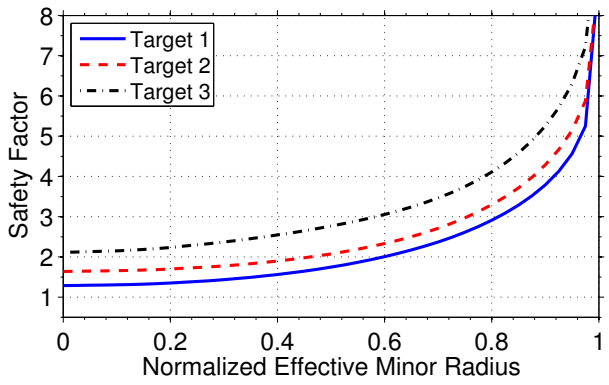

Figure 4.1: Safety factor profiles specified as to-be-achieved targets at the end of the current ramp-up phase of DIII-D plasma discharges. Target 1 is characterized by a minimum q-value of $q_{min} = 1.3$ and a q-value at 95% of the poloidal flux of $q_{95} = 4.4$. Target 2 is characterized by $q_{min} = 1.65$ and $q_{95} = 5.0$. Target 3 is characterized by $q_{min} = 2.1$ and $q_{95} = 6.2$.

4.3 Design and experimental testing of optimized startup trajectories

We now solve the actuator trajectory optimization problem (4.22)-(4.23) to reach a target safety factor profile at the end of the current ramp-up phase of the plasma discharge by employing the SQP solution method. Three different monotonically increasing q profiles (shown in Fig. 4.1) where specified as targets. The optimization is carried out over the time interval $t_{opt} = t \in [t_0, t_f] = [0.4, t_f]$ s, where t_f is the time that corresponds to the end of the current ramp-up phase and is employed as a design parameter. We begin by parameterizing the i-th actuator trajectory by n_{p_i} discrete parameters at the time points $t_{p_i} = [0.4, 0.5, 0.75, 1.0, \ldots, t_f]$ s. Next, the components of the total parameter vector (4.10) that are fixed, or not-to-be optimized, are chosen as discussed in section 4.2.3. Firstly, in order to acquire diagnostic data utilized by the real-time EFIT (rtEFIT) equilibrium reconstruction code [11] to reconstruct the plasma q profile, the 30L neutral beam injector is required to be on for 10 ms with the 30R neutral beam injector off. Therefore, we choose to modulate the 30L neutral

beam injector on for 10 ms and then off for 10 ms, which results in a constant average power of 1.1 MW being delivered to the plasma, i.e., $P_{nbi_{30\mathrm{L}}} = 1.1$ MW. Additionally, as the total amount of auxiliary power injected into the plasma is limited so that the plasma remains in the L-mode operating regime (see (4.17)-(4.19)) and the 30R neutral beam injector cannot actively be utilized for plasma control[3], we choose to fix the 30R neutral beam power at $P_{nbi_{30\mathrm{R}}} = 0.0$ MW. Secondly, it was decided prior to the execution of the plasma startup optimization experiments that after the L-mode current ramp-up phase of the discharge was complete (the phase of the discharge that the startup optimization experiments focused on), a significant amount of neutral beam power would be injected into the plasma to trigger the plasma to transition to the H-mode operating regime. This was done in order to keep the machine walls clean and free of impurities that may recycle into the plasma on subsequent experiments. As the co-current injection neutral beams (150L/R and 330L/R) were to be employed to transition the plasma to the H-mode operating regime, we choose to fix the 210L/R neutral beam powers at $P_{nbi_{210\mathrm{L/R}}} = 0.0$ MW. This choice was made to avoid the potential of triggering a plasma disruption by transitioning from a strong counter-rotating plasma (one with a significant amount of counter-current neutral beam injection) to a strong co-rotating plasma[4]. Thirdly, density control is challenging in experiments due to large particle recycling at the tokamak wall and to the difficulty of pumping particles out of the machine. Therefore, the line average electron density trajectory is chosen to not be optimized. As the particle confinement in the plasma is strongly dependent on the value of the total plasma current, the line average electron density trajectory is chosen to be proportional to the total plasma

[3]The 30R neutral beam injector could be modulated on for 10 ms and off for 10 ms out of phase with the 30L neutral beam injector and still satisfy the requirements needed to acquire diagnostic data. However, this would result in an additional constant average power of 1.1 MW being delivered to the plasma that cannot be manipulated to achieve the control objective.

[4]E-mail correspondence with Dr. Tim C. Luce and Dr. John R. Ferron at General Atomics, San Diego, CA, USA.

current trajectory following the expression[5]

$$\bar{n}_e(t)[10^{19}\mathrm{m}^{-3}] = 2.5 I_p(t)[\mathrm{MA}]. \tag{4.24}$$

Finally, all of the actuator values at the initial time $t_0 = 0.4$ s and the value of the total plasma current at the time t_f are chosen to be fixed. Therefore, the vector of to-be-optimized parameters is then given by

$$\theta = \big[P_{nbi_i}(0.5), P_{nbi_i}(0.75), \ldots, P_{nbi_i}(t_f), I_p(0.5), I_p(0.75), \ldots, I_p(t_f - 0.25)\big], \tag{4.25}$$

where $i \in$ [150L/R,330L/R], respectively. The value and shape of the q profile in the center of the plasma (typically in the spatial domain $\hat{\rho} \in [0, 0.4]$) is important to achieving and maintaining high performance plasmas [61,62]. As a result, the weight function $W_q(\hat{\rho})$ in (4.2) is chosen to place more emphasis on achieving the target q profile in the inner region of the plasma ($\hat{\rho} \in [0, 0.4]$) relative to the outer region.

The optimized parameters (4.25) (and associated actuator trajectories) determined by solving the optimization problem (4.22)-(4.23) are shown in Fig. 4.2 ($q^{tar}(\hat{\rho})$ chosen as target 1 in Fig. 4.1), Fig. 4.3 ($q^{tar}(\hat{\rho})$ chosen as target 2 in Fig. 4.1), and in Fig. 4.4 ($q^{tar}(\hat{\rho})$ chosen as target 3 in Fig. 4.1), respectively. For the various targets, the time that corresponds to the end of the current ramp-up phase is chosen as $t = 1.5$ s (target 1), $t = 1.25$ s (target 2), and $t = 1.0$ s (target 3), respectively. The optimized actuator trajectories exhibit a similar behavior for all of the targets. Firstly, a unique characteristic of the total plasma current trajectory is the regulation of the ramp-up rate, which is traditionally not done in tokamak experiments[6]. The plasma current trajectory is characterized by an initial ramp-up rate near the maximum allowable rate ($t \in [0.4, 0.5]$ s) followed by a gradual ramp-up rate near

[5]E-mail correspondence with Dr. Tim C. Luce at General Atomics, San Diego, CA, USA.

[6]Traditionally, the total plasma current is ramped up at fixed rate until the desired flattop value is reached.

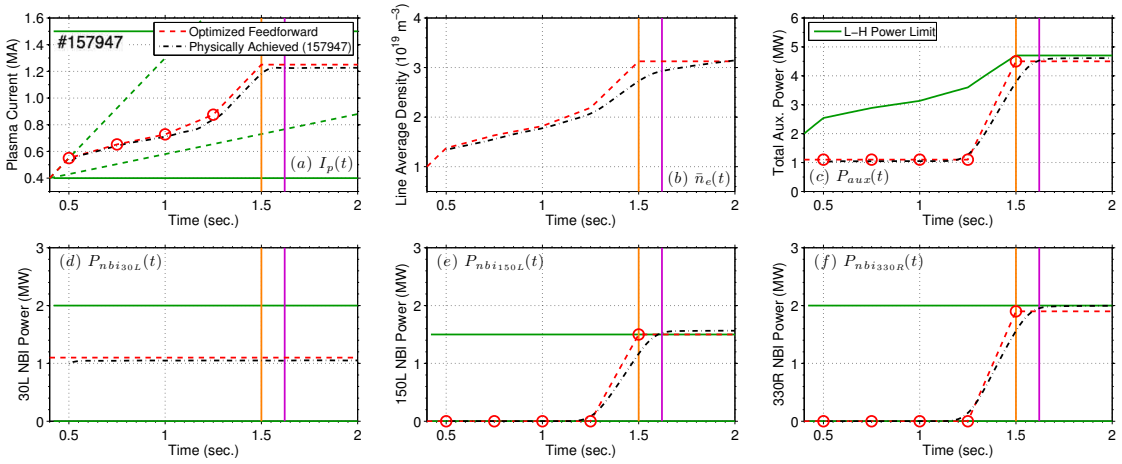

Figure 4.2: Optimized and physically achieved (DIII-D shot 157947) actuator trajectories for q profile target 1 in Fig. 4.1: (a) total plasma current, (b) line average electron density, (c) total amount of neutral beam injection power, and (d-f) individual neutral injection powers. The optimized 150R and 330L neutral beam injection powers are 0 MW (not shown). The optimization is carried out over the time interval $t_{opt} = t \in [0.4, 1.5]$ s. Additionally, the actuator magnitude (solid green) and rate (dash green) limits applied on the optimization problem solution are also shown (L-H power limit in (c) is given by (4.19)). The solid-orange and solid-purple lines indicate the time when the error between the achieved q profile and the target is at a minimum, i.e., when (4.2) is minimized, for the simulation and experimental tests, respectively.

the minimum allowable rate ($t \in [0.5, t_f - 0.25]$ s). During the last optimization time interval ($t \in [t_f - 0.25, t_f]$ s), the plasma current is again ramped-up at a rate near the maximum allowable rate, which is set to avoid triggering tearing modes due to a loss of magnetic shear near the plasma boundary, to the specified flattop value. This rapid ramp-up of the plasma current not only drives the system to the desired q profile near the plasma boundary, but also enhances the plasma confinement which raises the electron temperature and hence lowers the plasma resistivity. This in turn slows the penetration of the current density, which contributes to achieving the target q profile in the plasma core. Secondly, the auxiliary heating scheme is characterized by initially very little, if any, injected neutral beam power (other than the power injected in the 30L injector to acquire diagnostics). The off-axis neutral beam power ($P_{nbi_{150L}}$ for targets 1 and 2 and $P_{nbi_{150L/R}}$ for target 3) is rapidly injected late in

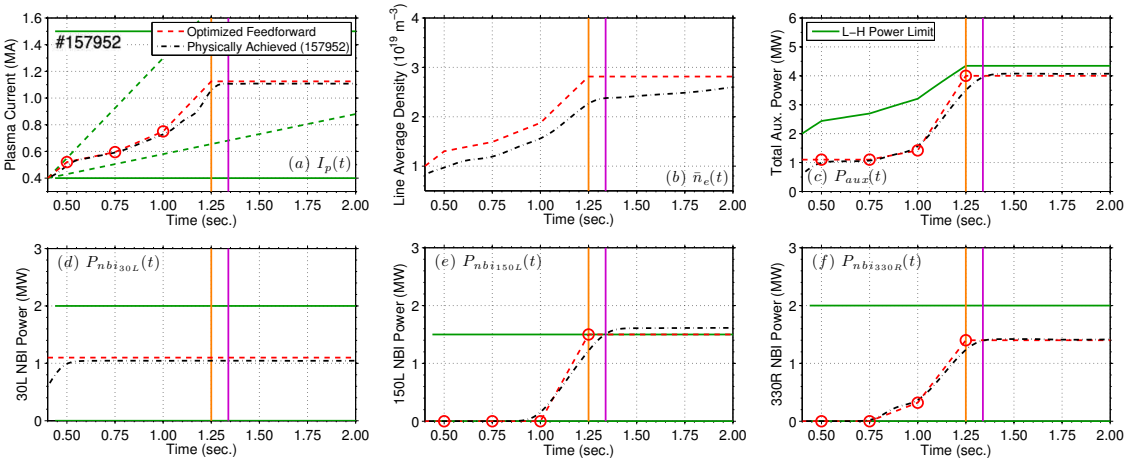

Figure 4.3: Optimized and physically achieved (DIII-D shot 157952) actuator trajectories for q profile target 2 in Fig. 4.1: (a) total plasma current, (b) line average electron density, (c) total amount of neutral beam injection power, and (d-f) individual neutral injection powers. The optimized 150R and 330L neutral beam injection powers are 0 MW (not shown). The optimization is carried out over the time interval $t_{opt} = t \in [0.4, 1.25]$ s. Additionally, the actuator magnitude (solid green) and rate (dash green) limits applied on the optimization problem solution are also shown (L-H power limit in (c) is given by (4.19)). The solid-orange and solid-purple lines indicate the time when the error between the achieved q profile and the target is at a minimum, i.e., when (4.2) is minimized, for the simulation and experimental tests, respectively.

the plasma current ramp-up phase ($t \in [t_f - 0.25, t_f]$ s) to set up a plasma state with off-axis auxiliary current drive, which is needed to achieve the target q profile in the plasma core. Additional neutral beam power is also rapidly injected during this phase ($P_{nbi_{330\mathrm{R}}}$ for targets 1 and 2) up to the maximum allowable total value (set to maintain the plasma in the L-mode operating regime (see (4.17)-(4.19))) to raise the electron temperature (lower the plasma resistivity) to contribute to achieving the target q profile in the plasma core (slows the penetration of the current density into the plasma core). Finally, it is worth noting, that if a mixed solution (one in which both co-current (150L/R and 330L/R) and counter-current (210L/R) neutral beam injection is allowed), the optimized auxiliary heating scheme solely employs the counter-current neutral beam power ($P_{nbi_{210\mathrm{L/R}}}$) late in the plasma current ramp-up phase for all of the targets. An example of this is shown in Fig. 4.5 where the target

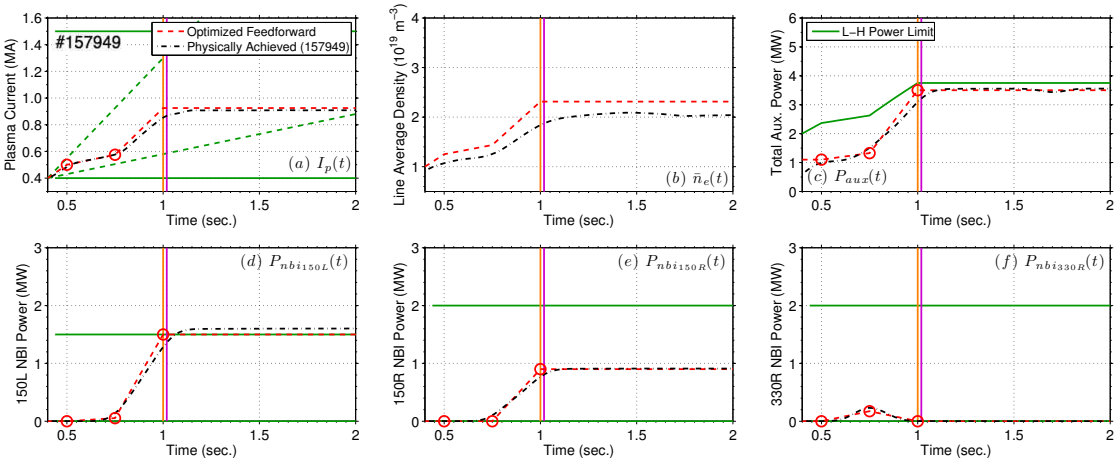

Figure 4.4: Optimized and physically achieved (DIII-D shot 157949) actuator trajectories for q profile target 3 in Fig. 4.1: (a) total plasma current, (b) line average electron density, (c) total amount of neutral beam injection power, and (d-f) individual neutral injection powers. The 30L neutral beam injection power is at a constant 1.1 MW and the optimized 330L neutral beam injection power is 0 MW (not shown). The optimization is carried out over the time interval $t_{opt} = t \in [0.4, 1.0]$ s. Additionally, the actuator magnitude (solid green) and rate (dash green) limits applied on the optimization problem solution are also shown (L-H power limit in (c) is given by (4.19)). The solid-orange and solid-purple lines indicate the time when the error between the achieved q profile and the target is at a minimum, i.e., when (4.2) is minimized, for the simulation and experimental tests, respectively.

q profile is chosen as target 2 in Fig. 4.1.

The actuator trajectories shown in Figs. 4.2-4.5 were tested through simulation with the physics-based model of the plasma dynamics tailored to DIII-D L-mode scenarios (described in section 2.7) and experimentally during DIII-D discharges 157947 (target 1), 157948, 157952, 158058 (target 2), and 157949 (target 3). The actuator values were held constant after the end of the plasma current ramp-up phase was complete, i.e., after the time t_f. It is important to note that the optimized trajectories represent the references to the dedicated control loops that command the DIII-D physical actuators. As shown in Fig. 4.2-4.5, the dedicated control loops were able to follow the requested trajectories reasonably well (note that the physically achieved neutral beam injection powers were not archived by the data acquisition system for

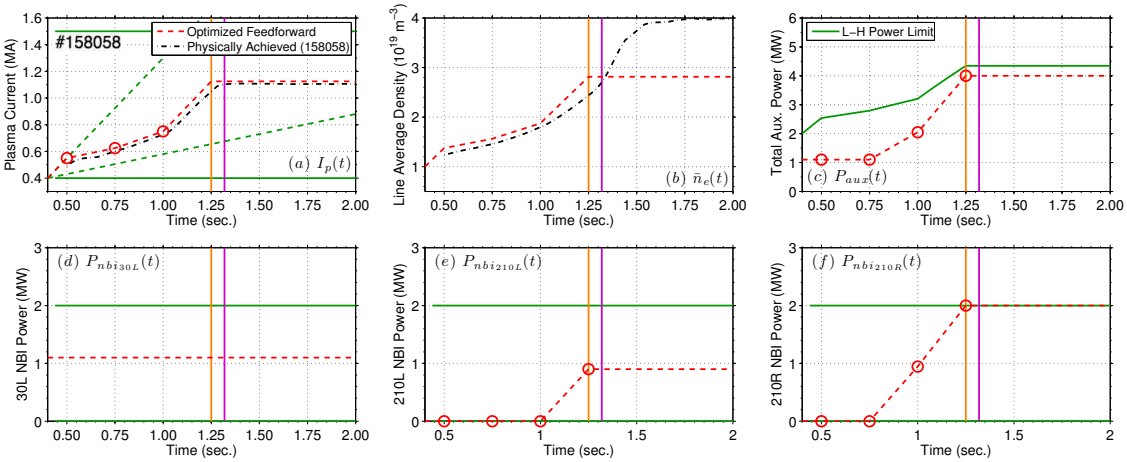

Figure 4.5: Optimized and physically achieved (DIII-D shot 158058) actuator trajectories for q profile target 2 in Fig. 4.1: (a) total plasma current, (b) line average electron density, (c) total amount of neutral beam injection power, and (d-f) individual neutral injection powers. Note that the physically achieved neutral beam injection powers were not archived by the data acquisition system for this discharge. The optimized 150L/R and 330L/R neutral beam injection powers are 0 MW (not shown). The optimization is carried out over the time interval $t_{opt} = t \in [0.4, 1.25]$ s. Additionally, the actuator magnitude (solid green) and rate (dash green) limits applied on the optimization problem solution are also shown (L-H power limit in (c) is given by (4.19)). The solid-orange and solid-purple lines indicate the time when the error between the achieved q profile and the target is at a minimum, i.e., when (4.2) is minimized, for the simulation and experimental tests, respectively.

discharge 158058).

A comparison of the target, physics-based model predicted, and experimentally achieved q profiles at the time when the error between the achieved q profile and the target is at a minimum, i.e., when (4.2) is minimized, is shown in Fig. 4.6. Also shown in the figures is a comparison of the assumed initial q profile that was employed to design the optimized startup trajectories and of the initial q profile achieved experimentally. Firstly, we see that a large discrepancy between the assumed (red dashed line + triangle in Fig. 4.6) and achieved (black dash-dotted line + circle in Fig. 4.6) initial q profile (at $t = t_0 = 0.4$ s) can occur due to the initial generation and formation of the plasma during the time interval $t \in [0, 0.4]$ s, the condition of the tokamak walls, and plasma impurities. Secondly, through simulation with the

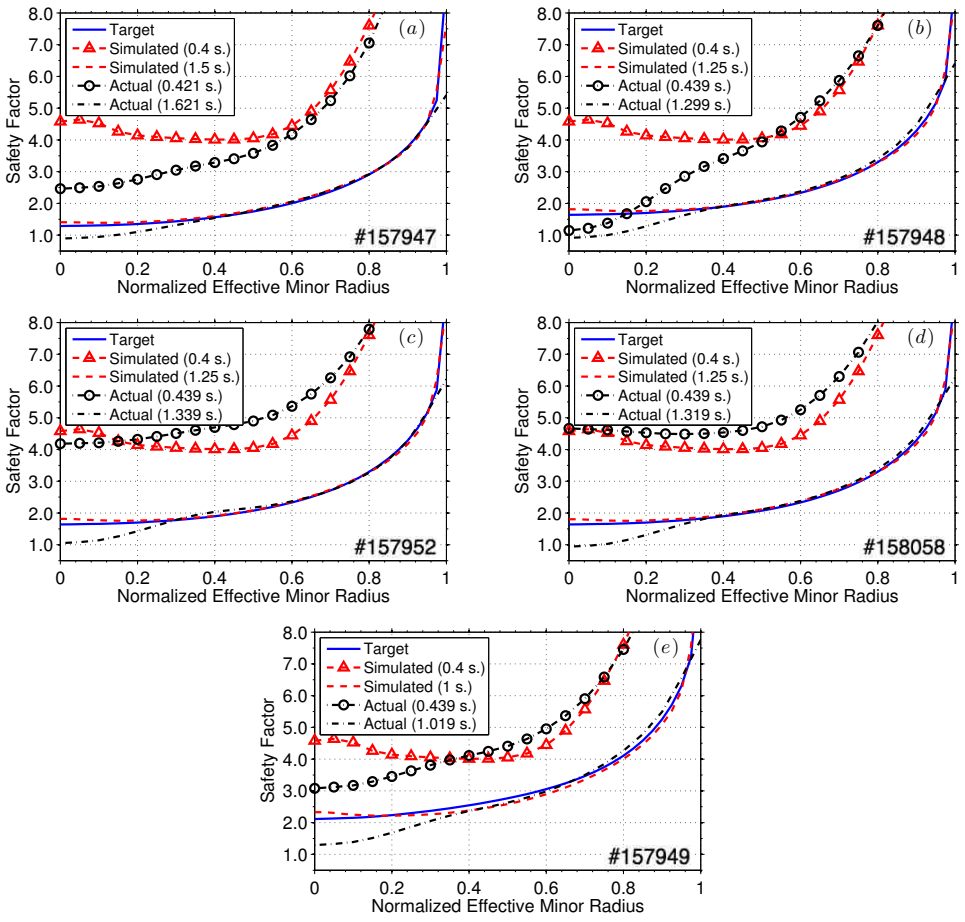

Figure 4.6: Best q profile target matching during the simulation and experimental testing of the optimized feedforward startup actuator trajectories to achieve the target profiles shown in Fig. 4.1: (a) target 1 (actuator trajectories shown in Fig. 4.2), (b-c) target 2 (actuator trajectories shown in Fig. 4.3), (d) target 2 (actuator trajectories shown in Fig. 4.5) and (e) target 3 (actuator trajectories shown in Fig. 4.4). DIII-D shot numbers are indicated in the figures.

physics-based model, it was shown that the optimized startup trajectories were able to steer the simulated plasma (red dashed line in Fig. 4.6) from the assumed initial condition through the tokamak operating space to achieve all of the target q profiles (blue line in Fig. 4.6) at the desired end time of the current ramp-up phase ($t_f = 1.5$ s for target 1, $t_f = 1.25$ s for target 2, $t_f = 1.0$ s for target 3). Finally, as shown in Fig. 4.6, the optimized startup trajectories were able to drive the experimental plasma (black dash-dotted line in Fig. 4.6) as close as possible to the all of the

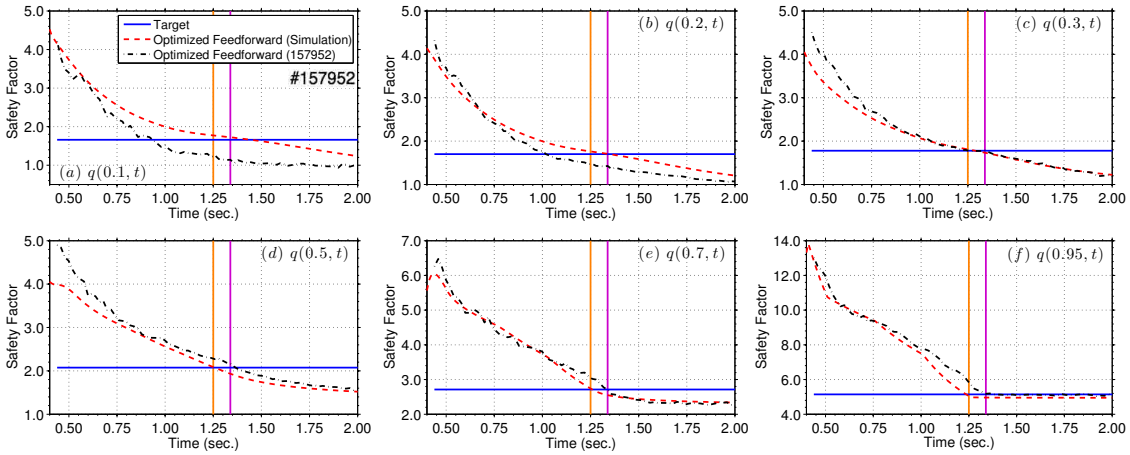

Figure 4.7: Simulated and experimental (DIII-D shot 157952) testing of optimized feedforward startup actuator trajectories to achieve target q profile 2 in Fig. 4.1 with co-current neutral beam injection (actuator trajectories shown in Fig. 4.3): Time traces of q at $\hat{\rho} = 0.1, 0.2, 0.3, 0.5, 0.7$, and 0.95. The solid-orange and solid-purple lines indicate the time when the error between the achieved q profile and the target is at a minimum, i.e., when (4.2) is minimized, for the simulation and experimental tests, respectively.

target q profiles at a time slightly after the desired end time of the current ramp-up phase. The delay in the best experimental target matching time is a result of the dedicated loops not exactly following the requested trajectories, particularly the total plasma current trajectory (shown in Figs. 4.2(a), 4.3(a), 4.4(a), and 4.5(a)). The experimentally achieved q profiles show an excellent match to the desired target profiles in the approximate spatial region $\hat{\rho} \in [0.3, 1]$ and exhibit a value below the desired target value in the plasma core. Note that the experimental q profile can not evolve much lower than a value of one due to the development of sawtooth oscillations (see section 4.2.5).

In order to gain some insight into the physical mechanism that results in the optimized startup trajectories not being able to achieve the target q profiles in the plasma core, time traces of q at various radial locations for DIII-D shots 157952 and 158058 (the discharges where the experimentally achieved and assumed initial q profiles exhibit the closest matching) are shown in Figs. 4.7 and 4.8, respectively. Firstly, as

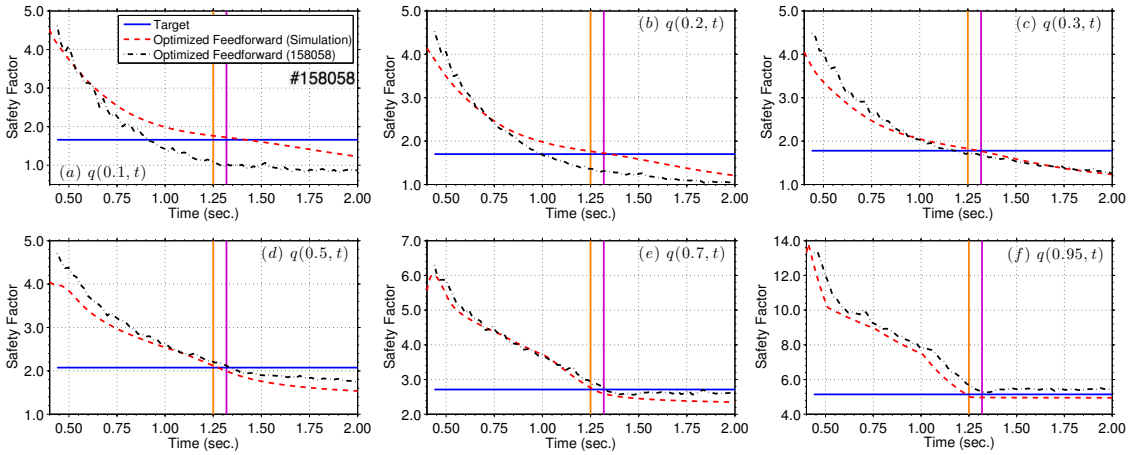

Figure 4.8: Simulated and experimental (DIII-D shot 158058) testing of optimized feedforward startup actuator trajectories to achieve target q profile 2 in Fig. 4.1 with counter-current neutral beam injection (actuator trajectories shown in Fig. 4.5): Time traces of q at $\hat{\rho} = 0.1, 0.2, 0.3, 0.5, 0.7$, and 0.95. The solid-orange and solid-purple lines indicate the time when the error between the achieved q profile and the target is at a minimum, i.e., when (4.2) is minimized, for the simulation and experimental tests, respectively.

shown in the figures, the experimentally achieved q profile evolution agrees well with the physics-based model predicted q profile evolution in the spatial region $\hat{\rho} \in [0.3, 1]$. Secondly, the experimentally achieved q profile evolution agrees reasonably well with the physics-based model predicted q profile evolution in the plasma core during the approximate time interval $t \in [0.4, 0.75)$ s. However, after this time, the experimental q profile evolves to a lower value than the physics-based model predicted q profile (see Figs. 4.7(a-b) and 4.8(a-b)). This indicates that the experimental current density diffuses towards the plasma core at a faster rate than predicted by the model[7]. Finally, as shown in the figures, there is no appreciable difference between the performance (in terms of driving the system to q profile target 2 in Fig. 4.1) of the optimized startup trajectories that utilized co-current neutral beam injection (Fig. 4.7) and counter-current neutral beam injection (Fig. 4.8), respectively.

As a result of the variability in the initial formation of the plasma as well as the

[7]In tokamaks, the local q-value is roughly inversely related to the local current density amplitude.

difference between the model predicted and experimentally observed current density diffusion rate during the experimental tests of the optimized startup trajectories, the target q profiles were unable to be achieved in the plasma core ($\hat{\rho} \in [0, 0.3)$) at the end of the current ramp-up phase of the discharge. Therefore to compensate for external disturbances (such as perturbed initial conditions and model uncertainty) and actuation limitations (either in regulation or faults), the feedforward trajectories need to be integrated together with a feedback control scheme, as discussed in the next section, to improve the ability to robustly achieve plasma target conditions.

4.4 Feedback control design

4.4.1 Partial differential equation model of system dynamics

We begin the design process by converting the physics model that describes the poloidal magnetic flux profile evolution in the tokamak (the magnetic diffusion equation) into a form suitable for feedback control design. The magnetic diffusion equation is given in (2.45) and restated here for convenience as

$$\frac{\partial \psi}{\partial t} = \frac{\eta(T_e)}{\mu_0 \rho_b^2 \hat{F}^2} \frac{1}{\hat{\rho}} \frac{\partial}{\partial \hat{\rho}} \left(\hat{\rho} \hat{F} \hat{G} \hat{H} \frac{\partial \psi}{\partial \hat{\rho}} \right) + R_0 \hat{H} \eta(T_e)(j_{aux} + j_{bs}), \tag{4.26}$$

with boundary conditions given by

$$\left. \frac{\partial \psi}{\partial \hat{\rho}} \right|_{\hat{\rho}=0} = 0 \qquad \left. \frac{\partial \psi}{\partial \hat{\rho}} \right|_{\hat{\rho}=1} = -k_{I_p} I_p(t), \tag{4.27}$$

where $\eta(\hat{\rho}, t)$ is the plasma resistivity, $T_e(\hat{\rho}, t)$ is the electron temperature, μ_0 is the vacuum magnetic permeability, $j_{aux}(\hat{\rho}, t)$ is the noninductive current density provided by the auxiliary sources, and $j_{bs}(\hat{\rho}, t)$ is the noninductive current density provided by the bootstrap current [60]. The parameters $\hat{F}(\hat{\rho})$, $\hat{G}(\hat{\rho})$, and $\hat{H}(\hat{\rho})$ are geometric

spatial factors pertaining to the magnetic configuration of a particular plasma MHD equilibrium (defined in (2.44)). The total auxiliary current drive is defined as

$$j_{aux} = \sum_j j_{nbi_j}, \tag{4.28}$$

where $j \in$ [30L/R,150L/R,210L/R,330L/R], and the individual auxiliary neutral beam current drives are modeled as (see (2.76) and section 2.7)

$$j_{nbi_j}(\hat{\rho}, t) = j_{nbi_j}^{ref}(\hat{\rho}) \frac{\sqrt{T_e(\hat{\rho}, t)}}{n_e(\hat{\rho}, t)} P_{nbi_j}(t), \tag{4.29}$$

where $j_{nbi_j}^{ref}$ is a normalized reference current density deposition profile for each of the sources, n_e is the electron density, and P_{nbi_j} is the power injected through the individual neutral beam injectors. The bootstrap current is proportional to the inverse of the poloidal flux gradient profile multiplied by the kinetic plasma profile gradients (see (2.81)), i.e.,

$$j_{bs}(\hat{\rho}, t) = \frac{k_{JkeV} R_0}{\hat{F}} \left(\frac{\partial \psi}{\partial \hat{\rho}} \right)^{-1} \left[2\mathcal{L}_{31} T_e \frac{\partial n_e}{\partial \hat{\rho}} + \{ 2\mathcal{L}_{31} + \mathcal{L}_{32} + \alpha \mathcal{L}_{34} \} n_e \frac{\partial T_e}{\partial \hat{\rho}} \right], \tag{4.30}$$

where $k_{JkeV} = 1.602 \times 10^{-16}$ J/keV and the coefficients $\mathcal{L}_{31}$, $\mathcal{L}_{32}$, $\mathcal{L}_{34}$, and α depend on the magnetic configuration of a particular plasma equilibrium and on particle collisionality in the plasma. For feedback control design, we chose to model the kinetic plasma parameters (electron density, electron temperature, and plasma resistivity) as a nominal model plus a bounded uncertain model. The feedback controller is then designed by employing *robust control techniques* [10] to achieve a desired closed-loop performance and ensure the closed-loop system remains stable for the range of the kinetic plasma parameters captured by the uncertain models.

Towards this goal, we define ranges in which the electron density and temperature profiles are expected to be in typical DIII-D L-modes scenarios, which are shown in

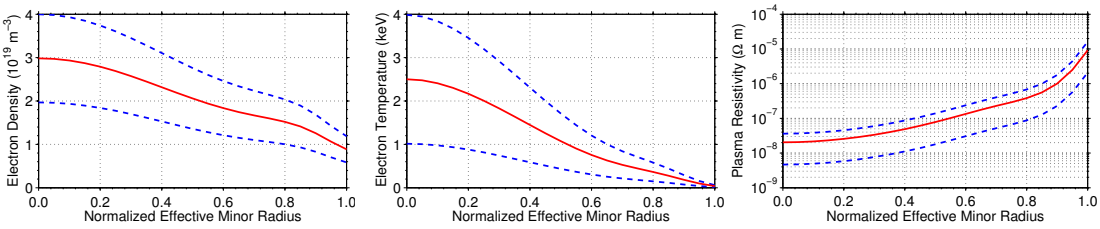

(a) n_e (b) T_e (c) η

Figure 4.9: Plasma parameter uncertainty ranges in DIII-D L-mode scenarios: (a) electron density, (b) electron temperature, and (c) plasma resistivity. Note: nominal values (solid) and minimum/maximum values (dash).

Figs. 4.9(a-b). For feedback control design, we model these kinetic plasma parameters as a nominal profile plus a bounded uncertain profile, i.e.,

$$n_e(\hat{\rho}) = n_e^{nom}(\hat{\rho}) + n_e^{unc}(\hat{\rho})\delta_{n_e}, \tag{4.31}$$

$$T_e(\hat{\rho}) = T_e^{nom}(\hat{\rho}) + T_e^{unc}(\hat{\rho})\delta_{T_e}, \tag{4.32}$$

where

$$\begin{aligned} n_e^{nom}(\hat{\rho}) &= \left[n_e^{max}(\hat{\rho}) + n_e^{min}(\hat{\rho})\right]/2, \\ T_e^{nom}(\hat{\rho}) &= \left[T_e^{max}(\hat{\rho}) + T_e^{min}(\hat{\rho})\right]/2, \\ n_e^{unc}(\hat{\rho}) &= \left[n_e^{max}(\hat{\rho}) - n_e^{min}(\hat{\rho})\right]/2, \\ T_e^{unc}(\hat{\rho}) &= \left[T_e^{max}(\hat{\rho}) - T_e^{min}(\hat{\rho})\right]/2, \end{aligned} \tag{4.33}$$

and δ_{T_e} and δ_{n_e} are uncertain parameters that satisfy $|\delta_{T_e}| \leq 1$ and $|\delta_{n_e}| \leq 1$. The plasma resistivity decreases as the electron temperature increases, therefore, the minimum plasma resistivity is defined by the maximum electron temperature, and the maximum plasma resistivity is defined by the minimum electron temperature, which are shown in Fig. 4.9(c). Additionally, the parameters $\sqrt{T_e}$ and $1/n_e$ are related to the electron temperature and density, respectively. For feedback control design, these

parameters are modeled as

$$\eta(\hat{\rho}) = \eta^{nom}(\hat{\rho}) + \eta^{unc}(\hat{\rho})\delta_{T_e}, \tag{4.34}$$

$$\sqrt{T_e(\hat{\rho})} = T_e^{nom'}(\hat{\rho}) + T_e^{unc'}(\hat{\rho})\delta_{T_e}, \tag{4.35}$$

$$1/n_e(\hat{\rho}) = n_e^{nom'}(\hat{\rho}) + n_e^{unc'}(\hat{\rho})\delta_{n_e}, \tag{4.36}$$

where

$$\begin{aligned}
\eta^{nom}(\hat{\rho}) &= \left[\eta^{max}(\hat{\rho}) + \eta^{min}(\hat{\rho})\right]/2, \\
T_e^{nom'}(\hat{\rho}) &= \left[\sqrt{T_e^{max}(\hat{\rho})} + \sqrt{T_e^{min}(\hat{\rho})}\right]/2, \\
n_e^{nom'}(\hat{\rho}) &= \left[n_e^{max}(\hat{\rho}) + n_e^{min}(\hat{\rho})\right] / \left[2n_e^{max}(\hat{\rho})n_e^{min}(\hat{\rho})\right], \\
\eta^{unc}(\hat{\rho}) &= \left[\eta^{min}(\hat{\rho}) - \eta^{max}(\hat{\rho})\right]/2, \\
T_e^{unc'}(\hat{\rho}) &= \left[\sqrt{T_e^{max}(\hat{\rho})} - \sqrt{T_e^{min}(\hat{\rho})}\right]/2, \\
n_e^{unc'}(\hat{\rho}) &= \left[n_e^{min}(\hat{\rho}) - n_e^{max}(\hat{\rho})\right] / \left[2n_e^{max}(\hat{\rho})n_e^{min}(\hat{\rho})\right].
\end{aligned} \tag{4.37}$$

Note that the plasma resistivity and $\sqrt{T_e}$ dependence on the electron temperature is modeled to first order to simplify the control design process.

Combining the magnetic diffusion equation (4.26) with the noninductive current-drive models (4.28)-(4.30) and the uncertain models (4.31)-(4.37), we obtain the PDE

governing the evolution of ψ that is used for feedback control design, which is expressed as

$$\begin{aligned}\frac{\partial\psi}{\partial t} &= \frac{(\eta^{nom}+\eta^{unc}\delta_{T_e})}{\mu_0\rho_b^2\hat{F}^2}\frac{1}{\hat{\rho}}\frac{\partial}{\partial\hat{\rho}}\left(\hat{\rho}\hat{F}\hat{G}\hat{H}\frac{\partial\psi}{\partial\hat{\rho}}\right)+R_0\hat{H}(\eta^{nom}+\eta^{unc}\delta_{T_e})\\ &\times\left(T_e^{nom'}+T_e^{unc'}\delta_{T_e}\right)\left\{n_e^{nom'}+n_e^{unc'}\delta_{n_e}\right\}\left(\sum_j j_{nbi_j}^{ref}(\hat{\rho})P_{nbi_j}(t)\right)\\ &+\frac{k_{JeV}R_0^2\hat{H}(\eta^{nom}+\eta^{unc}\delta_{T_e})}{\hat{F}}\left(\frac{\partial\psi}{\partial\hat{\rho}}\right)^{-1}\\ &\times\Bigg[2\mathcal{L}_{31}\left(T_e^{nom}+T_e^{unc}\delta_{T_e}\right)\frac{\partial}{\partial\hat{\rho}}\left\{n_e^{nom}+n_e^{unc}\delta_{n_e}\right\}\\ &+\left\{2\mathcal{L}_{31}+\mathcal{L}_{32}+\alpha\mathcal{L}_{34}\right\}\left\{n_e^{nom}+n_e^{unc}\delta_{n_e}\right\}\frac{\partial}{\partial\hat{\rho}}\left\{T_e^{nom}+T_e^{unc}\delta_{T_e}\right\}\Bigg]. \quad (4.38)\end{aligned}$$

By defining the quantities,

$$\begin{aligned}f_{\eta_1}(\hat{\rho}) &= \frac{\eta^{nom}}{\mu_0\hat{\rho}_b^2\hat{F}^2} \qquad f_{\eta_2}(\hat{\rho}) = \frac{\eta^{unc}}{\mu_0\hat{\rho}_b^2\hat{F}^2} \qquad D_\psi(\hat{\rho}) = \hat{F}\hat{G}\hat{H},\\ g_{nbi_j}(\hat{\rho}) &= R_0\hat{H}j_{nbi_j}^{ref}\eta^{nom}T_e^{nom'}n_e^{nom'} \qquad h_{nbi_j}(\hat{\rho}) = R_0\hat{H}j_{nbi_j}^{ref}\eta^{nom}T_e^{nom'}n_e^{unc'},\\ k_{nbi_j}(\hat{\rho}) &= R_0\hat{H}j_{nbi_j}^{ref}\left[\eta^{nom}T_e^{unc'}n_e^{nom'}+\eta^{unc}T_e^{nom'}n_e^{nom'}\right],\\ l_{nbi_j}(\hat{\rho}) &= R_0\hat{H}j_{nbi_j}^{ref}\left[\eta^{nom}T_e^{unc'}n_e^{unc'}+\eta^{unc}T_e^{nom'}n_e^{unc'}\right],\\ m_{nbi_j}(\hat{\rho}) &= R_0\hat{H}j_{nbi_j}^{ref}\eta^{unc}T_e^{unc'}n_e^{nom'} \qquad p_{nbi_j}(\hat{\rho}) = R_0\hat{H}j_{nbi_j}^{ref}\eta^{unc}T_e^{unc'}n_e^{unc'}, \quad (4.39)\end{aligned}$$

and

$$
\begin{aligned}
g_{bs}(\hat{\rho}) &= \frac{k_{JeV}R_0^2\hat{H}}{\hat{F}}\Bigg[2\mathcal{L}_{31}\eta^{nom}T_e^{nom}\frac{d}{d\hat{\rho}}\left(n_e^{nom}\right) \\
&\quad + \left\{2\mathcal{L}_{31}+\mathcal{L}_{32}+\alpha\mathcal{L}_{34}\right\}\eta^{nom}n_e^{nom}\frac{d}{d\hat{\rho}}\left(T_e^{nom}\right)\Bigg], \\
h_{bs}(\hat{\rho}) &= \frac{k_{JeV}R_0^2\hat{H}}{\hat{F}}\Bigg[2\mathcal{L}_{31}\eta^{nom}T_e^{nom}\frac{d}{d\hat{\rho}}\left(n_e^{unc}\right) \\
&\quad + \left\{2\mathcal{L}_{31}+\mathcal{L}_{32}+\alpha\mathcal{L}_{34}\right\}\eta^{nom}n_e^{unc}\frac{d}{d\hat{\rho}}\left(T_e^{nom}\right)\Bigg], \\
k_{bs}(\hat{\rho}) &= \frac{k_{JeV}R_0^2\hat{H}}{\hat{F}}\Bigg[2\mathcal{L}_{31}\left[\eta^{nom}T_e^{unc}\frac{d}{d\hat{\rho}}\left(n_e^{nom}\right)+\eta^{unc}T_e^{nom}\frac{d}{d\hat{\rho}}\left(n_e^{nom}\right)\right] \\
&\quad + \left\{2\mathcal{L}_{31}+\mathcal{L}_{32}+\alpha\mathcal{L}_{34}\right\}\left[\eta^{nom}n_e^{nom}\frac{d}{d\hat{\rho}}\left(T_e^{unc}\right)+\eta^{unc}n_e^{nom}\frac{d}{d\hat{\rho}}\left(T_e^{nom}\right)\right]\Bigg], \\
l_{bs}(\hat{\rho}) &= \frac{k_{JeV}R_0^2\hat{H}}{\hat{F}}\Bigg[2\mathcal{L}_{31}\left[\eta^{nom}T_e^{unc}\frac{d}{d\hat{\rho}}\left(n_e^{unc}\right)+\eta^{unc}T_e^{nom}\frac{d}{d\hat{\rho}}\left(n_e^{unc}\right)\right] \\
&\quad + \left\{2\mathcal{L}_{31}+\mathcal{L}_{32}+\alpha\mathcal{L}_{34}\right\}\left[\eta^{nom}n_e^{unc}\frac{d}{d\hat{\rho}}\left(T_e^{unc}\right)+\eta^{unc}n_e^{unc}\frac{d}{d\hat{\rho}}\left(T_e^{nom}\right)\right]\Bigg], \\
m_{bs}(\hat{\rho}) &= \frac{k_{JeV}R_0^2\hat{H}}{\hat{F}}\Bigg[2\mathcal{L}_{31}\eta^{unc}T_e^{unc}\frac{d}{d\hat{\rho}}\left(n_e^{nom}\right) \\
&\quad + \left\{2\mathcal{L}_{31}+\mathcal{L}_{32}+\alpha\mathcal{L}_{34}\right\}\eta^{unc}n_e^{nom}\frac{d}{d\hat{\rho}}\left(T_e^{unc}\right)\Bigg], \\
p_{bs}(\hat{\rho}) &= \frac{k_{JeV}R_0^2\hat{H}}{\hat{F}}\Bigg[2\mathcal{L}_{31}\eta^{unc}T_e^{unc}\frac{d}{d\hat{\rho}}\left(n_e^{unc}\right) \\
&\quad + \left\{2\mathcal{L}_{31}+\mathcal{L}_{32}+\alpha\mathcal{L}_{34}\right\}\eta^{unc}n_e^{unc}\frac{d}{d\hat{\rho}}\left(T_e^{unc}\right)\Bigg], \qquad (4.40)
\end{aligned}
$$

we can express (4.38) as

$$
\begin{aligned}
\frac{\partial\psi}{\partial t} &= f_{\eta_1}\frac{1}{\hat{\rho}}\frac{\partial}{\partial\hat{\rho}}\left(\hat{\rho}D_\psi\frac{\partial\psi}{\partial\hat{\rho}}\right)+f_{\eta_2}\frac{1}{\hat{\rho}}\frac{\partial}{\partial\hat{\rho}}\left(\hat{\rho}D_\psi\frac{\partial\psi}{\partial\hat{\rho}}\right)\delta_{T_e} \\
&\quad + \sum_j\left[g_{nbi_j}+h_{nbi_j}\delta_{n_e}+k_{nbi_j}\delta_{T_e}+l_{nbi_j}\delta_{T_e}\delta_{n_e}+m_{nbi_j}\delta_{T_e}^2+p_{nbi_j}\delta_{T_e}^2\delta_{n_e}\right]P_{nbi_j}(t) \\
&\quad + \left[g_{bs}+h_{bs}\delta_{n_e}+k_{bs}\delta_{T_e}+l_{bs}\delta_{T_e}\delta_{n_e}+m_{bs}\delta_{T_e}^2+p_{bs}\delta_{T_e}^2\delta_{n_e}\right]\left(\frac{\partial\psi}{\partial\hat{\rho}}\right)^{-1}. \qquad (4.41)
\end{aligned}
$$

From (4.1), we see that the rotational transform profile is inversely proportional to the

q profile (the variable we are ultimately interested in controlling) and proportional to the spatial gradient of the poloidal stream function. Therefore, we define the poloidal flux gradient profile as

$$\theta(\hat{\rho},t) \equiv \frac{\partial \psi}{\partial \hat{\rho}}. \tag{4.42}$$

Inserting (4.42) into (4.41) and differentiating the resulting equation with respect to $\hat{\rho}$, we obtain the following model of the θ profile dynamics

$$\begin{aligned}
\frac{\partial \theta}{\partial t} = & \left[q_{\eta_1} + q_{\eta_4}\delta_{T_e}\right]\frac{\partial^2 \theta}{\partial \hat{\rho}^2} + \left[q_{\eta_2} + q_{\eta_5}\delta_{T_e}\right]\frac{\partial \theta}{\partial \hat{\rho}} + \left[q_{\eta_3} + q_{\eta_6}\delta_{T_e}\right]\theta \\
& + \sum_j \left[g'_{nbi_j} + h'_{nbi_i}\delta_{n_e} + k'_{nbi_j}\delta_{T_e} + l'_{nbi_j}\delta_{T_e}\delta_{n_e} + m'_{nbi_j}\delta^2_{T_e} + p'_{nbi_j}\delta^2_{T_e}\delta_{n_e}\right]P_{nbi_j}(t) \\
& - \left[g_{bs} + h_{bs}\delta_{n_e} + k_{bs}\delta_{T_e} + l_{bs}\delta_{T_e}\delta_{n_e} + m_{bs}\delta^2_{T_e} + p_{bs}\delta^2_{T_e}\delta_{n_e}\right]\left(\frac{1}{\theta}\right)^2\frac{\partial \theta}{\partial \hat{\rho}} \\
& + \left[g'_{bs} + h'_{bs}\delta_{n_e} + k'_{bs}\delta_{T_e} + l'_{bs}\delta_{T_e}\delta_{n_e} + m'_{bs}\delta^2_{T_e} + p'_{bs}\delta^2_{T_e}\delta_{n_e}\right]\left(\frac{1}{\theta}\right),
\end{aligned} \tag{4.43}$$

where $(\cdot)' = d/d\hat{\rho}$ and

$$\begin{aligned}
q_{\eta_1}(\hat{\rho}) &= f_{\eta_1}(\hat{\rho})D_\psi(\hat{\rho}), \\
q_{\eta_2}(\hat{\rho}) &= f'_{\eta_1}(\hat{\rho})D_\psi(\hat{\rho}) + 2f_{\eta_1}(\hat{\rho})D'_\psi(\hat{\rho}) + f_{\eta_1}(\hat{\rho})D_\psi(\hat{\rho})/\hat{\rho}, \\
q_{\eta_3}(\hat{\rho}) &= f'_{\eta_1}(\hat{\rho})D_\psi(\hat{\rho})/\hat{\rho} + f'_{\eta_1}(\hat{\rho})D'_\psi(\hat{\rho}) - f_{\eta_1}(\hat{\rho})D_\psi(\hat{\rho})/\hat{\rho}^2 \\
&\quad + f_{\eta_1}(\hat{\rho})D'_\psi(\hat{\rho})/\hat{\rho} + f_{\eta_1}(\hat{\rho})D''_\psi(\hat{\rho}), \\
q_{\eta_4}(\hat{\rho}) &= f_{\eta_2}(\hat{\rho})D_\psi(\hat{\rho}), \\
q_{\eta_5}(\hat{\rho}) &= f'_{\eta_2}(\hat{\rho})D_\psi(\hat{\rho}) + 2f_{\eta_2}(\hat{\rho})D'_\psi(\hat{\rho}) + f_{\eta_2}(\hat{\rho})D_\psi(\hat{\rho})/\hat{\rho}, \\
q_{\eta_6}(\hat{\rho}) &= f'_{\eta_2}(\hat{\rho})D_\psi(\hat{\rho})/\hat{\rho} + f'_{\eta_2}(\hat{\rho})D'_\psi(\hat{\rho}) - f_{\eta_2}(\hat{\rho})D_\psi(\hat{\rho})/\hat{\rho}^2 \\
&\quad + f_{\eta_2}(\hat{\rho})D'_\psi(\hat{\rho})/\hat{\rho} + f_{\eta_2}(\hat{\rho})D''_\psi(\hat{\rho}).
\end{aligned} \tag{4.44}$$

The boundary conditions are given by

$$\theta(0,t) = 0 \qquad \theta(1,t) = -k_{I_p} I_p(t). \tag{4.45}$$

4.4.2 Model reduction via spatial discretization

We now approximate the governing infinite dimensional PDE (4.43) by a finite dimensional system of ordinary differential equations (ODEs) to obtain a model suitable for tracking feedback control design. This is achieved by discretizing (4.43) in space by using a truncated Taylor series expansion to approximate the spatial derivatives where the non-dimensional spatial domain ($\hat{\rho} \in [0,1]$) is represented by m_θ nodes. The spacing between the nodes ($\Delta\hat{\rho}$) is defined as $\Delta\hat{\rho} = 1/(m_\theta - 1)$. We employ central finite difference spatial derivative approximations of order $(\Delta\hat{\rho})^2$ in the interior node region, $2 \leq i \leq (m_\theta - 1)$. After applying the spatial derivative approximations to (4.43) for the interior nodes $i = [2, \ldots, m_\theta - 1]$, we obtain

$$\begin{aligned}
\dot{\theta}_i = {} & \left[q_{\eta_1}(\hat{\rho}_i) + q_{\eta_4}(\hat{\rho}_i)\delta_{T_e}\right] \frac{\theta_{i+1} - 2\theta_i + \theta_{i-1}}{(\Delta\hat{\rho})^2} \\
& + \left[q_{\eta_2}(\hat{\rho}_i) + q_{\eta_5}(\hat{\rho}_i)\delta_{T_e}\right] \frac{\theta_{i+1} - \theta_{i-1}}{2\Delta\hat{\rho}} + \left[q_{\eta_3}(\hat{\rho}_i) + q_{\eta_6}(\hat{\rho}_i)\delta_{T_e}\right] \theta_i \\
& + \sum_j \Big[g'_{nbi_j}(\hat{\rho}_i) + h'_{nbi_j}(\hat{\rho}_i)\delta_{n_e} + k'_{nbi_j}(\hat{\rho}_i)\delta_{T_e} + l'_{nbi_j}(\hat{\rho}_i)\delta_{T_e}\delta_{n_e} \\
& + m'_{nbi_j}(\hat{\rho}_i)\delta^2_{T_e} + p'_{nbi_j}(\hat{\rho}_i)\delta^2_{T_e}\delta_{n_e}\Big] P_{nbi_j}(t) \\
& - \Big[g_{bs}(\hat{\rho}_i) + h_{bs}(\hat{\rho}_i)\delta_{n_e} + k_{bs}(\hat{\rho}_i)\delta_{T_e} + l_{bs}(\hat{\rho}_i)\delta_{T_e}\delta_{n_e} + m_{bs}(\hat{\rho}_i)\delta^2_{T_e} \\
& + p_{bs}(\hat{\rho}_i)\delta^2_{T_e}\delta_{n_e}\Big] \left(\frac{1}{\theta_i}\right)^2 \frac{\theta_{i+1} - \theta_{i-1}}{2\Delta\hat{\rho}} \\
& + \Big[g'_{bs}(\hat{\rho}_i) + h'_{bs}(\hat{\rho}_i)\delta_{n_e} + k'_{bs}(\hat{\rho}_i)\delta_{T_e} + l'_{bs}(\hat{\rho}_i)\delta_{T_e}\delta_{n_e} + m'_{bs}(\hat{\rho}_i)\delta^2_{T_e} \\
& + p'_{bs}(\hat{\rho}_i)\delta^2_{T_e}\delta_{n_e}\Big] \left(\frac{1}{\theta_i}\right),
\end{aligned} \tag{4.46}$$

where θ_i and $\hat{\rho}_i$ are the values of θ and $\hat{\rho}$ at the discrete nodes, for $i = [2, \ldots, m_\theta - 1]$. The values of θ at the boundary nodes $i = 1$ and $i = m_\theta$ are obtained from the

boundary conditions (4.45) and are expressed as

$$\theta_1 = 0 \qquad \theta_{m_\theta} = -k_{I_p} I_p(t). \tag{4.47}$$

The discretized model can be written in a compact form as

$$\dot{x} = f_\theta(x, u, \delta), \tag{4.48}$$

$$\iota_i = -\frac{1}{B_{\phi,0}\rho_b^2 \hat{\rho}_i} x_i, \tag{4.49}$$

where $x = [\theta_2, \ldots, \theta_{m_\theta - 1}] \in \mathbb{R}^{n_\theta}$ is the state vector, ι_i is the value of ι at the discrete nodes, for $i = 2, \ldots, m_\theta - 1$, $u = [P_{nbi_{30\mathrm{L/R}}}, P_{nbi_{150\mathrm{L/R}}}, P_{nbi_{210\mathrm{L/R}}}, P_{nbi_{330\mathrm{L/R}}}, I_p] \in \mathbb{R}^9$ is the input vector, the uncertain parameter vector is $\delta = \left[\delta_{T_e}, \delta_{n_e}, \delta_{T_e}\delta_{n_e}, \delta_{T_e}^2, \delta_{T_e}^2 \delta_{n_e}\right] \in \mathbb{R}^5$, $f_\theta \in \mathbb{R}^{n_\theta}$ is a nonlinear function of the states, inputs, and uncertain parameters, and $n_\theta = m_\theta - 2$. The output vector is defined as $y = [\iota_2, \ldots, \iota_{m_\theta - 1}] \in \mathbb{R}^{n_\theta}$.

We define a nominal equilibrium point of the system (4.48) as

$$\dot{x}_{eq} = f_\theta(x_{eq}, u_{eq}, 0) = 0. \tag{4.50}$$

We can obtain a model suitable for tracking control design by defining the perturbation variables $\tilde{x}(t) = x(t) - x_{eq}$ and $u_{fb}(t) = u(t) - u_{eq}$, where $\tilde{x}(t)$ is the deviation away from the equilibrium state and $u_{fb}(t)$ is the output of the to-be-designed feedback controller. Linearizing (4.48) *with respect to the state and control input* around an equilibrium point defined by (4.50), we obtain

$$\dot{x}_{eq} + \dot{\tilde{x}} = f_\theta(x_{eq}, u_{eq}, \delta) + \left.\frac{\partial f_\theta}{\partial x}\right|_{(x_{eq}, u_{eq}, \delta)} \tilde{x} + \left.\frac{\partial f_\theta}{\partial u}\right|_{(x_{eq}, u_{eq}, \delta)} u_{fb}, \tag{4.51}$$

where $\partial f_\theta / \partial x \in \mathbb{R}^{n_\theta \times n_\theta}$ and $\partial f_\theta / \partial u \in \mathbb{R}^{n_\theta \times 9}$ are the Jacobians of the system. By

employing (4.50), we express (4.51) as

$$\dot{\tilde{x}} = \left.\frac{\partial f_\theta}{\partial x}\right|_{(x_{eq},u_{eq},\delta)} \tilde{x} + \left.\frac{\partial f_\theta}{\partial u}\right|_{(x_{eq},u_{eq},\delta)} u_{fb} + d_\delta, \tag{4.52}$$

where $d_\delta = f_\theta(x_{eq}, u_{eq}, \delta)$ is a disturbance. Finally, (4.52) is written as an explicit uncertain state-space system as

$$\begin{aligned} \dot{\tilde{x}} &= A\tilde{x} + Bu_{fb} + d_\delta, \\ y &= C\tilde{x} + Du_{fb}, \end{aligned} \tag{4.53}$$

where the state-space matrices have a structure of the form

$$\begin{aligned} A &= A_0 + \sum_{m=1}^{5} \delta_m A_m \qquad B = B_0 + \sum_{m=1}^{5} \delta_m B_m, \\ C &= C_0 + \sum_{m=1}^{5} \delta_m C_m \qquad D = D_0 + \sum_{m=1}^{5} \delta_m D_m, \end{aligned} \tag{4.54}$$

where A and B are the Jacobians $\partial f_\theta/\partial x$ and $\partial f_\theta/\partial u$ evaluated at (x_{eq}, u_{eq}, δ), respectively, A_i and B_i, for $i = 0, \ldots, 5$, are the components of the matrices A and B, respectively, $C_0 = \text{diag}\{-1/(B_{\phi,0}\rho_b^2\hat{\rho}_i)\}$, $D_0 = 0$, and $C_j = 0$ and $D_j = 0$, for $j = 1, \ldots, 5$.

4.4.3 Manipulation of dynamic model into robust control framework

We now exploit the structure of the state matrices in (4.54) to write the system (4.53) in the conventional $P - \Delta$ robust control framework (shown in the little purple box in Fig. 4.10), where P is the generalized transfer function of the system and $\Delta = \text{diag}\{\delta\}$ is a structured uncertainty matrix. The transfer function of a linear

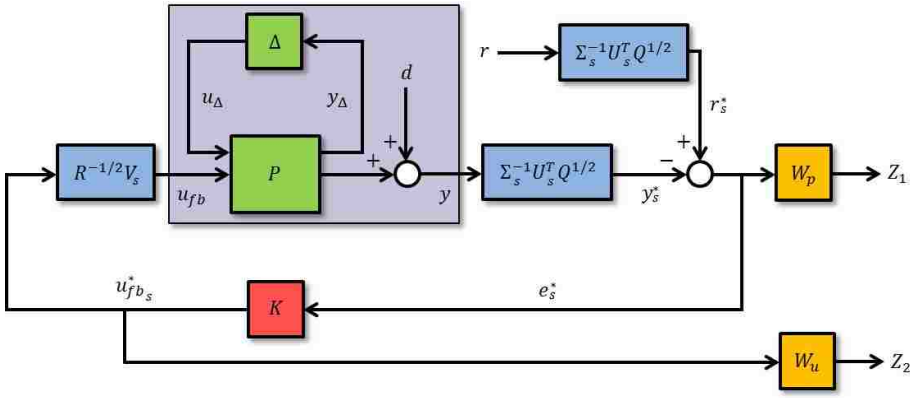

Figure 4.10: Schematic of control problem formulation for ι profile feedback control design in DIII-D L-mode scenarios.

system with state-space matrices A, B, C, and D can be written as an upper linear fractional transformation (LFT) as

$$G(s) = F_u\left(M_a, \frac{1}{s}I_{n_\theta}\right) = D + C(sI_{n_\theta} - A)^{-1}B,$$

where F_u is the upper LFT, the matrix M_a is defined as

$$M_a = \begin{bmatrix} A & B \\ C & D \end{bmatrix},$$

I_{n_θ} is an $n_\theta \times n_\theta$ identity matrix, and s denotes the Laplace variable. The nominal model will be coupled with the uncertain parameters in the transfer function representation of (4.53). By employing the method outlined in [138], we can separate the uncertain parameters from the nominal parameters to write the system (4.53) in the $P - \Delta$ robust control framework. The input-output equations of the system in this framework are expressed as

$$\begin{aligned} y_\Delta &= P_{11}u_\Delta + P_{12}u_{fb}, \\ y &= P_{21}u_\Delta + P_{22}u_{fb} + d, \end{aligned} \tag{4.55}$$

where P_{11}, P_{12}, P_{21}, and P_{22} are the component transfer functions of P that describe how the system inputs (u_Δ, u_{fb}) affect the system outputs (y_Δ, y) and d represents the effect that the disturbance d_δ has on the system outputs. An overview of the employed technique is provided in Appendix A.

4.4.4 Evaluation of relevant control channels

In order to acquire diagnostic data that is needed by the real-time EFIT (rtEFIT) equilibrium reconstruction code [11] to reconstruct the plasma q profile for feedback control, the 30L/R neutral beam powers need to be constant, and we do not utilize them for feedback control, i.e., $u_{fb} = 0$ for $P_{nbi_{30\mathrm{L/R}}}$. As a result, we have seven actuators to utilize in feedback, which implies we can independently control at most seven linear combinations of the system output. To evaluate the relevant control channels, we employ a singular value decomposition (SVD) of the nominal state-space system

$$y = G_0(s)u_{fb} = \left(C_0\left(sI_{n_\theta} - A_0\right)^{-1}B_0 + D_0\right)u_{fb} \tag{4.56}$$

at a particular frequency. The real approximation of the nominal input-output relation at a particular frequency $j\omega_{dc}$ is expressed as

$$\hat{y} = \hat{G}_0\hat{u}_{fb}, \tag{4.57}$$

where $\hat{G}_0$ denotes the real approximation of the complex matrix $G_0(j\omega_{dc})$ [10, 146]. Additionally, to weight the relative tracking performance and control effort, we introduce the positive definite weighting matrices $Q \in \mathbb{R}^{n_\theta \times n_\theta}$ and $R \in \mathbb{R}^{7\times 7}$. We next define the economy size SVD of the weighted matrix $\tilde{G}_0$ as $\tilde{G}_0 = Q^{1/2}\hat{G}_0R^{-1/2} = U\Sigma V^T$, where $\Sigma = \mathrm{diag}(\sigma_1, \sigma_2, \ldots, \sigma_7) \in \mathbb{R}^{7\times 7}$ is a diagonal matrix of singular values and $U \in \mathbb{R}^{n_\theta \times 7}$ and $V \in \mathbb{R}^{7\times 7}$ are matrices that possess the following properties

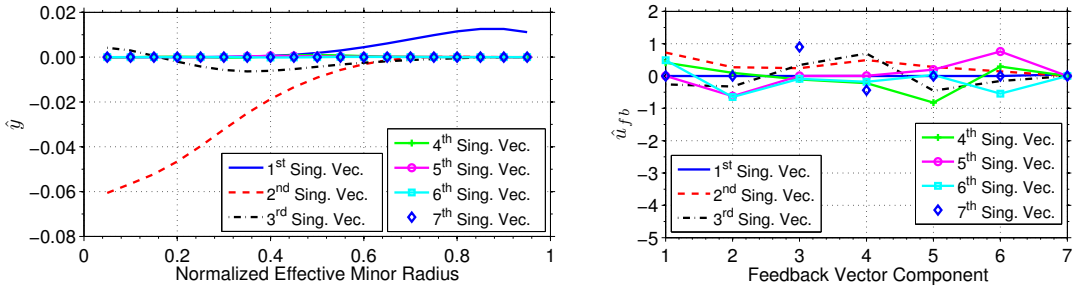

(a) $\hat{y}$ (b) $\hat{u}_{fb}$

Figure 4.11: Relevant control channels for ι profile control in DIII-D L-mode scenarios: (a) output and (b) input. The components of the control input vector are defined as $u_{fb} = [P_{nbi_{150L/R}}, P_{nbi_{210L/R}}, P_{nbi_{330L/R}}, I_p]|_{fb}$ where $u_{fb} = 0$ for $P_{nbi_{30L/R}}$.

$V^TV = VV^T = I, U^TU = I$, where I is a 7×7 identity matrix, and $(\cdot)^T$ denotes the matrix transpose. The input-output relation (4.57) is now expresses as

$$\hat{y} = Q^{-1/2}\tilde{G}_0 R^{1/2}\hat{u}_{fb} = Q^{-1/2}U\Sigma V^T R^{1/2}\hat{u}_{fb}. \tag{4.58}$$

The relevant control channels are then obtained from (4.58) and are shown in Fig. 4.11. The singular vectors for the obtainable outputs values are defined as $\hat{y} = Q^{-1/2}U\Sigma\hat{y}^*$, and the corresponding input singular vectors are defined as $\hat{u}_{fb} = R^{-1/2}V\hat{u}^*_{fb}$, where $\hat{y}^*$ and $\hat{u}^*_{fb}$ are the decoupled output and input, respectively, i.e., $\hat{y}^* = \hat{u}^*_{fb}$. By selecting the frequency as $\omega_{dc} = 25$ rad/s, the total plasma current (I_p) is exclusively utilized to control the ι profile near the plasma boundary (1st singular vector in Fig. 4.11) and the neutral beam injectors are employed to control the ι profile in the plasma core (second through seventh singular vectors in Fig. 4.11). By examining the second singular vector, we see that increasing all of the neutral beam powers ($\hat{u}_{fb} > 0$ in Fig. 4.11(b)) results in the ι profile decreasing (and hence the q profile increasing) in the plasma core ($\hat{y} < 0$ in Fig. 4.11(a)). Intuitively, increasing the off-axis, co-current (150L/R) and counter-current (210L/R) neutral beam injection power would result in a corresponding decrease in the total toroidal

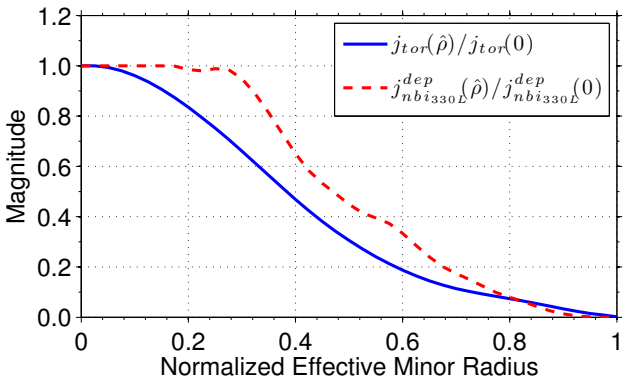

Figure 4.12: Normalized total toroidal current density (defined in (2.91)) and normalized 330L neutral beam injection current density in DIII-D L-mode scenarios.

current density in the plasma core (for a fixed value of the total plasma current), which agrees with the control input directions in Fig. 4.11. However, increasing the on-axis, co-current (330L/R) neutral beam injection power would intuitively result in an increase of the total toroidal current density in the plasma core (for a fixed value of the total plasma current), which does not agree with the control input directions in Fig. 4.11. See sections 2.6 and 4.3 for the relationship the local current density amplitude has to the local q-value in tokamaks. To understand this, the normalized total toroidal current density and the normalized 330L neutral beam injection current density in the considered DIII-D L-mode scenarios is shown in Fig. 4.12. As shown in the figure, the normalized current density deposition profile for the 330L neutral beam source exhibits a wider distribution than the normalized total toroidal current density. Therefore, the on-axis neutral beam sources have a similar effect to the one that the off-axis neutral beam sources have on the ι profile in the considered scenarios, i.e., increasing the on-axis neutral beam power will result in an decrease of the total toroidal current density in the plasma core (for a fixed value of the total plasma current), which agrees with the control input directions in Fig. 4.11.

We note that some of the singular values σ_i may have a small magnitude relative to the others and may be chosen to be neglected in the control synthesis to avoid

potentially spending a significant amount of control effort. Therefore, the singular values are partitioned into k_s significant singular values Σ_s and $7 - k_s$ negligible singular values Σ_{ns}. We then define the significant components of the output and input vectors as $\hat{y}_s^* = \Sigma_s^{-1} U_s^T Q^{1/2} \hat{y} \in \mathbb{R}^{k_s}$ and $\hat{u}_{fb_s}^* = V_s^T R^{1/2} \hat{u}_{fb} \in \mathbb{R}^{k_s}$, respectively, where $U_s \in \mathbb{R}^{n_\theta \times k_s}$ and $V_s \in \mathbb{R}^{7 \times k_s}$ are the components of U and V associated with the significant singular values. A detailed overview of the SVD technique employed to evaluate the relevant control channels is provided in Appendix B.

4.4.5 Feedback control problem formulation

It is desired that the output y be able to track a reference value r, therefore, we define the tracking error as $e = r - y$. The feedback control objectives are to maintain a small tracking error for any reference, reject the effects of the external disturbance, utilize as little feedback control effort as possible, and robustly stabilize the system by controlling the relevant channels of the system (4.55). This feedback control problem is formulated as shown in Fig. 4.10, where K is the to-be-designed feedback controller. The closed-loop system outputs are $Z_1 = W_p(s) e_s^*$ and $Z_2 = W_u(s) u_{fb_s}^*$, and the frequency dependent weight functions W_p and W_u are utilized to optimize the feedback performance. The nominal performance condition of the closed-loop system is expressed as

$$\begin{bmatrix} Z_1 \\ Z_2 \end{bmatrix} = \begin{bmatrix} W_p S_{DC_O} & -W_p S_{DC_O} \\ W_u K S_{DC_O} & -W_u K S_{DC_O} \end{bmatrix} \begin{bmatrix} r_s^* \\ d_s^* \end{bmatrix} = T_{zw} \begin{bmatrix} r_s^* \\ d_s^* \end{bmatrix}, \tag{4.59}$$

where T_{zw} is the closed-loop transfer function from the inputs (r_s^*, d_s^*) to the outputs (Z_1, Z_2), $d_s^* = \Sigma_s^{-1} U_s^T Q^{1/2} d$, and $S_{DC_O} = (I_{k_s} + \Sigma_s^{-1} U_s^T Q^{1/2} P_{22} R^{-1/2} V_s K)^{-1}$. See section 3.6 for an example of how this nominal performance condition is derived. Therefore, to achieve the closed-loop performance objectives (minimize tracking error,

reject effects of disturbance, utilize as little feedback as possible), the control problem is formulated as

$$\min_{K} \left|\left|T_{zw}\right|\right|_{\infty}, \ \ \forall\omega, \tag{4.60}$$

where $||\cdot||_{\infty}$ denotes the H_{∞} norm. See Appendix C for an introduction to the design of feedback controllers by employing the H_{∞} closed-loop shaping technique.

The feedback controller K obtained by solving (4.60) is written in state-space form as

$$\begin{aligned} \dot{x}_{fb} &= A^{*}_{fb}x_{fb} + B^{*}_{fb}e^{*}_{s}, \\ u^{*}_{fb_s} &= C^{*}_{fb}x_{fb} + D^{*}_{fb}e^{*}_{s}, \end{aligned} \tag{4.61}$$

where $x_{fb} \in \mathbb{R}^{n_{fb}}$ is the internal controller state vector, $A^{*}_{fb} \in \mathbb{R}^{n_{fb}\times n_{fb}}$, $B^{*}_{fb} \in \mathbb{R}^{n_{fb}\times k_s}$, $C^{*}_{fb} \in \mathbb{R}^{k_s\times n_{fb}}$ and $D^{*}_{fb} \in \mathbb{R}^{k_s\times k_s}$ are the controller system matrices, and n_{fb} is the number of controller states. For this controller design, the significant singular values are chosen as $\Sigma_s = \text{diag}\{\sigma_1, \sigma_2, \sigma_3\}$, which allows the feedback controller to actuate the total plasma current to control ι near the plasma boundary and the neutral beam injectors to control ι in the plasma core (see Fig. 4.11). Additionally, the value of the ι profile in the center of the plasma (typically in the spatial domain $\hat{\rho} \in [0, 0.3]$) and near the plasma boundary (typically in the spatial domain $\hat{\rho} \in [0.85, 1.0]$) is important to achieving high plasma performance and maintaining plasma stability [61,62]. As a result, the weight matrix Q utilized in the evaluation of the relevant control channels is chosen to place more emphasis on achieving the target ι profile in these spatial regions. By exploiting the block-diagonal structure of the uncertainty matrix, i.e., $\Delta = \text{diag}\{\delta\}$, we can analyze the the robust stability of the closed-loop system with the nominal controller. The block-diagonal uncertainty matrix structure allows us to

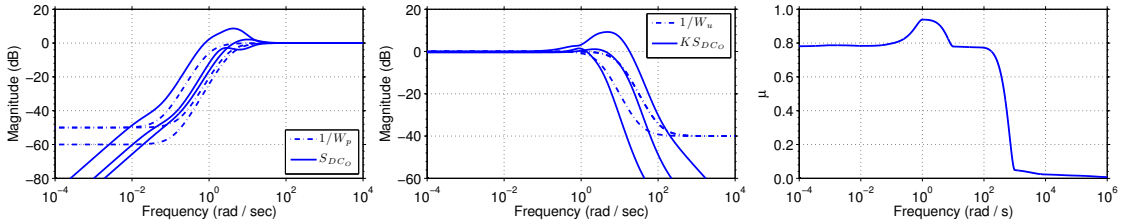

(a) (b) (c)

Figure 4.13: Singular value diagrams: (a) $1/W_p$ and S_{DC_O} and (b) $1/W_u$ and KS_{DC_O} and (c) structured singular value $\mu(N_{11}(j\omega))$ versus frequency. The robust stability condition is defined as $\mu(N_{11}(j\omega)) < 1 \; \forall\omega$ [10].

compute the structured singular value

$$\mu\left(N_{11}(j\omega)\right) = \frac{1}{\min\{k_m | \det\left(I - k_m N_{11}\Delta\right) = 0\}},$$

where $N_{11} = P_{11} - P_{12}R^{-1/2}V_s K S_{DC_O}\Sigma_s^{-1}U_s^T Q^{1/2}P_{21}$ (see section 3.6 for an example of how this transfer function is derived) is the closed-loop transfer function between the signals y_Δ and u_Δ shown in Fig. 4.10. To analyze the performance and robust stability of the closed-loop system, the singular value diagrams of the inverse of the performance weight functions and the achieved transfer functions S_{DC_O} and KS_{DC_O} are shown in Figs. 4.13(a-b) and a plot of the structured singular value $\mu(N_{11}(j\omega))$ versus frequency is shown in Fig. 4.13(c).

4.4.6 Anti-windup compensator design

In order to keep the closed-loop system well-behaved in the presence of actuator saturation, the feedback controller is augmented with an anti-windup compensator [140] that is designed to keep the controller request from significantly deviating from the range of physically achievable actuator values. The anti-windup compensator is

expressed as

$$\dot{x}_{aw} = A_{aw}x_{aw} + B_{aw}\left[sat(u) - u\right],$$
$$u_{aw} = C_{aw}x_{aw} + D_{aw}\left[sat(u) - u\right], \tag{4.62}$$

where the vector $x_{aw} \in \mathbb{R}^{n_{aw}}$ is the internal anti-windup compensator states, $A_{aw} \in \mathbb{R}^{n_{aw}\times n_{aw}}$, $B_{aw} \in \mathbb{R}^{n_{aw}\times 9}$, $C_{aw} \in \mathbb{R}^{9\times n_{aw}}$, and $D_{aw} \in \mathbb{R}^{9\times 9}$ are the anti-windup compensator system matrices, n_{aw} is the number of anti-windup compensator states, u_{aw} is the output of the anti-windup compensator, $sat(u)$ denotes the saturated output of the controller, the output of the controller is given by

$$u(t) = u_{ff}(t) + u_{fb}(t) + u_{aw}(t), \tag{4.63}$$

and u_{ff} is the feedforward control input. The number of anti-windup compensator states is chosen as $n_{aw} = 9$, and the anti-windup compensator system matrices are chosen as $A_{aw} = 0$, $B_{aw} = \text{diag}\{1\}$, $C_{aw} = \text{diag}\{\lambda_i\}$, $D_{aw} = 0$, where λ_i, for $i = \{1, \ldots, 9\}$, is the anti-windup gain for each individual actuator.

4.5 Optimized feedforward + feedback control algorithm performance testing in DIII-D experiments

In this section, we test the ability of the optimized feedforward (described in section 4.3) + feedback (4.61) control algorithm augmented with the anti-windup compensator (4.62) to reach a target safety factor profile at the end of the current ramp-up phase of the discharge in experiments in the DIII-D tokamak. We employ the general framework for real-time feedforward + feedback control of magnetic plasma profiles

implemented in the DIII-D Plasma Control System (PCS) described in section 3.7.2 to test the combined control algorithm. The feedback control algorithm designed in this chapter directly generates signals for the physical control variables. Therefore the NL Trans. Switch is set to the right position in Fig. 3.8. Also, the employed anti-windup scheme is designed to affect the output of the feedback portion of the feedforward + feedback controller. Therefore, the AW Switch is set to the left position in Fig. 3.8. Finally, the feedback control algorithm is implemented with a sampling time of 20 ms based on the modulation of the 30L neutral beam source utilized to acquire diagnostic data to reconstruct the q profile (see sections 3.7.2 and 4.3, respectively).

In order for the plasma to remain in the L-mode operating regime, the net power across the plasma surface needs to be lower than a threshold power (see (4.17)-(4.19)). Therefore, to ensure the combined optimized feedforward + feedback controller does not request a total amount of auxiliary power that exceeds the threshold power (4.19), we implement an additional saturation (after the Magnitude Saturation block in Fig. 3.8) on the individual neutral beam injection power requests. First, the expected threshold power (P_{lh}^{lim}) is calculated according to (4.19) as

$$P_{lh}^{lim}(t) = 2\left[\bar{n}_{e19}^{opt}(t)\right]^{3/4}, \tag{4.64}$$

where $\bar{n}_{e19}^{opt}$ is the optimized feedforward line average electron density (shown in Figs. 4.2(b), 4.3(b), 4.4(b), and 4.5(b)) in units of 10^{19} m^{-3}. Second, the total controller requested auxiliary power (P_{aux}^{req}) is computed as

$$P_{aux}^{req}(t) = \sum_i P_{nbi_i}^{req}(t), \tag{4.65}$$

where $i \in [30\text{L/R}, 150\text{L/R}, 210\text{L/R}, 330\text{L/R}]$ and $P_{nbi_i}^{req}$ is the controller requested individual neutral beam injection power (feedforward + feedback + anti-windup)

after the Magnitude Saturation block in Fig. 3.8. Thirdly, if the total controller requested auxiliary power (4.65) is greater than the expected threshold power (4.64), i.e., $P_{aux}^{req} > P_{lh}^{lim}$, a scale factor is computed as

$$P_{scale}(t) = \frac{P_{lh}^{lim}(t) - \left[P_{nbi_{30\mathrm{L}}}^{req} + P_{nbi_{30\mathrm{R}}}^{req}\right]}{P_{aux}^{req}(t) - \left[P_{nbi_{30\mathrm{L}}}^{req} + P_{nbi_{30\mathrm{R}}}^{req}\right]}, \tag{4.66}$$

and the controller requested individual neutral beam injection powers are scaled according to

$$\begin{aligned} P_{nbi_{30\mathrm{L}}}^{ref} &= P_{nbi_{30\mathrm{L}}}^{req}, \\ P_{nbi_{30\mathrm{R}}}^{ref} &= P_{nbi_{30\mathrm{R}}}^{req}, \\ P_{nbi_i}^{ref}(t) &= P_{scale}(t) P_{nbi_i}^{req}(t), \end{aligned} \tag{4.67}$$

where $i \in [150\mathrm{L/R}, 210\mathrm{L/R}, 330\mathrm{L/R}]$ to determine the individual neutral beam injections power references sent to the Dedicated Control Loops commanding the physical actuators in Fig. 3.8. If the total controller requested auxiliary power (4.65) is less than the expected threshold power (4.64), i.e., $P_{aux}^{req} < P_{lh}^{lim}$, the individual neutral beam injections power references sent to the Dedicated Control Loops are computed as

$$P_{nbi_i}^{ref}(t) = P_{nbi_i}^{req}(t), \tag{4.68}$$

where $i \in [30\mathrm{L/R}, 150\mathrm{L/R}, 210\mathrm{L/R}, 330\mathrm{L/R}]$. Finally, we set the reference for the feedback controller to follow (the vector r_M in Fig. 3.8) as the physics-based model predicted q profile evolution ($q^{FPD}(\hat{\rho}, t)$) achieved with the optimized feedforward trajectories designed in section 4.3 (for example see red dash-dotted lines in Figs. 4.6, 4.7, and 4.8, respectively) during the time interval $t \in [0.4, t_f]$, where $t_f = 1.5$ s for target 1, $t_f = 1.25$ s for target 2, and $t_f = 1.0$ s for target 3. After the time t_f, the reference is held constant at the physics-based model predicted q profile achieved

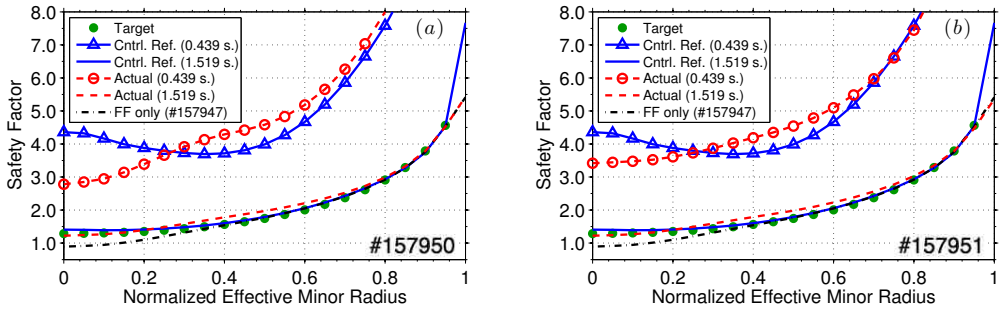

Figure 4.14: Best q profile target matching during experimental testing of optimized feedforward + feedback control algorithm to achieve q profile target 1. The target (green circle) is q profile target 1 shown in Fig. 4.1 and the reference q profile (Cntrl. Ref.) that the feedback controller was attempting to follow at the time $t = 0.439$ s is shown by the blue line + triangle and at the time $t = 1.519$ s is shown by the blue line. The best q profile matching to the reference (at the time t_f, i.e., $r_M(\hat{\rho}, t_f)$) with feedforward + feedback control is shown by the red dashed line and the best q profile matching to the reference (at the time t_f, i.e., $r_M(\hat{\rho}, t_f)$) with feedforward control is shown by the black dash-dotted line. DIII-D shot numbers are indicated in the figures.

at the time t_f, i.e.,

$$r_M(\hat{\rho}, t) = q^{FPD}(\hat{\rho}, t) \qquad \text{over } t \in [0.4, t_f] \text{ s},$$
$$r_M(\hat{\rho}, t) = q^{FPD}(\hat{\rho}, t_f) \qquad \text{over } t > t_f \text{ s}.$$

We now test the ability of the optimized feedforward + feedback control algorithm to achieve q profile target 1 (shown in Fig. 4.1) at the end of the current ramp-up phase in DIII-D shots 157950 and 157951. The feedforward actuator trajectories shown in Fig. 4.2 are used during these discharges. A comparison of the target, feedforward + feedback controlled, and feedforward controlled q profiles at the time when the error between the achieved q profile and the reference at the time t_f ($r_M(\hat{\rho}, t_f)$) is at a minimum, i.e., when (4.2) is minimized, is shown in Fig. 4.14. Also shown in the figures is a comparison of the reference initial q profile and of the initial q profile achieved experimentally. For both of the discharges, the initial q profile (red dashed line + circle in Fig. 4.14) is below the initial reference (blue line + triangle in Fig.

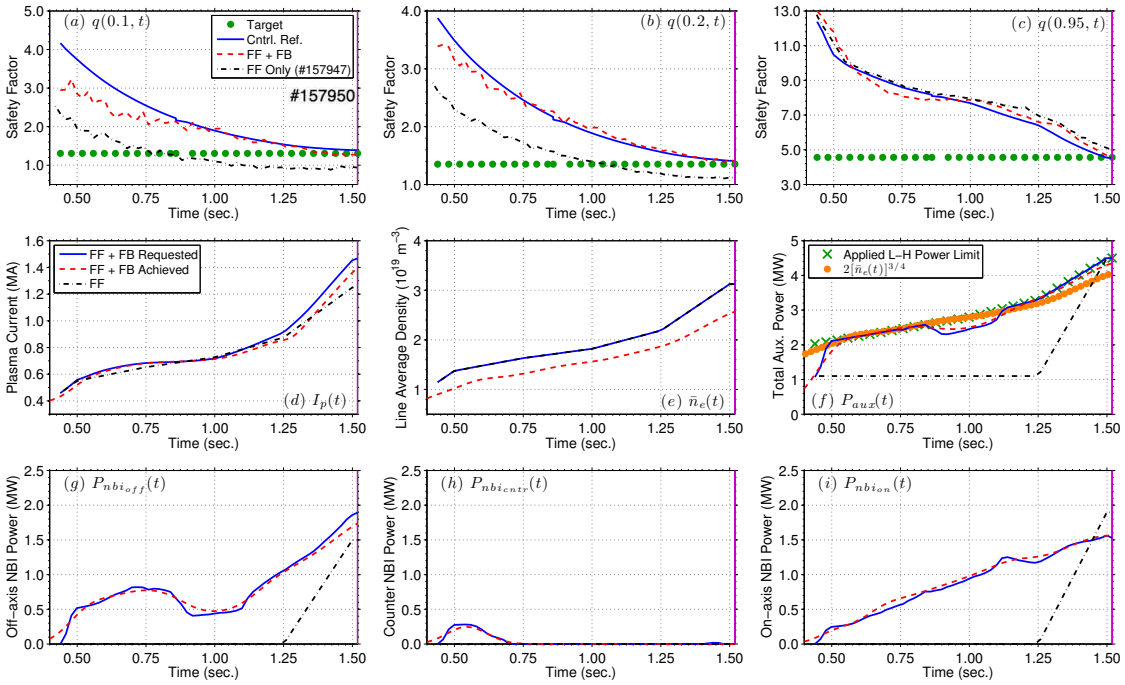

Figure 4.15: Experimental testing of optimized feedforward + feedback control algorithm to achieve q profile target 1 during DIII-D shot 157950: (a-c) time traces of q at $\hat{\rho} = 0.1, 0.2$, and 0.95, (d) total plasma current, (e) line average electron density, (f) total auxiliary power, and (g-i) neutral beam injection powers ($P_{nbi_{off}} = P_{nbi_{150\mathrm{L}}} + P_{nbi_{150\mathrm{R}}}$, $P_{nbi_{cntr}} = P_{nbi_{210\mathrm{L}}} + P_{nbi_{210\mathrm{R}}}$, $P_{nbi_{on}} = P_{nbi_{330\mathrm{L}}} + P_{nbi_{330\mathrm{R}}}$). In (a-c) the target (green circle) is q profile target 1 shown in Fig. 4.1 and the reference q profile evolution (Cntrl. Ref.) that the feedback controller was attempting to follow is shown by the blue line. In (f), the applied L-H power limit (green X) is given by (4.64) and the predicted L-to-H transition power (gold circle) is calculated according to (4.19) by using the physically achieved line average electron density (red dashed line in (e)).

4.14) in the plasma core. As shown in the figures, the feedback controller is able to reject the effects of the perturbed initial condition and drive the q profile (red dashed line in Fig. 4.14) as close to the reference (blue line in Fig. 4.14), and hence the target (green circle in Fig. 4.14), as possible across the entire spatial domain at the end of the current ramp-up phase. Also by examining the figures, we see that a very similar tracking performance is achieved (in terms of the achieved q profile and target matching) in both of the discharges, which shows that the addition of the feedback controller is able to improve the ability to robustly achieve the target compared with

feedforward-only control. To study how the feedback controller tracks the reference q profile evolution, time traces of q at various radial locations and a comparison of the actuator trajectories for DIII-D shot 157950 are shown in Fig. 4.15. Firstly, in response to the q profile in the plasma core initially being below the reference (Figs. 4.15(a-b)), the feedback controller rapidly increases the total auxiliary neutral beam injection power (blue line in Fig. 4.15(f)) up to the maximum allowable value (green X in Fig. 4.15(f)). This results in the q profile in the plasma core being driven from the low initial value to the reference during the time interval $t \in [1.0, 1.519]$ s. Also shown in the figures is how the feedback controller employs the various neutral beam groups (Figs. 4.15(g-i)) to track the reference q profile evolution in the plasma core. Finally, the feedback controller regulates the total plasma current to track the reference q profile evolution near the plasma boundary (Figs. 4.15(c-d)).

We now test the ability of the optimized feedforward + feedback control algorithm to achieve q profile target 2 (shown in Fig. 4.1) at the end of the current ramp-up phase in DIII-D shots 157958 and 158051. The feedforward actuator trajectories shown in Fig. 4.3 are used during these discharges. A time trace of q at $\hat{\rho} = 0.1$, a comparison of the total auxiliary neutral beam injection power, and a comparison of the target, feedforward + feedback controlled, and feedforward controlled q profiles at the time when the error between the achieved q profile and the reference at the time t_f ($r_M(\hat{\rho}, t_f)$) is at a minimum, i.e., when (4.2) is minimized, is shown in Fig. 4.16. For both of the discharges, the initial q profile (red dashed line + circle in Figs. 4.16(c)/(f)) is relatively close to the initial reference (blue line + triangle in Figs. 4.16(c)/(f)). Firstly, once the q profile in the plasma core evolves below the reference (Figs. 4.16(a)/(d)) at the approximate times of $t = 0.7$ s (157958) and $t = 0.55$ s (158051), the feedback controller rapidly increases the total auxiliary neutral beam injection power (blue line in Fig. 4.16(b)/(e)) up to the maximum allowable value (green X in Figs. 4.16(b)/(e)). This results in the q profile in the plasma core being

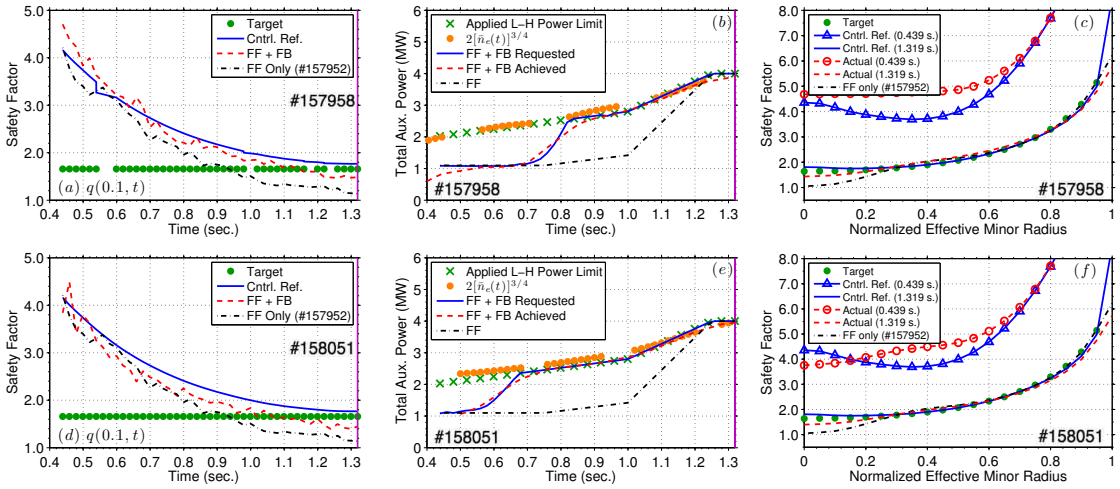

Figure 4.16: Experimental testing of optimized feedforward + feedback control algorithm to achieve q profile target 2 during DIII-D shots 157958 (top row) and 158051 (bottom row): (a)/(d) time trace of q at $\hat{\rho} = 0.1$, where the target (green circle) is q profile target 2 shown in Fig. 4.1 and the reference q profile evolution (Cntrl. Ref.) that the feedback controller was attempting to follow is shown by the blue line, (b)/(e) total auxiliary power, where the applied L-H power limit (green X) is given by (4.64) and the predicted L-to-H transition power (gold circle) is calculated according to (4.19) by using the physically achieved line average electron density, and (c)/(f) best q profile target matching, where the reference q profile (Cntrl. Ref.) that the feedback controller was attempting to follow at the time $t = 0.439$ s is shown by the blue line + triangle and at the time $t = 1.319$ s is shown by the blue line, the best q profile matching to the reference (at the time t_f, i.e., $r_M(\hat{\rho}, t_f)$) with feedforward + feedback control is shown by the red dashed line, and the best q profile matching to the reference (at the time t_f, i.e., $r_M(\hat{\rho}, t_f)$) with feedforward control is shown by the black dash-dotted line. DIII-D shot numbers are indicated in the figures.

driven closer to the reference in the feedforward + feedback controlled discharges relative to the feedforward-controlled discharge. However, the q profile in the plasma core was not able to be driven all of the way to the reference in the feedback-controlled discharges, even though the feedback controller requested the maximum allowable neutral beam injection power, which indicates that more auxiliary power is needed to achieve this target. Secondly, as shown in the figures, the feedback controller is able drive the q profile (red dashed line in Figs. 4.16(c)/(f)) as close to the reference (blue line in Figs. 4.16(c)/(f)), and hence the target (green circle in Figs. 4.16(c)/(f)), as

possible across the entire spatial domain at the end of the current ramp-up phase. Finally, we see that a very similar tracking performance is achieved (in terms of the achieved q profile and target matching) in both of the discharges, which again shows that the addition of the feedback controller is able to improve the ability to robustly achieve the target compared with feedforward-only control.

We now test the ability of the optimized feedforward + feedback control algorithm to achieve q profile target 3 (shown in Fig. 4.1) at the end of the current ramp-up phase in DIII-D shots 158052, 158055, and 158057. The feedforward actuator trajectories shown in Fig. 4.4 are used during these discharges. A comparison of the target, feedforward + feedback controlled, and feedforward controlled q profiles at the time when the error between the achieved q profile and the reference at the time t_f ($r_M(\hat{\rho}, t_f)$) is at a minimum, i.e., when (4.2) is minimized, and a comparison of the total auxiliary neutral beam injection power is shown in Fig. 4.17. For all of the discharges, the initial q profile (red dashed line + circle in Figs. 4.17(a)/(c)/(e)) is relatively close to the initial reference (blue line + triangle in Figs. 4.17(a)/(c)/(e)). During discharges 158052 and 158055, the feedback controller is able drive the q profile (red dashed line in Figs. 4.17(a)/(c)) as close to the reference (blue line in Figs. 4.17(a)/(c)) as possible across the entire spatial domain at the end of the current ramp-up phase. However, as observed in the previously discussed experiments, the q profile in the plasma core was not able to be driven all of the way to the reference in the feedback-controlled discharges even though the feedback controller requested the maximum allowable neutral beam injection power (Figs. 4.17(b)/(d)). Therefore, during discharge 158057, the maximum allowable total auxiliary power that the feedback controller can request is increased above the predicted L-to-H transition power (Fig. 4.17(f)). As shown in Fig. 4.17(e), the ability to request additional neutral beam power results in the ability to drive the q profile closer the reference across the entire spatial domain at the end of the current ramp-up phase during discharge 158057 compared to discharges

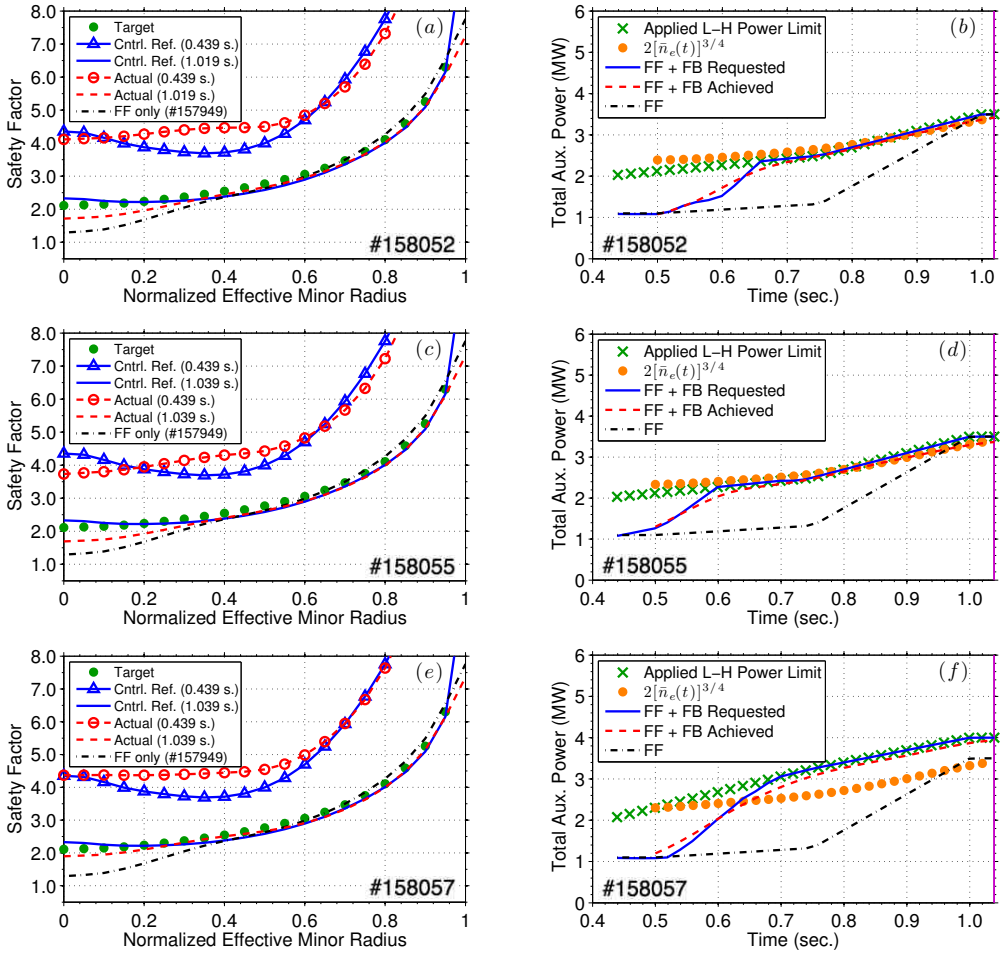

Figure 4.17: Experimental testing of optimized feedforward + feedback control algorithm to achieve q profile target 3 during DIII-D shots 158052 (top row), 158055 (middle row), and 158057 (bottom row): (a)/(c)/(e) best q profile target matching, where the target (green circle) is q profile target 3 shown in Fig. 4.1, the reference q profile (Cntrl. Ref.) that the feedback controller was attempting to follow at the time $t = 0.439$ s is shown by the blue line + triangle and at the best target matching time is shown by the blue line, the best q profile matching to the reference (at the time t_f, i.e., $r_M(\hat{\rho}, t_f)$) with feedforward + feedback control is shown by the red dashed line, and the best q profile matching to the reference (at the time t_f, i.e., $r_M(\hat{\rho}, t_f)$) with feedforward control is shown by the black dash-dotted line, and (b)/(d)/(f) total auxiliary power, where the applied L-H power limit (green X) is given by (4.64) and the predicted L-to-H transition power (gold circle) is calculated according to (4.19) by using the physically achieved line average electron density. DIII-D shot numbers are indicated in the figures.

158052 and 158055. As there is no transition to the H-mode operating regime in this discharge, this suggests that the threshold power (4.19) is indicative (not a hard limit) of transition. Finally, we see that a similar tracking performance is achieved (in terms of the achieved q profile and target matching) in all of the discharges, which again shows that the addition of the feedback controller is able to improve the ability to robustly achieve the target compared with feedforward-only control.

4.6 Conclusion

The reported advances demonstrate the potential physics-model-based profile control has to improve the reproducibility of plasma startup conditions in L-mode scenarios in the DIII-D tokamak by achieving a specified target q profile at the end of the current ramp-up phase of the discharge. Firstly, a numerical optimization algorithm to design feedforward trajectories for the available actuators, subject to the plasma dynamics as well as actuator, plasma state, and operating scenario constraints, that steer the plasma through the tokamak operating space to reach a target q profile was developed. A unique characteristic of the feedforward trajectories obtained by solving the optimization problem is the regulation of the plasma current ramp-up rate to achieve the target q profiles. The optimized actuator trajectories were successfully tested through simulation and subsequently tested in DIII-D experiments. The experimentally achieved q profiles showed a good match to the desired target profiles in the outer spatial region of the plasma. The experimental tests also indicated that the current density diffuses towards the plasma core at a faster rate than predicted by the model. Secondly, a robust feedback algorithm was synthesized to control the q profile dynamics to account for drifts due to external plasma disturbances. Experimental results in DIII-D demonstrated the potential of the combined feedforward + feedback controller to improve the ability to robustly achieve various different target q profiles

across the entire spatial domain at the end of the current ramp-up phase of the discharge. The control scheme developed in this chapter is extended to reactor relevant, high confinement (H-mode) scenarios in the DIII-D tokamak in next chapter.

Chapter 5

Current profile and stored energy control for the development and sustainment of advanced scenarios in the DIII-D tokamak

5.1 Introduction

A significant research thrust has been ongoing in the tokamak fusion community to find advanced, high performance operating scenarios with the goal of developing candidate scenarios for ITER [19]. These scenarios are characterized by a high fusion gain, good plasma confinement, magnetohydrodynamic (MHD) stability, and a noninductively driven plasma current. The development of these advanced scenarios is experimentally explored by specifying the device's actuator trajectory waveforms, such as the total plasma current and auxiliary heating and current-drive (H&CD) scheme, and analyzing the resulting plasma state evolution. This is conventionally referred to as advanced plasma scenario planning. Traditionally, these feedforward

actuator trajectories are developed through a substantial number of trial-and-error attempts and based on extensive experience gained during operation of a particular device. Two plasma profiles/parameters that are often used to define a plasma scenario are the safety factor profile (q profile), which is related to the stability and performance of the plasma, and the normalized plasma beta (β_N), which is a measure of the confinement efficiency of a particular plasma equilibrium.

In this chapter, the feedforward and feedback controllers designed in chapter 4 are extended to high confinement (H-mode) scenarios in the DIII-D tokamak. The physics-based model developed in chapter 2 is embedded in a numerical optimization algorithm to design feedforward trajectories for the available actuators (total plasma current, auxiliary H&CD system, line average electron density) that steer the plasma through the tokamak operating space to reach a target plasma state (characterized by the q profile and plasma β_N) in such a way that the achieved state is as stationary in time as possible. The proximity of the achieved plasma state to the predefined target state is formulated into a cost functional to be minimized. Additionally, actuator constraints, such as the maximum amount of auxiliary H&CD power and total plasma current ramp rate, and plasma state constraints, such as the minimum value of the q profile (to avoid the onset of MHD instabilities that degrade the performance of the plasma), are imposed on the solution of the optimization problem. The nonlinear, constrained, optimization problem is then to design actuator trajectories that minimize the cost functional subject to the plasma dynamics and the actuator and plasma state constraints. This optimization algorithm is developed to complement the experimental effort of advanced scenario planning in the DIII-D tokamak.

Additionally, feedback controllers for q profile and for simultaneous q profile and plasma stored energy control are designed following the approach presented in chapter 4, with the goal of rejecting external plasma disturbances to sustain the developed advanced scenarios. The auxiliary H&CD actuators on DIII-D considered in this

chapter are 6 individual electron cyclotron (EC) and 6 individual co-current neutral beam injection (NBI) sources, which are referred to by the names 30L/R, 150L/R, and 330L/R, where L and R denote left and right lines, respectively. In the H&CD scheme considered, the electron cyclotron (gyrotron) sources and the 150L/R NBI lines are utilized as off-axis H&CD sources, while the 30L/R and 330L/R NBI lines are utilized as on-axis H&CD sources. In the feedback control design, the individual EC sources are grouped together to form 1 effective EC source for control. Both the feedforward and feedback controllers are tested experimentally in DIII-D. The experimental tests demonstrate the potential physics-model-based profile control has to provide a systematic approach for the development and robust sustainment of advanced scenarios, as well as provide insight into physics aspects important to robust scenario execution. The q profile (not including energy control) feedback controller is shown to be able to effectively control the q profile when β_N is relatively close to the target, indicating the need for integrated q profile and β_N control to further enhance the ability to achieve robust scenario execution. Through simulations with the physics-based model developed in chapter 2, the ability of the combined q profile and stored energy feedback controller to track a desired target is demonstrated.

This chapter is organized as follows. In section 5.2, the actuator trajectory optimization problem is formulated. The optimization problem is solved by employing the sequential quadratic programming (SQP) technique [95], and the optimized actuator trajectories are tested in DIII-D experiments in section 5.3. In section 5.4, a robust feedback algorithm to simultaneously control the q profile and stored energy is designed. Experimental results in DIII-D are presented to demonstrate the potential of the q profile feedback controller (not including energy control) to improve the ability to robustly achieve target plasma scenarios, and simulation results are presented to demonstrate the ability of the combined q profile and stored energy feedback controller to track a desired target in sections 5.5 and 5.6, respectively. Finally, conclusions are

discussed in section 5.7.

5.2 Scenario planning by feedforward actuator trajectory optimization

The plasma parameters that characterize a tokamak operating scenario considered in this chapter are the q profile, the plasma β_N and the plasma loop-voltage profile (U_p). The relationship these quantities have to the plasma poloidal magnetic flux (Ψ) and plasma stored energy (E) are described in section 2.6 and are repeated here for convenience. The q profile is related to the spatial gradient of the poloidal magnetic flux and is defined as

$$q(\hat{\rho},t) = -\frac{d\Phi}{d\Psi} = -\frac{d\Phi}{2\pi d\psi} = -\frac{B_{\phi,0}\rho_b^2\hat{\rho}}{\partial\psi/\partial\hat{\rho}}, \tag{5.1}$$

where t is the time and ψ is the poloidal stream function, which is closely related to the poloidal magnetic flux ($\Psi = 2\pi\psi$). The normalized effective minor radius $\hat{\rho} = \rho/\rho_b$ is the spatial variable employed to index the magnetic flux surfaces, where ρ is the mean effective minor radius of the magnetic flux surface, i.e., $\Phi(\rho) = \pi B_{\phi,0}\rho^2$, Φ is the toroidal magnetic flux, $B_{\phi,0}$ is the vacuum toroidal magnetic field at the geometric major radius R_0 of the tokamak, and ρ_b is the mean effective minor radius of the last closed magnetic flux surface. The plasma β_N is related to the plasma stored energy and is defined as

$$\beta_N = \beta_t[\%]\frac{aB_{\phi,0}}{I_p[\mathrm{MA}]} \qquad \beta_t = \frac{\langle p\rangle_V}{B_{\phi,0}^2/(2\mu_0)} = \frac{(2/3)(E/V_p)}{B_{\phi,0}^2/(2\mu_0)}, \tag{5.2}$$

where β_t is the toroidal plasma beta [18], a is the plasma minor radius, I_p is the total plasma current, p is the plasma kinetic pressure, $\langle\cdot\rangle_V$ denotes the volume-average

operation $1/V_p \int_V (\cdot) dV$, V is the volume enclosed by a magnetic flux surface, V_p is the total plasma volume, and μ_0 is the vacuum magnetic permeability. The loop-voltage profile is related to the temporal derivative of the poloidal magnetic flux and is defined as

$$U_p(\hat{\rho}, t) = -\frac{\partial \Psi}{\partial t} = -2\pi \frac{\partial \psi}{\partial t}. \tag{5.3}$$

5.2.1 Target plasma state: Cost functional definition

The objective of the actuator trajectory optimization algorithm is to design actuator waveforms that steer the plasma from a particular initial condition through the tokamak operating space to reach a target state (defined in terms of the q profile ($q^{tar}(\hat{\rho})$) and normalized plasma beta (β_N^{tar})) at some time t_f during the plasma discharge in such a way that the achieved state is as stationary in time as possible. As the poloidal flux profile evolves with the slowest time constant in the plasma, if it reaches a stationary condition, i.e., $U_p(\hat{\rho}, t) =$ constant, all of the other plasma profiles have also reached a stationary condition. If $U_p(\hat{\rho}, t) = 0$, the total plasma current is completely driven by noninductive sources and this is referred to as a "steady-state" scenario. Therefore, the stationarity of the plasma state can be defined by the profile

$$g_{ss}(\hat{\rho}, t) = \frac{\partial U_p}{\partial \hat{\rho}}. \tag{5.4}$$

A stationary plasma state is reached when $g_{ss}(\hat{\rho}, t) = 0$. Therefore, the proximity of the achieved plasma state to the target state at the time t_f can be described by the cost functional

$$J(t_f) = k_{ss} J_{ss}(t_f) + k_q J_q(t_f) + k_{\beta_N} J_{\beta_N}(t_f), \tag{5.5}$$

where k_{ss}, k_q, and k_{β_N} are used to weight the relative importance of the plasma state characteristics and

$$J_q(t_f) = \int_0^1 W_q(\hat{\rho}) \left[q^{tar}(\hat{\rho}) - q(\hat{\rho}, t_f)\right]^2 d\hat{\rho}, \tag{5.6}$$

$$J_{ss}(t_f) = \int_0^1 W_{ss}(\hat{\rho}) \left[g_{ss}(\hat{\rho}, t_f)\right]^2 d\hat{\rho}, \tag{5.7}$$

$$J_{\beta_N}(t_f) = \left[\beta_N^{tar} - \beta_N(t_f)\right]^2, \tag{5.8}$$

where $W_q(\hat{\rho})$ and $W_{ss}(\hat{\rho})$ are positive functions used to weight which portions of the respective profiles are more important relative to the others.

5.2.2 Plasma state dynamics

In chapter 2, a general first-principles-driven (FPD), physics-based model of the poloidal magnetic flux profile (and hence the q profile and U_p profile) evolution was derived. The model was subsequently tailored to H-mode operating scenarios in the DIII-D tokamak in section 2.8. The nonlinear, physics-based partial differential equation (PDE) model of the poloidal flux evolution tailored to DIII-D H-mode scenarios is expressed as

$$\begin{aligned}\frac{\partial \psi}{\partial t} = {} & f_\eta(\hat{\rho})\, u_\eta(t) \frac{1}{\hat{\rho}} \frac{\partial}{\partial \hat{\rho}} \left(\hat{\rho} D_\psi(\hat{\rho}) \frac{\partial \psi}{\partial \hat{\rho}} \right) + \sum_{i=1}^{n_{ec}} f_{ec_i}(\hat{\rho})\, u_{ec_i}(t) \\ & + \sum_{i=1}^{n_{nbi}} f_{nbi_i}(\hat{\rho})\, u_{nbi_i}(t) + f_{bs}(\hat{\rho})\, u_{bs}(t) \left(\frac{\partial \psi}{\partial \hat{\rho}} \right)^{-1},\end{aligned} \tag{5.9}$$

with boundary conditions

$$\left.\frac{\partial \psi}{\partial \hat{\rho}}\right|_{\hat{\rho}=0} = 0 \qquad \left.\frac{\partial \psi}{\partial \hat{\rho}}\right|_{\hat{\rho}=1} = -k_{I_p} u_{I_p}(t), \tag{5.10}$$

where f_η, f_{ec_i}, f_{nbi_i}, and f_{bs} are defined in (2.85), D_ψ pertains to the magnetic configuration of a particular plasma equilibrium, n_{ec} and n_{nbi} are the number of electron cyclotron microwave launchers and neutral beam injectors, respectively, and k_{I_p} is a geometrical constant defined in (2.83). The diffusivity (u_η), interior (u_{ec_i}, u_{nbi_i}, u_{bs}), and boundary (u_{I_p}) control terms are expressed as

$$\begin{aligned}
u_\eta(t) &= \left[I_p(t)P_{tot}(t)^{1/2}\bar{n}_e(t)^{-1}\right]^{-3/2}, \\
u_{ec_i}(t) &= \left[I_p(t)P_{tot}(t)^{1/2}\bar{n}_e(t)^{-1}\right]^{-1/2}\bar{n}_e(t)^{-1}P_{ec_i}(t), \\
u_{nbi_i}(t) &= \left[I_p(t)P_{tot}(t)^{1/2}\bar{n}_e(t)^{-1}\right]^{-1}\bar{n}_e(t)^{-1}P_{nbi_i}(t), \\
u_{bs}(t) &= \left[I_p(t)P_{tot}(t)^{1/2}\bar{n}_e(t)^{-1}\right]^{-1/2}\bar{n}_e(t), \\
u_{I_p}(t) &= I_p(t),
\end{aligned} \tag{5.11}$$

where

$$P_{tot}(t) = P_{ohm}(t) + \sum_{i=1}^{n_{ec}} P_{ec_i}(t) + \sum_{i=1}^{n_{nbi}} P_{nbi_i}(t) - P_{rad}(t), \tag{5.12}$$

is the total power injected into the plasma, $P_{ohm}(t)$ is the ohmic power, $P_{ec_i}(t)$ and $P_{nbi_i}(t)$ are the individual gyrotron launcher and neutral beam injection powers, respectively, $P_{rad}(t)$ is the radiated power, and $\bar{n}_e(t)$ is the line average electron density. The evolution of the plasma stored energy (and hence the plasma β_N) is given by (2.59) and repeated here for convenience as

$$\frac{dE}{dt} = -\frac{E}{\tau_E(t)} + P_{tot}(t), \tag{5.13}$$

where $\tau_E(t)$ is the global energy confinement time. The energy confinement time scaling used in this work is the IPB98(y,2) scaling law [132].

We now spatially discretize the infinite dimensional PDE (5.9)-(5.10) by employing a finite difference method to simulate the physics-based model. The non-dimensional

spatial domain of interest ($\hat{\rho} \in [0,1]$) is represented by m_ψ discrete nodes. After spatially discretizing (5.9) and taking into account the boundary conditions (5.10), we obtain a nonlinear finite dimensional ordinary differential equation (ODE) model defined by

$$\dot{\hat{\psi}} = f_\psi(\hat{\psi}, u), \tag{5.14}$$

where $\hat{\psi} = [\psi_2, \ldots, \psi_{m_\psi - 1}]^T \in \mathbb{R}^{n_\psi}$ is the magnetic state vector, ψ_i, for $i = 2, \ldots, m_\psi - 1$, is the value of ψ at the i-th node, $u = [P_{ec_1}, \ldots, P_{ec_{n_{ec}}}, P_{nbi_1}, \ldots, P_{nbi_{n_{nbi}}}, \bar{n}_e, I_p]^T \in \mathbb{R}^{n_{act}}$ is the control input vector, $n_{act} = n_{ec} + n_{nbi} + 2$, $f_\psi \in \mathbb{R}^{n_\psi}$ is a nonlinear function of the plasma magnetic states and control inputs, and $n_\psi = m_\psi - 2$. By defining the plasma state vector as

$$x = \begin{bmatrix} \hat{\psi} \\ E \end{bmatrix} \in \mathbb{R}^{(n_\psi + 1)}, \tag{5.15}$$

we can write the magnetic and kinetic state dynamics as

$$\dot{x} = \begin{bmatrix} f_\psi(\hat{\psi}, u) \\ -\dfrac{E}{\tau_E(t)} + P_{tot}(x, u) \end{bmatrix} = F_{\psi,E}(x, u) \in \mathbb{R}^{(n_\psi + 1)}. \tag{5.16}$$

By employing a fully implicit numerical scheme, we can integrate (5.16) in time, i.e.,

$$\frac{x_{k+1} - x_k}{\Delta t} = F_{\psi,E}(x_{k+1}, u_k), \tag{5.17}$$

where x_k and u_k denote the state and control input, respectively, at the time step t_k, x_{k+1} denotes the state at the next time step t_{k+1}, and Δt is the simulation time step. The magnetic and thermal state evolution can be obtained by iteratively solving (5.17) at each time step from a given initial condition at time t_0, i.e., $x_0 = x(t_0)$.

5.2.3 Control actuator trajectory parameterization

The individual control actuator trajectories are parameterized in the same fashion as described in section 4.2.3, and the parameterization is repeated here for convenience. The trajectories of the i-th control actuator (u_i) are parameterized by a finite number of parameters (n_{p_i}) at discrete points in time (t_{p_i}), i.e., $t_{p_i} = [t_0, t_1, \ldots, t_k, \ldots, t_k = t_f] \in \mathbb{R}^{n_{p_i}}$. During the time interval $t \in (t_k, t_{k+1})$ the i-th control input is determined by linear interpolation as $u_i(t) = u_i(t_k) + [u_i(t_{k+1}) - u_i(t_k)]\,(t - t_k)/(t_{k+1} - t_k)$. By combining all of the parameters utilized to represent each individual actuator trajectory into a vector

$$\tilde{\theta} = \left[u_1^1, \ldots, u_1^{n_{p_1}}, \ldots, u_i^1, \ldots, u_i^{n_{p_i}}, \ldots, u_{n_{act}}^1, \ldots, u_{n_{act}}^{n_{p_{n_{act}}}}\right], \tag{5.18}$$

where $\tilde{\theta} \in \mathbb{R}^{n_p^{tot}}$ and $n_p^{tot} = \sum_{i=1}^{n_{act}} n_{p_i}$, the parameterized control actuator trajectories are given by

$$u(t) = \Pi(t)\tilde{\theta}, \tag{5.19}$$

where $\Pi(t) \in \mathbb{R}^{n_{act} \times n_p^{tot}}$ is a piecewise linear function of time. Some of the parameters in the vector (5.18) may be chosen to be fixed due to the desire to obtain an operating condition at the time t_f with a specific set of characteristics (a final plasma current ($I_p(t_f)$) and/or line average electron density ($\bar{n}_e(t_f)$)), or to provide the ability to acquire diagnostic data (constant power in a neutral beam injector). Therefore, the subset of free parameters in the vector (5.18) can be combined into a vector of to-be-optimized parameters which we define as $\theta \in \mathbb{R}^{n_{opt}}$ where $n_{opt} \leq n_p^{tot}$.

5.2.4 Actuator constraints

The actuator magnitude constraints are given by

$$I_p^{min} \leq I_p(t) \leq I_p^{max}, \tag{5.20}$$

$$P_{ec}^{min} \leq P_{ec_i}(t) \leq P_{ec}^{max}, \quad i = 1, \ldots, n_{ec} \tag{5.21}$$

$$P_{nbi}^{min} \leq P_{nbi_i}(t) \leq P_{nbi}^{max}, \quad i = 1, \ldots, n_{nbi}, \tag{5.22}$$

where $(\cdot)^{min}$ and $(\cdot)^{max}$ are the minimum and maximum limits, respectively. The actuator rate constraints are defined by

$$-I_{p,max}^{d'} \leq \frac{dI_p}{dt} \leq I_{p,max}^{u'}, \tag{5.23}$$

where $I_{p,max}^{d'}$ and $I_{p,max}^{u'}$ are the maximum total plasma current ramp-down and ramp-up rates, respectively. The actuator constraints (5.20)-(5.23) can be combined together and written in terms of the to-be-optimized parameters θ in a compact matrix form as

$$A_u^{lim}\theta \leq b_u^{lim}. \tag{5.24}$$

5.2.5 Plasma state and MHD stability constraints

The MHD stability limit related to the plasma magnetic states considered in this work is expressed as

$$q_{min}(t) \geq q_{min}^{lim}, \tag{5.25}$$

where $q_{min}(t) = \min\{q(\hat{\rho}, t)\}$ and q_{min}^{lim} is a constant chosen to be slightly greater than one to avoid the onset of sawtooth oscillations [18]. In order for the plasma to remain in the H-mode operating regime, the net power across the plasma surface, P_{net}, must

be greater than a threshold power, $P_{threshold}$, i.e.,

$$P_{net}(t) \geq P_{threshold}(t), \tag{5.26}$$

where

$$P_{net}(t) = P_{tot}(t) - \frac{dE}{dt} = \frac{E}{\tau_E(t)}, \tag{5.27}$$

and the threshold power is given in [143,144]. The final MHD stability limit considered in this work is given by

$$\bar{n}_{e20}(t) \leq n_g(t), \tag{5.28}$$

where $\bar{n}_{e20}(t)$ is the line average electron density evaluated in units of 10^{20} m^{-3} and

$$n_g(t) = \frac{I_p(t)[\mathrm{MA}]}{\pi a^2} \tag{5.29}$$

is referred to as the Greenwald density limit [147]. We next chose to formulate the constraints (5.25)-(5.26) as integral constraints [145], which provides the ability to reduce the number of constraints imposed on the optimization problem solution. An example of this is given for the constraint (5.25) as

$$c_q^{lim} = \int_{t_0}^{t_f} \max\{0, q_{min}^{lim} - q_{min}(t)\}dt \leq 0. \tag{5.30}$$

The MHD stability constraint (5.26) can be written in the form of (5.30) and combined together and written in a compact matrix form as

$$c_{mhd}^{lim}(x(t)) \leq 0. \tag{5.31}$$

As the MHD stability constraint (5.28) depends directly on the to-be-optimized parameters θ, it is included in the formulation of the actuator constraints (5.24).

5.2.6 Optimization problem statement and solution method

The nonlinear, constrained, actuator trajectory optimization problem is now to determine the to-be-optimized parameters θ that minimize the cost functional (5.5) subject to the plasma dynamics (5.16), the control actuator trajectory parameterization (5.19), the actuator constraints (5.24), and the plasma state and MHD stability constraints (5.31). This optimization problem is written mathematically as

$$\min_{\theta} \quad J(t_f) = J(\dot{x}(t_f), x(t_f)), \tag{5.32}$$

such that

$$\begin{aligned} \dot{x} &= F_{\psi,E}(x,u), \\ u(t) &= \Pi(t)\tilde{\theta}, \\ A_u^{lim}\theta &\leq b_u^{lim}, \\ c_{mhd}^{lim}(x(t)) &\leq 0. \end{aligned} \tag{5.33}$$

We solve this optimization problem by employing sequential quadratic programming (SQP) [95] as in section 4.2.6. An overview of the SQP technique is provided in Appendix E.

5.3 Design and experimental testing of optimized feedforward trajectories

We now solve the actuator trajectory optimization problem (5.32)-(5.33) to reach a target plasma state (such that the achieved state is in a stationary condition) at a time t_f during the plasma discharge by employing the SQP solution method. The

optimization is carried out over the time interval $t_{opt} = t \in [t_0, t_f] = [0.5, 3.0]$ s. We begin by parameterizing the i-th actuator trajectory by $n_{p_i} = 6$ discrete parameters at the time points $t_{p_i} = [0.5, 1.0, \ldots, 3.0]$ s. Next, the components of the total parameter vector (5.18) that are fixed, or not-to-be optimized, are chosen as discussed in section 5.2.3. Firstly, the total gyrotron power, $P_{ec_{tot}}(t)$, is chosen to be evenly distributed amongst the individual gyrotron launchers. Additionally, as the gyrotrons have a limited amount of total energy they can deliver in a plasma discharge, they are set to be inactive during the time interval $t \in [0.5, 2.5)$ s so they have the potential to be used at full power for the remainder of the discharge. Secondly, in order to acquire diagnostic data to reconstruct the q profile, the 30L/R neutral beam powers are fixed at a constant 1.1 MW. Thirdly, density control is challenging in experiments due to large particle recycling at the tokamak wall and to the difficulty of pumping particles out of the machine. Therefore, the line average electron density trajectory is chosen to not be optimized and is specified as follows: linearly ramped-up from an initial value of $\bar{n}_e(0.5) = 2 \times 10^{19}$ m^{-3} to a final value of $\bar{n}_e(2.0) = 4.2 \times 10^{19}$ m^{-3} and then held constant. Finally, all of the actuator values at the initial time $t_0 = 0.5$ s and the value of the total plasma current at the time $t_f = 3.0$ s are chosen to be fixed, i.e. they are not optimized. The vector of to-be-optimized parameters is then given by

$$\begin{aligned}\theta = \big[&P_{ec_{tot}}(2.5), P_{ec_{tot}}(3.0), P_{nbi_i}(1.0), \ldots, \\ &P_{nbi_i}(3.0), I_p(1.0), \ldots, I_p(2.5)\big],\end{aligned} \tag{5.34}$$

where $i \in$ [150L/R,330L/R], respectively. The value and shape of the q profile in the center of the plasma (typically in the spatial domain $\hat{\rho} \in [0, 0.4]$) is important to achieving and maintaining high performance plasmas [61,62]. As a result, the weight function $W_q(\hat{\rho})$ in (5.6) is chosen to place more emphasis on achieving the target q profile in the inner region of the plasma ($\hat{\rho} \in [0, 0.4]$) relative to the outer region.

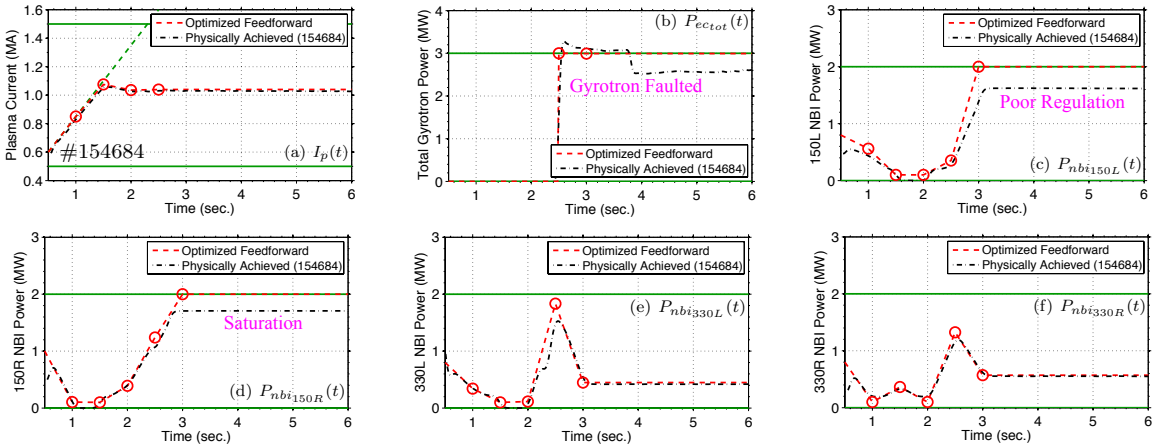

Figure 5.1: Optimized and physically achieved (DIII-D shot 154684) actuator trajectories: (a) total plasma current, (b) total electron cyclotron power (set to be inactive during the time interval $t \in [0.5, 2.5)$ s because of the limited amount of total energy the gyrotrons can deliver in one discharge), and (c-f) individual neutral beam injection powers. Actuator limitations (either in regulation or faults) are indicated in the respective figures. Additionally, the actuator magnitude (solid green) and rate (dash green) limits applied on the optimization problem solution are also shown. The actuator trajectories are represented by a finite number of parameters (optimized parameter denoted by red $\circ$) and the associated actuator trajectories (red - - line) are determined by linear interpolation during the time intervals between the individually optimized parameters.

The optimized parameters (5.34) (and associated actuator trajectories) determined by solving the optimization problem (5.32)-(5.33), with the target plasma state ($q^{tar}(\hat{\rho})$ and β_N^{tar}) chosen to be the q profile and β_N experimentally achieved at 3.0 s in DIII-D shot 150320, are shown in Fig. 5.1. Firstly, the total plasma current is ramped up at the maximum allowable rate, which is set to avoid triggering tearing modes due to a loss of magnetic shear near the plasma boundary, and exhibits a slight overshoot before settling to the specified final value. Secondly, the off-axis neutral beam power ($P_{nbi_{150L/R}}$) is gradually increased up to the maximum allowable value during the time interval $t \in [1.5, 3]$ s to set up a stationary plasma state with off-axis auxiliary current drive, which is needed to achieve the target q profile in the plasma core. Thirdly, the maximum amount of electron cyclotron power is injected into the plasma with the same objective, as well as to reach the target β_N. Finally,

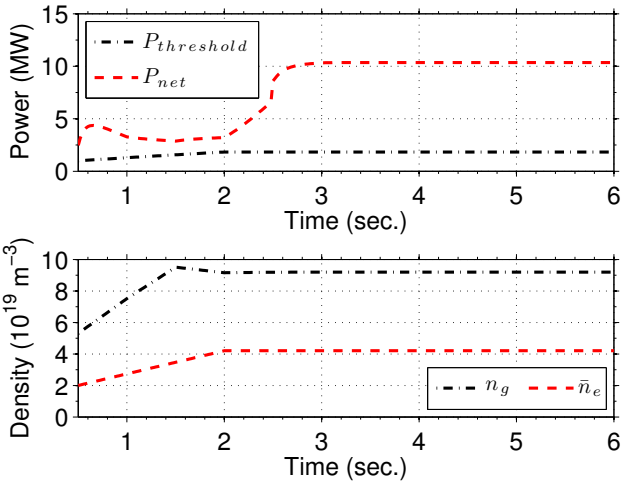

Figure 5.2: H-mode threshold (5.26) and density limit (5.28) conditions achieved with the actuator trajectories shown in Fig. 5.1 that are obtained by solving the optimization problem (5.32)-(5.33).

a moderate amount of on-axis neutral beam power ($P_{nbi_{330\mathrm{L/R}}}$) is injected into the plasma during the time interval $t \in [2, 3]$ s to set up a stationary state before settling to a relatively small amount that is needed to achieve the target β_N. As shown in Fig. 5.2, the optimized actuator trajectories satisfy the H-mode threshold (5.26) and density limit (5.28) constraints that are imposed on the solution of the optimization problem (5.32)-(5.33).

The actuator trajectories shown in Fig. 5.1 were tested through simulation with the physics-based model of the plasma dynamics tailored to DIII-D H-mode scenarios (described in section 2.8) and experimentally in DIII-D during shot 154684. As the optimized trajectories were designed to achieve a target plasma state at the time $t_f = 3.0$ s in such a way that the achieved state is as stationary in time as possible, the actuator values were held constant from the time t_f until the end of the discharge. It is important to note that the optimized trajectories represent the references to the dedicated control loops that command the DIII-D physical actuators, and as shown in Fig. 5.1, the dedicated control loops were able to follow the requested trajectories reasonably well. However, during DIII-D shot 154684, one of the gyrotrons faulted

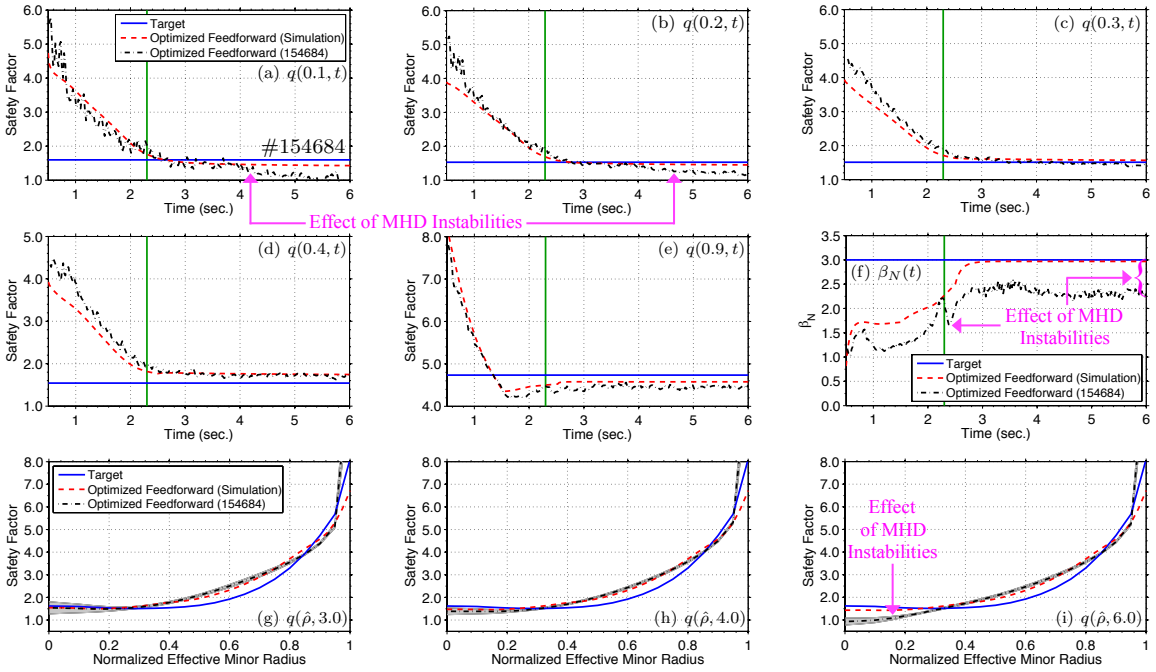

Figure 5.3: Simulated and experimental (DIII-D shot 154684) testing of optimized actuator trajectories: (a-e) time traces of q at $\hat{\rho} = 0.1, 0.2, 0.3, 0.4, 0.9$, (f) time trace of β_N, and (g-i) q profile at $t = 3.0, 4.0$, and 6.0 s. The solid green line denotes the onset of MHD instabilities during DIII-D shot 154684. Approximate error bars for the measured q profiles (obtained from rtEFIT [11]) are shown by the gray-shaded regions.

at approximately 3.8 s, the 150R neutral beam injector was saturated at its upper limit after 2.75 s, and the control loop commanding the 150L neutral beam injector was not able to follow the request after 2.5 s.

Time traces of q at various radial locations, a time trace of β_N, and a comparison of the target, physics-based model predicted, and experimentally achieved q profiles at various times is shown in Fig. 5.3. As shown, the optimized trajectories were able to drive the experimental plasma as close as possible to the desired stationary q profile at 3.0 s. However, at 2.3 s, MHD instabilities developed and persisted for the remainder of the discharge. The MHD instabilities degraded the plasma confinement characteristics (shown in the immediate reduction of β_N once the modes develop) and resulted in the inability to experimentally achieve the target β_N and maintain

the target q profile in the plasma core after 4.0 s. However, through simulation with the physics-based model, it was shown that the optimized trajectories were able to steer the simulated plasma to the stationary target in the absence of MHD modes. Finally, note the excellent agreement between the simulated and experimental q profile evolution during the time interval $t \in [0.5, 4.0]$ s, which provides confidence in the ability of the physics-based model to satisfactorily predict the evolution of the plasma for control algorithm design purposes.

As a result of the MHD instabilities that developed during the experimental test of the optimized trajectories, the target β_N was not able to be achieved and the target q profile was unable to be maintained in a stationary condition. Therefore to compensate for external disturbances (such as a reduction in confinement) and actuation limitations (either in regulation or faults), the feedforward trajectories need to be integrated together with a feedback control scheme, as discussed in the next section, to improve the ability to robustly achieve plasma target conditions.

5.4 Feedback control design

5.4.1 Partial differential equation model of system dynamics

We begin the design process by converting the physics model that describes the poloidal magnetic flux profile evolution in the tokamak (the magnetic diffusion equation) into a form suitable for control design. The magnetic diffusion equation is given in (2.45) and restated here for convenience as

$$\frac{\partial \psi}{\partial t} = \frac{\eta(T_e)}{\mu_0 \rho_b^2 \hat{F}^2} \frac{1}{\hat{\rho}} \frac{\partial}{\partial \hat{\rho}} \left(\hat{\rho} \hat{F} \hat{G} \hat{H} \frac{\partial \psi}{\partial \hat{\rho}} \right) + R_0 \hat{H} \eta(T_e)(j_{aux} + j_{bs}), \tag{5.35}$$

with boundary conditions given by

$$\left.\frac{\partial \psi}{\partial \hat{\rho}}\right|_{\hat{\rho}=0} = 0 \qquad \left.\frac{\partial \psi}{\partial \hat{\rho}}\right|_{\hat{\rho}=1} = -k_{I_p} I_p(t), \tag{5.36}$$

where $\eta(\hat{\rho}, t)$ is the plasma resistivity, $T_e(\hat{\rho}, t)$ is the electron temperature, $j_{aux}(\hat{\rho}, t)$ is the noninductive current density provided by the auxiliary sources, and $j_{bs}(\hat{\rho}, t)$ is the noninductive current density provided by the bootstrap current [60]. The parameters $\hat{F}(\hat{\rho})$, $\hat{G}(\hat{\rho})$, and $\hat{H}(\hat{\rho})$ are geometric spatial factors pertaining to the magnetic configuration of a particular plasma MHD equilibrium (defined in (2.44)). The total auxiliary current drive is generated by the gyrotron launchers and neutral beam injectors. The auxiliary gyrotron and neutral beam current drives are proportional to the current-drive efficiencies T_e/n_e and $\sqrt{T_e}/n_e$, respectively, where n_e is the electron density. The bootstrap current is proportional to the inverse of the poloidal flux gradient profile multiplied by the kinetic plasma profile gradients, i.e., $j_{bs} \propto (\partial\psi/\partial\hat{\rho})^{-1}[n_e \frac{\partial T_e}{\partial \hat{\rho}} + T_e \frac{\partial n_e}{\partial \hat{\rho}}]$. We chose to model the kinetic plasma parameters (electron density, electron temperature, and plasma resistivity) as a nominal model plus a bounded uncertain model. We then employ *robust control techniques* [10] to design a feedback controller that achieves a desired closed-loop performance while guaranteeing that the controller maintains closed-loop system stability for the range of the kinetic plasma parameters captured by the uncertain models.

Towards this goal, we define ranges in which the electron density and temperature profiles are expected to be in typical DIII-D advanced scenarios, which are shown in Figs. 5.4(a-b). For feedback control design, these parameters are modeled as a nominal profile plus a bounded uncertain profile, i.e.,

$$n_e(\hat{\rho}) = n_e^{nom}(\hat{\rho}) + n_e^{unc}(\hat{\rho})\delta_{n_e}, \tag{5.37}$$

$$T_e(\hat{\rho}) = T_e^{nom}(\hat{\rho}) + T_e^{unc}(\hat{\rho})\delta_{T_e}, \tag{5.38}$$

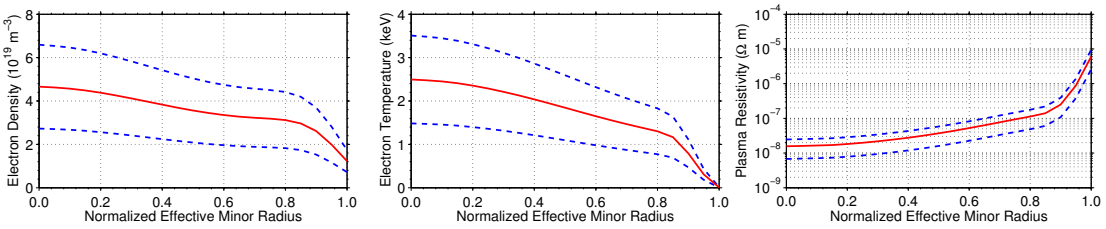

(a) n_e (b) T_e (c) η

Figure 5.4: Plasma parameter uncertainty ranges in DIII-D H-mode scenarios: (a) electron density, (b) electron temperature, and (c) plasma resistivity. Note: nominal values (solid) and minimum/maximum values (dash).

where the nominal (n_e^{nom}, T_e^{nom}) and uncertain profiles (n_e^{unc}, T_e^{unc}) are defined in terms of the maximum and minimum profiles shown in Figs. 5.4(a-b), with $|\delta_{T_e}| \leq 1$ and $|\delta_{n_e}| \leq 1$. The plasma resistivity is inversely related to the electron temperature (minimum resistivity is defined by the maximum electron temperature), and the resistivity range is shown in Fig. 5.4(c). Additionally, the parameters $\sqrt{T_e}$ and $1/n_e$ (note that $j_{nbi} \propto \sqrt{T_e}/n_e$ and $j_{ec} \propto T_e/n_e$) are related to the electron temperature and density, respectively. For feedback control design, these parameters are modeled as

$$\eta(\hat{\rho}) = \eta^{nom}(\hat{\rho}) + \eta^{unc}(\hat{\rho})\delta_{T_e}, \tag{5.39}$$

$$\sqrt{T_e(\hat{\rho})} = T_e^{nom'}(\hat{\rho}) + T_e^{unc'}(\hat{\rho})\delta_{T_e}, \tag{5.40}$$

$$1/n_e(\hat{\rho}) = n_e^{nom'}(\hat{\rho}) + n_e^{unc'}(\hat{\rho})\delta_{n_e}, \tag{5.41}$$

where the nominal (η^{nom}, $T_e^{nom'}$, $n_e^{nom'}$) and uncertain (η^{unc}, $T_e^{unc'}$, $n_e^{unc'}$) profiles are defined in terms of the maximum and minimum profiles shown in Fig. 5.4.

From (5.1), we see that the q profile is inversely related to the spatial gradient of the poloidal stream function, which we define as

$$\theta(\hat{\rho}, t) \equiv \frac{\partial \psi}{\partial \hat{\rho}}. \tag{5.42}$$

By combining the magnetic diffusion equation (5.35) with the noninductive current-drive models (auxiliary and bootstrap) and the models (5.37)-(5.41), and after some mathematical manipulations, we obtain the PDE governing the evolution of θ that is used for feedback control design, which is expressed as

$$\begin{aligned}\frac{\partial \theta}{\partial t} &= \left[q_{\eta_1} + q_{\eta_4}\delta_{T_e}\right]\frac{\partial^2 \theta}{\partial \hat{\rho}^2} + \left[q_{\eta_2} + q_{\eta_5}\delta_{T_e}\right]\frac{\partial \theta}{\partial \hat{\rho}} + \left[q_{\eta_3} + q_{\eta_6}\delta_{T_e}\right]\theta \\ &\quad + \sum_i \left[g_i' + h_i'\delta_{n_e} + k_i'\delta_{T_e} + l_i'\delta_{T_e}\delta_{n_e} + m_i'\delta_{T_e}^2 + p_i'\delta_{T_e}^2\delta_{n_e}\right]P_i(t) \\ &\quad - \left[g_{bs} + h_{bs}\delta_{n_e} + k_{bs}\delta_{T_e} + l_{bs}\delta_{T_e}\delta_{n_e} + m_{bs}\delta_{T_e}^2 + p_{bs}\delta_{T_e}^2\delta_{n_e}\right]\left(\frac{1}{\theta}\right)^2\frac{\partial \theta}{\partial \hat{\rho}} \\ &\quad + \left[g_{bs}' + h_{bs}'\delta_{n_e} + k_{bs}'\delta_{T_e} + l_{bs}'\delta_{T_e}\delta_{n_e} + m_{bs}'\delta_{T_e}^2 + p_{bs}'\delta_{T_e}^2\delta_{n_e}\right]\left(\frac{1}{\theta}\right), \end{aligned} \tag{5.43}$$

with boundary conditions

$$\theta(0,t) = 0 \qquad \theta(1,t) = -k_{I_p}I_p(t), \tag{5.44}$$

where $i \in \{ec_{tot}, nbi_{30\mathrm{L/R}}, nbi_{150\mathrm{L/R}}, nbi_{330\mathrm{L/R}}\}$, the parameters $q_{\eta_j}(\hat{\rho})$, for $j = 1, \ldots, 6$, $g_i(\hat{\rho})$, $h_i(\hat{\rho})$, $k_i(\hat{\rho})$, $l_i(\hat{\rho})$, $m_i(\hat{\rho})$, $p_i(\hat{\rho})$, $g_{bs}(\hat{\rho})$, $h_{bs}(\hat{\rho})$, $k_{bs}(\hat{\rho})$, $l_{bs}(\hat{\rho})$, $m_{bs}(\hat{\rho})$, $p_{bs}(\hat{\rho})$ are functions of space, $(\cdot)' = d/d\hat{\rho}$, and $P_i(t)$ is the total gyrotron launcher power and the individual neutral beam injection powers, respectively. See section 4.4.1 for an example of how (5.43) is derived. Additionally, for feedback control design, we approximate the plasma stored energy dynamics (5.13) as

$$\frac{dE}{dt} = -\frac{E}{\tau_E} + P_{aux}(t) = -\frac{E}{\tau_E} + \sum_i P_i(t), \tag{5.45}$$

where P_{aux} is the total auxiliary heating power. In (5.45), we have neglected the ohmic and radiated power to simplify the feedback control design as they are typically small compared to the auxiliary heating power in the scenarios considered.

5.4.2 Model reduction via spatial discretization

We spatially discretize the governing PDE (5.43) by employing a finite difference method, where the spatial domain of interest ($\hat{\rho} \in [0, 1]$) is represented as m_θ nodes, to obtain a model suitable for tracking control design. After spatially discretizing (5.43) and taking into account the boundary conditions (5.44), we obtain a nonlinear, finite dimensional, ordinary differential equation model defined by

$$\dot{\hat{\theta}} = f_\theta(\hat{\theta}, u, \delta), \tag{5.46}$$

where $\hat{\theta} = [\theta_2, \ldots, \theta_{m_\theta - 1}]^T \in \mathbb{R}^{n_\theta}$ is the magnetic state vector, θ_i, for $i = 2, \ldots, m_\theta - 1$, is the value of θ at the i-th node, $u = [P_{ec_{tot}}, P_{nbi_{30\mathrm{L/R}}}, P_{nbi_{150\mathrm{L/R}}}, P_{nbi_{330\mathrm{L/R}}}, I_p]^T \in \mathbb{R}^8$ is the input vector, the uncertain parameter vector is $\delta = \left[\delta_{T_e}, \delta_{n_e}, \delta_{T_e}\delta_{n_e}, \delta_{T_e}^2, \delta_{T_e}^2\delta_{n_e}\right]^T \in \mathbb{R}^5$, $f_\theta \in \mathbb{R}^{n_\theta}$ is a nonlinear function of the plasma magnetic states, control inputs, and uncertain parameters, and $n_\theta = m_\theta - 2$. By defining the plasma state vector as $x = [\hat{\theta}, E] \in \mathbb{R}^{(n_\theta + 1)}$, we can write the magnetic and kinetic state dynamics as

$$\dot{x} = \begin{bmatrix} f_\theta(\hat{\theta}, u, \delta) \\ -\dfrac{E}{\tau_E(t)} + \sum_{i=1}^{7} u_i \end{bmatrix} = F_{\theta,E}(x, u, \delta) \in \mathbb{R}^{(n_\theta + 1)}. \tag{5.47}$$

Linearizing (5.47) with respect to the state and control input around a nominal equilibrium point $(x_{eq}, u_{eq}, 0)$, we obtain a linear time-invariant (LTI) model given by

$$\begin{aligned} \dot{\tilde{x}} &= A\tilde{x} + Bu_{fb} + d_\delta, \\ y &= C\tilde{x} + Du_{fb}, \end{aligned} \tag{5.48}$$

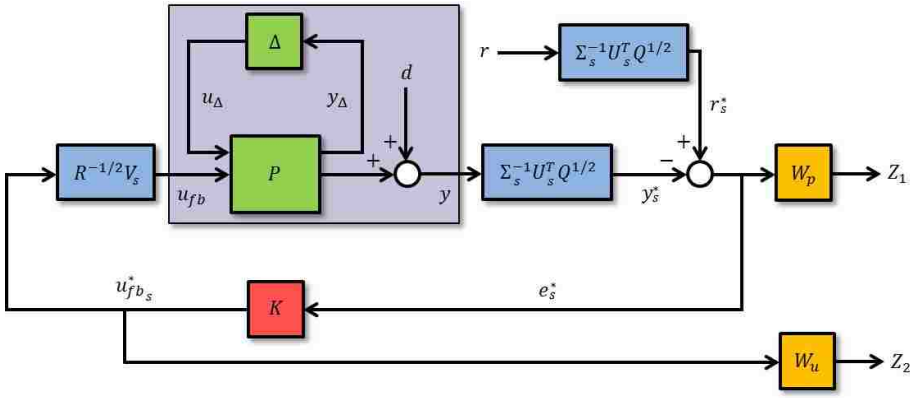

Figure 5.5: Schematic of control problem formulation for simultaneous θ profile + E feedback control design in DIII-D H-mode scenarios.

with

$$A = A_0 + \sum_{m=1}^{5} \delta_m A_m \qquad B = B_0 + \sum_{m=1}^{5} \delta_m B_m,$$
$$C = C_0 + \sum_{m=1}^{5} \delta_m C_m \qquad D = D_0 + \sum_{m=1}^{5} \delta_m D_m, \tag{5.49}$$

where $\tilde{x}(t) = x(t) - x_{eq}$, $u_{fb}(t) = u(t) - u_{eq}$ is the output of the to-be-designed feedback controller, $d_\delta = F_{\theta,E}(x_{eq}, u_{eq}, \delta)$, A and B are the Jacobians $\partial F_{\theta,E}/\partial x \in \mathbb{R}^{(n_\theta+1)\times(n_\theta+1)}$ and $\partial F_{\theta,E}/\partial u \in \mathbb{R}^{(n_\theta+1)\times 8}$, respectively, evaluated at (x_{eq}, u_{eq}, δ), A_i and B_i, for $i = 0, \ldots, 5$, are the components of the matrices A and B, respectively, C_0 is an $(n_\theta + 1) \times (n_\theta + 1)$ identity matrix, $D_0 = 0$, and $C_j = 0$ and $D_j = 0$, for $j = 1, \ldots, 5$.

5.4.3 Manipulation of dynamic model into robust control framework

By exploiting the structure of the of the state matrices in (5.49), the feedback system (5.48) can be written in the conventional $P - \Delta$ control framework (shown in the light purple box in Fig. 5.5), where P is the generalized plant and $\Delta = \text{diag}\{\delta_{T_e}, \delta_{n_e}\}$ is a structured uncertainty matrix, by employing the method outlined in [138]. The

system input-output equations in this framework are

$$\begin{aligned} y_\Delta &= P_{11}u_\Delta + P_{12}u_{fb}, \\ y &= P_{21}u_\Delta + P_{22}u_{fb} + d, \end{aligned} \tag{5.50}$$

where P_{11}, P_{12}, P_{21}, and P_{22} are the component transfer functions of the generalized plant P that are related to the system outputs (y_Δ, y) and inputs (u_Δ, u_{fb}), respectively, and d represents the effect that the disturbance d_δ has on the system outputs. An overview of the employed technique is provided in Appendix A.

5.4.4 Evaluation of relevant control channels

In order to acquire diagnostic data that is needed by the real-time EFIT (rtEFIT) equilibrium reconstruction code [11] to reconstruct the plasma q profile for feedback control, the 30L/R neutral beam powers need to be constant, and we do not utilize them for feedback control, i.e., $u_{fb} = 0$ for $P_{nbi_{30\mathrm{L/R}}}$. As a result, we have six actuators to utilize in feedback, which implies we can independently control at most six linear combinations of the system output. Therefore, we obtain the most relevant control channels from the nominal input-output relation at a particular frequency $j\omega_{dc}$, which is expressed as

$$\hat{y} = \hat{G}_0\hat{u}_{fb} = Q^{-1/2}\tilde{G}_0R^{1/2}\hat{u}_{fb} = Q^{-1/2}U\Sigma V^TR^{1/2}\hat{u}_{fb}. \tag{5.51}$$

The decoupled output and input are denoted by $\hat{y}^* = \Sigma^{-1}U^TQ^{1/2}\hat{y}$ and $\hat{u}^*_{fb} = V^TR^{1/2}\hat{u}_{fb}$, i.e., $\hat{y}^* = \hat{u}^*_{fb}$. The nominal system transfer function is expressed as $G_0(s) = C_0\left(sI_{n_\theta} - A_0\right)^{-1}B_0 + D_0$ and $\hat{G}_0$ denotes the real approximation of the complex matrix $G_0(j\omega_{dc})$ [10, 146]. The positive definite matrices $Q \in \mathbb{R}^{(n_\theta+1)\times(n_\theta+1)}$ and $R \in \mathbb{R}^{6\times6}$ are utilized to weight the relative tracking performance and control effort.

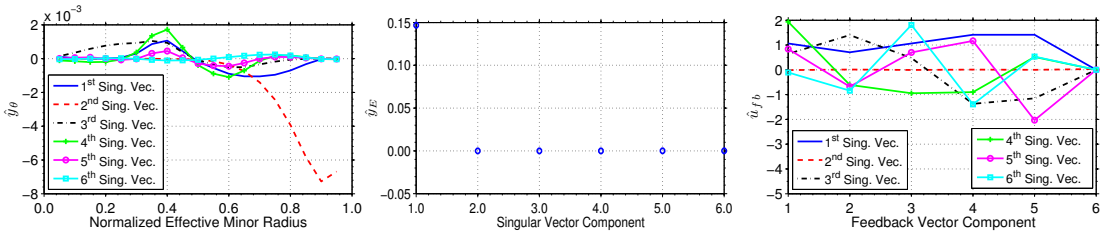

(a) $\hat{y}_\theta$ (b) $\hat{y}_E$ (c) $\hat{u}_{fb}$

Figure 5.6: Relevant control channels for θ profile + E control in DIII-D H-mode scenarios: (a-b) output and (c) input. The decoupled output is defined as $\hat{y} = [\hat{y}_\theta, \hat{y}_E]$ where $\hat{y}_\theta$ are the outputs associated with the magnetic states and $\hat{y}_E$ is the output associated with the kinetic states. The feedback vector components are $u_{fb} = [P_{ec_{tot}}, P_{nbi_{150\mathrm{L/R}}}, P_{nbi_{330\mathrm{L/R}}}, I_p]|_{fb}$ where $u_{fb} = 0$ for $P_{nbi_{30\mathrm{L/R}}}$.

Finally, the "weighted" transfer function $\tilde{G}_0$ and its economy size singular value decomposition (SVD) are defined as $\tilde{G}_0 = Q^{1/2}\hat{G}_0 R^{-1/2} = U\Sigma V^T$, where $\Sigma \in \mathbb{R}^{6\times 6}$ is a diagonal matrix of singular values and $U \in \mathbb{R}^{(n_\theta+1)\times 6}$ and $V \in \mathbb{R}^{6\times 6}$ are matrices that possess the following properties $V^TV = VV^T = I, U^TU = I$, where I is a 6×6 identity matrix. Some of the singular values may have a small magnitude relative to the others and may be chosen to be neglected in the control synthesis. Quantities associated with the significant singular values are denoted by a subscript s for the remainder of this chapter, i.e., $(\cdot)_s$. A detailed overview of the SVD technique employed to evaluate the relevant control channels is provided in Appendix B.

The relevant control channels are shown in Fig. 5.6. The frequency to evaluate the relevant control channels at is selected as $\omega_{dc} = 25$ rad/s, which results in the ability to exclusively utilize the total plasma current (I_p) to control the q profile near the plasma boundary (2nd singular vector in Figs. 5.6(a) and 5.6(c)). Additionally, by examining the third singular vector, we see that increasing the off-axis, co-current electron cyclotron ($P_{ec_{tot}}$) and neutral beam injection (150L/R) powers ($\hat{u}_{fb_i} > 0$ for $i = 1, 2, 3$ in Fig. 5.6(c)) and decreasing the on-axis, co-current (330L/R) neutral beam injection power ($\hat{u}_{fb_i} < 0$ for $i = 4, 5$ in Fig. 5.6(c)) results in the θ profile increasing (and hence the q profile increasing) in the plasma core ($\hat{y} > 0$ for $\hat{\rho} \in$

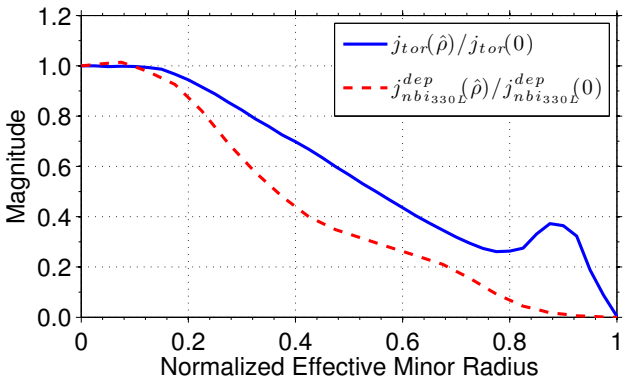

Figure 5.7: Normalized total toroidal current density (defined in (2.91)) and normalized 330L neutral beam injection current density in DIII-D H-mode scenarios.

$[0, 0.5)$ in Fig. 5.6(a)).[1] Intuitively, the effect that increasing the off-axis, co-current and decreasing the on-axis, co-current auxiliary current drive has on the q profile agrees with the control input directions in Fig. 5.6 as opposed to the nonintuitive behavior observed in section 4.4.4. To further study this, the normalized total toroidal current density and the normalized 330L neutral beam injection current density in the considered DIII-D H-mode scenarios is shown in Fig. 5.7. As shown in the figure, the normalized current density deposition profile for the 330L neutral beam source exhibits a narrower distribution than the normalized total toroidal current density. Therefore, increasing the on-axis, co-current (330L/R) neutral beam injection power would result in an increase of the total toroidal current density in the plasma core (for a fixed value of the total plasma current), which in turn would result in a decrease in the q-value (and hence the θ-value decreasing) in the plasma core. This behavior agrees with the control input directions in Fig. 5.6. See sections 2.6 and 4.3 for the relationship the local current density amplitude has to the local q-value in tokamaks.

[1] The employed coordinate system results in the θ profile having a negative magnitude. Therefore, a positive perturbation to this profile will result in a θ profile with a smaller magnitude in absolute value, i.e., the resulting θ profile will be less negative. This perturbation results in the q profile increasing as $q \propto -\theta^{-1}$.

5.4.5 Feedback control problem formulation

It is desired that the output y be able to track a reference value r, therefore, we define the tracking error as $e = r - y$. The feedback control problem is formulated as shown in Fig. 5.5, where K is the feedback controller, the closed-loop system outputs are $Z_1 = W_p e_s^*$ and $Z_2 = W_u u_{fb_s}^*$, and W_p and W_u are frequency dependent weight functions used to optimize the closed-loop performance. The nominal performance condition of the closed-loop system is expressed as

$$\begin{bmatrix} Z_1 \\ Z_2 \end{bmatrix} = \begin{bmatrix} W_p S_{DC_O} & -W_p S_{DC_O} \\ W_u K S_{DC_O} & -W_u K S_{DC_O} \end{bmatrix} \begin{bmatrix} r_s^* \\ d_s^* \end{bmatrix} \triangleq T_{zw} \begin{bmatrix} r_s^* \\ d_s^* \end{bmatrix} \quad \Rightarrow \quad \min_K \left|\left|T_{zw}\right|\right|_\infty, \quad \forall \omega, \tag{5.52}$$

where $S_{DC_O} = (I + \Sigma_s^{-1} U_s^T Q^{1/2} P_{22} R^{-1/2} V_s K)^{-1}$, $d_s^* = \Sigma_s^{-1} U_s^T Q^{1/2} d$, and $||\cdot||_\infty$ denotes the H_∞ norm. See section 3.6 for an example of how this nominal performance condition is derived, and see Appendix C for an introduction to the design of feedback controllers by employing the H_∞ closed-loop shaping technique. The feedback controller written in terms of the tracking error e and control input u_{fb} is expressed as

$$\begin{aligned} \dot{x}_{fb} &= A_{fb} x_{fb} + B_{fb} \Sigma_s^{-1} U_s^T Q^{1/2} e, \\ u_{fb} &= R^{-1/2} V_s C_{fb} x_{fb} + R^{-1/2} V_s D_{fb} \Sigma_s^{-1} U_s^T Q^{1/2} e, \end{aligned} \tag{5.53}$$

where x_{fb} is the internal controller state vector and A_{fb}, B_{fb}, C_{fb}, D_{fb} are the state-space matrices of the controller K that are determined by solving (5.52). The weight matrix Q utilized in the evaluation of the relevant control channels is chosen to place more emphasis on achieving the target q profile in the spatial regions $\hat{\rho} \in (0, 0.3]$ and $\hat{\rho} \in [0.85, 1.0)$ as the q-value in these spatial regions intimately affects the stability and performance of the plasma. To analyze the performance and robust stability of

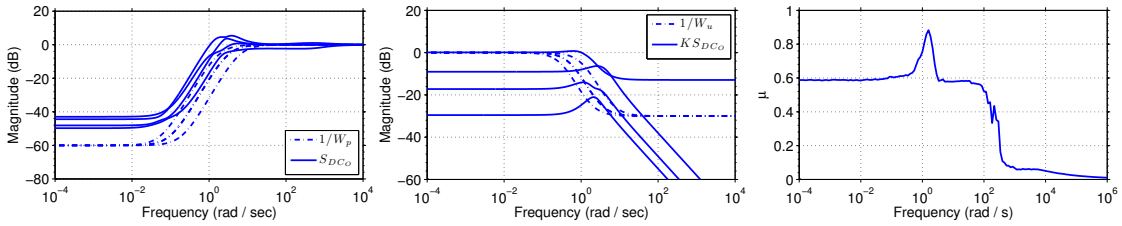

(a) (b) (c)

Figure 5.8: Singular values: (a) $1/W_p$ and S_{DC_o} and (b) $1/W_u$ and KS_{DC_o} and (c) $\mu(N_{11}(j\omega))$ versus frequency. The closed-loop robust stability condition is defined as $\mu(N_{11}(j\omega)) < 1$, $\forall\omega$ [10].

the closed-loop system, the singular value diagrams of the inverse of the performance weight functions and the achieved transfer functions S_{DC_O} and KS_{DC_O} are shown in Figs. 5.8(a-b) and a plot of the structured singular value $\mu(N_{11}(j\omega))$, which can be computed due to the block-diagonal structure of the uncertainty matrix Δ, versus frequency is shown in Fig. 5.8(c), where $N_{11} = P_{11} - P_{12}R^{-1/2}V_sKS_{DC_O}\Sigma_s^{-1}U_s^TQ^{1/2}P_{21}$ is the closed-loop transfer function between y_Δ and u_Δ in Fig. 5.5.

5.5 Performance testing of q profile feedback control algorithm in DIII-D experiments

In this section, we test the ability of the q profile feedback control algorithm (not including E feedback control) to reach, and subsequently maintain, a target safety factor profile in H-mode experiments in the DIII-D tokamak. The q profile controller is designed by solely focusing on (5.46). To ensure the closed-loop system remains well behaved in the presence of actuator magnitude saturation, the controller is augmented with an anti-windup compensator [140]. See section 4.4.6 for an example of the employed anti-windup scheme.

We employ the general framework for real-time feedforward + feedback control of magnetic plasma profiles implemented in the DIII-D Plasma Control System (PCS)

described in section 3.7.2 to test the control algorithm. The feedback control algorithm designed in this chapter directly generates signals for the physical control variables. Therefore the NL Trans. Switch is set to the right position in Fig. 3.8. Also, the employed anti-windup scheme is designed to affect the output of the feedback portion of the controller. Therefore, the AW Switch is set to the left position in Fig. 3.8. Finally, the feedback control algorithm is implemented with a sampling time of 20 ms based on the modulation of the 30L/R neutral beam sources utilized to acquire diagnostic data to reconstruct the q profile (see sections 3.7.2 and 4.3, respectively).

5.5.1 Reference tracking experimental testing of q profile controller

In a DIII-D discharge, robust tracking of a stationary target q profile was obtained in the presence of external plasma disturbances. In DIII-D shot 154359, the q profile feedback controller (not including E feedback control) was tested in a feedforward + feedback target tracking experiment. The target q profile ($q^{tar}(\hat{\rho},t)$) was obtained from the q profile achieved in DIII-D shot 150320 ($q^{320}(\hat{\rho},t)$) as follows:

$$
\begin{aligned}
&q^{tar}(\hat{\rho},t) = q^{320}(\hat{\rho},t) && \text{over } t \in [0.5, 2.0] \text{ s},\\
&q^{tar}(\hat{\rho},t) = q^{320}(\hat{\rho},2) + \left[q^{320}(\hat{\rho},5) - q^{320}(\hat{\rho},2)\right]\frac{(t-2)}{(5-2)} && \text{over } t \in (2.0, 4.0) \text{ s},\\
&q^{tar}(\hat{\rho},t) = q^{320}(\hat{\rho},5.0) && \text{over } t \in [4.0, 6.0] \text{ s}.
\end{aligned}
$$

The feedforward component of the control input was chosen to be the actuator trajectories achieved in DIII-D shot 150320. A key physics goal of plasma profile control is to be able to robustly reproduce target scenarios and enable controlled variation of specific characteristics of the profiles through feedback to better elucidate physics.

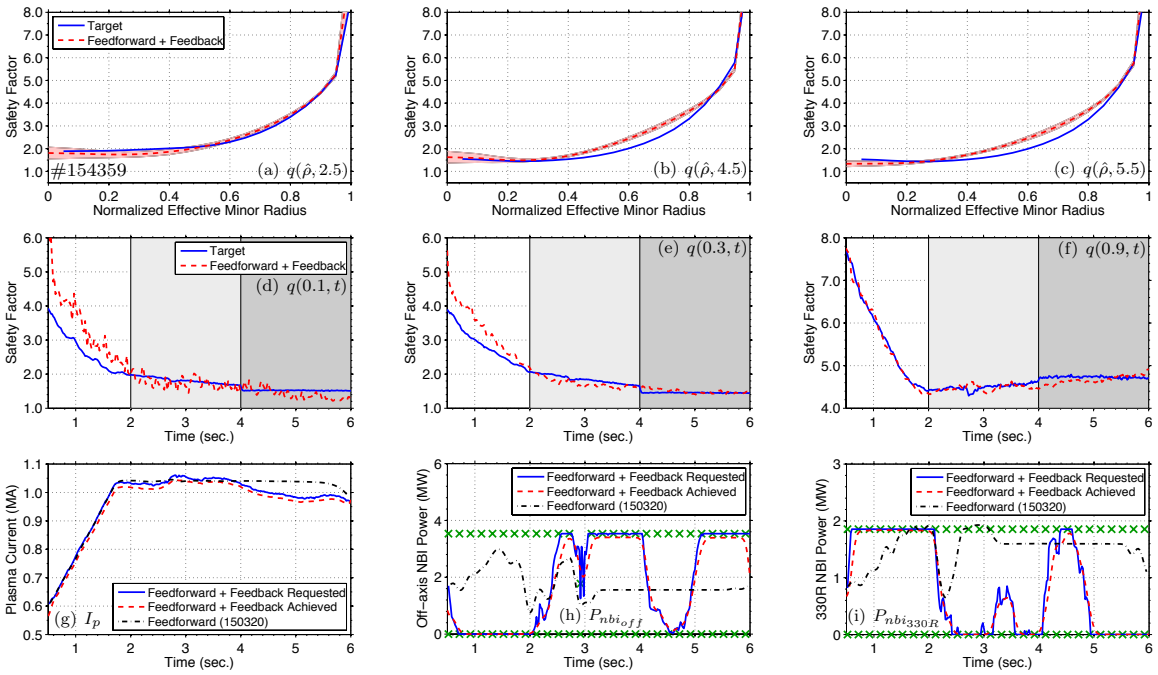

Figure 5.9: Experimental testing of q profile feedback controller during DIII-D shot 154359: (a-c) q profile at $t = 2.5, 4.5$, and 5.5 s, (d-f) time traces of q at $\hat{\rho} = 0.1, 0.3$, and 0.9, and (g-i) comparison of actuator trajectories ($P_{nbi_{off}} = P_{nbi_{150\mathrm{L}}} + P_{nbi_{150\mathrm{R}}}$). Approximate error bars for the measured q profiles (obtained from rtEFIT [11]) are shown by the red-shaded regions. Note: actuator limits denoted by green X.

A comparison of the target and experimentally achieved q profiles at various times, time traces of q at various radial locations, and a comparison of the actuator trajectories is shown in Fig. 5.9. As shown, the controller was able to drive the q profile to the target (specifically in the spatial regions where the tracking performance was more heavily weighted ($\hat{\rho} \in (0, 0.3]$ and $\hat{\rho} \in [0.85, 1.0)$)) and achieve a relatively stationary condition in the presence of perturbations in the initial conditions and actuator regulation disturbances. During the feedback-controlled discharge, the 30L/R neutral beam injectors were utilized at a constant power (total of 2 MW) to acquire diagnostic data while during the target discharge the power in these beams was increased from a low value (total of 1.2 MW) to a high value (total of 3.2 MW) at 3.0 s. Also, during the feedback-controlled discharge, the 330L neutral beam injector

and the gyrotron launchers were unavailable for feedback control due to errors in the setup. The 330L NBI delivered a constant 1.9 MW of power in the feedback-controlled discharge, and a constant 1.7 MW of power in the target discharge, during the time interval $t \in [2.5, 6.0]$ s. In the feedback-controlled discharge, the gyrotrons delivered a constant 1.6 MW of power during the time interval $t \in [2.5, 3.0]$ s and a constant 1.2 MW during the time interval $t \in (3.0, 6.0)$ s. In the target discharge, the gyrotrons delivered a constant 2.8 MW of power during the time interval $t \in [2.5, 6.0]$ s. Additionally, the flattop line average electron density in the feedback-controlled discharge was approximately 5% lower than in the target discharge during the approximate time interval $t \in (3.7, 5.4)$ s. The local q-value is roughly inversely related to the local current density amplitude in tokamaks, i.e., a low q profile is characterized by a high current profile and vice versa. The controller utilized the total plasma current to regulate the q profile near the plasma boundary (Figs. 5.9(f) and 5.9(g)) and modulated the mix of the on-and-off axis auxiliary current drives that were available for feedback control to track the target q profile in the plasma core (Figs. 5.9(d-e) and 5.9(h-i)). Firstly, during the time intervals $t \in [0.5, 2.0]$ s and $t \in (4.0, 5.0)$ s, the q-value in the plasma core is above the target. In response to this tracking error, the feedback controller decreases the off-axis neutral beam injection power ($P_{nbi_{off}}$) and increases the on-axis neutral beam power ($P_{nbi_{330\mathrm{R}}}$) to track the target q profile in plasma core. Secondly, during the time intervals $t \in (2.0, 4.0]$ s and $t \in [5.0, 6.0]$ s, the q-value in the plasma core is below the target. In response to this tracking error, the feedback controller increases the off-axis neutral beam injection power ($P_{nbi_{off}}$) and decreases the on-axis neutral beam power ($P_{nbi_{330\mathrm{R}}}$) to track the target q profile in plasma core. Finally, as shown in Fig. 5.10(a), the achieved β_N was relatively close to the target even though it was not feedback-controlled. This resulted in a similar bootstrap current profile in both the target and feedback-controlled discharges as shown in Fig. 5.10(b).

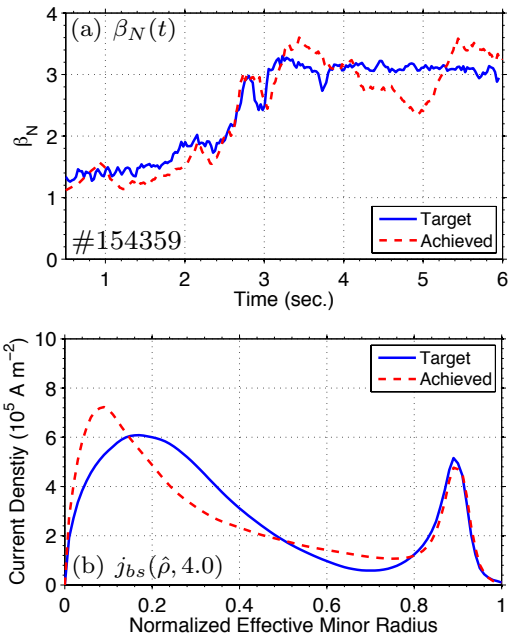

Figure 5.10: Comparison of (a) β_N and (b) bootstrap current profile j_{bs} (computed by TRANSP [12]) at 4.0 s. The bootstrap fraction in the target discharge was $f_{bs} = 38\%$ and in the feedback-controlled discharge was $f_{bs} = 39\%$ at 4.0 s. The bootstrap fraction is defined as $f_{bs} = I_{bs}/I_p$, where $I_{bs} = \int_0^1 j_{bs}(\hat{\rho}) \frac{\partial S}{\partial \hat{\rho}} d\hat{\rho}$ and S is the poloidal cross-sectional area enclosed by a magnetic flux surface.

5.5.2 Disturbance rejection experimental testing of q profile controller

In another DIII-D discharge, rejection of a disturbance purposely introduced in the initial q profile was obtained exclusively through feedback actuation. In DIII-D shot 154692, the q profile feedback controller (not including E feedback control) was tested in a pure feedback disturbance rejection experiment. The q profile evolution achieved in DIII-D shot 154358 was chosen as the target. A significant disturbance (low relative to the target) in the q profile at 0.5 s (when the feedback controller was turned on) was introduced to the plasma by delaying the time at which the plasma transitioned from the low confinement (L-mode) to the high confinement operating regime. This delay resulted in the inductive component of the plasma current profile diffusing in towards the center of the plasma at a faster rate than in the target shot. The feedforward

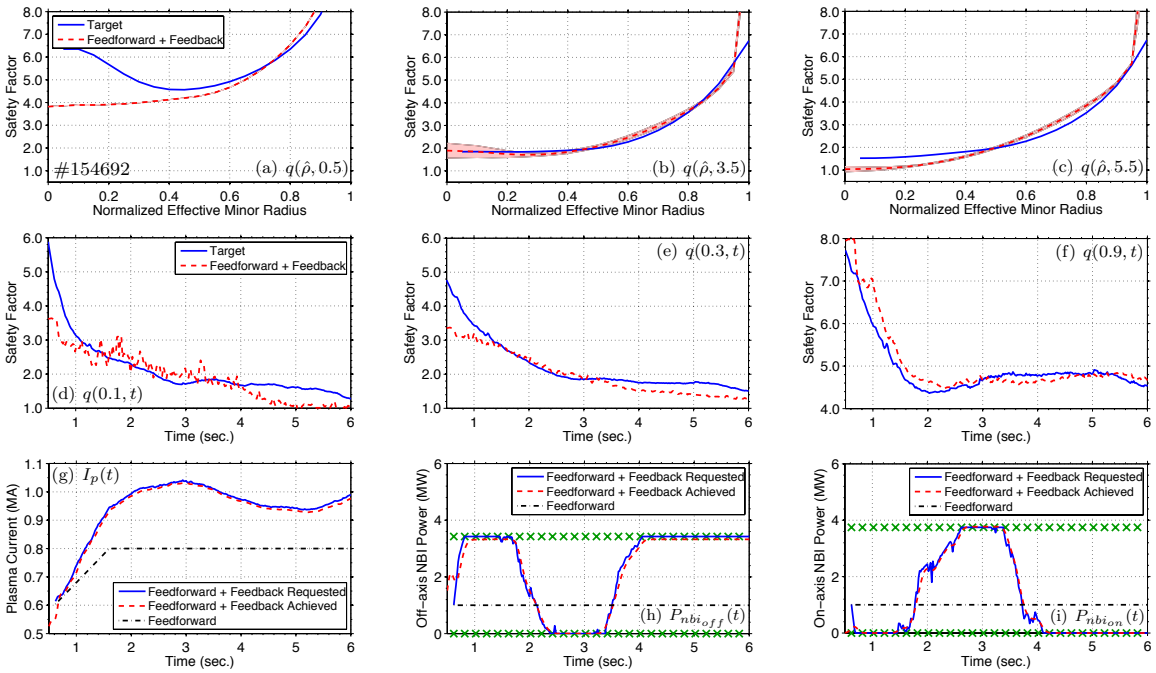

Figure 5.11: Experimental testing of q-profile feedback controller during DIII-D shot 154692: (a-c) q profile at $t = 0.5, 3.5$, and 5.5 s, (d-f) time trace of q at $\hat{\rho} = 0.1, 0.3$, and 0.9, and (g-i) comparison of actuator trajectories ($P_{nbi_{on}} = P_{nbi_{330\mathrm{L}}} + P_{nbi_{330\mathrm{R}}}$). Approximate error bars for the measured q profiles (obtained from rtEFIT [11]) are shown by the red-shaded regions. Note: actuator limits denoted by green X.

component of the control input was frozen after 1.6 s, therefore, the achieved profile regulation was obtained exclusively through feedback. Another important goal of profile control experiments is to investigate the minimum number of variables that must be controlled to achieve robust scenario execution.

A comparison of the target and experimentally achieved q profiles at various times, time traces of q at various radial locations, and a comparison of the actuator trajectories is shown in Fig. 5.11. As shown in the figures, the controller was able to reject the effects of the initial condition error and drive the q profile to the target during the time interval $t \in [0.5, 3.5]$ s in the presence of actuator regulation disturbances. In the feedback-controlled discharge, the gyrotrons were unavailable for feedback control due to errors in the setup and did not deliver any power to the plasma, while in the

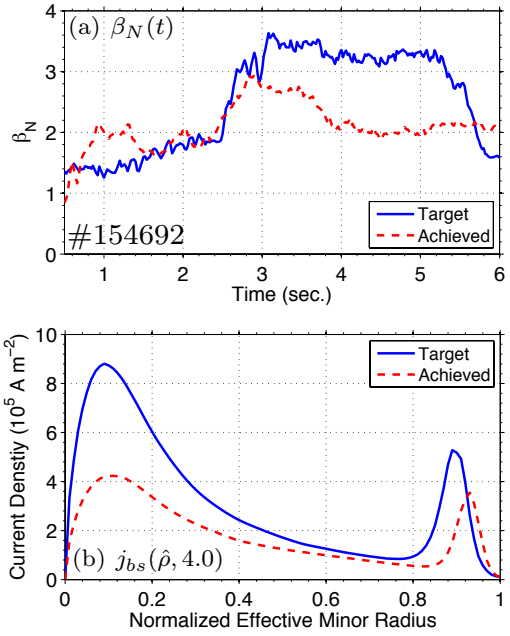

Figure 5.12: Comparison of (a) β_N and (b) bootstrap current profile (computed by TRANSP [12]) at 4.0 s. The bootstrap fraction in the target discharge was $f_{bs} = 39\%$ and in the feedback-controlled discharge was $f_{bs} = 27\%$ at 4.0 s.

target discharge, the gyrotrons delivered a constant 3 MW of power during the time interval $t \in [2.5, 6.0]$ s. Additionally, the flattop line average electron density in the feedback-controlled discharge was approximately 5-10% lower than in the target discharge during the approximate time interval $t \in (3.0, 5.0)$ s. The controller utilized the actuators to regulate the q profile across the spatial domain in the same way as in the previously discussed feedback experiment (Figs. 5.11(d-i)). However, even though the controller requested the maximum amount of off-axis auxiliary current drive during the time interval $t \in [4.0, 6.0]$ s, the q profile in the plasma core was unable to be maintained at the target. As shown in Fig. 5.12(a), the achieved β_N was relatively far away from the target during the time interval $t \in (3.0, 5.5]$ s. This resulted in a lower bootstrap current profile in the feedback-controlled discharge relative to the target as shown in Fig. 5.12(b). As the bootstrap current is an off-axis source of current, a lower bootstrap current may have contributed to the inability to maintain the q profile in the plasma core at the target during the feedback-controlled experiment.

5.6 Simulation testing of integrated q profile + E controller

In the previous section, the q profile feedback controller was shown to be able to effectively control the q profile when β_N is relatively close to the target. This indicates that an important aspect of achieving robust scenario execution is the need to simultaneously achieve a target q profile and β_N. In this section, the q profile + E feedback controller (5.53) is tested through simulations based on the physics-based model of the plasma poloidal magnetic flux profile and stored energy dynamics tailored to DIII-D H-mode scenarios described in section 2.8. First, a target q profile and β_N evolution is obtained by executing a feedforward-only simulation with the control input trajectories and initial conditions ($q(\hat{\rho}, 0.5)$ and $\beta_N(0.5)$) achieved in DIII-D shot 150318. Second, a nominal q profile and β_N evolution is obtained by executing a feedforward-only simulation with a nominal set of input trajectories and initial conditions. Finally, the ability of the algorithm to track the target evolutions that are obtained from the first simulation is determined by executing a feedforward + feedback simulation with the nominal input trajectories and initial conditions that are used in the second simulation. During the feedback-controlled simulation, the controller is inactive during the time interval $t = [0.5, 2.0]$ s. Simulated white noise is added to both the feedforward + feedback and feedforward simulations, respectively, to approximately replicate the noise level observed in the rtEFIT measurements during DIII-D operations.

A comparison of the target, feedforward + feedback controlled, and feedforward controlled q profiles at various times, time traces of q at various spatial locations, and a time trace of the plasma β_N is shown in Fig. 5.13. A comparison of the control inputs is shown in Fig. 5.14. As shown in the figures, the controller is able to drive the q profile and plasma β_N to the target evolutions once it becomes active at

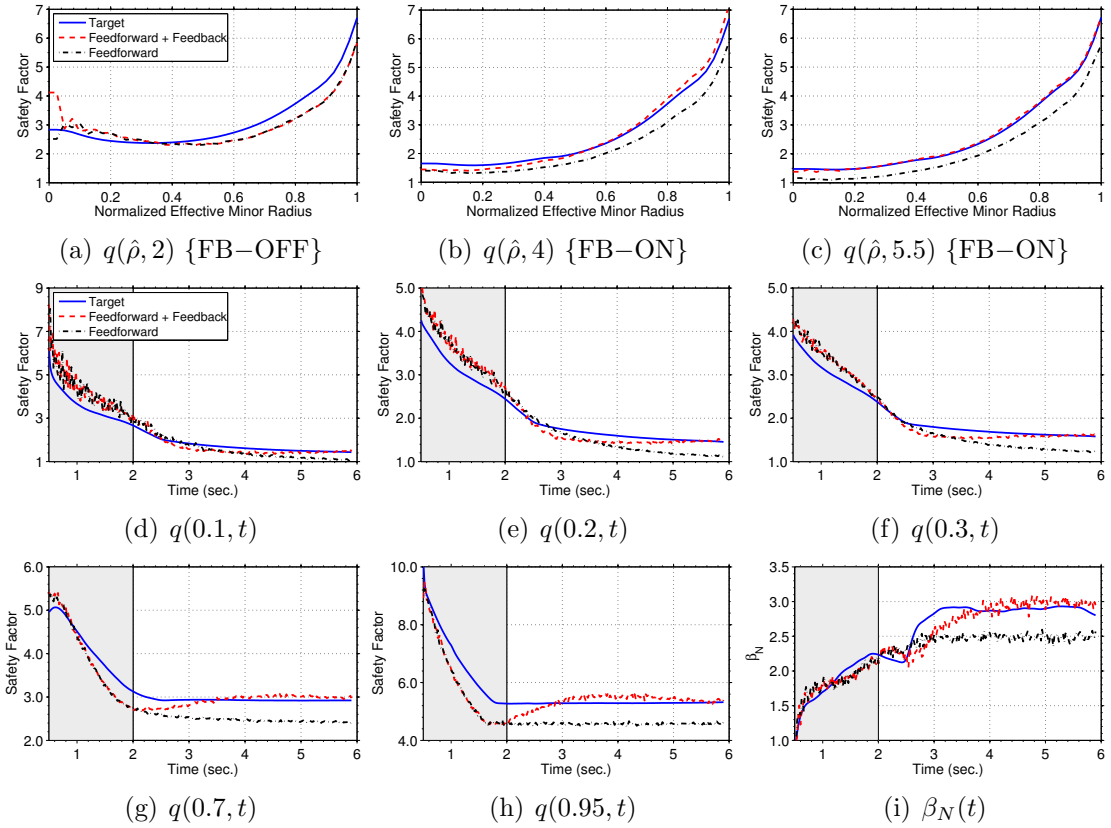

(a) $q(\hat{\rho}, 2)$ {FB−OFF} (b) $q(\hat{\rho}, 4)$ {FB−ON} (c) $q(\hat{\rho}, 5.5)$ {FB−ON}

(d) $q(0.1, t)$ (e) $q(0.2, t)$ (f) $q(0.3, t)$

(g) $q(0.7, t)$ (h) $q(0.95, t)$ (i) $\beta_N(t)$

Figure 5.13: Simulation testing of q profile + E feedback controller: (a-c) q profile at various times, (d-h) time trace of q at various spatial locations, and (i) time trace of plasma β_N. The gray-shaded region indicates when the feedback controller is inactive.

2.0 s in the presence of perturbations in the initial conditions and actuator regulation disturbances. During the feedback-controlled simulation, the 30L/R neutral beam injectors were utilized at a constant power while during the target simulation the power in these beams was increased from a low value to a high value at 3.0 s (see Figs. 5.14(d-e)). Additionally, the flattop line average electron density was approximately 5-10% higher than in the target simulation (see Fig. 5.14(b)). In the feedback-controlled simulation, firstly, the controller decreases the total plasma current to eliminate the error in q near the plasma boundary (see Figs. 5.13(g-h) and 5.14(a)). Secondly, at approximately 2.5 s, the value of q in the plasma core evolves below the

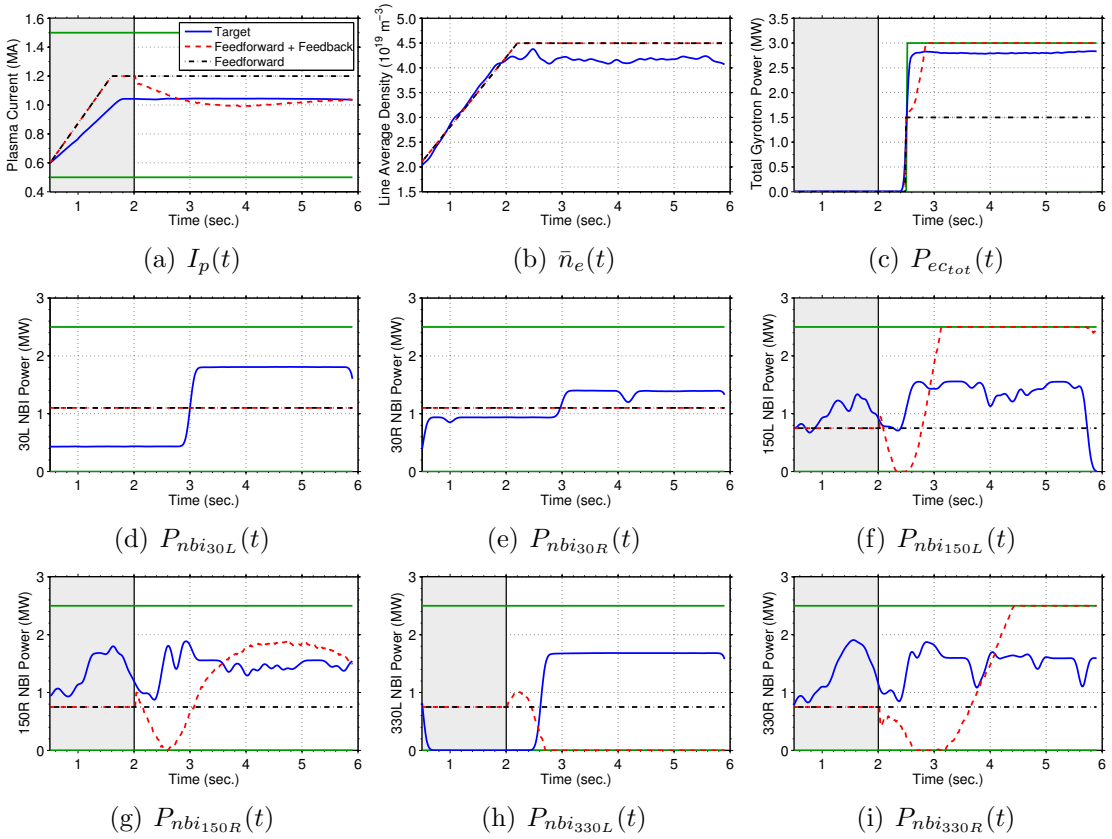

(a) $I_p(t)$ (b) $\bar{n}_e(t)$ (c) $P_{ec_{tot}}(t)$

(d) $P_{nbi_{30L}}(t)$ (e) $P_{nbi_{30R}}(t)$ (f) $P_{nbi_{150L}}(t)$

(g) $P_{nbi_{150R}}(t)$ (h) $P_{nbi_{330L}}(t)$ (i) $P_{nbi_{330R}}(t)$

Figure 5.14: Simulation testing of q profile + E feedback controller: Actuator trajectory comparison (actuator limits in solid green). The shaded gray region denotes when the feedback controller is not active. Note that the gyrotrons become available at 2.5 s and the line average electron density and the 30L/R neutral beam lines are not feedback controlled.

target value. In response, the controller decreases the on-axis auxiliary current drive ($P_{nbi_{330\mathrm{L/R}}}$) and increases the off-axis auxiliary current drive ($P_{ec_{tot}}$ and $P_{nbi_{150\mathrm{L/R}}}$) to track the target q profile in the plasma core (see Figs. 5.13(d-f), 5.14(c), and 5.14(f-i)). Finally, in order to track the target plasma β_N while maintaining good tracking of the q profile in the plasma core, the controller slowly increases the on-axis auxiliary heating (specifically $P_{nbi_{330\mathrm{R}}}$) beginning at approximately 3.25 s.

5.7 Conclusion

The reported advances demonstrate the potential physics-model-based profile control has to provide a systematic approach for the development and robust sustainment of advanced scenarios in DIII-D. These control algorithms also enable detailed study of the accuracy and validity of the relevant models themselves and can help clarify physics aspects important to robust scenario execution. A numerical optimization algorithm was developed to complement the experimental effort of advanced scenario planning in the DIII-D tokamak. At the core of the optimization algorithm is a nonlinear, physics-based, control-oriented model of the plasma dynamics. One direction of future work is to extend the physics-based model by coupling the poloidal magnetic flux profile dynamics together with the distributed dynamics of the electron temperature profile in order to better represent the effect the q profile has on plasma transport [59]. The optimized actuator trajectories were successfully tested through simulation, and an experimental test in DIII-D demonstrated the ability of the optimized trajectories to steer the plasma to a target stationary q profile. However, as observed in the experimental test, access to advanced scenarios can be limited by triggering MHD instabilities. Therefore, another direction of future work is to formulate additional plasma state constraints that can be imposed on the optimization problem solution to maintain distance from critical MHD stability limits, such as classical and neoclassical tearing modes.

As a result of the MHD instabilities that developed during the experimental test, the optimized feedforward trajectories were not able to achieve the target β_N and maintain a stationary q profile for the entirety of the plasma discharge. Therefore to account for external plasma disturbances (such as a reduction in confinement) and actuation limitations (either in actuator regulation or actuator faults), a feedback control scheme was developed to control the q profile. The ability of the q profile

feedback controller (not including energy control) to improve the ability to robustly achieve plasma target conditions was tested in DIII-D experiments. The q profile controller was shown to be able to effectively control the q profile when β_N is relatively close to the target. Therefore, these experiments indicate that another important aspect of achieving robust scenario execution is the need to simultaneously achieve a target q profile and β_N. Through simulations, the ability of an integrated q profile and stored energy feedback controller to track a desired target was demonstrated. Another direction of future work is to experimentally test the performance of the combined q profile and stored energy controller in DIII-D experiments. The development of these profile control capabilities may not only help achieve physics objectives on DIII-D, but will also help evaluate a control scheme that potentially can be utilized in future experiments and fusion power plants. The control scheme developed in this chapter is readily adaptable to a given operating scenario in a given machine of interest, as discussed in the following chapters, due to the strong first-principles dependence of the modeling and design approach used to synthesize controllers.

Chapter 6

Simultaneous closed-loop control of the safety factor profile and stored energy in burning plasma scenarios in the ITER tokamak

6.1 Introduction

The next phase of tokamak development is the ITER tokamak project [3]. ITER will be the first tokamak device to produce a significant amount of fusion power and hence be the first machine to explore the burning plasma operating regime. The current profile in the tokamak is intimately related to the plasma stability and energy/particle transport, and the plasma stored energy is intimately related to the amount of generated fusion power. As the current profile and the kinetic state of the plasma are tightly coupled, integrating methodologies for current profile control with strategies to control the kinetic state of the plasma is crucial to enabling stable plasma operation and maintaing a desired level of produced power. With this objective in

mind, in this chapter, an integrated physics-model-based feedback control algorithm is designed to track target safety factor profile (q profile) and stored energy evolutions in high confinement (H-mode) burning plasma scenarios in ITER.

The auxiliary heating and current-drive (H&CD) actuators on ITER considered in this chapter are three independently configurable electron cyclotron (gyrotron) launchers, one ion cyclotron launcher, and co-current-injection neutral beam launchers. In the considered operating scenarios, the neutral beam launchers are configured to inject particles at the same off-axis radial location, therefore, we group them together to form 1 effective neutral beam launcher for control. Additionally, the ion cyclotron launcher is configured to provide only heating power to the plasma. As a result, we design the feedback algorithm with a two loop structure. The first loop utilizes the total plasma current and exclusively the current-drive capabilities of the gyrotron and neutral beam launchers to control the q profile, and the second loop utilizes the ion cyclotron launcher to control the stored energy. This approach does not take into account the physical effects the actuators have on the q profile dynamics through plasma heating, which specifically affects the q profile evolution through resistive diffusion, auxiliary current-drive efficiency, and bootstrap current drive. Therefore, we employ the first-principles-driven (FPD), physics-based model of the plasma magnetic profile and stored energy evolution developed in chapter 2 to study the effect this unutilized control direction (pure plasma heating) has on the q profile dynamics in the considered H-mode ITER scenarios.

This chapter is organized as follows. In section 6.2, the effect that pure plasma heating has on the q profile is investigated. An integrated feedback algorithm to control the q profile and plasma stored energy is designed in section 6.3. The q profile portion of the feedback algorithm is designed to be robust to uncertainties in the electron density, electron temperature, and plasma resistivity. In section 6.4 the

feedback control algorithm is successfully tested in both reference tracking and disturbance rejection simulations with the physics-based model developed in chapter 2. The ability of the two control loops to interact together effectively is demonstrated by first tracking a nominal target, and then modulating the generated fusion power while maintaining the q profile in a stationary condition. Finally, a summary and discussion of some of the key practical issues investigated in this chapter for plasma profile control in ITER are presented in section 6.5.

6.2 Plasma heating effect on the safety factor profile

We first investigate the effect that pure plasma heating has on the safety factor profile in H-mode ITER scenarios using the physics-based model described in section 2.9. In order to illustrate the effect that the electron temperature, and hence the effect pure plasma heating, has on the q profile dynamics, we briefly describe the physics-based model. See chapter 2 for a detailed derivation/discussion of the models. The q profile is related to the plasma poloidal magnetic flux profile and is defined in (2.90) and repeated here for convenience as

$$q(\hat{\rho},t) = -\frac{d\Phi}{d\Psi} = -\frac{B_{\phi,0}\rho_b^2\hat{\rho}}{\partial\psi/\partial\hat{\rho}}, \tag{6.1}$$

where t is the time and ψ is the poloidal stream function, which is closely related to the poloidal magnetic flux Ψ ($\Psi = 2\pi\psi$). The spatial coordinate $\hat{\rho} = \rho/\rho_b$ is used to index the magnetic flux surfaces in the plasma, where ρ is the mean effective minor radius of a magnetic flux surface, i.e., $\Phi(\rho) = \pi B_{\phi,0}\rho^2$, Φ is the toroidal magnetic flux, $B_{\phi,0}$ is the vacuum toroidal magnetic field at the geometric major radius R_0 of the tokamak, and ρ_b is the mean effective minor radius the last closed magnetic

flux surface.

The evolution of the poloidal magnetic flux in a tokamak plasma is given by the magnetic diffusion equation (2.45) and is restated here for convenience as

$$\frac{\partial \psi}{\partial t} = \frac{\eta(T_e)}{\mu_0 \rho_b^2 \hat{F}^2} \frac{1}{\hat{\rho}} \frac{\partial}{\partial \hat{\rho}} \left(\hat{\rho} \hat{F} \hat{G} \hat{H} \frac{\partial \psi}{\partial \hat{\rho}} \right) + R_0 \hat{H} \eta(T_e) j_{ni}, \tag{6.2}$$

with boundary conditions

$$\frac{\partial \psi}{\partial \hat{\rho}}(0,t) = 0 \qquad \frac{\partial \psi}{\partial \hat{\rho}}(1,t) = -k_{I_p} I_p(t), \tag{6.3}$$

where η is the plasma resistivity, T_e is the electron temperature, μ_0 is the vacuum magnetic permeability, j_{ni} is the total noninductive current density, k_{I_p} is a geometric constant defined in (2.83), and I_p is the total plasma current. The parameters $\hat{F}$, $\hat{G}$, and $\hat{H}$ are geometric spatial factors pertaining to the magnetic configuration of a particular plasma equilibrium (defined in (2.44)). The plasma resistivity scales inversely with the electron temperature as

$$\eta(\hat{\rho}, t) \propto T_e(\hat{\rho}, t)^{-3/2}. \tag{6.4}$$

The total noninductive current is generated by the auxiliary sources and the bootstrap current (a self-generated noninductive source of plasma current) [60], i.e.,

$$j_{ni}(\hat{\rho}, t) = j_{aux}^{tot}(\hat{\rho}, t) + j_{bs}(\hat{\rho}, t) = \sum_{i=1}^{n_{aux}} j_{aux,i}(\hat{\rho}, t) + j_{bs}(\hat{\rho}, t), \tag{6.5}$$

where j_{aux}^{tot} is the total current density driven by the auxiliary sources, j_{bs} is the current density driven by the bootstrap current, $j_{aux,i}$ is the current density driven by the individual auxiliary sources, and n_{aux} is the number of auxiliary sources. The individual auxiliary current drives (electron cyclotron and neutral beam) are modeled

as

$$j_{aux,i}(\hat{\rho},t) = j_{aux,i}^{ref}(\hat{\rho})\frac{T_e(\hat{\rho},t)}{n_e(\hat{\rho},t)}P_{aux,i}(t), \tag{6.6}$$

where $j_{aux,i}^{ref}$ is a normalized reference current deposition profile for the i-th auxiliary source, the term T_e/n_e represents the current-drive efficiency, n_e is the electron density, and $P_{aux,i}$ is the i-th auxiliary power. The bootstrap current arises from the plasma radial pressure gradient that is produced by the magnetic confinement and is modeled as [134, 135]

$$j_{bs}(\hat{\rho},t) = \frac{k_{JkeV}R_0}{\hat{F}}\left(\frac{\partial\psi}{\partial\hat{\rho}}\right)^{-1}\left[2\mathcal{L}_{31}T_e\frac{\partial n_e}{\partial\hat{\rho}} + \{2\mathcal{L}_{31}+\mathcal{L}_{32}+\alpha\mathcal{L}_{34}\}\,n_e\frac{\partial T_e}{\partial\hat{\rho}}\right], \tag{6.7}$$

where $\mathcal{L}_{31}$, $\mathcal{L}_{32}$, $\mathcal{L}_{34}$, and α depend on the magnetic configuration of a particular plasma equilibrium and $k_{JkeV} = 1.602 \times 10^{-16}$ J/keV.

We investigate the effect that auxiliary heating has on the q profile in the presence of constant auxiliary current drive using the model described in section 2.9 by allowing the plasma to evolve to a stationary state with physical actuator quantities of $I_p = 11$ MA, $P_{ec_1} = P_{ec_2} = P_{ec_3} = 4$ MW (P_{ec_i} denotes the power injected through the individual electron cyclotron sources), $P_{nbi} = 20$ MW (P_{nbi} denotes the total power injected through the neutral beam injectors), and $\bar{n}_e = 7.35 \times 10^{19}$ m^{-3} ($\bar{n}_e$ denotes the line average electron density) under low ion cyclotron heating conditions ($P_{ic} = 5$ MW) and high ion cyclotron heating conditions ($P_{ic} = 20$ MW). Note that the power injected through the ion cyclotron launcher in ITER is constrained to the range $0 \text{ MW} \leq P_{ic} \leq 20$ MW. A comparison of the electron temperature and plasma resistivity before and after the heating power is increased is shown in Figs. 6.1(a-b). The increased heating power raises the electron temperature and lowers the plasma resistivity as expected from (6.4). A comparison of the auxiliary, bootstrap, and toroidal current density before and after the injected heating power into the plasma is increased is shown in Figs. 6.1(c-e). The effect of increasing the electron temperature

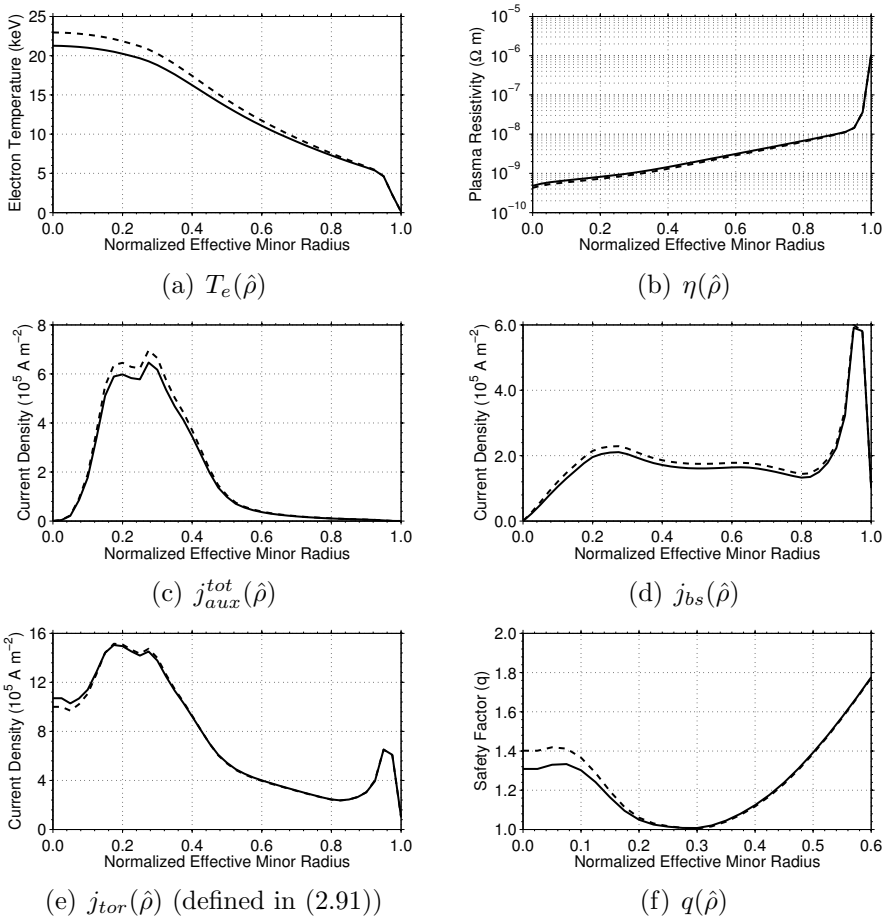

(a) $T_e(\hat{\rho})$ (b) $\eta(\hat{\rho})$

(c) $j_{aux}^{tot}(\hat{\rho})$ (d) $j_{bs}(\hat{\rho})$

(e) $j_{tor}(\hat{\rho})$ (defined in (2.91)) (f) $q(\hat{\rho})$

Figure 6.1: Comparison of stationary state plasma parameters in ITER at $I_p = 11$ MA with $P_{ec_1} = P_{ec_2} = P_{ec_3} = 4$ MW, $P_{nbi} = 20$ MW, $\bar{n}_e = 7.35 \times 10^{19}$ m^{-3}, and $P_{ic} = 5$ MW (solid) and $P_{ic} = 20$ MW (dash): (a) electron temperature, (b) plasma resistivity, (c) auxiliary current density, (d) bootstrap current density, (e) toroidal current density, and (f) q profile.

through plasma heating increases both the auxiliary and bootstrap current drives as expected from (6.6) and (6.7). The decrease in the plasma resistivity and the increases in both off-axis auxiliary co-current-drive and off-axis bootstrap co-current-drive results in the toroidal current density decreasing in the spatial region $\hat{\rho} \in [0, 0.2)$ and slightly increasing in the spatial region $\hat{\rho} \in [0.2, 0.4]$. Note that as the total plasma current remains constant, the increase in off-axis current density requires a corresponding decrease in on-axis current density. The effect this shift in equilibrium

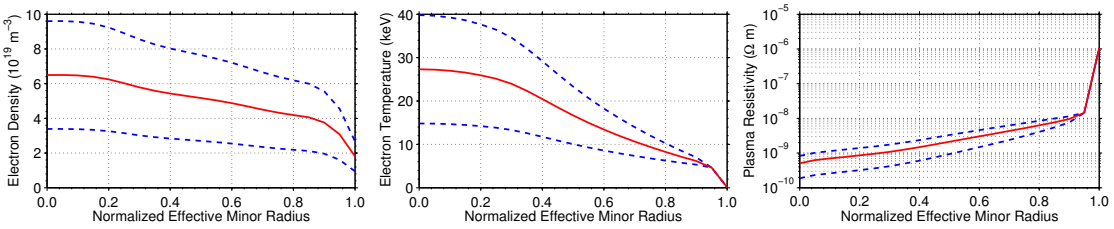

(a) n_e (b) T_e (c) η

Figure 6.2: Plasma parameter uncertainty ranges in ITER H-mode scenarios: (a) electron density, (b) electron temperature, and (c) plasma resistivity. Note: nominal values (solid) and minimum/maximum values (dash).

toroidal current density has on the q profile is shown in Fig. 6.1(f), which shows that pure plasma heating in the considered H-mode scenarios in ITER results in approximately a 5% increase in the q profile in the spatial region $\hat{\rho} \in [0, 0.2]$ with a negligible change outside this spatial region. Therefore, the actuators used for q profile control will attempt to counteract any q profile disturbance that results from plasma heating effects.

6.3 Feedback control design

6.3.1 Partial differential equation model of system dynamics

We begin by defining ranges in which the electron density and temperature profiles are expected to be in typical ITER high performance scenarios, which are shown in Figs. 6.2(a-b). We model these kinetic plasma parameters as a nominal profile plus a bounded uncertain profile, i.e.,

$$n_e(\hat{\rho}, t) = n_e^{nom}(\hat{\rho}) + n_e^{unc}(\hat{\rho})\delta_{n_e}(t), \tag{6.8}$$

$$T_e(\hat{\rho}, t) = T_e^{nom}(\hat{\rho}) + T_e^{unc}(\hat{\rho})\delta_{T_e}(t), \tag{6.9}$$

where the nominal (n_e^{nom}, T_e^{nom}) and uncertain (n_e^{unc}, T_e^{unc}) profiles are defined in terms of the maximum and minimum profiles shown in Figs. 6.2(a-b) and δ_{T_e} and δ_{n_e} are uncertain parameters that satisfy $|\delta_{T_e}| \leq 1$ and $|\delta_{n_e}| \leq 1$. As shown in (6.4), the plasma resistivity is inversely related to the electron temperature, and the resistivity range is shown in Fig. 6.2(c). Additionally, the parameter $1/n_e$ is related to the electron density. These kinetic plasma parameters are modeled as

$$\eta(\hat{\rho},t) = \eta^{nom}(\hat{\rho}) + \eta^{unc}(\hat{\rho})\delta_{T_e}(t), \tag{6.10}$$

$$1/n_e(\hat{\rho},t) = n_e^{nom'}(\hat{\rho}) + n_e^{unc'}(\hat{\rho})\delta_{n_e}(t), \tag{6.11}$$

where the nominal (η^{nom}, $n_e^{nom'}$) and uncertain (η^{unc}, $n_e^{unc'}$) profiles are defined in terms of the maximum and minimum profiles shown in Figs. 6.2(a) and 6.2(c), and the plasma resistivity dependence on the electron temperature is modeled to first order to simplify the control design process.

By combining the poloidal magnetic flux diffusion equation (6.2) with the models of the noninductive current-drive sources (6.5)-(6.7) and the models (6.8)-(6.11), the poloidal magnetic flux profile evolution is given by

$$\begin{aligned}
\frac{\partial \psi}{\partial t} = & \frac{(\eta^{nom} + \eta^{unc}\delta_{T_e})}{\mu_0 \rho_b^2 \hat{F}^2} \frac{1}{\hat{\rho}} \frac{\partial}{\partial \hat{\rho}} \left(\hat{\rho} \hat{F} \hat{G} \hat{H} \frac{\partial \psi}{\partial \hat{\rho}} \right) \\
& + R_0 \hat{H} (\eta^{nom} + \eta^{unc}\delta_{T_e}) \left(T_e^{nom} + T_e^{unc}\delta_{T_e}\right) \left\{ n_e^{nom'} + n_e^{unc'}\delta_{n_e} \right\} \\
& \times \left\{ j_{ec_1}^{ref} P_{ec_1}(t) + j_{ec_2}^{ref} P_{ec_2}(t) + j_{ec_3}^{ref} P_{ec_3}(t) + j_{nbi}^{ref} P_{nbi}(t) \right\} \\
& + \frac{k_{JkeV} R_0^2 \hat{H} (\eta^{nom} + \eta^{unc}\delta_{T_e})}{\hat{F}} \left(\frac{\partial \psi}{\partial \hat{\rho}} \right)^{-1} \\
& \times \Bigg[2\mathcal{L}_{31} \left(T_e^{nom} + T_e^{unc}\delta_{T_e}\right) \frac{\partial}{\partial \hat{\rho}} \left\{ n_e^{nom} + n_e^{unc}\delta_{n_e} \right\} \\
& + \left\{ 2\mathcal{L}_{31} + \mathcal{L}_{32} + \alpha \mathcal{L}_{34} \right\} \left\{ n_e^{nom} + n_e^{unc}\delta_{n_e} \right\} \frac{\partial}{\partial \hat{\rho}} \left\{ T_e^{nom} + T_e^{unc}\delta_{T_e} \right\} \Bigg].
\end{aligned} \tag{6.12}$$

From (6.1), we see that the safety factor profile is related to the spatial gradient of the

poloidal magnetic flux. Therefore, if we are able to control the poloidal flux gradient profile, which we define as

$$\theta(\hat{\rho},t) \equiv \partial\psi/\partial\hat{\rho}(\hat{\rho},t), \tag{6.13}$$

we will be able to control the q profile, assuming the system is indeed controllable. By grouping like terms, expanding (6.12) using the chain rule, inserting (6.13) into this expanded equation, and differentiating the resulting equation with respect to $\hat{\rho}$, the partial differential equation (PDE) governing the evolution of θ is expressed as

$$\begin{aligned}\frac{\partial\theta}{\partial t} = &\left[q_{\eta_1} + q_{\eta_4}\delta_{T_e}\right]\frac{\partial^2\theta}{\partial\hat{\rho}^2} + \left[q_{\eta_2} + q_{\eta_5}\delta_{T_e}\right]\frac{\partial\theta}{\partial\hat{\rho}} + \left[q_{\eta_3} + q_{\eta_6}\delta_{T_e}\right]\theta \\ &+ \sum_i \left[g_i' + h_i'\delta_{n_e} + k_i'\delta_{T_e} + l_i'\delta_{T_e}\delta_{n_e} + m_i'\delta_{T_e}^2 + p_i'\delta_{T_e}^2\delta_{n_e}\right]P_i(t) \\ &- \left[g_{bs} + h_{bs}\delta_{n_e} + k_{bs}\delta_{T_e} + l_{bs}\delta_{T_e}\delta_{n_e} + m_{bs}\delta_{T_e}^2 + p_{bs}\delta_{T_e}^2\delta_{n_e}\right]\left(\frac{1}{\theta}\right)^2\frac{\partial\theta}{\partial\hat{\rho}} \\ &+ \left[g_{bs}' + h_{bs}'\delta_{n_e} + k_{bs}'\delta_{T_e} + l_{bs}'\delta_{T_e}\delta_{n_e} + m_{bs}'\delta_{T_e}^2 + p_{bs}'\delta_{T_e}^2\delta_{n_e}\right]\left(\frac{1}{\theta}\right),\end{aligned} \tag{6.14}$$

with boundary conditions

$$\theta(0,t) = 0 \qquad \theta(1,t) = -k_{I_p}I_p(t), \tag{6.15}$$

where $i \in \{ec_1, ec_2, ec_3, nbi\}$, the parameters $q_{\eta_j}(\hat{\rho})$, for $j = 1,\ldots,6$, $g_i(\hat{\rho})$, $h_i(\hat{\rho})$, $k_i(\hat{\rho})$, $l_i(\hat{\rho})$, $m_i(\hat{\rho})$, $p_i(\hat{\rho})$, $g_{bs}(\hat{\rho})$, $h_{bs}(\hat{\rho})$, $k_{bs}(\hat{\rho})$, $l_{bs}(\hat{\rho})$, $m_{bs}(\hat{\rho})$, $p_{bs}(\hat{\rho})$ are functions of space, and $(\cdot)' = d/d\hat{\rho}(\cdot)$. See section 4.4.1 for an example of how (6.14) is derived. The first-principles-driven model (6.14)-(6.15) contains the physics information of how the control actuators, as well as the uncertain parameters δ_{n_e} and δ_{T_e}, influence the poloidal flux gradient profile dynamics, and the goal is to embed the physics into the feedback controller by converting the physics information into a form suitable to synthesize a feedback controller.

6.3.2 Model reduction via spatial discretization

We next seek a finite dimensional ordinary differential equation (ODE) model of the poloidal magnetic flux gradient profile dynamics to facilitate the synthesis of a feedback controller. An approximate ODE model is obtained by spatially discretizing the governing infinite dimensional PDE (6.14) using a truncated Taylor series expansion while leaving the time domain continuous [137]. The non-dimensional spatial domain of interest ($\hat{\rho} \in [0, 1]$) is represented as m_θ discrete nodes, and the spacing between the nodes ($\Delta\hat{\rho}$) is defined as $\Delta\hat{\rho} = 1/(m_\theta - 1)$. Central finite difference spatial derivative approximations of order $(\Delta\hat{\rho})^2$ are used in the interior node region, $2 \leq i \leq (m_\theta - 1)$. After applying the spatial derivative approximations to (6.14) and taking into account the boundary conditions (6.15), we obtain a nonlinear approximate finite dimensional ODE model defined by

$$\dot{x} = f_\theta(x, u_q, \delta), \tag{6.16}$$

where $x = [\theta_2, \theta_3, \ldots, \theta_{m_\theta - 1}]^T \in \mathbb{R}^{n_\theta}$ is the state vector, θ_i is the value of θ at the discrete spatial nodes, $u_q = [P_{ec_1}, P_{ec_2}, P_{ec_3}, P_{nbi}, I_p]^T \in \mathbb{R}^5$ is the control input vector, $\delta = \left[\delta_{T_e}, \delta_{n_e}, \delta_{T_e}\delta_{n_e}, \delta^2_{T_e}, \delta^2_{T_e}\delta_{n_e}\right] \in \mathbb{R}^5$ is the uncertain parameter vector, $f_\theta \in \mathbb{R}^{n_\theta}$ is a nonlinear function of the model parameters, the system states, the control inputs and the uncertain parameters, $n_\theta = m_\theta - 2$ and

$$\theta_1(t) = 0 \qquad \theta_{m_\theta}(t) = -k_{I_p} I_p(t). \tag{6.17}$$

Let $x_{ff}(t)$, $u_{ff_q}(t)$, and $\delta_{ff}(t)$ be a set of feedforward system trajectories, which satisfy

$$\dot{x}_{ff} = f_\theta(x_{ff}, u_{ff_q}, \delta_{ff}). \tag{6.18}$$

We can obtain a model suitable for tracking control design by defining the perturbation variables $\tilde{x}(t) = x(t) - x_{ff}(t)$ and $u_{fb_q}(t) = u_q(t) - u_{ff_q}(t)$, where $\tilde{x}(t)$ is the

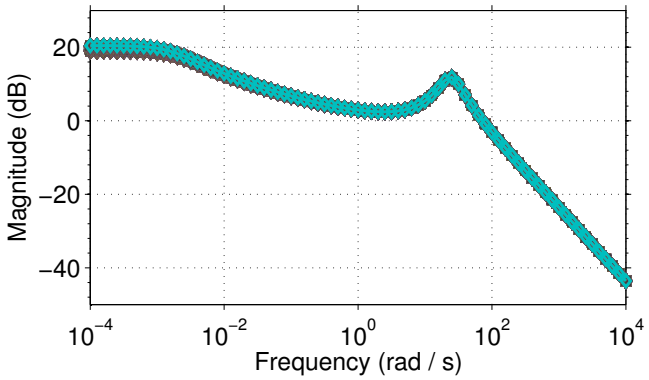

Figure 6.3: Magnitude of maximum singular value versus frequency of the linear model (6.19) along the nonlinear feedforward state and control input trajectories $x_{ff}(t)$ and $u_{ff}(t)$ for $\delta = 0$ and $d_\delta = 0$.

deviation away from the feedforward state trajectories and $u_{fb_q}(t)$ is the output of the to-be-designed feedback controller. Linearizing (6.16) *with respect to the state and control input* and using (6.18), we obtain a *linear time-variant* (LTV) system given by

$$\dot{\tilde{x}} = \left.\frac{\partial f_\theta}{\partial x}\right|_{(x_{ff},u_{ff_q},\delta)} \tilde{x} + \left.\frac{\partial f_\theta}{\partial u_q}\right|_{(x_{ff},u_{ff_q},\delta)} u_{fb_q} + d_\delta, \tag{6.19}$$

where $\partial f_\theta/\partial x \in \mathbb{R}^{n_\theta \times n_\theta}$ and $\partial f_\theta/\partial u_q \in \mathbb{R}^{n_\theta \times 5}$ are the system Jacobians, which depend on the uncertain parameters δ as well as the feedforward state and control input trajectories, and $d_\delta = f_\theta(x_{ff}, u_{ff_q}, \delta) - f_\theta(x_{ff}, u_{ff_q}, \delta_{ff})$. Figure 6.3 shows the maximum singular value versus frequency of the linear model (6.19) along the nonlinear feedforward state and control input trajectories for $\delta = 0$ and $d_\delta = 0$. As shown in the figure, the dynamic response of the system is weakly dependent on the feedforward state and input trajectories. Therefore, we evaluate the Jacobians at a specific feedforward state and input to obtain a linear time-invariant (LTI) model of the deviation dynamics given by

$$\begin{aligned} \dot{\tilde{x}} &= A\tilde{x} + Bu_{fb_q} + d_\delta, \\ y &= C\tilde{x} + Du_{fb_q}, \end{aligned} \tag{6.20}$$

with

$$A = A_0 + \sum_{m=1}^{5} \delta_m A_m \qquad B = B_0 + \sum_{m=1}^{5} \delta_m B_m,$$
$$C = C_0 + \sum_{m=1}^{5} \delta_m C_m \qquad D = D_0 + \sum_{m=1}^{5} \delta_m D_m, \tag{6.21}$$

where A and B are the Jacobians evaluated at a specific feedforward state and control input, A_i and B_i, for $i = 0, \ldots, 5$ are the component matrices of A and B, respectively, C_0 is an $n_\theta \times n_\theta$ identity matrix, $D_0 = 0$, and $C_j = 0$ and $D_j = 0$ for $j = 1, \ldots, 5$. In this chapter, we assume the plasma magnetic state is measurable and available for feedback control. The state-space system (6.20)-(6.21) is referred to as a linear *uncertain* system in the control theory literature, where A_0, B_0, C_0, and D_0 represent the nominal system and A_m, B_m, C_m, and D_m represent the influence each uncertain parameter δ_m has on the system.

6.3.3 Manipulation of dynamic model into robust control framework

The relationship between the inputs and outputs of a linear state-space system is given by the transfer function of the system $G(s)$, i.e., $y = G(s)u_{fb_q}$ where $G(s) = C(sI_{n_\theta} - A)^{-1}B + D$, I_{n_θ} is an $n_\theta \times n_\theta$ identity matrix, and s denotes the Laplace variable. We note that the nominal model will be coupled with the uncertain parameters in the transfer function representation of the uncertain system (6.20)-(6.21). As a result, we group the uncertain parameters into a *block-diagonal structured* uncertainty matrix $\Delta = \text{diag}\{\delta_{T_e}, \delta_{n_e}\}$ and write the system in the conventional $P - \Delta$ control framework (shown in the light purple box in Fig. 6.4) by employing the method outlined in [138], where $P(s)$ is the generalized transfer function of the system, in order to separate the uncertain parameters from the nominal parameters. If the transfer function $P \in$

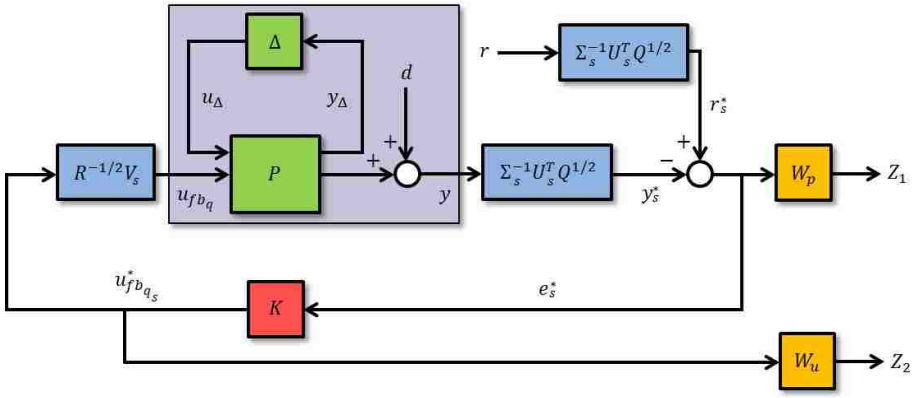

Figure 6.4: Schematic of control problem formulation for θ profile feedback control design in ITER H-mode scenarios. The uncertain state-space system (6.23) is shown in the light purple box. The blocks $\Sigma_s^{-1}U_s^TQ^{1/2}$ and $R^{-1/2}V_s$ are used to obtain a decoupled relationship between the outputs and inputs of the system, which allows us to design a square feedback controller $K \in \mathbb{R}^{k_s \times k_s}$. The outputs of the closed-loop system are defined as $Z_1 = W_p(s)e_s^* \in \mathbb{R}^{k_s}$ and $Z_2 = W_u(s)u^*_{fb_{q_s}} \in \mathbb{R}^{k_s}$, where $W_p \in \mathbb{R}^{k_s \times k_s}$ and $W_u \in \mathbb{R}^{k_s \times k_s}$ are frequency-dependent weight functions.

$\mathbb{R}^{(q_T+n_\theta)\times(q_T+5)}$, where q_T is the rank of the uncertainty matrix Δ, is partitioned as

$$P = \begin{bmatrix} P_{11} & P_{12} \\ P_{21} & P_{22} \end{bmatrix}, \tag{6.22}$$

the input-output equations of the system are

$$\begin{aligned} y_\Delta &= P_{11}u_\Delta + P_{12}u_{fb_q}, \\ y &= P_{21}u_\Delta + P_{22}u_{fb_q} + d, \end{aligned} \tag{6.23}$$

where $P_{11} \in \mathbb{R}^{q_T \times q_T}$, $P_{12} \in \mathbb{R}^{q_T \times 5}$, $P_{21} \in \mathbb{R}^{n_\theta \times q_T}$, $P_{22} \in \mathbb{R}^{n_\theta \times 5}$, $y_\Delta \in \mathbb{R}^{q_T}$, $u_\Delta \in \mathbb{R}^{q_T}$, $y \in \mathbb{R}^{n_\theta}$, $d \in \mathbb{R}^{n_\theta}$, and $u_{fb_q} \in \mathbb{R}^5$. The parameter d represents the effect the disturbance d_δ has on the system outputs. The relationship between the generalized transfer function $P(s)$, the uncertainty matrix Δ and the transfer function $G(s)$ is given by

$$G(s) = P_{22}(s) + P_{21}(s)\Delta\left[I_{q_T} - P_{11}(s)\Delta\right]^{-1}P_{12}(s), \tag{6.24}$$

where I_{q_T} is a $q_T \times q_T$ identity matrix. By examining (6.24), we see the transfer function P_{22} describes the nominal response of the system and the transfer functions P_{11}, P_{12}, and P_{21} describe how the uncertain parameters affect the system. An overview of the employed technique is provided in Appendix A.

6.3.4 Evaluation of relevant control channels

The target plasma state evolution is prescribed by a reference vector $r(t)$ and the control objective is the drive the system output $y(t)$ to the target evolution. Therefore, we define the tracking error $e(t)$ as

$$e(t) = r(t) - y(t). \tag{6.25}$$

As the number of outputs (n_θ) is larger than the number of inputs (5), the conditions to bring the tracking error exactly to zero are typically not met. As a result, only five linear combinations of the output of the system can be independently controlled, and we employ a singular value decomposition (SVD) of the nominal state-space system A_0, B_0, C_0, D_0 at a particular frequency to evaluate and decouple the most relevant input-output control channels. The relationship between the outputs y and inputs u_{fb_q} of the nominal linear state-space system is given by the transfer function of the nominal system which is expressed as $y = G_0(s)u_{fb_q}$, where $G_0(s) = C_0 \left(sI_{n_\theta} - A_0\right)^{-1} B_0 + D_0$ is the nominal transfer function.

The real approximation of the nominal input-output relation at a particular frequency $j\omega_{dc}$ is expressed as

$$\hat{y} = \hat{G}_0 \hat{u}_{fb_q}, \tag{6.26}$$

where $\hat{y}$ denotes the relevant output, $\hat{u}_{fb_q}$ denotes the relevant input, and $\hat{G}_0$ denotes the real approximation of the complex matrix $G_0(j\omega_{dc})$ [10,146]. In order to weight the

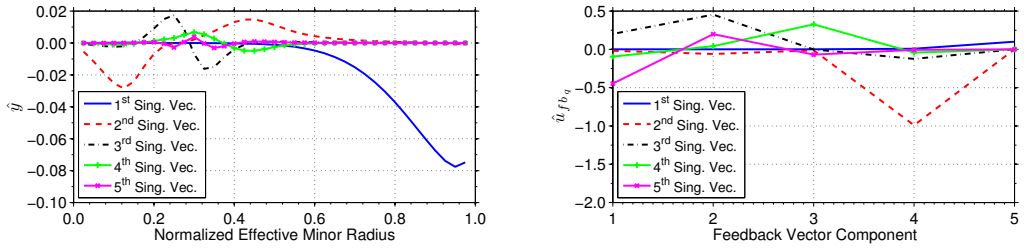

(a) (b)

Figure 6.5: Relevant control channels for θ profile control in ITER H-mode scenarios: (a) output and (b) input. Note the components of the control input vector are defined as $u_q = [P_{ec_1}, P_{ec_2}, P_{ec_3}, P_{nbi}, I_p]$.

tracking performance and control effort, we introduce the positive definite weighting matrices $Q \in \mathbb{R}^{n_\theta \times n_\theta}$ and $R \in \mathbb{R}^{5\times 5}$, and we define the "weighted" transfer function $\tilde{G}_0$ and its economy size singular value decomposition as $\tilde{G}_0 = Q^{1/2}\hat{G}_0 R^{-1/2} = U\Sigma V^T$, where $\Sigma = \text{diag}(\sigma_1, \sigma_2, \sigma_3, \sigma_4, \sigma_5) \in \mathbb{R}^{5\times 5}$ is a diagonal matrix of singular values and $U \in \mathbb{R}^{n_\theta \times 5}$ and $V \in \mathbb{R}^{5\times 5}$ are matrices that possess the following properties $V^T V = VV^T = I, U^T U = I$, where I is a 5×5 identity matrix, and $(\cdot)^T$ denotes the matrix transpose. The input-output relation (6.26) is now expressed as

$$\hat{y} = Q^{-1/2}\tilde{G}_0 R^{1/2}\hat{u}_{fb_q} = Q^{-1/2}U\Sigma V^T R^{1/2}\hat{u}_{fb_q}. \tag{6.27}$$

The singular vectors of the basis for the subspace of obtainable output values ($\hat{y} = Q^{-1/2}U\Sigma\hat{y}^*$), and hence the trackable components of the reference vector $\hat{r}$, as well as the corresponding input singular vectors ($\hat{u}_{fb_q} = R^{-1/2}V\hat{u}^*_{fb_q}$) are shown in Fig. 6.5, where $\hat{y}^*$ and $\hat{u}^*_{fb_q}$ denote the decoupled input and output, respectively, i.e., $\hat{y}^* = \hat{u}^*_{fb_q}$. It is reasonable to consider evaluating the relevant channels at a stationary state, i.e., $\omega_{dc} = 0$ rad/s. Figure 6.6 shows the response of the nominal system $y = G_0(s)u_{fb_q}$ to a 1 MA step input in the total plasma current. As shown in the figure, the response of the system is much slower in the plasma core compared to the response of the system near the plasma boundary. Therefore, evaluating the relevant control channels at a stationary state, i.e., using the total plasma current to control

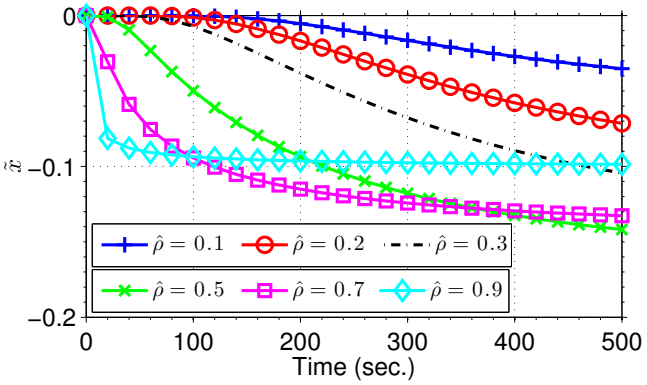

Figure 6.6: Response of the nominal state-space system $y = G_0(s)u_{fb_q}$ to a 1 MA step input in the plasma current. The system response is much faster near the plasma boundary compared to the response in the plasma core.

the q profile across the entire spatial domain, could lead to an undesirable transient closed-loop system response. As a result, we select the frequency as $\omega_{dc} = 10^{-1}$ rad/s, which allows us to utilize the total plasma current to control the q profile near the plasma boundary (1st singular vector in Fig. 6.5) and the gyrotron launchers and the neutral beam injectors to control the q profile near the center of the plasma (2nd singular vector in Fig. 6.5 is related to the neutral beams and the 3rd-5th singular vectors in Fig. 6.5 are related to the gyrotrons). Also, we note that the neutral beam injectors have a broad influence on the q profile while the gyrotron launchers have a more localized effect on the q profile, which is consistent with the noninductive current source profiles shown in Figs. 2.22(f).

As the magnitude of the singular value σ_i decreases, a larger amount of control effort is needed to produce a significant contribution to the profile. To avoid spending a lot of control effort for only a small improvement in the value of the tracking error $\left(\hat{e} = \hat{r} - \hat{y} = Q^{-1/2}U\Sigma(\hat{r}^* - \hat{y}^*)\right)$, where $\hat{r}^* = \Sigma^{-1}U^TQ^{1/2}\hat{r} \in \mathbb{R}^5$ represents the trackable components of the reference, we can partition the singular values into k_s significant singular values Σ_s and $5 - k_s$ negligible singular values Σ_{ns} and define the significant components of the reference, output, and input vectors as $\hat{r}_s^* = \Sigma_s^{-1}U_s^TQ^{1/2}\hat{r} \in \mathbb{R}^{k_s}$, $\hat{y}_s^* = \Sigma_s^{-1}U_s^TQ^{1/2}\hat{y} \in \mathbb{R}^{k_s}$, and $\hat{u}_{fb_{qs}}^* = V_s^TR^{1/2}\hat{u}_{fb_q} \in \mathbb{R}^{k_s}$,

where $U_s \in \mathbb{R}^{n_\theta \times k_s}$ and $V_s \in \mathbb{R}^{5 \times k_s}$ are the components of U and V associated with the significant singular values. A detailed overview of the SVD technique employed to evaluate the relevant control channels is provided in Appendix B.

6.3.5 Integrated feedback control synthesis

The feedback control objectives are to (i) maintain a small tracking error for any external reference input, (ii) reject the effects of any external disturbance input, (iii) utilize as little feedback control effort as possible, and (iv) ensure the closed-loop system remains stable for all allowable perturbations Δ, i.e., the ranges of the kinetic plasma parameters shown in Fig. 6.2, which is referred to as *robust stabilization* of the system in the control theory literature. We aim to achieve these control goals by controlling the relevant input-output channels of the system (6.23). This control problem is shown in Fig. 6.4, where K is the feedback controller, $Z_1 = W_p e_s^*$, $Z_2 = W_u u_{fb_{q_s}}^*$, and W_p and W_u are frequency dependent weight functions used to optimize the closed-loop performance. The nominal performance condition of the closed-loop system is expressed as

$$\begin{bmatrix} Z_1 \\ Z_2 \end{bmatrix} = \begin{bmatrix} W_p S_{DC_O} & -W_p S_{DC_O} \\ W_u K S_{DC_O} & -W_u K S_{DC_O} \end{bmatrix} \begin{bmatrix} r_s^* \\ d_s^* \end{bmatrix} = T_{zw} \begin{bmatrix} r_s^* \\ d_s^* \end{bmatrix}, \tag{6.28}$$

where $S_{DC_O} = (I_{k_s} + \Sigma_s^{-1} U_s^T Q^{1/2} P_{22} R^{-1/2} V_s K)^{-1}$ is the transfer function from the reference signal r_s^* to the error signal e_s^*, the function $K S_{DC_O}$ is the transfer function from the reference signal r_s^* to the feedback control signal $u_{fb_{q_s}}^*$, and $d_s^* = \Sigma_s^{-1} U_s^T Q^{1/2} d$. See section 3.6 for an example of how this nominal performance condition is derived. The frequency dependent weight functions $W_p(s) = \text{diag}\{W_{p_i}\} \in \mathbb{R}^{k_s \times k_s}$ and $W_u(s) = \text{diag}\{W_{u_i}\} \in \mathbb{R}^{k_s \times k_s}$ are used to shape the closed-loop transfer functions and are

parameterized as

$$W_{p_i}(s) = \frac{\left(s/\sqrt{M_{p_i}} + \omega_{p_i}\right)^2}{\left(s + \omega_{p_i}\sqrt{H^*_{p_i}}\right)^2} \qquad W_{u_i}(s) = \frac{\left(s/\sqrt{M_{u_i}} + \omega_{u_i}\right)^2}{\left(s + \omega_{u_i}\sqrt{H^*_{u_i}}\right)^2}, \tag{6.29}$$

where $i = 1, \ldots, k_s$, and M_{p_i}, $H^*_{p_i}$, ω_{p_i}, M_{u_i}, $H^*_{u_i}$, and ω_{u_i} are design parameters. Therefore, to achieve the performance conditions of the nominal closed-loop system, the control problem is formulated as

$$\min_K \left|\left|T_{zw}\right|\right|_\infty, \quad \forall\omega, \tag{6.30}$$

where $||\cdot||_\infty$ denotes the H_∞ norm. See Appendix C for an introduction to the design of feedback controllers by employing the H_∞ closed-loop shaping technique. The feedback controller K found by solving (6.30) is written in state-space form as

$$\begin{aligned} \dot{x}_{fb_q} &= A^*_{fb_q} x_{fb_q} + B^*_{fb_q} e^*_s, \\ u^*_{fb_{q_s}} &= C^*_{fb_q} x_{fb_q} + D^*_{fb_q} e^*_s, \end{aligned} \tag{6.31}$$

where the vector $x_{fb_q} \in \mathbb{R}^{n_{fb_q}}$ is the internal controller states, $A^*_{fb_q} \in \mathbb{R}^{n_{fb_q} \times n_{fb_q}}$, $B^*_{fb_q} \in \mathbb{R}^{n_{fb_q} \times k_s}$, $C^*_{fb_q} \in \mathbb{R}^{k_s \times n_{fb_q}}$, and $D^*_{fb_q} \in \mathbb{R}^{k_s \times k_s}$ are the controller system matrices, and n_{fb_q} is the number of q profile controller states. As the uncertainty has a block-diagonal structure, i.e., $\Delta = \text{diag}\{\delta\}$, we can compute the structured singular value $\mu\big(N_{11}(j\omega)\big)$ to determine the robust stability of the closed-loop system with the nominal controller (6.31), where N_{11} is the transfer function between y_Δ and u_Δ in Fig. 6.4. The closed-loop system is robustly stable for all allowable perturbations if and only if $\mu\big(N_{11}(j\omega)\big) < 1$, $\forall\omega$ [10]. To analyze the performance and robust stability of the closed-loop system, the singular value diagrams of the inverse of the performance weight functions and the achieved transfer functions S_{DC_O} and KS_{DC_O} are shown in Figs. 6.7(a-b) and a plot of μ versus frequency is shown in Fig. 6.7(c).

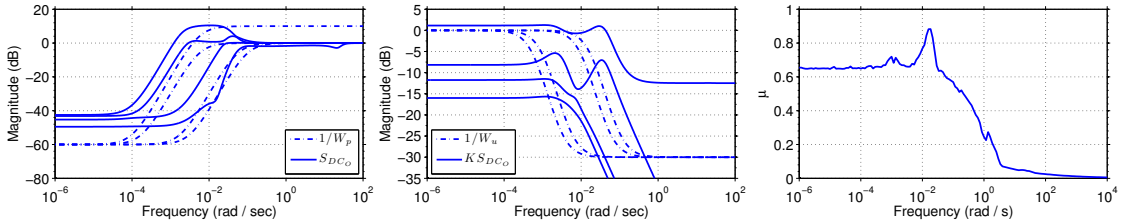

(a) (b) (c)

Figure 6.7: Singular value diagrams: (a) $1/W_p$ (dash-dotted) and S_{DC_o} (solid) and (b) $1/W_u$ (dash-dotted) and KS_{DC_o} (solid), and (c) μ versus frequency.

In the operating scenarios considered in this work, the ion cyclotron launcher is configured to provide only heating power to the plasma. Therefore, we employ the ion cyclotron launcher in a feedforward + feedback scheme, i.e., $P_{ic} = P_{ic_{ff}} + P_{ic_{fb}}$, where $P_{ic_{ff}}$ and $P_{ic_{fb}}$ are the feedforward and feedback components, respectively, to control the plasma stored energy (E). The stored energy feedback controller is expressed in state-space form as

$$\begin{aligned} \dot{x}_{fb_E} &= e_E, \\ P_{ic_{fb}} &= k_{I_{ic}} x_{fb_E} + k_{P_{ic}} e_E, \end{aligned} \tag{6.32}$$

where $x_{fb_E} \in \mathbb{R}^1$ is the internal controller state, $k_{P_{ic}}$ and $k_{I_{ic}}$ are the controller proportional and integral gains, $e_E = E_{tar} - E$ is the error in the stored energy, and E_{tar} is the desired stored energy reference.

6.3.6 Control algorithm structure

A schematic of the closed-loop control system structure is shown in Fig. 6.8. Due to limited actuation capabilities, such as the available amount of auxiliary heating and current-drive power, the integrated feedback control algorithm may drive the actuators to saturation, which could cause undesirable oscillations in the system to develop. Therefore, the feedback algorithm is complemented by and integrated together with

an anti-windup scheme [140] to ensure the closed-loop system remains well-behaved in the presence of actuator magnitude saturation. The anti-windup compensator is designed to keep the total control request

$$u = u_{ff} + u_{fb} + u_{aw}, \tag{6.33}$$

where the components of the control input vector are defined as

$$u = [P_{ec_1}, P_{ec_2}, P_{ec_3}, P_{nbi}, I_p, P_{ic}]^T \in \mathbb{R}^6, \tag{6.34}$$

and u_{aw} is the output of the anti-windup compensator, from significantly deviating from the range of physically achievable actuator values. See section 4.4.6 for an example of the employed anti-windup scheme.

6.4 Simulation testing of integrated feedback control algorithm performance

In this section, we test the integrated feedback control algorithm (6.31) and (6.32) augmented with the anti-windup compensator through simulation with the FPD, physics-based model of the poloidal magnetic flux profile evolution and the volume-averaged energy balance equation described in section 2.9. As the feedback algorithm is designed for the high performance phase of the discharge, all of the simulations are started just after the plasma transitions from the low confinement (L-mode) to the high confinement regime in these particular simulated scenarios during the current ramp-up phase at the time $t_0 = 45$ s. Additionally, in each simulation, the line average electron density evolution is linearly ramped up from an initial value of $\bar{n}_e(t_0) = 2.75 \times 10^{19}$ m^{-3} to a final value of $\bar{n}_e(86) = 7.35 \times 10^{19}$ m^{-3} and then held constant.

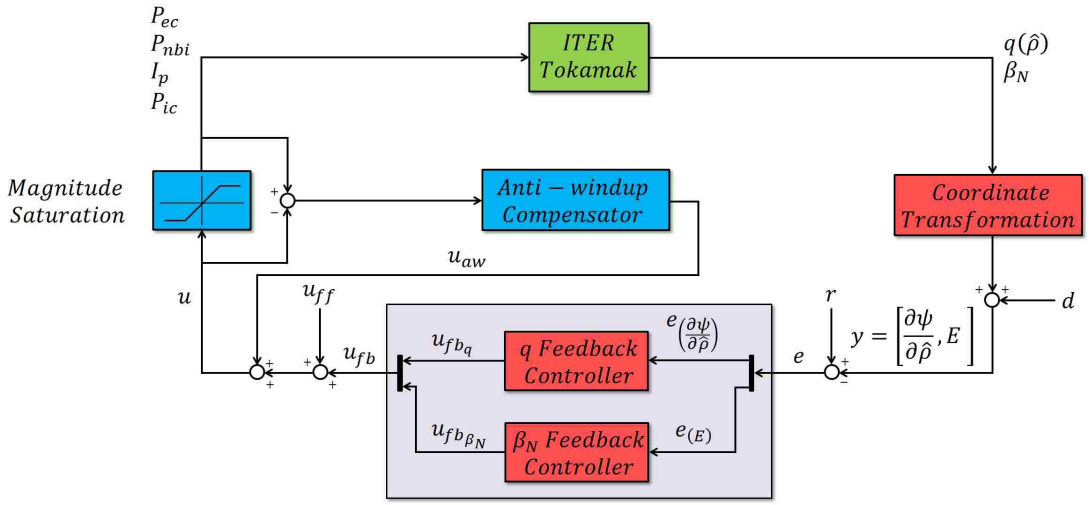

Figure 6.8: Schematic of closed-loop control system structure for simultaneous θ profile + E control for the ITER tokamak.. The coordinate transformation block converts the simulated plasma parameters to the parameters controlled by the feedback controller ($\theta = \partial\psi/\partial\hat{\rho}$ and E). The feedback controller reacts to the tracking error and outputs a feedback control request that drives the system in a direction to minimize the tracking error and reject the effects of any external disturbances. The anti-windup compensator reacts to the difference between the saturated and unsaturated actuator requests and outputs an anti-windup control request that minimizes the effects that actuator saturation has on the closed-loop system performance.

The integrated feedback control algorithm is implemented with a sampling time of 1 s in all of the feedback-controlled simulations, which is on the order of the energy confinement time and significantly smaller than the resistive current diffusion time in ITER. We now test the reference tracking and disturbance rejection capabilities of the feedback control algorithm, respectively. We emphasize the scenarios studied are not meant to be representative of any one specific standard ITER operating scenario but are meant to determine the ability of the feedback control algorithm to drive the plasma state evolution to a specified *physically achievable* target evolution.

6.4.1 Reference tracking

We now describe the setup for a test conducted to determine the reference tracking capabilities of the integrated feedback algorithm. First, a nominal q profile and stored energy evolution ($q_{nom}(\hat{\rho},t)$ and $E_{nom}(t)$) is obtained by executing a feedforward-only simulation with a nominal set of input trajectories (total plasma current, individual gyrotron launcher, ion cyclotron launcher, and neutral beam injection powers) and initial conditions. The final nominal plasma state is characterized by a slightly reversed shear q profile with q_{min} slightly greater than one, a total plasma current of $I_p = 11$ MA, a normalized plasma beta of $\beta_N \approx 2.2$, a fusion power of $P_{fus} \approx 390$ MW, and a total injected auxiliary heating power of $P_{aux}^{inj} = 43$ MW. Second, a perturbed q profile and stored energy evolution ($q_{pert}(\hat{\rho},t)$ and $E_{pert}(t)$) is obtained by executing a feedforward-only simulation with a perturbed set of input trajectories and initial conditions. Finally, the ability of the feedback algorithm to track a target plasma state evolution is determined by executing a feedforward + feedback simulation with the perturbed set of input trajectories and initial conditions. The target q profile and stored energy evolution ($q_{tar}(\hat{\rho},t)$ and $E_{tar}(t)$) is obtained from the nominal evolution as follows: $q_{tar}(\hat{\rho},t) = q_{nom}(\hat{\rho},t)$ during the time interval $t \in [45, 1600]$ s and

$$E_{tar}(t) = \begin{cases} E_{nom}(t) & 45 \text{ to } 1000 \text{ s} \\ 275 \text{ MJ } (\beta_N \approx 2.1, P_{fus} \approx 360 \text{ MW}) & 1000 \text{ to } 1300 \text{ s} \\ 297 \text{ MJ } (\beta_N \approx 2.25, P_{fus} \approx 410 \text{ MW}) & 1300 \text{ to } 1600 \text{ s} \end{cases} . \tag{6.35}$$

This target plasma state evolution provides the opportunity to test the ability of the feedback controller to both track a nominal plasma state evolution ($t \in [45, 1000]$ s)

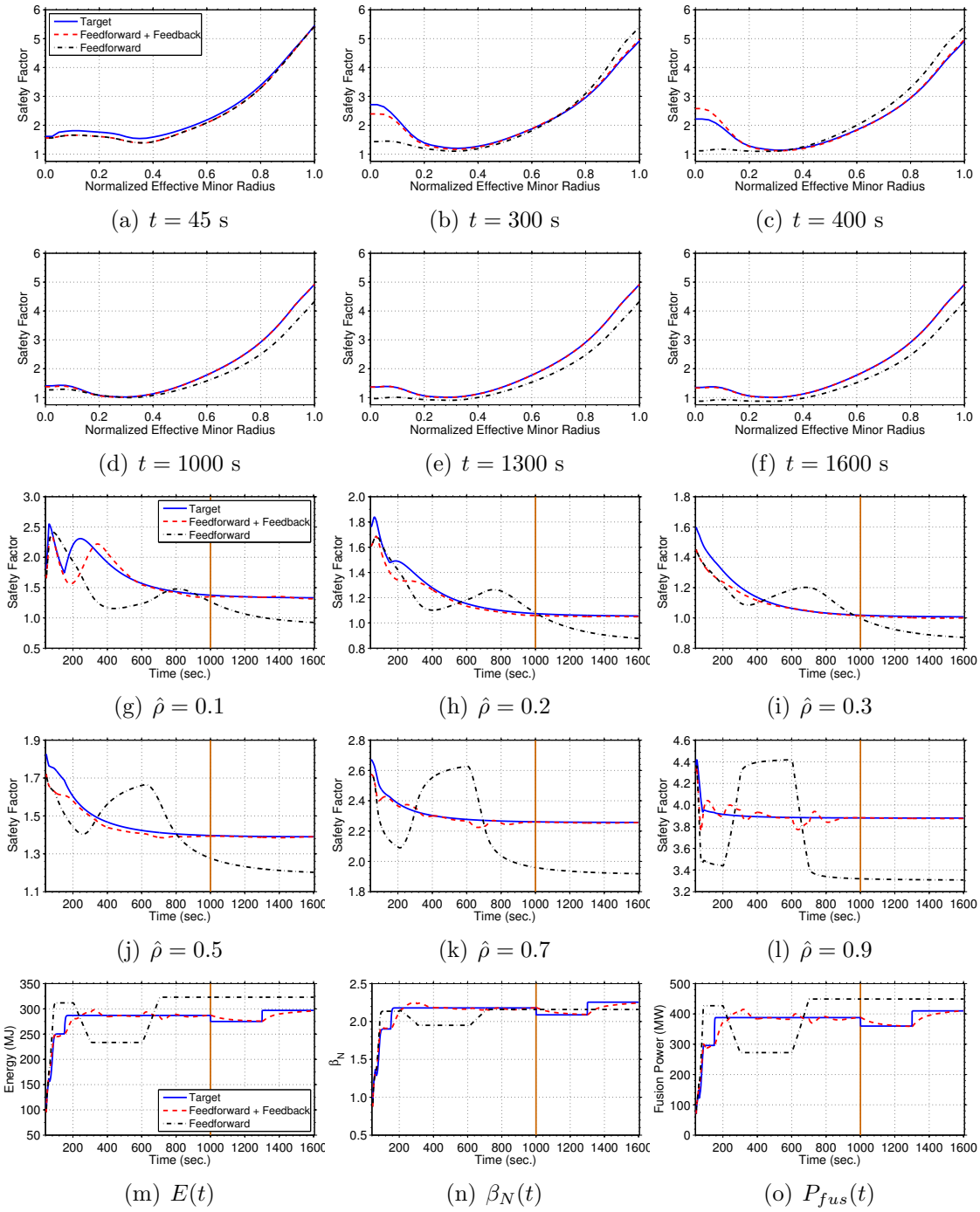

(a) $t = 45$ s (b) $t = 300$ s (c) $t = 400$ s

(d) $t = 1000$ s (e) $t = 1300$ s (f) $t = 1600$ s

(g) $\hat{\rho} = 0.1$ (h) $\hat{\rho} = 0.2$ (i) $\hat{\rho} = 0.3$

(j) $\hat{\rho} = 0.5$ (k) $\hat{\rho} = 0.7$ (l) $\hat{\rho} = 0.9$

(m) $E(t)$ (n) $\beta_N(t)$ (o) $P_{fus}(t)$

Figure 6.9: (a-f) Comparison of target, feedforward + feedback, and feedforward controlled q profiles at various times, (g-l) time traces of q at various radial locations, and (m-o) time traces of plasma stored energy, normalized β, and fusion power for the simulation in section 6.4.1. The solid-orange line denotes when the target q profile is maintained in a stationary condition while modifying the generated fusion power.

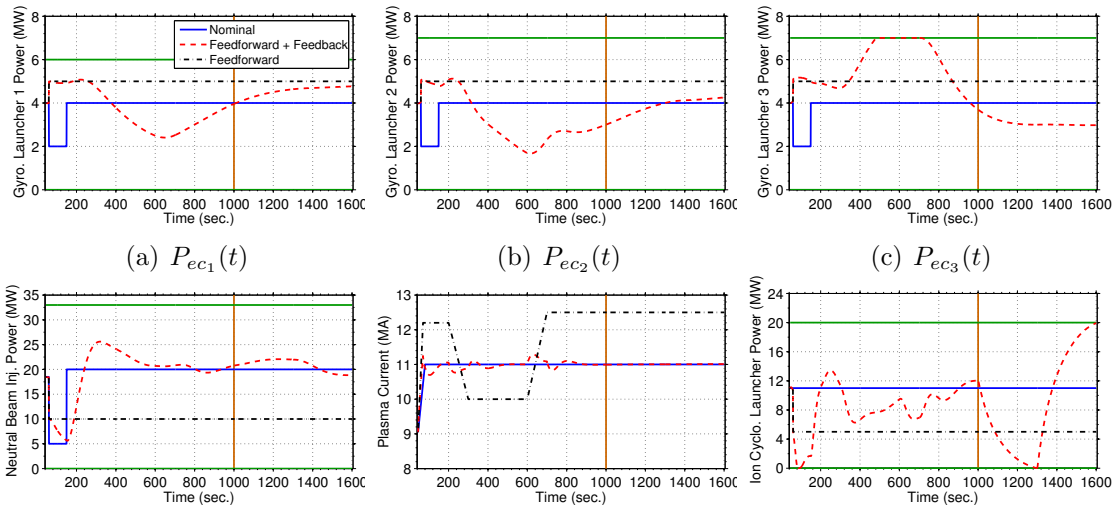

(a) $P_{ec_1}(t)$ (b) $P_{ec_2}(t)$ (c) $P_{ec_3}(t)$

(d) $P_{nbi}(t)$ (e) $I_p(t)$ (f) $P_{ic}(t)$

Figure 6.10: Control actuator trajectory comparison for the simulation in section 6.4.1: (a-c) individual gyrotron launcher powers, (d) neutral beam injection power, (e) total plasma current, and (f) ion cyclotron launcher power. The actuator magnitude limits are shown in solid-green. The solid-orange line denotes the time when the target q profile is maintained in a stationary condition while modifying the generated fusion power.

and maintain a stationary q profile while changing the generated fusion power ($t \in [1000, 1600]$ s).

A comparison of the FPD model predicted target, feedforward + feedback controlled, and feedforward controlled q profiles at various times, time traces of q at various normalized effective minor radii, and a comparison of the target, feedforward + feedback controlled, and feedforward controlled plasma stored energy, normalized beta, and fusion power as a function of time are shown in Fig. 6.9. The control inputs as a function of time are shown in Fig. 6.10. By examining the target plasma state evolution, we see that the time necessary for the plasma to reach an approximately stationary state is about 1000 s. During the feedback-controlled simulation, the initial q profile was lower than the target profile. As shown in the figures, the feedback controller is able to reject the effects of the perturbed initial condition and drive the plasma state evolution to the target evolution during the time interval $t \in [45, 1000]$ s

(nominal phase of simulation), which is not accomplished with feedforward-only control. The controller utilizes the neutral beam launchers and the total plasma current to react quickly to q profile tracking errors in the plasma core and near the plasma boundary, respectively. For example, during the feedback-controlled simulation during the time interval $t \in [150, 300]$ s, the q profile in the plasma core (Fig. 6.9(g)) evolves below the target, and in response, the controller increases the off-axis neutral beam power (Fig. 6.10(d)). Then during the time interval $t \in [300, 600]$ s, the q profile in the plasma core (Fig. 6.9(g)) evolves above the target, and in response, the controller decreases the off-axis neutral beam power (Fig. 6.10(d)). The controller utilizes the gyrotron launchers more subtly to eliminate more localized q profile tracking errors in the plasma core and the ion cyclotron launcher to eliminate plasma stored energy tracking errors. Additionally, the feedback controller is able to drive (i) the q profile to the target evolution with a control time constant of approximately 400 s in the core region of the plasma (roughly $\hat{\rho} \in [0, 0.4]$) and approximately 200 s in the outer region of the plasma (roughly $\hat{\rho} \in [0.4, 1]$), and (ii) the thermal plasma state to the target evolution with a control time constant of approximately 75 s. Finally during the time interval $t \in [1000, 1600]$ s, the controller is able to maintain the target stationary q profile while simultaneously changing the generated fusion power. The total plasma current and gyrotron launcher powers reach stationary values during this phase of the simulation. Therefore, the controller utilizes the neutral beam power to counteract the effect the changing ion cyclotron power (pure plasma heating to track the target thermal plasma state) has on the q profile, i.e., a lower ion cyclotron power results in a lower bootstrap current and a lower total auxiliary current (shown in section 6.2), and as a result a higher neutral beam power is needed to maintain a stationary q profile and vice versa.

6.4.2 Disturbance rejection

We now describe the setup for a test conducted to determine the disturbance rejection capabilities of the integrated feedback algorithm. First, a nominal q profile and stored energy evolution ($q_{nom}(\hat{\rho}, t)$ and $E_{nom}(t)$) is obtained by executing a feedforward-only simulation with a nominal set of input trajectories (total plasma current, individual gyrotron launcher, ion cyclotron launcher, and neutral beam injection powers) and initial conditions. The final nominal plasma state is characterized by a moderately reversed shear q profile with q_{min} slightly greater than one, a total plasma current of $I_p = 10.5$ MA, a normalized plasma beta of $\beta_N \approx 2.3$, a fusion power of $P_{fus} \approx 410$ MW, and a total injected auxiliary heating power of $P_{aux}^{inj} = 62$ MW. Second, a perturbed q profile and stored energy evolution ($q_{pert}(\hat{\rho}, t)$ and $E_{pert}(t)$) is obtained by executing a feedforward-only simulation with a perturbed set of input trajectories and initial conditions. Finally, the ability of the algorithm to track a target plasma state evolution is determined by executing a feedforward + feedback simulation with the perturbed set of input trajectories and initial conditions. The target q profile and stored energy evolution ($q_{tar}(\hat{\rho}, t)$ and $E_{tar}(t)$) is obtained from the nominal evolution as follows: $q_{tar}(\hat{\rho}, t) = q_{nom}(\hat{\rho}, t)$ during the time interval $t \in [45, 1600]$ s and

$$E_{tar}(t) = \begin{cases} E_{nom}(t) & 45 \text{ to } 1000 \text{ s} \\ 275 \text{ MJ } (\beta_N \approx 2.2, P_{fus} \approx 370 \text{ MW}) & 1000 \text{ to } 1300 \text{ s} \\ 297 \text{ MJ } (\beta_N \approx 2.35, P_{fus} \approx 420 \text{ MW}) & 1300 \text{ to } 1600 \text{ s} \end{cases} . \tag{6.36}$$

This target plasma state evolution provides the opportunity to test the ability of the feedback controller to both track a different nominal plasma state evolution ($t \in [45, 1000]$ s) and maintain a different stationary q profile while changing the generated fusion power ($t \in [1000, 1600]$ s). During the feedback-controlled simulation, the

feedback controller is turned on and off during the simulation according to

$$u_{fb} = \begin{cases} 45 \text{ to } 300 \text{ s} & \text{ON} \\ 300 \text{ to } 500 \text{ s} & \text{OFF} \\ 500 \text{ to } 1600 \text{ s} & \text{ON} \end{cases}, \tag{6.37}$$

to see the effect the disturbance has on the plasma state evolution and to determine the ability of the feedback controller to reject the disturbance and regulate the plasma state evolution around the target trajectories.

A comparison of the FPD model predicted target, feedforward + feedback controlled, and feedforward controlled q profiles at various times, time traces of q at various normalized effective minor radii, and a comparison of the target, feedforward + feedback controlled, and feedforward controlled plasma stored energy, normalized beta, and fusion power as a function of time are shown in Fig. 6.11. The control inputs as a function of time are shown in Fig. 6.12. By examining the target plasma state evolution, we see that the time necessary for the plasma to reach an approximately stationary state is again about 1000 s. During the feedback-controlled simulation, the initial q profile was higher than the target profile. As shown in the figures, the feedback controller is able to reject the effects of the perturbed initial condition and drive the q profile and plasma stored energy evolutions towards the desired target evolutions before the feedback controller is turned off at 300 s. During the time interval when the feedback controller is off in the feedback-controlled simulation ($t \in [300, 500]$ s), the plasma state evolves away from the target evolution towards the feedforward-only-controlled plasma state evolution. Once the feedback controller is turned on again at 500 s, it is once again able to drive the plasma state evolution towards the target evolution, which is not accomplished with feedforward-only control. The controller utilizes the actuators to control the plasma state in the same manner as observed in section 6.4.1, i.e., the neutral beam launchers and total

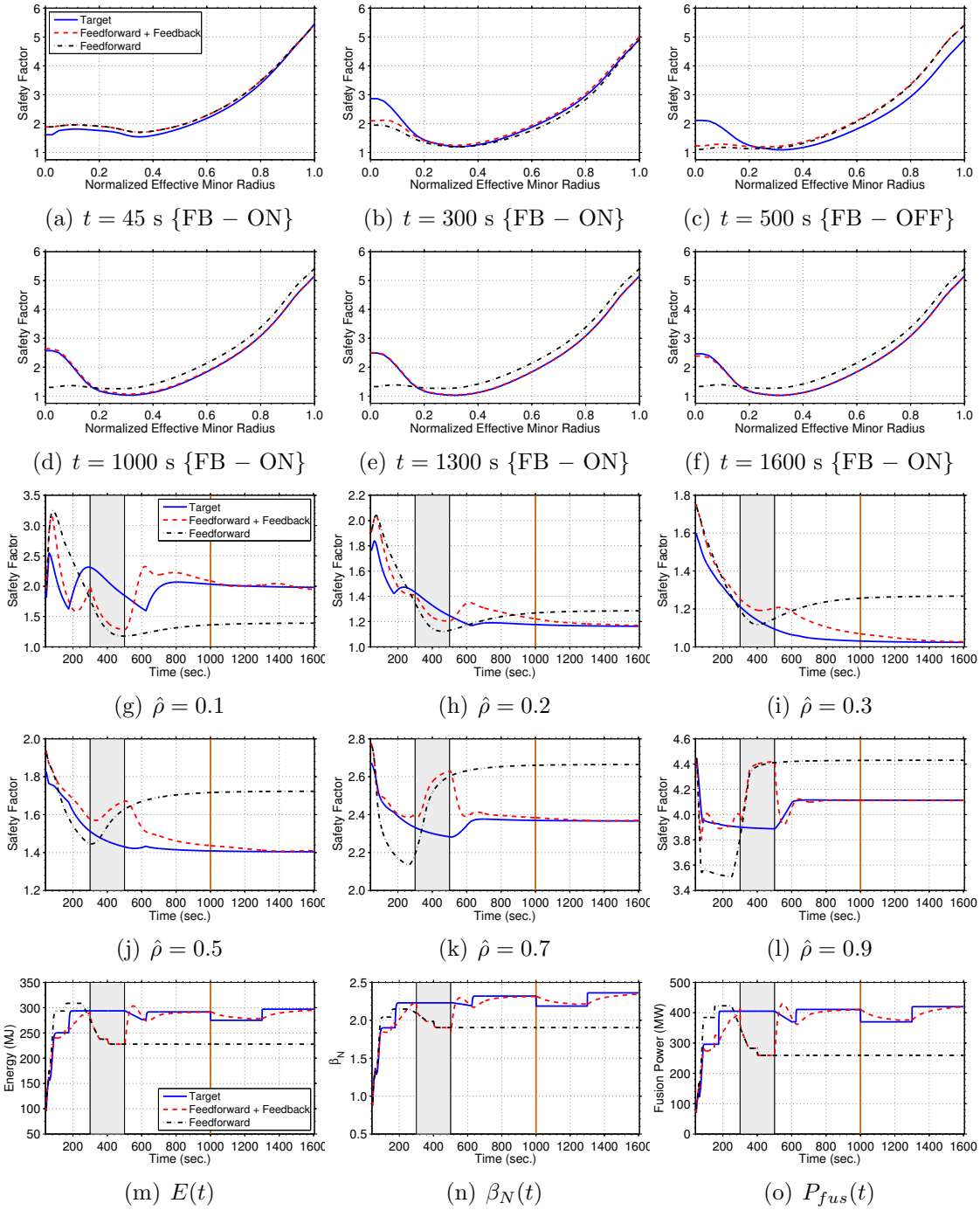

(a) $t = 45$ s {FB − ON} (b) $t = 300$ s {FB − ON} (c) $t = 500$ s {FB − OFF}

(d) $t = 1000$ s {FB − ON} (e) $t = 1300$ s {FB − ON} (f) $t = 1600$ s {FB − ON}

(g) $\hat{\rho} = 0.1$ (h) $\hat{\rho} = 0.2$ (i) $\hat{\rho} = 0.3$

(j) $\hat{\rho} = 0.5$ (k) $\hat{\rho} = 0.7$ (l) $\hat{\rho} = 0.9$

(m) $E(t)$ (n) $\beta_N(t)$ (o) $P_{fus}(t)$

Figure 6.11: (a-f) Comparison of target, feedforward + feedback, and feedforward controlled q profiles at various times, (g-l) time traces of q at various radial locations, and (m-o) time traces of plasma stored energy, normalized β, and fusion power for the simulation in section 6.4.2. The shaded gray region denotes when the feedback controller is not active. The solid-orange line denotes when the target q profile is maintained in a stationary condition while modifying the generated fusion power.

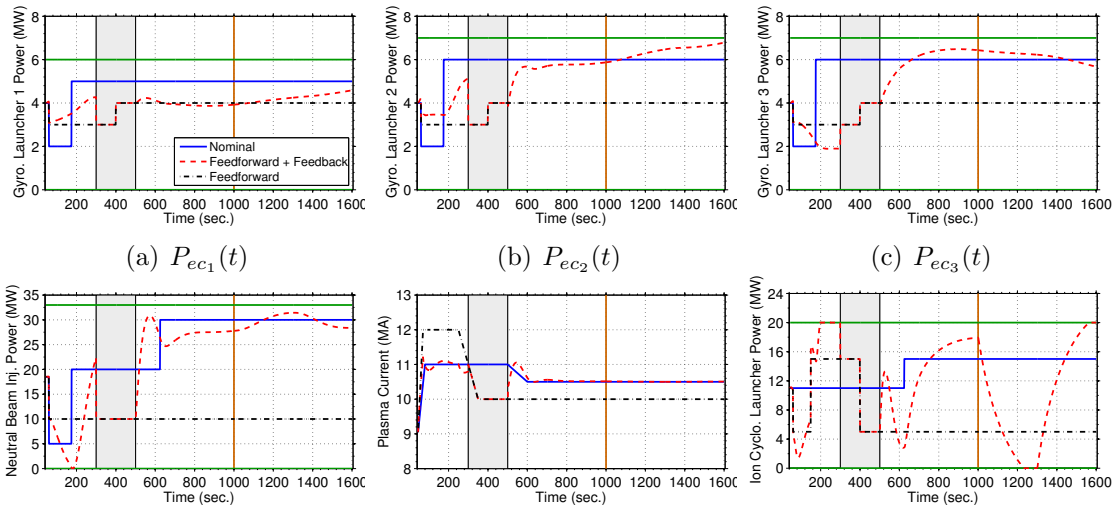

(a) $P_{ec_1}(t)$ (b) $P_{ec_2}(t)$ (c) $P_{ec_3}(t)$

(d) $P_{nbi}(t)$ (e) $I_p(t)$ (f) $P_{ic}(t)$

Figure 6.12: Control actuator trajectory comparison for the simulation in section 6.4.2: (a-c) individual gyrotron launcher powers, (d) neutral beam injection power, (e) total plasma current, and (f) ion cyclotron launcher power. The shaded gray region denotes when the feedback controller is not active. The actuator magnitude limits are shown in solid-green. The solid-orange line denotes the time when the target q profile is maintained in a stationary condition while modifying the generated fusion power.

plasma current to react quickly to q profile tracking errors in the plasma core and near the plasma boundary, respectively, the gyrotron launchers more subtly to eliminate localized q profile tracking errors in the plasma core, and the ion cyclotron launcher to eliminate plasma stored energy tracking errors. Additionally, the feedback controller is able to drive the plasma state to the target evolution with approximately the same control time constants observed in section 6.4.1. Finally, during the time interval $t \in [1000, 1600]$ s, the controller is able to maintain the target stationary q profile while simultaneously changing the generated fusion power in the same manner as observed in section 6.4.1.

6.5 Conclusion

An integrated model-based feedback control algorithm was designed to track target q profile and stored energy evolutions in H-mode burning plasma scenarios in ITER. The feedback controller was designed by embedding a FPD model of the plasma magnetic profile evolution into the control design process and to be *robust* to uncertainties in the electron density, electron temperature, and plasma resistivity profiles, which provides some additional confidence the algorithm can maintain closed-loop system stability in a variety of operating conditions. Additionally, the feedback controller is a computationally robust and efficient algorithm as it can be computed by a simple matrix multiplication of the controller matrices with the respective tracking errors, which is also advantageous for application in ITER from a computational point-of-view relative to other profile control algorithms that require real-time computation of various plasma profiles [107]. The feedback control algorithm was then successfully tested in reference tracking and disturbance rejection simulations with the FPD model of the plasma magnetic profile and stored energy evolution developed in chapter 2. The demonstrated ability of the feedback controller to (i) drive the system to multiple different operating points and (ii) maintain the q profile at a stationary target (to maintain plasma stability) while modulating the thermal state of the plasma (to respond to changing power demand) is an essential capability that will be needed for ITER, and eventually a commercial, power producing tokamak reactor.

As shown by the feedback-controlled simulations, the feedback controller augmented with the anti-windup compensator is able to drive the q profile and plasma stored energy to the target evolutions during both the transient and stationary-state phases of the simulations. The feedback control algorithm uses (i) the gyrotron launchers and the neutral beam injectors to control the q profile near the center of the plasma and the total plasma current to control the q profile near the plasma

boundary, as well as account for the effects the ion cyclotron launcher has on the electron temperature profile, which couples to the q profile evolution through the plasma resistivity, the auxiliary current-drive efficiency, and the bootstrap current drive, and (ii) the ion cyclotron launcher to control, and account for the effects the other actuators have on, the stored energy evolution. The integrated feedback control algorithm could be implemented in existing tokamak experiments by interfacing it with real-time measurements of the q profile and stored energy, respectively. These quantities can be obtained from a real-time Grad-Shafranov equation solver, such as real-time EFIT [11]. An example of how these measurements can be interfaced with the feedback controller can be found in chapter 3. Additionally, the control algorithm designed in this work represents a second layer of control in the overall scheme utilized to control the tokamak plasma, i.e., the actuator requests generated by the controller represent the reference values to the dedicated control loops commanding the physical actuators. Therefore, the control algorithm would also need to be interfaced with the dedicated control loops, for example a dedicated poloidal field coil controller that is designed to track a desired total plasma current request.

The time necessary for the plasma to reach an approximately stationary state in the simulations is about 1000 s, which represents a significant portion of (or even greater than in some cases) the total discharge length for many of the proposed ITER scenarios [148]. Therefore, active feedback control of the q profile evolution will be crucial to reject the effects any external disturbances have on the plasma evolution, maintain the plasma in a stable magnetohydrodynamic state, and maximize the plasma performance in ITER. As demonstrated, the feedback controller is able to drive the q profile to the target evolution in approximately 400 s in the plasma core and approximately 200 s in the outer region of the plasma, which represents a reasonable control time constant relative to the time necessary to reach a stationary plasma state. In the scenarios considered in this work, the auxiliary current-drive sources

(gyrotron and neutral beam launchers) are configured to inject power into the plasma away from the magnetic axis as shown in Fig. 2.22(f). Therefore, there is no direct way to control the q profile near the magnetic axis, which consequently contributes to the longer control time constant in the core region of the plasma relative to the outer region. Configuring the neutral beam launchers to inject power into the plasma both on-and-off axis would allow the q profile feedback controller to moderate the relative location of the noninductively-driven current in the plasma. This additional degree of control freedom may possibly allow for tighter control of the q profile, as well as reduce the control time constant, in the core region of the plasma.

As the q profile portion of the integrated feedback controller is designed to be robust to a range of kinetic plasma parameters, detailed real-time knowledge of these kinetic plasma profile evolutions may not be needed to actively control the q profile evolution, which is also advantageous for application in ITER and future reactors by requiring a smaller number of real-time diagnostics relative to other profile control algorithms [91, 93, 107]. Therefore, a separate dedicated control algorithm to control the thermal state of the plasma can be integrated together with the q profile feedback controller, as long as the electron density, electron temperature, and plasma resistivity profiles remain inside the ranges for which the q profile feedback controller ensures the closed-loop system remains stable. In this work, a proportional-integral feedback controller that utilizes the ion cyclotron launcher was designed to control the plasma stored energy evolution. However, if the ion cyclotron power request is driven to saturation by the feedback controller, the thermal state of the plasma is no longer controllable using this lone actuator. A subject of future work will be to (i) interface the q profile controller with a nonlinear burn controller [4] that utilizes not only auxiliary heating, but also the concept of isotopic fuel tailoring [149] and impurity injection to control the thermal state of the plasma, and (ii) test the control algorithms in closed-loop simulations with DINA-CH&CRONOS [5–9].

Finally, we have investigated many key practical issues for plasma profile control in ITER, which will be useful for the development of the ITER Plasma Control System that has recently been initiated. One of the more critical issues is whether plasma control can be achieved through the integration of separate individual control algorithms or whether a more fully integrated approach is required. As shown in the feedback-controlled simulations, it appears the integration of separate controllers may be able to achieve the plasma control performance requirements in ITER as long as the algorithms are *robust* to changes in the plasma parameters they are not specifically designed to control, and the target plasma state is *physically achievable*.

Chapter 7

Closed-loop control of the safety factor profile in the TCV tokamak

7.1 Introduction

In this chapter, feedback algorithms for safety factor profile (q profile) control in low confinement (L-mode) scenarios in the TCV tokamak are synthesized by embedding a first-principles-driven (FPD), physics-based model of the plasma dynamics into the control design process. As the current diffusion time constant in TCV (approximately 150 milliseconds in the scenarios studied) is much shorter than the plasma discharge length (approximately 2 seconds), TCV is an ideal machine to study the ability to actively control the q profile in tokamaks. The total plasma current, the auxiliary heating and current-drive (H&CD) system, and the line average electron density are the actuators that can be utilized to control the q profile in tokamaks. In this chapter, we first investigate the effect that the control input direction associated with pure plasma heating has on the q profile in L-mode operating scenarios in the TCV tokamak by utilizing the RAPTOR code [13–15]. This study indicates that pure auxiliary heating has a small effect on the q profile in the examined scenarios. Therefore, we

design feedback controllers that utilize the total plasma current, and exclusively the current-drive capabilities of the auxiliary sources, to control the q profile in TCV. The controllers are designed to put emphasis on achieving the target q profile in different spatial regions, to respond differently to errors in the q profile, and to be robust to uncertainties in the plasma electron temperature and plasma resistivity profiles. The performance of each controller is tested though simulations with the RAPTOR code, where the ability of each controller to track multiple different target profiles is demonstrated. The comparison of the closed-loop performance of these controllers is done in preparation for future q profile control experiments in TCV.

This chapter is organized as follows. In section 7.2, the effect that pure plasma heating has on the q profile is investigated. The feedback control problem formulation is presented in section 7.3. Three feedback controllers are designed, where the emphasis is placed on achieving the target in only the plasma core or both in the plasma core and near the plasma boundary. Additionally, the controllers are designed to either utilize the available actuators to control the q profile across the entire spatial domain or to utilize the auxiliary current drive actuators to control the q profile in the plasma core and the total plasma current to control the q profile near the plasma boundary. In section 7.4, the feedback controllers are tested in one target and two target simulations with the RAPTOR code. Finally, conclusions are discussed in section 7.5.

7.2 Plasma heating effect on the safety factor profile

The evolution of the poloidal magnetic flux in a tokamak plasma is given by the magnetic diffusion equation (2.45) and is restated here for convenience as

$$\frac{\partial \psi}{\partial t} = \frac{\eta(T_e)}{\mu_0 \rho_b^2 \hat{F}^2} \frac{1}{\hat{\rho}} \frac{\partial}{\partial \hat{\rho}} \left(\hat{\rho} \hat{F} \hat{G} \hat{H} \frac{\partial \psi}{\partial \hat{\rho}} \right) + R_0 \hat{H} \eta(T_e) j_{ni}, \tag{7.1}$$

with boundary conditions

$$\frac{\partial \psi}{\partial \hat{\rho}}(0,t) = 0 \qquad \frac{\partial \psi}{\partial \hat{\rho}}(1,t) = -k_{I_p} I_p(t), \tag{7.2}$$

where ψ is the poloidal stream function, which is closely related to the poloidal magnetic flux Ψ ($\Psi = 2\pi\psi$), t is the time, η is the plasma resistivity, T_e is the electron temperature, μ_0 is the vacuum magnetic permeability, j_{ni} is the total noninductive current density, k_{I_p} is a geometric constant defined in (2.83), and I_p is the total plasma current. The spatial coordinate $\hat{\rho} = \rho/\rho_b$ is used to index the magnetic flux surfaces in the plasma, where ρ is the mean effective minor radius of a magnetic flux surface, i.e., $\Phi(\rho) = \pi B_{\phi,0} \rho^2$, Φ is the toroidal magnetic flux, $B_{\phi,0}$ is the vacuum toroidal magnetic field at the geometric major radius R_0 of the tokamak, and ρ_b is the mean effective minor radius the last closed magnetic flux surface. The parameters $\hat{F}$, $\hat{G}$, and $\hat{H}$ are geometric spatial factors pertaining to the magnetic configuration of a particular plasma equilibrium (defined in (2.44)). The q profile is related to the poloidal magnetic flux and is defined in (2.90) and repeated here for convenience as

$$q(\hat{\rho},t) = -\frac{d\Phi}{d\Psi} = -\frac{B_{\phi,0} \rho_b^2 \hat{\rho}}{\partial \psi / \partial \hat{\rho}}. \tag{7.3}$$

In the development of the RAPTOR code [13–15], the magnetic diffusion equation

(7.1) is combined with physics-based models of varying degrees of complexity for the electron density, the electron temperature, the plasma resistivity, and the noninductive current sources to yield a model of the q profile dynamics suitable for control design. To illustrate the effect that the electron temperature, and hence pure plasma heating, has on these plasma properties, we briefly describe the physics-based models. The plasma resistivity scales inversely with the electron temperature as

$$\eta(\hat{\rho},t) \propto T_e(\hat{\rho},t)^{-3/2}. \tag{7.4}$$

The total noninductive current is generated by the auxiliary sources and the bootstrap current (a self-generated noninductive source of plasma current) [60], i.e.,

$$j_{ni}(\hat{\rho},t) = j_{aux}^{tot}(\hat{\rho},t) + j_{bs}(\hat{\rho},t) = \sum_{i=1}^{n_{aux}} j_{aux,i}(\hat{\rho},t) + j_{bs}(\hat{\rho},t), \tag{7.5}$$

where j_{aux}^{tot} is the total current density driven by the auxiliary sources, j_{bs} is the current density driven by the bootstrap current, $j_{aux,i}$ is the current density driven by the individual auxiliary sources, and n_{aux} is the number of auxiliary sources. The individual auxiliary current drives are modeled as

$$j_{aux,i}(\hat{\rho},t) = j_{aux,i}^{ref}(\hat{\rho}) \frac{T_e(\hat{\rho},t)}{n_e(\hat{\rho},t)} P_{aux,i}(t), \tag{7.6}$$

where $j_{aux,i}^{ref}$ is a normalized reference deposition profile for the i-th auxiliary source, the term T_e/n_e represents the current-drive efficiency, n_e is the electron density, and $P_{aux,i}$ is the i-th auxiliary power. The bootstrap current arises from the plasma radial pressure gradient that is produced by the magnetic confinement and is modeled as [134, 135]

$$j_{bs}(\hat{\rho},t) = \frac{k_{JkeV} R_0}{\hat{F}} \left(\frac{\partial \psi}{\partial \hat{\rho}} \right)^{-1} \left[2\mathcal{L}_{31} T_e \frac{\partial n_e}{\partial \hat{\rho}} + \{ 2\mathcal{L}_{31} + \mathcal{L}_{32} + \alpha \mathcal{L}_{34} \} n_e \frac{\partial T_e}{\partial \hat{\rho}} \right], \tag{7.7}$$

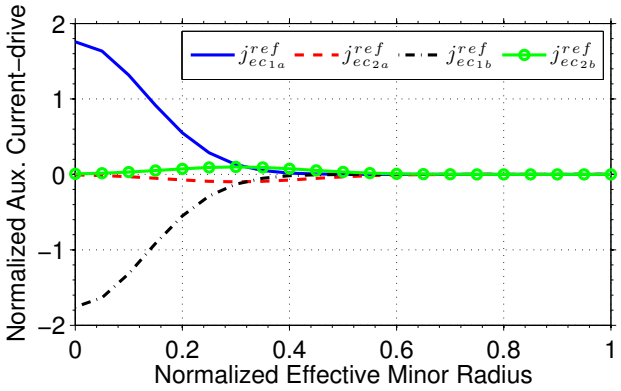

Figure 7.1: Normalized auxiliary current drive $\left(10^{20}\ \frac{\mathrm{m}^{-3}}{\mathrm{keV{\cdot}W}} \cdot \frac{\mathrm{A}}{\mathrm{m}^2}\right)$ in TCV.

where $\mathcal{L}_{31}$, $\mathcal{L}_{32}$, $\mathcal{L}_{34}$ and α depend on the magnetic configuration of a particular plasma equilibrium, $k_{JkeV} = 1.602 \times 10^{-16}$ J/keV, and we have assumed the electron and ion densities and temperatures, respectively, are equal.

The auxiliary H&CD actuators on TCV considered in this work are 4 electron cyclotron (gyrotron) launchers that are grouped into 2 clusters (denoted as a and b). The normalized reference current deposition profiles for each source are shown in Fig. 7.1. The gyrotrons in cluster a are: 1 on-axis co-current-injection source ($j^{ref}_{ec_{1a}}$ in Fig. 7.1) and 1 off-axis counter-current-injection source ($j^{ref}_{ec_{2a}}$ in Fig 7.1). The gyrotrons in cluster b are: 1 on-axis counter-current-injection source ($j^{ref}_{ec_{1b}}$ in Fig. 7.1) and 1 off-axis co-current-injection source ($j^{ref}_{ec_{2b}}$ in Fig. 7.1). As a result, there are two limiting auxiliary H&CD conditions that can be achieved with this configuration. The first condition is related to plasma heating power (P^h_{aux}) and is associated with the sum of the powers injected through the gyrotron clusters, i.e., $P^h_{aux} = 2(P_{ec_a} + P_{ec_b})$. The second condition is related to plasma current-drive power (P^{cd}_{aux}) and is associated with the difference of the powers injected through the gyrotron clusters, i.e., $P^{cd}_{aux} = P_{ec_a} - P_{ec_b}$. Note that if $P_{ec_a} = P_{ec_b}$, the auxiliary current drive would be zero as $j^{ref}_{ec_{1b}} = -j^{ref}_{ec_{1a}}$ and $j^{ref}_{ec_{2b}} = -j^{ref}_{ec_{2a}}$, i.e., pure plasma heating. If this change of coordinates is employed, the total auxiliary current drive

would be expressed as

$$j_{aux}^{tot}(\hat{\rho},t) = \left(j_{ec_{1a}}^{ref}(\hat{\rho}) + j_{ec_{2a}}^{ref}(\hat{\rho})\right)\frac{T_e(\hat{\rho},t)}{n_e(\hat{\rho},t)}P_{aux}^{cd}(t). \tag{7.8}$$

7.2.1 Auxiliary heating in presence of auxiliary current drive

We investigate the effect that auxiliary heating has on the q profile in the presence of constant auxiliary current drive using RAPTOR by allowing the plasma to evolve to a stationary state with a constant current-drive power $P_{aux}^{cd} = -0.1$ MW under moderate heating conditions ($P_{aux}^{h} = 1.0$ MW) and high heating conditions ($P_{aux}^{h} = 1.6$ MW) at two values of plasma current, $I_p = 140$ kA and $I_p = 185$ kA, respectively. The power injected through either of the clusters in TCV is constrained to the range $0.2 \text{ MW} \leq P_{ec_i} \leq 0.45$ MW, for $i \in$ [a,b]. A comparison of the electron temperature and plasma resistivity before and after the heating power is increased is shown in Figs. 7.2(a-b). The increased heating power raises the electron temperature (Fig. 7.2(a)) and lowers the plasma resistivity (Fig. 7.2(b)) at both values of total plasma current as expected from (7.4). A comparison of the auxiliary and bootstrap current densities before and after the heating power is increased is shown in Figs. 7.2(c-d). At both values of total plasma current, increasing the electron temperature through heating increases (in magnitude) both the auxiliary (Fig. 7.2(c)) and bootstrap (Fig. 7.2(d)) current drives as expected from (7.6)-(7.7). The increases in both on-axis auxiliary counter-current-drive (in negative direction) and off-axis bootstrap co-current-drive (in positive direction), and decrease in the plasma resistivity, results in the toroidal current density (Fig. 7.2(e)) decreasing in the spatial region $\hat{\rho} \in [0, 0.2]$. The effect that this shift in equilibrium toroidal current density has on the q profile is shown in Fig. 7.2(f), which shows the inverse relationship that exists between the current density and the q profile. From Fig. 7.2(f), we see that auxiliary heating in the presence of constant auxiliary current drive results in approximately a 5% increase

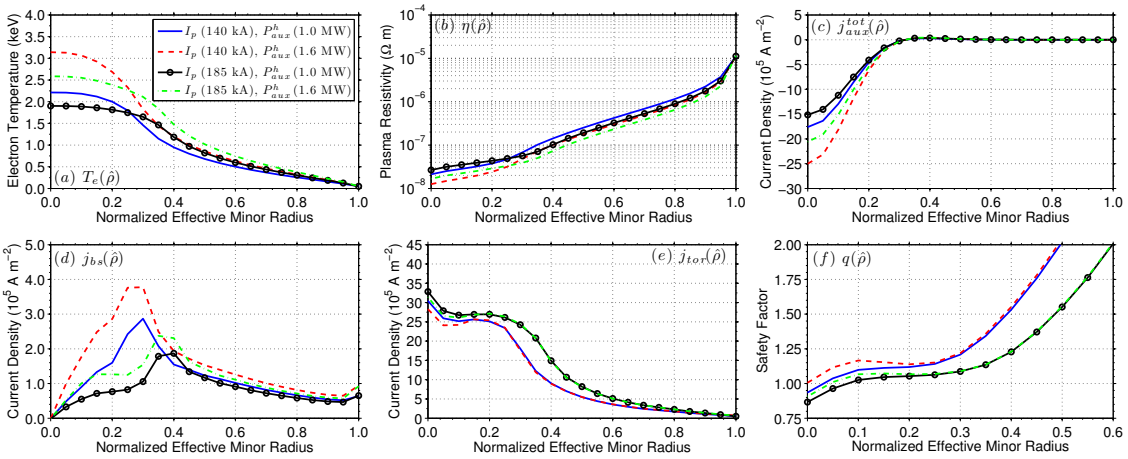

Figure 7.2: Comparison of stationary state plasma parameters under low and high plasma heating conditions with $P^{cd}_{aux} = -0.1$ MW.

in the q profile in the region $\hat{\rho} \in [0, 0.2]$ with a negligible change outside this spatial region. This is also the region where the auxiliary current drive has increased in magnitude (Fig. 7.2(c)).

7.2.2 Auxiliary heating in absence of auxiliary current drive

To study the relative importance of the current drive mechanisms (auxiliary and bootstrap), we investigate the effect that auxiliary heating has on the q profile in the absence of auxiliary current drive using RAPTOR by allowing the plasma to evolve to a stationary state with no current drive power $P^{cd}_{aux} = 0$ MW under low heating conditions ($P^h_{aux} = 0.8$ MW) and high heating conditions ($P^h_{aux} = 1.8$ MW) at two values of plasma current, $I_p = 140$ kA and $I_p = 185$ kA, respectively. A comparison of the electron temperature and plasma resistivity before and after the heating power is increased is shown in Figs. 7.3(a-b). The increased heating power again raises the electron temperature (Fig. 7.3(a)) and lowers the plasma resistivity (Fig. 7.3(b)) at both values of total plasma current as expected from (7.4). A comparison of the auxiliary and bootstrap current densities before and after the heating power is increased is shown in Figs. 7.3(c-d). Since $P^{cd}_{aux} = 0$ MW, there is no auxiliary current drive

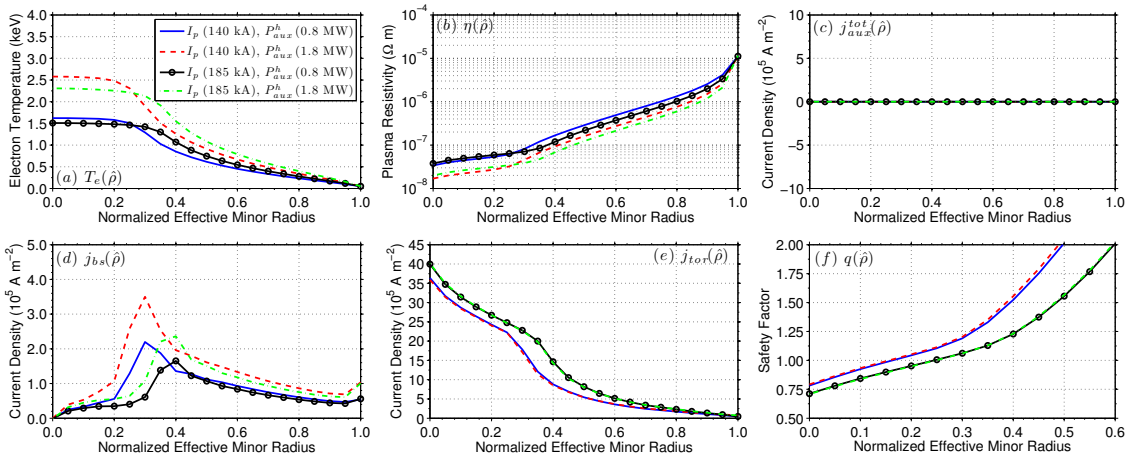

Figure 7.3: Comparison of stationary state plasma parameters under low and high plasma heating conditions with $P^{cd}_{aux} = 0$ MW.

(Fig. 7.3(c)). Again, at both values of total plasma current, increasing the electron temperature through heating increases the bootstrap current (Fig. 7.3(d)) as expected from (7.7). By comparing Fig. 7.2(d) and Fig. 7.3(d), we see that the bootstrap current drive behaves in a similar fashion in response to auxiliary heating independent of the presence or absence of auxiliary current drive. However, the increase in off-axis bootstrap co-current-drive and the decrease in plasma resistivity results in a small change in the toroidal current density (Fig. 7.3(e)), and correspondingly in a small change in the q profile as shown in Fig. 7.3(f), when auxiliary heating is applied without auxiliary current drive.

7.3 Feedback control design

As shown in the previous section, auxiliary heating has a small effect on the q profile in the absence of auxiliary current drive in the considered TCV scenarios. As a result, a q profile feedback controller that utilizes the total plasma current and exclusively the current-drive capabilities of the auxiliary sources is designed by employing the method utilized in chapters 4-6, and the controller will attempt to counteract any q

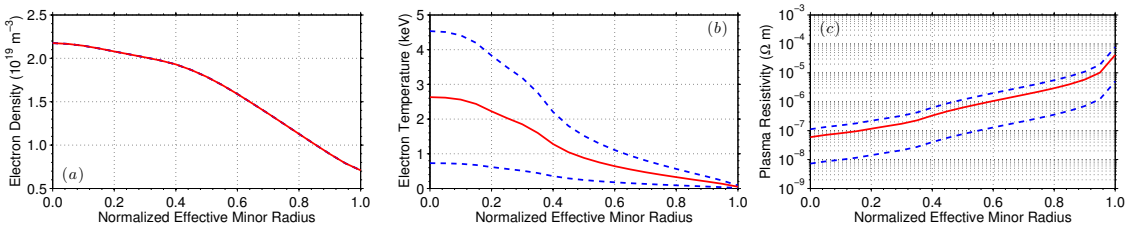

Figure 7.4: Plasma parameter uncertainty ranges in TCV L-mode scenarios: (a) electron density, (b) electron temperature, and (c) plasma resistivity. Note: nominal values (solid) and minimum/maximum values (dash).

profile disturbance that results from plasma heating effects.

7.3.1 Partial differential equation model of system dynamics

We begin by defining ranges in which the electron density profile, the electron temperature profile, and the plasma resistivity are expected to be in typical TCV L-mode scenarios, which are shown in Fig. 7.4. These parameters are modeled as

$$n_e(\hat{\rho}) = n_e^{nom}(\hat{\rho}), \tag{7.9}$$

$$T_e(\hat{\rho}) = T_e^{nom}(\hat{\rho}) + T_e^{unc}(\hat{\rho})\delta_{T_e}, \tag{7.10}$$

$$\eta(\hat{\rho}) = \eta^{nom}(\hat{\rho}) + \eta^{unc}(\hat{\rho})\delta_{T_e}, \tag{7.11}$$

where the nominal (n_e^{nom}, T_e^{nom}, η^{nom}) and uncertain (T_e^{unc}, η^{unc}) profiles are defined in terms of the maximum and minimum profiles and $|\delta_{T_e}| \leq 1$. Note that the dependence of the plasma resistivity on the electron temperature is modeled to first order to simplify the control design. Also, note that an uncertainty in the electron density profile can readily be incorporated in the formulation of the model, but for the scenarios considered, the electron density profile is assumed constant. By combining the magnetic diffusion equation (7.1) with the noninductive current-drive models

(7.5)-(7.7) and the uncertain models (7.9)-(7.11), we obtain

$$\begin{aligned}\frac{\partial \psi}{\partial t} = & \frac{(\eta^{nom}+\eta^{unc}\delta_{T_e})}{\mu_0 \rho_b^2 \hat{F}^2}\frac{1}{\hat{\rho}}\frac{\partial}{\partial \hat{\rho}}\left(\hat{\rho}\hat{F}\hat{G}\hat{H}\frac{\partial \psi}{\partial \hat{\rho}}\right) \\ & + \frac{R_0 \hat{H}(\eta^{nom}+\eta^{unc}\delta_{T_e})\left(T_e^{nom}+T_e^{unc}\delta_{T_e}\right)}{n_e^{nom}} \\ & \times \left\{ \left(j_{ec_{1a}}^{ref}+j_{ec_{2a}}^{ref}\right) P_{ec_a}(t) + \left(j_{ec_{1b}}^{ref}+j_{ec_{2b}}^{ref}\right) P_{ec_b}(t) \right\} \\ & + \frac{k_{JeV} R_0^2 \hat{H}(\eta^{nom}+\eta^{unc}\delta_{T_e})}{\hat{F}}\left(\frac{\partial \psi}{\partial \hat{\rho}}\right)^{-1} \\ & \times \Bigg[2\mathcal{L}_{31}\left(T_e^{nom}+T_e^{unc}\delta_{T_e}\right)\frac{\partial}{\partial \hat{\rho}}\left\{n_e^{nom}\right\} \\ & + \left\{2\mathcal{L}_{31}+\mathcal{L}_{32}+\alpha\mathcal{L}_{34}\right\} n_e^{nom}\frac{\partial}{\partial \hat{\rho}}\left\{T_e^{nom}+T_e^{unc}\delta_{T_e}\right\}\Bigg]. \end{aligned} \tag{7.12}$$

7.3.2 Model reduction via spatial discretization

From (7.3), we see that the rotational transform profile ($\iota = 1/q$) is dependent on the poloidal flux gradient profile, which we define as $\theta(\hat{\rho}, t) \equiv [\partial\psi/\partial\hat{\rho}(\hat{\rho}, t)]$. After some mathematical manipulations, a partial differential equation (PDE) model of the θ profile dynamics can be obtained from (7.12). Spatially discretizing this model by employing a finite difference method results in an ordinary differential equation model defined by

$$\begin{aligned} \dot{x} &= f_\theta(x, u, \delta), \\ y_i &= -\frac{1}{B_{\phi,0}\rho_b^2 \hat{\rho}_i} x_i, \end{aligned} \tag{7.13}$$

where $x = [\theta_i] \in \mathbb{R}^{n_\theta}$ is the state vector, $y = [\iota_i] \in \mathbb{R}^{n_\theta}$ is the output vector, θ_i, ι_i, and $\hat{\rho}_i$ are the values of θ, ι, and $\hat{\rho}$ at the discrete nodes, for $i = [2, \ldots, m_\theta - 1]$, $u = [P_{ec_a}, P_{ec_b}, I_p] \in \mathbb{R}^3$ is the control input vector, $\delta = \left[\delta_{T_e}, \delta_{T_e}^2\right] \in \mathbb{R}^2$ is the uncertain parameter vector, $f_\theta \in \mathbb{R}^{n_\theta}$ is a nonlinear function, $n_\theta = m_\theta - 2$, and m_θ is the number of nodes utilized to represent the spatial domain. After linearizing (7.13)

with respect to the state and control input around a nominal operating point (x_{eq}, u_{eq}) characterized by $\delta = 0$, i.e., $f(x_{eq}, u_{eq}, 0) = 0$, we obtain

$$\begin{aligned} \dot{\tilde{x}} &= A(\delta)\tilde{x} + B(\delta)u_{fb} + d_\delta, \\ y &= C\tilde{x} + Du_{fb}, \end{aligned} \tag{7.14}$$

where $\tilde{x} = x - x_{eq}$, $u_{fb} = u - u_{eq}$ is the output of the to-be-designed feedback controller, $d_\delta = f(x_{eq}, u_{eq}, \delta)$, $A(\delta)$ and $B(\delta)$ are the Jacobians $\partial f_\theta / \partial x \in \mathbb{R}^{n_\theta \times n_\theta}$ and $\partial f_\theta / \partial u \in \mathbb{R}^{n_\theta \times 3}$ evaluated at (x_{eq}, u_{eq}, δ), $C = \text{diag}\{-1/(B_{\phi,0}\rho_b^2\hat{\rho}_i)\} \in \mathbb{R}^{n_\theta \times n_\theta}$ and $D = 0$.

7.3.3 Evaluation of relevant control channels

As there are only three control inputs, we can at most independently control three linear combinations of the system output. Therefore, we obtain the most relevant control channels from the nominal input-output relation at a particular frequency $j\omega_{dc}$, which is expressed as $\hat{y} = \hat{G}_0\hat{u}_{fb} = Q^{-1/2}\tilde{G}_0R^{1/2}\hat{u}_{fb} = Q^{-1/2}U\Sigma V^TR^{1/2}\hat{u}_{fb}$. The decoupled output and input are denoted by $\hat{y}^* = \Sigma^{-1}U^TQ^{1/2}\hat{y}$ and $\hat{u}^*_{fb} = V^TR^{1/2}\hat{u}_{fb}$, i.e., $\hat{y}^* = \hat{u}^*_{fb}$. The nominal system transfer function is expressed as $G_0(s) = C\left(sI_{n_\theta} - A(0)\right)^{-1}B(0)$, where s denotes the Laplace variable and I_{n_θ} denotes an $n_\theta \times n_\theta$ identity matrix, and $\hat{G}_0$ denotes the real approximation of the complex matrix $G_0(j\omega_{dc})$ [10, 146]. The positive definite matrices $Q \in \mathbb{R}^{n_\theta \times n_\theta}$ and $R \in \mathbb{R}^{3\times 3}$ are utilized to weight the relative tracking performance and control effort. Finally, the "weighted" transfer function $\tilde{G}_0$ and its economy size singular value decomposition are defined as $\tilde{G}_0 = Q^{1/2}\hat{G}_0R^{-1/2} = U\Sigma V^T$, where $\Sigma \in \mathbb{R}^{3\times 3}$ is a diagonal matrix of singular values and $U \in \mathbb{R}^{n_\theta \times 3}$ and $V \in \mathbb{R}^{3\times 3}$ are matrices that possess the following properties $V^TV = VV^T = I, U^TU = I$. Some of the singular values may have a small magnitude relative to the others and may be chosen to be

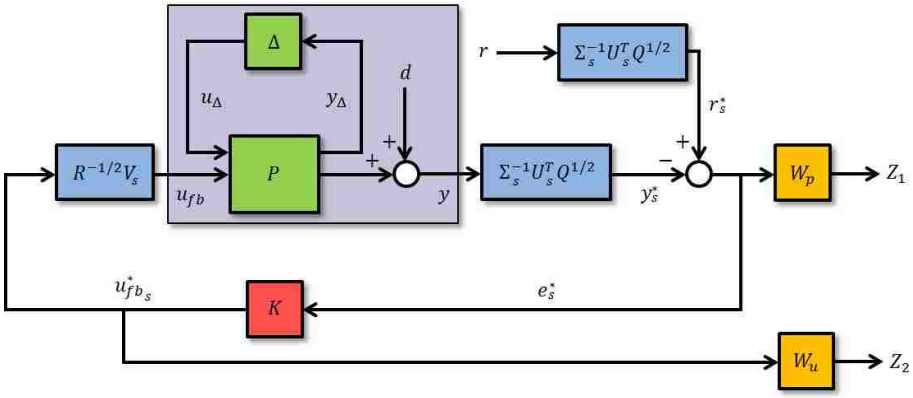

Figure 7.5: Schematic of control problem formulation for ι profile feedback control design in TCV L-mode scenarios.

neglected in the control synthesis. Quantities associated with the significant singular values are denoted by a subscript s for the remainder of this chapter, i.e., $(\cdot)_s$. A detailed overview of the singular value decomposition technique employed to evaluate the relevant control channels is provided in Appendix B.

7.3.4 Feedback control problem formulation

The feedback control problem is formulated as shown in Fig. 7.5, where r is the reference value, the tracking error is defined as $e = r - y$, and K is the to-be-designed feedback controller. The feedback system (7.14) is written in the conventional $P - \Delta$ robust control framework, where P is the generalized transfer function and $\Delta = \text{diag}\{\delta_{T_e}\}$ is a structured uncertainty matrix, by employing the method described in [138]. An overview of the employed technique is provided in Appendix A. The closed-loop system outputs are Z_1 and Z_2 and the frequency dependent weight functions W_p and W_u are utilized to optimize the feedback performance. The control problem is formulated as (see Fig. 8.3)

$$\min_K \left|\left|T_{zw}\right|\right|_\infty, \quad \forall\omega \qquad T_{zw} = \begin{bmatrix} W_p S_{DC_O} & -W_p S_{DC_O} \\ W_u K S_{DC_O} & -W_u K S_{DC_O} \end{bmatrix}, \tag{7.15}$$

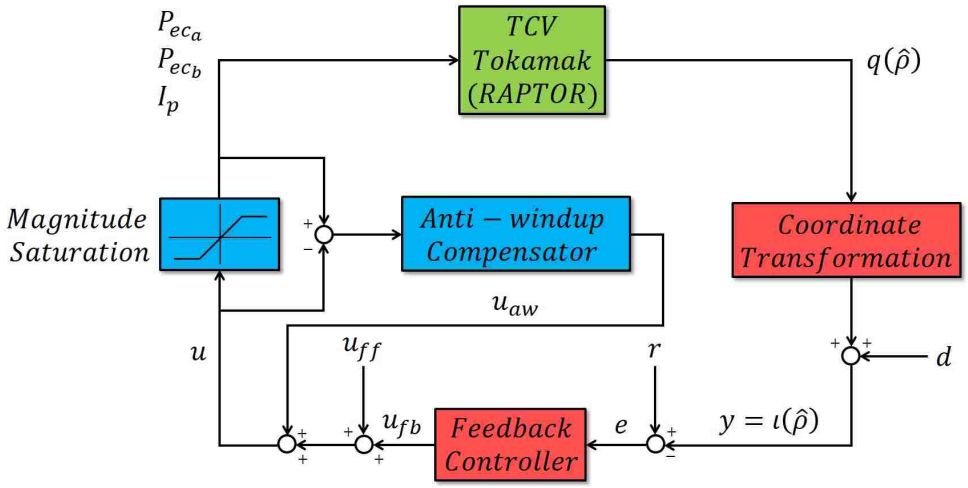

Figure 7.6: Schematic of closed-loop control system structure for ι profile control for the TCV tokamak.

where T_{zw} is the closed-loop transfer function from the inputs (r_s^*, d_s^*) to the outputs (Z_1, Z_2), $d_s^* = \Sigma_s^{-1} U_s^T Q^{1/2} d$, $S_{DC_O} = (I + \Sigma_s^{-1} U_s^T Q^{1/2} P_{22} R^{-1/2} V_s K)^{-1}$, P_{22} is the component transfer function of P from u_{fb} to y, and $||\cdot||_\infty$ denotes the H_∞ norm. See section 3.6 for an example of how this nominal performance condition is derived. The feedback controller K is obtained by solving (7.15) and is designed such that the closed-loop system is stable for all allowable perturbations (checked by computing the structured singular value [10]). See Appendix C for an introduction to the design of feedback controllers by employing the H_∞ closed-loop shaping technique.

A schematic of the closed-loop control system structure is shown in Fig. 7.6. To ensure the closed-loop system remains well-behaved in the presence of actuator magnitude saturation, the feedback controller is augmented by an anti-windup compensator [140]. See section 4.4.6 for an example of the employed anti-windup scheme.

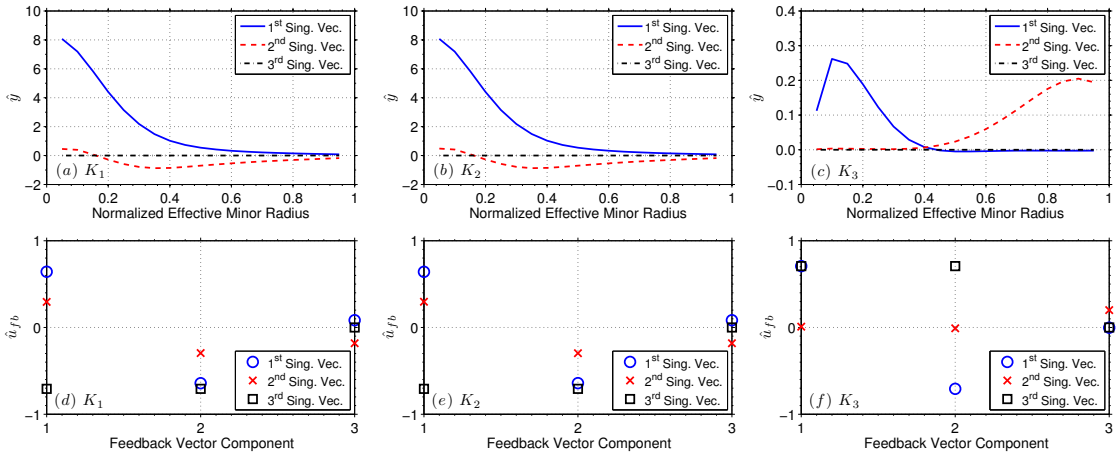

Figure 7.7: Relevant control channels for ι profile control in TCV L-mode scenarios: (a-c) output ($\hat{y} = Q^{-1/2}U\Sigma\hat{y}^*$) and (d-f) input ($\hat{u}_{fb} = R^{-1/2}V\hat{u}^*_{fb}$). The feedback vector components are defined as $u_{fb} = [P_{ec_a}, P_{ec_b}, I_p]\,|_{fb}$.

7.4 Control algorithm performance testing in TCV RAPTOR simulations

In this section, the closed-loop performances of three feedback controllers are compared in TCV L-mode scenarios using RAPTOR [13–15]. The value and shape of the q profile in the plasma core is important due to its close relationship to both plasma performance [61, 62] and stability limits [63, 64]. Additionally, it may also be desirable to achieve a q profile with a specific value near the plasma boundary to obtain plasmas with a desired total plasma current. The weight matrix Q utilized in the evaluation of the relevant control channels can be utilized to place more emphasis on achieving the target q profile in different spatial regions. The relevant control channels of the first controller (denoted as K_1) are evaluated at a frequency of $\omega_{dc} = 0$ rad/s with emphasis placed on achieving the target q profile in the spatial region $\hat{\rho} \in [0, 0.4]$. The second controller (denoted as K_2) is designed in the same way as controller K_1 but with emphasis placed on achieving the target q profile in the spatial regions $\hat{\rho} \in [0, 0.4]$ and $\hat{\rho} \in [0.7, 0.8]$. Finally, the relevant control channels of the third controller (denoted as K_3) are evaluated at a frequency of $\omega_{dc} = 1500$

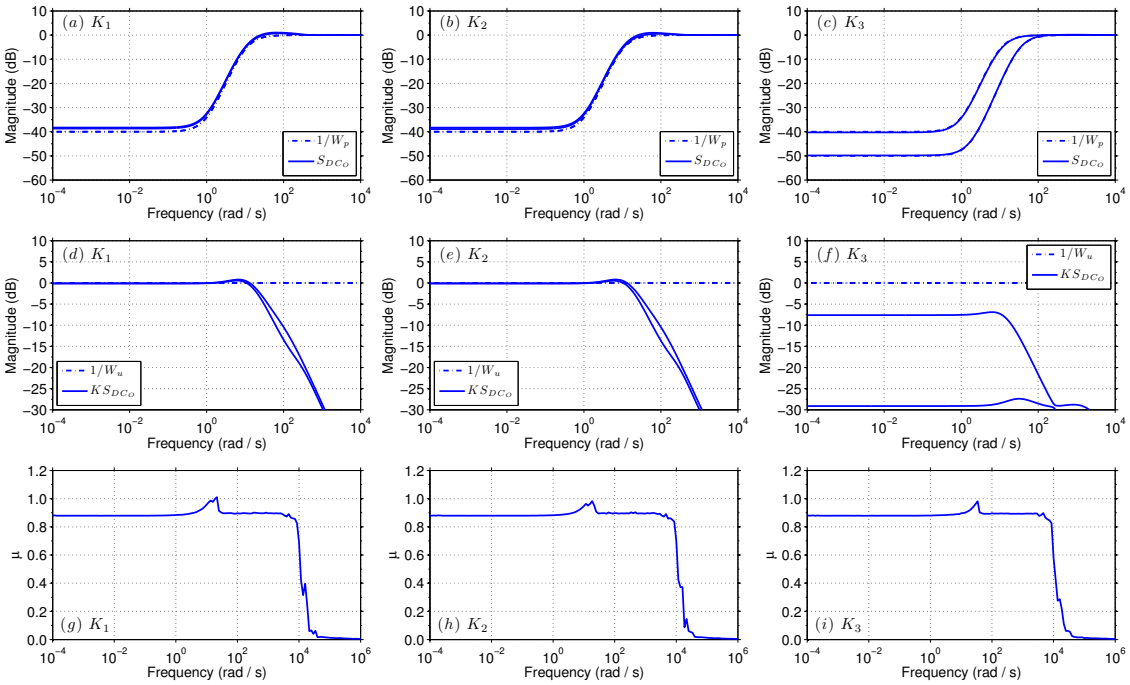

Figure 7.8: (a-f) Nominal performance (tracking and control effort) and (g-i) structured singular value versus frequency for the three controllers. The closed-loop robust stability condition is defined as $\mu(N_{11}(j\omega)) < 1$, $\forall\omega$ [10], where N_{11} is the transfer function between y_Δ and u_Δ in Fig. 7.5.

rad/s with emphasis placed on achieving the target q profile in the spatial regions $\hat{\rho} \in [0, 0.4]$ and $\hat{\rho} \in [0.7, 0.8]$.

The relevant control channels of the three controllers are shown in Fig. 7.7. First, we note that the third actuation direction (□) for all of the controllers (Figs. 7.7(d-f)) is associated with auxiliary heating (equal contributions from P_{ec_a} and P_{ec_b} in the same direction and no contribution from I_p), which is negligible in this control design approach. Second, we see that the control inputs are coupled for controllers K_1 and K_2, i.e., the first (○) and second (×) input singular vectors have contributions from all three actuators (Figs. 7.7(d-e)). In contrast, the gyrotron and total plasma current actuation directions are decoupled for controller K_3 (Fig. 7.7(f)), i.e., the first singular vector only has contributions from P_{ec_a} and P_{ec_b} and the second singular vector only has a contribution from I_p. The bandwidth of the gyrotron control direction for

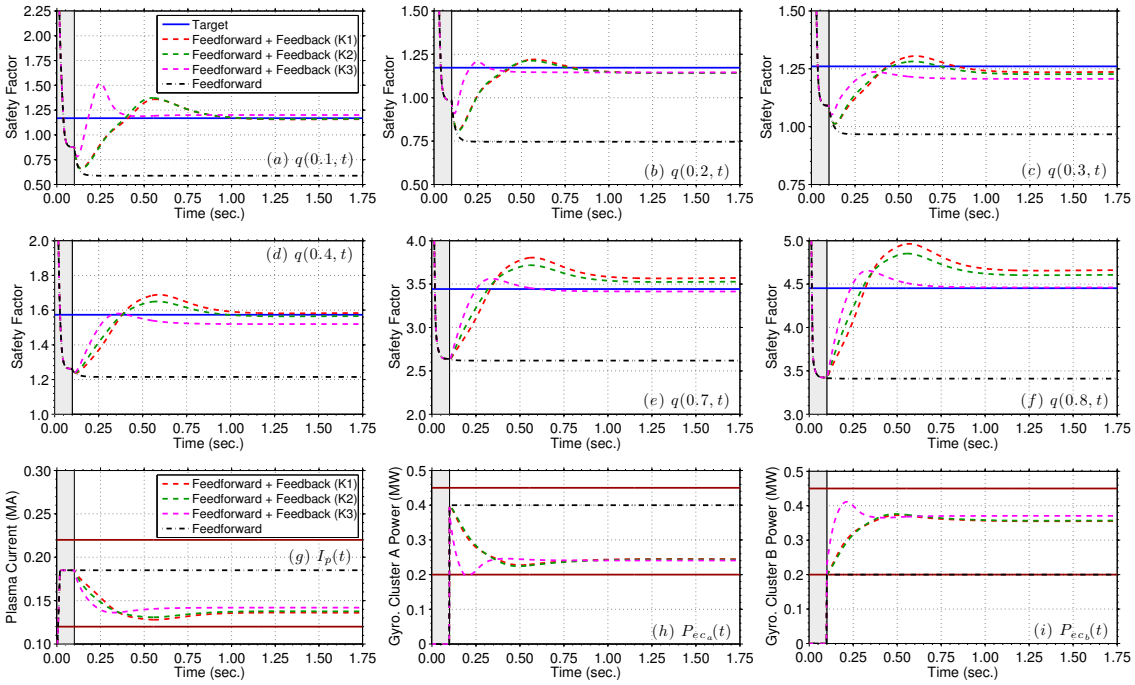

Figure 7.9: Time traces of outputs (q) and inputs (I_p, P_{ec_a}, P_{ec_b}) for simulation in section 7.4.1. Gray-shaded region denotes when feedback controller is off. Actuator limits (solid brown).

controller K_3 is set at a slightly higher value relative to the other control directions. This is enabled because the actuation directions are decoupled in controller K_3. To analyze the performance and robust stability of the closed-loop system with the three controllers, the singular value diagrams of the inverse of the performance weight functions and the achieved transfer functions S_{DC_O} and KS_{DC_O} are shown in Figs. 7.8(a-f) and a plot of μ versus frequency is shown in Fig. 7.8(g-i) for the three controllers. As shown in the figures, all of the controllers achieve nominal performance and are able to robustly stabilize the closed-loop system (marginal stability is reached with controller K_1 at the approximate frequency of 10 rad/s).

7.4.1 One target simulation

In this section the feedback controllers are tested in a one target simulation with RAPTOR. A q profile achieved in TCV with a total plasma current of 140 kA and

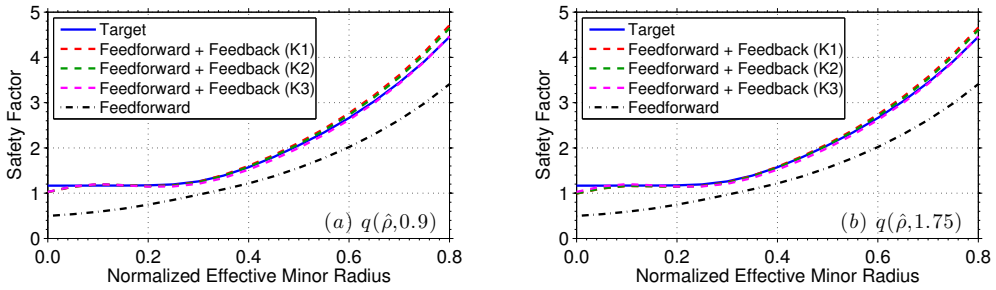

Figure 7.10: Comparison of target, feedforward + feedback controlled, and feedforward controlled q profiles at various times for simulation in section 7.4.1.

counter-current-injection auxiliary power is chosen as the target. First, a nominal q profile evolution is obtained by executing a feedforward-only simulation with a nominal set of input trajectories. Next, the ability of each of the controllers to track the target is determined by executing feedforward + feedback simulations with the nominal inputs. During the feedback-controlled simulations, the controller is inactive during the time interval $t \in [0, 0.1]$ s.

Time traces of q at various spatial locations and a comparison of the control inputs as a function of time are shown in Fig. 7.9. A comparison of the target, feedforward + feedback controlled, and feedforward controlled q profiles at various times is shown in Fig. 7.10. Once the controllers become active at 0.1 s, they are able to drive the q profile towards the target. In tokamaks, the local q-value is roughly inversely related to the local current density amplitude. In the feedback-controlled simulations, all of the controllers decrease the total plasma current and the auxiliary power in the cluster a gyrotrons and increase the auxiliary power in the cluster b gyrotrons to track the target. The controller K_3 is able to respond to the error in the plasma core faster than controllers K_1 and K_2 due to the slightly higher bandwidth of the gyrotron control direction for controller K_3. Additionally, the error near the plasma boundary is eliminated by controller K_3, whereas there is a small tracking error obtained with controllers K_1 and K_2. However, the error near the plasma boundary obtained with controller K_2 is smaller than the error obtained with controller K_1 due to the higher

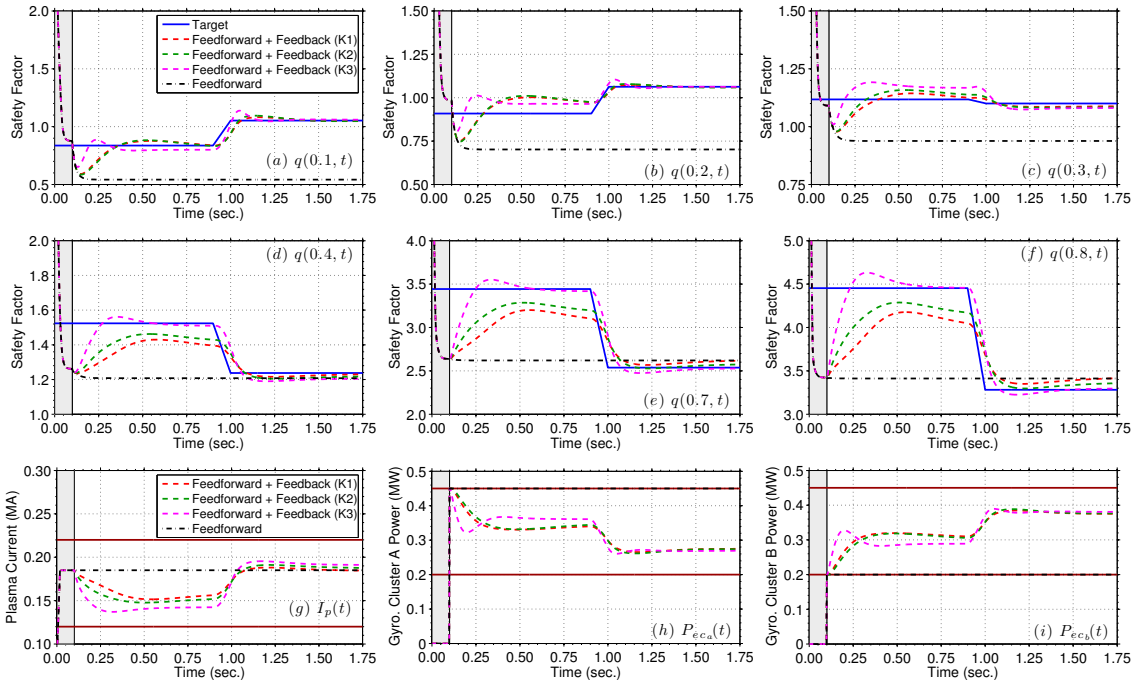

Figure 7.11: Time traces of outputs (q) and inputs (I_p, P_{ec_a}, P_{ec_b}) for simulation in section 7.4.2. Gray-shaded region denotes when feedback controller is off. Actuator limits (solid brown).

weight placed on achieving the target in this spatial region for controller K_2.

7.4.2 Two target simulation

In this section the feedback controllers are tested in a two target simulation with RAPTOR. A q profile achieved in TCV with a total plasma current of 140 kA and co-current-injection auxiliary power is chosen as the target during the time interval $t \in [0, 0.9]$ s. During the time interval $t \in [1.0, 1.75]$ s, a q profile achieved in TCV with a total plasma current of 190 kA and counter-current-injection auxiliary power is chosen as the target. The target during the time interval $t \in (0.9, 1.0)$ s is obtained by linear interpolation. First, a nominal q profile evolution is obtained by executing a feedforward-only simulation with a nominal set of input trajectories. Next, the ability of each of the controllers to track the target is determined by executing feedforward + feedback simulations with the nominal inputs. During the feedback-controlled

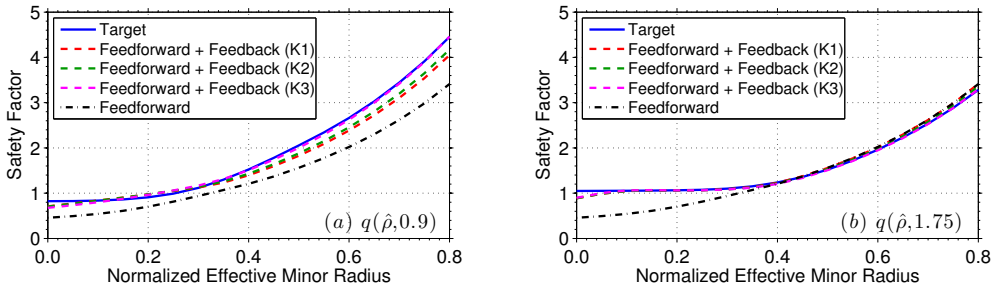

Figure 7.12: Comparison of target, feedforward + feedback controlled, and feedforward controlled q profiles at various times for simulation in section 7.4.2.

simulations, the controller is inactive during the time interval $t \in [0, 0.1]$ s.

Time traces of q at various spatial locations and a comparison of the control inputs as a function of time are shown in Fig. 7.11. A comparison of the target, feedforward + feedback controlled, and feedforward controlled q profiles at various times is shown in Fig. 7.12. Once the controllers become active at 0.1 s, they are able to drive the q profile towards the first target. In the feedback-controlled simulations, all of the controllers decrease the total plasma current and the cluster a gyrotron power, while increasing the cluster b gyrotron power, to track the first target. For controllers K_1 and K_2 the actuators are utilized to control the q profile across the entire spatial domain (Figs. 7.7(a-b)). Therefore, in response to the q-value being above the target at $\hat{\rho} = 0.2, 0.3$ (current density to low), the controllers K_1 and K_2 increase the total plasma current (relative to controller K_3) to lower the q-value at these locations (the current density at these locations will increase as the current applied at the plasma boundary propagates towards the plasma core). As a result of the increased current density, a tracking error at $\hat{\rho} = 0.4, 0.7, 0.8$ is obtained with controllers K_1 and K_2. However, the error obtained with controller K_2 is smaller than the error obtained with controller K_1 (see section 7.4.1). In contrast, for controller K_3, the gyrotrons are utilized to control the q profile in the plasma core and the total plasma current is utilized to control the q profile near the plasma boundary (Fig. 7.7(c)). Therefore, controller K_3 does not increase the total plasma current to decrease the

error at $\hat{\rho} = 0.2, 0.3$, and as a result, good tracking control performance is achieved at $\hat{\rho} = 0.4, 0.7, 0.8$. When the target profile is switched, a similar tracking performance is achieved in the plasma core ($\hat{\rho} = 0.1, 0.2, 0.3$) with all of the controllers. Finally, with controllers K_1 and K_2 a smaller error at $\hat{\rho} = 0.4$ is obtained at the expense of achieving a larger error at $\hat{\rho} = 0.7, 0.8$ (relative to controller K_3).

7.5 Conclusion

Auxiliary heating was shown to have a relatively small effect on the q profile in the absence of auxiliary current drive in the studied TCV scenarios. As a result, we designed feedback controllers that exclusively utilized the current-drive capabilities of the auxiliary sources to control the q profile in TCV. The algorithms were designed to put emphasis on achieving the target q profile in different spatial regions and to respond differently to errors in the q profile. The closed-loop performance of each controller was tested and compared through simulations with the RAPTOR code. Our future work includes testing the controllers experimentally in TCV by utilizing the closed-loop plasma state observer developed in [150] to reconstruct the q profile in real-time.

Chapter 8

Simultaneous closed-loop current and electron temperature profile control in the TCV tokamak

8.1 Introduction

The current profile and the electron temperature profile are intimately coupled in tokamak plasmas through resistive diffusion, auxiliary current-drive efficiency, bootstrap current drive, ohmic heating, and plasma energy/particle transport. As these physical mechanisms play a critical role in the fusion gain, plasma confinement, magnetohydrodynamic (MHD) stability, and fraction of noninductively driven current of a tokamak operation scenario, developing integrated strategies for current profile and electron temperature profile control is crucial to developing the ability to robustly achieve and maintain desired plasma targets. In this chapter, we extend the methodology developed in chapter 7 for safety factor profile (q profile) control in the TCV tokamak to synthesize a feedback algorithm for simultaneous safety factor and electron temperature profile control in TCV following a FPD, physics-based approach.

The plasma poloidal magnetic flux (Ψ) and electron temperature (T_e) dynamics are governed by an infinite dimensional nonlinear, coupled physics model that is described by the magnetic diffusion equation [124] and the electron heat transport equation [7]. The rotational transform (ι) profile, defined as $\iota = 1/q$, is proportional to the spatial gradient of Ψ, and therefore represents a natural plasma property conducive for feedback control. In this chapter, an integrated feedback controller is designed to track target ι and T_e profiles by embedding the partial differential equation (PDE) models of the Ψ and T_e dynamics into the control design process. We model the electron thermal conductivity profile as an uncertainty and design the controller to be robust to an expected uncertainty range. The actuators used to control the ι and T_e profiles are the total plasma current and the auxiliary heating and current-drive (H&CD) system. The performance of the integrated controller is demonstrated though simulations with the RAPTOR code [13–15] by first tracking a nominal target, and then modulating the T_e profile between equilibrium points while maintaining the ι profile in a stationary condition.

This chapter is organized as follows. In section 8.2, the physics model that governs the evolution of the current and electron temperature profiles is converted into a form suitable for control design. The PDE model is spatially discretized by employing a finite difference method in section 8.3, and in section 8.4, the discretized model is formulated into a robust control design framework. In section 8.5, the part of the plant output that we can effectively control is determined by employing a singular value decomposition of the nominal plant model, and in section 8.6, the integrated feedback controller is synthesized by first considering the nominal model and then analyzing the stability of the closed-loop system in the presence of the model uncertainty. Closed-loop simulations with the RAPTOR code are presented in section 8.7 to demonstrate the ability of the controller to drive the system to multiple different operating points. Finally, conclusions are discussed in section 8.8.

8.2 Model of system dynamics

A well confined tokamak plasma MHD equilibrium is characterized by the formation of nested toroidal surfaces of constant poloidal magnetic flux. Any quantity that is constant on these magnetic flux surfaces can be used to index them. In this work, the spatial coordinate $\hat{\rho} = \rho/\rho_b$ is used to index the magnetic flux surfaces, where ρ is the mean effective minor radius of a magnetic flux surface, i.e., $\Phi(\rho) = \pi B_{\phi,0}\rho^2$, Φ is the toroidal magnetic flux, $B_{\phi,0}$ is the vacuum toroidal magnetic field at the geometric major radius R_0 of the tokamak, and ρ_b is the mean effective minor radius of the last closed magnetic flux surface.

The rotational transform is related to the spatial gradient of the poloidal magnetic flux and is defined as

$$\iota(\hat{\rho}, t) = \frac{1}{q(\hat{\rho}, t)} = -\frac{d\Psi}{d\Phi} = -\frac{\partial\psi/\partial\hat{\rho}}{B_{\phi,0}\rho_b^2\hat{\rho}}, \tag{8.1}$$

where t is the time and $\psi(\hat{\rho}, t)$ is the poloidal stream function, which is closely related to the poloidal magnetic flux $\Psi(\hat{\rho}, t)$, i.e., $(\Psi = 2\pi\psi)$. The poloidal magnetic flux dynamics in a tokamak plasma are given by the magnetic diffusion equation in (2.45) and restated here for convenience as

$$\frac{\partial\psi}{\partial t} = \frac{\eta(T_e)}{\mu_0\rho_b^2\hat{F}^2}\frac{1}{\hat{\rho}}\frac{\partial}{\partial\hat{\rho}}\left(\hat{\rho}\hat{F}\hat{G}\hat{H}\frac{\partial\psi}{\partial\hat{\rho}}\right) + R_0\hat{H}\eta(T_e)j_{ni}, \tag{8.2}$$

with boundary conditions

$$\frac{\partial\psi}{\partial\hat{\rho}}(0, t) = 0 \qquad \frac{\partial\psi}{\partial\hat{\rho}}(1, t) = -k_{I_p}I_p, \tag{8.3}$$

where $\eta(\hat{\rho}, t)$ is the plasma resistivity, $T_e(\hat{\rho}, t)$ is the electron temperature, μ_0 is the vacuum magnetic permeability, $j_{ni}(\hat{\rho}, t)$ is the total noninductive current density, k_{I_p}

is a geometrical constant defined in (2.83), and $I_p(t)$ is the total plasma current. The parameters $\hat{F}(\hat{\rho})$, $\hat{G}(\hat{\rho})$, and $\hat{H}(\hat{\rho})$ are geometric spatial factors pertaining to the magnetic configuration of a particular plasma MHD equilibrium (defined in (2.44)).

Assuming diffusion is the dominant heat transport mechanism in the tokamak plasma, the electron temperature dynamics are given by the electron heat transport equation in (2.48) and restated here for convenience as

$$\frac{3}{2}\frac{\partial}{\partial t}\left[n_e T_e\right] = \frac{1}{\rho_b^2 \hat{H}}\frac{1}{\hat{\rho}}\frac{\partial}{\partial \hat{\rho}}\left[\hat{\rho}\frac{\hat{G}\hat{H}^2}{\hat{F}}\left(\chi_e n_e \frac{\partial T_e}{\partial \hat{\rho}}\right)\right] + Q_e, \tag{8.4}$$

with boundary conditions

$$\frac{\partial T_e}{\partial \hat{\rho}}(0,t) = 0 \qquad T_e(1,t) = T_{e,bdry}, \tag{8.5}$$

where $n_e(\hat{\rho},t)$ is the electron density, $\chi_e(\hat{\rho},t)$ is the electron thermal conductivity, $Q_e(\hat{\rho},t)$ is the total electron heating power density, and $T_{e,bdry}$ is the electron temperature at the plasma boundary, which is assumed constant.

In order to convert the physics models of the plasma poloidal magnetic flux and electron temperature dynamics (8.2) and (8.4) into a form suitable to design a feedback controller, we develop simplified physics-based models of the plasma resistivity, noninductive current sources, electron heating sources, and electron thermal conductivity. See chapter 2 for a detailed derivation/discussion of the models, and in particular, section 2.10 where the models are tailored to the TCV tokamak.

8.2.1 Plasma resistivity modeling

The plasma resistivity scales inversely with the electron temperature as

$$\eta(\hat{\rho},t) = \frac{k_{sp}(\hat{\rho}) Z_{eff}}{T_e(\hat{\rho},t)^{3/2}}, \tag{8.6}$$

where k_{sp} is a spatial profile and Z_{eff} is the effective average charge of the ions in the plasma, which is assumed constant in space and time.

8.2.2 Noninductive current drive modeling

The total noninductive current density is generated by the combination of the auxiliary sources and the bootstrap current [60], i.e.,

$$j_{ni}(\hat{\rho},t) = \sum_{i=1}^{n_{aux}} j_{aux,i}(\hat{\rho},t) + j_{bs}(\hat{\rho},t), \tag{8.7}$$

where $j_{aux,i}$ is the current density driven by the individual auxiliary sources, j_{bs} is the current density driven by the bootstrap current, and n_{aux} is the number of auxiliary sources. The individual auxiliary current drives are modeled as

$$j_{aux,i}(\hat{\rho},t) = j_{aux,i}^{ref}(\hat{\rho})\frac{T_e(\hat{\rho},t)}{n_e(\hat{\rho},t)}P_{aux,i}(t), \tag{8.8}$$

where $j_{aux,i}^{ref}$ is a normalized reference current density deposition profile for the i-th auxiliary source, T_e/n_e represents the current-drive efficiency (for electron cyclotron current-drive [66]), and $P_{aux,i}$ is the i-th auxiliary power. The bootstrap current is a self-generated current in the plasma which arises from the radial pressure gradient that is produced by the magnetic confinement [60], and is modeled as [134, 135]

$$\begin{aligned} j_{bs}(\hat{\rho},t) = \frac{k_{JkeV}R_0}{\hat{F}}\left(\frac{\partial\psi}{\partial\hat{\rho}}\right)^{-1}\Bigg[&2\mathcal{L}_{31}T_e(\hat{\rho},t)\frac{\partial n_e}{\partial\hat{\rho}}(\hat{\rho},t) \\ &+\left\{2\mathcal{L}_{31}+\mathcal{L}_{32}+\alpha\mathcal{L}_{34}\right\}n_e(\hat{\rho},t)\frac{\partial T_e}{\partial\hat{\rho}}(\hat{\rho},t)\Bigg], \end{aligned} \tag{8.9}$$

where $\mathcal{L}_{31}(\hat{\rho})$, $\mathcal{L}_{32}(\hat{\rho})$, $\mathcal{L}_{34}(\hat{\rho})$, and $\alpha(\hat{\rho})$ depend on the magnetic configuration of a particular plasma equilibrium, $k_{JkeV} = 1.602 \times 10^{-16}$ J/keV, and we have assumed the electron and ion densities and temperatures, respectively, are equal.

8.2.3 Electron heating power density modeling

The total electron heating power density is expressed as

$$Q_e(\hat{\rho},t) = \frac{1}{k_{JkeV}}\left[Q_{e,ohm}(\hat{\rho},t) + \sum_{i=1}^{n_{aux}} Q_{e,aux_i}(\hat{\rho},t) - Q_{e,rad}(\hat{\rho},t)\right], \tag{8.10}$$

where $Q_{e,ohm}$ is the ohmic heating power density, Q_{e,aux_i} is the power density produced by the individual auxiliary sources, and $Q_{e,rad}$ is the radiated power density. The ohmic power density is modeled as

$$Q_{e,ohm}(\hat{\rho},t) = j_{tor}(\hat{\rho},t)^2\eta(\hat{\rho},t), \tag{8.11}$$

where the total toroidal current density is expressed as [70]

$$j_{tor}(\hat{\rho},t) = -\frac{1}{\mu_0\rho_b^2 R_0\hat{H}}\frac{1}{\hat{\rho}}\frac{\partial}{\partial\hat{\rho}}\left(\hat{\rho}\hat{G}\hat{H}\frac{\partial\psi}{\partial\hat{\rho}}\right). \tag{8.12}$$

The individual auxiliary power densities are modeled as

$$Q_{e,aux_i}(\hat{\rho},t) = Q_{aux_i}^{ref}(\hat{\rho})P_{aux_i}(t), \tag{8.13}$$

where $Q_{aux,i}^{ref}$ is a normalized reference power density deposition profile for the i-th auxiliary source. The radiated power density (for Bremsstrahlung radiation) is modeled as [18]

$$Q_{e,rad}(\hat{\rho},t) = k_{brem}Z_{eff}n_e(\hat{\rho},t)^2\sqrt{T_e(\hat{\rho},t)}, \tag{8.14}$$

where $k_{brem} = 5.5\times10^{-37}$ $\mathrm{Wm}^3/\sqrt{\mathrm{keV}}$ is the Bremsstrahlung radiation coefficient.

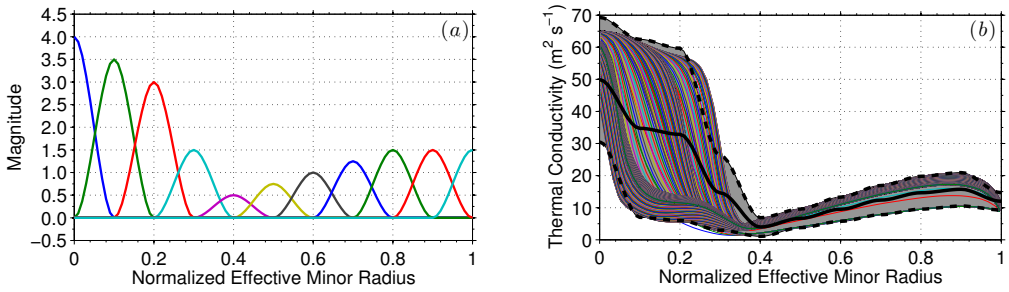

Figure 8.1: (a) Cubic spline basis functions used to model χ_e and (b) the χ_e uncertainty range (gray-shaded region) captured by the model (8.15)-(8.16). The nominal model (characterized by $\delta_\alpha = 0$) is shown by the solid black line, and the maximum/minimum values (characterized by $\delta_\alpha = 1$ and $\delta_\alpha = -1$, respectively) are shown by the dashed black lines. The multicolored lines show the various χ_e profiles that are achieved during a typical TCV simulated discharge using RAPTOR [13–15].

8.2.4 Electron thermal conductivity modeling

From (8.6), (8.8), and (8.9), we see that the electron temperature is coupled to the poloidal magnetic flux dynamics through resistive diffusion, auxiliary current-drive efficiency, and bootstrap current drive. From (8.11)-(8.12), we see that the poloidal magnetic flux is coupled to the electron temperature dynamics through ohmic heating. Additionally, the local thermal transport, i.e., χ_e, is intimately dependent on the local magnetic state of the plasma [61, 62]. However, it is extremely difficult to develop closed-form expressions that accurately represent this complex interaction. Therefore, in this work we model the thermal conductivity as a nominal model plus a bounded uncertainty. We represent the thermal conductivity by a finite number of elements n_α as

$$\chi_e(\hat{\rho}) \approx \sum_{\alpha=1}^{n_\alpha} \Lambda_\alpha(\hat{\rho})\gamma_\alpha, \tag{8.15}$$

where $\Lambda_\alpha(\hat{\rho})$ are basis functions and

$$\gamma_\alpha = \gamma_\alpha^{nom} + \gamma_\alpha^{unc}\delta_\alpha, \tag{8.16}$$

where γ_α^{nom} and γ_α^{unc} are constants that define the range for each γ_α such that each uncertainty δ_α satisfies the condition $|\delta_\alpha| \leq 1$. The basis functions $\Lambda_\alpha(\hat{\rho})$ are chosen as cubic splines and are shown in Fig. 8.1(a). The evolution of the thermal conductivity profile during a typical TCV simulated discharge using RAPTOR [13–15] is shown in Fig. 8.1(b). Based on this data, we can obtain values for γ_α^{nom} and γ_α^{unc} in (8.16) by projecting (8.15) onto a set of trial functions $\Lambda_\beta(\hat{\rho})$ and integrating over the spatial domain, i.e.,

$$\int_0^1 \Lambda_\beta(\hat{\rho})\chi_e(\hat{\rho})d\hat{\rho} \approx \sum_{\alpha=1}^{n_\alpha} \int_0^1 \Lambda_\beta(\hat{\rho})\Lambda_\alpha(\hat{\rho})d\hat{\rho}\gamma_\alpha^*. \tag{8.17}$$

By choosing $\beta = \alpha$, (8.17) can be written in matrix form as

$$A_{\beta\alpha}\Gamma_\alpha^* = b_\beta, \tag{8.18}$$

where

$$A_{\beta\alpha} = \begin{bmatrix} \int_0^1 \Lambda_1(\hat{\rho})\Lambda_1(\hat{\rho})d\hat{\rho} & \dots & \int_0^1 \Lambda_1(\hat{\rho})\Lambda_{n_\alpha}(\hat{\rho})d\hat{\rho} \\ \vdots & \ddots & \vdots \\ \int_0^1 \Lambda_{n_\alpha}(\hat{\rho})\Lambda_1(\hat{\rho})d\hat{\rho} & \dots & \int_0^1 \Lambda_{n_\alpha}(\hat{\rho})\Lambda_{n_\alpha}(\hat{\rho})d\hat{\rho} \end{bmatrix}$$

$$\Gamma_\alpha^* = \begin{bmatrix} \gamma_1^* \\ \vdots \\ \gamma_{n_\alpha}^* \end{bmatrix} \qquad b_\beta = \begin{bmatrix} \int_0^1 \Lambda_1(\hat{\rho})\chi_e(\hat{\rho})d\hat{\rho} \\ \vdots \\ \int_0^1 \Lambda_{n_\alpha}(\hat{\rho})\chi_e(\hat{\rho})d\hat{\rho} \end{bmatrix}. \tag{8.19}$$

For each RAPTOR simulated χ_e, we solve (8.18) for Γ_α^*, and the parameters γ_α^{nom} and γ_α^{unc} in (8.16) are then calculated as

$$\begin{aligned} \gamma_\alpha^{nom} &= \left[\max(\gamma_\alpha^*) + \min(\gamma_\alpha^*)\right]/2, \\ \gamma_\alpha^{unc} &= \left[\max(\gamma_\alpha^*) - \min(\gamma_\alpha^*)\right]/2. \end{aligned} \tag{8.20}$$

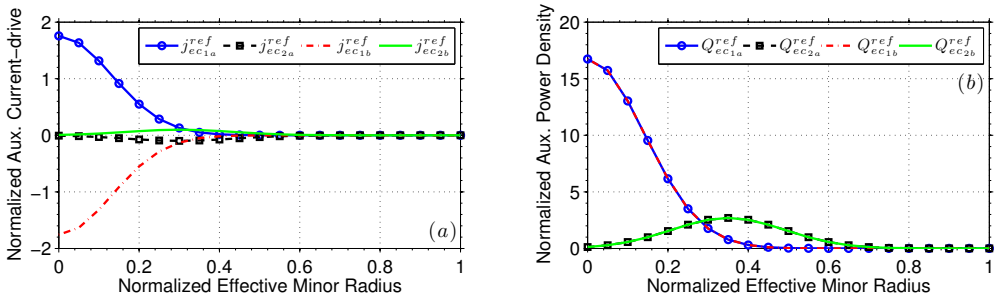

Figure 8.2: Normalized auxiliary electron cyclotron (a) current drive $\left(10^{20}\ \frac{\mathrm{m}^{-3}}{\mathrm{keV}\cdot\mathrm{W}}\cdot\frac{\mathrm{A}}{\mathrm{m}^2}\right)$ and (b) power density $\left(\mathrm{m}^{-3}\right)$ in the TCV tokamak.

The thermal conductivity uncertainty range captured by the model (8.15)-(8.16) with the parameters γ_α^{nom} and γ_α^{unc} defined by (8.20) is shown in Fig. 8.1(b). As shown in the figure, the majority of the thermal conductivity profiles fall within the range captured by the model.

8.2.5 Partial differential equation model of system dynamics

The auxiliary H&CD actuators on TCV considered in this work are 4 electron cyclotron (gyrotron) launchers that are grouped into 2 clusters (denoted as a and b). The respective current drive and power density deposition profiles for each source are shown in Fig. 8.2. The gyrotrons in cluster a are configured as follows: 1 on-axis heating and co-current-injection source ($j_{ec_{1a}}^{ref}$ and $Q_{ec_{1a}}^{ref}$ in Fig. 8.2) and 1 off-axis heating and counter-current-injection source ($j_{ec_{2a}}^{ref}$ and $Q_{ec_{2a}}^{ref}$ in Fig. 8.2), and the gyrotrons in cluster b are configured as follows: 1 on-axis heating and counter-current-injection source ($j_{ec_{1b}}^{ref}$ and $Q_{ec_{1b}}^{ref}$ in Fig. 8.2) and 1 off-axis heating and co-current-injection source ($j_{ec_{2b}}^{ref}$ and $Q_{ec_{2b}}^{ref}$ in Fig. 8.2). Also, note that the electron density could be utilized as an actuator, but for the scenarios considered in this work the electron density profile is assumed constant.

By combining the magnetic diffusion equation (8.2) with the resistivity model

(8.6), the noninductive current drive models (8.7)-(8.9), and defining the quantities

$$f_\eta(\hat{\rho}) = \frac{k_{sp} Z_{eff}}{\mu_0 \rho_b^2 \hat{F}^2} \qquad D_\psi(\hat{\rho}) = \hat{F}\hat{G}\hat{H},$$
$$g_{ec_i}(\hat{\rho}) = \frac{R_0 \hat{H} k_{sp} Z_{eff} j_{ec_i}^{ref}}{n_e} \qquad f_{bs_1}(\hat{\rho}) = \frac{k_{JkeV} R_0^2 k_{sp} Z_{eff} \hat{H}}{\hat{F}},$$
$$f_{bs_2}(\hat{\rho}) = 2\mathcal{L}_{31} \frac{dn_e}{d\hat{\rho}} \qquad f_{bs_3}(\hat{\rho}) = \left\{2\mathcal{L}_{31} + \mathcal{L}_{32} + \alpha \mathcal{L}_{34}\right\} n_e,$$

for $i \in$ [1a,2a,1b,2b], we obtain

$$\begin{aligned}\frac{\partial \psi}{\partial t} = {} & f_\eta \frac{1}{T_e^{3/2}} \frac{1}{\hat{\rho}} \frac{\partial}{\partial \hat{\rho}} \left(\hat{\rho} D_\psi \frac{\partial \psi}{\partial \hat{\rho}} \right) \\ & + \frac{1}{T_e^{1/2}} \left(\left[g_{ec_{1a}} + g_{ec_{2a}} \right] P_{ec_a}(t) + \left[g_{ec_{1b}} + g_{ec_{2b}} \right] P_{ec_b}(t) \right) \\ & + f_{bs_1} \left(\frac{\partial \psi}{\partial \hat{\rho}} \right)^{-1} \frac{1}{T_e^{3/2}} \left(f_{bs_2} T_e + f_{bs_3} \frac{\partial T_e}{\partial \hat{\rho}} \right). \end{aligned} \tag{8.21}$$

By combining the electron heat transport equation (8.4) with the electron heat source models (8.10)-(8.14), the thermal conductivity model (8.15)-(8.16), and defining the quantities

$$f_{T_e}(\hat{\rho}) = \frac{2}{3} \frac{1}{\rho_b^2 \hat{H} n_e} \qquad D_{T_e}(\hat{\rho}) = \frac{\hat{G}\hat{H}^2 n_e}{\hat{F}},$$
$$f_{j_{tor}}(\hat{\rho}) = \frac{2}{3} \frac{k_{sp} Z_{eff}}{k_{JkeV} n_e} \left(\frac{1}{\mu_0 \rho_b^2 R_0 \hat{H}} \right)^2 \qquad D_{j_{tor}}(\hat{\rho}) = \hat{G}\hat{H},$$
$$f_{rad}(\hat{\rho}) = \frac{2}{3} \frac{k_{brem} Z_{eff} n_e^2}{k_{JkeV} n_e} \qquad m_{ec_i}(\hat{\rho}) = \frac{2}{3} \frac{Q_{ec_i}^{ref}}{k_{JkeV} n_e},$$

for $i \in$ [1a,2a,1b,2b], we obtain

$$\begin{aligned}\frac{\partial T_e}{\partial t} = & f_{T_e}\frac{1}{\hat{\rho}}\frac{\partial}{\partial\hat{\rho}}\left[\hat{\rho}D_{T_e}\left(\sum_{\alpha=1}^{n_\alpha}\Lambda_\alpha\left\{\gamma_\alpha^{nom}+\gamma_\alpha^{unc}\delta_\alpha\right\}\right)\frac{\partial T_e}{\partial\hat{\rho}}\right] \\ & + f_{j_{tor}}\frac{1}{\hat{\rho}^2}\left[\frac{\partial}{\partial\hat{\rho}}\left(\hat{\rho}D_{j_{tor}}\frac{\partial\psi}{\partial\hat{\rho}}\right)\right]^2\frac{1}{T_e^{3/2}} - f_{rad}T_e^{1/2} \\ & + \left[m_{ec_{1a}}+m_{ec_{2a}}\right]P_{ec_a}(t) + \left[m_{ec_{1b}}+m_{ec_{2b}}\right]P_{ec_b}(t). \end{aligned} \tag{8.22}$$

From (8.1), we see that the rotational transform is related to the spatial gradient of the poloidal flux, which we define as

$$\theta(\hat{\rho},t) \equiv [\partial\psi/\partial\hat{\rho}(\hat{\rho},t)]. \tag{8.23}$$

By inserting (8.23) into (8.21)-(8.22) and after copious application of the chain rule, we obtain PDE models of the θ and T_e profile dynamics that are expressed as

$$\begin{aligned}\frac{\partial\theta}{\partial t} = & \frac{1}{T_e^{3/2}}\left[q_{\eta_1}\frac{\partial^2\theta}{\partial\hat{\rho}^2}+q_{\eta_2}\frac{\partial\theta}{\partial\hat{\rho}}+q_{\eta_3}\theta\right] - \frac{3}{2}\frac{1}{T_e^{5/2}}\frac{\partial T_e}{\partial\hat{\rho}}\left[q_{\eta_1}\frac{\partial\theta}{\partial\hat{\rho}}+q_{\eta_4}\theta\right] \\ & + \frac{1}{T_e^{1/2}}\left\{\left[g'_{ec_{1a}}+g'_{ec_{2a}}\right]P_{ec_a}(t)+\left[g'_{ec_{1b}}+g'_{ec_{2b}}\right]P_{ec_b}(t)\right\} \\ & - \frac{1}{2}\frac{1}{T_e^{3/2}}\frac{\partial T_e}{\partial\hat{\rho}}\left\{\left[g_{ec_{1a}}+g_{ec_{2a}}\right]P_{ec_a}(t)+\left[g_{ec_{1b}}+g_{ec_{2b}}\right]P_{ec_b}(t)\right\} \\ & + \frac{1}{\theta}\frac{1}{T_e^{3/2}}\left[f'_{bs_1}-f_{bs_1}\frac{1}{\theta}\frac{\partial\theta}{\partial\hat{\rho}}-\frac{3}{2}f_{bs_1}\frac{1}{T_e}\frac{\partial T_e}{\partial\hat{\rho}}\right]\left(f_{bs_2}T_e+f_{bs_3}\frac{\partial T_e}{\partial\hat{\rho}}\right) \\ & + f_{bs_1}\frac{1}{\theta}\frac{1}{T_e^{3/2}}\left(f'_{bs_2}T_e+\left\{f_{bs_2}+f'_{bs_3}\right\}\frac{\partial T_e}{\partial\hat{\rho}}+f_{bs_3}\frac{\partial^2 T_e}{\partial\hat{\rho}^2}\right) \end{aligned} \tag{8.24}$$

and

$$\begin{aligned}\frac{\partial T_e}{\partial t} = f_{T_e}\Bigg[& \left\{\frac{1}{\hat{\rho}}D_{T_e} + D'_{T_e}\right\}\left(\sum_{\alpha=1}^{n_\alpha}\Lambda_\alpha\left\{\gamma_\alpha^{nom} + \gamma_\alpha^{unc}\delta_\alpha\right\}\frac{\partial T_e}{\partial\hat{\rho}}\right) \\ & + D_{T_e}\left(\sum_{\alpha=1}^{n_\alpha}\Lambda'_\alpha\left\{\gamma_\alpha^{nom} + \gamma_\alpha^{unc}\delta_\alpha\right\}\frac{\partial T_e}{\partial\hat{\rho}}\right) \\ & + D_{T_e}\left(\sum_{\alpha=1}^{n_\alpha}\Lambda_\alpha\left\{\gamma_\alpha^{nom} + \gamma_\alpha^{unc}\delta_\alpha\right\}\frac{\partial^2 T_e}{\partial\hat{\rho}^2}\right)\Bigg] \\ & + f_{j_{tor}}\frac{1}{\hat{\rho}^2}\left[\left\{D_{j_{tor}} + \hat{\rho}D'_{j_{tor}}\right\}\theta + \hat{\rho}D_{j_{tor}}\frac{\partial\theta}{\partial\hat{\rho}}\right]^2\frac{1}{T_e^{3/2}} - f_{rad}T_e^{1/2} \\ & + \left[m_{ec_{1a}} + m_{ec_{2a}}\right]P_{ec_a}(t) + \left[m_{ec_{1b}} + m_{ec_{2b}}\right]P_{ec_b}(t), \end{aligned} \tag{8.25}$$

where $(\cdot)' = d/d\hat{\rho}$ and

$$\begin{aligned} q_{\eta_1}(\hat{\rho}) &= f_\eta(\hat{\rho})D_\psi(\hat{\rho}), \\ q_{\eta_2}(\hat{\rho}) &= f'_\eta(\hat{\rho})D_\psi(\hat{\rho}) + 2f_\eta(\hat{\rho})D'_\psi(\hat{\rho}) + f_\eta(\hat{\rho})D_\psi(\hat{\rho})/\hat{\rho}, \\ q_{\eta_3}(\hat{\rho}) &= f'_\eta(\hat{\rho})D_\psi(\hat{\rho})/\hat{\rho} + f'_\eta(\hat{\rho})D'_\psi(\hat{\rho}) - f_\eta(\hat{\rho})D_\psi(\hat{\rho})/\hat{\rho}^2 \\ &\quad + f_\eta(\hat{\rho})D'_\psi(\hat{\rho})/\hat{\rho} + f_\eta(\hat{\rho})D''_\psi(\hat{\rho}), \\ q_{\eta_4}(\hat{\rho}) &= f_\eta(\hat{\rho})D_\psi(\hat{\rho})/\hat{\rho} + f_\eta(\hat{\rho})D'_\psi(\hat{\rho}). \end{aligned}$$

8.3 Model reduction via spatial discretization

To obtain a model suitable for tracking feedback control design, the governing infinite dimensional PDEs (8.24) and (8.25) are approximated by a finite dimensional system of ordinary differential equations (ODEs). This is achieved by representing the spatial domain ($\hat{\rho} \in [0, 1]$) as m discrete nodes and approximating the spatial derivatives using a finite difference method of order $(\Delta\hat{\rho})^2$, where $\Delta\hat{\rho} = 1/(m-1)$ is the spacing between the evenly distributed nodes. After applying the spatial derivative approximations to (8.24) and (8.25) for the interior nodes $i = [2, \ldots, m-1]$, we

obtain

$$
\begin{aligned}
\dot{\theta}_i = & \frac{1}{T_{e_i}^{3/2}} \left[q_{\eta_1}(\hat{\rho}_i) \frac{\theta_{i+1} - 2\theta_i + \theta_{i-1}}{(\Delta\hat{\rho})^2} + q_{\eta_2}(\hat{\rho}_i) \frac{\theta_{i+1} - \theta_{i-1}}{2\Delta\hat{\rho}} + q_{\eta_3}(\hat{\rho}_i)\theta_i \right] \\
& - \frac{3}{2} \frac{1}{T_{e_i}^{5/2}} \frac{T_{e_{i+1}} - T_{e_{i-1}}}{2\Delta\hat{\rho}} \left[q_{\eta_1}(\hat{\rho}_i) \frac{\theta_{i+1} - \theta_{i-1}}{2\Delta\hat{\rho}} + q_{\eta_4}(\hat{\rho}_i)\theta_i \right] \\
& + \frac{1}{T_{e_i}^{1/2}} \left\{ \left[g'_{ec_{1a}}(\hat{\rho}_i) + g'_{ec_{2a}}(\hat{\rho}_i) \right] P_{ec_a}(t) + \left[g'_{ec_{1b}}(\hat{\rho}_i) + g'_{ec_{2b}}(\hat{\rho}_i) \right] P_{ec_b}(t) \right\} \\
& - \frac{1}{2} \frac{1}{T_{e_i}^{3/2}} \frac{T_{e_{i+1}} - T_{e_{i-1}}}{2\Delta\hat{\rho}} \left\{ \left[g_{ec_{1a}}(\hat{\rho}_i) + g_{ec_{2a}}(\hat{\rho}_i) \right] P_{ec_a}(t) + \left[g_{ec_{1b}}(\hat{\rho}_i) + g_{ec_{2b}}(\hat{\rho}_i) \right] P_{ec_b}(t) \right\} \\
& + \frac{1}{\theta_i} \frac{1}{T_{e_i}^{3/2}} \left[f'_{bs_1}(\hat{\rho}_i) - f_{bs_1}(\hat{\rho}_i) \frac{1}{\theta_i} \frac{\theta_{i+1} - \theta_{i-1}}{2\Delta\hat{\rho}} - \frac{3}{2} f_{bs_1}(\hat{\rho}_i) \frac{1}{T_{e_i}} \frac{T_{e_{i+1}} - T_{e_{i-1}}}{2\Delta\hat{\rho}} \right] \\
& \times \left(f_{bs_2}(\hat{\rho}_i) T_{e_i} + f_{bs_3}(\hat{\rho}_i) \frac{T_{e_{i+1}} - T_{e_{i-1}}}{2\Delta\hat{\rho}} \right) \\
& + f_{bs_1}(\hat{\rho}_i) \frac{1}{\theta_i} \frac{1}{T_{e_i}^{3/2}} \left(f'_{bs_2}(\hat{\rho}_i) T_{e_i} + \left\{ f_{bs_2}(\hat{\rho}_i) + f'_{bs_3}(\hat{\rho}_i) \right\} \frac{T_{e_{i+1}} - T_{e_{i-1}}}{2\Delta\hat{\rho}} \right. \\
& \left. + f_{bs_3}(\hat{\rho}_i) \frac{T_{e_{i+1}} - 2T_{e_i} + T_{e_{i-1}}}{(\Delta\hat{\rho})^2} \right)
\end{aligned} \tag{8.26}
$$

and

$$
\begin{aligned}
\dot{T}_{e_i} = & f_{T_e}(\hat{\rho}_i) \left[\left\{ \frac{1}{\hat{\rho}_i} D_{T_e}(\hat{\rho}_i) + D'_{T_e}(\hat{\rho}_i) \right\} \left(\sum_{\alpha=1}^{n_\alpha} \Lambda_\alpha(\hat{\rho}_i) \left\{ \gamma_\alpha^{nom} + \gamma_\alpha^{unc} \delta_\alpha \right\} \frac{T_{e_{i+1}} - T_{e_{i-1}}}{2\Delta\hat{\rho}} \right) \right. \\
& + D_{T_e}(\hat{\rho}_i) \left(\sum_{\alpha=1}^{n_\alpha} \Lambda'_\alpha(\hat{\rho}_i) \left\{ \gamma_\alpha^{nom} + \gamma_\alpha^{unc} \delta_\alpha \right\} \frac{T_{e_{i+1}} - T_{e_{i-1}}}{2\Delta\hat{\rho}} \right) \\
& \left. + D_{T_e}(\hat{\rho}_i) \left(\sum_{\alpha=1}^{n_\alpha} \Lambda_\alpha(\hat{\rho}_i) \left\{ \gamma_\alpha^{nom} + \gamma_\alpha^{unc} \delta_\alpha \right\} \frac{T_{e_{i+1}} - 2T_{e_i} + T_{e_{i-1}}}{(\Delta\hat{\rho})^2} \right) \right] \\
& + f_{j_{tor}}(\hat{\rho}_i) \frac{1}{\hat{\rho}_i^2} \left[\left\{ D_{j_{tor}}(\hat{\rho}_i) + \hat{\rho}_i D'_{j_{tor}}(\hat{\rho}_i) \right\} \theta_i + \hat{\rho}_i D_{j_{tor}}(\hat{\rho}_i) \frac{\theta_{i+1} - \theta_{i-1}}{2\Delta\hat{\rho}} \right]^2 \frac{1}{T_{e_i}^{3/2}} \\
& - f_{rad}(\hat{\rho}_i) T_{e_i}^{1/2} + \left[m_{ec_{1a}}(\hat{\rho}_i) + m_{ec_{2a}}(\hat{\rho}_i) \right] P_{ec_a}(t) + \left[m_{ec_{1b}}(\hat{\rho}_i) + m_{ec_{2b}}(\hat{\rho}_i) \right] P_{ec_b}(t),
\end{aligned} \tag{8.27}
$$

where θ_i, T_{e_i}, and $\hat{\rho}_i$ are the values of θ, T_e, and $\hat{\rho}$ at the discrete nodes, for $i = [2, \ldots, m-1]$. The values of θ and T_e at the boundary nodes $i = 1$ and $i = m$ are

obtained from the boundary conditions (8.3) and (8.5) and are expressed as

$$\theta_1 = 0 \qquad T_{e_1} = \frac{4T_{e_2} - T_{e_3}}{3}, \tag{8.28}$$

$$\theta_m = -k_{I_p} I_p(t) \qquad T_{e_m} = T_{e,bdry}. \tag{8.29}$$

The discretized model can be written in a compact form as

$$\dot{\hat{\theta}} = F_\theta(\hat{\theta}, \hat{T}_e, u), \tag{8.30}$$

$$\dot{\hat{T}}_e = F_{T_e}(\hat{\theta}, \hat{T}_e, u, \delta), \tag{8.31}$$

$$\iota_i = -\frac{1}{B_{\phi,0}\rho_b^2 \hat{\rho}_i}\theta_i, \tag{8.32}$$

where $\hat{\theta} = [\theta_2, \ldots, \theta_{m-1}] \in \mathbb{R}^n$, $\hat{T}_e = [T_{e_2}, \ldots, T_{e_{m-1}}] \in \mathbb{R}^n$, ι_i is the value of ι at the discrete nodes, for $i = [2, \ldots, m-1]$, $u = [P_{ec_a}, P_{ec_b}, I_p] \in \mathbb{R}^3$ is the control input vector, $\delta = [\delta_1, \ldots, \delta_{n_\alpha}] \in \mathbb{R}^{n_\alpha}$ is the uncertain parameter vector, $F_\theta \in \mathbb{R}^n$ and $F_{T_e} \in \mathbb{R}^n$ are nonlinear functions, and $n = m - 2$. By defining the state vector as $x = [\hat{\theta}, \hat{T}_e] \in \mathbb{R}^{2n}$, we can write the state dynamics as

$$\dot{x} = \begin{bmatrix} F_\theta(\hat{\theta}, \hat{T}_e, u) \\ F_{T_e}(\hat{\theta}, \hat{T}_e, u, \delta) \end{bmatrix} = F_{\theta,T_e}(x, u, \delta) \in \mathbb{R}^{2n}. \tag{8.33}$$

The output vector is defined as $y = [\hat{\iota}, \hat{T}_e] \in \mathbb{R}^{2n}$, where $\hat{\iota} = [\iota_2, \ldots, \iota_{m-1}] \in \mathbb{R}^n$.

We define an equilibrium point of the system (8.33) as

$$\dot{x}_{eq} = F_{\theta,T_e}(x_{eq}, u_{eq}, 0) = 0. \tag{8.34}$$

We can obtain a model suitable for tracking control design by defining the perturbation variables $\tilde{x}(t) = x(t) - x_{eq}$ and $u_{fb}(t) = u(t) - u_{eq}$, where $\tilde{x}(t)$ is the deviation

away from the equilibrium state and $u_{fb}(t)$ is the output of the to-be-designed feedback controller. Linearizing (8.33) *with respect to the state and control input* around an equilibrium point defined by (8.34), we obtain

$$\dot{x}_{eq} + \dot{\tilde{x}} = F_{\theta,T_e}(x_{eq}, u_{eq}, \delta) + \left.\frac{\partial F_{\theta,T_e}}{\partial x}\right|_{(x_{eq},u_{eq},\delta)} \tilde{x} + \left.\frac{\partial F_{\theta,T_e}}{\partial u}\right|_{(x_{eq},u_{eq},\delta)} u_{fb}, \tag{8.35}$$

where $\partial F_{\theta,T_e}/\partial x \in \mathbb{R}^{2n\times 2n}$ and $\partial F_{\theta,T_e}/\partial u \in \mathbb{R}^{2n\times 3}$ are the Jacobians of the system. By employing (8.34), we express (8.35) as

$$\dot{\tilde{x}} = \left.\frac{\partial F_{\theta,T_e}}{\partial x}\right|_{(x_{eq},u_{eq},\delta)} \tilde{x} + \left.\frac{\partial F_{\theta,T_e}}{\partial u}\right|_{(x_{eq},u_{eq},\delta)} u_{fb} + d_\delta, \tag{8.36}$$

where $d_\delta = F_{\theta,T_e}(x_{eq}, u_{eq}, \delta)$ is a disturbance. Finally, (8.36) is written as an explicit uncertain state-space system as

$$\begin{aligned} \dot{\tilde{x}} &= A(\delta)\tilde{x} + Bu_{fb} + d_\delta, \\ y &= C\tilde{x} + Du_{fb}, \end{aligned} \tag{8.37}$$

where $A(\delta)$ and B are the Jacobians $\partial F_{\theta,T_e}/\partial x \in \mathbb{R}^{2n\times 2n}$ and $\partial F_{\theta,T_e}/\partial u \in \mathbb{R}^{2n\times 3}$ evaluated at (x_{eq}, u_{eq}, δ),

$$C = \begin{bmatrix} C_\iota & 0 \\ 0 & C_{T_e} \end{bmatrix},$$

where $C_\iota = \text{diag}\{-1/(B_{\phi,0}\rho_b^2\hat{\rho}_i)\} \in \mathbb{R}^{n\times n}$, $C_{T_e} = \text{diag}\{1\} \in \mathbb{R}^{n\times n}$, and $D = 0$. The structure of the matrix $A(\delta)$ is of the form

$$A(\delta) = A_0 + \sum_{i=1}^{n_\alpha} \delta_i A_i, \tag{8.38}$$

where A_0 represents the nominal system response and A_i represents the influence that the uncertain parameter δ_i has on the system response.

8.4 Manipulation of dynamic model into robust control framework

We now exploit the structure of the matrix $A(\delta)$ in (8.38) to write the system (8.37) in the conventional $P-\Delta$ robust control framework (shown in the little purple box in Fig. 8.3), where P is the generalized transfer function of the system and $\Delta = \text{diag}\{\delta\}$ is a structured uncertainty matrix. The transfer function of a linear system with state-space matrices A, B, C, and D can be written as an upper linear fractional transformation (LFT) as

$$G(s) = F_u\left(M_a, \frac{1}{s}I\right) = D + C(sI - A)^{-1}B, \tag{8.39}$$

where F_u is the upper LFT, the matrix M_a is defined as

$$M_a = \begin{bmatrix} A & B \\ C & D \end{bmatrix}, \tag{8.40}$$

I is an identity matrix with the appropriate dimensions, and s denotes the Laplace variable. The nominal model will be coupled with the uncertain parameters in the transfer function representation of (8.37). By employing the method outlined in [138], we can separate the uncertain parameters from the nominal parameters to write the system (8.37) in the $P-\Delta$ robust control framework. The input-output equations of the system in this framework are expressed as

$$\begin{aligned} y_\Delta &= P_{11}u_\Delta + P_{12}u_{fb}, \\ y &= P_{21}u_\Delta + P_{22}u_{fb} + d, \end{aligned} \tag{8.41}$$

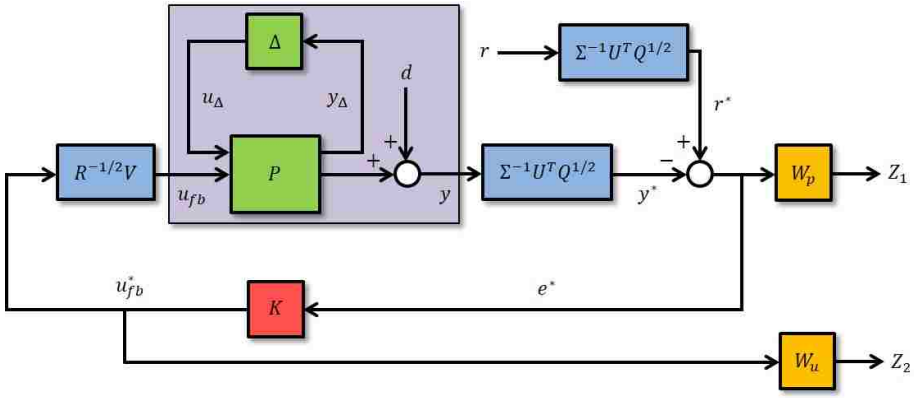

Figure 8.3: Schematic of control problem formulation for simultaneous $\iota + T_e$ profile feedback control design in TCV L-mode scenarios.

where P_{11}, P_{12}, P_{21}, and P_{22} are the component transfer functions of P that describe how the system inputs (u_Δ, u_{fb}) affect the system outputs (y_Δ, y) and d represents the effect that the disturbance d_δ has on the system outputs. An overview of the employed technique is provided in Appendix A.

8.5 Evaluation of relevant control channels

The feedback system (8.41) is an underactuated system, i.e., there are $2n$ outputs but only 3 inputs. Therefore, at most 3 linear combinations of the system output can be controlled. In this work, we employ a singular value decomposition (SVD) of the nominal input-output relation

$$y = G_0(s)u_{fb} \quad \text{where} \quad G_0(s) = C\left(sI - A(0)\right)^{-1}B + D$$

at a particular frequency to choose the output directions (and associated input directions) to control. The real approximation of the nominal input-output relation at a particular frequency $j\omega_{dc}$ is expressed as

$$\hat{y} = \hat{G}_0\hat{u}_{fb}, \tag{8.42}$$

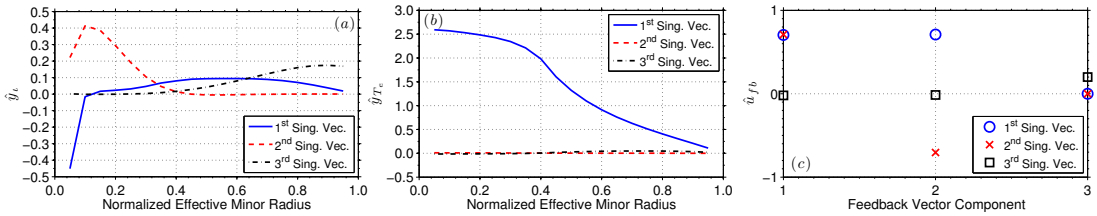

Figure 8.4: Relevant control channels for ι and T_e profile control in TCV L-mode scenarios: (a-b) output and (c) input. The output is defined as $\hat{y} = [\hat{y}_\iota, \hat{y}_{T_e}]$, where $\hat{y}_\iota$ are the system outputs associated with the rotational transform, and $\hat{y}_{T_e}$ are the system outputs associated with the electron temperature. The feedback vector components are $u_{fb} = [P_{ec_a}, P_{ec_b}, I_p]\,|_{fb}$.

where $\hat{G}_0$ denotes the real approximation of the complex matrix $G_0(j\omega_{dc})$ [10, 146]. We next define the "weighted" transfer function $\tilde{G}_0$ and its economy size singular value decomposition as $\tilde{G}_0 = Q^{1/2}\hat{G}_0 R^{-1/2} = U\Sigma V^T$, where $\Sigma \in \mathbb{R}^{3\times 3}$ is a diagonal matrix of singular values, and $U \in \mathbb{R}^{2n\times 3}$ and $V \in \mathbb{R}^{3\times 3}$ are matrices that possess the following properties $V^TV = VV^T = I, U^TU = I$. We have introduced the positive definite matrices $Q \in \mathbb{R}^{2n\times 2n}$ and $R \in \mathbb{R}^{3\times 3}$ to weight the relative tracking performance and control effort. The input-output relation (8.42) is now expressed as

$$\hat{y} = \hat{G}_0\hat{u}_{fb} = Q^{-1/2}\tilde{G}_0 R^{1/2}\hat{u}_{fb} = Q^{-1/2}U\Sigma V^T R^{1/2}\hat{u}_{fb}.$$

The singular vectors of the basis for the subspace of obtainable output values ($\hat{y} = Q^{-1/2}U\Sigma\hat{y}^*$) and the corresponding input singular vectors ($\hat{u}_{fb} = R^{-1/2}V\hat{u}^*_{fb}$) are shown in Fig. 8.4, where $\hat{y}^*$ and $\hat{u}^*_{fb}$ are the decoupled output and input, i.e., $\hat{y}^* = \hat{u}^*_{fb}$. A detailed overview of the SVD technique employed to evaluate the relevant control channels is provided in Appendix B. In this work, the frequency to evaluate the relevant channels at is chosen as $\omega_{dc} = 250$ rad/s. By examining Fig. 8.4, we see that this choice allows us to utilize the gyrotrons (P_{ec_a} and P_{ec_b} in opposite directions) to control the ι profile in the plasma core through auxiliary current drive, the total plasma current to control the ι profile near the plasma boundary, and the gyrotrons (P_{ec_a} and P_{ec_b} in the same direction) to control the electron temperature profile. Also

by examining Fig. 8.4, we can see the difference in time scales between the rotational transform and electron temperature dynamics. From Figs. 8.4(a) and (c), we see that at a frequency of 250 rad/s the effect of modifying the total plasma current at the plasma boundary has not had time to propagate to the core of the plasma, whereas from Fig. 8.4(b), we see that the effects of the actuators on the electron temperature have fully propagated across the entire spatial domain. As a result, we see that the electron temperature dynamics are governed by a faster time constant than the rotational transform dynamics.

8.6 Feedback control problem formulation

The feedback control problem is formulated as shown in Fig. 8.3, where r is the reference value, $e = r - y$ is the tracking error, and K is the to-be-designed feedback controller. The closed-loop system outputs are Z_1 and Z_2, and the frequency dependent weight functions W_p and W_u are utilized to optimize the feedback performance. The feedback control objectives are to maintain a small tracking error for any reference, reject the effects of the external disturbance, utilize as little feedback control effort as possible, and robustly stabilize the system by controlling the relevant input and output channels of the system (8.41). The control problem is formulated as

$$\min_{K} \left|\left|T_{zw}\right|\right|_{\infty}, \ \forall\omega \qquad T_{zw} = \begin{bmatrix} W_p S_{DC_O} & -W_p S_{DC_O} \\ W_u K S_{DC_O} & -W_u K S_{DC_O} \end{bmatrix}, \tag{8.43}$$

which represents the closed-loop nominal performance condition. The function T_{zw} is the closed-loop transfer function from the inputs (r^*, d^*) to the outputs (Z_1, Z_2), $d^* = \Sigma^{-1}U^T Q^{1/2} d$, and $S_{DC_O} = (I + \Sigma^{-1}U^T Q^{1/2} P_{22} R^{-1/2} V K)^{-1}$. See section 3.6 for an example of how this nominal performance condition is derived. See Appendix C for an introduction to the design of feedback controllers by employing the H_∞

closed-loop shaping technique. The feedback controller K obtained by solving (8.43) is written in state-space form as

$$\dot{x}_{fb} = A^*_{fb} x_{fb} + B^*_{fb} e^*,$$
$$u^*_{fb} = C^*_{fb} x_{fb} + D^*_{fb} e^*,$$

where $x_{fb} \in \mathbb{R}^{n_{fb}}$ is the internal controller state vector, $A^*_{fb} \in \mathbb{R}^{n_{fb} \times n_{fb}}$, $B^*_{fb} \in \mathbb{R}^{n_{fb} \times 3}$, $C^*_{fb} \in \mathbb{R}^{3 \times n_{fb}}$ and $D^*_{fb} \in \mathbb{R}^{3 \times 3}$ are the controller system matrices, and n_{fb} is the number of controller states. Equivalently, the controller can be written in terms of the tracking error e and control input u_{fb} as

$$\begin{aligned} \dot{x}_{fb} &= A_{fb} x_{fb} + B_{fb} e, \\ u_{fb} &= C_{fb} x_{fb} + D_{fb} e, \end{aligned} \tag{8.44}$$

where

$$\begin{aligned} A_{fb} &= A^*_{fb}, \\ B_{fb} &= B^*_{fb} \Sigma^{-1} U^T Q^{1/2}, \\ C_{fb} &= R^{-1/2} V C^*_{fb}, \\ D_{fb} &= R^{-1/2} V D^*_{fb} \Sigma^{-1} U^T Q^{1/2}. \end{aligned}$$

To analyze the performance of the closed-loop system, the singular value diagrams of the inverse of the performance weight functions and the achieved transfer functions S_{DC_O} and KS_{DC_O} are shown in Fig. 8.5(a-b). As shown in the figure, the controller achieves nominal performance. The robust stability of the closed-loop system with the nominal controller is analyzed by exploiting the block-diagonal structure of the uncertainty matrix, i.e., $\Delta = \text{diag}\{\delta\}$, which allows us to compute the structured

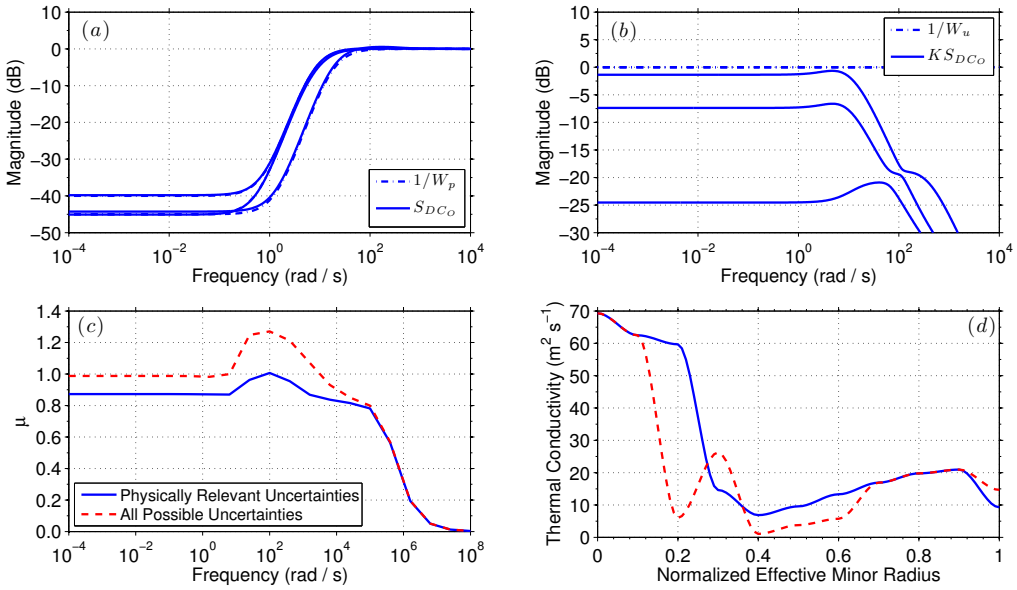

Figure 8.5: (a) Nominal performance (tracking), (b) nominal performance (control effort), (c) structured singular value versus frequency for physically relevant (solid) and all possible (dashed) uncertainties according to the model (8.15)-(8.16), and (d) the corresponding χ_e that results in the largest μ-value at a frequency of 100 rad/s for each respective case in (c). The robust stability condition is defined as $\mu(N_{11}(j\omega)) < 1 \ \forall\omega$ [10].

singular value

$$\mu\left(N_{11}(j\omega)\right) = \frac{1}{\min\{k_m | \det\left(I - k_m N_{11}\Delta\right) = 0\}},$$

where $N_{11} = P_{11} - P_{12}R^{-1/2}VKS_{DC_O}\Sigma^{-1}U^TQ^{1/2}P_{21}$ (see section 3.6 for an example of how this transfer function is derived) is the closed-loop transfer function between the signals y_Δ and u_Δ shown in Fig. 8.3. A plot of μ versus frequency is shown in Fig. 8.5(c). As shown in the figure, for all possible uncertainties (dashed line in Fig. 8.5(c)) according to the model (8.15)-(8.16), the nominal controller does not achieve robust stability. However, by comparing the thermal conductivity profile that results in the largest μ-value for this case (dashed line in Fig. 8.5(d)) to the thermal conductivity profiles predicted by RAPTOR in Fig. 8.1(b), we see that the model (8.15)-(8.16) can allow unphysical thermal conductivity profiles. Therefore, we restrict the uncertainties in the model (8.15)-(8.16) by requiring that the resulting

thermal conductivity profile should satisfy

$$\frac{\partial \chi_e}{\partial \hat{\rho}} < 0 \text{ for } \hat{\rho} \in [0, 0.35] \quad \text{and} \quad \frac{\partial \chi_e}{\partial \hat{\rho}} > 0 \text{ for } \hat{\rho} \in [0.45, 0.85].$$

We then recompute μ, and as shown by the solid line in Fig. 8.5(c), the nominal controller achieves robust stability for this subset of uncertainties (marginal stability is reached at a frequency of 100 rad/s).

8.7 Control algorithm performance testing in TCV RAPTOR simulations

We now test the closed-loop performance of the integrated $\iota + T_e$ profile feedback controller (8.44) in TCV RAPTOR [13–15] simulations. In order to the ensure a fair assessment of the controller performance, the target plasma state must be physically achievable, i.e., the ι and T_e profiles that are specified as targets in the simulations must be compatible with each other. In this work, we obtain T_e profiles that are compatible with specific ι profiles by executing RAPTOR simulations with ι profile control only (see chapter 7) and taking the resulting T_e profile as a nominal compatible target.

The controller is tested with two different sets of ι and T_e profile targets to assess the ability of the controller to drive the system to multiple different operating points. In all cases the target profiles are specified in the same way. The ι profile target is held constant for the duration of the simulation, and the nominal compatible T_e profile is chosen as the target during the time interval $t \in [0, 1)$ s. During the time interval $t \in [1, 1.4)$ s, the nominal compatible T_e profile is scaled down by 10%, and the resulting profile is specified as the target. Finally, the nominal compatible T_e profile is scaled up by 10%, and the resulting profile is specified as the target during

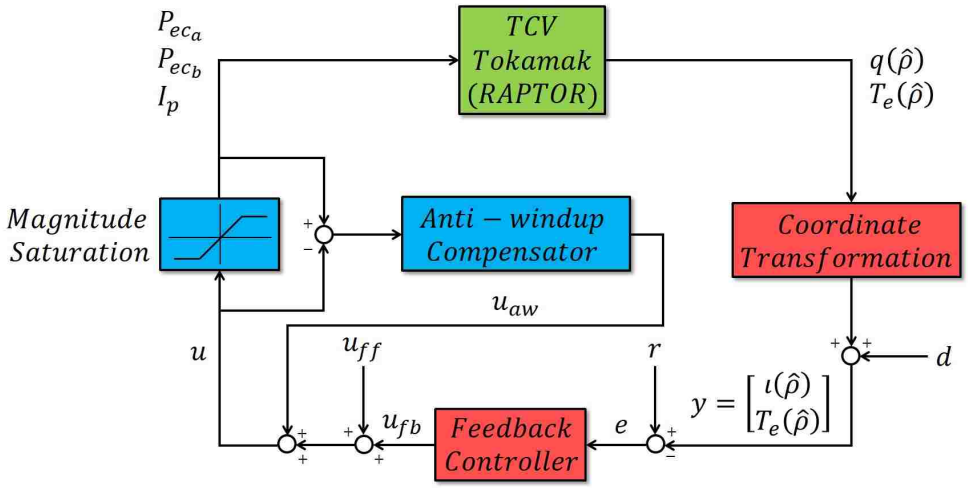

Figure 8.6: Schematic of closed-loop control system structure for simultaneous $\iota + T_e$ profile control for the TCV tokamak.

the time interval $t \in [1.4, 2]$ s. Specifying the target evolution in this way provides the opportunity to (i) test the ability of the controller to track a nominal ι and T_e profile evolution ($t \in [0, 1)$ s) and (ii) assess the ability of the controller to modulate individual quantities (T_e profile) while simultaneously maintaining other quantities (ι profile) in a stationary condition ($t \in [1, 2]$ s).

The sequence of simulations to test the controller performance are also executed in the same way. First, a nominal ι and T_e profile evolution is obtained by executing a feedforward-only simulation with a nominal set of input trajectories. Next, the ability of the controller to track the target is determined by executing a feedforward + feedback simulation with the nominal input trajectories. During the feedback-controlled simulations, the controller is inactive during the time interval $t \in [0, 0.1]$ s. The simulation results are presented in terms of the achieved q profile ($q = 1/\iota$) as this is the quantity most often utilized in the literature to specify the magnetic state of the plasma.

A schematic of the closed-loop control system structure is shown in Fig. 8.6. To ensure the closed-loop system remains well-behaved in the presence of actuator

magnitude saturation, the feedback controller is augmented by an anti-windup compensator [140]. See section 4.4.6 for an example of the employed anti-windup scheme.

8.7.1 Broad T_e profile with $q(0,t) = 1.05$ and $q(0.8,t) = 3.3$

In this section, a q profile achieved in the TCV tokamak with a total plasma current of 190 kA and counter-current-injection auxiliary power is chosen as the target. The corresponding nominal electron temperature profile that is specified as the target exhibits a broad profile shape. Time traces of q and T_e at various spatial locations, a comparison of the target, feedforward + feedback controlled, and feedforward controlled q and T_e profiles, and a comparison of the control inputs is shown in Fig. 8.7. Once the controller becomes active at 0.1 s, it is able to drive the ι and T_e profiles to the target during the nominal phase of the simulation ($t \in [0,1)$ s) by increasing the total plasma current and the cluster b gyrotron power and decreasing the cluster a gyrotron power. During the time interval $t \in [1,2]$ s, the controller is able to modulate the T_e profile between equilibrium points while maintaining the q profile in a relatively stationary condition by rejecting the effects the changing electron temperature has on the magnetic profile dynamics (see (8.6), (8.8), and (8.9)).

8.7.2 Narrow T_e profile with $q(0,t) = 1.17$ and $q(0.8,t) = 4.5$

In this section, a q profile achieved in the TCV tokamak with a total plasma current of 140 kA and counter-current-injection auxiliary power is chosen as the target. The corresponding nominal electron temperature profile that is specified as the target exhibits a narrow profile shape. Time traces of q and T_e at various spatial locations, a comparison of the target, feedforward + feedback controlled, and feedforward controlled q and T_e profiles, and a comparison of the control inputs is shown in Fig. 8.8. When the controller becomes active at 0.1 s, it is again able to drive the ι and T_e

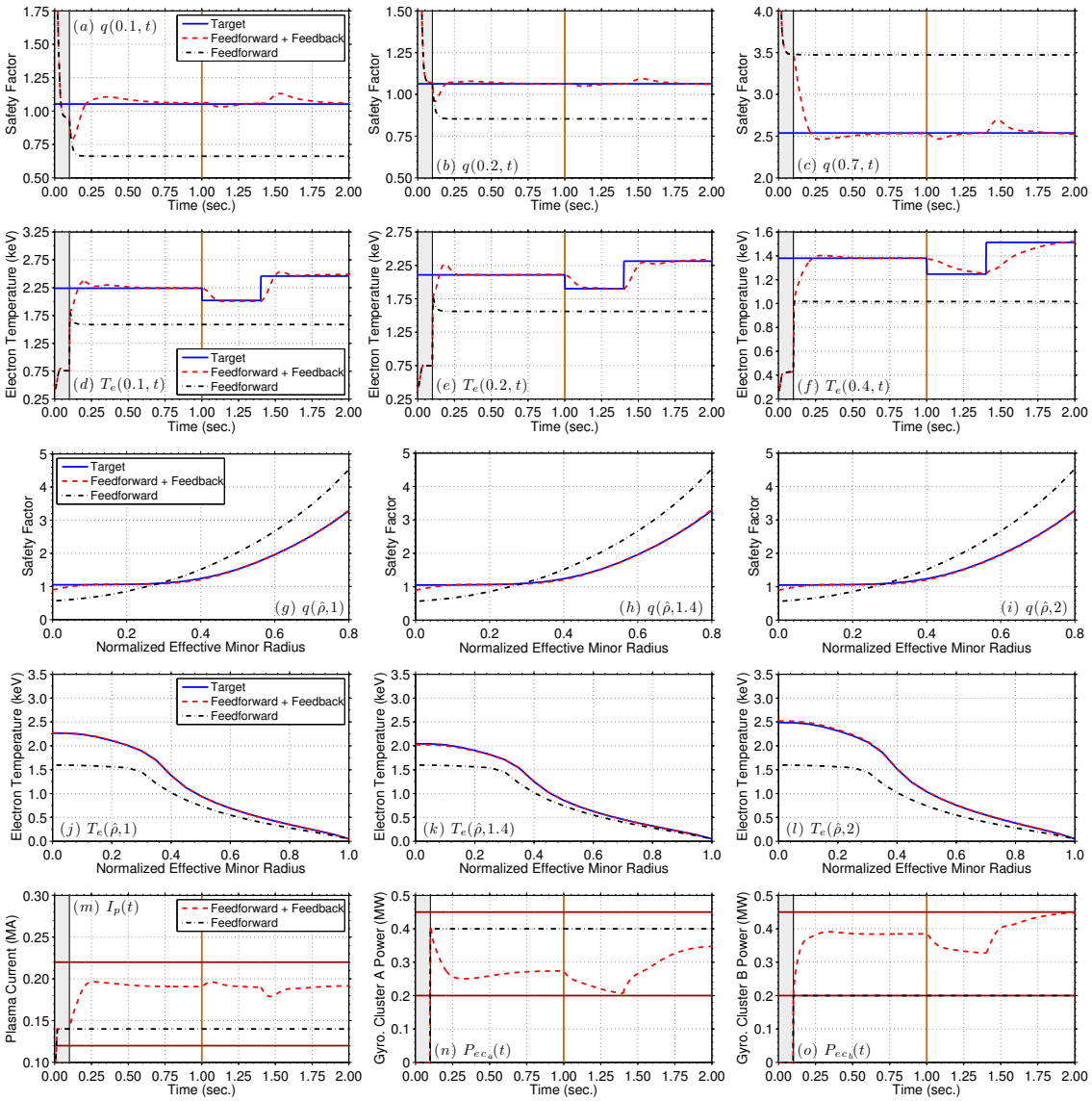

Figure 8.7: (a-f) Time traces of outputs (q, T_e) at various radial locations, (g-l) comparison of target, feedforward + feedback, and feedforward controlled outputs $(q(\hat{\rho})$ and $T_e(\hat{\rho}))$ at various times, and (m-o) comparison of control inputs $(I_p, P_{ec_a}, P_{ec_b})$ for the simulation in section 8.7.1. The solid-orange line denotes when the target q profile is maintained in a stationary condition while modifying the T_e profile. Feedback controller off (gray-shaded region) and actuator limits (solid brown).

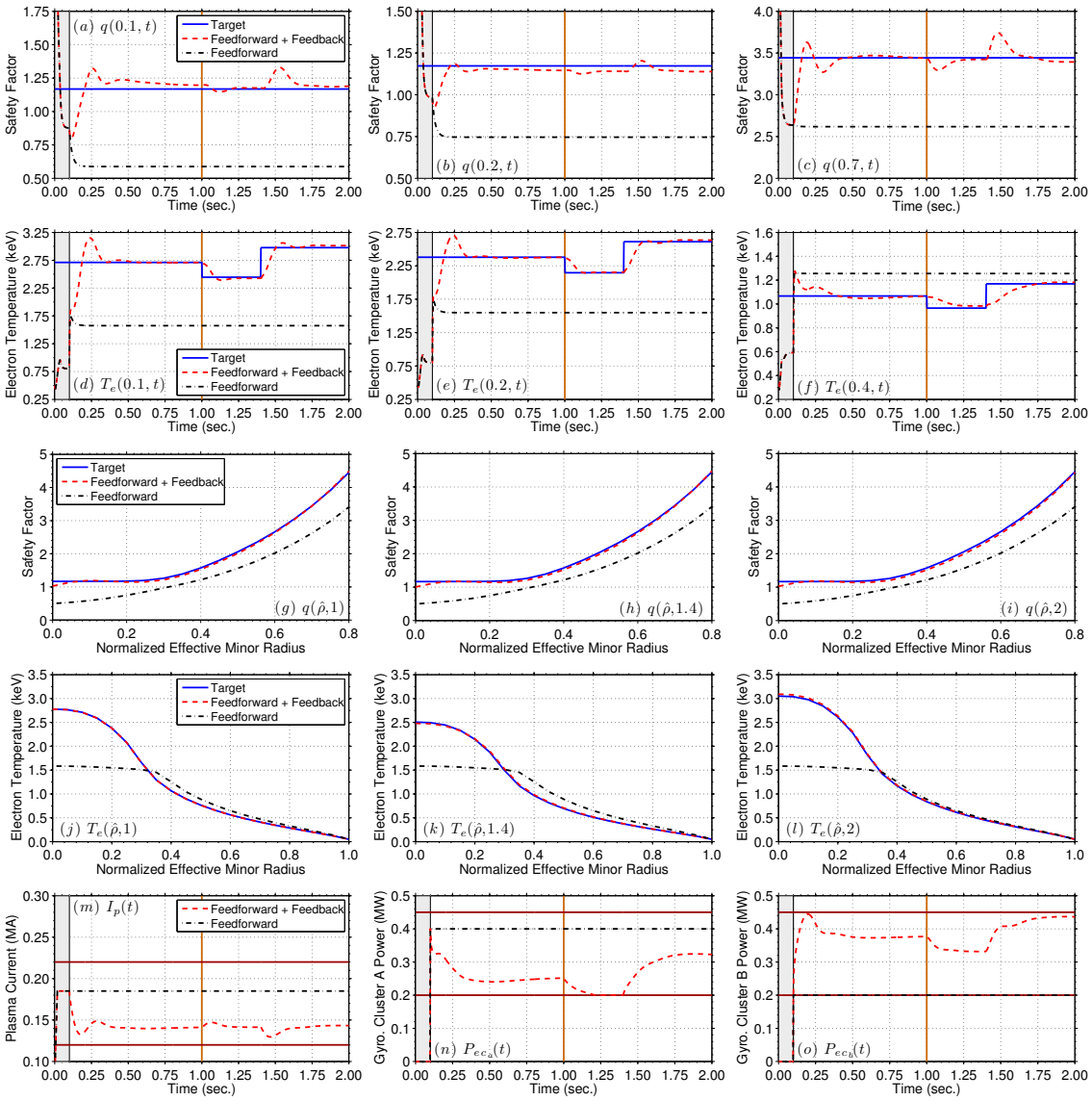

Figure 8.8: (a-f) Time traces of outputs (q, T_e) at various radial locations, (g-l) comparison of target, feedforward + feedback, and feedforward controlled outputs $(q(\hat{\rho})$ and $T_e(\hat{\rho}))$ at various times, and (m-o) comparison of control inputs $(I_p, P_{ec_a}, P_{ec_b})$ for the simulation in section 8.7.2. The solid-orange line denotes when the target q profile is maintained in a stationary condition while modifying the T_e profile. Feedback controller off (gray-shaded region) and actuator limits (solid brown).

profiles to the target during the nominal phase of the simulation ($t \in [0, 1)$ s) by decreasing the total plasma current and the cluster a gyrotron power and increasing the cluster b gyrotron power. Once again, the controller is able to modulate the T_e profile between equilibrium points while maintaining the q profile in a relatively stationary condition during the time interval $t \in [1, 2]$ s.

8.8 Conclusion

An integrated feedback algorithm for ι and T_e profile control in tokamaks was developed following a FPD, physics-based modeling approach. The electron thermal conductivity profile was modeled as a nominal profile plus a bounded uncertainty, and the controller was designed to be robust to an expected range of uncertainty. The performance of the controller was demonstrated through RAPTOR simulations of the TCV tokamak plasma dynamics. One direction of future work is to develop a model of χ_e that naturally predicts physically relevant profiles. Additionally, our future work includes utilizing the closed-loop plasma state observer developed in [150] to reconstruct the ι and T_e profiles in real-time to experimentally test the controller in TCV.

Chapter 9

Conclusions and future work

The work in this dissertation has focused on developing algorithms for current profile and combined current profile + thermal state control in nuclear fusion tokamak reactors. In this chapter, the contributions of this dissertation are summarized, and some possible directions of future research are discussed.

9.1 Contributions

The contributions of this dissertation are as follows:

1. A general physics-based modeling approach was developed to convert the physics model that describes the current profile evolution in the tokamak into a form suitable for control design. This was accomplished by developing physics-based, control-oriented models of the electron density, the electron temperature, the plasma resistivity, and the noninductive current drives in response to the available control actuators. This first-principles-driven (FPD) model (as well as the accompanying numerical simulation code) is readily tailored to a given operating scenario in a given machine of interest. In this dissertation, the model was

tailored to low confinement (L-mode) and high confinement (H-mode) scenarios in DIII-D, H-mode burning plasma scenarios in ITER, and L-mode scenarios in TCV, demonstrating the flexibility of the employed methodology. The model's predictive capabilities were demonstrated through comparison to the evolution of experimentally-achieved/advanced-simulation-predicted plasma parameters. In addition to the control applications developed in this dissertation, the physics-based modeling approach and numerical simulation code were employed to develop and test other current profile control algorithms for the DIII-D tokamak [100, 101, 151] and the National Spherical Torus Experiment Upgrade (NSTX-U) tokamak [152–154], and are currently being extended to the EAST tokamak.

2. A general framework for real-time feedforward + feedback control of magnetic and kinetic plasma profiles was implemented in the DIII-D Plasma Control System (PCS). A tokamak simulation model (Simserver) that can interface with the control algorithm implemented in the DIII-D PCS was developed, which enabled closed-loop simulations with the real-time code to be executed to debug the algorithm prior to experimental testing. In addition to the controllers tested in this dissertation, the control framework and Simserver were employed to implement, debug, and experimentally test the controllers developed in [77, 78, 98–105] for current profile control in DIII-D.

3. A numerical optimization algorithm to synthesize feedforward trajectories for the tokamak actuators that steer the plasma through the tokamak operating space to achieve a predefined target scenario, subject to actuator and plasma state constraints, was developed. At the core of the optimization algorithm is

the developed FPD, physics-based model of the plasma dynamics. By exploiting the computational efficiency of the embedded physics-based model, the optimization problem was iteratively solved by employing the sequential quadratic programming technique. The optimization algorithm was utilized to optimize plasma startup conditions by achieving a target current profile at the end of the current ramp-up phase in DIII-D L-mode scenarios and to reach a target plasma state characterized by a desired current profile and stored energy in a stationary manner in DIII-D H-mode scenarios. In addition, the developed numerical optimization algorithm is currently being employed to develop actuator trajectories for advanced scenario planning in the NSTX-U tokamak.

4. Following a FPD, physics-based approach, robust feedback algorithms for current profile control, combined current profile + stored energy control, and simultaneous current profile + electron temperature profile control were designed for various operating scenarios in multiple tokamaks, which demonstrates the flexibility of the employed methodology.

5. DIII-D experimental tests demonstrated the potential physics-model-based profile control has to provide a systematic approach for the development and robust sustainment of tokamak operating scenarios. The ability of the feedforward + feedback control algorithm to improve the reproducibility of plasma startup conditions in L-mode scenarios in the DIII-D tokamak was demonstrated by achieving various target q profiles at the end of the current ramp-up phase of the discharge. The ability of the optimized feedforward trajetories to steer the plasma to a target stationary current profile, and the ability of the current profile feedback controller to improve the ability to robustly achieve plasma target conditions, in DIII-D H-mode scenarios was demonstrated. These experiments,

along with those described in [98–101], mark the first time ever FPD, model-based, closed-loop full magnetic profile control was successfully demonstrated in a tokamak device.

6. ITER and TCV simulation tests showed the ability to simultaneously control the magnetic and thermal state dynamics in tokamak plasmas. The ITER simulations demonstrated the ability to drive the current profile to a stationary target while simultaneously modulating the amount of fusion power that is generated. The TCV simulations demonstrated the ability to drive the current and electron temperature profiles to a self consistent target, as well as to maintain the current profile in a stationary condition while simultaneously modulating the electron temperature profile between equilibrium points. The ability to maintain the current profile at a stationary target (to maintain plasma stability) while modulating the thermal state of the plasma (to respond to changing power demand) is an essential capability that will be needed for a commercial, power producing tokamak reactor.

9.2 Future work

In order for candidate control solutions to truly be considered for application on ITER, they need to be developed and routinely used in existing tokamak experiments. The DIII-D experiments discussed in this dissertation demonstrate the potential physics-model-based current profile control has to improve the reproducibility of tokamak operating scenarios. However, current profile control is currently not routinely utilized in everyday tokamak operation. Therefore additional experimental testing of current profile controllers, and eventually integrated current profile and electron temperature profile controllers, in various tokamaks is needed.

The feedback control algorithm developed for combined current profile + stored

energy control in burning plasma ITER scenarios represents a foundation for integrated current profile and burn condition control in ITER. Additionally, the ability to simultaneously control the current and electron temperature profiles was demonstrated in TCV simulations. However, the developed algorithms solely employ auxiliary heating to control the plasma thermal state. If the auxiliary heating is driven to saturation, the thermal state of the plasma is no longer controllable using this lone actuator. Therefore, integrating the current profile controller with strategies that utilize not only auxiliary heating, but also the concepts of isotopic fuel tailoring and impurity injection to control the thermal state of the plasma [4] would be desirable. Additionally, the control algorithm needs to be more rigorously tested in simulations with advanced physics-based simulation codes, such as DINA-CH&CRONOS [5–9].

The current profile is not a directly measurable quantity and is reconstructed for feedback control by combining diagnostic measurements with a real-time Grad-Shafranov equilibrium solver, which is the case for the rtEFIT algorithm [11] utilized at the DIII-D tokamak. However, the accuracy of this reconstruction method is limited by the difficulty of obtaining reliable internal plasma diagnostic measurements with adequate spatial and temporal resolution to obtain a complete description of the current profile evolution during the discharge. An alternative approach that warrants additional exploration is constructing the current profile in real-time by synthesizing a closed-loop observer following a FPD approach. This approach has recently been investigated for application in TCV [13, 150].

Advanced high performance operating scenarios operate close to operational boundaries in terms of proximity to stability limits and actuation capabilities to maximize plasma performance. In these operating scenarios, magnetohydrodynamic (MHD) instabilities, such as neoclassical tearing modes (NTMs), can be triggered, which limit the plasma performance and can lead to plasma terminating disruptions. As the actuators utilized to stabilize these instabilities are also used to control the current

and electron temperature profiles, integrated algorithms for profile control and MHD instability stabilization/suppression need to be explored.

Bibliography

[1] L. M. Hively, "Special Topic: Conventional Computations Forms for Maxwellian Reactivities," *Nuclear Fusion*, vol. 17, no. 4, pp. 873–876, 1977.

[2] R. C. Wolf, "Internal Transport Barriers in Tokamak Plasmas," *Plasma Physics and Controlled Fusion*, vol. 45, pp. R1–R91, 2003.

[3] ITER Organization, [Online]. Available: http://www.iter.org.

[4] M. D. Boyer, "Nonlinear Burn Condition and Kinetic Profile Control in Tokamak Fusion Reactors," Ph.D. dissertation, Lehigh University, 2014.

[5] S. H. Kim *et al.*, "Full Tokamak Discharge Simulation of ITER by Combining DINA-CH and CRONOS," *Plasma Phys. and Control. Fusion*, vol. 51, no. 10, p. 105007, 2009.

[6] J.-Y. Favez *et al.*, "Comparing TCV Experimental VDE Responses with DINA Code Simulations," *Plasma Phys. and Control. Fusion*, vol. 44, pp. 171–193, 2002.

[7] V. Basiuk *et al.*, "Simulations of Steady-state Scenarios for Tore Supra using the CRONOS Code," *Nucl. Fusion*, vol. 43, pp. 822–830, 2003.

[8] K. Besseghir, J. Garcia, J.-F. Artaud, F. Imbeaux, R. R. Khayrutdinov, J. B. Lister, V. E. Lukash, and P. Maget, "Achieving and Sustaining Advanced Scenarios in ITER Modelled by CRONOS and DINA-CH," *Plasma Phys. and Control. Fusion*, vol. 55, p. 125012, 2013.

[9] K. Besseghir, "Free-Boundary Simulations of ITER Advanced Scenarios," Ph.D. dissertation, École Polytechnique Fédérale de Lausanne (EPFL), 2013.

[10] S. Skogestad and I. Postlethwaite, *Multivariable Feedback Control Analysis and Design.* Wiley, New York, 2005.

[11] J. Ferron *et al.*, "Real time Equilibrium Reconstruction for Tokamak Discharge Control," *Nuclear Fusion*, vol. 38, no. 7, pp. 1055–1066, 1998.

[12] R. J. Hawryluk *et al.*, "An Empirical Approach to Tokamak Transport," in *Physics of Plasmas Close to Thermonuclear Conditions,* ed B. Coppi *et al.*, vol 1, 1980, pp. 19–46.

[13] F. Felici *et al.*, "Real-time Physics-model-based Simulation of the Current Density Profile in Tokamak Plasmas," *Nuclear Fusion*, vol. 51, no. 8, p. 083052, 2011.

[14] F. Felici and O. Sauter, "Nonlinear model-based optimization of actuator trajectories for tokamak plasma profile control," *Plasma Phys. and Control. Fusion*, vol. 54, p. 025002, 2012.

[15] F. Felici, "Real-Time Control of Tokamak Plasmas: from Control of Physics to Physics-Based Control," Ph.D. dissertation, École Polytechnique Fédérale de Lausanne (EPFL), 2011.

[16] T. Appenzaler, "The End of Cheap Oil," *Nat. Geograph.*, vol. 205, no. 6, pp. 80–109, 2004.

[17] A. Pironti and M. Walker, "Control of Tokamak Plasmas," *IEEE Control Systems Magazine*, vol. 25, no. 5, pp. 24–29, 2005.

[18] J. Wesson, *Tokamaks*. Oxford, UK: Clarendon Press, 2004.

[19] T. Taylor *et al.*, "Physics of advanced tokamaks," *Plasma Phys. and Control. Fusion*, vol. 39, pp. B47–B73, 1997.

[20] A. Pironti and M. Walker, "Fusion, Tokamaks, and Plasma Control," *IEEE Control Systems Magazine*, vol. 25, no. 5, pp. 30–43, 2005.

[21] M. Walker *et al.*, "Emerging Applications in Tokamak Plasma Control," *IEEE Control Systems Magazine*, vol. 26, pp. 35–63, 2006.

[22] M. Garibbai *et al.*, "The New Control Scheme for the JET Plasma Position and Current Control System," in *15^{th} SOFE Conference*, 1996, pp. 33–36.

[23] D. Humphreys *et al.*, "Initial Implementation of a Multivariable Plasma Shape and Position Controller on the DIII-D Tokamak," in *IEEE International Conference on Control Applications*, 2000.

[24] R. Albanese *et al.*, "Plasma Response Models for Current, Shape, and Position Control in JET," *Fusion Engineering and Design*, vol. 66-68, pp. 715–718, 2003.

[25] M. Ariola *et al.*, "Plasma Shape Control for the JET Tokamak," *IEEE Control Systems Magazine*, vol. 25, no. 5, pp. 65–75, 2005.

[26] M. Walker and D. Humphreys, "Valid Coordinate Systems for Lin- earized Plasma Shape Response Models in Tokamaks," *Fusion Science and Technology*, vol. 50, no. 4, pp. 473–489, 2006.

[27] D. Gates *et al.*, "Plasma Shape Control on the National Spherical Torus Experiment (NSTX) Using Real-time Equilibrium Reconstruction," *Nuclear Fusion*, vol. 46, pp. 17–23, 2006.

[28] Y. Mitrishkin, A. Korostelev *et al.*, "Design and Modeling of ITER Plasma Magnetic Control System in Plasma Current Ramp-up Phase on DINA Code," in *IEEE Conference on Decision and Control*, 2009.

[29] G. Ambrosino *et al.*, "Design and Implementation of an Output Regulation Controller for the JET Tokamak," *IEEE Transactions on Control Systems Technology*, vol. 16, no. 6, pp. 1101–1111, 2008.

[30] W. Shi *et al.*, "Multivariable Model-Based Shape Control for the National Spherical Torus Experiment (NSTX)," *Fusion Engineering and Design*, vol. 86, no. 6-8, pp. 1107–1111, 2011.

[31] W. Shi, J. Barton *et al.*, "Multivariable Multi-Model-based Magnetic Control System for the Current Ramp-up Phase in the National Spherical Torus Experiment (NSTX)," in *50th IEEE Conference on Decision and Control and European Control Conference Proceedings (Orlando, FL, USA)*, 2011, pp. 2632–2637.

[32] A. M. Garofalo *et al.*, "Resistive Wall Mode Dynamics and Active Feedback Control in DIII-D," *Nuclear Fusion*, vol. 41, p. 1171, 2001.

[33] M. Okabayashi *et al.*, "Active Feedback Stabilization of the Resistive Wall Mode on the DIII-D Device," *Phys. Plasmas*, vol. 8, p. 2071, 2001.

[34] A. K. Sen *et al.*, "Optimal Control of Tokamak Resistive Wall Modes in the Presence of Noise," *Phys. Plasmas*, vol. 10, p. 4350, 2003.

[35] E. J. Strait *et al.*, "Resistive Wall Mode Stabilization with Internal Feedback Coils in DIII-D," *Phys. Plasmas*, vol. 11, p. 2505, 2004.

[36] S. Sabbagh *et al.*, "The ResistiveWall Mode and Feedback Control Physics Design in NSTX," *Nuclear Fusion*, vol. 44, p. 560, 2004.

[37] S. Mauel *et al.*, "Dynamics and Control of Resistive Wall Modes with Magnetic Feedback Control Coils: Experiment and Theory," *Nuclear Fusion*, vol. 45, p. 285, 2005.

[38] M. Okabayashi *et al.*, "Control of the Resistive Wall Mode with Internal Coils in the DIII-D Tokamak," *Nuclear Fusion*, vol. 45, p. 1715, 2005.

[39] Z. Sun *et al.*, "Adaptive Optimal Stochastic State Feedback Control of Resistive Wall Modes in Tokamaks," *Phys. Plasmas*, vol. 13, p. 012512, 2006.

[40] O. Katsuro-Hopkins *et al.*, "Enhanced ITER Resistive Wall Mode Feedback Performance Using Optimal Control Techniques," *Nuclear Fusion*, vol. 47, p. 1157, 2007.

[41] J. Dalessio, E. Schuster, D. Humphreys, M. Walker *et al.*, "Model-based Robust Control of Resistive Wall Modes via μ Synthesis," *Fusion Science and Technology*, vol. 55, pp. 163–179, 2009.

[42] A. Isayama *et al.*, "Complete Stabilization of a Tearing Mode in Steady State High-β_p H-mode Discharges by the First Harmonic Electron Cyclotron Heating/current drive on JT-60U," *Plasma Physics and Controlled Fusion*, vol. 42, p. L37, 2000.

[43] D. A. Humphreys *et al.*, "Active Control for Stabilization of Neoclassical Tearing Modes," *Physics of Plasmas*, vol. 13, p. 056113, 2006.

[44] A. Manini *et al.*, "Development of a Feedback System to Control MHD Instabilities in ASDEX Upgrade," *Fusion Engineering and Design*, vol. 82, p. 995, 2007.

[45] B. A. Hennen *et al.*, "Real-time Control of Tearing Modes Using a Line-of-sight Electron Cyclotron Emission Diagnostic," *Plasma Physics and Controlled Fusion*, vol. 52, p. 104006, 2010.

[46] F. Felici *et al.*, "Integrated Real-time Control of MHD Instabilities using Multi-beam ECRH/ECCD Systems on TCV," *Nuclear Fusion*, vol. 52, p. 074001, 2012.

[47] W. Wehner and E. Schuster, "Control-oriented Modelling for Neoclassical Tearing Mode Stabilization via Minimum-seeking Techniques," *Nuclear Fusion*, vol. 52, p. 074003, 2012.

[48] E. Kolemen *et al.*, "State-of-the-art Neoclassical Tearing Mode Control in DIII-D using Real-time Steerable Electron Cyclotron Current Drive Launchers," in *24th IAEA Fusion Energy Conference (San Diego, CA, USA)*, paper PD/1-1, 2012.

[49] D. A. Humphreys *et al.*, "Development of ITER-relevant Plasma Control Solutions at DIII-D," *Nuclear Fusion*, vol. 47, p. 943, 2007.

[50] X. Litaudon *et al.*, "Towards Fully Non-inductive Current Drive Operation in JET," *Plasma Physics and Controlled Fusion*, vol. 44, p. 1057, 2002.

[51] S. Coda *et al.*, "High-bootstrap, Noninductively Sustained Electron Internal Transport Barriers in the Tokamak a Configuration Variable," *Physics of Plasmas*, vol. 12, p. 056124, 2005.

[52] M. Murakami *et al.*, "Progress Toward Fully Noninductive, High Beta Conditions in DIII-D," *Physics of Plasmas*, vol. 13, p. 056106, 2006.

[53] C. Gormezano *et al.*, "Progress in the ITER Physics Basis Chapter 6: Steady State Operation," *Nuclear Fusion*, vol. 47, p. S285, 2007.

[54] C. T. Holcomb *et al.*, "Optimizing Stability, Transport, and Divertor Operation Through Plasma Shaping for Steady-state Scenario Development in DIII-D," *Physics of Plasmas*, vol. 16, p. 056116, 2009.

[55] T. Suzuki *et al.*, "Development of Advanced Operation Scenarios in Weak Magnetic-shear Regime on JT-60U," *Nuclear Fusion*, vol. 49, p. 085003, 2009.

[56] Y. Sakamoto *et al.*, "Development of Reversed Shear Plasmas with High Bootstrap Current Fraction Towards Reactor Relevant Regime in JT-60U," *Nuclear Fusion*, vol. 49, p. 095017, 2009.

[57] N. Oyama and the JT-60 Team, "Overview of JT-60U Results Towards the Establishment of Advanced Tokamak Operation," *Nuclear Fusion*, vol. 49, p. 104007, 2009.

[58] I. Voitsekhovitch *et al.*, "Non-inductive Current Drive and Transport in high β_N plasmas in JET," *Nuclear Fusion*, vol. 49, p. 055026, 2009.

[59] J. Ferron *et al.*, "Optimization of the Safety Factor Profile for High Noninductive Current Fraction Discharges in DIII-D," *Nuclear Fusion*, vol. 51, p. 063026, 2011.

[60] A. G. Peeters, "The bootstrap current and its consequences," *Plasma Phys. and Control. Fusion*, vol. 42, pp. B231–B242, 2000.

[61] R. E. Waltz *et al.*, "Advances in the Simulation of Toroidal Gyro-Landau Fluid Model Turbulence," *Physics of Plasmas*, vol. 2, p. 2408, 1995.

[62] C. C. Petty *et al.*, "Experimental Constraints on Transport from Dimensionless Parameter Scaling Studies ," *Physics of Plasmas*, vol. 5, p. 1695, 1998.

[63] J. Ferron *et al.*, "Optimization of DIII-D Advanced Tokamak Discharges with Respect to the β Limit," *Physics of Plasmas*, vol. 12, p. 056126, 2005.

[64] T. C. Hender *et al.*, "Chapter 3: MHD Stability, Operational Limits and Disruptions," *Nuclear Fusion*, vol. 47, p. S128, 2007.

[65] P. A. Politzer and G. D. Porter, "Power Threshold for Neutral Beam Current Drive," *Nucl. Fusion*, vol. 30, no. 8, p. 1605, 1990.

[66] T. C. Luce *et al.*, "Generation of Localized Noninductive Current by Electron Cyclotron Waves on the DIII-D Tokamak," *Physical Review Letters*, vol. 83, no. 22, p. 4550, 1999.

[67] O. Sauter *et al.*, "Beta Limits in Long-pulse Tokamak Discharges," *Physics of Plasmas*, vol. 4, p. 1654, 1997.

[68] H. St. John, T. S. Taylor, Y. R. Lin-Liu, and A. D. Turnbull, "Transport Simulation of Negative Magnetic Shear Discharges," in *Proc. 15th Int. Conf. on Plasma Physics and Controlled Nuclear Fusion Research (Seville, Spain, 1994)*, vol. 3 (Vienna: IAEA), 1996, p. 603.

[69] J. Crotinger *et al.*, in *Technical Report UCRL-ID-126284 LLNL*, 1997.

[70] G. V. Pereverzev *et al.*, "ASTRA Automated System for Transport Analysis in a Tokamak," in *Technical Report 5/98 IPP Report*, 2002.

[71] J. M. Park *et al.*, "Experiment and Modeling of ITER Demonstration Discharges in the DIII-D Tokamak," in *Proc. 23rd Int. Conf. on Fusion Energy (Daejeon, Korea, 2010)*, paper EXC/P2-05, 2010.

[72] L. Laborde *et al.*, "A Model-based Technique for Integrated Real-time Profile Control in the JET Tokamak," *Plasma Physics and Controlled Fusion*, vol. 47, pp. 155–183, 2005.

[73] D. Moreau *et al.*, "Real-time Control of the q-profile in JET for Steady State Advanced Tokamak Operation," *Nuclear Fusion*, vol. 43, pp. 870–882, 2003.

[74] D. Moreau, D. Mazon *et al.*, "A Two-time-scale Dynamic-model Approach for Magnetic and Kinetic Profile Control in Advanced Tokamak Scenarios on JET," *Nuclear Fusion*, vol. 48, no. 10, p. 106001, 2008.

[75] J. Ferron *et al.*, "Feedback Control of the Safety Factor Profile Evolution during Formation of an Advanced Tokamak Discharge," *Nuclear Fusion*, vol. 46, p. L13, 2006.

[76] D. Moreau *et al.*, "Plasma Models for Real-time Control of Advanced Tokamak Scenarios ," *Nuclear Fusion*, vol. 51, no. 6, p. 063009, 2011.

[77] W. Shi, W. Wehner, J. Barton, M. D. Boyer, E. Schuster *et al.*, "Multivariable Robust Control of the Plasma Rotational Transform Profile for Advanced Tokamak Scenarios in DIII-D," in *2012 American Control Conference (Montreal, QC, Canada)*, 2012, pp. 5037–5042.

[78] W. Wehner *et al.*, "Optimal Feedback Control of the Poloidal Magnetic Flux Profile in the DIII-D Tokamak Based on Identified Plasma Response Models," in *2012 American Control Conference (Montreal, QC, Canada)*, 2012, pp. 5049–5054.

[79] O. Barana *et al.*, "Feedback Control of the Lower Hybrid Power Deposition Profile on Tore Supra," *Plasma Physics and Controlled Fusion*, vol. 49, pp. 947–967, 2007.

[80] T. Wijnands *et al.*, "Feedback Control of the Current Profile on Tore Supra," *Nuclear Fusion*, vol. 37, pp. 777–791, 1997.

[81] T. Suzuki *et al.*, "Recent RF Experiments and Application of RF Waves to Real-Time Control of Safety Factor Profile in JT-60U," in *AIP Conference Proceedings (Park City, UT, USA)*, 2005, pp. 279–286.

[82] T. Suzuki, S. Ide, T. Oikawa, T. Fujita, M. Ishikawa, M. Seki *et al.*, "Off-axis Current Drive and Real-time Control of Current Profile in JT-60U," *Nuclear Fusion*, vol. 48, p. 045002, 2008.

[83] Y. Ou, T. C. Luce, E. Schuster *et al.*, "Towards Model-Based Current Profile Control at DIII-D," *Fusion Engineering and Design*, vol. 82, pp. 1153–1160, 2007.

[84] E. Witrant *et al.*, "A Control-oriented model of the Current Profile in Tokamak Plasma," *Plasma Phys and Control Fusion*, vol. 49, pp. 1075–1105, 2007.

[85] Y. Ou and E. Schuster, "On Stability of Receding Horizon Control of Bilinear Parabolic PDE Systems," in *49th IEEE Conference on Decision and Control (Atlanta, GA, USA)*, 2010.

[86] Y. Ou, C. Xu, and E. Schuster, "Robust Control Design for the Poloidal Magnetic Flux Profile Evolution in the Presence of Model Uncertainties," *IEEE Transactions on Plasma Science*, vol. 38, pp. 375–382, 2010.

[87] Y. Ou, C. Xu, E. Schuster, T. C. Luce *et al.*, "Optimal Tracking Control of Current Profile in Tokamaks," *IEEE Transactions on Control Systems Technology*, vol. 19, pp. 432–441, 2011.

[88] C. Xu, Y. Ou, and E. Schuster, "Sequential Linear Quadratic Control of Bilinear Parabolic PDEs based on POD Model Reduction," *Automatica*, vol. 47, pp. 418–426, 2011.

[89] Y. Ou, C. Xu, E. Schuster, T. C. Luce, J. R. Ferron, M. L. Walker, and D. A. Humphreys, "Receding-Horizon Optimal Control of the Current Profile Evolution During the Ramp-Up Phase of a Tokamak Discharge," *Control Engineering Practice*, vol. 19, pp. 22–31, 2011.

[90] C. Xu, Y. Ou, and E. Schuster, "Receding Horizon Control of the Magnetic Flux Bilinear PDE based on Sequential Linear Quadratic Control," in *7th International Congress on Industrial and Applied Mathematics (Vancouver, Canada)*, 2011.

[91] O. Gaye *et al.*, "Sliding Mode Stabilization of the Current Profile in Tokamak Plasmas," in *50th IEEE Conference on Decision and Control (Orlando, FL, USA)*, 2011, pp. 2638–2643.

[92] A. Gahlawat *et al.*, "Bootstrap Current Optimization in Tokamaks using Sum-of-Squares Polynomials," in *51st IEEE Conference on Decision and Control (Maui, HI, USA)*, 2012, pp. 4359–4365.

[93] F. Argomedo *et al.*, "Lyapunov-based Distributed Control of the Safety-factor Profile in a Tokamak Plasma," *Nuclear Fusion*, vol. 53, no. 3, p. 033005, 2013.

[94] N. M. T. Vu, R. Nouailletas, L. Lefevre, and S. Bremond, "An IDA-PBC Approach for the Control of 1D Plasma Profile in Tokamaks," in *52nd IEEE Conference on Decision and Control (Florence, Italy)*, 2013, pp. 4176–4181.

[95] J. Nocedal and S. J. Wright, *Numerical optimization*. Springer, New York, 2006.

[96] Y. Ou, C. Xu, E. Schuster *et al.*, "Design and simulation of extremum-seeking open-loop optimal control of current profile in the DIII-D tokamak," *Plasma Phys. and Control. Fusion*, vol. 50, p. 115001, 2008.

[97] C. Xu, Y. Ou, J. Dalessio, E. Schuster *et al.*, "Ramp-up phase current profile control of tokamak plasmas via nonlinear programming," *IEEE Transactions on Plasma Science*, vol. 38, pp. 163–173, 2010.

[98] M. D. Boyer, J. E. Barton, E. Schuster *et al.*, "First-principles-driven Model-based Current Profile Control for the DIII-D Tokamak via LQI Optimal Control," *Plasma Phys. Control. Fusion*, vol. 55, p. 105007, 2013.

[99] M. D. Boyer, J. E. Barton, E. Schuster, M. L. Walker *et al.*, "Backstepping Control of the Toroidal Plasma Current Profile in the DIII-D Tokamak," *IEEE Transactions on Control Systems Technology*, vol. 22, no. 5, pp. 1725–1739, 2014.

[100] M. D. Boyer, J. E. Barton, W. Shi, W. P. Wehner, E. Schuster, J. R. Ferron, M. L. Walker, D. A. Humphreys, F. Turco, T. C. Luce, R. D. Johnson, and B. G. Penaflor, "Simultaneous Boundary and Distributed Feedback Control of the Current Profile in H-mode Discharges on DIII-D," in *19th IFAC World Congress (Cape Town, South Africa)*, 2014, pp. 1568–1573.

[101] W. Wehner, W. Shi, J. Barton, E. Schuster *et al.*, "First-Principles-Driven Model-Based Control of the Poloidal Magnetic Flux Profile at the DIII-D Tokamak," in *19th IFAC World Congress*, 2014, pp. 10 319–10 324.

[102] W. Shi, W. Wehner, J. Barton, M. D. Boyer, E. Schuster *et al.*, "A Two-time-scale Model-based Combined Magnetic and Kinetic Control System for Advanced Tokamak Scenarios on DIII-D," in *51st IEEE Conference on Decision and Control (Maui, HI, USA)*, 2012, pp. 4347–4352.

[103] D. Moreau *et al.*, "Integrated Magnetic and Kinetic Control of Advanced Tokamak Scenarios based on Data-driven Models," in *24th IAEA Fusion Energy Conference (San Diego, CA, USA)*, paper ITR/P1-20, 2012.

[104] W. Shi, W. Wehner, J. Barton, M. D. Boyer, E. Schuster *et al.*, "PTRANSP Simulation and Experimental Test of a Robust Current Profile and β_N Controller for Off-axis Current-drive Scenarios in the DIII-D Tokamak," in *2013*

American Control Conference Proceedings (Washington DC, USA), 2013, pp. 1225–1230.

[105] D. Moreau *et al.*, "Integrated Magnetic and Kinetic Control of Advanced Tokamak Plasmas on DIII-D based on Data-driven Models," *Nuclear Fusion*, vol. 53, p. 063020, 2013.

[106] J. F. Artaud *et al.*, "Simulations of Steady-state Scenarios for Tore Supra using the CRONOS Code," *Nuclear Fusion*, vol. 50, p. 043001, 2010.

[107] S. H. Kim and J. B. Lister, "A Potentially Robust Plasma Profile Control Approach for ITER using Real-time Estimation of Linearized Profile Response Models," *Nuclear Fusion*, vol. 52, p. 074002, 2012.

[108] J. E. Barton, K. Besseghir, J. Lister, and E. Schuster, "Towards First-principles Control-oriented Modeling of the Magnetic and Kinetic Plasma Profile Evolutions in ITER," in *54th Annual Meeting of the APS Division of Plasma Physics (Providence, RI, USA)*, http://meetings.aps.org/link/BAPS.2012.DPP.JP8.125, 2012.

[109] J. E. Barton, W. Shi, K. Besseghir, J. Lister, A. Kritz, E. Schuster *et al.*, "Physics-based Control-oriented Modeling of the Safety Factor Profile Dynamics in High Performance Tokamak Plasmas," in *52nd IEEE Conference on Decision and Control (Florence, Italy)*, 2013, pp. 4182–4187.

[110] J. Barton, E. Schuster, M. L. Walker, and D. A. Humphreys, "Robust Control of the Spatial Current Profile in the DIII-D Tokamak," in *53rd Annual Meeting of the APS Division of Plasma Physics (Salt Lake Cite, UT, USA)*, http://meetings.aps.org/link/BAPS.2011.DPP.TP9.34, 2011.

[111] J. E. Barton *et al.*, "First-Principles Model-based Robust Control of the Current Profile Evolution in the DIII-D Tokamak," in *2012 American Control Conference (Montreal, QC, Canada)*, 2012, pp. 2134–2140.

[112] J. E. Barton, M. D. Boyer, W. Shi, W. P. Wehner, E. Schuster *et al.*, "First-principles Model-based Closed-loop Control of the Current Profile Dynamic Evolution on DIII-D," in *24th IAEA Fusion Energy Conference (San Diego, CA, USA)*, paper EX/P2-09, 2012.

[113] J. E. Barton, M. D. Boyer, W. Shi, E. Schuster *et al.*, "Toroidal Current Profile Control During Low Confinement Mode Plasma Discharges in DIII-D via First-principles-driven Model-based Robust Control Synthesis," *Nucl. Fusion*, vol. 52, p. 123018, 2012.

[114] J. Barton, E. Schuster, M. L. Walker, and D. A. Humphreys, "Closed-Loop Simulation of Model-Based Current Profile Control with the DIII-D Plasma Control System," in *52nd Annual Meeting of the APS Division of Plasma Physics (Chicago, IL, USA)*, http://meetings.aps.org/link/BAPS.2010.DPP.GP9.51, 2010.

[115] J. Barton, Y. Ou, C. Xu, E. Schuster *et al.*, "Simserver Simulation of a Model-based Current Profile Controller in the DIII-D Plasma Control System," *Fusion Engineering and Design*, vol. 86, no. 6-8, pp. 1116–1119, 2011.

[116] J. E. Barton, W. P. Wehner, E. Schuster, T. C. Luce, G. L. Jackson, J. R. Ferron, D. A. Humphreys, and A. W. Hyatt, "Optimization of the Current Ramp-up Phase in DIII-D via Physics-model-based Control of Plasma Safety Factor Profile Dynamics," in *56th Annual Meeting of the APS Division of Plasma Physics*, 2014.

[117] J. E. Barton, E. Schuster, M. L. Walker, and D. A. Humphreys, "Physics-model-based Actuator Trajectory Optimization and Feedback Control of the Safety Factor Profile and Internal Energy Dynamics in DIII-D," in *55th Annual Meeting of the APS Division of Plasma Physics (Denver, CO, USA)*, http://meetings.aps.org/link/BAPS.2013.DPP.BP8.100, 2013.

[118] J. E. Barton, W. Shi, E. Schuster, T. C. Luce, J. R. Ferron, M. L. Walker, D. A. Humphreys, F. Turco, R. D. Johnson, and B. G. Penaflor, "Nonlinear Physics-model-based Actuator Trajectory Optimization for Advanced Scenario Planning in the DIII-D Tokamak," in *19th IFAC World Congress (Cape Town, South Africa)*, 2014, pp. 671–676.

[119] J. E. Barton, M. D. Boyer, W. Shi, W. P. Wehner, E. Schuster, J. R. Ferron, M. L. Walker, D. A. Humphreys, T. C. Luce, F. Turco, R. D. Johnson, and B. G. Penaflor, "Experimental and Simulation Testing of Physics-model-based Safety Factor Profile and Internal Energy Feedback Controllers in DIII-D Advanced Tokamak Scenarios," in *19th IFAC World Congress (Cape Town, South Africa)*, 2014, pp. 5223–5228.

[120] J. E. Barton, M. D. Boyer, W. Shi, W. P. Wehner, E. Schuster *et al.*, "Physics-model-based Control of the Plasma Current Profile Dynamics for the Development and Sustainment of Advanced Scenarios in DIII-D," in *25th IAEA Fusion Energy Conference (Saint Petersburg, Russia)*, paper PPC/P2-32, 2014.

[121] J. E. Barton, K. Besseghir, J. Lister, and E. Schuster, "Robust Control of the Safety Factor Profile and Stored Energy Evolutions in High Performance Burning Plasma Scenarios in the ITER Tokamak," in *52nd IEEE Conference on Decision and Control (Florence, Italy)*, 2013, pp. 4194–4199.

[122] J. E. Barton, E. Schuster, F. Felici, and O. Sauter, "Closed-loop Control of the Safety Factor Profile in the TCV Tokamak," in *53rd IEEE Conference on Decision and Control*, 2014.

[123] J. E. Barton, W. P. Wehner, E. Schuster, F. Felici, and O. Sauter, "Simultaneous Closed-loop Control of the Current and Electron Temperature Profiles in the TCV Tokamak," *submitted to 2015 American Control Conference*, 2014.

[124] F. Hinton and R. Hazeltine, "Theory of Plasma Transport in Toroidal Confinement Systems," *Rev. Mod. Phys.*, vol. 48, pp. 239–308, 1976.

[125] J. Blum, *Numerical Simulation and Optimal Control in Plasma Physics: With Applications to Tokamaks*. Wiley, Paris, 1989.

[126] V. D. Shafranov, "Plasma Equilibrium in a Magnetic Field," *Reviews of Plasma Physics*, vol. 2, p. 103, 1966.

[127] J. P. Freidberg, *Ideal Magnetohydrodynamics*. Plenum Press, New York, NY, 1987.

[128] G. W. Hammett and F. W. Perkins, "Fluid Moment Models for Landau Damping with Application to the Ion-temperature-gradient Instability," *Phys. Rev. Lett.*, vol. 64.25, pp. 3019–3022, 1990.

[129] R. E. Waltz *et al.*, "A Gyro-Landau-fluid Transport Model," *Physics of Plasmas*, vol. 4.7, pp. 2482–2496, 1997.

[130] S. C. Jardin, M. G. Bell, and N. Pomphrey, "TSC Simulation of Ohmic Discharges in TFTR," *Nuclear Fusion*, vol. 33.3, p. 371, 1993.

[131] M. Erba *et al.*, "Validation of a New Mixed Bohm/gyro-Bohm Model for Electron and Ion Heat Transport Against the ITER, Tore Supra and START Database Discharges," *Nuclear Fusion*, vol. 38.7, p. 1013, 1998.

[132] ITER Physics Basis, *Nuclear Fusion*, vol. 39, p. 2137, 1999.

[133] R. J. Goldston, "Energy Confinement Scaling in Tokamaks: Some Implications of Recent Experiments with Ohmic and Strong Auxiliary Heating," *Plasma Physics and Controlled Fusion*, vol. 26, p. 87, 1984.

[134] O. Sauter *et al.*, "Neoclassical Conductivity and Bootstrap Current Formulas for General Axisymmetric Equilibria and Arbitrary Collisionality Regime," *Physics of Plasmas*, vol. 6, no. 7, p. 2834, 1999.

[135] O. Sauter *et al.*, "Erratum: Neoclassical Conductivity and Bootstrap Current Formulas for General Axisymmetric Equilibria and Arbitrary Collisionality Regime [Phys. Plasmas 6, 2834 (1999)]," *Physics of Plasmas*, vol. 9, no. 12, p. 5140, 2002.

[136] J.-F. Artaud, F. Imbeaux, T. Aniel, V. Basiuk, L.-G. Eriksson, G. Giruzzi, G. T. Hoang, G. Huysmans, E. Joffrin, Y. Peysson, M. Schneider, and P. Thomas, "Predictive Integrated Modelling for ITER Scenarios," in *32nd EPS Conference on Plasma Physics (Tarragona, Spain)*, vol. 29C (ECA), 2005, pp. P–1.035.

[137] W. Schiesser, *The Numerical Method of Lines: Integration of Partial Differential Equations*. Academic Press, San Diego, 1991.

[138] A. Packard, "Whats New with μ: Structured Uncertainty in Multivariable Control," Ph.D. dissertation, Univ. of Calif., Berkeley, 1988.

[139] D. Piglowski *et al.*, "Enhancements in the Second Generation DIII-D Digital Plasma Control System," *Fusion Engineering and Design*, vol. 82, pp. 1058–1063, 2007.

[140] L. Zaccarian and A. R. Teel, *Modern Anti-windup Synthesis: Control Augmentation for Actuator Saturation.* Princeton, New Jersey: Princeton University Press, 2011.

[141] E. Schuster *et al.*, "Antiwindup Scheme for Plasma Shape Control with Rate and Magnitude Actuation Constraints in the DIII-D Tokamak," in *IEEE Conference on Decision and Control*, 2003.

[142] M. Walker *et al.*, "Advances in Integrated Plasma Control on DIII-D," *Fusion Engineering and Design*, vol. 82, pp. 1051–1057, 2007.

[143] Y. Martin *et al.*, "Power requirements for accessing the H-mode in ITER," *Journal of Physics: Conference Series*, vol. 123, p. 012033, 2008.

[144] E. Righi *et al.*, "Isotope Scaling of the H-mode Power Threshold on JET," *Nuclear Fusion*, vol. 39, no. 3, p. 309, 1999.

[145] K. Teo *et al.*, *A unified computational approach to optimal control problems.* Wiley, New York, 1991.

[146] J. Edmunds and B. Kouvaritakis, "Extensions of the Frame Alignment Technique and Their uses in the Characteristic Locus Design Method," *International Journal of Control*, vol. 29, no. 5, pp. 787–796, 1979.

[147] M. Greenwald *et al.*, "A new look at density limits in tokamaks," *Nuclear Fusion*, vol. 28, p. 2199, 1988.

[148] A. Sips, "Advanced Scenarios for ITER Operation," *Plasma Physics and Controlled Fusion*, vol. 47, pp. A19–A40, 2005.

[149] L. Baylor, P. Parks, T. Jernigan, J. Caughman, S. Combs, C. Foust, W. A. Houlberg, S. Maruyama, and D. Rasmussen, "Pellet Fueling and Control of Burning Plasmas in ITER," *Nuclear Fusion*, vol. 47, pp. 443–448, 2007.

[150] F. Felici *et al.*, "A Dynamic State Observer for Real-time Reconstruction of the Tokamak Plasma Profile State and Disturbances," in *2014 American Control Conference*, 2014, pp. 4816–4823.

[151] W. Shi, J. E. Barton, W. Wehner, M. D. Boyer, E. Schuster *et al.*, "First-principles-driven Control of the Rotational Transform Profile in High Performance Discharges in the DIII-D Tokamak," in *52nd IEEE Conference on Decision and Control (Florence, Italy)*, 2013, pp. 4170–4175.

[152] Z. Ilhan, J. Barton, W. Shi, E. Schuster *et al.*, "Physics-based Control-oriented Modeling of the Current Profile Evolution in NSTX-Upgrade," in *55th Annual Meeting of the APS Division of Plasma Physics*, http://meetings.aps.org/link/BAPS.2013.DPP.NP8.41, 2013.

[153] Z. Ilhan, J. Barton, W. Wehner, E. Schuster *et al.*, "First-Principles-Driven Model-Based Optimal Control of the Current Profile in NSTX-U," in *56th Annual Meeting of the APS Division of Plasma Physics*, 2014.

[154] Z. O. Ilhan, W. Wehner, J. Barton, E. Schuster, D. Gates, S. Gerhardt, and J. Menard, "First-Principles-Driven Model-Based Optimal Control of the Current Profile in NSTX-U," *submitted to 2015 American Control Conference*, 2014.

[155] G. Ambrosino *et al.*, "Optimal steady-state control for linear non right-invertible systems," *IET Control Theory and Applications*, vol. 1, no. 3, pp. 604–610, 2007.

[156] G. Golub and C. F. V. Loan, *Matrix Computations, 3rd Ed.* Baltimore, Maryland: Johns Hopkins University Press, 1996.

Appendix A

Manipulation of linear uncertain state-space system into a robust control framework

In this appendix, we provide an overview of a technique employed to manipulate a linear uncertain state-space system with a defined structure into a conventional robust control framework. The derivation follows the one originally described in [138]. We begin by considering a general linear uncertain state-space system described by

$$\begin{aligned} \dot{x} &= Ax + Bv_{FB}, \\ y &= Cx + Dv_{FB}, \end{aligned} \tag{A.1}$$

where $x \in \mathbb{R}^n$ is the system state, $v_{FB} \in \mathbb{R}^m$ is the control input, $y \in \mathbb{R}^p$ is the system output, and the state-space matrices have a structure defined by

$$\begin{aligned} A &= A_0 + \sum_{i=1}^{n_\delta} \delta_i A_i^* \qquad B = B_0 + \sum_{i=1}^{n_\delta} \delta_i B_i^*, \\ C &= C_0 + \sum_{i=1}^{n_\delta} \delta_i C_i^* \qquad D = D_0 + \sum_{i=1}^{n_\delta} \delta_i D_i^*, \end{aligned} \tag{A.2}$$

where $\delta = [\delta_1, \ldots, \delta_i, \ldots, \delta_{n_\delta}] \in \mathbb{R}^{n_\delta}$ is the uncertain parameter vector, the matrices A_0, B_0, C_0, D_0 represent the nominal response of the system, and the matrices A_i^*, B_i^*, C_i^*, D_i^* represent the influence each uncertain parameter δ_i has on the system response.

A linear system with state-space matrices A, B, C, D has a transfer function representation $G(s) = C(sI_n - A)^{-1}B + D$, where s denotes the Laplace variable, I_n denotes an $n \times n$ identity matrix, and $y = G(s)v_{FB}$. By defining the matrix

$$M_a = \begin{bmatrix} A & B \\ C & D \end{bmatrix}, \tag{A.3}$$

the system transfer function $G(s)$ can be written as a linear fractional transformation (LFT) as

$$\begin{aligned} G(s) &= D + C(sI_n - A)^{-1}B = D + C\frac{1}{s}I_n\left(I_n - A\frac{1}{s}I_n\right)^{-1}B \\ &= M_{a_{22}} + M_{a_{21}}\frac{1}{s}I_n\left(I_n - M_{a_{11}}\frac{1}{s}I_n\right)^{-1}M_{a_{12}} = F_u\left(M_a, \frac{1}{s}I_n\right), \end{aligned} \tag{A.4}$$

where F_u denotes the upper LFT. The block diagram of the system transfer function

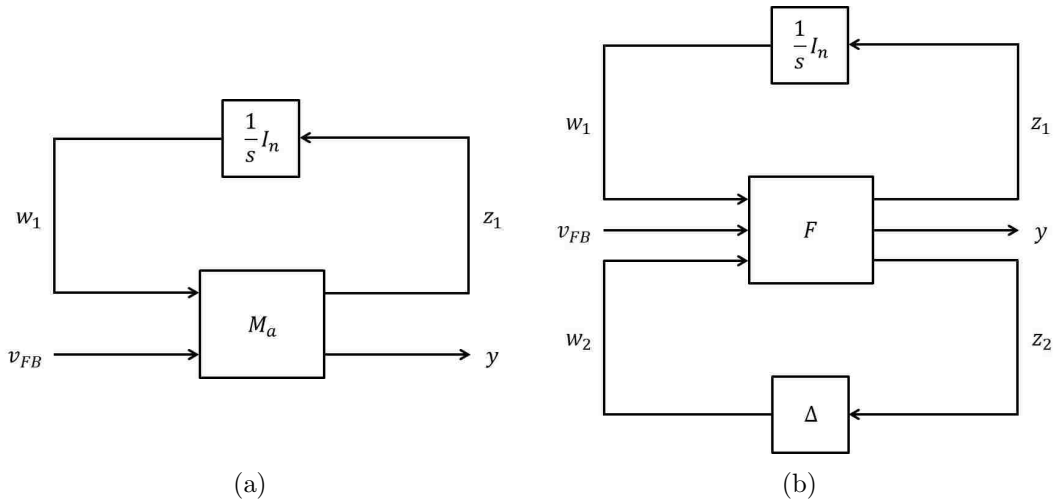

Figure A.1: Transfer function $G(s)$ (a) represented as a LFT and (b) with uncertainty Δ pulled out.

$G(s)$ (A.4) is shown in Fig. A.1(a) with equivalent equations

$$\begin{aligned} w_1 &= \frac{1}{s} I_n z_1, \\ y &= F_u\left(M_a, \frac{1}{s} I_n\right) v_{FB} = G(s) v_{FB}. \end{aligned} \tag{A.5}$$

By employing (A.2), the matrix M_a, defined in (A.3), is written in the form of a general state-space uncertainty as

$$M_a = \begin{bmatrix} A_0 + \sum_{i=1}^{n_\delta} \delta_i A_i^* & B_0 + \sum_{i=1}^{n_\delta} \delta_i B_i^* \\ C_0 + \sum_{i=1}^{n_\delta} \delta_i C_i^* & D_0 + \sum_{i=1}^{n_\delta} \delta_i D_i^* \end{bmatrix}. \tag{A.6}$$

By exploiting the structure of the state matrices in (A.6), the uncertainty is formulated into a LFT by achieving the smallest possible number of repeated blocks [138]. With this purpose in mind, the matrix J_i is formed as

$$J_i = \begin{bmatrix} A_i^* & B_i^* \\ C_i^* & D_i^* \end{bmatrix} \in \mathbb{R}^{(n+p)\times(n+m)}. \tag{A.7}$$

By using singular value decomposition and grouping terms, the matrix J_i is expressed as

$$J_i = U_i \Sigma_i V_i^* = (U_i \sqrt{\Sigma_i})(\sqrt{\Sigma_i} V_i^*) = \begin{bmatrix} L_i \\ W_i \end{bmatrix} \cdot \begin{bmatrix} R_i \\ Z_i \end{bmatrix}^*, \tag{A.8}$$

where $[\cdot]^*$ denotes the complex conjugate transpose. If the rank of the matrix J_i is q_i, then each inner matrix has the following dimensions

$$L_i \in \mathbb{R}^{n \times q_i} \quad W_i \in \mathbb{R}^{p \times q_i} \quad R_i \in \mathbb{R}^{n \times q_i} \quad Z_i \in \mathbb{R}^{m \times q_i}. \tag{A.9}$$

By employing (A.8), the uncertainty is written as

$$\delta_i J_i = \begin{bmatrix} L_i \\ W_i \end{bmatrix} [\delta_i I_{q_i}] \begin{bmatrix} R_i \\ Z_i \end{bmatrix}^*, \tag{A.10}$$

where I_{q_i} is a $q_i \times q_i$ identity matrix. Finally the matrix M_a, defined in (A.6), is expressed as

$$M_a = \begin{bmatrix} A_0 & B_0 \\ C_0 & D_0 \end{bmatrix} + \sum_{i=1}^{n_\delta} \delta_i J_i = F_{11} + F_{12} \Delta F_{21} \tag{A.11}$$

where

$$F_{11} = \begin{bmatrix} A_0 & B_0 \\ C_0 & D_0 \end{bmatrix} \qquad F_{12} = \begin{bmatrix} L_1 & \dots & L_{n_\delta} \\ W_1 & \dots & W_{n_\delta} \end{bmatrix},$$
$$F_{21} = \begin{bmatrix} R_1^* & Z_1^* \\ \vdots & \vdots \\ R_{n_\delta}^* & Z_{n_\delta}^* \end{bmatrix} \qquad \Delta = \begin{bmatrix} \delta_1 I_{q_1} & & 0 \\ & \ddots & \\ 0 & & \delta_{n_\delta} I_{q_{n_\delta}} \end{bmatrix}. \tag{A.12}$$

The representation of the matrix M_a, defined in (A.11), is equal to the lower LFT

$$\begin{aligned} M_a &= F_l(F, \Delta) = F_{11} + F_{12}\Delta(I_{q_T} - F_{22}\Delta)^{-1}F_{21} \\ &= F_{11} + F_{12}\Delta F_{21} \end{aligned} \tag{A.13}$$

where

$$F = \begin{bmatrix} F_{11} & F_{12} \\ F_{21} & 0 \end{bmatrix}, \tag{A.14}$$

q_T is the total rank of the Δ matrix given by

$$q_T = \sum_{i=1}^{n_\delta} q_i, \tag{A.15}$$

I_{q_T} denotes a $q_T \times q_T$ identity matrix, and F_l denotes the lower LFT.

The block diagram of the system is now drawn as in Fig. A.1(b) with equivalent equations

$$\begin{aligned} w_1 &= \frac{1}{s} I_n z_1 \qquad\qquad w_2 = \Delta z_2, \\ y &= F_u\left(F_l(F, \Delta), \frac{1}{s} I_n\right) v_{FB} = G(s) v_{FB}. \end{aligned} \tag{A.16}$$

The transfer function $G(s)$ of the uncertain state-space model is next expressed as

$$\begin{aligned} G(s) &= F_u\left(M_a, \frac{1}{s} I_n\right) = F_u\left(F_l(F, \Delta), \frac{1}{s} I_n\right) \\ &= F_l\left(F_u\left(F, \frac{1}{s} I_n\right), \Delta\right) = F_l(P', \Delta). \end{aligned} \tag{A.17}$$

For convention purposes, it is necessary to move the uncertainty to create an upper LFT by employing the definition

$$G(s) = F_l(P', \Delta) = F_u(P, \Delta), \tag{A.18}$$

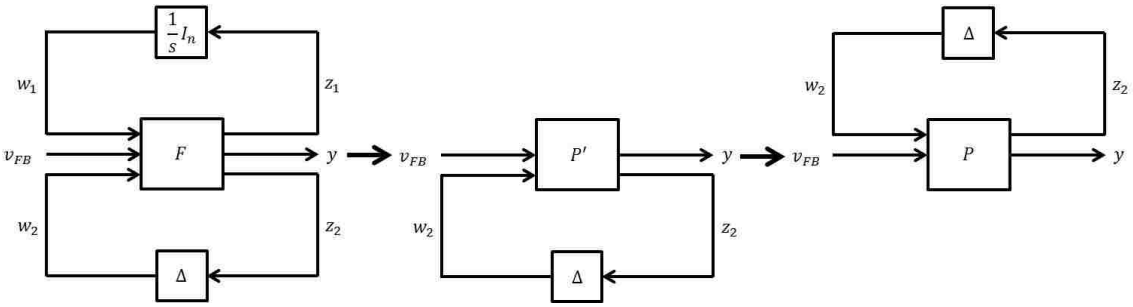

Figure A.2: Block diagram manipulation to obtain plant P.

where

$$P' = \begin{bmatrix} P_{22} & P_{21} \\ P_{12} & P_{11} \end{bmatrix} \qquad P = \begin{bmatrix} P_{11} & P_{12} \\ P_{21} & P_{22} \end{bmatrix}. \tag{A.19}$$

The corresponding block diagram manipulation is shown in Fig. A.2. The input-output equations of the system in this robust control framework are given by

$$\begin{aligned} z_2 &= P_{11}w_2 + P_{12}v_{FB}, \\ y &= P_{21}w_2 + P_{22}v_{FB}, \end{aligned} \tag{A.20}$$

where $P_{11} \in \mathbb{R}^{q_T \times q_T}$, $P_{12} \in \mathbb{R}^{q_T \times m}$, $P_{21} \in \mathbb{R}^{p \times q_T}$, $P_{22} \in \mathbb{R}^{p \times m}$, $z_2 \in \mathbb{R}^{q_T}$, $w_2 \in \mathbb{R}^{q_T}$, $y \in \mathbb{R}^p$, and $v_{FB} \in \mathbb{R}^m$.

Appendix B

Evaluation of relevant control channels via singular value decomposition

In this appendix, we provide an overview of a technique employed to evaluate the relevant control channels of an underactuated linear system (one that has more to-be-controlled outputs than available manipulatable inputs) by employing singular value decomposition (SVD). More details regarding this technique can be found in [155].

We begin by considering a general linear state-space system described by

$$\begin{aligned} \dot{x} &= Ax + Bu_{fb}, \\ y &= Cx + Du_{fb}, \end{aligned} \tag{B.1}$$

where $x \in \mathbb{R}^n$ is the system state, $u_{fb} \in \mathbb{R}^m$ is the control input, $y \in \mathbb{R}^p$ is the system output, A, B, C, D are the system state-space matrices, and $p > m$. The relationship between the outputs y and the inputs u_{fb} of the system (B.1) is expressed in terms

of the system transfer function $G(s)$ which is defined as

$$y = G(s)u_{fb} \qquad \text{where } G(s) = C(sI_n - A)^{-1}B + D, \tag{B.2}$$

where s denotes the Laplace variable and I_n is an $n \times n$ identity matrix. For a given set of constant inputs, the system (B.2) will reach a steady-state condition defined by a constant output, provided that the system is internally stable. These constant outputs and inputs define a particular equilibrium point of the system. It is desired that the outputs reach a set point, or reference to-be-tracked, which we denote as $r \in \mathbb{R}^p$, and the tracking error is defined as

$$e = r - y. \tag{B.3}$$

A feedback controller can then be designed to manipulate the control inputs u_{fb} to minimize (B.3). The conditions to bring the tracking error exactly to zero are typically not met because the number of controlled outputs (p) is larger than the number of controlled inputs (m). As a result, we can only independently control m linear combinations of the output of the system. The technique we employ to evaluate and decouple the most relevant control channels is based on a SVD of the state-space system (B.1) at a particular frequency $j\omega_{dc}$.

The real approximation of (B.2) at a particular frequency $j\omega_{dc}$ is expressed as

$$\hat{y} = \hat{G}\hat{u}_{fb}, \tag{B.4}$$

where $\hat{G}$ denotes the real approximation of the complex matrix $G(j\omega_{dc})$ [10, 146]. To begin the process of determining the relevant control channels, we consider a

performance index $\hat{J}$, which is defined as

$$\hat{J} = \hat{e}^T Q \hat{e} = (\hat{r} - \hat{y})^T Q (\hat{r} - \hat{y}), \tag{B.5}$$

where $Q \in \mathbb{R}^{p \times p}$ is a symmetric positive definite matrix that is used to weight which components of the tracking error, relative to the other components, are more important to minimize and $(\cdot)^T$ denotes the matrix transpose. We introduce another positive definite matrix $R \in \mathbb{R}^{m \times m}$ to weight which inputs have more control authority relative to the other inputs. We then define the "weighted" transfer function $\tilde{G}_0$ and its "economy" size SVD [156] as

$$\tilde{G} = Q^{\eta} \hat{G} R^{-\eta} = U \Sigma V^T, \tag{B.6}$$

where $\Sigma = \text{diag}\{\sigma_1, \sigma_2, \ldots, \sigma_m\} \in \mathbb{R}^{m \times m}$ is a diagonal matrix of singular values with $\sigma_1 > \sigma_2 > \ldots > \sigma_m > 0$, $U \in \mathbb{R}^{p \times m}$ and $V \in \mathbb{R}^{m \times m}$ are matrices that possess the following properties

$$V^T V = V V^T = I_m \qquad U^T U = I_m, \tag{B.7}$$

where I_m is an $m \times m$ identity matrix, and $\eta = 1/2$ is chosen to enable the performance index (B.5) to be written as a function of Σ as will be shown below.

By employing (B.6), the input-output relation (B.4) is now expressed as

$$\hat{y} = Q^{-1/2} \tilde{G} R^{1/2} \hat{u}_{fb} = Q^{-1/2} U \Sigma V^T R^{1/2} \hat{u}_{fb}. \tag{B.8}$$

We note that the columns of the matrix $Q^{-1/2} U \Sigma$ define a basis for the subspace of obtainable output values, and as a result, any obtainable output can be written as a linear combination $\hat{y}^* \in \mathbb{R}^m$ of the basis vectors, i.e.,

$$\hat{y} = Q^{-1/2} U \Sigma \hat{y}^* \iff \hat{y}^* = \Sigma^{-1} U^T Q^{1/2} \hat{y}. \tag{B.9}$$

This implies only the component of the reference vector which also lies in this subspace will be able to be tracked in steady state. As a result, we decompose the reference vector into a trackable component $\hat{r}_t$ and a non-trackable component r_{nt}, i.e., $r = \hat{r}_t + r_{nt}$. As the trackable component lies in the subspace of obtainable output values it can also be written as a linear combination $\hat{r}^* \in \mathbb{R}^m$ of the basis vectors, i.e.,

$$\hat{r}_t = Q^{-1/2} U \Sigma \hat{r}^* \Longleftrightarrow \hat{r}^* = \Sigma^{-1} U^T Q^{1/2} (\hat{r}_t + r_{nt}), \tag{B.10}$$

where $\Sigma^{-1} U^T Q^{1/2} r_{nt} = 0$ because the non-trackable component does not lie in the obtainable output subspace. By defining

$$\hat{u}^*_{fb} = V^T R^{1/2} \hat{u}_{fb} \Longleftrightarrow \hat{u}_{fb} = R^{-1/2} V \hat{u}^*_{fb}, \tag{B.11}$$

where $\hat{u}^*_{fb} \in \mathbb{R}^m$, a one-to-one relationship between $\hat{y}^*$ and $\hat{u}^*_{fb}$ is obtained by using (B.9) and (B.8) as

$$\begin{aligned} \hat{y}^* &= \Sigma^{-1} U^T Q^{1/2} \hat{y} \\ &= \Sigma^{-1} U^T Q^{1/2} Q^{-1/2} U \Sigma V^T R^{1/2} \hat{u}_{fb} = \hat{u}^*_{fb}. \end{aligned} \tag{B.12}$$

By utilizing (B.10) and (B.9), the performance index (B.5) is now written as

$$\begin{aligned} \hat{J} = \hat{e}^T Q \hat{e} &= (\hat{r} - \hat{y})^T Q (\hat{r} - \hat{y}) \\ &= (\hat{r}^* - \hat{y}^*)^T \Sigma U^T Q^{-1/2} Q Q^{-1/2} U \Sigma (\hat{r}^* - \hat{y}^*) \\ &= \left(\hat{r}^* - \hat{y}^*\right)^T \Sigma^2 (\hat{r}^* - \hat{y}^*) = \sum_{i=1}^{m} \sigma_i^2 \left(\hat{r}^*_i - \hat{y}^*_i\right)^2, \end{aligned} \tag{B.13}$$

where σ_i denotes the i-th singular value, $\hat{r}^*_i$ denotes the i-th component of $\hat{r}^*$, and $\hat{y}^*_i$ denotes the i-th component of $\hat{y}^*$.

We note that the i-th singular value acts as a weight parameter for the i-th

component of the tracking error in (B.13). It is possible that two sequential singular values could exhibit a large difference in magnitude, i.e., $\sigma_i \gg \sigma_{i+1}$. Therefore, no matter how large the component of the tracking error associated with σ_{i+1} is, its contribution to the overall value of performance index will be small compared to the component of the tracking error associated with σ_i. As a result, if we take all of the singular values into account, we could spend a lot of control effort for only a small improvement in the value of the performance index (B.13). To avoid this penalty, we partition the singular values into k_s significant singular values Σ_s and $m - k_s$ negligible singular values Σ_{ns}, and introduce the partitions

$$U = \begin{bmatrix} U_s & U_{ns} \end{bmatrix} \qquad V = \begin{bmatrix} V_s & V_{ns} \end{bmatrix} \qquad \Sigma = \begin{bmatrix} \Sigma_s & 0 \\ 0 & \Sigma_{ns} \end{bmatrix}, \tag{B.14}$$

$$\hat{r}^* = \begin{bmatrix} \hat{r}_s^* \\ \hat{r}_{ns}^* \end{bmatrix} \qquad \hat{y}^* = \begin{bmatrix} \hat{y}_s^* \\ \hat{y}_{ns}^* \end{bmatrix} \qquad \hat{u}_{fb}^* = \begin{bmatrix} \hat{u}_{fb_s}^* \\ \hat{u}_{fb_{ns}}^* \end{bmatrix}, \tag{B.15}$$

where $U_s \in \mathbb{R}^{p \times k_s}$, $\Sigma_s \in \mathbb{R}^{k_s \times k_s}$, $V_s \in \mathbb{R}^{m \times k_s}$, $\hat{r}_s^* \in \mathbb{R}^{k_s}$, $\hat{y}_s^* \in \mathbb{R}^{k_s}$, and $\hat{u}_{fb_s}^* \in \mathbb{R}^{k_s}$. By employing the partitions (B.14), the properties (B.7) are expressed as

$$\begin{aligned} V^T V &= \begin{bmatrix} V_s^T \\ V_{ns}^T \end{bmatrix} \begin{bmatrix} V_s & V_{ns} \end{bmatrix} = \begin{bmatrix} V_s^T V_s & V_s^T V_{ns} \\ V_{ns}^T V_s & V_{ns}^T V_{ns} \end{bmatrix} = \begin{bmatrix} I_{k_s} & 0 \\ 0 & I_{m-k_s} \end{bmatrix} \\ U^T U &= \begin{bmatrix} U_s^T \\ U_{ns}^T \end{bmatrix} \begin{bmatrix} U_s & U_{ns} \end{bmatrix} = \begin{bmatrix} U_s^T U_s & U_s^T U_{ns} \\ U_{ns}^T U_s & U_{ns}^T U_{ns} \end{bmatrix} = \begin{bmatrix} I_{k_s} & 0 \\ 0 & I_{m-k_s} \end{bmatrix}. \end{aligned} \tag{B.16}$$

By employing (B.14)-(B.15), a reduced form of the performance index (B.13) is written as

$$\hat{J}_s = \left(\hat{r}_s^* - \hat{y}_s^*\right)^T \Sigma_s^2 \left(\hat{r}_s^* - \hat{y}_s^*\right) = \sum_{i=1}^{k_s} \sigma_i^2 \left(\hat{r}_i^* - \hat{y}_i^*\right)^2, \tag{B.17}$$

where

$$\hat{r}_s^* = \Sigma_s^{-1} U_s^T Q^{1/2} (\hat{r}_t + r_{nt}),$$
$$\hat{y}_s^* = \Sigma_s^{-1} U_s^T Q^{1/2} \hat{y}. \tag{B.18}$$

By employing (B.18) and (B.8), a reduced form of the decoupled system $\hat{y}^* = \hat{u}_{fb}^*$ (B.12) is expressed as

$$\begin{aligned}
\hat{y}_s^* &= \Sigma_s^{-1} U_s^T Q^{1/2} \hat{y} = \Sigma_s^{-1} U_s^T Q^{1/2} Q^{-1/2} U \Sigma V^T R^{1/2} \hat{u}_{fb} \\
&= \Sigma_s^{-1} U_s^T \begin{bmatrix} U_s & U_{ns} \end{bmatrix} \begin{bmatrix} \Sigma_s & 0 \\ 0 & \Sigma_{ns} \end{bmatrix} \begin{bmatrix} V_s^T \\ V_{ns}^T \end{bmatrix} R^{1/2} \hat{u}_{fb} \\
&= \Sigma_s^{-1} \begin{bmatrix} I_{k_s} & 0 \end{bmatrix} \begin{bmatrix} \Sigma_s V_s^T \\ \Sigma_{ns} V_{ns}^T \end{bmatrix} R^{1/2} \hat{u}_{fb} = \hat{u}_{fb_s}^*,
\end{aligned} \tag{B.19}$$

where we have defined

$$\hat{u}_{fb_s}^* = V_s^T R^{1/2} \hat{u}_{fb} \Longleftrightarrow \hat{u}_{fb} = R^{-1/2} V_s \hat{u}_{fb_s}^*. \tag{B.20}$$

Appendix C

Fundamentals of feedback control design by H_∞ closed-loop shaping

In this appendix, we provide an overview of the fundamentals of feedback control design by employing the H_∞ closed-loop shaping technique. More details regarding this technique can be found in [10].

The H_∞ norm of any stable transfer function $F(s)$, where s denotes the Laplace variable, represents the maximum gain in any direction at any frequency between the outputs and inputs of $F(s)$ and is expressed mathematically as

$$||F(s)||_\infty = \max_\omega \bar{\sigma}(F(j\omega)), \tag{C.1}$$

where $||\cdot||_\infty$ denotes the H_∞ norm and $\bar{\sigma}(F(j\omega))$ denotes the maximum singular value of the function F at each frequency ω. For single-input-single-output (SISO) systems, specifications on the shape of the frequency response of the magnitude of the transfer function F, which is denoted as $|F|$, can be captured by an upper bound, $1/|W_f(s)|$, on the magnitude of F, where $W_f(s)$ is a weight function. This frequency

dependent specification is expressed mathematically as

$$\begin{aligned} & |F(j\omega)| < 1/|W_f(j\omega)|, \quad \forall\omega \\ \Leftrightarrow \quad & |W_f F| < 1, \quad \forall\omega \quad \Leftrightarrow \quad ||W_f F||_\infty < 1, \end{aligned} \tag{C.2}$$

where the last equivalence relationship follows from the definition of the H_∞ norm (C.1). This method is easily extendable to multi-input-multi-output (MIMO) systems and yields the same H_∞ relationship between the weight function and the transfer function shown in (C.2).

We begin by considering a general linear state-space system described by

$$\begin{aligned} \dot{x} &= Ax + Bu, \\ y &= Cx + Du, \end{aligned} \tag{C.3}$$

where $x \in \mathbb{R}^n$ is the system state, $u \in \mathbb{R}^m$ is the control input, $y \in \mathbb{R}^p$ is the system output, and A, B, C, D are the system state-space matrices. The relationship between the outputs y and the inputs u of the system (C.3) can be expressed in terms of the system transfer function $G(s)$, which is defined as

$$y = G(s)u \qquad \text{where } G(s) = C(sI_n - A)^{-1}B + D, \tag{C.4}$$

where s denotes the Laplace variable and I_n is an $n \times n$ identity matrix.

A conventional block diagram of a feedback control system is shown in Fig. C.1, where G is the system transfer function, K is the feedback controller, r is the desired reference (set point), d is an uncontrolled disturbance, y is the system output, and n is the measurement noise. The goal of the feedback control design problem is to design a controller that outputs a control signal u that drives the system output to the desired set point, thus minimizing the tracking error e. In order to understand

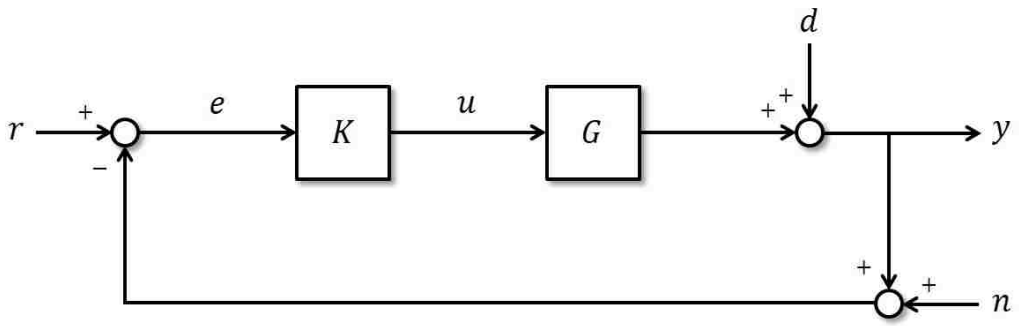

Figure C.1: Block diagram of conventional feedback control system.

how the external system inputs (r, d, n) affect the system outputs (y), tracking error (e), and control signal (u), the closed-loop system transfer functions are expressed as

$$y = \frac{GK}{I+GK}r + \frac{I}{I+GK}d - \frac{GK}{I+GK}n, \tag{C.5}$$

$$e = \frac{I}{I+GK}r - \frac{I}{I+GK}d - \frac{I}{I+GK}n, \tag{C.6}$$

$$u = K\frac{I}{I+GK}r - K\frac{I}{I+GK}d - K\frac{I}{I+GK}n. \tag{C.7}$$

By employing the definitions

$$S = \frac{I}{I+GK}, \tag{C.8}$$

$$T = \frac{GK}{I+GK}, \tag{C.9}$$

$$I = S + T, \tag{C.10}$$

where S is the sensitivity function and T is the complementary sensitivity function, we can express (C.5)-(C.7) as

$$y = Tr + Sd - Tn, \tag{C.11}$$

$$e = Sr - Sd - Sn, \tag{C.12}$$

$$u = KSr - KSd - KSn. \tag{C.13}$$

The feedback control objectives are to 1.) stabilize the system, 2.) maintain a small tracking error for any reference, 3.) reject the effects of any external disturbance, 4.) minimize the effect measurement noise has on the closed-loop system, and 5.) utilize as little feedback control effort as possible. These control objectives can be translated into desired values of the closed-loop transfer functions in various frequency ranges as follows:

1.) For unstable systems, the feedback controller must first stabilize the system. In the case of the linear system (C.3) considered here, the feedback controller needs to ensure all of the closed-loop system poles (eigenvalues) lie in the open left-half plane, i.e., all of the poles have a negative real part.

2.) Typically references are low frequency signals, therefore, for good reference tracking ($y \to r$), the magnitude of the transfer function S should approach zero and the magnitude of the transfer function T should approach one at low frequencies, i.e., $|S| \to 0$ and $|T| \to 1$ as $s \to 0$ (see (C.11) and (C.12)). Note that both of these conditions can be met by satisfying one of them due to (C.10).

3.) Additionally, disturbances are typically low frequency in nature as well, therefore, to reject the effects an external disturbance has on the system output, the magnitude of the transfer function S should approach zero at low frequencies, i.e., $|S| \to 0$ as $s \to 0$ (see (C.11) and (C.12)).

4.) Typically measurement noise is a high frequency signal. In order to minimize the effect of noise on the closed-loop system, the peak magnitude of the transfer function S should be suppressed. Additionally, the magnitude of the transfer function S should approach one and the magnitude of the transfer function T should approach zero at high frequencies, i.e., $|S| \to 1$ and $|T| \to 0$ as $s \to \infty$ (see (C.11) and (C.12)). Note that both of these conditions can be met by satisfying one of them due to (C.10).

5.) In order to minimize the amount of control effort used to achieve good reference tracking ($y \to r$) and disturbance rejection, the magnitude of the transfer function KS should be minimized at low frequencies. In addition, the feedback controller should not react to high frequency noise, so the magnitude of the transfer function KS should approach zero at high frequencies, i.e., $|KS| \to 0$ as $s \to \infty$ (see (C.13)).

By utilizing the results of (C.2), the control design problem can be formulated as the following stacked H_∞ minimization problem

$$\min_K \left\| \begin{matrix} W_p S \\ W_u K S \end{matrix} \right\|_\infty, \qquad \forall \omega. \tag{C.14}$$

The functions $W_p(s)$ and $W_u(s)$ are used to place upper bounds $1/\bar{\sigma}\big(W_p(j\omega)\big)$ and $1/\bar{\sigma}\big(W_u(j\omega)\big)$ on the shape of the frequency responses of the magnitude of the closed-loop transfer functions S and KS, respectively. One possible parameterization of the the weight functions is $W_p = \text{diag}\{W_{p_i}\} \in \mathbb{R}^{p \times p}$ and $W_u = \text{diag}\{W_{u_i}\} \in \mathbb{R}^{m \times m}$ where

$$W_{p_i}(s) = \frac{\big(s/\sqrt{M_{p_i}} + \omega_{p_i}\big)^2}{\big(s + \omega_{p_i}\sqrt{H^*_{p_i}}\big)^2} \qquad W_{u_i}(s) = \frac{\big(s/\sqrt{M_{u_i}} + \omega_{u_i}\big)^2}{\big(s + \omega_{u_i}\sqrt{H^*_{u_i}}\big)^2}, \tag{C.15}$$

where the design parameters M_{p_i} and M_{u_i} are related to the high frequency behavior, the design parameters $H^*_{p_i}$ and $H^*_{u_i}$ are related to the low frequency behavior, and the design parameters ω_{p_i} and ω_{u_i} are related to the bandwidth of the upper bounds $1/\bar{\sigma}\big(W_{p_i}(j\omega)\big)$ and $1/\bar{\sigma}\big(W_{u_i}(j\omega)\big)$, respectively [10]. The design parameters can be chosen so the shape of the frequency response of the upper bounds coincides with the desired shape of the frequency response of the closed-loop transfer functions previously described.

The H_∞ closed-loop shaping technique is now applied to the following linear SISO system

$$\begin{aligned} \dot{x} &= -\frac{1}{\tau}x + \frac{1}{\tau}u, \\ y &= x, \end{aligned} \tag{C.16}$$

where τ is a constant. For $\tau < 0$, the uncontrolled ($u = 0$) system (C.16) is unstable. For this example we set $\tau = -3$, therefore, feedback is necessary to stabilize the closed-loop system. The various design parameters in the weight functions (C.15) are chosen as $M_p = 1$, $\omega_p = 10^{0.5}$, $H_p^* = 10^{-3}$, $M_u = 10^{-3}$, $\omega_u = 10^{2.5}$, and $H_u^* = 1$, and the designed H_∞ closed-loop shaping controller is denoted as

$$K_{cls}(s) = K(s), \tag{C.17}$$

where K is obtained by solving (C.14). It is worth noting, that in order to guarantee that the closed-loop system will be able to track step changes in the reference signal, the controller should include a pure integrator ($1/s$). This characteristic could be captured by selecting the design parameter $H_p^* = 0$, however, this may result in numerical problems with the algorithm employed to solve (C.14) [10]. Therefore, an alternative approach is to augment the H_∞ closed-loop shaping controller (C.17) with a compensator as

$$K_{cls}^{int}(s) = K_{cls}(s)\left[\frac{\omega_{int}}{s}\left(\frac{s}{\omega_{int}} + 1\right)\right]^{n_{int}}, \tag{C.18}$$

where n_{int} is the number of integrators to be added. The design parameter ω_{int} determines the frequency range ($\omega \in [0, \omega_{int}]$) over which the compensator will affect the response of the controller K_{cls} to error signals, i.e., the controller transfer function $K_{cls}(s)$ will be unmodified for frequencies in the range $\omega \in (\omega_{int}, \infty]$. For this example we select $n_{int} = 1$ and $\omega_{int} = 0.05$.

The time response of the system (C.16) with the various designed controllers is shown in Fig. C.2. For comparisons sake, a conventional proportional-integral (PI) controller is also designed as

$$K_{PI}(s) = \left(k_P + k_I \frac{1}{s}\right), \tag{C.19}$$

where k_P is the proportional gain and k_I is the integral gain. For this example we select $k_P = k_I = -5$. As shown in Figs. C.2(a-b), the response of the system with the PI controller (C.19) and the loop-shaping controller (C.18) is very similar when there is no measurement noise, i.e., $n = 0$ in Fig. C.1, and the controllers are able to track the desired set point (target). When measurement noise is present, the controllers are still able to track the desired set point (shown in Fig. C.2(c)), however, as shown in Fig. C.2(d), the PI controller reacts significantly more to the noise than the loop-shaping controller. To understand this, the frequency response of the designed controllers, as well as the frequency response of the various closed-loop transfer functions, is shown in Fig. C.3. As shown in Fig. C.3(a), the frequency response of the loop-shaping controllers rolls off at high frequencies, whereas the frequency response of the PI controller does not. The effect that this has on the closed-loop transfer function between the control input and noise signals KS (see (C.13)) is shown in Fig. C.3(c), which results in the PI controller reacting to noise more than the loop-shaping controllers. Finally, the steady-state response (with no measurement noise) of the system (C.16) with the various designed controllers is shown in Figs. C.2(e-f). As the PI (C.19) and augmented loop-shaping (C.18) controllers have a pure integrator (shown in Figs. C.3(a-b), i.e., $|K| \to \infty$ and $|S| \to 0$ as $s \to 0$), they are able to track the desired set point with zero steady-state error, while a small steady-state error is achieved with the loop-shaping controller (C.17).

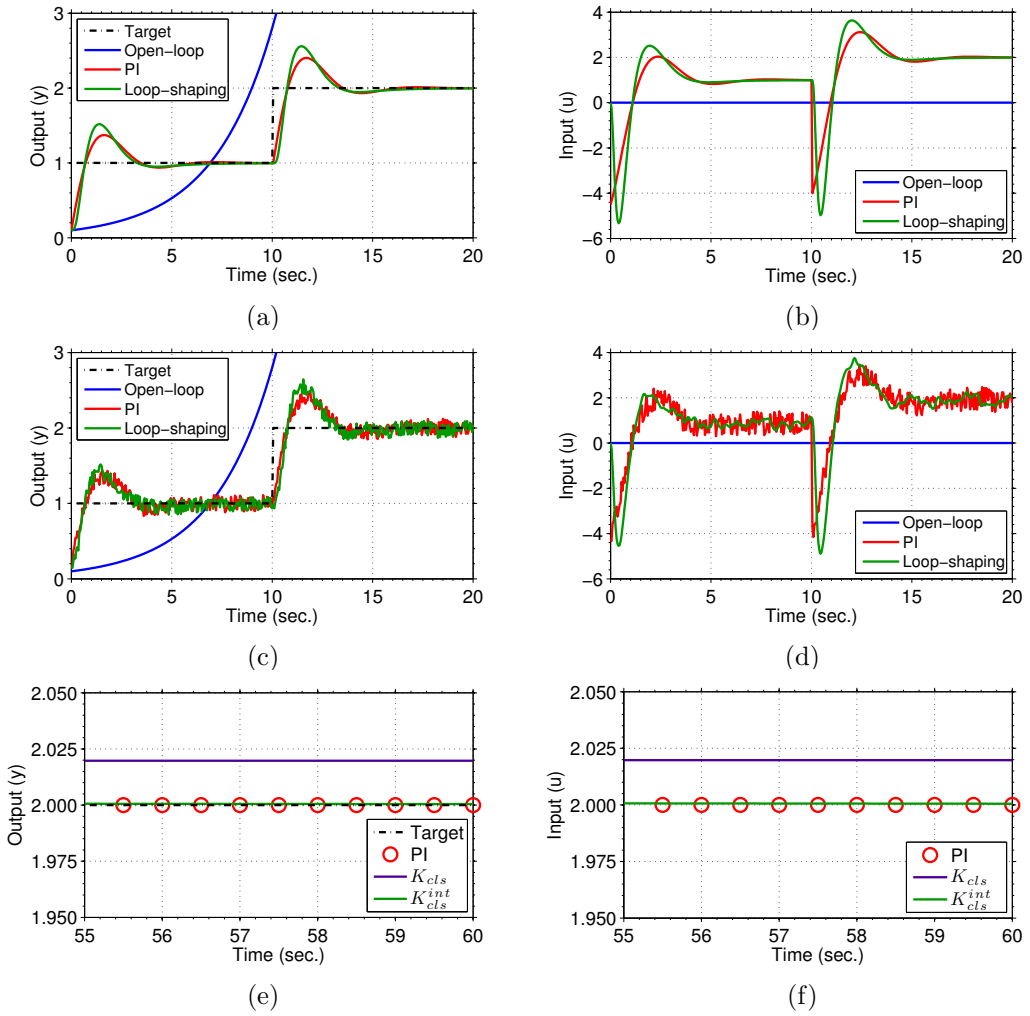

Figure C.2: Time response of the system (C.16) with the various designed controllers: (a-b) without measurement noise, (c-d) with measurement noise, and (e-f) in steady state.

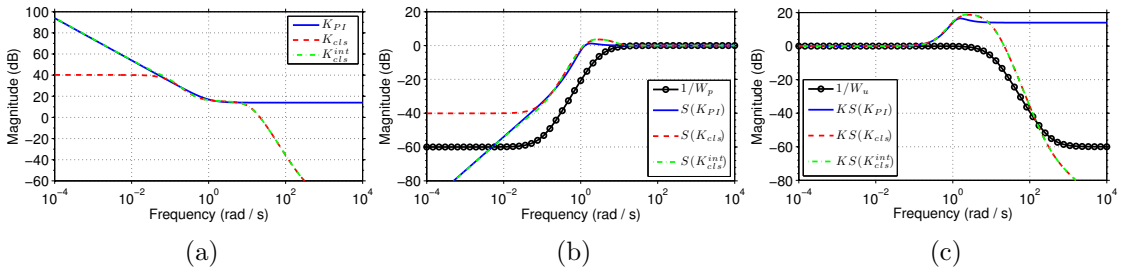

Figure C.3: Singular value diagrams of: (a) feedback controllers, (b) sensitivity function (and associated weight function $1/W_p$ for H_∞ design) achieved with the controllers in (a), and (c) transfer function KS (and associated weight function $1/W_u$ for H_∞ design) achieved with the controllers in (a).

Appendix D

Interfacing feedback controller with available rtEFIT measurements

In this appendix, we describe the coordinate transformation algorithm implemented in the DIII-D Plasma Control System (PCS) to construct the magnetic profiles available for real-time feedback control on the normalized effective minor radius spatial domain $\hat{\rho}$ from the data provided by the real-time EFIT (rtEFIT) equilibrium reconstruction code [11]. The measurements that are available in real-time on the normalized flux spatial domain ψ_n are shown in Table D.1. The normalized flux ψ_n is defined as

$$\psi_n = \frac{\psi - \psi_{axis}}{\psi_{bdry} - \psi_{axis}}. \tag{D.1}$$

The safety factor $q(\psi_n^{rt})$ is provided by rtEFIT at 64 evenly spaced points

$$\psi_n^{rt} = 0, 1/64, 2/64, \ldots, 63/64. \tag{D.2}$$

Table D.1: Measurements Available in Real-time

Measurement	Description	Units
$q(\psi_n^{rt})$	Safety factor on normalized flux spatial domain	None
ψ_{axis}	Poloidal stream function on magnetic axis	Wb/rad
ψ_{bdry}	Poloidal stream function on plasma boundary	Wb/rad
I_p^{meas}	Plasma current	MA

We begin the magnetic profile construction algorithm by determining the normalized effective minor radius coordinates associated with the rtEFIT normalized flux coordinates (D.2).

D.1 Computing normalized effective minor radius coordinates

The basic definition of the safety factor is

$$q = -\frac{d\Phi}{d\Psi} = -\frac{d\Phi}{2\pi d\psi}, \tag{D.3}$$

which we use to calculate the toroidal flux coordinates $\Phi(\psi_n^{rt})$ corresponding to the values of $q(\psi_n^{rt})$ provided by rtEFIT. By using the relationship

$$d\psi = \big(\psi_{bdry} - \psi_{axis}\big) d\psi_n, \tag{D.4}$$

we integrate (D.3) to obtain

$$\int_{\psi_{axis}}^{\psi} d\Phi = \Phi(\psi) - \Phi(\psi_{axis}) = -2\pi \int_{\psi_{axis}}^{\psi} q(\psi) d\psi,$$

$$\Phi(\psi_n) - \Phi(0) = -2\pi \int_0^{\psi_n} \big(\psi_{bdry} - \psi_{axis}\big) q(\psi_n) d\psi_n,$$

$$\Phi(\psi_n) = -2\pi \int_0^{\psi_n} \big(\psi_{bdry} - \psi_{axis}\big) q(\psi_n) d\psi_n, \tag{D.5}$$

where $\Phi(0) = 0$ by definition. By numerically integrating the right hand side of (D.5) by employing trapezoidal integration, we compute the toroidal flux coordinates $\Phi(\psi_n^{rt}\big|_k)$, $2 \leq k \leq 64$, as

$$\begin{aligned}\Phi(\psi_n^{rt}\big|_k) &= \frac{2\pi(\psi_{axis} - \psi_{bdry})}{2} \frac{1}{64} \sum_{j=2}^{k} \left[q(\psi_n^{rt}\big|_{j-1}) + q(\psi_n^{rt}\big|_j) \right] \\ &= \Phi(\psi_n^{rt}\big|_{k-1}) + \frac{2\pi(\psi_{axis} - \psi_{bdry})}{2} \frac{1}{64} \left[q(\psi_n^{rt}\big|_{k-1}) + q(\psi_n^{rt}\big|_k) \right], \end{aligned} \tag{D.6}$$

where $\Phi(\psi_n^{rt}|_1) = 0$. Because the safety factor is not computed at the plasma boundary by rtEFIT, we employ the approximation $q(\psi_n^{rt}\big|_{65}) = q(\psi_n^{rt}\big|_{64})$ to compute Φ at the plasma boundary. This approximation results in

$$\Phi(\psi_n^{rt}\big|_{65}) = \Phi(\psi_n^{rt}\big|_{64}) + 2\pi(\psi_{axis} - \psi_{bdry}) \frac{1}{64} q(\psi_n^{rt}\big|_{64}). \tag{D.7}$$

By using the relationship between the toroidal flux coordinates and the mean effective minor radius ρ

$$\Phi = \pi B_{\phi,0} \rho^2, \tag{D.8}$$

Table D.2: Magnetic Profiles Available in Real-time

Profile	Description	Units
$q(\hat{\rho})$	Safety factor on normalized ρ spatial domain	None
$i(\hat{\rho})$	Rotational transform on normalized ρ spatial domain	None
$\Psi(\hat{\rho})$	Poloidal magnetic flux on normalized ρ spatial domain	Wb
$\theta(\hat{\rho}) = \partial\psi/\partial\hat{\rho}$	Poloidal flux gradient on normalized ρ spatial domain	Wb/rad

where $B_{\phi,0}$ is the the vacuum toroidal magnetic field at the geometric major radius of the tokamak, we calculate the mean effective minor radius $\rho(\psi_n^{rt}\big|_k)$, $1 \leq k \leq 65$, as

$$\rho(\psi_n^{rt}\big|_k) = \sqrt{\frac{\Phi(\psi_n^{rt}\big|_k)}{\pi B_{\phi,0}}}. \tag{D.9}$$

The normalized minor radius $\hat{\rho}(\psi_n^{rt}\big|_k)$, $1 \leq k \leq 65$, is then computed as

$$\hat{\rho}(\psi_n^{rt}\big|_k) = \frac{\rho(\psi_n^{rt}\big|_k)}{\rho(\psi_n^{rt}\big|_{65})}. \tag{D.10}$$

We now know the normalized minor radius coordinates associated with the rtEFIT normalized flux coordinates (D.2), which we use to construct the magnetic profiles available for real-time control on the desired spatial domain.

D.2 Constructing magnetic profiles available for real-time control

Due to the unique relationship between the normalized effective minor radius coordinates (D.10) and the rtEFIT normalized flux coordinates (D.2), we can construct the desired magnetic profiles available for real-time control shown in Table D.2 from the measurements $q(\psi_n^{rt})$ provided by rtEFIT.

D.2.1 Safety factor profile: q

The safety factor profile $q(\hat{\rho}(\psi_n^{rt}\big|_k))$, $1 \leq k \leq 64$, is computed as

$$q(\hat{\rho}(\psi_n^{rt}\big|_k)) = q(\psi_n^{rt}\big|_k). \tag{D.11}$$

As the safety factor is not computed at the plasma boundary by rtEFIT, we employ the approximation

$$q(\hat{\rho}(\psi_n^{rt}\big|_{65})) = q(\psi_n^{rt}\big|_{64}) \tag{D.12}$$

to compute the safety factor at the plasma boundary.

D.2.2 Rotational transform profile: i

The rotational transform profile is defined as $i = 1/q$, therefore, $i(\hat{\rho}(\psi_n^{rt}\big|_k))$, $1 \leq k \leq 64$, is computed as

$$i(\hat{\rho}(\psi_n^{rt}\big|_k)) = \frac{1}{q(\psi_n^{rt}\big|_k)}. \tag{D.13}$$

As the safety factor is not computed at the plasma boundary by rtEFIT, we employ the approximation

$$i(\hat{\rho}(\psi_n^{rt}\big|_{65})) = \frac{1}{q(\psi_n^{rt}\big|_{64})} \tag{D.14}$$

to compute the rotational transform at the plasma boundary.

D.2.3 Poloidal magnetic flux profile: Ψ

The relationship between the poloidal flux Ψ and the poloidal stream function ψ is

$$\Psi = 2\pi\psi. \tag{D.15}$$

Therefore, we use (D.1) and (D.2) to compute the poloidal flux profile $\Psi(\hat{\rho}(\psi_n^{rt}|_k))$, $1 \leq k \leq 65$, as

$$\Psi(\hat{\rho}(\psi_n^{rt}|_k)) = 2\pi\left(\psi_{axis} + \frac{k-1}{64}(\psi_{bdry} - \psi_{axis})\right). \tag{D.16}$$

D.2.4 Poloidal magnetic flux gradient profile: θ

By using the definition of the safety factor (D.3), the relationship between Φ and ρ (D.8), and the definition of the normalized effective minor radius (D.10), the safety factor can be expressed as

$$q = -\frac{B_{\phi,0}\rho_b\rho}{\theta}. \tag{D.17}$$

Therefore, the poloidal flux gradient profile $\theta(\hat{\rho}(\psi_n^{rt}|_k))$, $1 \leq k \leq 64$, is computed as

$$\theta(\hat{\rho}(\psi_n^{rt}|_k)) = -\frac{B_{\phi,0}\rho(\psi_n^{rt}|_{65})\rho(\psi_n^{rt}|_k)}{q(\psi_n^{rt}|_k)}. \tag{D.18}$$

If (D.18) is used to compute θ at the plasma boundary, the construction algorithm will fail because of the approximation $q(\psi_n^{rt}|_{65}) = q(\psi_n^{rt}|_{64})$. In order to overcome this construction failure at the plasma boundary, the constructed poloidal flux gradient at the plasma boundary is computed as

$$\theta(\hat{\rho}(\psi_n^{rt}|_{65})) = -k_{I_p}I_p^{meas}. \tag{D.19}$$

This definition is consistent with the boundary conditions (2.83) of the magnetic diffusion equation model of the poloidal flux profile evolution in the tokamak.

D.3 Computing selected magnetic profile

The selected magnetic profile is denoted as $y_M(\hat{\rho}(\psi_n^{rt}))$. The spatial domain that the magnetic profile can be controlled on in real-time is 21 evenly spaced points

$$\hat{\rho} = 0, 0.05, 0.1, 0.15, \ldots, 1. \tag{D.20}$$

Therefore, to complete the magnetic profile construction algorithm, the selected magnetic profile $y_M(\hat{\rho}(\psi_n^{rt}))$ is interpolated onto the spatial domain (D.20).

Appendix E

Overview of sequential quadratic programming

In this appendix, we provide an overview of the sequential quadratic programming (SQP) solution method for a general nonlinear program (NLP) defined by

$$\min_{v} \quad \mathcal{J}(z, v), \tag{E.1}$$

such that

$$f(z, v) = 0, \tag{E.2}$$

where $\mathcal{J}$ is a scalar-valued function to be minimized, z is the system state, v is the manipulated control input, and f is a general nonlinear function. More details regarding this technique can be found in [95]. To simplify the explanation of the SQP technique, we only consider equality constraints in the form of (E.2). We begin by defining the system Hamiltonian as

$$\mathcal{H}(z, v, \lambda) = \mathcal{J}(z, v) + \lambda^T f(z, v), \tag{E.3}$$

where λ is a to-be-determined Lagrange multiplier. An incremental change in the Hamiltonian with respect to changes in the parameters is given to first order by

$$d\mathcal{H} = \mathcal{H}_z dz + \mathcal{H}_v dv + \mathcal{H}_\lambda d\lambda, \tag{E.4}$$

where $(\cdot)_i = \frac{\partial(\cdot)}{\partial i}$ for $i \in [z, v, \lambda]$. At a local minimum (z^*, v^*, λ^*), $d\mathcal{H}$ must be zero for all increments dz, dv, $d\lambda$. Therefore, the first-order optimality conditions for the NLP (E.1)-(E.2) are given by the nonlinear equations

$$\begin{aligned}
\mathcal{H}_z(z^*, v^*, \lambda^*) &= \mathcal{J}_z(z^*, v^*) + (\lambda^*)^T f_z(z^*, v^*) = 0, \\
\mathcal{H}_v(z^*, v^*, \lambda^*) &= \mathcal{J}_v(z^*, v^*) + (\lambda^*)^T f_v(z^*, v^*) = 0, \\
\mathcal{H}_\lambda(z^*, v^*, \lambda^*) &= f(z^*, v^*) = 0.
\end{aligned} \tag{E.5}$$

One approach to solving the NLP (E.1)-(E.2) is to assume we have an iteration

$$\left(z^{(k+1)}, v^{(k+1)}, \lambda^{(k+1)}\right) = \left(z^{(k)}, v^{(k)}, \lambda^{(k)}\right) + \left(\zeta^{(k)}, \xi^{(k)}, \sigma^{(k)}\right)$$

that is converging to the solution (z^*, v^*, λ^*) of (E.5), where $(\zeta^{(k)}, \xi^{(k)}, \sigma^{(k)})$ are search directions. Assuming the current estimate $(z^{(k)}, v^{(k)}, \lambda^{(k)})$ is close to (z^*, v^*, λ^*), we can linearize (E.5) around the current estimate, i.e.,

$$\begin{aligned}
0 = {} & \mathcal{H}_z(z^{(k)}, v^{(k)}, \lambda^{(k)}) + \mathcal{H}_{zz}(z^{(k)}, v^{(k)}, \lambda^{(k)})\zeta^{(k)} \\
& + \mathcal{H}_{zv}(z^{(k)}, v^{(k)}, \lambda^{(k)})\xi^{(k)} + \mathcal{H}_{z\lambda}(z^{(k)}, v^{(k)}, \lambda^{(k)})\sigma^{(k)}, \\
0 = {} & \mathcal{H}_v(z^{(k)}, v^{(k)}, \lambda^{(k)}) + \mathcal{H}_{vz}(z^{(k)}, v^{(k)}, \lambda^{(k)})\zeta^{(k)} \\
& + \mathcal{H}_{vv}(z^{(k)}, v^{(k)}, \lambda^{(k)})\xi^{(k)} + \mathcal{H}_{v\lambda}(z^{(k)}, v^{(k)}, \lambda^{(k)})\sigma^{(k)}, \\
0 = {} & \mathcal{H}_\lambda(z^{(k)}, v^{(k)}, \lambda^{(k)}) + \mathcal{H}_{\lambda z}(z^{(k)}, v^{(k)}, \lambda^{(k)})\zeta^{(k)} \\
& + \mathcal{H}_{\lambda v}(z^{(k)}, v^{(k)}, \lambda^{(k)})\xi^{(k)} + \mathcal{H}_{\lambda\lambda}(z^{(k)}, v^{(k)}, \lambda^{(k)})\sigma^{(k)},
\end{aligned} \tag{E.6}$$

where $(\cdot)_{ij} = \frac{\partial^2(\cdot)}{\partial i \partial j}$ for $i \in [z, v, \lambda]$ and $j \in [z, v, \lambda]$. From (E.5), we note that

$$\mathcal{H}_{z\lambda} = \mathcal{H}_{\lambda z} = f_z \qquad \mathcal{H}_{v\lambda} = \mathcal{H}_{\lambda v} = f_v \qquad \mathcal{H}_{\lambda\lambda} = 0,$$

which allows us to write (E.6) in matrix form as

$$\left.\begin{bmatrix} \mathcal{H}_{zz} & \mathcal{H}_{zv} & f_z \\ \mathcal{H}_{vz} & \mathcal{H}_{vv} & f_v \\ f_z & f_v & 0 \end{bmatrix}\right|_{(z^{(k)}, v^{(k)}, \lambda^{(k)})} \begin{bmatrix} \zeta^{(k)} \\ \xi^{(k)} \\ \sigma^{(k)} \end{bmatrix} = - \left.\begin{bmatrix} H_z \\ H_v \\ f \end{bmatrix}\right|_{(z^{(k)}, v^{(k)}, \lambda^{(k)})} . \tag{E.7}$$

The search directions $(\zeta^{(k)}, \xi^{(k)}, \sigma^{(k)})$ can then be obtained by solving (E.7). It can be shown that the first-order optimality condition of the quadratic program (QP)

$$\min_{\xi^{(k)}} \quad \mathcal{L}(\zeta^{(k)}, \xi^{(k)})\big|_{(z^{(k)}, v^{(k)}, \lambda^{(k)})}, \tag{E.8}$$

such that

$$f(z^{(k)}, v^{(k)}) + \left.\begin{bmatrix} f_z & f_v \end{bmatrix}\right|_{(z^{(k)}, v^{(k)})} \begin{bmatrix} \zeta^{(k)} \\ \xi^{(k)} \end{bmatrix} = 0, \tag{E.9}$$

where

$$\mathcal{L} = \mathcal{H} + \begin{bmatrix} \mathcal{H}_z & \mathcal{H}_v \end{bmatrix} \begin{bmatrix} \zeta^{(k)} \\ \xi^{(k)} \end{bmatrix} + \frac{1}{2} \begin{bmatrix} \zeta^{(k)} & \xi^{(k)} \end{bmatrix} \begin{bmatrix} \mathcal{H}_{zz} & \mathcal{H}_{zv} \\ \mathcal{H}_{vz} & \mathcal{H}_{vv} \end{bmatrix} \begin{bmatrix} \zeta^{(k)} \\ \xi^{(k)} \end{bmatrix},$$

with Lagrange multiplier $\sigma^{(k)}$, is given by (E.7). Therefore from the sequence of quadratic programs (E.8)-(E.9) (denoted as $\text{QP}^{(k)}$), which represent a quadratic approximation of $\mathcal{H}$ subject to a linear approximation of f around the current estimate $(z^{(k)}, v^{(k)}, \lambda^{(k)})$, search directions for the original NLP (E.1)-(E.2) can be obtained.

Curriculum vitae

Education

Doctor of Philosophy, Mechanical Engineering
Lehigh University, Bethlehem, PA - GPA: 4.0 Dec. 2014
Advisor: Prof. Eugenio Schuster

Bachelor of Science, Mechanical Engineering, Aerospace Engineering Minor
Lehigh University, Bethlehem, PA - GPA: 3.95, *Summa Cum Laude* May 2009

Skills and Expertise

- First-principles-driven (physics-based) modeling and model validation, numerical simulation, nonlinear optimization, multivariable model-based feedback control, and analysis of complex physical system dynamics
- Implementing, validating, and experimentally testing real-time control algorithms
- Experience in dynamic system analysis and various applications of control engineering: distributed parameter and nonlinear systems, robust, adaptive and state-space control, system identification (data-driven modeling)
- Knowledge in: numerical methods, fluid mechanics, unsteady and turbulent flow, aerodynamics, heat and mass transfer, thermodynamics, nuclear reactor engineering, mechanics of materials, electrical engineering
- Computer: MATLAB/Simulink, C/C++ Programming Language, LabVIEW, SolidWorks, LaTex, Microsoft Office (PowerPoint, Word and Excel), Unix

Professional Experience

Lehigh University Department of Mechanical Engineering and Mechanics, Bethlehem, PA
Research Assistant Aug. 2009 – Dec. 2014

- Developed nonlinear, control-oriented, partial differential equation models of plasma current and electron temperature dynamics in nuclear fusion magnetic confinement tokamak devices via first-principle-driven, physics-based methods
- Tailored models to multiple operating scenarios in various tokamak devices and validated model prediction against experimentally achieved and simulated tokamak data
- Embedded model into nonlinear, constrained optimization algorithm to numerically design feedforward trajectories for actuators that steer plasma through tokamak operating space to reach specified targets

- Synthesized model-based, robust feedback algorithms for control of distributed current profile, distributed current profile + internal energy, and distributed current and electron temperature profiles in various tokamaks
- Demonstrated ability of feedforward and feedback control algorithms to robustly drive plasma to relevant targets and avoid stability limits through MATLAB/Simulink numerical simulations of plasma dynamics in multiple tokamaks, specifically: DIII-D (modern, medium-sized device in San Diego, CA), ITER (future large-scale device under construction in Cadarache, France), TCV (modern medium-sized device in Lausanne, Switzerland)
- DIII-D tokamak experimental evaluation of control performance:
  - Implemented general framework for real-time feedforward + feedback control (in C language) of plasma profiles in DIII-D tokamak's Plasma Control System
  - Interfaced feedback controller with available real-time measurements
  - Successfully demonstrated performance of optimized feedforward and feedback algorithms to investigate and clarify physics aspects important to robust tokamak operation

École Polytechnique Fédérale de Lausanne (EPFL)
Centre de Recherches en Physique des Plasmas (CRPP), Lausanne, Switzerland
Research Assistant — March – May 2012

- Developed general physics-based modeling approach to convert physics models that describe tokamak plasma current profile and internal energy dynamics into form suitable for control design for reactor relevant scenarios
- Validated plasma state evolution predicted by control-oriented model against simulated ITER tokamak data
- Assisted in instruction of basic control theory course for graduate students at CRPP

General Atomics — Fusion Energy Research Group, San Diego, CA
Research Assistant — May – Aug. 2010

- Developed MATLAB/Simulink simulation model (S-function in C language) of tokamak plasma current profile and internal energy dynamics that can interface with DIII-D tokamak's Plasma Control System to test implementation of real-time control code in closed-loop simulations prior to experimental testing

Bechtel Marine Propulsion Corporation — Bettis Atomic Power Laboratory, Pittsburgh, PA
Research Intern — May – Aug. 2009, Dec. 2008 – Jan. 2009, May – Aug. 2008

- Developed a LabVIEW application to map various kinds of temperature calculations onto a 3D model of a test piece as colors in real time to concisely provide operator with physical sense of events occurring in test section
- Updated data acquisition code to be compatible with designed application

Consol Energy Incorporated Research and Development Division, Pittsburgh, PA
Research Intern Dec. 2007 – Jan. 2008, May – Aug. 2007

- Composed process flow diagrams and wrote detailed descriptions of subsystems of Pressurized Fluidized Bed Combustion Technology-Pilot Test Facility (PFBC-PTF) (next generation coal power plant to burn waste coal)
- Designed a pressurization system to test flow of coal-paste fuel under plant operating conditions
- Collaborated with other engineers to update Piping and Instrumentation Diagrams (P&IDs), and ran water treatment and gas analyzer systems, of PFBC-PTF

Teaching Experience

Lehigh University, Bethlehem, PA

Introduction to Engineering Practice Instructor: Aug. – Dec. 2013

- Developed mini-wind-turbine design project to introduce first year students to mechanical engineering principles

Numerical Methods in Mechanical Engineering Teaching Assistant: Aug. – Dec. 2013

- Ran laboratory sessions designed to reinforce and clarify concepts of engineering applications of Excel, simple numerical methods, and basic MATLAB

Nuclear Fusion and Radiation Protection Teaching Assistant: Aug. – Dec. 2012

- Taught lectures on design of nuclear fusion tokamak devices, radioactivity, and various radioactive decay processes as well as graded exams and homework assignments

Graphics for Engineering Design Teaching Assistant: Aug. – Dec. 2011

Honors and Awards

- **Graduate education (2009–2014)**: Participant of *62nd Meeting of Nobel Laureates (dedicated to Physics)*, Student best paper award finalist (IEEE ACC 2012), Rossin Doctoral Fellow (2010), Lehigh University Fellowship (2009), Elizabeth Major Nevius Award (2009), President's Scholar (2009)
- **Undergraduate education (2005–2009)**: Dean's List (all semesters), Ferdinand P. Beer Award (2009), H.R. and Y.B. Wei Prize (2009), Charles F. Homewood Memorial Scholarship (2008), Class of 1904 Award (2008), Bill Hardy Award (2007), Pi Tau Sigma Award (2007), John R. Wagner Award (2007), Rossin Junior Fellows, Pi Tau Sigma Honorary Mechanical Engineering Fraternity, Tau Beta Pi Engineering Honor Society

Journal Publications

Justin E. Barton, William P. Wehner, Eugenio Schuster, Federico Felici and Olivier Sauter, "Current and electron temperature profile control in TCV via physics-model-based control synthesis," in preparation.

J. E. Barton, W. P. Wehner, E. Schuster, T. C. Luce, G. L. Jackson, J. R. Ferron, D. A. Humphreys, A. W. Hyatt, R. D. Johnson and B. G. Penaflor, "Current ramp-up optimization in DIII-D via physics-model-based safety factor profile control," in preparation.

Justin E. Barton, Mark D. Boyer, Wenyu Shi, William P. Wehner, Eugenio Schuster, John R. Ferron, Michael L. Walker, David A. Humphreys, Tim C. Luce, Francesca Turco, Ben G. Penaflor and Robert D. Johnson, "Physics-model-based nonlinear actuator trajectory optimization and safety factor profile feedback control for advanced scenario development in DIII-D," in preparation for submission to *Nuclear Fusion*.

Justin E. Barton, Karim Besseghir, Jo Lister and Eugenio Schuster, "Physics-based control-oriented modeling and robust feedback control of the plasma safety factor profile and stored energy dynamics in ITER," in preparation for submission to *Plasma Physics and Controlled Fusion*.

S. Coda for the TCV team (**J.E. Barton**), "The science program of the TCV tokamak: exploring fusion reactor and power plant concepts," in preparation for submission to *Nuclear Fusion*.

Mark D. Boyer, **Justin Barton**, Eugenio Schuster, Tim C. Luce, John R. Ferron, Michael L. Walker, David A. Humphreys, Ben G. Penaflor and Robert D. Johnson, "Backstepping control of the toroidal plasma current profile in the DIII-D tokamak," *IEEE Transactions on Control Systems Technologies*, vol. 22, no. 5, p. 1725-39, 2014.

Mark D. Boyer, **Justin Barton**, Eugenio Schuster, Tim C. Luce, John R. Ferron, Michael L. Walker, David A. Humphreys, Ben G. Penaflor and Robert D. Johnson, "First-principles-driven model-based current profile control for the DIII-D tokamak via LQI optimal control," *Plasma Physics and Controlled Fusion*, vol. 55, p. 105007, 2013.

D. Moreau, M.L. Walker, J.R. Ferron, F. Liu, E. Schuster, **J.E. Barton**, M.D. Boyer, K.H. Burrell, S.M. Flanagan, P. Gohil, R.J. Groebner, C.T. Holcomb, D.A. Humphreys, A.W. Hyatt, R.D. Johnson, R.J. La Haye, J. Lohr, T.C. Luce, J.M. Park, B.G. Penaflor, W. Shi, F. Turco, W. Wehner, and ITPA-IOS group members and experts, "Integrated magnetic and kinetic control of advanced tokamak plasmas on DIII-D based on data-driven models," *Nuclear Fusion*, vol. 53, p. 063020, 2013.

Justin E. Barton, Mark D. Boyer, Wenyu Shi, Eugenio Schuster, Tim C. Luce, John R. Ferron, Michael L. Walker, David A. Humphreys, Ben G. Penaflor and Robert D. Johnson,"Toroidal current profile control during low confinement mode plasma discharges in DIII-D via first-principles-driven model-based robust control synthesis," *Nuclear Fusion*, vol. 52, p. 123018, 2012.

Justin Barton, Yongsheng Ou, Chao Xu, Eugenio Schuster and Michael Walker, "Simserver simulation of a model-based current profile controller in the DIII-D plasma control system," *Fusion Engineering and Design*, vol. 86, no. 6-8, pp. 1116-1119, 2011.

Refereed Conference Publications

Justin E. Barton, William P. Wehner, Eugenio Schuster, Federico Felici and Olivier Sauter, "Simultaneous closed-loop control of the current and electron temperature profiles in the TCV tokamak," submitted to *2015 American Control Conference*, July 1-3, 2015.

William P. Wehner, **Justin Barton** and Eugenio Schuster, "Toroidal rotation profile control for the DIII-D tokamak," submitted to *2015 American Control Conference*, July 1-3, 2015.

Zeki Okan Ilhan, William Wehner, **Justin Barton**, Eugenio Schuster, David Gates, Stefan Gerhardt, and Jonathan Menard, "First-principles-driven model-based optimal control of the current profile in NSTX-U," submitted to *2015 American Control Conference*, July 1-3, 2015.

Justin E. Barton, Eugenio Schuster, Federico Felici and Olivier Sauter, "Closed-loop control of the safety factor profile in the TCV tokamak," in *53rd IEEE Conference on Decision and Control*, December 15-17, 2014.

Justin E. Barton, Wenyu Shi, Eugenio Schuster, Tim C. Luce, John R. Ferron, Michael L. Walker, David A. Humphreys, Francesca Turco, Robert D. Johnson and Ben G. Penaflor, "Nonlinear physics-model-based actuator trajectory optimization for advanced scenario planning in the DIII-D tokamak," in *19th IFAC World Congress*, pp. 671-676, August 24-29, 2014.

Justin E. Barton, Mark D. Boyer, Wenyu Shi, William P. Wehner, Eugenio Schuster, John R. Ferron, Michael L. Walker, David A. Humphreys, Tim C. Luce, Francesca Turco, Robert D. Johnson and Ben G. Penaflor, "Experimental and simulation testing of physics-model-based safety factor profile and internal energy feedback controllers in DIII-D advanced tokamak scenarios," in *19th IFAC World Congress*, pp. 5223-5228, August 24-29, 2014.

Mark D. Boyer, **Justin Barton**, Wenyu Shi, William Wehner, Eugenio Schuster, John Ferron, Michael Walker, David Humphreys, Francesca Turco, Tim Luce, Robert Johnson and Benjamin Penaflor, "Simultaneous boundary and distributed feedback control of the current profile in H-mode discharges on DIII-D ," in *19th IFAC World Congress*, pp. 1568-1573, August 24-29, 2014.

William Wehner, Wenyu Shi, **Justin Barton**, Eugenio Schuster, Michael L. Walker, John R. Ferron, Tim C. Luce, Francesca Turco, David A. Humphreys, Ben G. Penaflor and Robert D. Johnson, "First-principles-driven model-based control of the poloidal magnetic flux profile in the DIII-D tokamak," in *19th IFAC World Congress*, pp. 10319-10324, August 24-29, 2014.

Justin E. Barton, Karim Besseghir, Jo Lister and Eugenio Schuster, "Robust control of the safety factor profile and stored energy evolutions in high performance burning plasma scenarios in the ITER tokamak," in *52nd IEEE Conference on Decision and Control*, pp. 4194-4199, December 10-13, 2013.

Justin E. Barton, Wenyu Shi, Karim Besseghir, Jo Lister, Arnold Kritz, Eugenio Schuster, Michael L. Walker, David A. Humphreys, Tim C. Luce and John R. Ferron, "Physics-based control-oriented modeling of the safety factor profile dynamics in high performance tokamak plasmas," in *52nd IEEE Conference on Decision and Control*, pp. 4182-4187, December 10-13, 2013.

Wenyu Shi, **Justin E. Barton**, William Wehner, Mark D. Boyer, Eugenio Schuster, and Arnold Kritz, "First-principles-driven control of the rotational transform profile in high performance discharges in the DIII-D tokamak," in *52nd IEEE Conference on Decision and Control*, pp. 4170-4175, December 10-13, 2013.

Wenyu Shi, William Wehner, **Justin Barton**, Mark D. Boyer, Eugenio Schuster, Arnold Kritz, Didier Moreau, Tim C. Luce, John R. Ferron, Michael L. Walker, David A. Humphreys, Ben G. Penaflor and Robert D. Johnson, "PTRANSP simulation and experimental test of a robust current profile and β_N controller for off-axis current-drive scenarios in the DIII-D tokamak," in *2013 American Control Conference*, pp. 1225-1230, June 17-19, 2013.

Mark D. Boyer, **Justin Barton**, Eugenio Schuster, Michael L. Walker, Tim C. Luce, John R. Ferron, Ben G. Penaflor, Robert D. Johnson and David A. Humphreys, "Current profile tracking for the DIII-D tokamak via LQI optimal control," in *51st IEEE Conference on Decision and Control*, pp. 4341-4346, December 10-13, 2012.

Wenyu Shi, William Wehner, **Justin Barton**, Mark D. Boyer, Eugenio Schuster, Didier Moreau, Tim C. Luce, John R. Ferron, Michael L. Walker, David A. Humphreys, Ben G. Penaflor and Robert D. Johnson, "A two-time-scale model-based combined magnetic and kinetic control system for advanced tokamak scenarios on DIII-D," in *51st IEEE Conference on Decision and Control*, pp. 4347-52, December 10-13, 2012.

Justin E. Barton, Mark D. Boyer, Wenyu Shi, Eugenio Schuster, Tim C. Luce, John R. Ferron, Michael L. Walker, David A. Humphreys, Ben G. Penaflor and Robert D. Johnson, "First-principle model-based robust control of the current profile evolution in the DIII-D tokamak," in *2012 American Control Conference*, pp. 2134-2140, June 27-29, 2012, (Student best paper award finalist).

Mark D. Boyer, **Justin Barton**, Eugenio Schuster, Tim C. Luce, John R. Ferron, Michael L. Walker, David A. Humphreys, Ben G. Penaflor and Robert D. Johnson, "Backstepping control of the plasma current profile in the DIII-D tokamak," in *2012 American Control Conference*, pp. 2996-3001, June 27-29, 2012.

Wenyu Shi, William Wehner, **Justin Barton**, Mark D. Boyer, Eugenio Schuster, Didier Moreau, Tim C. Luce, John R. Ferron, Michael L. Walker, David A. Humphreys, Ben G. Penaflor and Robert D. Johnson, "Multivariable robust control of the plasma rotational transform profile for advanced tokamak scenarios in DIII-D," in *2012 American Control Conference*, pp. 5037-5042, June 27-29, 2012.

Wenyu Shi, **Justin Barton**, Majed Alsarheed and Eugenio Schuster, "Multivariable multi-model-based magnetic control system for the current ramp-up phase in the National Spherical Torus Experiment (NSTX)," in *50th IEEE Conference on Decision and Control and European Control Conference*, pp. 2632-2637, December 12-15, 2011.

Justin Barton, Yongsheng Ou, Chao Xu, Eugenio Schuster and Michael Walker, "Poloidal magnetic flux profile control in tokamaks via normalized coprime factorization robust control," in *2011 IEEE International Conference on Control Applications*, pp. 49-54, September 28-30, 2011.

Conference Publications (Refereed Synopsis)

J.E. Barton, M.D. Boyer, W. Shi, W.P. Wehner, E. Schuster, J.R. Ferron, M.L. Walker, D.A. Humphreys, T.C. Luce, B.G. Penaflor and R.D. Johnson,"Physics-model-based control of the plasma current profile dynamics for the development and sustainment of advanced scenarios in DIII-D," in *25th IAEA Fusion Energy Conference*, paper PPC/P2-32, October 13-18, 2014.

S. Coda for the TCV team (**J.E. Barton**), "The science program of the TCV tokamak: exploring fusion reactor and power plant concepts," in *25th IAEA Fusion Energy Conference*, paper OV/4-2, October 13-18, 2014.

J.E. Barton, M.D. Boyer, W. Shi, W.P. Wehner, E. Schuster, T.C. Luce, J.R. Ferron, M.L. Walker, D.A. Humphreys, B.G. Penaflor and R.D. Johnson,"First-principles model-based closed-loop control of the current profile dynamic evolution on DIII-D," in *24th IAEA Fusion Energy Conference*, paper EX/P2-09, October 8-13, 2012.

D. Moreau, M.L. Walker, J.R. Ferron, F. Liu, E. Schuster, J.F. Artaud, **J.E. Barton**, M.D. Boyer, K.H. Burrell, S.M. Flanagan, J. Garcia, P. Gohil, R.J. Groebner, C.T. Holcomb, D.A. Humphreys, A.W. Hyatt, R.D. Johnson, R.J. La Haye, J. Lohr, T.C. Luce, R. Nouailletas, J.M. Park, B.G. Penaflor, W. Shi, F. Turco, W. Wehner, and ITPA-IOS group members and experts, "Integrated magnetic and kinetic control of advanced tokamak scenarios based on data-driven models," in *24th IAEA Fusion Energy Conference*, paper ITR/P1-20, October 8-13, 2012.

Presentations

J. E. Barton, W. P. Wehner, E. Schuster, T. C. Luce, G. L. Jackson, J. R. Ferron, D. A. Humphreys and A. W. Hyatt, "Optimization of the current ramp-up phase in DIII-D via physics-model-based control of plasma safety factor profile dynamics," *56th Annual Meeting of the APS Division of Plasma Physics*, New Orleans, Louisiana, October 27-31, 2014.

Justin E. Barton, Mark D. Boyer, Wenyu Shi, William P. Wehner, Eugenio Schuster, John R. Ferron, Michael L. Walker, David A. Humphreys, Tim C. Luce, Francesca Turco, Wayne Solomon, Robert D. Johnson, Ben G. Penaflor, Karim Besseghir, Jo Lister, "Physics-model-based control of the plasma safety factor profile dynamics in tokamaks," *Princeton Plasma Physics Laboratory Seminar*, Princeton, New Jersey, June 10, 2014.

Justin E. Barton, Mark D. Boyer, Wenyu Shi, William P. Wehner, Eugenio Schuster, John R. Ferron, Michael L. Walker, David A. Humphreys, Tim C. Luce, Francesca Turco, Wayne Solomon, Robert D. Johnson and Ben G. Penaflor, "Physics-model-based safety factor profile and internal energy control in advanced tokamak scenarios," *18th Workshop on MHD Stability Control*, Santa Fe, New Mexico, November 18-20, 2013.

Justin E. Barton, Eugenio Schuster, Michael L. Walker, David A. Humphreys, "Physics-model-based actuator trajectory optimization and feedback control of the safety factor profile and internal energy dynamics in DIII-D," *55th Annual Meeting of the APS Division of Plasma Physics*, Denver, Colorado, November 11-15, 2013.

Justin E. Barton, Karim Besseghir, Jo Lister and Eugenio Schuster, "Towards first-principles control-oriented modeling of the magnetic and kinetic plasma profile evolutions in ITER," *54th Annual Meeting of the APS Division of Plasma Physics*, Providence, Rhode Island, October 29 - November 2, 2012.

Justin E. Barton, Mark D. Boyer, Wenyu Shi, Eugenio Schuster, Tim C. Luce, John R. Ferron, Michael L. Walker, David A. Humphreys, Ben G. Penaflor and Robert D. Johnson, "Toroidal current profile control in tokamaks via first principles-driven model-based control synthesis," *EPFL CRPP Seminar*, Lausanne, Switzerland, March 12, 2012.

Justin E. Barton, Mark D. Boyer, Wenyu Shi, Eugenio Schuster, Michael L. Walker and David A. Humphreys, "Robust control of the spatial current profile in the DIII-D tokamak," *53rd Annual Meeting of the APS Division of Plasma Physics*, Salt Lake City, Utah, November 14-18, 2011.

Justin Barton, Yongsheng Ou, Chao Xu, Eugenio Schuster and Michael Walker, "Poloidal magnetic flux profile control in tokamaks via normalized coprime factorization robust control," *National Control Engineering Students Workshop*, College Park, Maryland, April 28 - May 1, 2011.

Justin Barton, Eugenio Schuster, Michael Walker and David Humphreys, "Simserver simulation of model-based current profile controllers in the DIII-D plasma control system," *52nd Annual Meeting of the APS Division of Plasma Physics*, Chicago, Illinois, November 8-12, 2010.

Justin Barton, Yongsheng Ou, Chao Xu, Eugenio Schuster and Michael Walker, "Simserver simulation of a model-based current profile controller in the DIII-D plasma control system," *26th Symposium on Fusion Technology*, Porto, Portugal, September 27 - October 1, 2010.

Justin Barton, Yongsheng Ou, Chao Xu, Eugenio Schuster and Michael Walker, "Simserver simulation of a model-based current profile controller in the DIII-D plasma control system," *4th ITER International Summer School*, Austin, Texas, May 31 - June 4, 2010.